

Giovanni Seminara
Stefano Lanzoni
Nicoletta Tambroni

Theoretical Morphodynamics: River Meandering

STUDIES IN SCIENCES AND TECHNOLOGY

- 2 -

STUDIES IN SCIENCES AND TECHNOLOGY

Editor-in-Chief

Paolo Maria Mariano, University of Florence, Italy

Scientific Board

Michele Benzi, Scuola Normale of Pisa, Italy

Kaushik Bhattacharya, California Institute of Technology, United States

John Dainton, University of Liverpool, United Kingdom

Marc Geers, Eindhoven University of Technology, Netherlands

Krishna Kannan, Indian Institute of Technology Madras, India

Martin Kruzik, Institute of Information Theory and Automation Czech Academy of Sciences, Slovakia

Xanthippi Markenscoff, University of California, United States

Fabrizio Mollaioli, Sapienza University of Rome, Italy

Domenico Mucci, University of Parma, Italy

Maria Patrizia Pera, University of Florence, Italy

Anja Schlömerkemper, University of Würzburg, Germany

Reuven Segev, Ben-Gurion University of the Negev, Israel

Giovanni Seminara, University of Genoa, Italy

Marco Spadini, University of Florence, Italy

David John Steigmann, University of California Berkeley, United States

Paolo Vannucci, University of Versailles Saint-Quentin-en-Yvelines, France

Giovanni Seminara, Stefano Lanzoni, Nicoletta Tambroni

Theoretical Morphodynamics: River Meandering

FIRENZE UNIVERSITY PRESS
2023

Theoretical Morphodynamics: River Meandering / Giovanni Seminara, Stefano Lanzoni, Nicoletta Tambroni. – Firenze : Firenze University Press, 2023.
(Studi scientifici e tecnici ; 2)
<https://books.fupress.com/isbn/9791221503036>

ISBN 979-12-215-0302-9 (Print)
ISBN 979-12-215-0303-6 (PDF)
ISBN 979-12-215-0304-3 (XML)
DOI 10.36253/979-12-215-0303-6

Graphic design: Alberto Pizarro Fernández, Lettera Meccanica SRLs
Front cover image: © azmansinoby123rf.com

Volume published with the support of Università degli studi di Padova - Dipartimento di Ingegneria civile, edile ed ambientale – ICEA. (University of Padua - Department of Civil, Environmental and Architectural Engineering.)

Peer Review Policy

Peer-review is the cornerstone of the scientific evaluation of a book. All FUP's publications undergo a peer-review process by external experts under the responsibility of the Editorial Board and the Scientific Boards of each series (DOI 10.36253/fup_best_practice.3).


Referee List

In order to strengthen the network of researchers supporting FUP's evaluation process, and to recognise the valuable contribution of referees, a Referee List is published and constantly updated on FUP's website (DOI 10.36253/fup_referee_list).

Firenze University Press Editorial Board

M. Garzaniti (Editor-in-Chief), M.E. Alberti, F. Vittorio Arrigoni, E. Castellani, F. Ciampi, D. D'Andrea, A. Dolfi, R. Ferrise, A. Lambertini, R. Lanfredini, D. Lippi, G. Mari, A. Mariani, P.M. Mariano, S. Marinai, R. Minuti, P. Nanni, A. Orlandi, I. Palchetti, A. Perulli, G. Pratesi, S. Scaramuzzi, I. Stolzi.

FUP Best Practice in Scholarly Publishing (DOI 10.36253/fup_best_practice)

 The online digital edition is published in Open Access on www.fupress.com.

Content license: except where otherwise noted, the present work is released under Creative Commons Attribution 4.0 International license (CC BY 4.0: <http://creativecommons.org/licenses/by/4.0/legalcode>). This license allows you to share any part of the work by any means and format, modify it for any purpose, including commercial, as long as appropriate credit is given to the author, any changes made to the work are indicated and a URL link is provided to the license.

Metadata license: all the metadata are released under the Public Domain Dedication license (CC0 1.0 Universal: <https://creativecommons.org/publicdomain/zero/1.0/legalcode>).

© 2023 Author(s)

Published by Firenze University Press
Firenze University Press
Università degli Studi di Firenze
via Cittadella, 7, 50144 Firenze, Italy
www.fupress.com

*This book is printed on acid-free paper
Printed in Italy*

Contents

Foreword	5
<i>Giovanni Seminara, Stefano Lanzoni, Nicoletta Tambroni</i>	
1. Introduction	7
1.1 Early interest in meandering	7
1.2 Meandering as one of the possible fluvial patterns in sedimentary environments	8
1.3 The life cycle of alluvial meanders	10
1.4 Ubiquitousness of meandering patterns in nature	14
1.5 Plan of the Monograph	19
2. Hydrodynamics of sinuous channels	21
2.1 Dimensional formulation	21
2.1.1 Curved channels	21
2.1.2 Governing equations	22
2.1.3 Closure of the governing equations	24
2.1.4 Boundary conditions	25
2.2 Dimensionless formulation	26
2.2.1 Scaling	26
2.2.2 Formulation of the hydrodynamic problem in dimensionless form	29
2.3 Classification of meander bends	33
2.4 Flow in constant curvature wide channels	35
2.4.1 Formulation for the steady state	35
2.4.2 Fully developed steady flow in mildly curved channels: free vortex effect and the role of curvature	38
2.4.3 Fully developed steady flow in mildly curved channels: the role of bed topography	44
2.5 Steady flow in weakly meandering channels	51
2.6 Sharp bends	61
2.6.1 Enhancement and saturation of the centrifugally driven secondary flow	61
2.6.2 Outer bank secondary cells	66
2.6.3 Flow separation	70

CONTENTS

2.6.4	Modeling the hydrodynamics of sharp bends	71
2.7	Modeling the hydrodynamics of natural meanders: rational approximations or empirical modeling?	73
3.	Forced bars in sinuous channels	77
3.1	Formulation of the problem of morphodynamics of sinuous channels	77
3.1.1	The motion of the solid phase in sinuous channels: dimensional formulation	77
3.1.2	The motion of the solid phase in sinuous channels: dimensionless formulation	80
3.2	Forced (point) bars in single bends of cohesionless channels with constant curvature	82
3.2.1	Fully developed point bar in mildly curved bends: linear theory	82
3.2.2	Finite amplitude fully developed point bars in mildly constant curvature bends	86
3.3	Finite amplitude morphodynamics in meandering channels	94
3.3.1	Finite amplitude bars in slowly varying meandering channels with constant width	94
3.3.2	Extension to the case of meandering channels undergoing spatial variations of channel width	100
3.4	Further approaches to the morphodynamics of sinuous channels	101
3.4.1	Laboratory observations: bed topography in movable bed meandering channels with a Kinoshita planform	101
3.4.2	Field observations: three-dimensional flow structure and bed morphology in large elongated meander loops	102
3.4.3	Coupled hydro-morphodynamic simulations at the meander reach scale	103
3.4.4	Field observations through remote sensing	103
4.	The theory of river meanders	107
4.1	Introduction	107
4.2	Depth averaged model of meander morphodynamics	108
4.3	Resonance in meandering channels	112
4.3.1	Linear theory and the resonance mechanism	112
4.3.2	Weakly nonlinear theory of near resonant meanders	116
4.3.3	The nonlinear response far from resonance	120
4.4	Morphodynamic influence	121
4.4.1	What influence?	121
4.4.2	The exact solution of the linear problem of meander morphodynamics	123
4.4.3	Testing linear predictions in the sub-resonant case: downstream influence	128
4.4.4	Testing linear predictions in the super-resonant case: upstream influence	129
4.4.5	Morphodynamic regime in the field	132

4.5	Free bar suppression in meandering channels	134
4.5.1	Experimental and field observations	134
4.5.2	Theoretical interpretation of the suppression mechanism	135
5.	Planform evolution of meandering rivers	143
5.1	Bank erosion and migration rules	143
5.2	The integro-differential equation of planform evolution	146
5.3	Meander formation: an instability process	148
5.3.1	Modern field and laboratory observations	148
5.3.2	Bend instability: linear theory	154
5.4	Nonlinear evolution from incipient meandering to neck cutoff: the origin of fattening and skewing of meander bends	159
5.4.1	Formulation	159
5.4.2	A Landau-Stuart amplitude equation for the fundamental harmonic	161
5.4.3	Can meanders of permanent form exist?	161
5.4.4	General features of the planform development of river meanders in the sub-resonant and super-resonant cases	162
5.4.5	The nature of bend instability in the nonlinear regime	165
5.5	Beyond neck cutoff: Long-term evolution	166
5.5.1	Further effects generating the complexity of meander patterns	167
5.5.2	Numerical simulations	167
5.5.3	Results of numerical simulations: sub- versus super-resonant	170
5.5.4	Effects of floodplain heterogeneity	172
5.5.5	Long-term meander evolution in the light of the modern paradigms of complexity	175
5.6	Planform evolution and meander width	185
5.6.1	The equilibrium approach: Spatial variations of channel width in meandering channels at equilibrium	185
5.6.2	The dynamic approach: Coevolution of meander width and sinuosity	190
5.7	Mechanics of chute-cutoffs	196
6.	Additional features of fluvial meandering	201
6.1	Sorting effects on fluvial meanders	201
6.2	Meanders in mixed bedrock-alluvial channels	205
6.2.1	Morphodynamics of mixed bedrock-alluvial meandering channels	205
6.2.2	How do meanders incise bedrock?	208
7.	Concluding remarks	215
8.	Mathematical Appendix	219
8.1	Forced oscillations and resonance	219

CONTENTS

8.1.1	Toy model	219
8.1.2	Free oscillations: Temporal normal modes	219
8.1.3	Free oscillations: spatial modes	220
8.1.4	Forced oscillations: linear solution at the steady state and resonance	221
8.1.5	Forced oscillations: weakly nonlinear solution	221
8.2	Interaction between temporal free modes and forced modes	227
9.	Bibliography	233
10.	Notations	247

Foreword

Giovanni Seminara, Stefano Lanzoni, Nicoletta Tambroni

In the previous Monograph (Seminara *et al.*, 2023) we have laid down, in a coherent fashion, the foundations of the theory of morphodynamics of fluvial sedimentary patterns and discussed its applications to the morphodynamics of straight channels. The knowledge we have built up is the appropriate starting point to apply our analysis to the two main classes of river planforms, namely meandering and braiding, encountered in nature. The present Monograph restricts its attention to meandering rivers, leaving to a future Monograph the task to assess the available knowledge on braiding rivers. Hereafter, any Chapter, Section, Equation, or Figure of the previous Monograph will be distinguished from those of the present Monograph by adding the suffix (I), e.g. Section 1.2 of the previous Monograph will be referred to as Section 1.2(I). As the contents of this book are a follow up of the previous Monograph, we are equally indebted to the members of the 'enlarged Genoa group' as well as to the outstanding colleagues mentioned in Acknowledgments (I), for sharing with us ideas, friendship, and enthusiasm. We are also particularly grateful to the several scientists who granted us their permission to use figures contained in their dissertations or provided us with modified versions of figures contained in their published material. Let us list them.

- Jorge Abad kindly granted us his permission to use Figure 3.8 of his PhD Dissertation;
- Giovanni Cecconi kindly made Figure 13 available to us;
- Esther Eke kindly granted her permission to use Figures 3.11 and 3.13 of her PhD Dissertation;
- Theodore Fuller kindly granted his permission to use Figure 2.9 of his PhD Dissertation;
- Kory Konsoer kindly granted us his permission to use Figures 3.1, 3.5 and 5.5 of his PhD Dissertation;
- Rossella Luchi kindly granted her permission to use Figures 4.2, 4.6, 4.7, and 6.23 of her PhD Dissertation. Rossella also made Figures 116 and 117 available to us;
- Jagriti Mishra kindly granted her permission to use Figures 2.1 and 2.10 of her PhD Dissertation;
- Federico Monegaglia kindly granted his permission to use Figures 6.8 and 6.27 of his PhD Dissertation and made Figure 120 available to us;
- Yarko Nino kindly granted his permission to use Figures 6.23 and 6.24 of his MSc Dissertation;
- Elli Papangelakis kindly made available to us Figure 132;
- Jonathan Schwenk kindly granted his permission to use Figure 4.13 of his PhD Dissertation;
- Luca Solari kindly provided Figure 81;

Thanks are also due to two anonymous Referees. Their reviews of our original manuscript suggested splitting the book into two distinct monographs (the present monograph and the previous one). Implementing this suggestion has largely improved readability and clarity of the contents of the monographs.

Finally, our families have supported our efforts and fully deserve that this book be dedicated to them.

1. Introduction

1.1. Early interest in meandering

The word *meander* is the English version of the Latin word *maeander* (*Μαίανδρος* in ancient Greek), the name of a sinuous river flowing in the southwestern region of the modern Turkey (Figure 1).

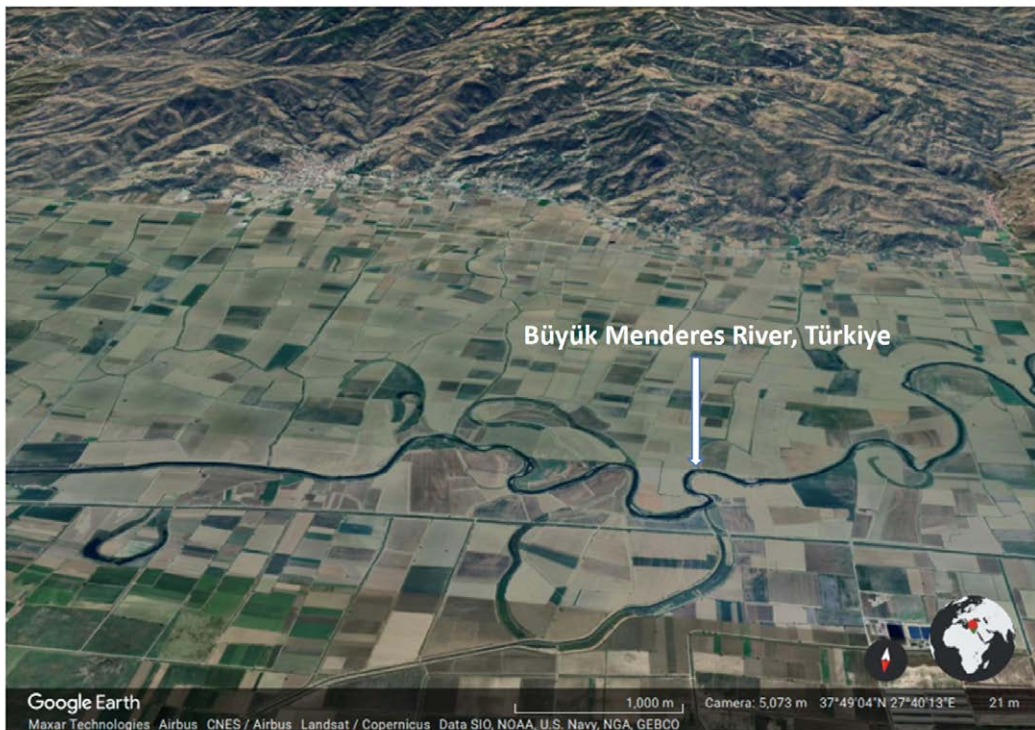


Figura 1. Satellite image of the *Büyük Menderes* river, which flows in the southwestern region of the modern Turkey. Its sinuous course and its original name (*maeander* in latin) are the origin of the meaning of the modern word *meander*. Source: Google Earth: lat. 37° 49' 04" N; lon., 27° 40' 13" E.

In modern times, this river is called *Büyük Menderes*, it flows west through the *Büyük Menderes* graben and debouches into the Aegean Sea, south of Izmir and not far from the ancient Ionian

city of Miletus. Since the time of Classical Greece the word meander has then been employed to describe sinuous rivers and winding patterns.

Various features of meandering rivers, notably their ubiquitousness and their striking regularity, have long attracted the attention of historians (Xenophon, circa 370 B.C.; Titus Livius, 9 B.C.), geographers (Strabo, around 10 A.D.), poets (Ovidio, 8 A.D.) and painters. Among the latter a prominent role was played by Leonardo, who paid particular attention to the course of the Arno River, both for scientific interest and for engineering purposes. Leonardo's observations of meandering patterns are reported in the form of sketches in many of his codices (e.g. Figure 2). We have not found in Leonardo's sketches any sign suggesting that he had already captured

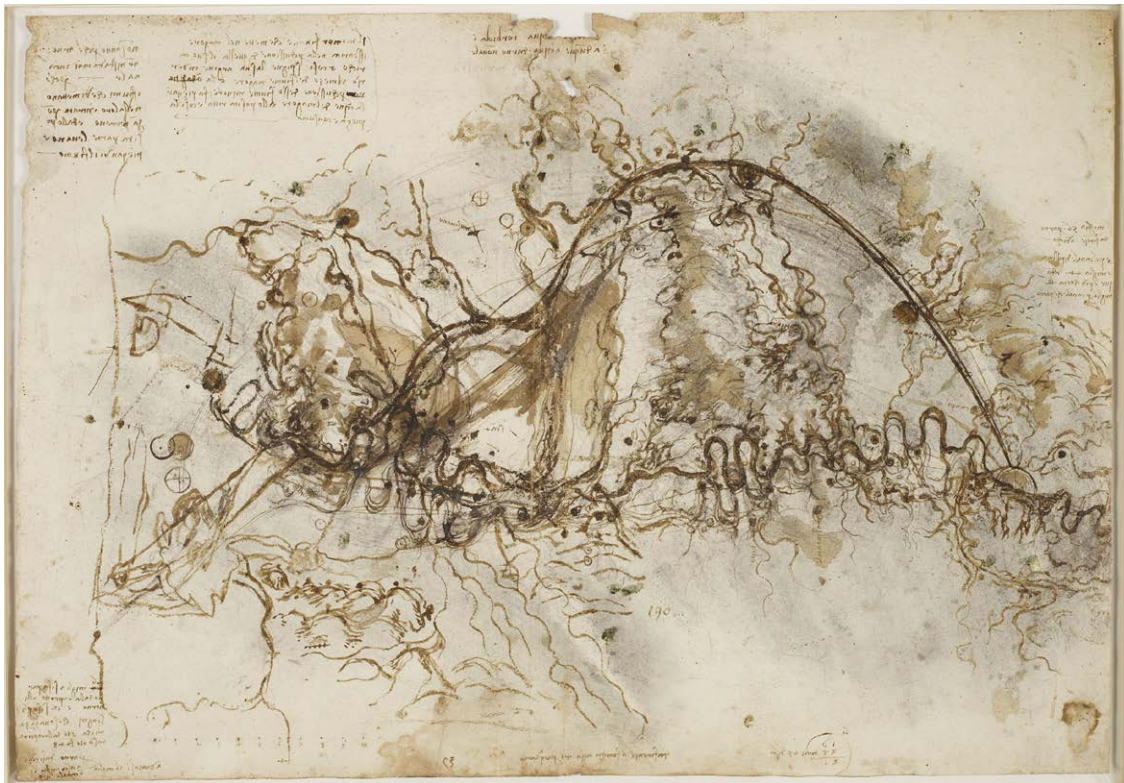


Figura 2. Map conserved at the Royal Collection of Windsor (RL 12279): this is one of Leonardo's sketches showing the planform of the Arno River downstream of Florence (Credit: Royal Collection Trust / © His Majesty King Charles III 2023).

characteristic morphological features of river meanders (e.g. upstream skewing of meander loops) that will be detected in modern observations. However, this aspect would deserve to be further explored.

1.2. Meandering as one of the possible fluvial patterns in sedimentary environments

In our previous Monograph (Seminara *et al.*, 2023), we have pointed out the ubiquitous nature of the *bar* unit as the fundamental building block of fluvial sedimentary patterns. This led us to investigate in depth the origin and development of bars in straight channels. The most striking feature of the bar unit is that it gives rise to the winding of the thread of high velocity: hence, the tendency of the stream to follow a meandering path is an ubiquitous feature of fluvial patterns in straight, meandering and braiding rivers.

In particular, the presence of a single row of bars is a major ingredient of meandering rivers. However, this feature does not tell the whole story about the nature of river meandering. In other

words, *meandering is not simply associated with a winding thalweg*. What distinguishes meandering from straight channels is the fact that in a meandering river *the channel axis follows a winding path*, hence meanders form and evolve in response to *planform forcing*.

Channel curvature adds additional features to the hydrodynamics and morphodynamics of straight channels. In particular, an additional, curvature driven, component of secondary flow arises and contributes to the accumulation of sediments in the inner part of the bend and to bottom scour at the outer portion of the bend. The sequence of riffles and pools thus formed looks very similar to the single row of bars which forms in straight channels with non-erodible banks (Figure 3). However, a major difference exists between *alternate bars* and the so called *point bars* observed in meandering rivers: typically alternate bars migrate slowly downstream, whereas point bars are quasi-steady features which keep *attached* to the bends.



Figure 3. Sequence of point bars displayed by the meandering White River (Indiana, USA). (Credit: Google Earth: lat 39° 20' 44" N; lon. 86° 38' 06" W).

The fact that alternate bars are intrinsically distinct from point bars is demonstrated by a major observation originally made by Kinoshita and Miwa (1974): the two patterns may coexist in weakly meandering channels where alternate bars migrating through the meandering channel have been observed both in the field and in the laboratory (e.g. Figure 4).

The above observations suggest that the knowledge we have established on the issue of why and when alternate bars form in straight alluvial channels does not answer the question of why and when meanders form. We will see that the two issues are somehow related to one another but they are distinct. The theory we will discuss in Chapters 4 and 5 provides answers to both questions and clarifies the conceptual distinction between the formation of alternate bars and meanders.

Just like bars, meandering also arises from an instability process. However, in the meander case, it is the occurrence of *perturbations of the channel planform* to trigger instability. The response of flow and bed topography to spatially periodic perturbations of the channel alignment essentially

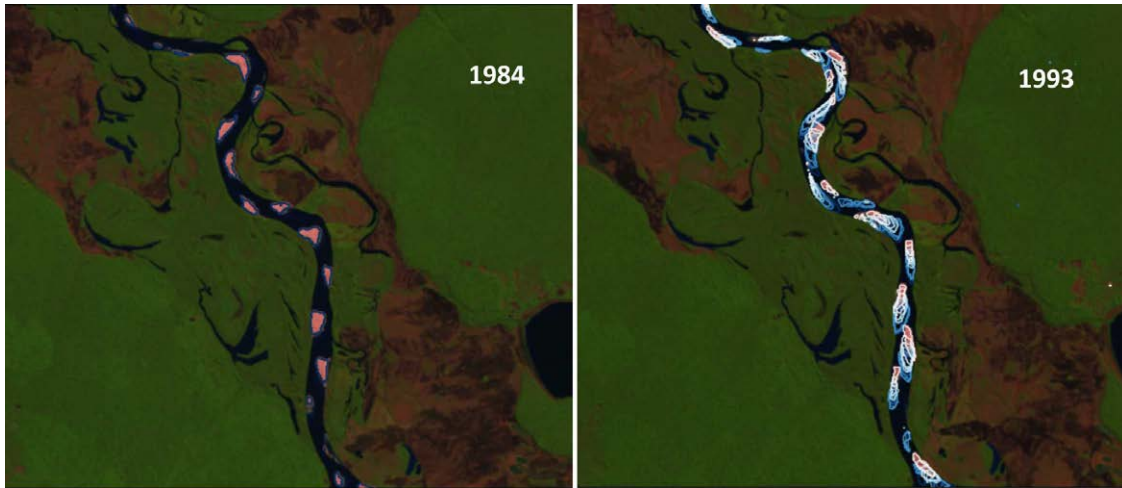


Figura 4. Satellite observations of the downstream shift of alternate bars migrating through the Rio Xingu (Brazil). Contours show the annual position of bare sediment (reproduced from Figure 6.27 of Monegaglia, 2017).

consists of the development of a sequence of *point bars*. Depending on the wavelength of planform perturbations the response of the flow may, in turn, promote further erosion of the outer bends and accretion at the inner bends, leading to meander growth and meander migration. This overall process is intermittent but, on large time scales, it may be viewed as a continuous process which leads from incipient meander formation (meander birth) to the disappearance of the meander loop (meander death) and the re-initiation of the whole cycle.

Again, planform instability is the crucial mechanism but it does not tell the whole story of meander formation. A second major ingredient is needed in order for the channel to maintain its coherence, i.e. its ability to grossly conserve its width throughout the planform evolution process. This ingredient is the *presence of some apparent or real cohesion of the banks*, brought up by the presence of vegetation or by a bank composition comprising a significant mud-clay content. In the absence of any of the latter features, i.e. with purely cohesionless banks, laboratory observations show that an initial straight channel invariably evolves into a braiding pattern.

But let us go back to meander evolution. Although meanders are obviously not living organisms, however the picture they offer in the field suggests that they typically undergo a life cycle.

1.3. The life cycle of alluvial meanders

What triggers meandering initiation in alluvial rivers is the occurrence of some initial perturbation of the planform configuration. Often such perturbation arises as a consequence of the *death* of a previous meander (Figure 5). Meanders then grow and migrate downstream. Field observations (e.g. Nanson and Hickin (1983)) show that, typically, as meanders develop, the downstream migration speed of meander trains decreases monotonically down to very small values at the late development stage. While migrating, bends amplify and the rate of bend amplification grows up to a peak and then slowly decays. As a result, meanders lengthen continuously so that the *channel sinuosity*, defined as the ratio between meander intrinsic wavelength and meander cartesian wavelength, also increases. Values of channel sinuosity of mature meanders of alluvial rivers fall typically in the range 2-3.

Meanders develop mature shapes (e.g. Figure 6) that display a variety of interesting features. They may form either *single* or *multiple* loops, as well as *compound* bends.

A first successful mathematical representation of the shape of single loops was suggested by Langbein and Leopold (1966) based on an analysis of the planform shape of the Mississippi at Greenville. These Authors called such a representation a *sine generated shape*. Essentially, they noted that it is the *curvature* rather than the lateral coordinate of the channel axis to exhibit



Figure 5. Typical examples of meandering pattern: the Alatna River (Alaska) showing juvenile meanders arising after the abandonment of mature loops (Google maps, lat. $67^{\circ} 21' 18.4''$ N; lon. $153^{\circ} 40' 04.2''$ W).

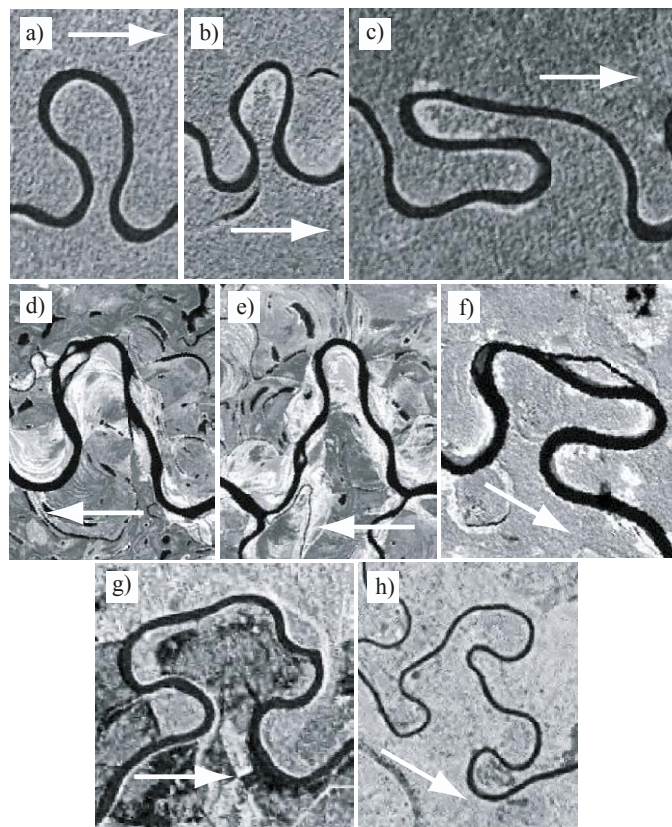


Figure 6. Typical examples of bend shapes observed in meandering rivers. (a) Upstream- and (b) downstream-skewed bends, (c-f) compound bends, and (g,h) multiple loops. The river locations are: northern Papua New Guinea (a-c), Alaska (Porcupine River) (d,e), Peru (Rio Madre de Dios) (f), western Canada (g), and Peru (h). The images have been obtained from the Landsat mosaic image Web sites: <https://zulu.ssc.nasa.gov/mrsid/> (a,b,c,g, and h) and <http://glcfapp.umiacs.umd.edu/> (Figures d-f). The arrows indicate flow direction (reproduced from Frascati and Lanzoni, 2009).

a sinusoidal dependence on the longitudinal intrinsic coordinate. More precisely, Langbein and Leopold (1966) suggest that single meander loops are generated by a sine curve defined by the following equation:

$$\vartheta = \vartheta_1 \sin \lambda(s - s_0). \quad (1)$$

Here ϑ is the angle that the tangent to the channel axis forms with the axis of the valley, s is the

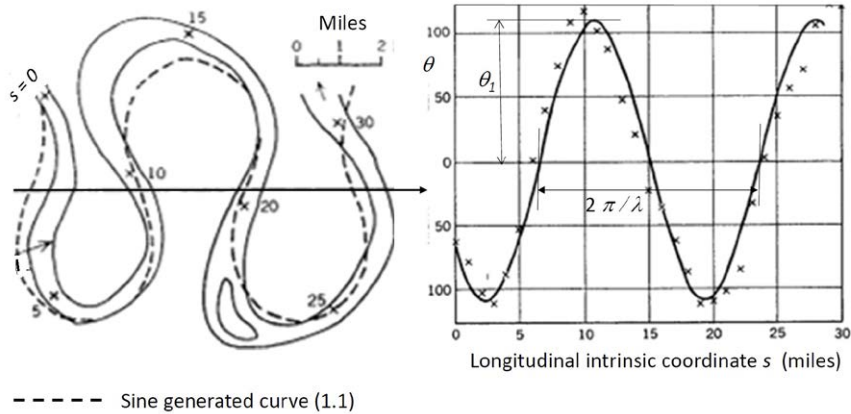


Figure 7. Langbein and Leopold's fitting of the sine generated curve on the shape of a meander of the Mississippi River at Greenville (modified from Langbein and Leopold, 1966).

intrinsic longitudinal coordinate and $\lambda (\equiv 2\pi/L_s)$ is the *intrinsic meander wavenumber*, with L_s *intrinsic meander wavelength*. Moreover, ϑ_1 is an amplitude parameter which controls the amount of horseshoe looping. Recalling that the curvature of the channel axis $\mathcal{C}(s)$ is defined as $-\partial\vartheta/\partial s$, it follows that channel curvature also obeys the sine generated shape suggested by Langbein and Leopold (1966). There are, of course, plenty of irregular meanders in nature (see Figure 6d-h) but those that are fairly regular do conform reasonably to the sine generated shape, as shown by Figure 7.

The above fit is overall fairly satisfactory but fails to reproduce two important features that meanders develop as they evolve, namely fattening and skewing of their shape. This was noted long before Langbein and Leopold (1966)'s paper by Kinoshita (1961) who suggested a slightly modified form of the sine generated curve which is now known as *Kinoshita curve*. It reads:

$$\vartheta = \vartheta_1 \sin(\lambda s) + \vartheta_{3r} \cos(3\lambda s) + \vartheta_{3i} \sin(3\lambda s). \quad (2)$$

Here, corrections of the sine generated shape include terms proportional to the third harmonics of the fundamental spatial oscillation. Fattening and skewing of the meander loop do arise from these third harmonics. Fattening is associated with negative values of ϑ_{3r} (Figure 8 c,d) and upstream (downstream) skewing with positive (negative) values of ϑ_{3i} (Figure 8 e-h).

It is sometimes stated that one can infer from an aerial photo what is the flow direction of a meandering river, simply assuming that meanders are upstream skewed. While this statement certainly applies to the regular meander train depicted in figure 7, Figures 6 and 9 show that river patterns may develop multiple loops, comprising single loops that may display both downstream and upstream skewing. Figure 9 also shows that the final stage of meander development, which closes the meander cycle, is *meander death*. Death typically occurs as the meander loop is abandoned in favor of a hydraulically more efficient fluvial path through a process called *neck cutoff*. The abandoned loop forms a so called *oxbow lake*, i.e. a pond separated from the river, which is eventually buried into the valley plain.

An alternative way meander loops may choose to *die* is through the mechanism of the so called *chute cutoff*. In this case the meander loop is bypassed by a new channel that cuts through the

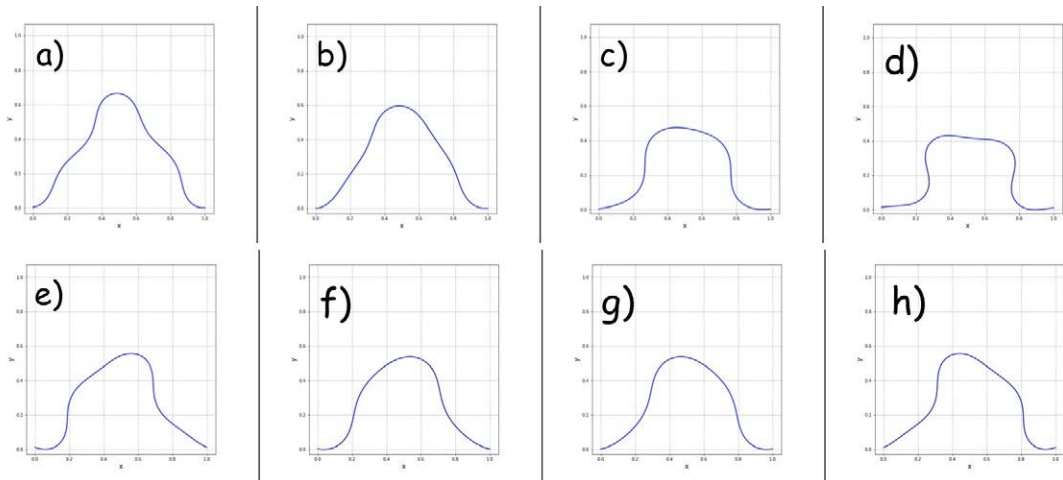


Figure 8. Typical shapes of meander bends generated through the Kinoshita curve (2). The curves have been computed setting $\vartheta_1 = 4/\pi$ and using the following couples of values for the skewing and fattening coefficients, $\vartheta_{3r}, \vartheta_{3i}$: (a) 0.13,0.5; (b) 0.13,0.25; (c) 0.13,-0.25; (d) 0.13,-0.5; (e) -0.4,0; (f) -0.2,0; (g) 0.2,0; (h) 0.4,0.

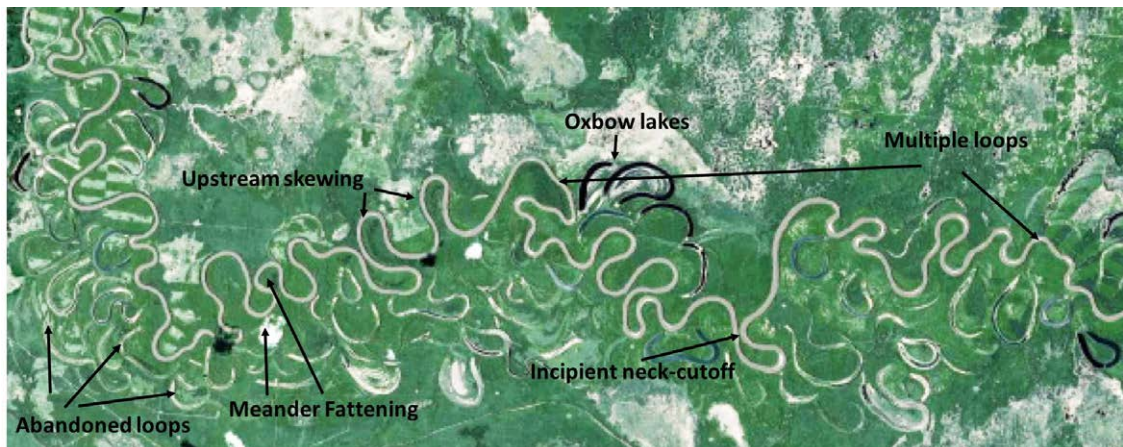


Figure 9. Typical example of meandering patterns: Chinchaga River, Alberta (Canada) showing several features of mature meandering, namely skewing, fattening, multiple loops, oxbow lakes, incipient neck cutoff and abandoned loops. (Credit: Google Earth. lat., $58^{\circ} 46' 29.24''$ N; lon., $118^{\circ} 23' 35.04''$ O)

portion of the floodplain enclosed by the loop (Figure 10). For this process to occur, unlike in the case of neck cutoff, the floodplain adjacent to the channel must be inundated. The chute incision leads to channel shortening, enhanced downstream sediment delivery, and a consequent rearrangement of the meandering pattern. The original meander loop is usually filled with sediments and disappears but it may also *survive*.

The picture depicted above applies whenever the alluvial river is able to develop without any geological constraint. A striking example of the effects of a geological constraint is the presence of confining valley walls that reduce the lateral degree of freedom of meander evolution. Preventing free meander amplification, lateral constraints lead to a sort of highly skewed *equilibrium meander train* like the one observed in the Beaver river (Canada) (Figure 11).

Note that, in the absence of geological constraint, no equilibrium meandering pattern has ever been detected and theoretical arguments do support the latter observations.

Each stage of meander development outlined above has distinct characteristics and poses

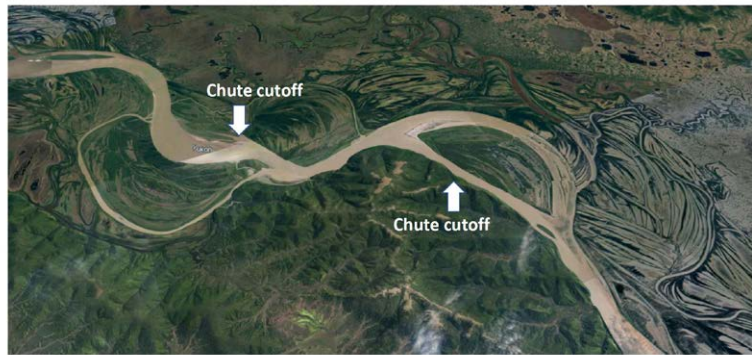


Figura 10. Formation of chute cutoffs in a meandering river. Yukon River, Alaska. (Google Earth, lat. $61^{\circ} 59' 50.9''$ N; lon. $160^{\circ} 01' 37.5''$ W).



Figura 11. The equilibrium meander train formed in the Beaver river (Canada) whose planform evolution is constrained by the valley walls. (Credit: Google Earth. lat. $54^{\circ} 22' 49.6''$ N; lon. $110^{\circ} 15' 36.9''$ W).

challenging problems of physical and mathematical interpretation that will be dealt with in the various chapters of the present Monograph. However, before we outline our program, let us make a short digression to emphasize how general is the occurrence of meander patterns in terrestrial and even in planetary environments.

1.4. Ubiquitousness of meandering patterns in nature

In the previous section we have invariably referred to alluvial rivers, which is undoubtedly the environment which our collective imagination associates most frequently to meandering patterns. However, meandering is an ubiquitous feature in many other environments. Let us have a brief glance at some interesting examples.

Incised meanders in bedrock

As discussed in Chapter 7 of Seminara *et al.* (2023), river channels grossly fall into two main categories, namely alluvial and bedrock channels. In spite of the absence of an alluvial bed and of



Figura 12. The spectacular sequence of meanders of the San Juan River in southeast Utah. This river incised straight down for several hundred feet while maintaining a highly sinuous and regular pattern. Elevation increases from dark to light. (Google Maps, lat. $37^{\circ} 09' 39.2''$ N; lon. $109^{\circ} 55' 31.6''$ W).

the bedform patterns associated with it, bedrock channels display some of the most spectacular meandering patterns observed in nature (Figure 12).

The available knowledge on bedrock meanders, including the known attempts to understand their origin, will be discussed in Section 6.2.1. It suffices here to note that meanders in rock are purely erosional features, hence the essential process governing river incision is the mechanism of bedrock erosion. As discussed in Chapter 7 of Seminara *et al.* (2023), a variety of erosion mechanisms have been explored in recent years and the subject has progressed significantly. This notwithstanding, attempts at modeling the actual process whereby the spectacular meandering patterns depicted in Figure 12 develop from an initially flat floodplain, are still in their infancy.

Tidal meanders

Transitional environments (estuaries and lagoons) host equally fascinating meandering patterns (Figure 13). The characteristics of tidal meanders are similar to those of fluvial meanders, with tidal bars and bank cohesion playing a similar role. However, tidal meanders also exhibit features distinct from those of alluvial rivers. This is not surprising as tidal flow, unlike fluvial flow, is oscillatory and, in tide dominated environments, its direction changes every half a cycle. Moreover, the longitudinal characteristics of tidal channels vary on a spatial scale which is much smaller than in the fluvial case.

In spite of an apparently striking dissimilarity of the governing processes, planform dimensions of tidal and fluvial meanders consistently scale with local channel width. Moreover, once normalized by channel width, observed migration rates of tidal and fluvial meanders are remarkably similar. Indeed, also tidal meanders may be obliterated by neck cutoffs (Figure 14). Essentially, meandering tidal channels recapitulate many fluvial counterparts owing to large gradients of tidal prisms across meander wavelengths (Finotello *et al.*, 2018).



Figura 13. A fascinating image of a network of meandering channels in Venice lagoon. Courtesy of G. Cecconi.

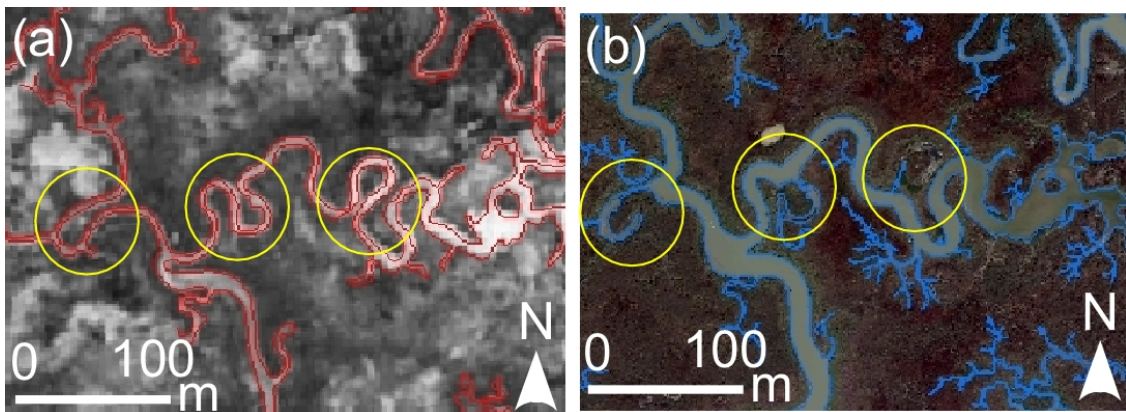


Figura 14. Neck cutoffs of two meander loops in the Pagliaga salt marsh of Venice lagoon are clearly detected comparing a picture taken in (a) 1954 with the corresponding picture taken in (b) 2010.

However, statistical analysis of meandering patterns extracted from satellite images indicate that tidal and fluvial meanders disclose fingerprints of the different physical processes they are shaped by (Marani *et al.*, 2002; Finotello *et al.*, 2020). Specifically, the Kinoshita shape does not fit

tidal meanders due to the presence of even harmonics and skewness of meander loops is not clearly detectable. Overall tidal meanders are less morphologically complex and display more spatially homogeneous characteristics as compared to fluvial meanders. This finding can be explained by the quite regular action exerted by repeated tides in carving tidal meanders, as well as by the higher lithological homogeneity of the substrates they typically cut through.

The above findings are based on the analysis of planform geometries and, at the moment, lack a well established theoretical explanation. Tidal Morphodynamics is thus an important chapter of Theoretical Morphodynamics that will deserve a specific Monograph of the present Series.

Meanders of turbidity currents

As discussed in the Introductory Monograph (Blondeaux *et al.*, 2018), turbidity currents are sediment-laden flows that transport large amounts of sediments from the coastal region into and across the continental shelf, where they incise the submarine hillslopes and form giant submarine fans at the foot of the shelf. The fans are cut by extensive submarine channels where billions of tonnes of sediment may be transported. Typically, submarine channels are highly sinuous (Figure

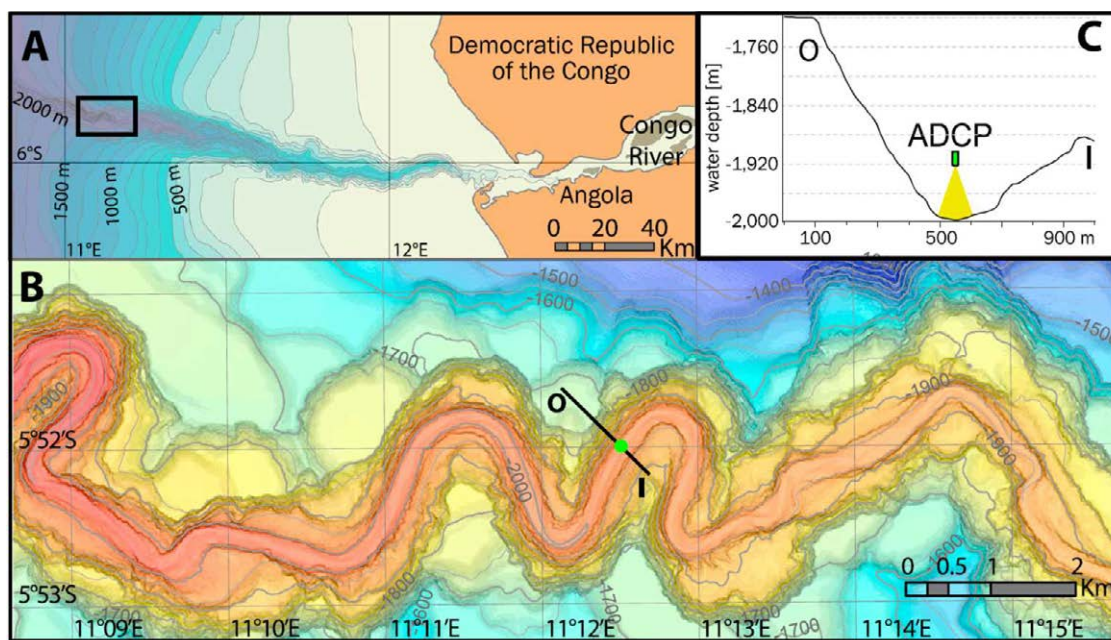


Figura 15. The giant turbidity current cutting the submarine fan of the Congo River (Congo Democratic Republic) displays a meandering planform (reproduced from Azpiroz-Zabala *et al.*, 2017, open access under the terms of the Creative Commons CC BY license).

15) and channel curvature drives significant secondary currents. The structure of these secondary flows is affected by an effect that is not present in the fluvial case, namely a lateral pressure gradient due to cross-flow variations in flow stratification. The complexity of the flow-sediment field leaves several unsettled issues, still subject to intense debate (Azpiroz-Zabala *et al.*, 2017).

The formation of meandering turbidity currents is also affected by their ability to build up self-formed levees through flow-sediment exchange with the surrounding submarine fan. Self confinement prevents spreading and contributes to determine the ability of turbidity currents to persist over enormous longitudinal distances. Erosion of the outer bank and deposition at the inner bank are also observed and may lead to significant lateral channel migration.

Supraglacial Meanders

The ablation zone of glaciers and ice sheets exhibits the presence of networks of channels cut by surface meltwater during the summer season. The resulting supraglacial streams typically follow meandering paths. Supraglacial meandering is due to a mechanism of lateral melting and consequent lateral channel migration, driven by channel curvature which enhances heat transfer to the surrounding ice at outer bends. Supraglacial meanders have characteristics similar to those of alluvial meanders (Parker, 1975). Their wavelengths scale with channel width, with a rough estimate for meander wavelength as equal to eight times channel width. They also experience



Figura 16. Supraglacial meanders on the Mendenhall Glacier, Alaska (credit: Mendenhall glacier streams-Bing images).

downstream migration (Karlstrom *et al.*, 2013) and neck cutoffs (Knighton, 1981).

Planetary Meanders

The occurrence of sedimentary patterns, and in particular of fluvial meanders, has also been discovered in other planets of the solar system. This is a topic of major interest as it may contribute to clarifying the distribution in space and time of liquid water in other planets. The discovery of landform complexes whose characteristics (planform and altimetry, structure, and erosional features) are suggestive of materials deposited within an aqueous sedimentary environment, have been reported in the recent literature. Figure 17 shows a sequence of tight meander bends at the Edge of the Aeolis Planum region of the Mars planet. Matsubara *et al.* (2014) note the presence of *apparent cutoffs and parallel lineations that resemble scroll bar deposits in terrestrial meandering*. The formation of multiple loops is also notable. Matsubara *et al.* (2014) point out that the above observations substantiate the idea that meandering channels can develop in the absence of vegetation. From an analysis of terrestrial rivers that show little vegetation cover, they conclude that bank cohesion, required to promote meandering, may be provided by an unusually high content of mud (silt/clay) (41% in the meandering Quinn River, Nevada, USA) whose flocculation and deposition may be induced by the presence of dissolved salts in river waters. On the contrary, the role of permafrost in promoting cohesion did not emerge from observations of the sinuous Usuktuk River near Barrow, Alaska, which exhibited no exposed permafrost on its stream banks.

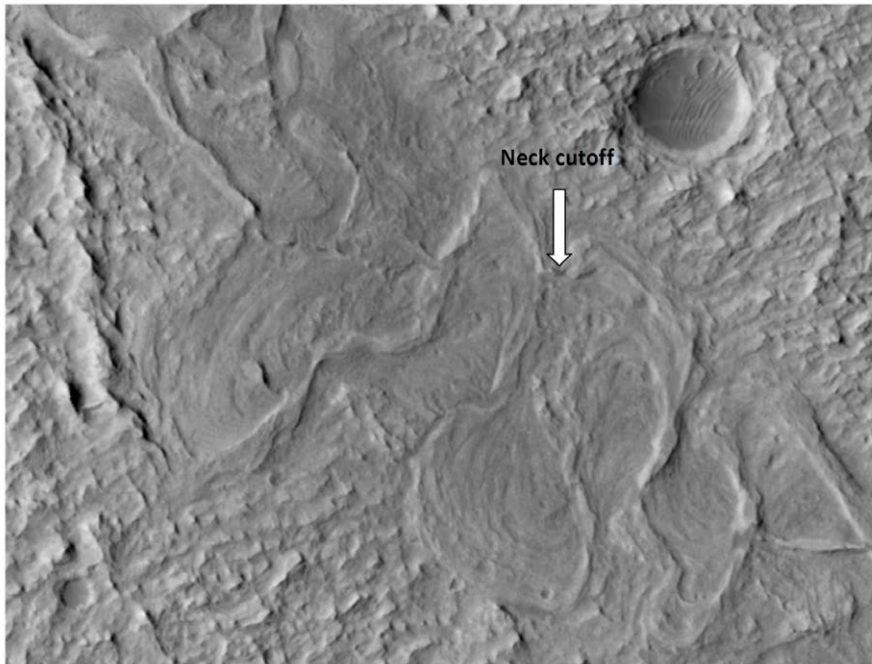


Figura 17. Fossil highly sinuous inverted meandering channel and floodplain at the Edge of Aeolis Planum of the Mars planet. Relief inversion is the effect of wind erosion, whereby finer sediments are removed from the floodplain and the channel bed turns into a ridge. Note the remnants of previous meander loops and the neck cutoff possibly occurred shortly before flow ceased (Howard, 2009) (Credit: NASA/JPL-Caltech/UArizona, HIRISE image PSP_006683_1740).

The Authors conclude that the former mechanism was likely responsible for the formation of Aeolis Dorsa Martian meanders.

Many issues arise when one attempts to understand what geophysical conditions were in place when sedimentary patterns so strikingly similar to terrestrial ones formed. This makes the subject of Planetary Morphodynamics extremely fascinating and, not surprisingly, such to attract the interest of some of the best scientists in the morphological community.

1.5. Plan of the Monograph

The present Monograph is intended for a reader at the postgraduate level who has been exposed to the content of the previous Monograph (Seminara *et al.*, 2023). There, we have assessed the available knowledge on the hydrodynamics and morphodynamics of straight channels, exploring the notion of equilibrium channels and their response to large scale perturbations of the bed topography leading to the development of free and forced bars.

In the present Monograph, we move to analyze the response of channels to perturbations of the planform shape. This is a complex issue that requires various preliminary steps. The first step is to analyze the flow perturbations induced by the curvature of the channel axis in channels with assigned bed topography. This analysis is presented in Chapter 2 and can be pursued analytically in mildly curved bends, which are frequently encountered in nature. The main outcome of this analysis is the prediction of the 3D structure of the two components of secondary flow. The curvature driven component arises from the need to compensate for the in-balance between vertically increasing centrifugal force and constant lateral pressure gradient acting on fluid particles; the topographically driven component arises from pure continuity requirements. The case of sharp bends is not amenable to simple analytical treatment and displays a number of novel features, most notably the possibility of flow separation at the inner bends and the formation

of secondary cells at the outer bends.

The second step is to understand the morphodynamic consequences of the occurrence of secondary flows, namely the formation of forced bars, consisting in the accumulation of sediments at the inner bends, coupled with the bed scour experienced by the outer bends. This analysis, pursued in Chapter 3, is again analytically feasible in the case of mildly curved bends, whilst numerical analysis, laboratory and field observations are the appropriate tools for the case of sharp bends.

At this stage, the reader has acquired some understanding of flow and bed topography in curved channels. This is the appropriate starting point to proceed to the planform stability analysis discussed in Chapter 4. Essentially, one looks at flow-topography response of the initially equilibrium channel to harmonic perturbations of the channel alignment and seeks conditions such that bank erosion reinforces the planform perturbation. This will require to establish some erosion rule coupling bank erosion to perturbations of the flow field relative to the basic equilibrium state. A number of interesting features arise. In particular, planform perturbations may resonate with the natural *bar* response of the channel. Moreover, the presence of a meandering channel reach may be morphodynamically felt either downstream or upstream, through forced bar oscillations. Finally, the theory allows for the analysis of the interaction between free and forced bars and shows that alternate bars are unable to migrate through meandering channels when their curvature exceeds some threshold value.

The reasonable success achieved with the help of the general formulation proposed above has encouraged various Authors to extend it to the prediction of the planform evolution of meandering rivers. This is discussed in Chapter 5. We first derive an integro-differential equation of planform evolution in intrinsic coordinates, that requires to be coupled with some *erosion rule* relating the intensity and location of bank erosion to the perturbation of the flow field. The solution of this equation in the linear regime confirms the nature of meander formation as an instability process. A complete analytical solution is then obtained to describe the nonlinear evolution of the meandering channel from incipient meandering to neck cutoff, displaying the fattened and skewed shape of mature meander bends associated with Kinoshita shape and even compound loops of the kind displayed in Figure 9. The only feature that does not naturally emerge from those numerical simulations is the occurrence of chute cutoffs: they are then discussed separately at the end of the chapter. Theory also shows that meanders of permanent form do not exist. To proceed beyond neck cutoff and investigate the long-term evolution of meandering, numerical simulations are needed. They show that in the long term the reach averaged channel sinuosity tends asymptotically to a dynamical stationary state characterized by fluctuations around a constant value, essentially controlled by the occurrence of neck cutoffs. The existence of seemingly universal features of meander behavior has stimulated several attempts to apply modern paradigms of complexity to meander evolution, that are critically reviewed. This completes the theory of fluvial meandering in the alluvial case and for uniform sediments.

The latter two constraints are relaxed in Chapter 6.

We know from Chapter 7(I) that the heterogeneous character of fluvial sediments gives rise to a number of so called *sorting effects*. In particular, in Section 6.1.1 we will see that field observations show that point bars on the inside of bends tend to be finer than the pools at the outer bends. Moreover, the upper parts of point bars display a tendency to be coarser upstream and finer downstream. We will review few contributions aimed at providing a theoretical explanation of the latter observations. It turns out that sorting in meandering rivers has so far been interpreted in terms of the dependence of the lateral tangential component of particle weight on particle size. However, available models do not appear to be fully satisfactory, even if one restricts oneself to the case of dominant bedload.

In Section 6.2 we then relax the alluvial constraint and discuss the morphodynamics of meanders in mixed bedrock-alluvial channels, in the light of the general formulation for the morphodynamics of mixed alluvial-bedrock channels discussed in Chapter 7(I). The Section ends with some thoughts on the open issue of how meanders incise bedrocks.

The final Chapter of the Monograph is devoted to a glance at the future.

2. Hydrodynamics of sinuous channels

In this Chapter we concentrate on the hydrodynamics of fixed bed bends and introduce the reader to the variety of physical mechanisms which arise when an incompressible fluid flows in a curved open channel, at sufficiently large Reynolds numbers for the flow to be fully turbulent.

2.1. Dimensional formulation

2.1.1 Curved channels

We consider a curved open channel with the following characteristics (Figure 18).

- The channel axis is a curved line in the 3-D space. Below, we refer the flow to an orthogonal system of coordinates (s , n and z , respectively). The longitudinal s axis is curvilinear and is the projection of the channel axis onto a horizontal plane. The transverse rectilinear axis n is horizontal and orthogonal to the s axis. The s, n, z system is characterized by the following metric coefficients:

$$h_s = \frac{r_0(s) + n}{r_0(s)}, \quad h_n = 1, \quad h_z = 1. \quad (3a,b,c)$$

Note that h_s accounts mathematically for the fact that if one walks in the longitudinal direction along the s coordinate line, the distance he travels increases as the lateral coordinate increases. Indeed, h_s measures the ratio between the longitudinal arc length at the lateral coordinate n and the corresponding arc length at the channel axis (Figure 18c).

- The radius of curvature of the longitudinal axis is a function of the longitudinal coordinate: hence $r_0 = r_0(s)$.
- The channel cross sections, defined as the intersections of the channel with planes orthogonal to the channel axis, are assumed to have constant width ($2B$).
- The channel bed as well as the channel banks are non erodible.

These assumptions require some comments in order to fully appreciate a few subtle implications. The first note concerns the channel axis. In nature, the axis is a line which does not lie on a plane, hence, besides exhibiting a *bending curvature*, it is also characterized by some (albeit fairly weak) degree of *torsion*. We have chosen an orthogonal coordinate system defined on a horizontal plane, thus avoiding the formal complications that would arise adopting an intrinsic coordinate system tied to the channel axis. As discussed below, this approach is definitely much simpler. However, a small complication arises: since the longitudinal axis lies on a horizontal plane, the basic uniform state, besides a dominant longitudinal component, will include a small vertical component. The second note refers to the notion of *channel width*. A *stage independent* channel width is unambiguously defined for rectangular channels. In nature, the notion of channel width is less obvious: if it is identified with the width of the free surface at the given cross section, then it is in general a *stage dependent* quantity. We will come back to this issue further on, whilst, for the time being, we restrict ourselves to the case of rectangular channels.

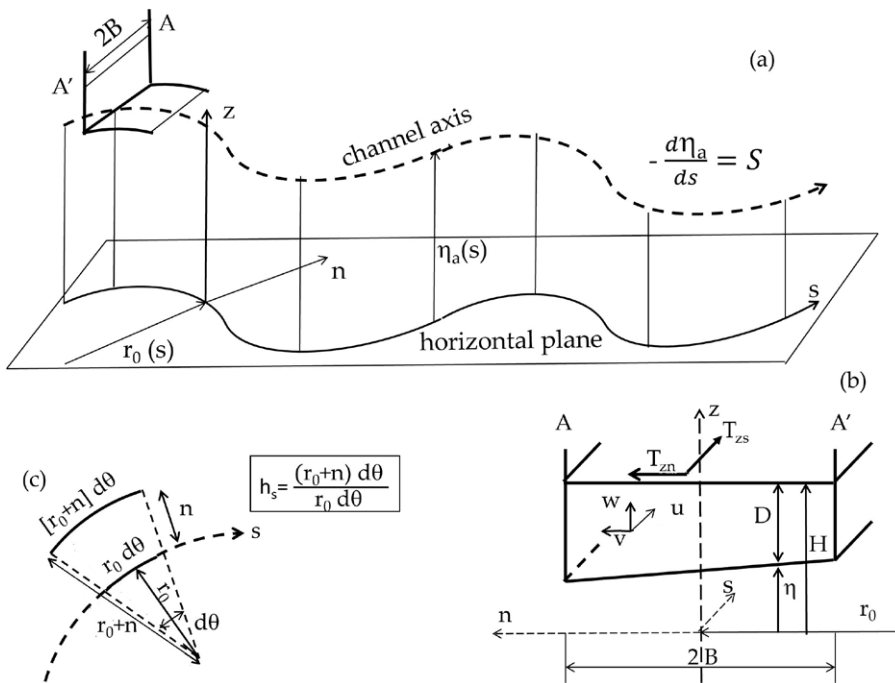


Figura 18. Sketch of a sinuous open channel and notations.

2.1.2 Governing equations

The mathematical formulation of the hydrodynamic problem is obtained, as discussed in Chapter 2(I), imposing the mass conservation and the momentum principle for the fluid phase, along with appropriate boundary conditions at the free surface, at the channel bottom and at the channel banks. Moreover, the initial state of the system must be assigned. The choice of the governing equations depends on how detailed we wish the description of the turbulent flow field to be. Although the use of LES (Large Eddy Simulation) techniques have been proposed for detailed simulations of morphodynamic processes (van Balen *et al.*, 2009; Nabi *et al.*, 2012), for the purposes of bend morphodynamics it is most often sufficient to rely on a Reynolds averaged formulation.

Conservation equations of mass and momentum of the fluid phase.

Let us write the dimensional form of the Reynolds averaged mass and momentum conservation equations for the fluid phase in the orthogonal curvilinear coordinates introduced in Section 2.1.1:

$$\frac{1}{h_s} \frac{\partial u_s}{\partial s} + \frac{1}{h_s} \frac{\partial (h_s u_n)}{\partial n} + \frac{\partial u_z}{\partial z} = 0, \quad (4a)$$

$$\begin{aligned} \rho \left(\frac{\partial u_s}{\partial t} + \frac{u_s}{h_s} \frac{\partial u_s}{\partial s} + u_n \frac{\partial u_s}{\partial n} + u_z \frac{\partial u_s}{\partial z} + \frac{u_s u_n}{h_s} \frac{\partial h_s}{\partial n} \right) = \\ - \frac{1}{h_s} \frac{\partial P}{\partial s} + \frac{\partial T_{zs}^t}{\partial z} + \frac{1}{h_s} \frac{\partial T_{ss}^t}{\partial s} + \frac{1}{h_s} \frac{\partial (h_s T_{ns}^t)}{\partial n} + \frac{T_{sn}^t}{h_s} \frac{\partial h_s}{\partial n}, \end{aligned} \quad (4b)$$

$$\begin{aligned} \rho \left(\frac{\partial u_n}{\partial t} + \frac{u_s}{h_s} \frac{\partial u_n}{\partial s} + u_n \frac{\partial u_n}{\partial n} + u_z \frac{\partial u_n}{\partial z} - \frac{u_s^2}{h_s} \frac{\partial h_s}{\partial n} \right) = \\ - \frac{\partial P}{\partial n} + \frac{\partial T_{zn}^t}{\partial z} + \frac{\partial T_{nn}^t}{\partial n} + \frac{1}{h_s} \frac{\partial T_{sn}^t}{\partial s} + \frac{T_{nn}^t - T_{ss}^t}{h_s} \frac{\partial h_s}{\partial n}, \end{aligned} \quad (4c)$$

$$\begin{aligned} \rho \left(\frac{\partial u_z}{\partial t} + \frac{u_s}{h_s} \frac{\partial u_z}{\partial s} + u_n \frac{\partial u_z}{\partial n} + u_z \frac{\partial u_z}{\partial z} \right) = \\ - \frac{\partial P}{\partial z} + \frac{\partial T_{zz}^t}{\partial z} + \frac{\partial T_{nz}^t}{\partial n} + \frac{1}{h_s} \frac{\partial T_{sz}^t}{\partial s} + \frac{T_{nz}^t}{h_s} \frac{\partial h_s}{\partial n} - \rho g. \end{aligned} \quad (4d)$$

Here, u_s, u_n, u_z are the longitudinal, lateral and vertical components of the Reynolds averaged velocity vector, respectively. Moreover, P is the average pressure, including the isotropic contribution $-(2/3)\rho\mathcal{K}$ arising from the Boussinesq linear closure (see eq. 2.44(I)). Finally, the quantities T_{ij}^t ($i, j = s, n, z$) are the deviatoric components of the Reynolds stress tensor.

Vorticity transport equation

In curvilinear coordinates, the components of the instantaneous vorticity vector have the form:

$$\omega_s = \frac{\partial v_z}{\partial n} - \frac{\partial v_n}{\partial z}, \quad \omega_n = \frac{\partial v_s}{\partial z} - \frac{1}{h_s} \frac{\partial v_z}{\partial s}, \quad \omega_z = \frac{1}{h_s} \left(\frac{\partial v_n}{\partial s} - \frac{v_s}{r_0} \right) - \frac{\partial v_s}{\partial n}. \quad (5)$$

Similar expressions (with v_s, v_n, v_z replaced by u_s, u_n, u_z , respectively) hold for the mean vorticity vector $\mathbf{\Omega} \equiv (\Omega_s, \Omega_n, \Omega_z)$ in turbulent flows.

For the present purposes, it is useful to report the dimensional form of the governing equation for the longitudinal component ω_s of the instantaneous vorticity vector. Using the present curvilinear coordinates, from equation (2.10)(I) one finds:

$$\begin{aligned} \frac{\partial \omega_s}{\partial t} + \frac{v_s}{h_s} \frac{\partial \omega_s}{\partial s} + v_n \frac{\partial \omega_s}{\partial n} + v_z \frac{\partial \omega_s}{\partial z} = \frac{\omega_s}{h_s} \frac{\partial v_s}{\partial s} + \omega_n \frac{\partial v_s}{\partial n} + \omega_z \frac{\partial v_s}{\partial z} + \frac{1}{h_s} \left(\frac{v_n \omega_s - v_s \omega_n}{r_0} \right) \\ + \nu \left(\nabla^2 \omega_s + \frac{2}{h_s^2 r_0} \frac{\partial \omega_n}{\partial s} - \frac{\omega_s}{h_s^2 r_0^2} - \frac{\omega_n}{h_s^3 r_0^2} \frac{\partial r_0}{\partial s} \right), \end{aligned} \quad (6)$$

where

$$\nabla^2 = \frac{1}{h_s} \frac{\partial}{\partial s} \left(\frac{1}{h_s} \frac{\partial}{\partial s} \right) + \frac{1}{h_s} \frac{\partial}{\partial n} \left(h_s \frac{\partial}{\partial n} \right) + \frac{\partial^2}{\partial z^2}. \quad (7)$$

Similarly, one may derive from equation (2.43)(I) the governing equation for the longitudinal component Ω_s of the mean vorticity vector, to find:

$$\begin{aligned}
 \frac{\partial \Omega_s}{\partial t} + \frac{u_s}{h_s} \frac{\partial \Omega_s}{\partial s} + u_n \frac{\partial \Omega_s}{\partial n} + u_z \frac{\partial \Omega_s}{\partial z} &= \frac{\Omega_s}{h_s} \frac{\partial u_s}{\partial s} + \Omega_n \frac{\partial u_s}{\partial n} + \Omega_z \frac{\partial u_s}{\partial z} + \frac{1}{h_s} \left(\frac{u_n \Omega_s - u_s \Omega_n}{r_0} \right) \\
 - \frac{1}{\rho} \left[\frac{1}{h_s} \frac{\partial^2}{\partial z^2} - \frac{\partial}{\partial n} \left(\frac{1}{h_s} \frac{\partial}{\partial n} \right) \right] (h_s T_{nz}^t) &- \frac{1}{\rho} \frac{\partial}{\partial z} \left(\frac{1}{h_s} \frac{\partial T_{sn}^t}{\partial s} \right) + \frac{1}{\rho} \frac{\partial}{\partial n} \left(\frac{1}{h_s} \frac{\partial T_{sz}^t}{\partial s} \right) \\
 - \frac{1}{\rho h_s r_0} \frac{\partial}{\partial z} (T_{nn}^t - T_{ss}^t) &- \frac{1}{\rho} \frac{\partial^2}{\partial z \partial n} (T_{nn}^t - T_{zz}^t) \\
 + \nu \left(\nabla^2 \Omega_s + \frac{2}{h_s^2 r_0} \frac{\partial \Omega_n}{\partial s} - \frac{\Omega_s}{h_s^2 r_0^2} - \frac{\Omega_n}{h_s^3 r_0^2} \frac{\partial r_0}{\partial s} \right). &
 \end{aligned} \tag{8}$$

In Section 2.6.2, this equation will be used to analyze the variety of mechanisms that control the generation of secondary flows in sharply curved channels.

2.1.3 Closure of the governing equations

As discussed in Section 2.2.8(I), Reynolds averaging requires some closure relationships for the Reynolds stresses. In the present context, a least complex closure able to capture the main ingredients of the process can be obtained taking advantage of the slowly varying character of the flow field typical of fluvial hydrodynamics at sufficiently large scales. This approach is commonly and successfully employed in 1-D hydraulic modeling where the flow is treated as a slowly varying sequence of locally and instantaneously uniform flows. This idea can reasonably be pursued also in curvilinear flows, provided sinuosity is weak and the channel is sufficiently wide that the boundary layers at the channel banks play a passive role. If we exclude for the time being the case of sharp, narrow bends, we may rely on the Boussinesq closure and model the eddy viscosity ν_T using its uniform form (see eq. 2.84(I)), expressed in terms of the local and instantaneous flow field. Under these assumptions we may write:

$$\nu_T = u_\tau D(s, n, t) \mathcal{N}(\zeta). \tag{9}$$

Here, $D(s, n, t)$ is the local instantaneous value of flow depth, where the word '*instantaneous*' refers to the possibility that the Reynolds averaged flow may undergo temporal variations due, e.g. to the propagation of a flood. Also, $\mathcal{N}(\zeta)$ is a function describing the shape of the vertical distribution of the eddy viscosity expressed in terms of the normalized vertical coordinate ζ . This variable, which maps the physical z -domain $[\eta, H]$ into the ζ -range $[0, 1]$, is defined as follows:

$$\zeta = \frac{z - \eta}{H - \eta} = \frac{z - \eta}{D}. \tag{10}$$

Finally, u_τ is the local instantaneous value of the friction velocity. We recall that the friction velocity is defined as the square of the ratio between the modulus τ_η of the flow shear stress acting on the bed and the flow density ρ . For a general flow field, denoting by \mathbf{T} the stress tensor, by \mathbf{t} the stress vector ($\equiv \mathbf{T} \cdot \hat{\mathbf{n}}$) and by $\hat{\mathbf{n}}$ the unit vector in the outer normal direction (Figure 19), one may write:

$$\tau_\eta = |\mathbf{t}_\eta - (\mathbf{t}_\eta \cdot \hat{\mathbf{n}}_\eta) \hat{\mathbf{n}}_\eta|. \tag{11}$$

The Boussinesq closure for T_{ij}^t ($i, j = s, n, z$) reads:

$$\frac{T_{ij}^t}{\rho} = 2\nu_T D_{ij}, \tag{12}$$

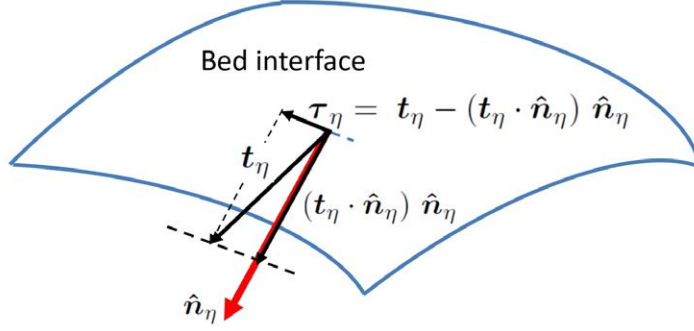


Figure 19. Sketch illustrating the decomposition of the stress vector acting at the bed interface into its normal and tangential components

with ν_T eddy viscosity expressed in the slowly varying form (9) and D_{ij} Reynolds averaged strain rate tensor. In our curvilinear orthogonal system, one finds:

$$\frac{T_{zs}^t}{\rho} = \nu_T \left(\frac{\partial u_s}{\partial z} + \frac{1}{h_s} \frac{\partial u_z}{\partial s} \right); \quad \frac{T_{ns}^t}{\rho} = \nu_T \left(\frac{\partial u_s}{\partial n} + \frac{1}{h_s} \frac{\partial u_n}{\partial s} - \frac{u_s}{h_s} \frac{\partial h_s}{\partial n} \right); \quad (13a)$$

$$\frac{T_{nz}^t}{\rho} = \nu_T \left(\frac{\partial u_n}{\partial z} + \frac{\partial u_z}{\partial n} \right); \quad \frac{T_{ss}^t}{\rho} = 2\nu_T \left(\frac{1}{h_s} \frac{\partial u_s}{\partial s} + \frac{u_n}{h_s} \frac{\partial h_s}{\partial n} \right); \quad (13b)$$

$$\frac{T_{nn}^t}{\rho} = 2\nu_T \left(\frac{\partial u_n}{\partial n} \right); \quad \frac{T_{zz}^t}{\rho} = 2\nu_T \left(\frac{\partial u_z}{\partial z} \right). \quad (13c)$$

2.1.4 Boundary conditions

The boundary conditions to be associated with the above conservation equations are obtained from those presented in Section 2.2.6(I) (equations 2.35(I), 2.36(I) and 2.40(I)), written in the present curvilinear coordinates. They read as follows.

No slip at the solid boundaries:

$$u_s = u_n = u_z = 0 \quad [-B < n < B, \quad z = \eta + z_0(n)], \quad (14a)$$

$$u_s = u_n = u_z = 0 \quad [\eta(n) < z < H(n), \quad n = \pm B \mp n_0(z)], \quad (14b)$$

with $z_0(n)$ and $n_0(z)$ conventional distances from the bed and channel banks, respectively, where no slip must be imposed in the turbulent flow.

The free surface is a material surface:

At the free surface:

$$\left[-\frac{\partial H}{\partial t} - \frac{u_s}{h_s} \frac{\partial H}{\partial s} - u_n \frac{\partial H}{\partial n} + u_z \right]_{H(s,n,t)} = 0. \quad (15)$$

The free surface is stress free.

Employing eq. 2.17(I), the unit vector orthogonal to the free surface $\hat{\mathbf{n}}_H$ is found to have the form:

$$\hat{\mathbf{n}}_H = \frac{\left(-\frac{1}{h_s} \frac{\partial H}{\partial s}; -\frac{\partial H}{\partial n}; 1\right)}{\sqrt{1 + \left(\frac{1}{h_s} \frac{\partial H}{\partial s}\right)^2 + \left(\frac{\partial H}{\partial n}\right)^2}}. \quad (16)$$

The dynamic condition at the free surface (equation 2.37(I)), projected into the longitudinal, lateral and vertical directions then reads:

$$\left[(-P + T_{ss}^t)\hat{\mathbf{n}}_{Hs} + T_{ns}^t\hat{\mathbf{n}}_{Hn} + T_{zs}^t\hat{\mathbf{n}}_{Hz}\right]_H = 0, \quad (17a)$$

$$\left[T_{sn}^t\hat{\mathbf{n}}_{Hs} + (-P + T_{nn}^t)\hat{\mathbf{n}}_{Hn} + T_{zn}^t\hat{\mathbf{n}}_{Hz}\right]_H = 0, \quad (17b)$$

$$\left[T_{sz}^t\hat{\mathbf{n}}_{Hs} + T_{nz}^t\hat{\mathbf{n}}_{Hn} + (-P + T_{zz}^t)\hat{\mathbf{n}}_{Hz}\right]_H = 0. \quad (17c)$$

Open boundaries

Open boundaries are the end cross sections, located at $s = 0$ and $s = L_r$, with L_r the intrinsic length of the curved channel reach under consideration. The specification of suitable conditions at these boundaries is a delicate issue that will be discussed in various specific cases.

2.2. Dimensionless formulation

In order to seek simplifications of the above mathematical problem, appropriate to the variety of contexts that can be found in nature, it is useful to reformulate it in dimensionless form. We then need to choose appropriate scales for the independent and dependent variables.

2.2.1 Scaling

The reference uniform flow

Flows in curved channels can be thought of as curvature driven perturbations of flows in straight channels. It is thus natural to refer the flow quantities to those corresponding to a uniform flow in a straight open channel with width equal to that of the curved channel and slope equal to some suitably defined measure of the *average* slope of the channel. The reader should again appreciate the subtlety of this concept. In the field, a curved channel can hardly be characterized by a constant slope ($-d\eta_a/ds$ in Figure 18). Hence, at least in general, one has to choose a characteristic channel reach and define an average channel slope in that reach, that may be used to calculate the characteristics of the reference uniform flow.

Following the notations employed in Section 2.3.3(I), we denote by D_u , U_u , C_{fu} , F_{ru} and $u_{\tau u}$ the flow depth, the cross sectionally averaged flow speed, the friction coefficient, the Froude number and the friction velocity (averaged over the boundary) of the reference uniform flow, respectively. We recall that the above quantities satisfy the following relationships:

$$u_{\tau u}^2 = \frac{\bar{\tau}_u}{\rho} = C_{fu} U_u^2 = g S R_u = \frac{g S D_u}{1 + \frac{1}{\beta_u}}, \quad (18a)$$

$$F_{ru}^2 = \frac{U_u^2}{g D_u}. \quad (18b)$$

Here, $\bar{\tau}_u$ is the uniform shear stress averaged over the wet boundary and R_u is the hydraulic radius of the reference flow. Moreover, $2\beta_u$ is the width to depth ratio of the uniform stream, hence:

$$\beta_u = \frac{B}{D_u}. \quad (19)$$

Finally, the kinematic eddy viscosity of the reference flow has the form (84)(I):

$$\nu_{T_u} = u_{\tau_u} D_u \mathcal{N}(\zeta). \quad (20)$$

Dimensionless variables

Let us make the independent variables dimensionless. The natural scales for the lateral and vertical coordinates are the channel half-width B and the reference uniform flow depth D_u , respectively. The scale of spatial variations of the flow field in the longitudinal direction may be externally forced (e.g. some meander wavelength in meandering channels) or internally generated (e.g. the spatial scale of flow adjustment to entrance conditions). Let us denote this scale by L . Similarly, the scale of temporal variations of the flow field may be externally forced (e.g. the time scale of a forced hydrograph) or internally generated (e.g. the temporal scale of flow adjustment to initial conditions). Let us denote this scale by T_0 .

We then introduce the following dimensionless variables:

$$\tilde{t} = \frac{t}{T_0}, \quad \tilde{s} = \frac{s}{L}, \quad \tilde{n} = \frac{n}{B}, \quad (\tilde{z}, \tilde{D}, \tilde{\eta}) = \frac{(z, D, \eta)}{D_u}. \quad (21)$$

One further geometric property of the channel needs appropriate scaling. Let R_0 denote some appropriate measure of the radius of curvature of the channel axis, say its minimum value in the reach under consideration. Let us then write:

$$\tilde{r}_0 = \frac{r_0}{R_0}, \quad h_s = \frac{\tilde{r}_0(\tilde{s}) + \nu_0 \tilde{n}}{\tilde{r}_0(\tilde{s})} = 1 + \nu_0 \mathcal{C}(\tilde{s}) \tilde{n}, \quad (22)$$

Here, \mathcal{C} and ν_0 are the *dimensionless curvature of the channel axis* and a *dimensionless curvature parameter* respectively, such that

$$\mathcal{C}(\tilde{s}) = \frac{1}{\tilde{r}_0(\tilde{s})}, \quad \nu_0 = \frac{B}{R_0}. \quad (23)$$

Let us finally make the stresses and the eddy viscosity ν_T dimensionless. The natural scale of pressure is the hydrostatic pressure associated with the reference flow depth D_u . Reynolds stresses are conveniently scaled by the average shear stress of the reference uniform flow $\rho u_{\tau_u}^2$. Hence, recalling (18a), we write:

$$\tilde{P} = \frac{P}{\rho g D_u}, \quad \tilde{T}_{ij}^t = \frac{T_{ij}^t}{\rho u_{\tau_u}^2} \quad (i, j = \tilde{s}, \tilde{n}, \tilde{z}). \quad (24)$$

The definition of eddy viscosity determines its natural scale as the ratio between the scale of Reynolds stress $\rho u_{\tau_u}^2$ and the scale of the vertical velocity gradient U_u/D_u of the reference flow, namely:

$$\tilde{\nu}_T = \frac{\nu_T}{u_{\tau_u} D_u}. \quad (25)$$

Next, let us examine the scales of the longitudinal, lateral and vertical components of the flow velocity. While U_u is a correct measure of the size of the basic uniform flow field, it does not necessarily measure the sizes of the longitudinal, lateral and vertical perturbations of the flow

velocity, which depend on what drives them. These sizes can be estimated analyzing the balances between the various contributions to the continuity and momentum equations. Let us clarify this point.

Consider the lateral component of the momentum equation (4c) and assume that the dominant frictional term $\left(\frac{\partial}{\partial z}[\nu_T \frac{\partial u_n}{\partial z}]\right)$ is balanced by the *centrifugal term* $\left(\frac{u_s^2}{h_s} \frac{\partial h_s}{\partial n}\right)$: then, adopting the scales (21) and using R_0 as scale for the radius of curvature of the channel axis and $u_{\tau u} D_u$ as scale for the eddy viscosity, one readily finds that:

$$u_n \sim \mathcal{O}(\delta U_u), \quad (26)$$

where δ is the following dimensionless parameter:

$$\delta = \frac{D_u}{R_0 \sqrt{C_{fu}}}. \quad (27)$$

A second mechanism driving the development of secondary flow is the so called *topographic steering*: variations of flow depth due to variations of bed elevation give rise to longitudinal variations of longitudinal velocity, which produce lateral variations of lateral velocity by simple continuity requirements (recall eq. (4a)). Assuming that variations of longitudinal velocity are of the order of the velocity itself, say U_u , the required balance between the latter two effects in eq. (4a) implies that:

$$u_n \sim \mathcal{O}\left(\frac{B}{L} U_u\right). \quad (28)$$

As discussed below, both dimensionless parameters δ and B/L are typically small in natural meanders, which implies that *secondary flows are typically an order of magnitude smaller than the primary flow*.

Similar arguments may be pursued when seeking the appropriate scale of the perturbations of the longitudinal velocity u_s . The reader will readily show that, balancing the dominant frictional term $\frac{\partial}{\partial z}[\frac{\partial u_s}{\partial z}]$ in (4b) with *longitudinal convection* $\frac{u_s}{h_s} \frac{\partial u_s}{\partial s}$ the perturbation of longitudinal velocity Δu_s satisfies the following scaling relationship:

$$\Delta u_s \sim \mathcal{O}(\mathfrak{L} U_u) \quad (29)$$

where

$$\mathfrak{L} = \frac{D_u}{L \sqrt{C_{fu}}}. \quad (30)$$

Balancing *lateral convection* $u_n \frac{\partial u_s}{\partial n}$ one finds a similar scale for Δu_s if topography dominates, i.e. if the scale (28) is employed for u_n . Alternatively, using the centrifugal scaling (26), one finds:

$$\Delta u_s \sim \mathcal{O}(\mathfrak{b} \delta U_u) \quad (31)$$

where

$$\mathfrak{b} = \frac{D_u}{B \sqrt{C_{fu}}}. \quad (32)$$

Finally, balancing the dominant frictional term $\frac{\partial}{\partial z}[\frac{\partial u_s}{\partial z}]$ in (4b) with the *local inertia* $\frac{\partial u_s}{\partial t}$ the perturbation of longitudinal velocity Δu_s satisfies the following scaling relationship:

$$\Delta u_s \sim \mathcal{O}(\sigma U_u). \quad (33)$$

where

$$\sigma = \frac{D_u}{L_{T_0} \sqrt{C_{fu}}}. \quad (34)$$

Here L_{T_0} is a convective length scale, defined as the path length of a particle moving with the reference uniform speed U_u in the reference time T_0 .

The scale of the vertical velocity component u_z is determined by flow continuity. Balancing $\frac{\partial u_z}{\partial z}$ with $\frac{1}{h_s} \frac{\partial(h_s u_n)}{\partial n}$, one readily finds that $u_z \sim \mathcal{O}(V/\beta_u)$, having denoted by V the scale of u_n .

The above analysis suggests that perturbations of the flow velocity scale with the reference uniform speed U_u multiplied by various dimensionless parameters each associated with one of the mechanisms driving the flow perturbations. Below, we will then adopt the choice to scale the longitudinal and lateral components of velocity by U_u and the vertical component by U_u/β_u . Hence, we write:

$$\tilde{u}_s = \frac{u_s}{U_u}, \quad \tilde{u}_n = \frac{u_n}{U_u}, \quad \tilde{u}_z = \frac{u_z}{U_u/\beta_u}. \quad (35)$$

This choice implies that *the various dimensionless parameters presented above will appear in the dimensionless form of the governing equations.*

Finally, the scale ΔH of longitudinal perturbations of the free surface elevation H is typically determined by a balance between the perturbation of the longitudinal pressure gradient ($\frac{1}{\rho} \frac{\partial \Delta P}{\partial s}$) and the perturbation of longitudinal convection ($u_s \frac{\partial u_s}{\partial s}$) in the momentum equation. Assuming a hydrostatic distribution of the mean pressure, the former scales with $(g \Delta H/L)$, whilst convection scales with $(U_u \Delta U/L)$, where ΔU is the scale of perturbations of longitudinal velocity associated with the assumed perturbation of the free surface elevation. Assuming that $\Delta U \sim U_u$, one finds that $\Delta H \sim F_{ru}^2 D_u$. Note that this scaling is consistent with the well known observation that perturbations of the free surface in subcritical flows are typically much weaker than perturbations experienced in supercritical flows. It is then convenient to write:

$$\tilde{H} = \frac{H}{F_{ru}^2 D_u}. \quad (36)$$

2.2.2 Formulation of the hydrodynamic problem in dimensionless form

Governing equations

Let us first examine the vertical component of the Reynolds equations. With the help of (21), (25) and (35), it takes the following dimensionless form:

$$\begin{aligned} \frac{\partial \tilde{P}}{\partial \tilde{z}} &= -1 - \mathfrak{b} F_{ru}^2 C_{fu} \left[\sigma \frac{\partial \tilde{u}_z}{\partial \tilde{t}} + \frac{\mathfrak{L}}{h_s} \tilde{u}_s \frac{\partial \tilde{u}_z}{\partial \tilde{s}} + \mathfrak{b} \left(\tilde{u}_n \frac{\partial \tilde{u}_z}{\partial \tilde{n}} + \tilde{u}_z \frac{\partial \tilde{u}_z}{\partial \tilde{z}} \right) \right] \\ &+ F_{ru}^2 C_{fu} \left[\frac{\partial \tilde{T}_{zz}^t}{\partial \tilde{z}} + \sqrt{C_{fu}} \left(\mathfrak{b} \frac{\partial \tilde{T}_{nz}^t}{\partial \tilde{n}} + \frac{\mathfrak{L}}{h_s} \frac{\partial \tilde{T}_{sz}^t}{\partial \tilde{s}} + \frac{\delta}{h_s} C \tilde{T}_{nz}^t \right) \right] \\ &= -1 + \mathcal{O}(C_{fu}) \end{aligned} \quad (37)$$

Noting that the friction coefficient C_{fu} takes values typically in the range 10^{-2} - 10^{-3} and the aspect ratio is large, the above equation reduces to the hydrostatic approximation for the mean pressure field $\tilde{P}(s, n, z)$. Moreover, as shown below (equation (47)), at the free surface the condition of

vanishing normal stress reduces to the condition of vanishing mean pressure. Hence, \tilde{P} is the solution of the following differential problem:

$$\frac{\partial \tilde{P}}{\partial \tilde{z}} = -1, \quad (38a)$$

$$\tilde{P}|_{F_{ru}^2 \tilde{H}} = 0. \quad (38b)$$

The dimensionless mean pressure is then solved in terms of the free surface elevation as follows:

$$\tilde{P} = F_{ru}^2 \tilde{H}(s, n) - \tilde{z}. \quad (39)$$

With the help of (39) the mean pressure can be removed from the longitudinal and the lateral components of the Reynolds equations, and the pressure gradient can be replaced by the slope of the free surface. The resulting dimensionless mass and momentum conservation equations (along s and n) then become:

$$\frac{\mathfrak{L}}{\mathfrak{b}} \frac{1}{h_s} \frac{\partial \tilde{u}_s}{\partial \tilde{s}} + \frac{\partial \tilde{u}_n}{\partial \tilde{n}} + \frac{\partial \tilde{u}_z}{\partial \tilde{z}} = -\frac{\delta}{\mathfrak{b} h_s} \mathcal{C}(\tilde{s}) \tilde{u}_n, \quad (40a)$$

$$\begin{aligned} \sigma \frac{\partial \tilde{u}_s}{\partial \tilde{t}} + \frac{\mathfrak{L}}{h_s} \tilde{u}_s \frac{\partial \tilde{u}_s}{\partial \tilde{s}} + \mathfrak{b} \left(\tilde{u}_n \frac{\partial \tilde{u}_s}{\partial \tilde{n}} + \tilde{u}_z \frac{\partial \tilde{u}_s}{\partial \tilde{z}} \right) + \frac{\delta \mathcal{C}}{h_s} \tilde{u}_s \tilde{u}_n = -\frac{\mathfrak{L}}{h_s} \frac{\partial \tilde{H}}{\partial \tilde{s}} \\ + \sqrt{C_{fu}} \frac{\partial \tilde{T}_{zs}^t}{\partial \tilde{z}} + C_{fu} \left(\frac{\mathfrak{L}}{h_s} \frac{\partial \tilde{T}_{ss}^t}{\partial \tilde{s}} + \mathfrak{b} \frac{\partial \tilde{T}_{ns}^t}{\partial \tilde{n}} + 2\delta \frac{\mathcal{C}}{h_s} \tilde{T}_{ns}^t \right), \end{aligned} \quad (40b)$$

$$\begin{aligned} \sigma \frac{\partial \tilde{u}_n}{\partial \tilde{t}} + \frac{\mathfrak{L}}{h_s} \tilde{u}_s \frac{\partial \tilde{u}_n}{\partial \tilde{s}} + \mathfrak{b} \left(\tilde{u}_n \frac{\partial \tilde{u}_n}{\partial \tilde{n}} + \tilde{u}_z \frac{\partial \tilde{u}_n}{\partial \tilde{z}} \right) - \frac{\delta \mathcal{C}}{h_s} \tilde{u}_s^2 = -\mathfrak{b} \frac{\partial \tilde{H}}{\partial \tilde{n}} \\ + \sqrt{C_{fu}} \frac{\partial \tilde{T}_{zn}^t}{\partial \tilde{z}} + C_{fu} \left[\mathfrak{b} \frac{\partial \tilde{T}_{nn}^t}{\partial \tilde{n}} + \frac{\mathfrak{L}}{h_s} \frac{\partial \tilde{T}_{ns}^t}{\partial \tilde{s}} + \frac{\delta \mathcal{C}}{h_s} (\tilde{T}_{nn}^t - \tilde{T}_{ss}^t) \right]. \end{aligned} \quad (40c)$$

Closure relationships

The closure relationships adopted for weakly sinuous wide channels (13) are also readily made dimensionless.

Recalling (20) and (25), the dimensionless form of the eddy viscosity of the reference uniform flow reads:

$$\tilde{\nu}_{Tu} = \mathcal{N}(\zeta). \quad (41)$$

The dimensionless closure relationships take the form

$$\tilde{T}_{zs}^t = \frac{\tilde{\nu}_T}{\sqrt{C_{fu}}} \left(\frac{\partial \tilde{u}_s}{\partial \tilde{z}} + \mathfrak{b} C_{fu} \frac{\mathfrak{L}}{h_s} \frac{\partial \tilde{u}_z}{\partial \tilde{s}} \right), \quad (42a)$$

$$\tilde{T}_{zn}^t = \frac{\tilde{\nu}_T}{\sqrt{C_{fu}}} \left(\frac{\partial \tilde{u}_n}{\partial \tilde{z}} + \mathfrak{b}^2 C_{fu} \frac{\partial \tilde{u}_z}{\partial \tilde{n}} \right), \quad (42b)$$

$$\tilde{T}_{sn}^t = \tilde{\nu}_T \left(\mathfrak{b} \frac{\partial \tilde{u}_s}{\partial \tilde{n}} + \frac{\mathfrak{L}}{h_s} \frac{\partial \tilde{u}_n}{\partial \tilde{s}} - \frac{\tilde{u}_s}{h_s} \delta \mathcal{C} \right), \quad (42c)$$

$$\tilde{T}_{ss}^t = 2 \frac{\tilde{\nu}_T}{h_s} \left(\mathfrak{L} \frac{\partial \tilde{u}_s}{\partial \tilde{s}} + \delta \mathcal{C} \tilde{u}_n \right), \quad (42d)$$

$$\tilde{T}_{nn}^t = 2 \tilde{\nu}_T \mathfrak{b} \frac{\partial \tilde{u}_n}{\partial \tilde{n}}, \quad (42e)$$

$$\tilde{T}_{zz}^t = 2 \tilde{\nu}_T \mathfrak{b} \frac{\partial \tilde{u}_z}{\partial \tilde{z}}. \quad (42f)$$

Boundary conditions

- *No slip at the solid boundaries:*

$$\tilde{u}_s = \tilde{u}_n = \tilde{u}_z = 0 \quad [-1 < \hat{n} < 1, \quad \tilde{z} = \tilde{\eta} + \tilde{z}_0(\tilde{n})], \quad (43a)$$

$$\tilde{u}_s = \tilde{u}_n = \tilde{u}_z = 0 \quad [\hat{\eta} < \tilde{z} < F_{ru}^2 \tilde{H}, \quad \tilde{n} = \pm 1]. \quad (43b)$$

- *Kinematic condition at the free surface.*

$$\mathbf{b} \tilde{u}_z \Big|_{F_{ru}^2 \tilde{H}} = F_{ru}^2 \left[\sigma \frac{\partial \tilde{H}}{\partial \tilde{t}} + \frac{\mathfrak{L}}{h_s} \tilde{u}_s \frac{\partial \tilde{H}}{\partial \tilde{s}} + \mathbf{b} \tilde{u}_n \frac{\partial \tilde{H}}{\partial \tilde{n}} \right]_{F_{ru}^2 \tilde{H}}. \quad (44)$$

- *Vanishing normal stress at the free surface.*

$$\left[-\tilde{P} \hat{n}_z + F_{ru}^2 C_{fu} (\tilde{T}_{sz} \hat{n}_s + \tilde{T}_{nz} \hat{n}_n + \tilde{T}_{zz} \hat{n}_z) \right]_{F_{ru}^2 \tilde{H}} = 0, \quad (45)$$

where the components of the unit vector $\hat{\mathbf{n}}_H$ have the following dimensionless forms:

$$\hat{n}_s = -\frac{F_{ru}^2 C_{fu}}{h_s} \mathfrak{L} \frac{\partial \tilde{H}}{\partial \tilde{s}} \hat{n}_z, \quad (46a)$$

$$\hat{n}_n = -F_{ru}^2 \sqrt{C_{fu}} \mathbf{b} \frac{\partial \tilde{H}}{\partial \tilde{n}} \hat{n}_z, \quad (46b)$$

$$\hat{n}_z = \frac{1}{\sqrt{1 + F_{ru}^4 C_{fu} \left[\left(\frac{\mathfrak{L}}{h_s} \frac{\partial \tilde{H}}{\partial \tilde{s}} \right)^2 + \mathbf{b}^2 \left(\frac{\partial \tilde{H}}{\partial \tilde{n}} \right)^2 \right]}}. \quad (46c)$$

With the help of (46), neglecting terms of order $\mathcal{O}(C_{fu}^{1/2})$ or smaller, the condition (45) may be approximated by the much simpler condition:

$$\tilde{P} \Big|_{F_{ru}^2 \tilde{H}} = 0. \quad (47)$$

- *Vanishing tangential stress at the free surface.*

$$\left[-\tilde{P} \hat{n}_s + F_{ru}^2 C_{fu} (\tilde{T}_{ss}^t \hat{n}_s + \tilde{T}_{ns}^t \hat{n}_n + \tilde{T}_{zs}^t \hat{n}_z) \right]_{F_{ru}^2 \tilde{H}} = 0, \quad (48a)$$

$$\left[-\tilde{P} \hat{n}_n + F_{ru}^2 C_{fu} (\tilde{T}_{sn}^t \hat{n}_s + \tilde{T}_{nn}^t \hat{n}_n + \tilde{T}_{zn}^t \hat{n}_z) \right]_{F_{ru}^2 \tilde{H}} = 0. \quad (48b)$$

The general form of (48) appears to be quite complicated. However, the reader will readily check that terms proportional to \hat{n}_{hz} are dominant and the above relationships reduce to the simplest conditions:

$$\tilde{T}_{zs}^t \Big|_{F_{ru}^2 \tilde{H}} = 0, \quad \tilde{T}_{zn}^t \Big|_{F_{ru}^2 \tilde{H}} = 0. \quad (49)$$

We also perform the coordinate transformation (10). In general, \tilde{H} and \tilde{D} are both functions of \tilde{t} , \tilde{s} and \tilde{n} , hence the temporal and spatial derivatives must be replaced as follows:

$$\frac{\partial}{\partial \tilde{t}} \rightarrow \frac{\partial}{\partial \tilde{t}} - \left(\frac{F_{ru}^2}{\tilde{D}} \frac{\partial \tilde{H}}{\partial \tilde{t}} + \frac{\zeta - 1}{\tilde{D}} \frac{\partial \tilde{D}}{\partial \tilde{t}} \right) \frac{\partial}{\partial \zeta}, \quad (50a)$$

$$\frac{\partial}{\partial \tilde{s}} \rightarrow \frac{\partial}{\partial \tilde{s}} - \left(\frac{F_{ru}^2}{\tilde{D}} \frac{\partial \tilde{H}}{\partial \tilde{s}} + \frac{\zeta - 1}{\tilde{D}} \frac{\partial \tilde{D}}{\partial \tilde{s}} \right) \frac{\partial}{\partial \zeta}, \quad (50b)$$

$$\frac{\partial}{\partial \tilde{n}} \rightarrow \frac{\partial}{\partial \tilde{n}} - \left(\frac{F_{ru}^2}{\tilde{D}} \frac{\partial \tilde{H}}{\partial \tilde{n}} + \frac{\zeta - 1}{\tilde{D}} \frac{\partial \tilde{D}}{\partial \tilde{n}} \right) \frac{\partial}{\partial \zeta}, \quad (50c)$$

$$\frac{\partial}{\partial \tilde{z}} \rightarrow \frac{1}{\tilde{D}} \frac{\partial}{\partial \zeta}, \quad (50d)$$

With the help of all the above assumptions, and neglecting the higher order contributions ($\mathcal{O}(C_{fu})$ or smaller) of all the Reynolds stresses except for \tilde{T}_{zs}^t and \tilde{T}_{zn}^t , we may rewrite the governing equations (40a), (40b) and (40c) in the following form:

$$\begin{aligned} \frac{\mathfrak{L}}{\mathfrak{b}} \frac{1}{h_s} \left[\frac{\partial \tilde{u}_s}{\partial \tilde{s}} - \left(\frac{F_{ru}^2}{\tilde{D}} \frac{\partial \tilde{H}}{\partial \tilde{s}} + \frac{\zeta - 1}{\tilde{D}} \frac{\partial \tilde{D}}{\partial \tilde{s}} \right) \frac{\partial \tilde{u}_s}{\partial \zeta} \right] + \frac{\partial \tilde{u}_n}{\partial \tilde{n}} - \left(\frac{F_{ru}^2}{\tilde{D}} \frac{\partial \tilde{H}}{\partial \tilde{n}} + \frac{\zeta - 1}{\tilde{D}} \frac{\partial \tilde{D}}{\partial \tilde{n}} \right) \frac{\partial \tilde{u}_n}{\partial \zeta} \\ + \frac{1}{\tilde{D}} \frac{\partial \tilde{u}_z}{\partial \zeta} = -\frac{\delta}{\mathfrak{b} h_s} \mathcal{C}(\tilde{s}) \tilde{u}_n, \end{aligned} \quad (51a)$$

$$\begin{aligned} \sigma \left[\frac{\partial \tilde{u}_s}{\partial \tilde{t}} - \left(\frac{F_{ru}^2}{\tilde{D}} \frac{\partial \tilde{H}}{\partial \tilde{t}} + \frac{\zeta - 1}{\tilde{D}} \frac{\partial \tilde{D}}{\partial \tilde{t}} \right) \frac{\partial \tilde{u}_s}{\partial \zeta} \right] + \frac{\mathfrak{L}}{h_s} \tilde{u}_s \left[\frac{\partial \tilde{u}_s}{\partial \tilde{s}} - \left(\frac{F_{ru}^2}{\tilde{D}} \frac{\partial \tilde{H}}{\partial \tilde{s}} + \frac{\zeta - 1}{\tilde{D}} \frac{\partial \tilde{D}}{\partial \tilde{s}} \right) \frac{\partial \tilde{u}_s}{\partial \zeta} \right] \\ + \mathfrak{b} \left\{ \tilde{u}_n \left[\frac{\partial \tilde{u}_s}{\partial \tilde{n}} - \left(\frac{F_{ru}^2}{\tilde{D}} \frac{\partial \tilde{H}}{\partial \tilde{n}} + \frac{\zeta - 1}{\tilde{D}} \frac{\partial \tilde{D}}{\partial \tilde{n}} \right) \frac{\partial \tilde{u}_s}{\partial \zeta} \right] + \frac{\tilde{u}_z}{\tilde{D}} \frac{\partial \tilde{u}_s}{\partial \zeta} \right\} + \frac{\delta \mathcal{C}}{h_s} \tilde{u}_s \tilde{u}_n = \\ - \frac{\mathfrak{L}}{h_s} \frac{\partial \tilde{H}}{\partial \tilde{s}} + \frac{1}{\tilde{D}^2} \frac{\partial}{\partial \zeta} \left(\tilde{\nu}_T \frac{\partial \tilde{u}_s}{\partial \zeta} \right), \end{aligned} \quad (51b)$$

$$\begin{aligned} \sigma \left[\frac{\partial \tilde{u}_n}{\partial \tilde{t}} - \left(\frac{F_{ru}^2}{\tilde{D}} \frac{\partial \tilde{H}}{\partial \tilde{t}} + \frac{\zeta - 1}{\tilde{D}} \frac{\partial \tilde{D}}{\partial \tilde{t}} \right) \frac{\partial \tilde{u}_n}{\partial \zeta} \right] + \frac{\mathfrak{L}}{h_s} \tilde{u}_s \left[\frac{\partial \tilde{u}_n}{\partial \tilde{s}} - \left(\frac{F_{ru}^2}{\tilde{D}} \frac{\partial \tilde{H}}{\partial \tilde{s}} + \frac{\zeta - 1}{\tilde{D}} \frac{\partial \tilde{D}}{\partial \tilde{s}} \right) \frac{\partial \tilde{u}_n}{\partial \zeta} \right] \\ + \mathfrak{b} \left\{ \tilde{u}_n \left[\frac{\partial \tilde{u}_n}{\partial \tilde{n}} - \left(\frac{F_{ru}^2}{\tilde{D}} \frac{\partial \tilde{H}}{\partial \tilde{n}} + \frac{\zeta - 1}{\tilde{D}} \frac{\partial \tilde{D}}{\partial \tilde{n}} \right) \frac{\partial \tilde{u}_n}{\partial \zeta} \right] + \frac{\tilde{u}_z}{\tilde{D}} \frac{\partial \tilde{u}_n}{\partial \zeta} \right\} - \frac{\delta \mathcal{C}}{h_s} \tilde{u}_s^2 = \\ - \mathfrak{b} \frac{\partial \tilde{H}}{\partial \tilde{n}} + \frac{1}{\tilde{D}^2} \frac{\partial}{\partial \zeta} \left(\tilde{\nu}_T \frac{\partial \tilde{u}_n}{\partial \zeta} \right). \end{aligned} \quad (51c)$$

Moreover the metric coefficient h_s reads:

$$h_s = 1 + \nu_0 \mathcal{C} \tilde{n} = 1 + \frac{\delta}{\mathfrak{b}} \mathcal{C} \tilde{n}. \quad (52)$$

The boundary conditions associated with the above equations are also simplified and read:

$$\tilde{u}_s = \tilde{u}_n = \tilde{u}_z = 0 \quad (\zeta = \zeta_0(\tilde{n}), \quad -1 < \tilde{n} < 1), \quad (53a)$$

$$\tilde{u}_s = \tilde{u}_n = \tilde{u}_z = 0 \quad (0 < \zeta < 1, \quad \tilde{n} = \pm 1), \quad (53b)$$

$$\mathfrak{b} \tilde{u}_z = F_{ru}^2 \left[\sigma \frac{\partial \tilde{H}}{\partial \tilde{t}} + \frac{\mathfrak{L}}{h_s} \tilde{u}_s \frac{\partial \tilde{H}}{\partial \tilde{s}} + \mathfrak{b} \tilde{u}_n \frac{\partial \tilde{H}}{\partial \tilde{n}} \right] \quad (\zeta = 1), \quad (53c)$$

$$\tilde{T}_{zs}^t = \tilde{T}_{zn}^t = 0 \quad \Rightarrow \quad \frac{\partial \tilde{u}_s}{\partial \zeta} = \frac{\partial \tilde{u}_n}{\partial \zeta} = 0 \quad (\zeta = 1). \quad (53d)$$

Summary of the relevant dimensionless parameters

From the above formulation a number of dimensionless parameters emerge.

Two of them, the aspect ratio β_u and the curvature ratio ν_0 , are of purely geometric nature. The friction coefficient C_{fu} and the Froude number F_{ru} , control the hydrodynamics of the basic uniform flow.

Flow perturbations driven by the forcing effects of curvature and bed topography involve four further dimensionless parameters:

$$\sigma = \frac{D_u}{L_{T_0} \sqrt{C_{fu}}}, \quad \mathfrak{L} = \frac{D_u}{L \sqrt{C_{fu}}}, \quad \delta = \frac{D_u}{R_0 \sqrt{C_{fu}}}, \quad \mathfrak{b} = \frac{D_u}{B \sqrt{C_{fu}}}, \quad (54)$$

As discussed in Section 2.2.1, their physical meaning is straightforward: each of them measures the ratio between friction and one of the inertial effects, namely local inertia in σ , longitudinal convection in \mathfrak{L} , centrifugal inertia in δ and lateral convection in \mathfrak{b} .

We also point out that an alternative choice of dimensionless parameters would be:

$$\frac{\sigma}{\mathfrak{b}} = \frac{B}{L_{T_0}}, \quad \frac{\mathfrak{L}}{\mathfrak{b}} = \frac{B}{L}, \quad \frac{\delta}{\mathfrak{b}} = \nu_0 = \frac{B}{R_0}. \quad (55)$$

Since, for meandering rivers, \mathfrak{b} is often $\mathcal{O}(1)$ (see the next Section), the above two choices are equivalent. The former parameters (54) will be employed in this Chapter and the next one, whereas, for convenience, the latter parameters (55) will be used in Chapter 4 and Chapter 5.

2.3. Classification of meander bends

It is useful at this stage to analyze the range of values attained by the above dimensionless parameters. This analysis will help us introduce a mechanistic classification of meander bends to be exploited in the formulation of appropriate models of the hydrodynamics and morphodynamics of meandering channels. Below, we follow the lead of Bolla Pittaluga and Seminara (2011) who analyzed the database by Lagasse *et al.* (2004), referring to roughly 1500 meander bends of 139 rivers in the USA. The dataset contains aerial photos, detailed historical data, information on the mean daily and annual peak discharge for the gage nearest to the site. Using these data, Bolla Pittaluga and Seminara (2011) calculated the values of various dimensionless parameters for each meander bend and determined the histograms and the cumulative frequency curves reported in Figure 20. Based on the above estimates, we can classify bends according to a variety of criteria.

Mild versus sharp bends: the δ parameter

The parameter δ plays a central role in the lateral momentum equation (51c), where it multiplies the centripetal acceleration term. Indeed, as discussed later in this Chapter, bend hydrodynamics is controlled by the development of a lateral slope of the free surface. This slope, in turn, gives rise to a lateral pressure gradient that provides the centripetal force acting on fluid particles moving along curvilinear trajectories. However, the lateral pressure gradient is constant along the vertical direction, whereas the required centripetal force increases from zero at the bed to a maximum at the free surface. As a result of this unbalance, a secondary circulation arises, directed outward close to the free surface and inward close to the bed. The intensity of this centrifugally driven secondary flow is $\mathcal{O}(\delta)$. It is then reasonable to define a bend as *mildly curved* provided $\delta \ll 1$, and *sharp* if $\delta \sim \mathcal{O}(1)$. A mildly curved bend is thus a bend with a fairly weak centrifugally induced secondary flow, while a sharp bend is characterized by a strong centrifugally induced circulation. Figure 20a suggests that mildly curved bends are fairly common in nature, as 50% of the meander bends analyzed in the considered dataset are characterized by a value of the parameter δ below 0.18. As mentioned in the previous Section, similar arguments would apply to ν_0 . Hence a small ν_0 is also associated with mild meandering.

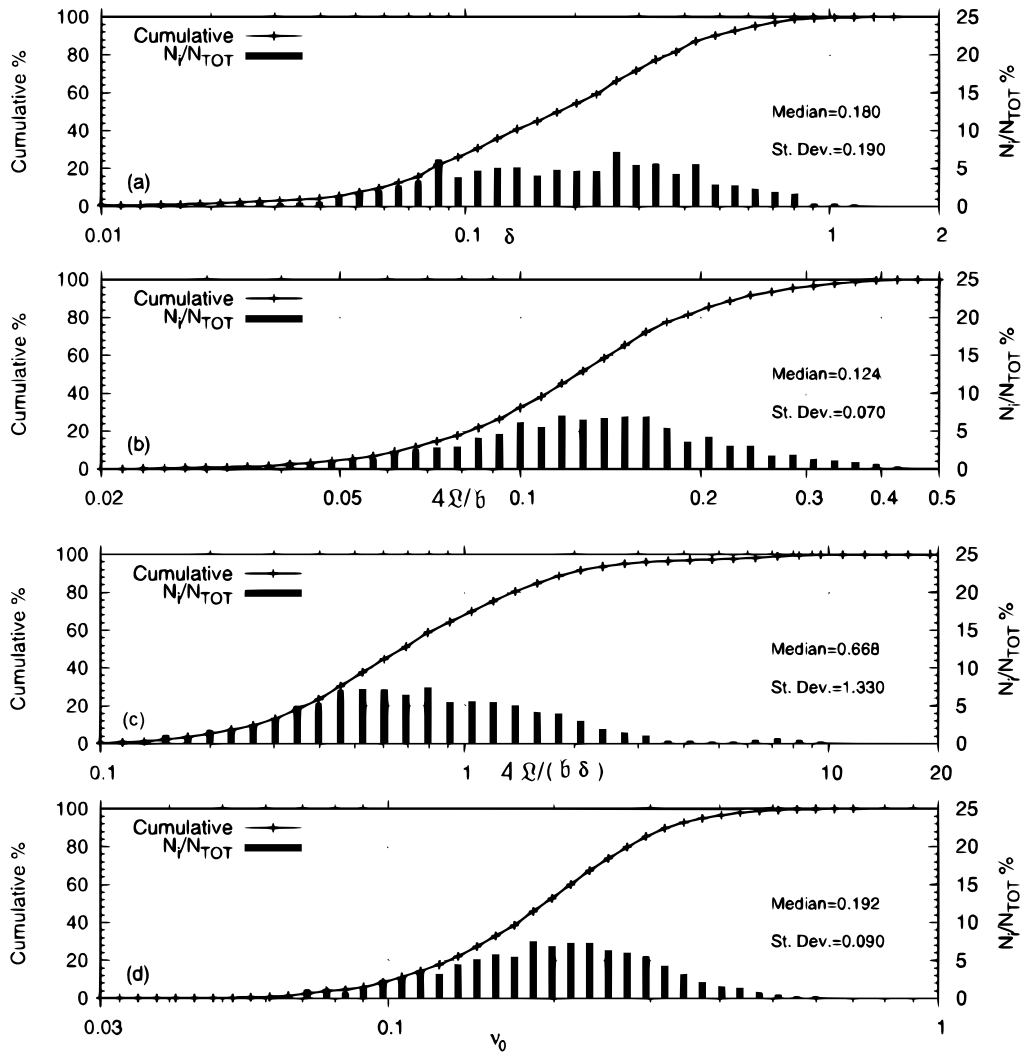


Figure 20. Typical frequency distributions and cumulative frequency curves of the parameters δ , $4\mathcal{L}/b$, $4\mathcal{L}/(b\delta)$ and ν_0 extracted by Bolla Pittaluga and Seminara (2011) from the database of Lagasse *et al.* (2004). Also shown are median values as well as standard deviations (modified from Bolla Pittaluga and Seminara, 2011)

Long versus short bends: topographic steering and the \mathcal{L} parameter

In cohesionless channels the bed is erodible. As a result, the secondary flow transports sediment towards the inner bank where point bars build up, while pools develop at the outer bank. Note that the perturbations of bottom topography thus established are by no means necessarily small relative to the average flow depth. What may be expected to keep small is the *lateral slope* of the bed. However, a small lateral slope may build up a finite perturbation of bed elevation provided the channel is not too narrow. In other words, the flow depth in the cross section of mildly curved bends may undergo variations of the order of the average flow depth.

Note that the development of bed topography drives an additional source of secondary flow through the mechanism that was called *topographic steering* by Dietrich and Smith (1983) and was outlined in Section 2.2.1. Essentially, the bar-pool pattern generated by the action of centrifugally driven secondary flow in meandering channels is associated with longitudinal variations of flow

depth and flow velocity that, by simple continuity requirements, give rise to the development of a further contribution to the lateral component of the flow velocity, i.e. a topographical component of the secondary flow.

In Section 2.2.1 we showed that, balancing the orders of magnitude of the first two terms in equation (51a) topographic steering is found to satisfy the scaling $u_n \sim \mathcal{O}(u_s B/L)$. We then describe a bend as long or short depending on the parameter $B/L = \mathfrak{L}/\mathfrak{b}$ being small or $\mathcal{O}(1)$. In other words, a *long* bend generates a fairly weak topographically induced secondary flow, while in a *short* bend the latter contribution is strong. Figure 20b suggests that long bends are fairly common in nature, as the median value of the parameter $4B/L$ is roughly equal to 0.124. Note that the factor 4 is included because the spatial scale on which the amplitude of the secondary flow varies in the longitudinal direction is a quarter wavelength. Again, one should appreciate that, in a long bend, the perturbations of bottom elevation driven by the action of topographic steering are not necessarily small relative to the average flow depth.

The mathematical problem formulated in the previous sections can be solved numerically and various solutions have indeed been presented in the literature. However, in order to introduce the reader to the full complexity of bend hydrodynamics, it is instructive to investigate analytically a sequence of simple configurations illustrating the variety of physical mechanisms operating in the process. This is the goal we will pursue in the next two sections.

2.4. Flow in constant curvature wide channels

2.4.1 Formulation for the steady state

We start with the simplest configuration, consisting of a sufficiently wide (large β_u) rectangular channel consisting of an upstream straight reach connected downstream to a long bend (small \mathfrak{L}) with constant curvature $1/R_0$ (Figure 21a). Under these conditions, the reference uniform flow is unambiguously defined in the straight upstream reach. Moreover, we assume that *the channel axis of the bend is a circular helix*, i.e. a curve in three-dimensional space such that the tangent line at any point makes a constant angle with the axis of the helix (the z -axis in Figure 21b). In other words, with this special assumption, the longitudinal slope S of the channel axis in the curved reach is a constant, that we may take to coincide with the slope of the straight channel located upstream.

The mathematical advantage of the assumption that the channel has a wide section is that we may neglect contributions proportional to powers of $1/\beta_u$. Clearly, this scheme has important physical limitations that must be fully appreciated. Essentially, the approach does not hold in the boundary layers adjacent to the channel banks. There, the flow properties vary much faster than we assumed when we scaled the lateral coordinate by the channel half width B (recall equation (21)c). In mathematical terms, a straightforward expansion of the flow field in inverse powers of β_u (implicit in our approach) is *not uniformly valid*. It applies only to the *outer region*, namely the region outside the boundary layers forming at the banks. The formulation in the boundary layers differs from that in the outer region and could be obtained by rescaling the lateral coordinate by the characteristic thickness of the boundary layer which is $\mathcal{O}(D_u)$. It is within these boundary layers that the flow field adjusts to the requirement of no slip at the side walls. Fortunately, for the present purposes, we do not need to include the solution in the side wall boundary layers. We then restrict ourselves to the outer region and do not enforce no slip at the channel banks.

The dimensionless formulation of the problem for the steady state is readily obtained from the general formulation presented in the previous section by stipulating that:

$$\mathcal{C} = 1, \quad \frac{\partial}{\partial t} \equiv 0, \quad \beta_u \gg 1. \quad (56)$$

Note that, for the sake of simplicity, *the tilde will be removed and variables will implicitly be assumed dimensionless throughout*. Moreover, we set $L = B$ as, in constant curvature channels, no external longitudinal scale can be identified. As a result, we will replace the parameter \mathfrak{L} with \mathfrak{b}

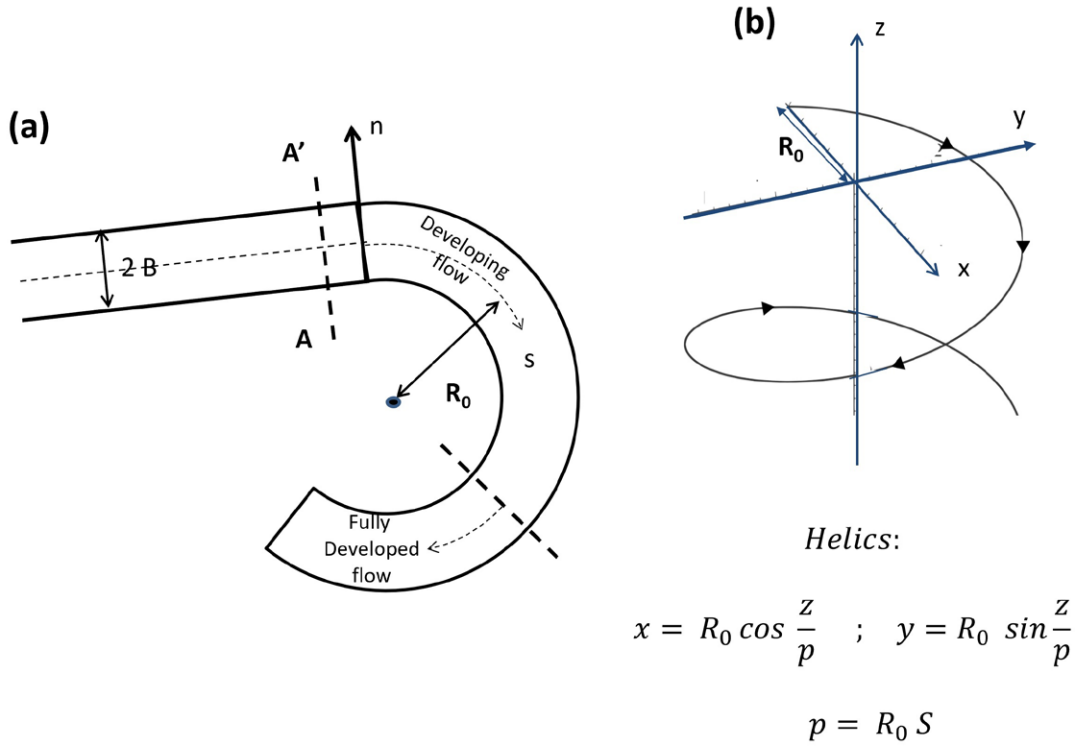


Figura 21. (a) Sketch of a constant curvature rectangular channel. (b) Sketch and equation of a helix: S is the slope of the channel, p is the pitch of the helix.

in the governing equations (51a)-(51c), which can be rewritten as follows:

$$\frac{1}{h_s} \left[\frac{\partial u_s}{\partial s} - \left(\frac{F_{ru}^2}{D} \frac{\partial H}{\partial s} + \frac{\zeta - 1}{D} \frac{\partial D}{\partial s} \right) \frac{\partial u_s}{\partial \zeta} \right] + \left[\frac{\partial u_n}{\partial n} - \left(\frac{F_{ru}^2}{D} \frac{\partial H}{\partial n} + \frac{\zeta - 1}{D} \frac{\partial D}{\partial n} \right) \frac{\partial u_n}{\partial \zeta} \right] + \frac{1}{D} \frac{\partial u_z}{\partial \zeta} = -\frac{\delta}{b h_s} u_n, \quad (57a)$$

$$\frac{1}{D^2} \frac{\partial}{\partial \zeta} \left(\nu_T \frac{\partial u_s}{\partial \zeta} \right) = \frac{b}{h_s} \frac{\partial H}{\partial s} + \frac{b}{h_s} u_s \left[\frac{\partial u_s}{\partial s} - \left(\frac{F_{ru}^2}{D} \frac{\partial H}{\partial s} + \frac{\zeta - 1}{D} \frac{\partial D}{\partial s} \right) \frac{\partial u_s}{\partial \zeta} \right] + b \left\{ u_n \left[\frac{\partial u_s}{\partial n} - \left(\frac{F_{ru}^2}{D} \frac{\partial H}{\partial n} + \frac{\zeta - 1}{D} \frac{\partial D}{\partial n} \right) \frac{\partial u_s}{\partial \zeta} \right] + \frac{u_z}{D} \frac{\partial u_s}{\partial \zeta} \right\} + \frac{\delta}{h_s} u_s u_n, \quad (57b)$$

$$\frac{1}{D^2} \frac{\partial}{\partial \zeta} \left(\nu_T \frac{\partial u_n}{\partial \zeta} \right) = \frac{b}{h_s} \frac{\partial H}{\partial n} + \frac{b}{h_s} u_s \left[\frac{\partial u_n}{\partial s} - \left(\frac{F_{ru}^2}{D} \frac{\partial H}{\partial s} + \frac{\zeta - 1}{D} \frac{\partial D}{\partial s} \right) \frac{\partial u_n}{\partial \zeta} \right] + b \left\{ u_n \left[\frac{\partial u_n}{\partial n} - \left(\frac{F_{ru}^2}{D} \frac{\partial H}{\partial n} + \frac{\zeta - 1}{D} \frac{\partial D}{\partial n} \right) \frac{\partial u_n}{\partial \zeta} \right] + \frac{u_z}{D} \frac{\partial u_n}{\partial \zeta} \right\} - \frac{\delta}{h_s} C u_s^2. \quad (57c)$$

The metric coefficient h_s reads:

$$h_s = 1 + \nu_0 n = 1 + \frac{\delta}{b} n. \quad (58)$$

The boundary conditions associated with the above governing equations are also simplified and

read:

$$u_s = u_n = u_z = 0 \quad (\zeta = \zeta_0), \quad (59a)$$

$$u_z = F_{ru}^2 \left[\frac{u_s}{h_s} \frac{\partial H}{\partial s} + u_n \frac{\partial H}{\partial n} \right] \quad (\zeta = 1), \quad (59b)$$

$$\frac{\partial u_s}{\partial \zeta} = \frac{\partial u_n}{\partial \zeta} = 0 \quad (\zeta = 1). \quad (59c)$$

Finally, an integral condition must be satisfied, such to ensure that the flow discharge does not vary in the longitudinal direction, hence:

$$\int_{-1}^1 \left(D \int_{\zeta_0}^1 u_s d\zeta \right) dn = 2. \quad (60)$$

In constant curvature bends with rectangular cross section, the bend hydrodynamics is dominated by two effects: the so called *free vortex effect* and the generation of a *curvature driven secondary flow*. The first is related to the fact that, entering the bend, the fluid feels a variation of the longitudinal bed slope in the lateral direction. Indeed, the length of the circular path connecting two cross sections increases proceeding from the inner to the outer channel bank, hence the bed-slope decreases outwards (Figure 22). This is a *metric effect* which tends to accelerate the inner flow and retard the outer flow (like in a free vortex). The second effect is due to the curvature of the channel banks that forces fluid particles to follow curved streamlines. This is only possible provided particles are able to develop a centripetal acceleration. The mechanism to provide such an acceleration is the establishment of an inward directed pressure gradient, which requires that the free surface develops a lateral slope. This leads to the generation of a secondary flow controlled by the imbalance between the required centripetal acceleration (which is proportional to the square of the local velocity) and the available lateral pressure gradient. More precisely, the lateral pressure gradient is insufficient for the high momentum fluid located in the upper part of the cross section, which is then displaced from the inner to the outer channel bank. On the contrary, the lateral pressure gradient exceeds the centripetal acceleration required by the low momentum fluid located in the lower part of the cross section, which is then forced to move in the inward direction close to the bed (Figure 22). The curvature driven secondary circulation develops in space starting

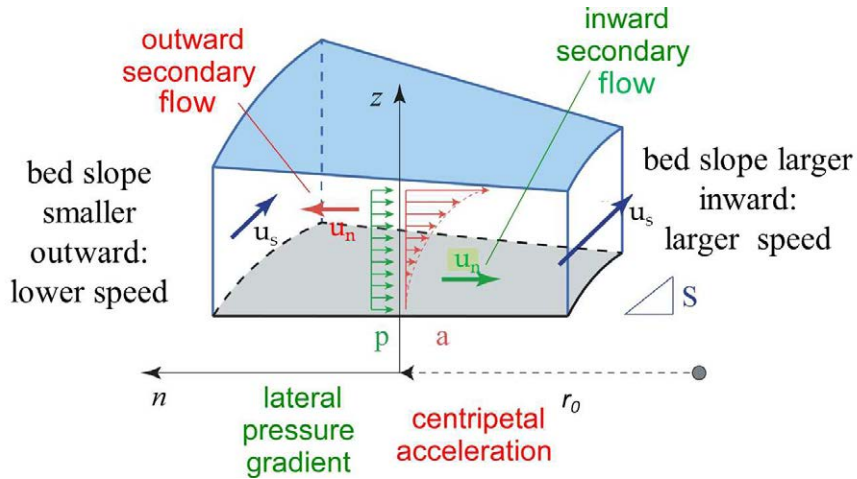


Figure 22. Sketch of the mechanism of generation of the *free vortex effect* and *curvature driven secondary flow*

from the bend inlet until the flow reaches a new (*fully developed*) uniform state, albeit no longer unidirectional.

It is instructive to start investigating this fully developed flow field.

2.4.2 Fully developed steady flow in mildly curved channels: free vortex effect and the role of curvature

In the fully developed case, the formulation is obtained from that presented in the previous section by simply assuming that the velocity field and the gradient of free surface elevation, i.e. the flow properties in the governing momentum equations, do not vary in the longitudinal direction. Note that the governing equations of the problem, even in the case of wide channels, retain their nonlinear character, hence they are non amenable to simple analytical treatment in general. A fully analytical approach is, however, possible in a particular, yet non trivial, case, namely for *weakly curved* bends, which is discussed in detail below starting from the case of flat laterally horizontal bottom. Let us then employ the *mildly curved* approximation and assume:

$$\nu_0 \ll 1, \quad \delta \ll 1. \quad (61)$$

Note that these two constraints are essentially equivalent, as discussed in Section 2.3.

Let us then get advantage from (61) to seek a solution for the flow field expanded in powers of the small parameter δ in a neighborhood of the uniform solution as follows:

$$\begin{aligned} [u_s, u_n, u_z, H, D, \nu_T] = & \\ & \delta^0 [u_{s0}(\zeta), 0, u_{z0}(\zeta), H_u(s) + h_0, D_0, \nu_{T0}(\zeta)] + \\ & \delta [u_{s1}(n, \zeta), u_{n1}(\zeta), u_{z1}(n, \zeta), h_1(n), D_1(n), \nu_{T1}(n, \zeta)] + \mathcal{O}(\delta^2), \end{aligned} \quad (62)$$

where, due to the fixed character of the bed, the flow depth is expressed in terms of free surface elevation as follows:

$$D_0 = 1 + F_{ru}^2 h_0, \quad D_1(n) = F_{ru}^2 h_1(n). \quad (63)$$

At the leading order of approximation u_{s0} and u_{z0} are only functions of the normalized vertical coordinate ζ . We also allow for the possibility that an s -independent correction (h_0) of the uniform free surface elevation ($H_u(s)$) be needed to satisfy the integral constraint (60).

Moreover, a simple closure for ν_T is justified by the assumptions of wide cross section and mildly curved bend. We assume that the eddy viscosity retains the same vertical dependence it experiences in a straight channel but its amplitude varies in the lateral direction in direct proportion to the local values of the friction velocity and flow depth. Hence we write:

$$\nu_T = \sqrt{\frac{C_f}{C_{fu}}} U(n) D(n) \mathcal{N}(\zeta), \quad (64)$$

where $\mathcal{N}(\zeta)$ is the dimensionless form of the eddy viscosity of the reference uniform flow (see Section 2.3.4(I)) and $U(n)$ denotes the vertically averaged longitudinal component of the dimensionless flow velocity defined in the form:

$$U(n) = \frac{1}{D} \int_{\eta+z_0}^{Fr^2H} u_s dz = \int_{\zeta_0}^1 u_s d\zeta = U_0 + \delta U_1 + \mathcal{O}(\delta^2) \quad (65)$$

Using Strickler relationship for C_f , with the channel roughness taken to be laterally constant, such that $(C_f)^{-\frac{1}{2}} = \frac{k_s}{\sqrt{g}} D^{1/6}$ (in dimensional form), then, in dimensionless form, one finds that $\sqrt{C_f} = \sqrt{C_{fu}} D^{-1/6}$ and eq. (64) becomes:

$$\nu_T = U(n) D^{\frac{5}{6}}(n) \mathcal{N}(\zeta), \quad (66)$$

We now substitute from (62) into (66) and, with the help of simple algebra, find:

$$\nu_T = \nu_{T0} + \delta \nu_{T1} + \mathcal{O}(\delta^2) \quad (67)$$

where

$$\nu_{T0} = \mathcal{N}(\zeta) U_0 D_0^{5/6}, \quad \nu_{T1} = \nu_{T0} \left(\frac{U_1}{U_0} + \frac{5}{6} \frac{D_1}{D_0} \right). \quad (68a,b)$$

We may now substitute from the expansions (62) and (67) into the governing equations (57) and the related boundary conditions (59), to obtain the following problems at the various orders of approximation in δ .

$\mathcal{O}(\delta^0)$

Let us first consider the continuity equation (57a) which shows that at the leading order, a small vertical component of velocity must be allowed, such that:

$$-F_{ru}^2 \frac{dH_u}{ds} \frac{du_{s0}}{d\zeta} + \frac{du_{z0}}{d\zeta} = 0, \quad (69)$$

and the kinematic boundary condition (59b), which reads:

$$u_{z0} = F_{ru}^2 \frac{dH_u}{ds} u_{s0} \quad (\zeta = 1). \quad (70a)$$

The above differential equation is readily solved to obtain:

$$u_{z0}(\zeta) = F_{ru}^2 \frac{dH_u}{ds} u_{s0}(\zeta). \quad (71)$$

The reader will readily appreciate that u_{z0} is needed in order for the vectorial composition of u_{s0} and u_{z0} to generate a *longitudinal* component of the flow velocity aligned with the channel axis. Indeed, recalling the different scales used for u_s and u_z , the requirement that the vector \mathbf{u}_0 be aligned with the channel axis implies that the ratio u_{z0}/u_{s0} must be equal to $-\beta_u S$ (see sketch in Figure 23). Indeed, in a uniform flow and with the present scaling, one may write:

$$\frac{dH_u}{ds} = -\frac{B}{F_{ru}^2 D_u} S = -\beta_u C_{fu} = -\frac{\sqrt{C_{fu}}}{\mathfrak{b}}. \quad (72)$$

Equating the $\mathcal{O}(\delta^0)$ terms in (57b), one finds the following problem:

$$\frac{1}{D_0^2} \frac{d}{d\zeta} \left(\nu_{T0} \frac{du_{s0}}{d\zeta} \right) = \mathfrak{b} \frac{dH_u}{ds} + \frac{\mathfrak{b}}{D_0} \frac{du_{s0}}{d\zeta} \underbrace{\left(u_{z0} - u_{s0} F_{ru}^2 \frac{dH_u}{ds} \right)}_{\text{vanishing by (71)}} = -\sqrt{C_{fu}}, \quad (73)$$

$$u_{s0}|_{\zeta_0} = 0, \quad \frac{du_{s0}}{d\zeta} \Big|_1 = 0, \quad (74)$$

where use has been made of (71) that shows that the term in square brackets in the right hand side of (73) vanishes. Hence, at the leading order of approximation, the longitudinal flow of weakly

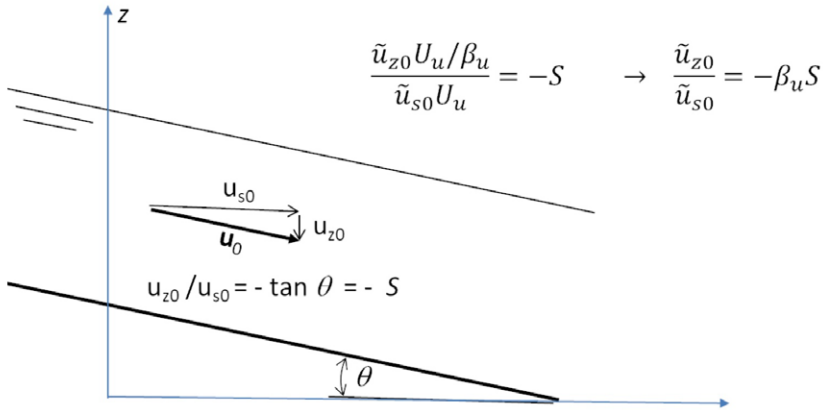


Figura 23. Sketch illustrating the physical interpretation of the component u_{z0} of the vertical velocity

curved wide bends does neither feel the metric effect nor the lateral momentum transfer driven by the secondary flow. Moreover, recalling (68a), one readily shows that it is convenient to set:

$$u_{s0} = U_0 \mathcal{F}_0(\zeta), \quad U_0 = D_0^{7/12}. \quad (75)$$

With the help of (75), the differential problem given by (73), (74) becomes identical with that governing the undisturbed uniform turbulent flow in infinitely wide straight open channels (see Section 2.3.4(I)) which admits of the following solution:

$$\mathcal{F}_0(\zeta) = \left[\frac{\sqrt{C_{fu}}}{k} \ln \left(\frac{\zeta}{\zeta_0} \right) + W_f(\zeta) \right]. \quad (76)$$

Here k is the Von Karman constant, ζ_0 is the scaled distance from the bed where no-slip is conventionally enforced and $W_f(\zeta)$ is the so called wake function (2.66(I)), the specific form of which depends on the particular choice made for the vertical distribution of eddy viscosity $\mathcal{N}(\zeta)$ (see Section 2.3.4(I)). Note that, as a result of scaling, the vertical average of $\mathcal{F}_0(\zeta)$ is equal to one.

Let us finally check whether a correction of the flow depth is required to satisfy the integral constraint (60) at the open boundary. At $\mathcal{O}(\delta^0)$ it leads to the following condition:

$$D_0 \int_{\zeta_0}^1 \left(\int_{-1}^1 u_{s0} dn \right) d\zeta = (1 + F_{ru}^2 h_0)^{19/12} \int_{\zeta_0}^1 \mathcal{F}_0(\zeta) d\zeta \int_{-1}^1 dn = 2, \quad (77)$$

which is satisfied by the simplest requirement:

$$h_0 = 0. \quad (78)$$

Hence, at the leading order, no correction of the free surface elevation is needed and the solution is identical to the straight channel solution, i.e. $D_0 = 1$, $U_0 = 1$.

$\mathcal{O}(\delta)$

Proceeding to the next order, i.e. equating the $\mathcal{O}(\delta)$ terms in the governing equations and boundary conditions, one finds a sequence of differential problems for u_{s1} , u_{n1} and u_{z1} .

Let us then analyze flow continuity, which reads:

$$\frac{\partial u_{n1}}{\partial n} + \frac{\partial u_{z1}}{\partial \zeta} + F_{ru}^2 \frac{dH_u}{ds} \frac{\partial}{\partial \zeta} \left(-u_{s1} + \frac{n}{\mathfrak{b}} u_{s0} \right) + F_{ru}^2 h_1 \frac{d}{d\zeta} \underbrace{\left(-u_{z0} + u_{s0} F_{ru}^2 \frac{dH_u}{ds} \right)}_{\text{vanishing by (71)}} = 0. \quad (79)$$

This equation allows one to determine the vertical component of velocity once its lateral and longitudinal components are known. Indeed, integration of (79) with the help of (70a) and recalling that the no slip condition is enforced at ζ_0 , gives:

$$u_{z1}(\zeta) = -\frac{\partial}{\partial n} \int_{\zeta_0}^{\zeta} u_{n1} d\zeta' + F_{ru}^2 \frac{dH_u}{ds} \left(u_{s1} - \frac{n}{\mathfrak{b}} u_{s0} \right). \quad (80)$$

On the other hand, the kinematic boundary condition at the free surface (59b) at $\mathcal{O}(\delta)$ provides the following constraint:

$$u_{z1} = F_{ru}^2 \frac{dH_u}{ds} \left[u_{s1} - \frac{n}{\mathfrak{b}} u_{s0} \right] \quad (\zeta = 1). \quad (81)$$

Computing (80) for $\zeta=1$ and using (81), we end up with the condition that the integral $\int_{\zeta_0}^1 u_{n1} d\zeta$ must keep constant in the lateral direction. This constant must however vanish owing to no-flux constraint at the channel banks. The lateral velocity must thus satisfy the following requirement:

$$\int_{\zeta_0}^1 u_{n1} d\zeta = 0. \quad (82)$$

We can next solve the lateral component of the momentum equation which, at $\mathcal{O}(\delta)$, reads:

$$\begin{aligned} \frac{\partial}{\partial \zeta} \left[\mathcal{N}(\zeta) \frac{\partial u_{n1}}{\partial \zeta} \right] &= \mathfrak{b} \frac{dh_1}{dn} - u_{s0}^2 + \mathfrak{b} \frac{\partial u_{n1}}{\partial \zeta} \underbrace{\left(u_{z0} - u_{s0} F_{ru}^2 \frac{dH_u}{ds} \right)}_{\text{vanishing by (71)}} \\ &= \mathfrak{b} \frac{dh_1}{dn} - u_{s0}^2, \end{aligned} \quad (83)$$

where use has again been made of (71). This equation represents the mathematical expression of the mechanism of generation of secondary flow illustrated in Figure 22. The differential system given by (83) and the associated boundary conditions

$$u_{n1}|_{\zeta_0} = 0, \quad \frac{\partial u_{n1}}{\partial \zeta} \Big|_1 = 0, \quad (84)$$

is readily solved in the form:

$$u_{n1}(\zeta) = \mathfrak{b} \frac{dh_1}{dn} \mathcal{G}_{10}(\zeta) - \mathcal{G}_{11}(\zeta). \quad (85)$$

Here,

$$\mathcal{G}_{10}(\zeta) = -\frac{1}{\sqrt{C_{fu}}} \mathcal{F}_0(\zeta), \quad (86)$$

while the function $\mathcal{G}_{11}(\zeta)$ is the solution of the following boundary value problem:

$$\frac{d}{d\zeta} \left[\mathcal{N}(\zeta) \frac{d\mathcal{G}_{11}}{d\zeta} \right] = \mathcal{F}_0^2, \quad (87)$$

$$\mathcal{G}_{11}|_{\zeta_0} = 0, \quad \frac{d\mathcal{G}_{11}}{d\zeta}\Big|_1 = 0. \quad (88)$$

Requiring that the solution (85) satisfies the integral constraint (82), one eventually determines the lateral slope of the free surface dh_1/dn required for the net lateral flux to vanish:

$$\frac{dh_1}{dn} = a_1 = -\beta_u C_{fu} I_{\mathcal{G}_{11}}, \quad (89)$$

having denoted by I_f the integral $\int_{\zeta_0}^1 f d\zeta$. Hence,

$$h_1 = h_{10} + h_{11}(n) = h_{10} + a_1 n, \quad (90)$$

with h_{10} lateral average of h_1 .

The final form of u_{n1} then reads:

$$u_{n1} = \mathcal{F}_0(\zeta) I_{\mathcal{G}_{11}} - \mathcal{G}_{11}(\zeta). \quad (91)$$

The Figure 24 shows the vertical distribution of the secondary flow velocity $u_{n1}(\zeta)$ predicted for a given value of the friction coefficient.

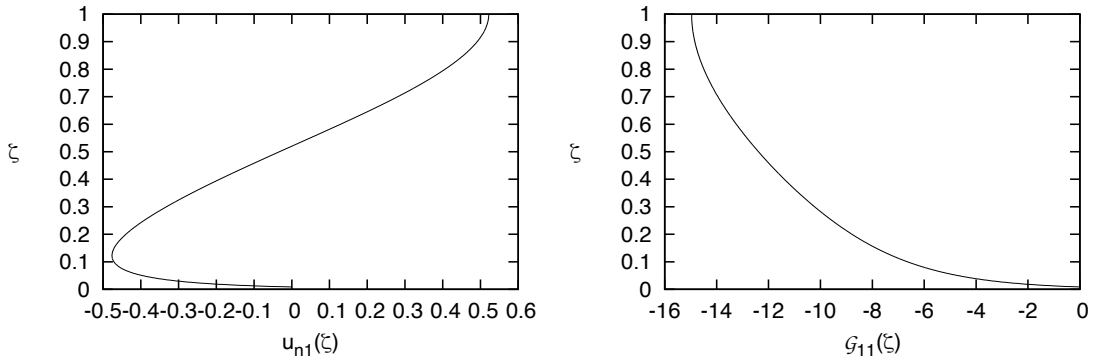


Figure 24. Left: The vertical distribution of the secondary flow velocity $u_{n1}(\zeta)$ predicted for the value 0.01 of the unperturbed friction coefficient C_{fu} and for the \mathcal{N} distribution proposed by Rattray and Mitsuda (1974). Right: The function $\mathcal{G}_{11}(\zeta)$.

The governing equation for u_{s1} reads:

$$\begin{aligned} \frac{\partial}{\partial \zeta} \left[\mathcal{N}(\zeta) \frac{\partial u_{s1}}{\partial \zeta} \right] - 2 F_{ru}^2 h_1 \frac{d}{d\zeta} \left[\mathcal{N}(\zeta) \frac{du_{s0}}{d\zeta} \right] + \frac{\partial}{\partial \zeta} \left[\left(\frac{5}{6} F_{ru}^2 h_1 + U_1 \right) \mathcal{N}(\zeta) \frac{du_{s0}}{d\zeta} \right] = \\ - n \frac{dH_u}{ds} + \mathfrak{b} \left(\frac{\partial u_{s1}}{\partial \zeta} - F_{ru}^2 h_1 \frac{du_{s0}}{d\zeta} \right) \underbrace{\left(u_{z0} - u_{s0} F_{ru}^2 \frac{dH_u}{ds} \right)}_{\text{vanishing by (71)}} \\ + \frac{du_{s0}}{d\zeta} \underbrace{\left[F_{ru}^2 \frac{dH_u}{ds} (n u_{s0} - \mathfrak{b} u_{s1}) + \mathfrak{b} u_{z1} \right]}_{\text{vanishing by (80)}} \end{aligned} \quad (92)$$

$$u_{s1}|_{\zeta_0} = 0, \quad \frac{\partial u_{s1}}{\partial \zeta}\Big|_1 = 0, \quad (93)$$

where we have again assumed that $dh_{10}/ds \equiv 0$.

This system can be largely simplified using (71) and (80) to find:

$$\frac{\partial}{\partial \zeta} \left[\mathcal{N}(\zeta) \frac{\partial u_{s1}}{\partial \zeta} \right] = \left(-\frac{7}{6} F_{ru}^2 h_1 + U_1 + \frac{n}{\mathfrak{b}} \right) \sqrt{C_{fu}}, \quad (94)$$

$$u_{s1} \Big|_{\zeta_0} = 0, \quad \frac{\partial u_{s1}}{\partial \zeta} \Big|_1 = 0. \quad (95)$$

Hence, it turns out that the $\mathcal{O}(\delta)$ correction of the longitudinal component of velocity u_{s1} is driven by three effects associated with the three terms on the right handside of equation (94). The first is a *topographic* contribution associated with variations of the local flow depth. The second is driven by the *perturbation of the friction velocity* which affects the eddy viscosity. The last term accounts for the *metric effect* whereby the flow in the inner region is faster than in the outer region.

By analogy to the $\mathcal{O}(\delta^0)$ problem, this differential system is immediately solved in the form:

$$u_{s1} = \mathcal{F}_0(\zeta) \left(-\frac{n}{\mathfrak{b}} - U_1 + \frac{7}{6} F_{ru}^2 h_1 \right). \quad (96)$$

In order to determine the depth averaged value $U_1(n)$, we simply apply its definition (65) to find:

$$U_1(n) = \int_{\zeta_0}^1 u_{s1} d\zeta \quad \Rightarrow \quad U_1 = \frac{1}{2} \left(-\frac{n}{\mathfrak{b}} + \frac{7}{6} F_{ru}^2 h_1 \right). \quad (97)$$

At last, the integral constraint (60), expanded in powers of δ , at first order gives:

$$\int_{\zeta_0}^1 d\zeta \int_{-1}^1 (u_{s1} + u_{s0} F_{ru}^2 h_1) dn = \int_{-1}^1 U_1(n) dn + 2 F_{ru}^2 h_{10} = \frac{19}{6} F_{ru}^2 h_{10} = 0. \quad (98)$$

Hence, we end up with the trivial conclusion that h_{10} must vanish, i.e. the average flow depth is not perturbed by the effect of curvature. Note that this result is strictly connected to the linear nature of the analysis and to the horizontal configuration of the bed. Indeed, the lateral dependence of u_{s1} has vanishing mean, hence no correction of the average flow depth is needed. Recalling the solution (90) for $h_1(n)$, it follows that the complete solution for the longitudinal component of the flow velocity up to $\mathcal{O}(\delta^2)$ reads:

$$\begin{aligned} u_s &= \mathcal{F}_0(\zeta) \left[1 + \frac{1}{2} \delta \left(-\frac{n}{\mathfrak{b}} + \frac{7}{6} F_{ru}^2 h_{11} \right) + \mathcal{O}(\delta^2) \right] \\ &= \mathcal{F}_0(\zeta) \left[1 - \frac{1}{2} \frac{\delta}{\mathfrak{b}} \left(1 + \frac{7}{6} \sqrt{C_{fu}} F_{ru}^2 I_{G_{11}} \right) n + \mathcal{O}(\delta^2) \right]. \end{aligned} \quad (99)$$

The above solution predicts that, in the fully developed regime, *the thread of high velocity is still located at the inner bend* (where $n < 0$). This is the so called *free vortex effect* and arises from the fact that in wide and weakly curved bends with laterally horizontal bed the lateral transfer of longitudinal momentum arises only at second order. As a consequence, it is a fairly weak effect, so that the outward metric reduction of the bed slope, which is the origin of the free vortex effect, prevails. The solution also shows that the free vortex contribution is corrected by the effect of the lateral slope of the free surface whereby the flow depth increases outward and the flow experiences an acceleration. However, the latter mechanism is typically small in subcritical flows (recall Figure 24b which suggests that $I_{G_{11}}$ is negative and the modulus of the quantity $\sqrt{C_{fu}} I_{G_{11}} / \mathfrak{b}$ is smaller than one). Hence, the free vortex effect prevails. This is clearly illustrated by Figure 25 which shows that the effect of increasing the value of δ is to enhance the flow acceleration at the inner bend relative to the outer bend.

These results confirm also the pioneering observations of Rozovskij (1957) reported in Figure 26. The reader will note that the fluid speed, starting from the entrance of the 180° bend, accelerates

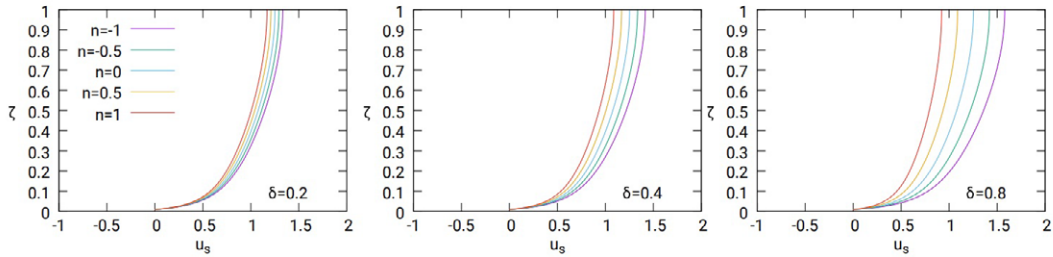


Figure 25. Vertical distribution of the dimensionless longitudinal component of the velocity u_s in the fully developed flow in a curved rectangular channel with constant curvature at different lateral positions ($n=-1, -0.5, 0, 0.5$ and 1), for the $\mathcal{N}(\zeta)$ distribution proposed by Rattray and Mitsuda (1974), with $C_{fu} = 0.01$, $b=2$, $F_{ru}=0.37$ and different values of the curvature parameter δ .

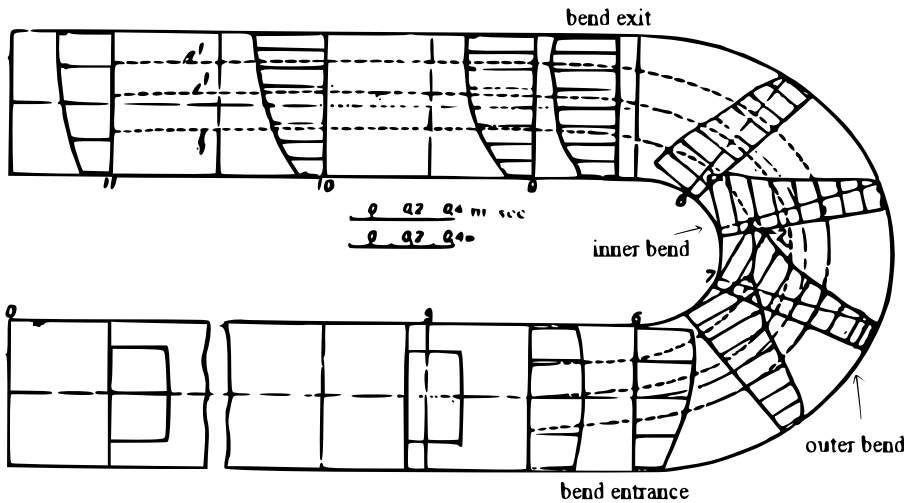


Figure 26. Spatial development of the flow speed at the free surface of a constant curvature channel bend with rectangular cross section, hence with laterally horizontal bed (reproduced from Rozovskij, 1957).

at the inner bank and decelerates close to the outer bank. The thread of high velocity shifts towards the outer bank only close to the bend exit and persists in the downstream rectilinear reach where the uniform distribution is slowly recovered.

2.4.3 Fully developed steady flow in mildly curved channels: the role of bed topography

The secondary flow investigated in the previous Section was driven by a single mechanism, namely, *streamline curvature*. However, in meandering rivers a second component of the secondary flow plays a major role. Essentially, the bed undergoes longitudinal variations of bed elevation that force, by simple continuity requirements, the generation of a *topographically driven* secondary flow. This mechanism, called *topographic steering*, is illustrated in Figure 27 and its importance was originally pointed out by Yen (1970) and Dietrich and Smith (1983). The latter Authors state that: "*Forces arising from topographically induced spatial accelerations are of the same order of magnitude as the downstream boundary shear stress and water surface slope force components, so they must be modeled as zero-order, not first- or second-order, effects*".

Below, we illustrate the role of bed topography by analyzing the fully developed flow in wide rectangular channels with constant weak curvature and prescribed laterally sloping bed. The analysis thus requires small adjustments of that pursued in the previous section.

We again assume that the channel axis is the circular helix determined by the intersection of

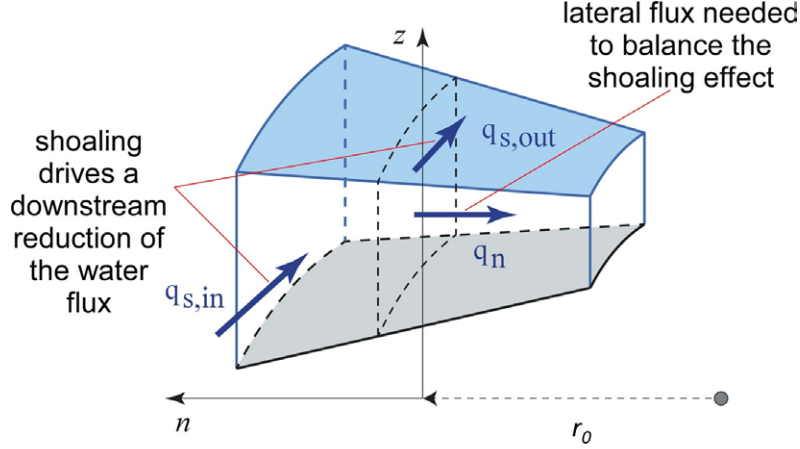


Figure 27. Sketch of the mechanism of *topographic steering*.

the bottom with the curved surface $n = 0$. Again, the longitudinal slope of the channel axis is constant and will be taken to coincide with the slope S of the straight upstream channel. Let us also adopt the same scaling employed in the previous section and assume that the lateral distribution of the dimensionless bed elevation η at a cross section located in the fully developed region of the flow can be written in the form (Figure 28):

$$\eta(s, n) = \eta_a(s) + \eta_d(n), \quad -\frac{d\eta_a}{ds} = \frac{B}{D_u} S, \quad (100)$$

with $\eta_a(s)$ dimensionless bed elevation at the channel axis and $\eta_d(n)$ local deviation of dimensionless bed elevation from the flat horizontal configuration considered in the previous section. Also, the longitudinal scale L has again been taken to coincide with the channel half-width B , given the fully developed nature of the flow field.

Let us express the dimensionless free surface elevation H in the form:

$$H = H_u(s) + h(n), \quad (101)$$

having denoted by h its perturbation relative to the *undisturbed straight uniform value* $H_u(s)$. Note that, due to the fully developed nature of the examined configuration, h can only be a function of the lateral coordinate. As a result, the flow depth is immediately expressed in terms of the perturbation of free surface elevation as follows:

$$D(n) = F_{ru}^2 H - \eta = 1 - \eta_d(n) + F_{ru}^2 h(n), \quad (102)$$

as $F_{ru}^2 H_u(s) - \eta_a(s) = 1$ (see Figure 28). In other words, the flow depth varies laterally due to the fixed prescribed shape of the bottom and undergoes further variations driven by the perturbation of free surface elevation.

Having restricted ourselves to the case of *wide weakly curved* bends, satisfying the conditions (61), we adapt the expansion (62) to the new channel configuration and write it in the form:

$$\begin{aligned} & [u_s, u_n, u_z, h, D, \nu_T] = \\ & [u_{s0}(n, \zeta), 0, u_{z0}(n, \zeta), h_0, D_0(n), \nu_{T0}(n, \zeta)] + \\ & \delta [u_{s1}(n, \zeta), u_{n1}(n, \zeta), u_{z1}(n, \zeta), h_1(n), D_1(n), \nu_{T1}(n, \zeta)] + \mathcal{O}(\delta^2). \end{aligned} \quad (103)$$

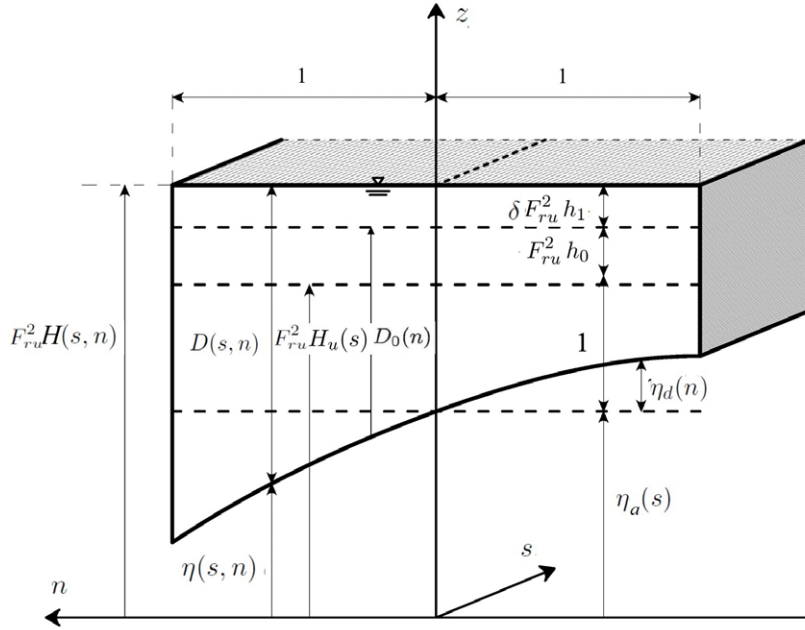


Figure 28. Constant curvature rectangular channel with laterally sloping bed: sketch and notations in terms of dimensionless variables.

where, recalling (102), we may write:

$$D_0(n) = 1 + F_{ru}^2 h_0 - \eta_d(n), \quad D_1(n) = F_{ru}^2 h_1(n). \quad (104a,b)$$

The quantity h_0 is independent of the lateral and longitudinal coordinates and represents a correction of the average flow depth that is needed in order to satisfy the integral constraint (60) at the open boundary.

The closure (66) must also be adapted, as $D(n)$ and $U(n)$ must now be expanded according to (103). Again, adopting the Strickler's formula for C_f , one finds:

$$\nu_{T0} = \mathcal{N}(\zeta) D_0^{5/6}(n) U_0(n), \quad \nu_{T1} = \nu_{T0} \left[\frac{U_1(n)}{U_0(n)} + \frac{5}{6} \frac{F_{ru}^2 h_1(n)}{D_0(n)} \right]. \quad (105a,b)$$

Substituting from (103) into the governing equations (57) and related boundary conditions, the analysis proceeds along the lines of the corresponding analysis described in the previous section.

$\mathcal{O}(\delta^0)$

At the leading order of approximation, one finds:

$$\frac{1}{D_0^2} \frac{\partial}{\partial \zeta} \left(\nu_{T0} \frac{\partial u_{s0}}{\partial \zeta} \right) = \mathfrak{b} \frac{dH_u}{ds} + \frac{\mathfrak{b}}{D_0} \frac{\partial u_{s0}}{\partial \zeta} \underbrace{\left(u_{z0} - u_{s0} F_{ru}^2 \frac{dH_u}{ds} \right)}_{\text{vanishing by (71)}} = -\sqrt{C_{fu}}, \quad (106)$$

$$u_{s0}|_{\zeta_0} = 0, \quad \frac{\partial u_{s0}}{\partial \zeta} \Big|_1 = 0, \quad (107)$$

where use has been made of the relationship (71), that the reader will readily show applies also in the present case. Setting $u_{s0} = U_0(n) \mathcal{F}_0(\zeta)$ and recalling equation (105a), one finds that the lateral coordinate can be scaled out of (106) provided one sets $U_0 = D_0^{7/12}$.

The complete solution for u_{s0} then reads:

$$u_{s0} = D_0(n)^{7/12} \mathcal{F}_0(\zeta). \quad (108)$$

Hence, *the first (and largest) effect of bed topography is that the lateral variations of the flow depth give rise to $\mathcal{O}(1)$ variations of the longitudinal velocity u_{s0} whereby the flow speed increases in the direction of increasing flow depth.*

As mentioned above, this solution must also satisfy the integral constraint (60) at any order of approximation. At the leading order, the following relationship is readily obtained:

$$\int_{-1}^1 D_0^{19/12} dn = 2. \quad (109)$$

Recalling (104a), it turns out that for any given function $\eta_d(n)$, this is an implicit equation for h_0 . Hence: *at the leading order of approximation, the longitudinal slope of the free surface in the curved reach is equal to its value in the straight reach and the flow satisfies the integral constraint by simply varying uniformly its average flow depth.*

$\mathcal{O}(\delta)$

At first order, the problem for the lateral component of velocity u_{n1} is found to read:

$$\begin{aligned} \frac{1}{D_0^2} \frac{\partial}{\partial \zeta} \left(\nu_{T0} \frac{\partial u_{n1}}{\partial \zeta} \right) &= \mathfrak{b} \frac{dh_1}{dn} - u_{s0}^2 + \frac{\mathfrak{b}}{D_0} \frac{\partial u_{n1}}{\partial \zeta} \underbrace{\left(u_{z0} - u_{s0} F_{ru}^2 \frac{dH_u}{ds} \right)}_{\text{vanishing by (71)}} \\ &= \mathfrak{b} \frac{dh_1}{dn} - D_0^{7/6} \mathcal{F}_0^2, \end{aligned} \quad (110)$$

$$u_{n1}|_{\zeta_0} = 0, \quad \frac{\partial u_{n1}}{\partial \zeta} \Big|_1 = 0. \quad (111)$$

The problem for the lateral component of velocity is forced by a centripetal acceleration which is now proportional to $D_0(n)^{7/6}$, i.e. it depends on the lateral coordinate n . Again, setting

$$u_{n1} = U_1(n) \mathcal{G}_1(\zeta), \quad (112)$$

the reader will readily verify that the lateral coordinate can be scaled out of the governing equation for u_{n1} provided one sets:

$$u_{n1} = D_0(n)^{7/4} \mathcal{G}_1(\zeta), \quad \frac{dh_1}{dn} = a_1 D_0(n)^{7/6}, \quad (113a,b)$$

The above assumption implies that:

- the differential problem for the function $\mathcal{G}_1(\zeta)$ is identical to that given by (83) and (84);
- with the use of the equivalent of the integral constraint (82), derived below, the constant a_1 is shown to be given by a relationship identical to (89);
- the function h_1 is readily obtained from the integration of (113b) and reads:

$$h_1 = a_1 \int D_0^{7/6} dn + h_{10}. \quad (114)$$

Having determined u_{n1} we can then calculate the $\mathcal{O}(\delta)$ component of the vertical velocity u_{z1} from the continuity equation (57a), which can be written in the form:

$$\begin{aligned} \frac{1}{D_0} \frac{\partial u_{z1}}{\partial \zeta} &= \frac{F_{ru}^2 h_1}{D_0^2} \underbrace{\left(\frac{\partial u_{z0}}{\partial \zeta} - \frac{\partial u_{s0}}{\partial \zeta} F_{ru}^2 \frac{dH_u}{ds} \right)}_{\text{vanishing by (71)}} + \frac{F_{ru}^2}{D_0} \frac{dH_u}{ds} \left(\frac{\partial u_{s1}}{\partial \zeta} - \frac{n}{\mathfrak{b}} \frac{\partial u_{s0}}{\partial \zeta} \right) \\ &\quad - \frac{\partial u_{n1}}{\partial n} + \frac{(\zeta - 1)}{D_0} \frac{dD_0}{dn} \frac{\partial u_{n1}}{\partial \zeta}. \end{aligned} \quad (115)$$

This is immediately solved, using (71) and imposing the no slip condition for u_{z1} at the bed. One finds:

$$u_{z1} = F_{ru}^2 \frac{dH_u}{ds} \left(u_{s1} - \frac{n}{\mathfrak{b}} u_{s0} \right) + (\zeta - 1) \frac{dD_0}{dn} u_{n1} - \frac{\partial}{\partial n} \left(D_0 \int_{\zeta_0}^{\zeta} u_{n1} d\zeta' \right). \quad (116)$$

The kinematic boundary condition at the free surface (53c), evaluated at $\mathcal{O}(\delta)$ gives:

$$u_{z1} = F_{ru}^2 \frac{dH_u}{ds} \left[u_{s1} - \frac{n}{\mathfrak{b}} u_{s0} \right] \quad (\zeta = 1). \quad (117a)$$

With the latter condition, the solution (116) leads to the constraint:

$$\frac{\partial}{\partial n} \left(D_0 \int_{\zeta_0}^{\zeta} u_{n1} d\zeta' \right) = 0. \quad (118)$$

This is readily integrated imposing the boundary condition of vanishing lateral flux at the channel banks. Since $D_0(\pm 1) \neq 0$, a constraint for $\mathcal{G}_1(\zeta)$ identical to (82) is finally obtained.

The $\mathcal{O}(\delta)$ correction for the longitudinal velocity u_{s1} is the solution of the following differential system:

$$\begin{aligned} \frac{1}{D_0^2} \frac{\partial}{\partial \zeta} \left(\nu_{T0} \frac{\partial u_{s1}}{\partial \zeta} \right) &= \\ &\frac{1}{D_0^2} \left(2 \frac{F_{ru}^2 h_1}{D_0} - \frac{U_1}{U_0} - \frac{5}{6} \frac{F_{ru}^2 h_1}{D_0} \right) \frac{\partial}{\partial \zeta} \left(\nu_{T0} \frac{\partial u_{s0}}{\partial \zeta} \right) - \mathfrak{b} \frac{dH_u}{ds} \frac{n}{\mathfrak{b}} + \\ &\left[\frac{\mathfrak{b}}{D_0} \frac{\partial u_{s1}}{\partial \zeta} - \mathfrak{b} \frac{F_{ru}^2 h_1}{D_0^2} \frac{\partial u_{s0}}{\partial \zeta} \right] \underbrace{\left(u_{z0} - u_{s0} F_{ru}^2 \frac{dH_u}{ds} \right)}_{\text{vanishing by (71)}} + \\ &\frac{\mathfrak{b}}{D_0} \frac{\partial u_{s0}}{\partial \zeta} \left[u_{z1} + F_{ru}^2 \frac{dH_u}{ds} \left(\frac{n}{\mathfrak{b}} u_{s0} - u_{s1} \right) \right] + \\ &\mathfrak{b} u_{n1} \left[\frac{\partial u_{s0}}{\partial n} - \frac{\zeta - 1}{D_0} \frac{dD_0}{dn} \frac{\partial u_{s0}}{\partial \zeta} \right], \end{aligned} \quad (119)$$

$$u_{s1}|_{\zeta_0} = 0, \quad \frac{\partial u_{s1}}{\partial \zeta} \Big|_1 = 0. \quad (120)$$

With the help of (71), (116) and some algebra, this system reduces to the form:

$$\begin{aligned} \frac{1}{D_0^{7/12}} \frac{\partial}{\partial \zeta} \left[\mathcal{N}(\zeta) \frac{\partial u_{s1}}{\partial \zeta} \right] &= \sqrt{C_{fu}} \left(\frac{U_1}{U_0} - \frac{7}{6} \frac{F_{ru}^2 h_1}{D_0} + \frac{n}{\mathfrak{b}} \right) \\ &\quad + \mathfrak{b} D_0^{4/3} \frac{dD_0}{dn} \left(\frac{7}{12} \mathcal{G}_1 \mathcal{F}_0 - \frac{11}{4} \frac{d\mathcal{F}_0}{d\zeta} \int_{\zeta_0}^{\zeta} \mathcal{G}_1 d\zeta' \right), \end{aligned} \quad (121)$$

$$u_{s1}|_{\zeta_0} = 0, \quad \frac{\partial u_{s1}}{\partial \zeta} \Big|_1 = 0, \quad (122)$$

showing that the correction of longitudinal velocity is driven not only by the free vortex (metric) effect and the $\mathcal{O}(\delta)$ corrections of the eddy viscosity as in the case of a laterally horizontal bed (see equation (94)), but also by the convective effect of secondary flow, which plays a major role.

The solution of (121) and (122), reads:

$$u_{s1} = \left(\frac{7}{6} F_{ru}^2 h_1 D_0^{-5/12} - D_0^{7/12} \frac{n}{\mathfrak{b}} - U_1 \right) \mathcal{F}_0(\zeta) + \mathfrak{b} D_0^{23/12} \frac{dD_0}{dn} \mathcal{F}_{11}(\zeta), \quad (123)$$

where the function $\mathcal{F}_{11}(\zeta)$ satisfies the following boundary value problem:

$$\frac{d}{d\zeta} \left[\mathcal{N}(\zeta) \frac{d\mathcal{F}_{11}}{d\zeta} \right] = \frac{7}{12} \mathcal{G}_1 \mathcal{F}_0 - \frac{11}{4} \frac{d\mathcal{F}_0}{d\zeta} \int_{\zeta_0}^{\zeta} \mathcal{G}_1 d\zeta', \quad (124)$$

$$\mathcal{F}_{11}|_{\zeta_0} = 0, \quad \frac{d\mathcal{F}_{11}}{d\zeta} \Big|_1 = 0. \quad (125)$$

The depth averaged velocity at $\mathcal{O}(\delta)$ is found integrating in ζ the solution (123) to find:

$$U_1 = \frac{1}{2} D_0^{7/12} \left(\frac{7}{6} F_{ru}^2 \frac{h_1}{D_0} - \frac{n}{\mathfrak{b}} \right) + \frac{1}{2} \mathfrak{b} D_0^{23/12} \frac{dD_0}{dn} I_{\mathcal{F}_{11}}. \quad (126)$$

Substituting from (126) into (123) one ends up with the following relationship for the first order correction of the longitudinal velocity:

$$u_{s1} = D_0^{7/12} \left(\frac{7}{6} F_{ru}^2 \frac{h_1}{D_0} - \frac{n}{\mathfrak{b}} \right) \frac{\mathcal{F}_0}{2} + \mathfrak{b} D_0^{23/12} \frac{dD_0}{dn} \left(\mathcal{F}_{11} - \mathcal{F}_0 \frac{I_{\mathcal{F}_{11}}}{2} \right). \quad (127)$$

This solution clarifies that topographic steering has additional hydrodynamic effects besides that found at leading order where the outer flow was deeper, hence faster than the inner shallower flow. At first order, three contributions emerge. A correction associated with the perturbation of free surface elevation, a metric effect that accelerates the inner flow relative to the outer flow, and the effect of the lateral transfer of longitudinal momentum which is strongly dependent on the lateral distribution of the flow depth.

In order to complete the solution, we need to determine the $\mathcal{O}(\delta)$ correction of the average free surface elevation $F_{ru}^2 h_{10}$. The constraint (60), imposed at $\mathcal{O}(\delta)$, leads to the following relationship:

$$\int_{\zeta_0}^1 \left[\int_{-1}^1 (F_{ru}^2 h_1 u_{s0} + D_0 u_{s1}) dn \right] d\zeta = 0. \quad (128)$$

Substituting from (127), (108) and (114) into (128) and performing the integration, one finds the following equation for h_{10} :

$$\begin{aligned} N_{(7/12)} F_{ru}^2 h_{10} &= \frac{6}{19\mathfrak{b}} \int_{-1}^1 n D_0^{19/12} dn - a_1 F_{ru}^2 \int_{-1}^1 D_0^{7/12} dn \left(\int D_0^{7/6} dn \right) \\ &\quad - \frac{72}{893} \mathfrak{b} I_{\mathcal{F}_{11}} \left[D_0^{47/12} \right]_{-1}^1, \end{aligned} \quad (129)$$

where we have used the following notation:

$$N_{(a)} \equiv \int_{-1}^1 (D_0)^a dn. \quad (130)$$

Particular cases

The first particular case is the laterally horizontal bed case considered in the previous section. The reader will readily check that, setting $D_0 = 1$ in the above solution, one recovers immediately the solution obtained in Section 2.4.2.

Let us next consider a less trivial particular case. Let bed elevation be linearly decreasing in the outer lateral direction, such that:

$$\eta = \eta_a - S_n n \quad \Rightarrow \quad D_0 = 1 + F_{ru}^2 h_0 + S_n n = \bar{D}_0 + S_n n, \quad (131)$$

with η_a dimensionless bed elevation at the centerline, S_n the lateral bed slope an $\mathcal{O}(1)$ quantity, and $\bar{D}_0 (\equiv 1 + F_{ru}^2 h_0)$ the laterally averaged dimensionless flow depth at leading order.

With the latter assumptions the quantity $N_{(a)}$ is readily expressed in the following form:

$$N_{(a)} = \frac{1}{S_n(a+1)} [(\bar{D}_0 + S_n)^{a+1} - (\bar{D}_0 - S_n)^{a+1}], \quad (132)$$

An implicit equation for \bar{D}_0 , or equivalently for h_0 , is obtained from the constraint (109), which reads:

$$N_{(19/12)} = 2. \quad (133)$$

Using (132) and using a trial and error procedure one finds the solution plotted in Figure 29.

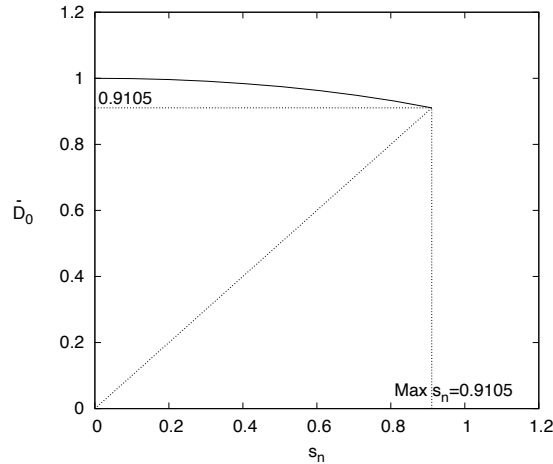


Figure 29. Relationship between the lateral slope of the bed profile in a constant curvature bend and reduction of the mean flow depth relative to its value in the straight upstream reach.

Note that, *as the lateral slope of the bed profile increases, the mean flow depth in the curved reach \bar{D}_0 decreases relative to its value in the upstream straight reach.* This is a consequence of the fact that the flow discharge per unit width is nonlinearly dependent on the local flow depth with exponent larger than one. As a result the faster flow in the outer half of the cross section prevails on the slower flow in the inner half. A flow depth lower than in the straight reach is thus needed to allow the flow of the prescribed discharge. Also, note that *a threshold value for S_n exists, above which the flow in the curved reach can no longer fill the entire channel width.* This is an obvious corollary of the previous observation. As S_n increases, the minimum flow depth decreases and the lowering of the free surface increases, until the free surface emerges at the inner wall and, consequently, $\bar{D}_0 = S_n = 0.5 (31/12)^{12/19} = 0.9105$.

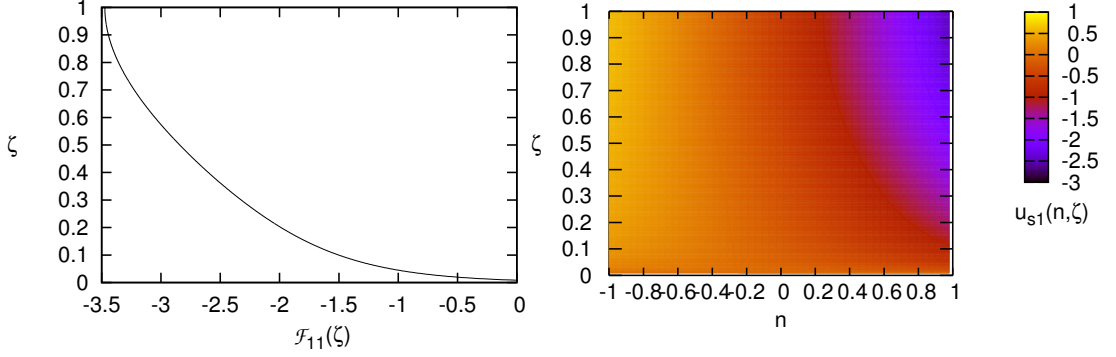


Figure 30. Left panel: The function $\mathcal{F}_{11}(\zeta)$ contributing to the $\mathcal{O}(\delta)$ correction for the longitudinal velocity u_{s1} is plotted for a given value of the friction coefficient $C_{fu} = 0.01$ and for the $\mathcal{N}(\zeta)$ distribution proposed by Rattray and Mitsuda (1974). Right panel: Distribution of $u_{s1}(\zeta, n)$ for $S_n=0.5$, $\mathfrak{b}=2$, and $F_{ru}=0.37$.

Next, we can solve (124), (125) for \mathcal{F}_{11} . The function $\mathcal{F}_{11}(\zeta)$ is plotted in the left panel of Figure 30.

We then derive the function $h_1(n)$ from the integration of (114), to find:

$$h_1(n) = \frac{6 a_1}{13 S_n} D_0^{13/6} + h_{10}, \quad (134)$$

where the quantity h_{10} is determined as a function of S_n , solving (129) to find:

$$h_{10} = -\frac{6}{13} \frac{a_1}{S_n} \frac{N_{(33/12)}}{N_{(7/12)}} - \frac{6}{19} \mathfrak{b} S_n \frac{I_{\mathcal{F}_{11}}}{F_{ru}^2} \frac{N_{(35/12)}}{N_{(7/12)}} + \frac{72}{589} \frac{1}{\mathfrak{b} S_n F_{ru}^2} \left[\frac{(\bar{D}_0 + S_n)^{31/12} + (\bar{D}_0 - S_n)^{31/12}}{N_{(7/12)}} - \frac{N_{(31/12)}}{N_{(7/12)}} \right]. \quad (135)$$

Finally, we substitute from (134) into (127) and derive the solution for the first order correction of the longitudinal velocity u_{s1} . The distribution of $u_{s1}(\zeta, n)$ is plotted in the right panel of Figure 30 for given values of the relevant physical parameters.

Results for the main properties of the flow and topography fields are plotted in Figure 31. Figure 31a and Figure 31b show the lateral distributions of the flow depth at the lowest order D_0 and the coefficient h_1 of the first order perturbation, respectively. Note that the latter quantity increases strongly with the slope S_n such to make the perturbation expansion progressively invalid. The same argument applies to the contribution of the lateral transfer of longitudinal momentum (last term in the right hand side of (127)) which is proportional both to S_n and to a power of D_0 close to two. As a result, the present expansion is expected to hold for values of δ decreasing as S_n increases.

For a low value of δ (0.1) Figure 31g shows that the longitudinal velocity peaks at the outer wall and is minimum at the inner wall, i.e. the effect of topography is to reverse the pattern found in the horizontal bed case ($S_n = 0$) for values of the lateral slope S_n as large as 0.75. Increasing the value of δ (0.2), Figure 31h shows that the trend is similar, though, increasing S_n , the velocity peak tends to be displaced towards the central region.

The three contributions to the order δ correction of the depth averaged longitudinal velocity (equation (126)) are shown in Figure 32. Note that the lateral transfer contribution is everywhere negative and dominant.

2.5. Steady flow in weakly meandering channels

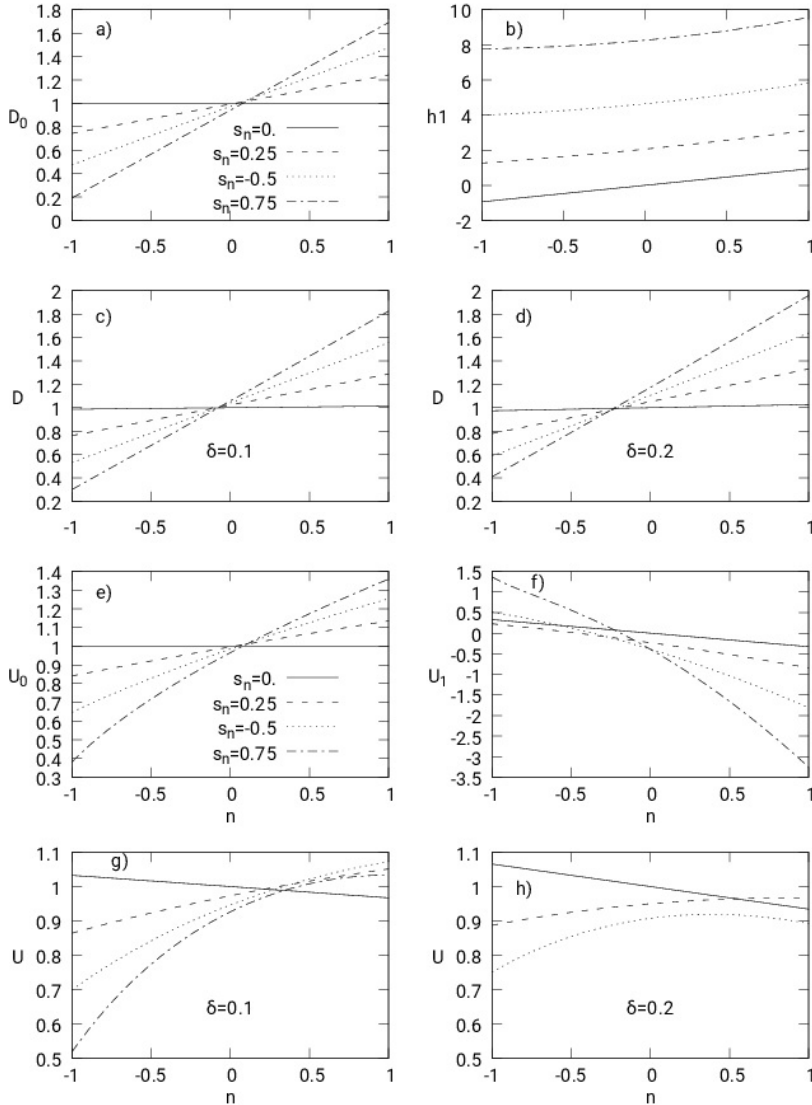


Figure 31. (a) and (b) lateral distributions of the flow depth at the lowest order D_0 and the coefficient h_1 of the first order perturbation, respectively. (c) and (d) lateral distributions of the flow depth D for $\delta = 0.1$ and $\delta = 0.2$. (e) and (f) lateral distributions of the leading order and first order longitudinal component of the depth averaged velocity, respectively. (g) and (h) lateral distributions of the longitudinal component of the depth averaged velocity U for $\delta = 0.1$ and $\delta = 0.2$. Calculations have been performed employing the $\mathcal{N}(\zeta)$ distribution proposed by Rattray and Mitsuda (1974) and assuming $C_{fu} = 0.01$, $b=1.2$, $F_{r-u}=0.37$ and different values of S_n .

We now extend our analysis to the case of a weakly meandering channel with spatially variable topography. The novel feature is the fact that the channel is now characterized by *curvature of the channel axis that varies along the longitudinal coordinate s* . Let $\mathcal{C}(s)$ denote the dimensionless curvature of the longitudinal coordinate line, with s dimensionless and scaled by the meander length L . Below, we still employ dimensionless variables and remove the tilde for simplicity.

The scaling quantities, denoted by the subscript u , will be the properties of the uniform flow of the given fluid discharge in a rectangular channel with constant width $2B$, laterally horizontal bed and constant longitudinal bed slope S , equal to the constant slope of the channel axis. The latter is

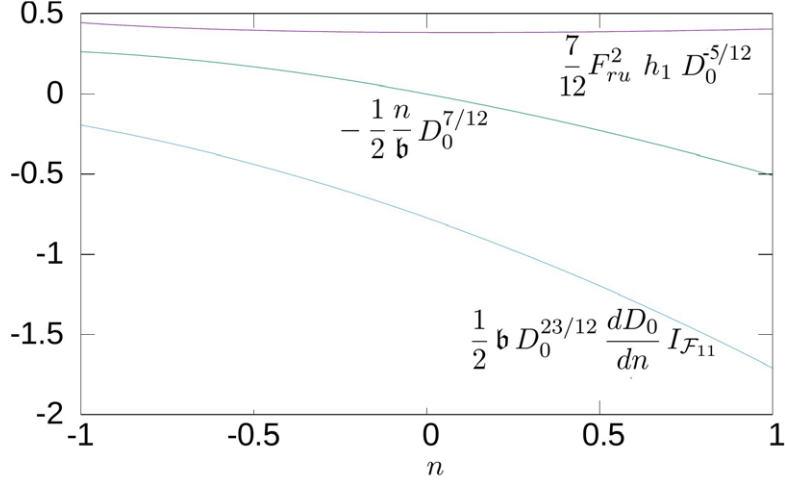


Figure 32. Lateral distribution of the three terms contributing to U_1 in equation (126) for the $\mathcal{N}(\zeta)$ distribution proposed by Rattray and Mitsuda (1974), $C_{fu} = 0.01$, $b=1.2$, $F_{ru}=0.37$ and $S_n = 0.5$.

the curved three-dimensional line $\eta = \eta_a(s)$ lying on the vertical ($z - s$) surface and characterized by constant slope $S = -(D_u/L) d\eta_a/ds$. The effect of a spatially variable topography will be included assuming that the dimensionless elevation of the channel bottom η reads:

$$\eta(s, n) = \eta_a(s) + \eta_d(n) \mathcal{C}(s - \varphi). \quad (136)$$

Hence, superimposed on its constant longitudinal average slope S , the bed displays a lateral slope which undergoes longitudinal harmonic oscillations with wavelength equal to the meander wavelength and spatial lag φ relative to curvature (Figure 33). These oscillations generate a harmonic sequence of *fixed* riffles and pools out of phase relative to curvature as observed in meandering rivers.

Let us employ the usual notations and set:

$$H(s, n) = H_u(s) + h(s, n). \quad (137)$$

The dimensionless flow depth $D(s, n)$ can then be written in the form:

$$D(s, n) = 1 - \eta_d(n) \mathcal{C}(s - \varphi) + F_{ru}^2 h(s, n). \quad (138)$$

The formulation of the hydrodynamic problem in dimensionless form is obtained from the general formulation presented in Section 2.2 by setting:

$$\frac{\partial}{\partial t} \equiv 0, \quad \beta_u \gg 1. \quad (139)$$

Again we seek a fully analytical approach for *weakly meandering* channels, such that the parameter δ may be taken to be small (see equation 61). The further parameter \mathfrak{L} (recall the definition (54b)) accounts for the spatial forcing arising from the longitudinally varying curvature. We assume that the rate of longitudinal variations is *slow*, i.e. the meander wavelength L is sufficiently large to set:

$$\mathfrak{L} = \Lambda \delta \ll 1, \quad (140)$$

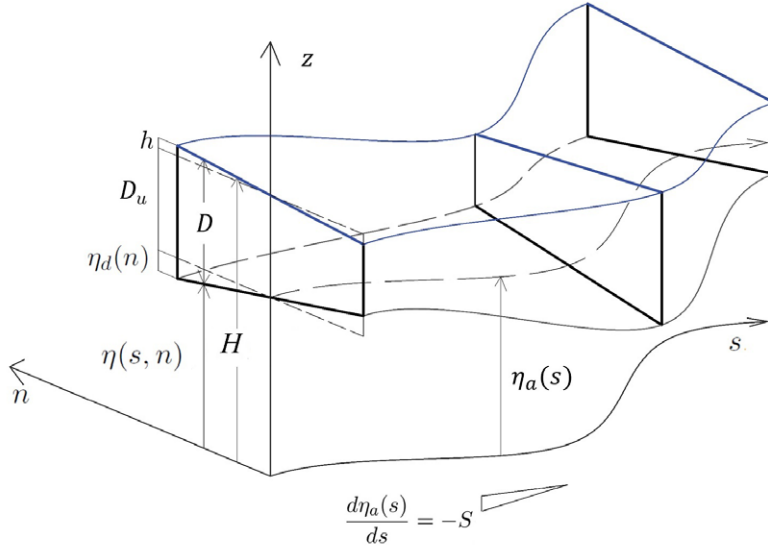


Figure 33. Sketch of a meandering channel with fixed bed and lateral bed slope subject to spatial oscillations lagging ahead of curvature. Quantities in the figure are dimensional.

with

$$\Lambda = \frac{R_0}{L} \sim \mathcal{O}(1). \quad (141)$$

With the above assumptions, the analysis for this problem follows the lines of the approach employed in the previous Sections and is reported below.

We seek a solution for the flow field expanded in powers of the small parameter δ as follows:

$$\begin{aligned} [u_s, u_n, u_z, H, D, \nu_T] = & \\ & + \delta^{-1} [0, 0, 0, h_u(s), 0, 0] \\ & + \delta^0 [u_{s0}(s, n, \zeta), 0, u_{z0}(s, n, \zeta), h_0(s), D_0(s, n), \nu_{T0}(s, n, \zeta)] \\ & + \delta [u_{s1}(s, n, \zeta), u_{n1}(s, n, \zeta), u_{z1}(s, n, \zeta), h_1(s, n), D_1(s, n), \nu_{T1}(s, n, \zeta)] \\ & + \mathcal{O}(\delta^2). \end{aligned} \quad (142)$$

A few comments are in order.

In the present context, the free surface elevation associated with the basic uniform state gives rise to an $\mathcal{O}(\delta^{-1})$ contribution to the free surface slope. This is readily explained noting that:

$$F_{ru}^2 H_u(s) = \eta_a(0) + 1 - \frac{L}{D_u} S s \quad \Rightarrow \quad H_u(s) = H_u(0) - \frac{\sqrt{C_{fu}}}{\Lambda \delta} s = H_u(0) + \frac{h_u(s)}{\delta}. \quad (143)$$

This feature is a consequence of the scaling employed for the longitudinal coordinate, that involves the *slow* longitudinal scale L .

The closure for ν_T is identical to (105) except for the fact that the flow depth D and the depth averaged speed U are now functions of both s and n .

Finally, the presence of a leading order term in the expansion for the vertical component of the flow velocity arises from the usual argument already clarified in the previous sections.

We may now substitute from (136), (139), (142), (105), (143), (144) into the governing equations and related boundary conditions presented in Section 2.2. Equating likewise powers of δ , we find a sequence of differential problems.

$\mathcal{O}(\delta^0)$

The flow depth $D_0(s, n)$ reads:

$$D_0(s, n) = 1 - \eta_d(n) \mathcal{C}(s - \varphi) + F_{ru}^2 h_0(s), \quad (144)$$

where $F_{ru}^2 h_0(s)$ is the leading order perturbation of the free surface elevation, to be determined.

The *continuity equation*, at the leading order, reads:

$$\frac{1}{D_0} \left[-\frac{\Lambda F_{ru}^2}{\mathfrak{b}} \frac{dh_u}{ds} \frac{\partial u_{s0}}{\partial \zeta} + \frac{\partial u_{z0}}{\partial \zeta} \right] = 0. \quad (145)$$

This may immediately be integrated with the help of the kinematic boundary condition (53c) to give an expression for u_{z0} similar to (71), namely

$$u_{z0}(s, n, \zeta) = \frac{\Lambda}{\mathfrak{b}} F_{ru}^2 \frac{dh_u}{ds} u_{s0}(s, n, \zeta). \quad (146)$$

At the leading order of approximation, the *longitudinal momentum equation* leads to a differential problem similar to the corresponding problem for the case treated in Section 2.4.3. A similar solution is thus found:

$$u_{s0}(s, n, \zeta) = U_0(s, n) \mathcal{F}_0(\zeta) = D_0(s, n)^{7/12} \mathcal{F}_0(\zeta). \quad (147)$$

Again, *the first (and largest) effect of the laterally and longitudinally varying topography is the onset of $\mathcal{O}(1)$ lateral and longitudinal variations of u_{s0} described by the function $D_0^{7/12}$* . Note that variations of u_{s0} are not in phase with variations of D_0 in spite of the large wavelength assumption (140) whereby longitudinal derivatives of u_{s0} do not appear at leading order. Indeed, a phase lag arises from the nonlinear dependence of u_{s0} from D_0 .

The integral constraint (60), at leading order, leads to the following relationship:

$$\int_{-1}^1 D_0^{19/12} dn = \int_{-1}^1 [1 - \eta_d(n) \mathcal{C}(s - \varphi) + F_{ru}^2 h_0(s)]^{19/12} dn = 2. \quad (148)$$

This is an equation for $h_0(s)$ which can be solved, for given values of the parameters F_{ru} and φ , once the lateral structure of bed elevation is assigned. Below we will examine the particular case of linearly sloping beds.

$\mathcal{O}(\delta)$

Let us move to the *lateral component of the momentum equation* which, at $\mathcal{O}(\delta)$, reads:

$$\begin{aligned} D_0^{-7/12} \frac{\partial}{\partial \zeta} \left[\mathcal{N}(\zeta) \frac{\partial u_{n1}}{\partial \zeta} \right] &= \mathfrak{b} \frac{\partial h_1}{\partial n} - \mathcal{C}(s) D_0^{7/6} \mathcal{F}_0^2(\zeta) + \\ &\quad \frac{\mathfrak{b}}{D_0} \frac{\partial u_{n1}}{\partial \zeta} \underbrace{\left[u_{z0} - \frac{\Lambda}{\mathfrak{b}} u_{s0} F_{ru}^2 \frac{dh_u}{ds} \right]}_{\text{vanishing by (145)}} \\ &= \mathfrak{b} \frac{\partial h_1}{\partial n} - \mathcal{C}(s) D_0^{7/6} \mathcal{F}_0^2(\zeta), \end{aligned} \quad (149)$$

$$u_{n1}|_{\zeta_0} = 0, \quad \frac{\partial u_{n1}}{\partial \zeta} \Big|_1 = 0. \quad (150)$$

where use has been made of (145). The solution for u_{n1} is readily obtained in the form:

$$u_{n1} = -\frac{\mathfrak{b}}{\sqrt{C_{fu}}} D_0^{7/12} \mathcal{F}_0(\zeta) \frac{\partial h_1}{\partial n} - \mathcal{C}(s) D_0^{7/4} \mathcal{G}_{11}(\zeta), \quad (151)$$

where the function $\mathcal{G}_{11}(\zeta)$ is identical to the solution of the differential problem (87), (88) and the quantity $\partial h_1 / \partial n$ is yet to be determined.

Let us next consider the *continuity equation* at $\mathcal{O}(\delta)$, which reads:

$$\begin{aligned} \frac{1}{D_0} \frac{\partial u_{z1}}{\partial \zeta} + \frac{\Lambda}{\mathfrak{b}} \left\{ \frac{\partial u_{s0}}{\partial s} - \left[\frac{F_{ru}^2}{D_0} \frac{dh_0}{ds} + \frac{\zeta - 1}{D_0} \frac{\partial D_0}{\partial s} \right] \frac{\partial u_{s0}}{\partial \zeta} \right\} \\ + \frac{\partial u_{n1}}{\partial n} - \frac{\zeta - 1}{D_0} \frac{\partial D_0}{\partial n} \frac{\partial u_{n1}}{\partial \zeta} - \frac{\Lambda}{\mathfrak{b}} \frac{F_{ru}^2}{D_0} \frac{dh_u}{ds} \left[-\frac{n}{\mathfrak{b}} \mathcal{C}(s) \frac{\partial u_{s0}}{\partial \zeta} + \frac{\partial u_{s1}}{\partial \zeta} \right] \\ - \frac{D_1}{D_0^2} \underbrace{\left[-\frac{\Lambda}{\mathfrak{b}} F_{ru}^2 \frac{dh_u}{ds} \frac{\partial u_{s0}}{\partial \zeta} + \frac{\partial u_{z0}}{\partial \zeta} \right]}_{\text{vanishing by (145)}} = 0, \end{aligned} \quad (152)$$

where the last term in the left hand side vanishes due to the relationship (145). Imposing the no slip condition at the bed, with the help of (147) and (151), some algebra allows us to solve this equation for u_{z1} to give:

$$\begin{aligned} u_{z1} = & -\frac{\Lambda}{\mathfrak{b}} \mathcal{I}_{\mathcal{F}_0} \frac{\partial(U_0 D_0)}{\partial s} + \frac{\Lambda}{\mathfrak{b}} u_{s0} \left[F_{ru}^2 \frac{dh_0}{ds} + (\zeta - 1) \frac{\partial D_0}{\partial s} \right] \\ & - \frac{\partial}{\partial n} (D_0 \mathcal{I}_{u_{n1}}) + (\zeta - 1) \frac{\partial D_0}{\partial n} u_{n1} \\ & - \frac{F_{ru}^2}{\mathfrak{b}} \sqrt{C_{fu}} \left[u_{s1} - \frac{n}{\mathfrak{b}} \mathcal{C}(s) u_{s0} \right], \end{aligned} \quad (153)$$

having denoted by \mathcal{I}_f the integral $\int_{\zeta_0}^{\zeta} f d\zeta'$.

We next expand the kinematic boundary condition at the free surface (53c). At $\mathcal{O}(\delta)$ one finds:

$$u_{z1}|_1 = \frac{\Lambda}{\mathfrak{b}} u_{s0}|_1 F_{ru}^2 \frac{dh_0}{ds} - \frac{\sqrt{C_{fu}}}{\mathfrak{b}} F_{ru}^2 \left[u_{s1}|_1 - \frac{n}{\mathfrak{b}} \mathcal{C}(s) u_{s0}|_1 \right]. \quad (154)$$

Evaluating $u_{z1}|_1$ from (153), substituting into (154) one finds the following differential equation:

$$\frac{\Lambda}{\mathfrak{b}} \mathcal{I}_{\mathcal{F}_0} \frac{\partial(U_0 D_0)}{\partial s} + \frac{\partial}{\partial n} (D_0 \mathcal{I}_{u_{n1}}) = 0 \quad (155)$$

The reader will readily show that (155) is simply the depth integrated version of the continuity equation in dimensionless form at $\mathcal{O}(\delta)$. Using the solution (151) for u_{n1} , the latter equation transforms into a differential equation for h_1 , which reads:

$$\frac{\mathfrak{b}}{\sqrt{C_{fu}}} \frac{\partial}{\partial n} \left(U_0 D_0 \frac{\partial h_1}{\partial n} \right) + I_{\mathcal{G}_{11}} \frac{\partial D_0^{11/4}}{\partial n} \mathcal{C}(s) - \frac{\Lambda}{\mathfrak{b}} \frac{\partial(U_0 D_0)}{\partial s} = 0, \quad (156)$$

and must be solved along with the no lateral flux condition at the walls. Recalling (151), the latter condition reads:

$$\left[\int_{\zeta_0}^1 u_{n1} d\zeta \right]_{s,-1} = 0 \quad \Rightarrow \quad \frac{\partial h_1}{\partial n} \Big|_{s,-1} = -\frac{\sqrt{C_{fu}} I_{\mathcal{G}_{11}}}{\mathfrak{b}} \mathcal{C}(s) D_0^{7/6} \Big|_{s,-1}. \quad (157)$$

We may next define:

$$h_1(s, n) = h_{10}(s) + h_{11}(s, n), \quad (158)$$

with $h_{11}(s, n)$ obtained from direct integration of (156, 157) and an arbitrary choice for $h_{11}|_{n=-1}$, say $h_{11}|_{n=-1} = 0$. Indeed, it is the function $h_{10}(s)$ which ultimately sets the value of h_1 in $n = -1$. In order to enforce the integral constraint at the open boundary which determines the function $h_{10}(s)$, we need to know the solution for the longitudinal component of the secondary flow u_{s1} .

Evaluating the equation (57b) at $\mathcal{O}(\delta)$ it is found that the correction u_{s1} of the longitudinal velocity satisfies the following differential problem:

$$\begin{aligned} \frac{1}{U_0} \frac{\partial}{\partial \zeta} \left[\mathcal{N}(\zeta) \frac{\partial u_{s1}}{\partial \zeta} \right] &= \sqrt{C_{fu}} \left(-\frac{7}{6} \frac{D_1}{D_0} + \frac{U_1}{U_0} + \frac{n}{\mathfrak{b}} \mathcal{C}(s) \right) + \Lambda \frac{dh_0}{ds} \\ &+ \Lambda u_{s0} \left[\frac{\partial u_{s0}}{\partial s} - \frac{\zeta - 1}{D_0} \frac{\partial D_0}{\partial s} \frac{\partial u_{s0}}{\partial \zeta} \right] - \frac{\Lambda u_{s0}}{D_0} \frac{\partial u_{s0}}{\partial \zeta} F_{ru}^2 \frac{dh_0}{ds} \\ &- \frac{\Lambda F_{ru}^2}{D_0} \frac{dh_u}{ds} \frac{\partial u_{s0}}{\partial \zeta} \left[u_{s1} - \frac{n}{\mathfrak{b}} \mathcal{C}(s) u_{s0} \right] \\ &+ \mathfrak{b} u_{n1} \left[\frac{\partial u_{s0}}{\partial n} - \frac{\zeta - 1}{D_0} \frac{\partial D_0}{\partial n} \frac{\partial u_{s0}}{\partial \zeta} \right] + \frac{\mathfrak{b}}{D_0} u_{z1} \frac{\partial u_{s0}}{\partial \zeta} \\ &+ \frac{\mathfrak{b}}{D_0} \left(\frac{\partial u_{s1}}{\partial \zeta} - \frac{F_{ru}^2 h_1}{D_0} \frac{\partial u_{s0}}{\partial \zeta} \right) \underbrace{\left(u_{z0} - \frac{\Lambda}{\mathfrak{b}} u_{s0} F_{ru}^2 \frac{dh_u}{ds} \right)}_{\text{vanishing by (145)}}, \end{aligned} \quad (159)$$

$$u_{s1}|_{\zeta=\zeta_0} = 0, \quad \frac{\partial u_{s1}}{\partial \zeta} \Big|_{\zeta=1} = 0. \quad (160)$$

Using the solutions for u_{z0} , u_{n1} , u_{z1} and the equation (156), with the help of a considerable amount of algebra, the latter equation reduces to the form:

$$\begin{aligned} \frac{\partial}{\partial \zeta} \left[\mathcal{N}(\zeta) \frac{\partial u_{s1}}{\partial \zeta} \right] &= \sqrt{C_{fu}} D_0^{7/12} \left(-\frac{7}{6} \frac{F_{ru}^2 h_1}{D_0} + \frac{U_1}{U_0} + \frac{n}{\mathfrak{b}} \mathcal{C}(s) + \frac{\Lambda}{\sqrt{C_{fu}}} \frac{dh_0}{ds} \right) \\ &+ \frac{7}{12} D_0^{3/4} \left(\Lambda \frac{\partial D_0}{\partial s} - \frac{\mathfrak{b}^2}{\sqrt{C_{fu}}} \frac{\partial D_0}{\partial n} \frac{\partial h_1}{\partial n} \right) \mathcal{F}_0^2 \\ &+ \mathfrak{b} D_0^{23/12} \frac{\partial D_0}{\partial n} \mathcal{C}(s) \left[\frac{11}{4} \frac{d\mathcal{F}_0}{d\zeta} (\mathcal{I}_{\mathcal{G}_{11}} - \mathcal{I}_{\mathcal{F}_0} \mathcal{I}_{\mathcal{G}_{11}}) - \frac{7}{12} \mathcal{F}_0 \mathcal{G}_{11} \right], \end{aligned} \quad (161)$$

$$u_{s1}|_{\zeta=\zeta_0} = 0, \quad \frac{\partial u_{s1}}{\partial \zeta} \Big|_{\zeta=1} = 0. \quad (162)$$

This system is solved to give:

$$u_{s1} = u_{10}(s, n) \mathcal{F}_0(\zeta) + \sum_{j=1,2} u_{1j}(s, n) \mathcal{F}_{1j}(\zeta). \quad (163)$$

Here, the coefficients $u_{10}(s, n)$ and $u_{1j}(s, n)$ ($j = 1 - 2$) read:

$$u_{10} = D_0^{7/12} \left[\frac{7}{6} \frac{F_{ru}^2 h_1}{D_0} - \frac{U_1}{U_0} - \frac{n}{\mathfrak{b}} \mathcal{C}(s) - \frac{\Lambda}{\sqrt{C_{fu}}} \frac{dh_0}{ds} \right], \quad (164a)$$

$$u_{11} = \frac{7}{12} D_0^{3/4} \left[\Lambda \frac{\partial D_0}{\partial s} - \frac{\mathfrak{b}^2}{\sqrt{C_{fu}}} \frac{\partial D_0}{\partial n} \frac{\partial h_1}{\partial n} \right], \quad (164b)$$

$$u_{12} = \mathfrak{b} D_0^{23/12} \frac{\partial D_0}{\partial n} \mathcal{C}(s). \quad (164c)$$

Moreover, the functions $\mathcal{F}_{1j}(\zeta)$ ($j = 1, 2$) satisfy the following differential systems:

$$\frac{d}{d\zeta} \left[\mathcal{N}(\zeta) \frac{d\mathcal{F}_{1j}}{d\zeta} \right] = \Phi_{1j}, \quad (j = 1, 2) \quad (165a)$$

$$\mathcal{F}_{1j}|_{\zeta_0} = 0, \quad \frac{d\mathcal{F}_{1j}}{d\zeta} \Big|_1 = 0, \quad (165b)$$

with the functions Φ_{1j} ($j = 1, 2$) having the following form:

$$\Phi_{11} = \mathcal{F}_0^2, \quad \Phi_{12} = \left[\frac{11}{4} \frac{d\mathcal{F}_0}{d\zeta} (\mathcal{I}_{\mathcal{G}_{11}} - \mathcal{I}_{\mathcal{F}_0} I_{\mathcal{G}_{11}}) - \frac{7}{12} \mathcal{F}_0 \mathcal{G}_{11} \right]. \quad (166)$$

Finally, let us determine the quantity $h_{10}(s)$ needed to satisfy the integral constraint (60) at any cross section. At $\mathcal{O}(\delta)$ this constraint takes again the form (128). Substituting from (147), (158), (163) and (164) into (128) and performing the integration, one ends up with an expression for $h_{10}(s)$ that may be written in the compact form:

$$h_{10}(s) = - \left(\int_{-1}^1 D_0^{7/12} dn \right)^{-1} \left[\int_{-1}^1 h_{11} D_0^{7/12} dn + \frac{12}{19 F_{ru}^2} \int_{-1}^1 U_{11} D_0 dn \right], \quad (167)$$

where we have employed the following notations:

$$U_1 = I_{u_{s1}} = \frac{7}{12} D_0^{-5/12} F_{ru}^2 h_1 + U_{11}, \quad (168a)$$

$$U_{11}(s, n) = D_0^{7/12} \left[- \frac{n}{2\mathfrak{b}} \mathcal{C}(s) - \frac{\Lambda}{2\sqrt{C_{fu}}} \frac{dh_0}{ds} \right] + \frac{1}{2} \sum_{j=1,2} u_{1j} I_{\mathcal{F}_{1j}}. \quad (168b)$$

In summary, the main physical features of the solution are as follows.

At leading order the flow is purely longitudinal. It retains the form (108) though the amplitude $D_0^{7/12}$ is now a function of both the longitudinal and lateral coordinates (see equation (138)). Hence, *the first (and major) effect of topography is again to give rise to $\mathcal{O}(1)$ lateral and longitudinal variations of u_{s0} . Note that variations of u_{s0} are not in phase with variations of D_0 in spite of the large wavelength assumption (140) as a phase lag arises from the nonlinear dependence of u_{s0} from D_0 .* This nonlinear dependence of the longitudinal velocity on the flow depth has a second major implication. In order to satisfy the integral constraint (60) the longitudinal slope of the free surface must undergo $\mathcal{O}(1)$ spatial variations described by the function $-dh_0/ds$.

At $\mathcal{O}(\delta)$ one finds the usual corrections of the main longitudinal flow. The lateral component of the flow velocity u_{n1} is again forced by two effects. The first is the lateral slope of the free surface $\partial h_1/\partial n$, which is here an oscillating function of the longitudinal coordinate. The second is the centripetal acceleration associated with the curvilinear character of the longitudinal flow, which drives a contribution proportional to the local curvature of the channel axis $\mathcal{C}(s)$. However, unlike the constant curvature case, the lateral slope of the free surface is not determined by the condition that the secondary flow must have vanishing mean. Indeed, a topographically driven component of the secondary flow with non vanishing depth-average arises from the longitudinal dependence of the flow depth.

Similarly, continuity suggests that the vertical correction u_{z1} of the flow velocity also involves topographically driven contributions associated with the spatial variations of the longitudinal and lateral fluxes.

The longitudinal correction u_{s1} , besides the metric effect and the corrections of eddy viscosity due to perturbations of the flow depth and average flow velocity, feels the effects of convection of longitudinal momentum by the secondary flow. This is due to the spatially varying topography which determines $\mathcal{O}(1)$ lateral variations of the longitudinal velocity.

Finally, an s -dependent correction of the laterally averaged free surface elevation, h_{10} , is needed in order to satisfy the integral constraint (60) at any cross section.

Pictures of the spatial distribution of the secondary flow and of the dependence of the lateral slope on the longitudinal coordinate for different values of the relevant parameters are given below for the particular case of sine generated meanders.

The particular case of sine generated meanders

Let us now consider a particular case. Let the dimensionless curvature of the channel axis read:

$$\mathcal{C}(s) = \cos(2\pi s) = \frac{1}{2} \exp(2\pi i s) + c.c. . \quad (169)$$

This is the so called *sine generated curve* that Langbein and Leopold (1966) have suggested to be a good fit of observed shapes of meandering channels. With the above choice, *the scaling curvature* R_0^{-1} *is the peak curvature at the bend apex* and the scaling length L *is the intrinsic meander wavelength* (i.e. the wavelength defined along the channel axis).

Next, let us assume that the lateral slope of the bed is constant and write:

$$\eta_d(n) = -S_n n. \quad (170)$$

Thus, bed oscillations have peak dimensionless scour-deposit equal to $\pm S_n$. The constant lateral slope assumed for the bed profile is obviously the simplest choice to investigate the role of bed topography. The actual profile established in cohesionless meandering channels is determined by their morphodynamics and will be investigated in the next Chapter.

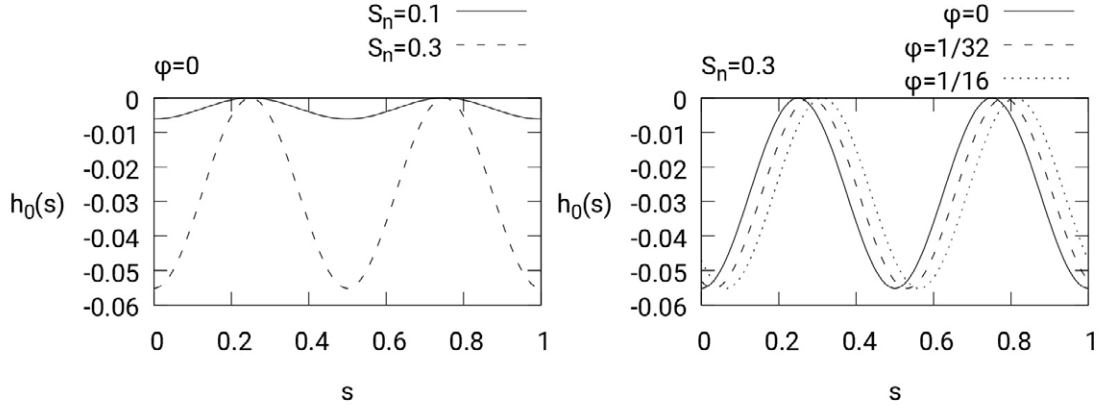


Figure 34. The leading order correction of the free surface elevation $h_0(s)$ in a meandering channel with fixed bed and lateral bed slope subject to sine generated spatial oscillations. The function $h_0(s)$ is plotted for $F_{ru} = 0.04$ and various values of the lateral bed slope S_n and of its phase lag φ relative to curvature.

Substituting from (170) into (148) one finds:

$$\begin{aligned} \frac{31}{6} S_n \cos 2\pi(s - \varphi) &= [1 + S_n \cos 2\pi(s - \varphi) + F_{ru}^2 h_0(s)]^{31/12} \\ &\quad - [1 - S_n \cos 2\pi(s - \varphi) + F_{ru}^2 h_0(s)]^{31/12}. \end{aligned} \quad (171)$$

This is an algebraic equation for $h_0(s)$ to be solved for given values of the parameters F_{ru} , S_n and φ which is readily shown to reduce to (133) in the particular case of fully developed flow and constant curvature. Moreover, the reader will readily show that expanding (171) in a neighborhood

of $S_n = 0$, equation (171) reduces to (77), i.e. the particular case of fully developed flow and constant curvature and $h_0(s)$ identically vanishes. The function $h_0(s)$ is plotted in Figure 34 for various values of parameters S_n and φ . It turns out that $h_0(s)$ is invariably negative. Hence *the flow depth required to let the given discharge flow steadily in a meandering channel with laterally sloping bed is everywhere lower than the flow depth needed to allow for the uniform flow of the same discharge in an equivalent meandering channel with laterally horizontal bed*. This is not surprising: since the speed is nonlinearly dependent on flow depth, the increase of water flux driven by the outer deepening of the cross section prevails on the decrease of water flux associated with the inner depth reduction, hence the average flow depth must decrease. Also, the spatial oscillations of the lateral bed slope drive analogous *spatial oscillations of the average free surface elevation*. Note that the frequency of the spatial oscillations of $h_0(s)$ is twice the fundamental meander frequency. Indeed, as the balance of the water flux is insensitive to the sign of the lateral bed slope. These results confirm qualitatively the earlier observations of Hooke (1974) (see Figure 3 of Hooke, 1974).

Similarly, substituting from (170) into (156) and its associated boundary conditions, the solution for $h_{11}(s, n)$ is readily obtained numerically at each cross section

Having determined the functions $h_0(s)$ and $h_{11}(s, n)$ we can then solve for $u_{n1}(s, n, \zeta)$ using (151). In Figure 35 we plot the spatial distribution of the depth averaged lateral velocity $V_1(s, n) = I_{un1}$ and the dependence of its peak in a meander wavelength on the lateral bed slope S_n and on the dimensionless meander wavelength D_u/L , for given values of the relevant physical parameters (note that d_s is the relative roughness d/D_u).

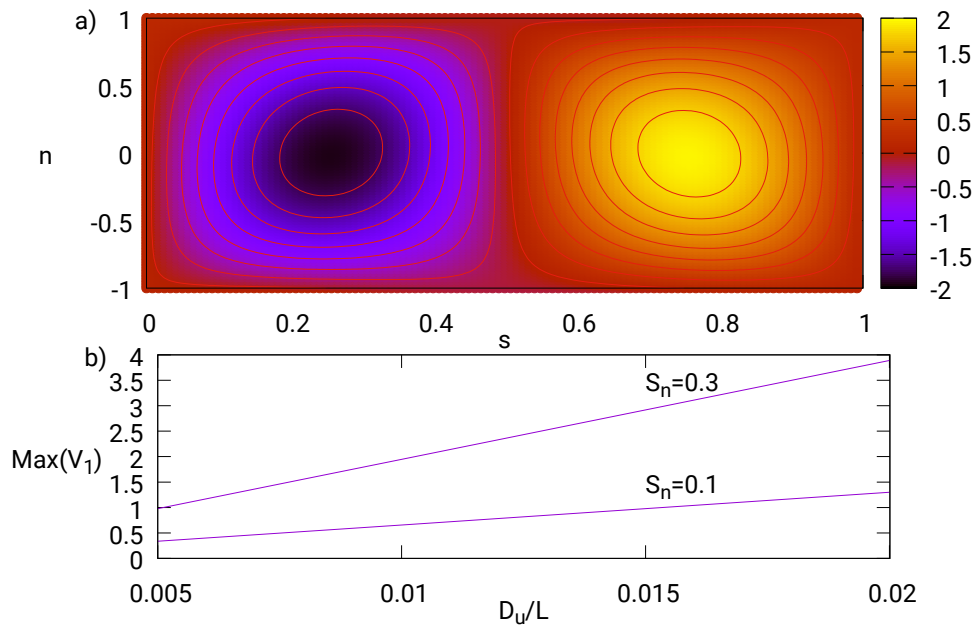


Figure 35. (a) The spatial distribution of the depth averaged first order component of the lateral velocity $V_1(s, n)$ for a meandering channel with meander wavelength $L = 10^2 D_u$, fixed bed and lateral bed slope $S_n = 0.3$ subject to spatial oscillations $\eta(s, n) = \eta_a - S_n n \cos(2\pi s)$. (b) The peak of $V_1(s, n)$ in a meander wavelength is plotted versus D_u/L for various values of the lateral slope S_n . In both plots the relevant dimensionless parameters take the following values: $\varphi = 0$, $C_{fu} = 0.01$, $\delta = 0.06$, $b = 1.23$, $F_{ru} = 0.4$, corresponding to $\nu_0 = 0.05$, $\beta_u = 8$, $\tau_{*u} = 0.1$, $d_s = 0.01$.

We can then proceed to solve (156), (157) for $h_{11}(s, n)$ with the boundary condition $h_{11}|_{n=-1} = 0$. Next, we evaluate the function $h_{10}(s)$ from (167). Finally, we use (158) to evaluate the function $h_1(s, n)$. The lateral average $h_{1avg}(s, n)$ of the function $h_1(s, n)$ and the function $h_1(s, n) - h_{1avg}(s)$ are plotted in Figure 36, for given values of the relevant parameters.

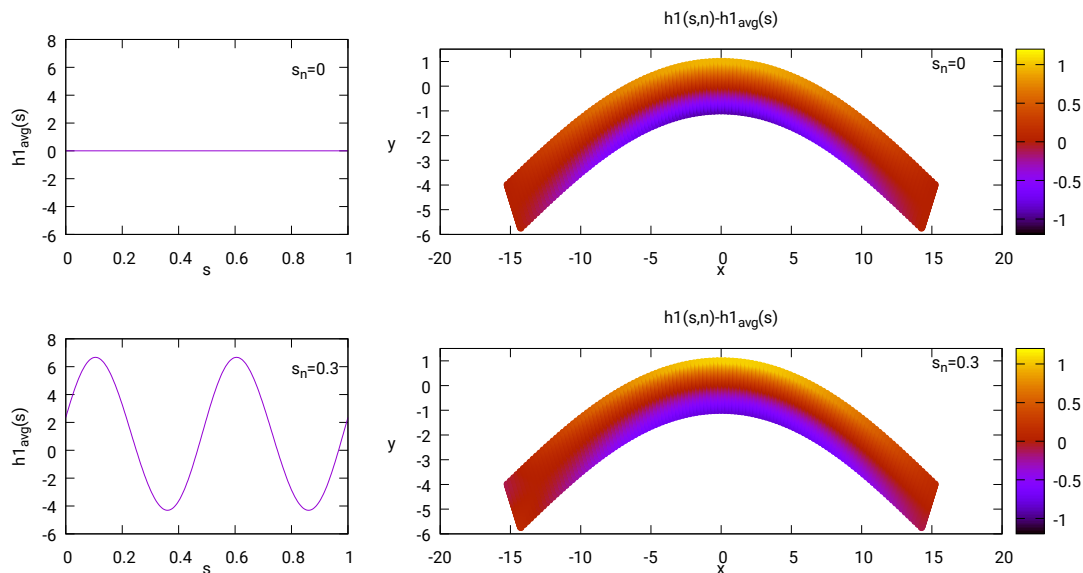


Figure 36. The lateral average $h_{1,avg}(s, n)$ of the function $h_1(s, n)$ (left panels) and the function $h_1(s, n) - h_{1,avg}(s)$ (right panels) are plotted for given values of the relevant parameters: $\varphi = 0$, $C_{fu} = 0.01$, $\delta = 0.06$, $b = 1.23$, $F_{ru} = 0.4$, corresponding to $\nu_0 = 0.05$, $\beta_u = 8$, $\tau_{*u} = 0.1$, $d_s = 0.01$. *Top:* $S_n = 0$, *Bottom:* $S_n = 0.3$. Note that the dimensionless Cartesian coordinates x and y are scaled by half the channel width B , with $x = 0$ corresponding to $s = 0$ and $x = 15$ to $s = 0.25$.

In the case of laterally horizontal bottom (upper plots) the lateral slope of the free surface is in phase with curvature. Moreover, no $\mathcal{O}(\delta)$ correction of the laterally averaged free surface elevation is needed in order to satisfy the constraint of constant flow discharge. In the case of laterally sloping bottom (lower plots) an $\mathcal{O}(\delta)$ correction of the laterally averaged free surface elevation is needed and is found to undergo periodic oscillations with spatial frequency twice the meander frequency.

Finally, from the differential systems (165a)-(165b) we can derive the solution for the $\mathcal{O}(\delta)$ correction of the longitudinal velocity. The resulting depth averaged velocity field $U(s, n)$ is plotted in Figure 37. Note the distinct behavior of the longitudinal velocity field in the cases of laterally horizontal and laterally sloping topographies. In the former case, the metric effect dominates such that the thread of high velocity lies close to the inner bank at the bend apex and the velocity pattern is in phase with curvature. In the latter case, topography dominates and the thread of high velocity moves towards the outer bank. Moreover, topography drives a phase lag between velocity pattern and channel curvature, the former lags behind the latter, the more so as φ increases. These results are in qualitative agreement with the early model of Smith and McLean (1984).

2.6. Sharp bends

As discussed in Section 2.3, sharp bends are characterized by values of channel curvature large enough for both the δ and ν_0 parameters to attain finite values. Figure 20 shows that a small fraction of bends observed in nature are indeed sharp. In the last decade, the hydrodynamics of sharp bends has received considerable attention in a sequence of papers of Blanckaert and his coworkers. Let us examine what novel features are brought up when channel curvature assumes large value.

2.6.1 Enhancement and saturation of the centrifugally driven secondary flow

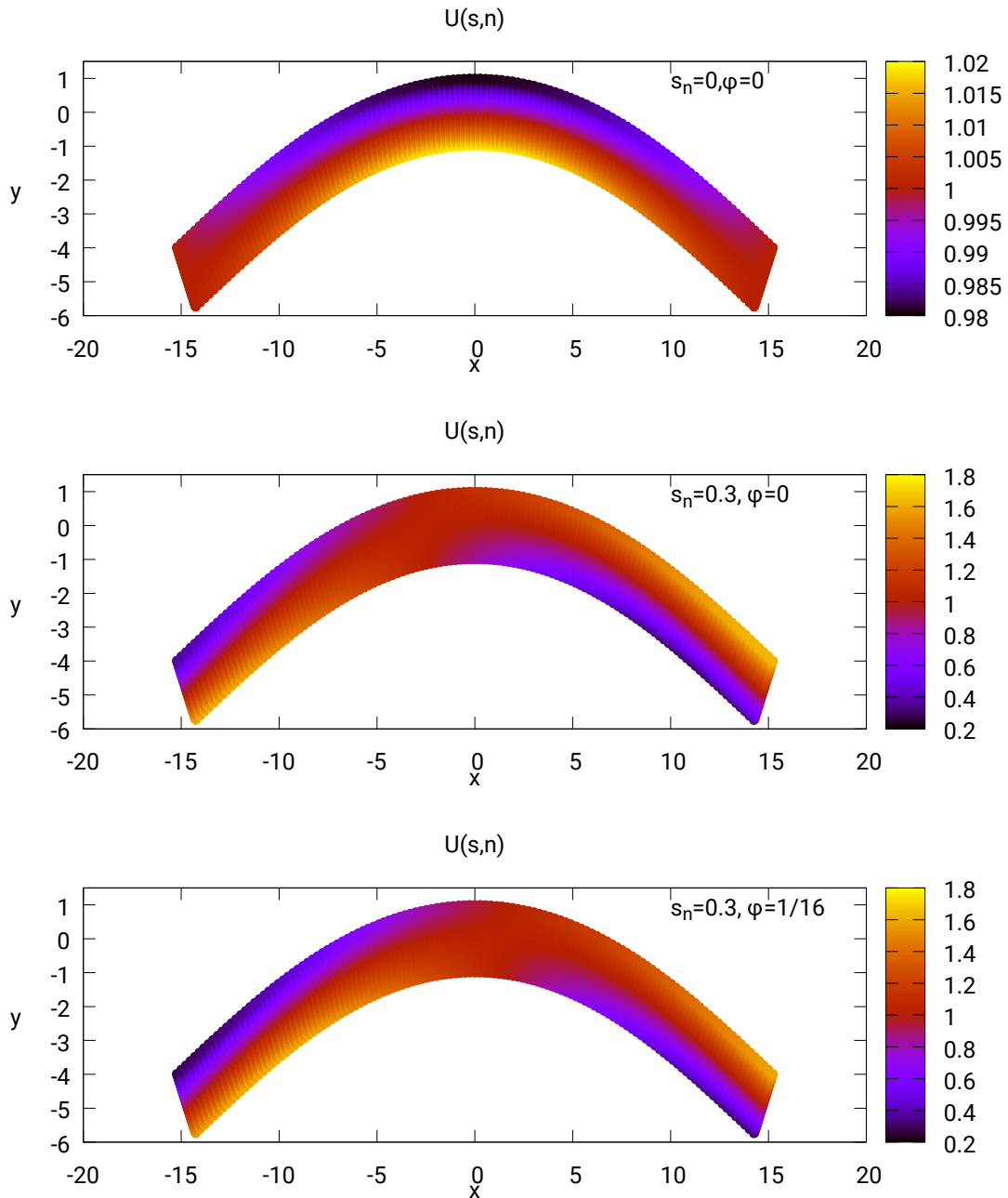


Figura 37. Longitudinal and lateral distributions of the dimensionless longitudinal component of the depth averaged velocity $U(s, n)$ for the following values of the relevant physical parameters: $C_{fu} = 0.01$, $\delta=0.06$, $b=1.23$, $F_{ru}=0.4$, corresponding to $\nu_0=0.05$, $\beta_u=8$, $\tau_{*u}=0.1$, $d_s=0.01$. *Upper plot*: laterally horizontal bed ($S_n = 0$); *middle plot*: $S_n = 0.3$ $\varphi = 0$; *lower plot*: $S_n = 0.3$ $\varphi = 1/16$

The first effect to be considered is the *failure of the linear framework*. This has some obvious consequences. Consider first the case of constant curvature channels under fully developed conditions. A glance at the equations (57) suggests that various contributions to the continuity

and momentum equations are no longer negligible. In particular, the lateral component of the secondary flow u_n is now an $\mathcal{O}(1)$ quantity forced not only by the centripetal acceleration and the lateral pressure gradient (last and second term on the right hand side of equation (57c)), but also by the convective contributions. Similarly, the longitudinal flow component u_s is no longer slightly perturbed with respect to the primary uniform flow. Rather, it feels the metric effect (first term in the right hand side of equation (57b)) as an $\mathcal{O}(1)$ perturbation whereby the longitudinal flow experiences non negligible lateral variations even in the case of flat horizontal bed. The longitudinal flow is further deformed by the convective transport of longitudinal momentum (last two terms in the right hand side of equation (57b)). This effect has already emerged in the context of the linear analysis of laterally tilted bed discussed in Section 2.4.3. However, for weakly curved bends, convection is an $\mathcal{O}(\delta)$ effect because the longitudinal velocity has $\mathcal{O}(1)$ lateral variations (associated with $D_0^{7/12}$) but the secondary flow (u_n) is small, whilst in sharp bends, convection is an $\mathcal{O}(1)$ effect because the secondary flow is no longer small. Finally, modifications of the turbulent closure might be needed because the turbulence characteristics are likely altered with respect to the straight channel case.

An attempt to quantify the above effects was made in a series of papers of Blanckaert and coworkers (Blanckaert *et al.*, 2008; Zeng *et al.*, 2008b; Duarte, 2008; Blanckaert, 2009, 2011). They performed a series of 12 laboratory experiments in a 1.3 m wide laboratory flume, consisting of a 193° constant curvature bend (radius of curvature of the centerline $R_0 = 1.7$ m) and two straight reaches, 9 m and 5 m long, located upstream and downstream, respectively. Here, we refer to three of the five fixed bed experiments (F119000, F169000, F219000) reviewed in Blanckaert (2011), where the bed was flat and roughened by glueing 2 mm sand. The values of the relevant dimensionless parameters in the various runs fell in the following ranges: $\nu_0 = 0.31$ -0.38; $\delta = 0.94$ -1.9; $F_{ru}^2 = 0.068$ -0.17; $b = 0.21$ -0.41. Recalling Figure 20 and the definitions introduced in Section 2.3, the above values of ν_0 and δ fall in the upper range of values observed in nature and are definitely characteristic of sharp bends. The main outcomes of the laboratory observations are summarized below.

Spatial evolution and saturation of the secondary flow

As we know, the generation of the secondary flow is associated with the development of a lateral slope of the free surface. Figure 38 shows that the slope starts developing upstream of the bend

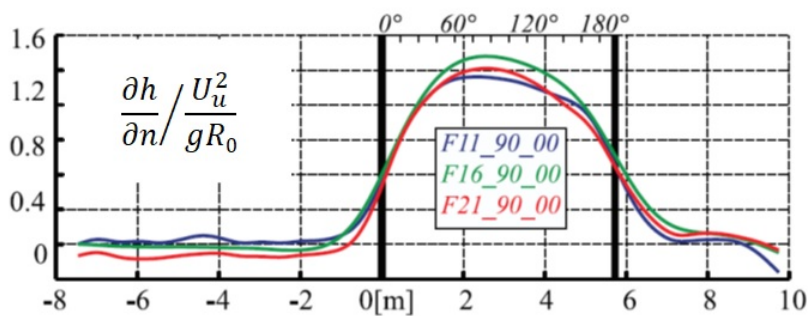


Figure 38. Lateral slope of the free surface $\partial h/\partial n$ scaled by $U_u^2/(gR_0)$, estimated by Blanckaert (2009) through a linear interpolation of the values measured in experiments F119000, F169000 and F219000 (reproduced from Blanckaert, 2009, under the permission of JGR, license number 5718281385915).

entrance, then increases to reach its peak ($\simeq 1.4$) between 60° and 90°. The water surface slope then decreases down to about half its peak at the bend exit. Blanckaert (2009) notes that this

suggests that overshooting of its equilibrium value occurs in the first part of the bend. The transverse slope finally decays rapidly within 1 m downstream of the bend exit.

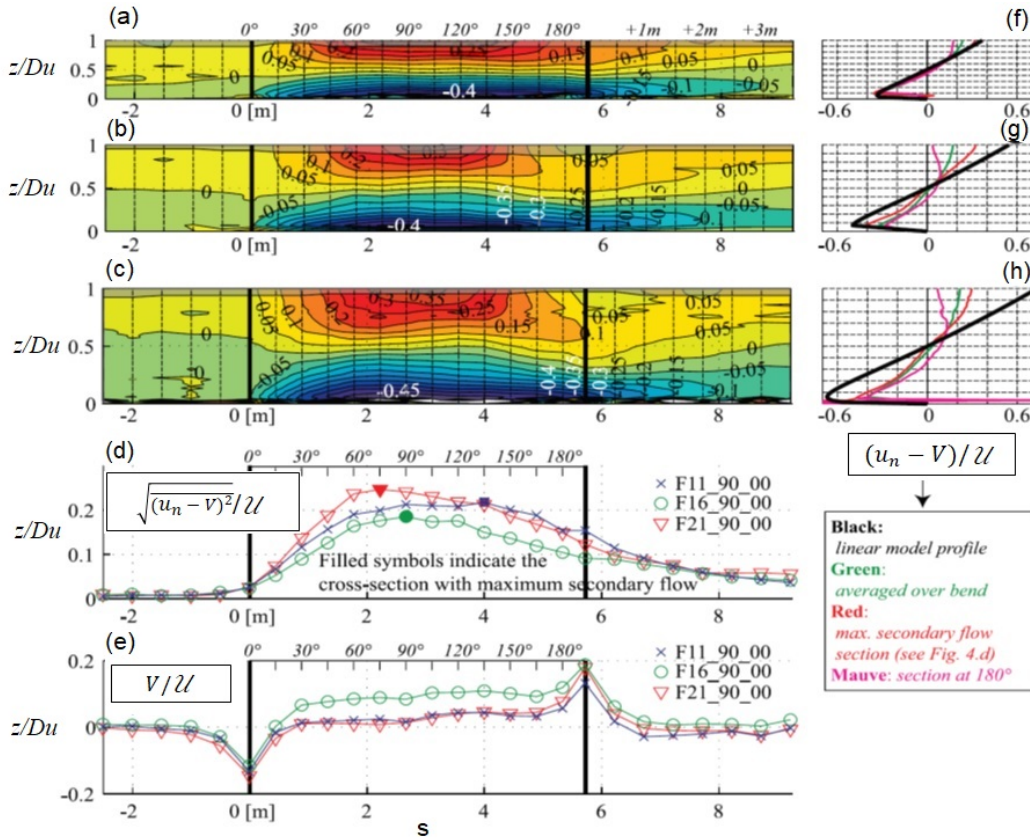


Figure 39. (a-f) Intensity of the zero-average component $u_n - V$ of the secondary flow, scaled by the undisturbed cross-sectionally averaged speed U and measured along the centerline in the experiments (a,b) F119000 ($\delta=0.94$), (c,d) F169000 ($\delta=1.39$) and (e,f) F219000 ($\delta=1.9$) of Blanckaert (2009). (a,b,c) Isovels; (f,g,h) Vertical distributions.

V is the depth average of the lateral velocity component. Plots are distorted by a factor 10. (d,e) Streamwise distribution of (d) the root mean square intensity of the zero-average component of the secondary flow and (h) of the depth-averaged lateral component of the secondary flow, both scaled by U and measured along the centerline (reproduced from Blanckaert, 2009, under the permission of JGR, license number 5718281385915).

Figure 39 shows three examples of the spatial evolution along the channel centerline of the depth-averaged component V and the zero-average component $(u_n - V)$ of the lateral velocity, both scaled by the undisturbed cross-sectionally averaged speed U_u . In all cases the secondary flow develops at the bend entrance, then increases, reaches a peak at a cross section between 60° and 135° to decrease in the downstream portion of the bend. In the straight reach following the bend the secondary flow rapidly decays. Note that the intensity of the secondary flow is not sensitive to the increase of the δ parameter in the range 0.94-1.9. Moreover, significant inward (outward) values of V are observed near the bend entrance (exit).

The observation that secondary flow does no longer vary in the upper range of δ values was described as a *saturation effect*. This is also illustrated in Figure 40, plotting the streamwise component of the dimensionless mean flow vorticity Ω_s , scaled by (U_u/D_u) . The values of the maximum vertically averaged values of Ω_s observed in the three experiments (0.35, 0.45 and 0.39) do confirm that the intensity of the secondary flow did not increase with δ (taking the values 0.94, 1.39 and 1.9, respectively), at least within the experimental uncertainty that was estimated as less than 20 %.

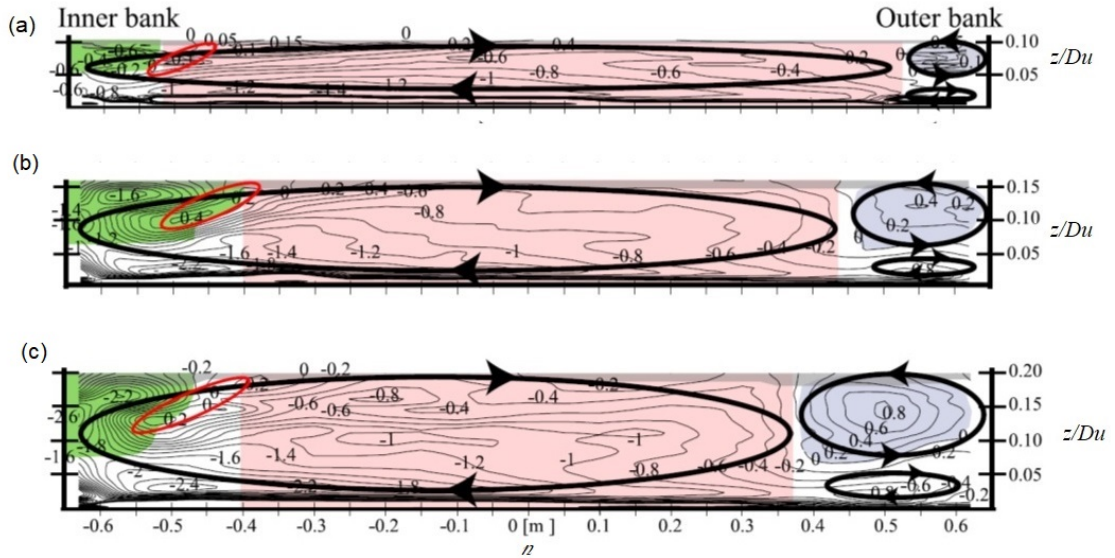


Figure 40. Values of the streamwise component of the dimensionless mean flow vorticity Ω_s (scaled by U_u/D_u) in the experiments $F119000$ ($\delta = 0.94$, $\Omega_s = -0.35$), $F169000$ ($\delta = 1.39$, $\Omega_s = -0.45$) and $F219000$ ($\delta = 1.9$, $\Omega_s = -0.39$) reported by Blanckaert (2011) emphasizing the presence of a main circulation cell (red area). Measurements refer to the cross sections where the secondary flow reached its peak intensity according to the centerline measurements of Blanckaert (2009). The minimum vertically averaged values of Ω_s observed for the three runs are -0.35 , -0.45 and -0.39 , respectively. The vorticity patterns also show the formation of two outer bank secondary cells (grey area) and an inner bank flow separation (green area) (reproduced from Blanckaert, 2011, under the permission of JGR, license number 5718280961502).

Shape of the vertical profile of the streamwise velocity

The shape of the vertical profile of the streamwise velocity is deformed with respect to the logarithmic shape of a straight channel. This is shown in Figure 41 plotting the streamwise velocity u_s scaled by the local depth-averaged velocity U , observed along the centerline in the three experiments. The profile shape varies from the classical logarithmic distribution in the straight reach upstream of the bend to a slightly perturbed shape with velocity increasing (decreasing) near the surface (bed) in the initial part of the bend. The shape is then progressively and strongly deformed such to exhibit its maximum close to the bed and a progressively lower minimum close to the free surface. This mechanism was first pointed out by de Vriend (1981) and was further analyzed by Blanckaert and Graf (2004) and Blanckaert and de Vriend (2003) in terms of a feedback between streamwise and cross-stream velocities whereby the deformation of the secondary flow damps the driving mechanism of the latter. It is this feedback that ultimately generates the saturation of the secondary flow in very sharp bends.

Turbulence characteristics

Energy losses are enhanced relative to the case of straight channels (about 40% higher in the sharp bends investigated by Blanckaert, 2009). This observation is associated with the observed increase of turbulent kinetic energy (more than twice its straight value) due to an increased production rate, which is also displayed by the increased velocity gradient in the near bed region driven by the deformation of the velocity profile. And again, energy losses and turbulence intensity do not increase linearly with the δ parameter and saturate in the very high curvature range. The interested reader is referred to the quoted papers for further details of the relevant processes.

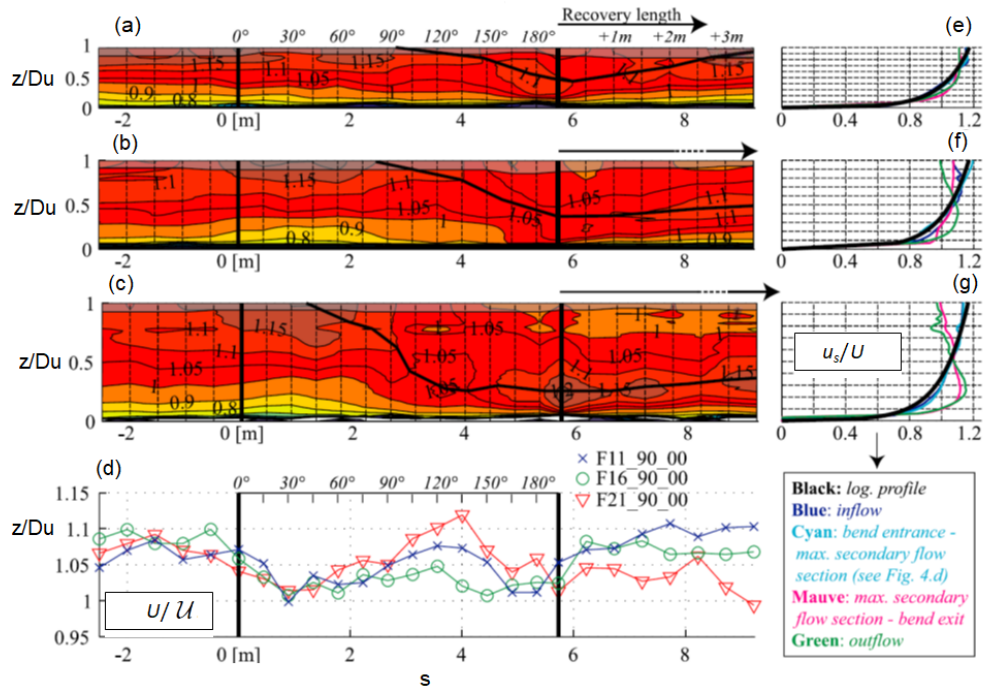


Figura 41. Streamwise velocity u_s , scaled by the local depth-averaged streamwise velocity U observed along the centerlines in the experiments (a,e) F119000, (b,f) F169000 and (c,g) F219000 reported by Blanckaert (2009). (a,b,c) Isovels of u_s/U ; (e,f,g) Vertical profiles of u_s/U . Black line: location where u_s displays its maximum. Plots are distorted by a factor 10. (d) Streamwise distribution along the channel centerline of the depth-averaged streamwise velocity U scaled by the cross-sectional averaged streamwise velocity, \mathcal{U} (see legend) (reproduced from Blanckaert, 2009, under the permission of JGR, license number 5718281385915).

The conclusion of Blanckaert (2009) is that the dominant mechanism emerged from the considered experiments is the role of the curvature-induced secondary flow directly or indirectly responsible for the processes mentioned above. However, as noted by the Author himself, this conclusion is strongly dependent on the fixed bed and the rectangular cross section adopted in the laboratory experiments. These features prevent the occurrence of the effect associated with bed deformation driven by the mobile character of the bottom in meandering real rivers. These aspects will be dealt with in the next Chapter.

2.6.2 Outer bank secondary cells

Figure (40) shows that, besides the main secondary cell that forms in the core region of the flow, two additional secondary cells are present close to the outer bank. The formation of these cells in open channel flows has been known for a long time since the early laboratory observations of Mockmore (1943), the field observations of Bathurst *et al.* (1977) and Bridge and Jarvis (1977), followed by a number of later contributions (see references quoted in Blanckaert *et al.*, 2012).

This phenomenon deserves some attention because it may directly affect the stress acting on the outer bank, although its effect on the mechanism of bank erosion is not agreed. On one hand, Bathurst *et al.* (1979) emphasize the destabilizing effect of the advection of high momentum fluid towards the bed, on the other hand Christensen *et al.* (1999) and others suggest that the outer cells protect the bank from the action of the high speed fluid displaced towards the bank by the secondary flow in the core region. The extensive work performed by Blanckaert and his coworkers on this subject has addressed various issues, as outlined below.

Dependence of the strength of outer cells on channel curvature

Although outer cells are known to exist also in mildly curved bends, Figure 40 shows that their strength does increase rapidly with curvature intensity, measured by the parameter δ .

Spatial evolution of outer cells

Observations performed by Markham and Thorne (1992) in a natural meander bend, as well as those made by Blanckaert (2009) in a laboratory flume, identified the separation between the central region and the outer cells as marked by the existence of vertical spiral vortices (Figure 42). The formation of the outer cells starts at the bend inlet. Their width increases in the initial part of the bend where the curvature of the outer bank increases and tends to a nearly constant value starting from a cross section at about 60° .

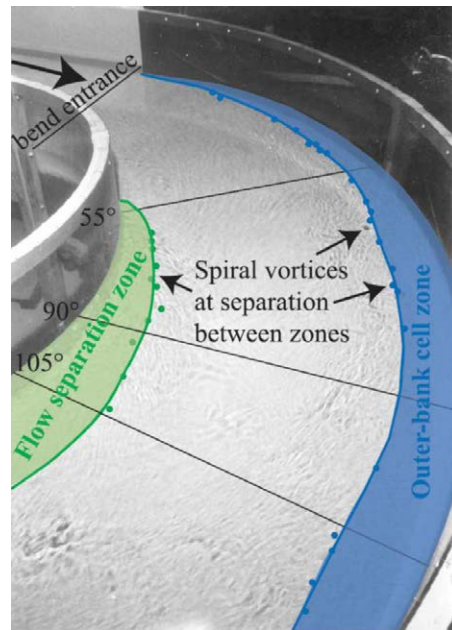


Figure 42. The picture shows the strip where the outer cell was confined in the F169000 experiment reported by Blanckaert (2011). Separation from the central region is marked by the presence of vertical spiral vortices. Also shown is the inner separation zone (reproduced from Blanckaert, 2011, under the permission of JGR, license number 5718280961502).

Occurrence of the outer cells and their dependence on the roughness and inclination of the outer bank

This aspect of the problem was treated by Blanckaert *et al.* (2012). In this paper, the assumption that outer bank cells would occur near steep banks but not near shelving ones (Bathurst *et al.*, 1977, 1979; Thorne and Hey, 1979), was shown to be incorrect. However, the strength of the outer cells nearly halved as the bank inclination was reduced from 90° to 30° . This suggests that the relevance of the phenomenon is limited to steep banks, that are known to be characteristic of sharp bends (Leopold and Wolman, 1960; Thorne *et al.*, 1995).

Moreover, Blanckaert *et al.* (2012) observations showed that the width and intensity of the outer cell as well as its protective effect are enhanced if the bank roughness increases.

Why do outer cells form?

This process has similarities with the formation of Görtler vortices (Görtler, 1955) in laminar flow past concave walls (Figure 43a). It is well known that Görtler vortices arise from a centrifugal

instability of the boundary layer flow, similar to the better known Taylor instability that leads to the formation of counter-rotating vortices in Couette flow between rotating circular cylinders.

An even closer analogy may be drawn between the development of secondary flows in open channels and the *laminar flow in curved pipes*. This flow was investigated in the early work of Dean (1927) who showed that, for weakly curved bends, the unbalance between the lateral pressure gradient and the required centripetal force gives rise to a secondary motion, superposed on the primary flow. The secondary circulation consists of a pair of counter-rotating cells, called *Dean vortices* (Figure 43b). The dimensionless parameter controlling the onset and the intensity of secondary flow is the so called Dean number $De = \frac{Ua}{\nu} \sqrt{a/R}$, i.e. the product of the Reynolds number times the square root of the ratio of the pipe radius a to the radius of curvature R of the pipe axis. The Dean number can be shown to measure the ratio between the square root of the product of inertial to centripetal forces (which promote secondary flows) and viscous forces (that tend to suppress secondary flows).

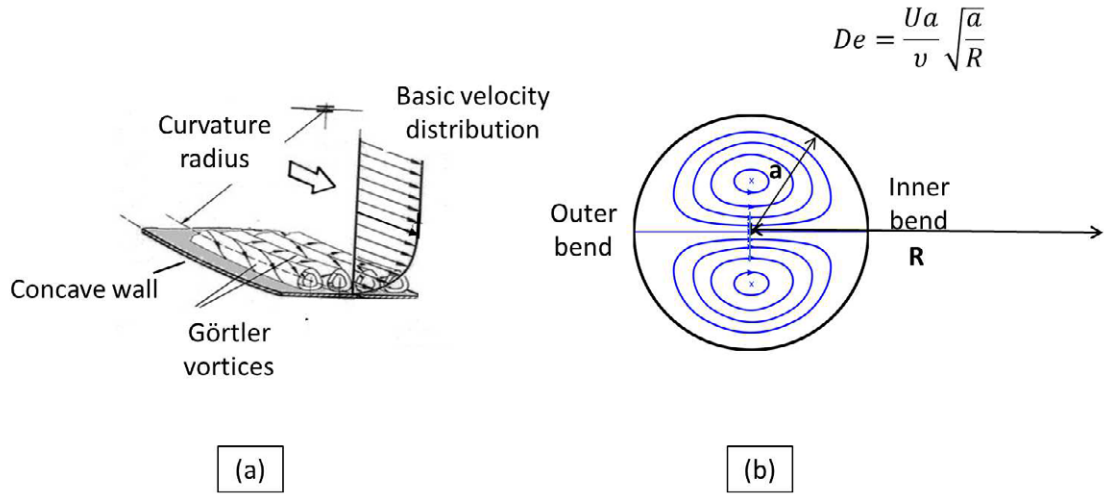


Figure 43. (a) Sketch of Görtler vortices generated by an instability of the boundary layer flow over concave walls. (b) Sketch of secondary laminar flow in curved pipes, according to the solution obtained by Dean (1927).

For *laminar* flows in curved open channels with rectangular cross sections, numerical (Cheng *et al.*, 1976; de Vriend, 1981; Winters, 1987) and experimental (Hille *et al.*, 1985) studies exhibit a notable feature. Besides the main secondary cell that forms in the central region, an outer-bank cell appears as the Dean number exceeds a critical value. This suggests the occurrence of a flow instability and a bifurcation process. The works of de Vriend (1981) and Blanckaert and de Vriend (2004) have identified a possible origin of the instability. In brief, the main action driving the formation of secondary cells is the centripetal force. Moreover, the evolution equation of the longitudinal component of the vorticity vector, which is expression of the secondary flow (Figure 44), shows that the driving centripetal term in this equations reads:

$$-\frac{v_s \omega_n}{h_s r_0}, \quad (172)$$

where $\omega_n \equiv -\partial v_s / \partial z$.

Indeed, under steady and fully developed conditions, the equation (6) for the longitudinal component of the vorticity ω_s , becomes:

$$v_n \frac{\partial \omega_s}{\partial n} + v_z \frac{\partial \omega_s}{\partial z} = \omega_n \frac{\partial v_s}{\partial n} + \omega_z \frac{\partial v_s}{\partial z} + \frac{v_n \omega_s}{r_0 h_s} - \boxed{\frac{v_s \omega_n}{r_0 h_s}} + \nu \left(\nabla^2 \omega_s - \frac{\omega_s}{h_s^2 r_0^2} \right). \quad (173)$$

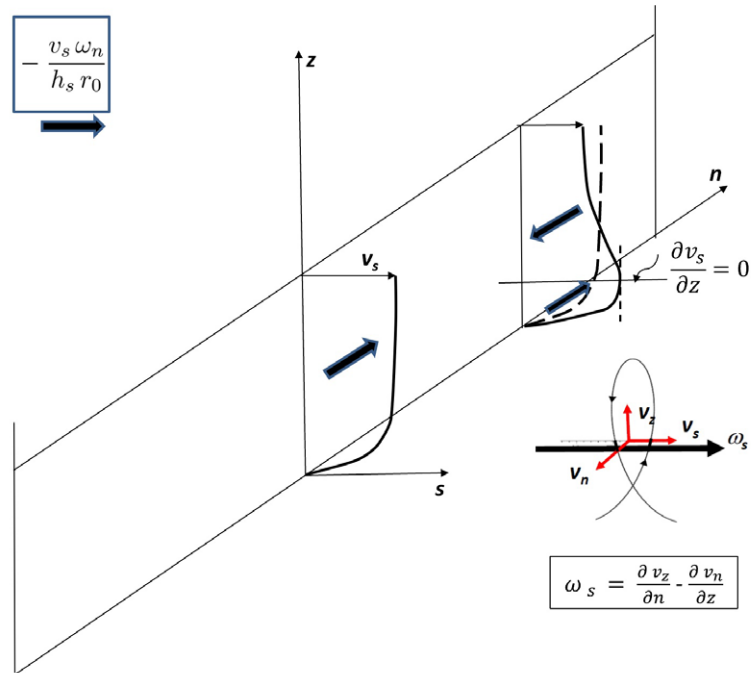


Figure 44. Sketch illustrating the change of direction of the centripetal term $-v_s \omega_n / (r_0 h_s)$ in the vorticity equation. The profile of longitudinal velocity v_s deforms owing to the momentum redistribution associated with the action of the secondary flow.

Hence, the centripetal term is significantly affected by the momentum redistribution associated with the action of the secondary flow that deforms the shape of the v_s -profile. Most notable, in this respect, is the fact that the lateral component of the vorticity ω_n , hence the driving centripetal term changes sign in the upper part of the water column as the peak of v_s is displaced towards the lower part of the water column. According to Blanckaert and de Vriend (2004) this change of sign is a triggering condition for the formation of the outer-bank cell (Figure 44).

In turbulent flows, besides the mechanism of secondary flow generation discussed so far (*secondary flow of first kind* according to Prandtl, 1942), an additional mechanism (*secondary flow of the second kind*) exists. As discussed in Section 2.3.6(I), this is caused by the anisotropy of turbulent normal stresses and, unlike the former type, is obviously a feature only observed in turbulent flows.

The centrifugal mechanism and the turbulent straight mechanisms coexist in curved turbulent flows. Blanckaert and de Vriend (2004) have analyzed experimentally this issue in detail by measuring the size of different terms appearing in the evolution equation (6) for the longitudinal component of vorticity Ω_s . In summary, results show that the sign of the centrifugal term $-u_s \Omega_n / (r_0 h_s)$ in the Reynolds-averaged counterpart of equation (173) is consistent with the sense of rotation of the outer-bank cell. In other words, centrifugal effects do contribute to the intensity of outer bank secondary cell. Moreover, it appears that the anisotropy of the cross-stream turbulent normal stresses T_{nn}^t and T_{zz}^t and the cross-stream turbulent shear stress T_{nz}^t play the same role in the Reynolds-averaged vorticity equation (8). Finally, the anisotropy of normal stresses driven by the free surface does not differ significantly from that generated by the banks.

The above picture has been confirmed by detailed numerical tests performed with the help of the LES technique by Booi (2003) (see also van Balen *et al.*, 2009; Constantinescu *et al.*, 2011) on open-channel turbulent flow in a mildly curved ($\nu_0 = 0.06$, $\delta = 0.26$) 180° bend with laterally

horizontal bed. Results confirm many of the findings of linear theories. In particular, the secondary flow in the core region of the cross-section is fairly weak (about 10% of the bulk velocity). Also, a counter rotating secondary cell forms at the outer bank, its strength is weaker than that of the primary helical motion and centrifugal terms play a crucial role in the process controlling its formation. Turbulence anisotropy is significant close to the side walls, negligible in the core region. Finally, simulations confirm the analysis of the transfer of kinetic energy proposed by Blanckaert and de Vriend (2004). Essentially, mean flow kinetic energy is dominantly transferred to turbulence, especially in the boundary layers near the bottom. However, a small negative contribution (i.e. from turbulence to the mean motion) occurs via the cross-stream turbulent stresses in the region where the outer bank circulation cells form. According to Blanckaert and de Vriend (2004), this contribution, although negligible when compared with the total kinetic energy transferred from the mean flow to turbulence, plays an essential role in the formation of the circulation cells. It is the actual reason why linear turbulence closure models (e.g. the standard \mathcal{K} - ϵ model with an isotropic eddy viscosity), fail to reproduce the formation of the outer bank cells, as noted by Demuren and Rodi (1986) and confirmed by Booij (2003).

2.6.3 Flow separation

The interest in the process of flow separation with the consequent formation of a recirculation zone at the (convex) inner bank of meandering rivers arose in the 1960, when Bagnold (1960) proposed some theoretical speculations to explain the observation that the flow resistance of sinuous open channels displays a minimum for values of the curvature ratio (ν_0) in the range 0.25-0.33. This issue was also investigated in the laboratory by Leopold *et al.* (1960). The latter paper provided experimental evidence of a discontinuous increase in resistance occurring in sharply sinuous channels with fairly small wavelength when the flow Froude number exceeded a threshold value dependent on the curvature ratio. This discontinuity was associated with the formation of a recirculating flow driven by the high curvature of the inner bends, producing a *dead zone of weak reverse flow immediately past the apex*. The main effect of this macro-eddy was to restrict the primary flow to a narrower cross section.

The problem was then left unexplored for longer than a decade, until Leeder and Bridges (1975) performed some field observations of flow separation in natural meander bends and attempted to define an empirical criterion for predicting the onset of separation. These Authors also suggested that flow separation at the inner bank is likely to favor meander migration as it reduces the effective width of the flow and moves the thread of high velocity towards the outer bank.

Further attention on the process had to wait nearly three decades, when Ferguson *et al.* (2003) investigated flow separation along the inner banks of two sharp meander bends combining field measurements of flow velocity with three-dimensional CFD simulations. The main feature pointed out in the conclusions of this investigation was that, in contrast with suggestion by Leeder and Bridges (1975), the reduction of the effective width of the primary flow is counterbalanced by an increase in flow depth, such that the flow decelerates along the outer bank from the bend inlet to its apex. Moreover, the helicoidal secondary flow at the outer bank was only present in the upstream portion of the bend, where peak bottom stresses (and consequently potential peak erosion) were experienced. This is in contrast with what is commonly observed in most weakly curved bends. Detailed analysis of the three-dimensional structure of the flow field in the recirculating eddy was also reported.

More recently, as discussed in the previous section, detailed laboratory observations of the flow in a very sharp bend were performed by Blanckaert and coworkers. Results were reported in several papers. In particular, an interesting comparison between the flow separation observed at the (convex) inner bank under fixed and mobile bed conditions was made by Blanckaert (2010) (but see also Blanckaert, 2011). Although the morphodynamics of sinuous channels with cohesionless bed will be treated in the next Chapter, it is appropriate to anticipate the main outcome of the above comparison. Indeed, as expected, the characteristics of flow separation in the two cases turn out to be fundamentally different (Figure 45). In the fixed bed case, separation is induced by the high curvature of the inner bank slightly upstream of the bend apex, in the high speed region induced by the free vortex effect. In the mobile bed case, the free vortex effect is superseded by

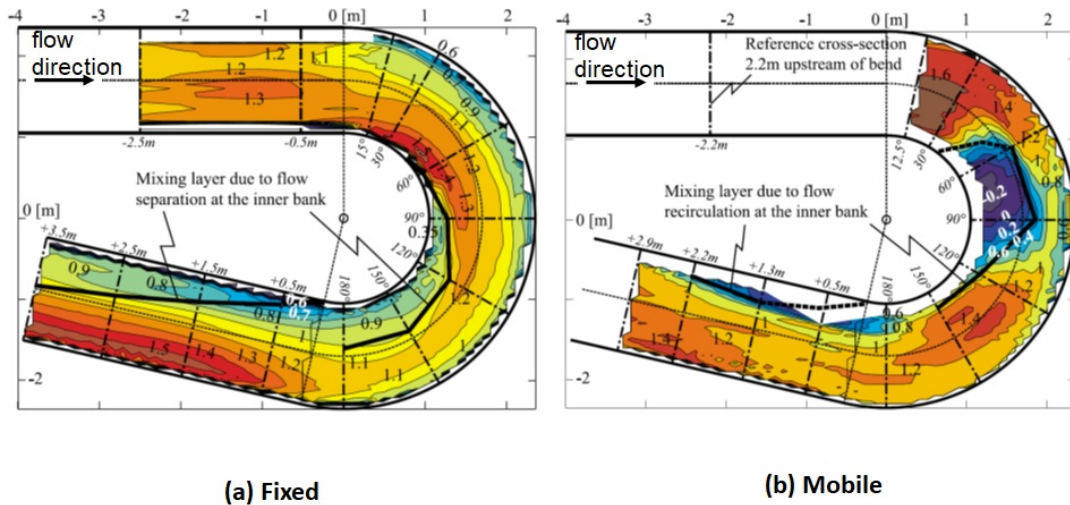


Figure 45. Longitudinal mean flow velocity u at the free surface, scaled by the cross sectionally averaged speed U in the (a) F169000 fixed bed experiment and (b) the M169000 mobile bed experiment of Blanckaert (2011) (reproduced from Blanckaert, 2011, under the permission of JGR, license number 5718280961502).

the formation of a point bar close to the inner bend. This leads to the formation of a low velocity recirculation bubble that traps sediments promoting the accretion of the inner bank. The point bar and the separation zone also have the effect to move the thread of high velocity towards the outer bank. The effective width of the flow is thus sharply reduced, with the primary and secondary flows concentrated in the outer half of the cross section. This promotes outer bank erosion, which is further enhanced by the observed peaking of the longitudinal velocity near the toe of the outer bank. This is roughly the state of the art, summarized in the conclusions of Blanckaert (2011): “*The control parameters of inner-bank separation remain unknown, but the results suggest that inner-bank flow separation enhances meander migration*”.

2.6.4 Modeling the hydrodynamics of sharp bends

The above discussion suggests that, in order to model all the features characteristic of the turbulent flow in sharp bends, one needs to employ fairly sophisticated turbulent models. Possible choices encompass the DNS simulations, the LES approach or a RANS nonlinear closure model. None of these approaches is appropriate to morphodynamic investigations of large scale fluvial processes. However, besides their scientific value, the information provided by these investigations may help in the formulation of simplified models more suitable to fluvial morphodynamics.

We are aware of no DNS simulation of turbulent flow in curved open channels, whilst LES simulations referring to weakly curved bends have been discussed in Section 2.6.2. LES simulations of a sharply curved meandering open channel flow have been reported by Stoesser *et al.* (2010), who compared their output with results obtained with the help of standard RANS closures. They are discussed below, along with results of a few further RANS numerical investigations listed in Figure 46.

The first application of advanced RANS modeling to the turbulent flow in curved bends is due to Demuren and Rodi (1986), who developed a previous work of Leschziner and Rodi (1979). They solved numerically the three-dimensional Reynolds averaged Navier-Stokes equations, closed by the classical $K-\epsilon$ turbulence model (Launder and Spalding, 1974) with the following approximations: (i) molecular diffusion terms were neglected, hence the viscous sublayer was not resolved and empirical wall functions were employed; (ii) a shear-layer approximation was adopted such that turbulent diffusion of momentum in the streamwise direction was neglected; (iii) the influence of curvature on turbulence was ignored. Results of simulations were tested by comparison with

Authors	Bend angle	β_u	ν_0	δ	Closure	Experimental Validation
Demuren and Rodi (1986)	1 meander 7 meanders	10.15 2.24	0.14 0.14	0.26 0.35	$K-\varepsilon$	Chang (1971) Fukuoka (1971)
Shimizu et al. (1990)	180°	6.3	0.5	0.41	Zero order	Rozovskij (1957)
Khosronejad et al. (2007)	S-shaped flume	1.67	0.2	1.7	$K-\varepsilon$, $K-\omega$	Ghanmi (1999)
Zeng et al. (2008b)	193°	4.1	0.39	1.01	$K-\omega$ SST Spalart-Almaras	Blanckaert (2002)
Stoesser et al. (2010)	two 180° bends	1.45	0.125	1.45	$K-\varepsilon$, $K-\omega$, LES	Siebert (1982)

Figure 46. Summary of numerical investigations on the hydrodynamics of sharply curved bends appeared in the literature.

measurements of Chang (1971) and Fukuoka (1971). Comparison was reasonably successful except for the inability of the model to predict the occurrence of the small counter-rotating outer bank cells.

Few years later Shimizu *et al.* (1990) performed a similar exercise using a much simpler closure model, namely a zero-order closure achieved by simply assuming a structure for the eddy viscosity. Comparison with the experiments of Rozovskij (1957) for a fixed-bed rectangular cross-section was fairly reasonable in spite of the relative simplicity of the closure adopted (which obviously prevented the generation of the outer bank cell) and the quite sharp nature of the bend (Figure 47). In particular, the dominance of the free vortex effect in the initial portion of the bend and the progressive shift of the thread of high velocity towards the outer bend were successfully reproduced.

More recently, Khosronejad *et al.* (2007) employed a low-turbulence Reynolds number version of the $K-\omega$ closure model of Wilcox (1994), as well as the classical $K-\varepsilon$ model, and adopted the rigid lid approximation. The latter consists of assuming that the kinematic boundary condition at the free surface may be reduced to a condition of vanishing normal component of the flow velocity. The validation of the model was based on the experimental observations of Ghanmi (1999), performed on a S-shaped sharply curved and very narrow flume with an horizontal fixed bed.

A step forward was made in the investigation of Zeng *et al.* (2008b), who extended a previous version of Zeng *et al.* (2008a). The novel features of this work were: (i) the mathematical formulation was expressed in terms of generalized curvilinear coordinates such that the code was potentially suitable to irregular geometries; (ii) the turbulent closure relied on the low-Reynolds number versions of either the $K-\omega$ Shear Stress Transport (SST) model (Menter, 1994) or the Spalart-Almaras (SA) model (Spalart, 2000). These turbulence closure models can account for the effects of bed roughness using a mesh fine enough in the direction normal to the bed such that wall functions were no longer needed. The model was applied to the flat bed configuration of experiment H89 by Blanckaert (2002). A summary of the comparison between simulated results and observations is plotted in Figure 48.

In particular, Figure 48a shows that the displacement of the thread of high streamwise velocity in the outward direction and its persistence in the straight outflow reach are reproduced in the simulation, though some differences emerge in the region where the fast flow detaches from the inner wall. A second feature observed in the experiment is reproduced. The cross-stream circulation increases in the first half of the bend, it reaches a peak in the cross section at 90°, it then decreases to about half its peak value at the bend exit and decays in the straight outflow reach. As expected, the formation of weaker counter-rotating cells of cross-stream circulation at the outer bank is not captured by the simulation. A related deficiency is the inability of simulations to capture

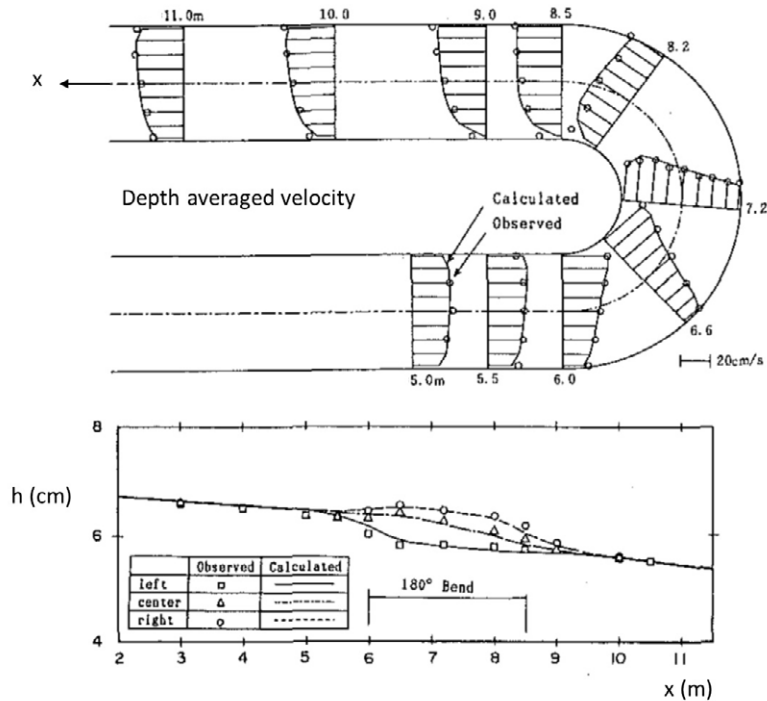


Figura 47. Comparison between three-dimensional simulations of Shimizu *et al.* (1990) and observations of Rozovskij (1957). (a) Depth averaged longitudinal velocity; (b) water-surface elevation (modified from Shimizu *et al.*, 1990)

the decrease of streamwise velocities toward the water surface and the reversal of the measured vertical gradient of the lateral velocity close to the outer bank.

The last numerical investigation is due to Stoesser *et al.* (2010), who modeled the experimental configuration tested by Siebert (1982). This consisted of a sequence of two 180° bends bridged by a short straight reach. A distinct feature of the apparatus was the very small width to depth ratio of the channel ($\beta_u = 1.45$), that was hardly representative of natural rivers. Three numerical approaches were employed by Stoesser *et al.* (2010): RANS with either \mathcal{K} - ω or \mathcal{K} - ϵ closure models, and LES. Moreover, wall functions and rigid lid approximation were used as boundary conditions at the solid wall and free surface, respectively. Results of the calculations showed that the performance of the two RANS approaches was quite similar, whilst LES simulations displayed some distinct differences. A surprising feature of simulated secondary flows was the presence of an outer bank cell in the output of RANS simulations, an unexpected result given the isotropic character of the closures employed. However, the degree of generality of these findings is not clear and may only be ascertained extending the simulations to the case of wider bends, where the interaction between core flow and side wall boundary layers is not as strong as in the present context.

2.7. Modeling the hydrodynamics of natural meanders: rational approximations or empirical modeling?

The discussion proposed in the last section has shown that fully three-dimensional flow models can capture most of the important features of the turbulent flow field observed in fairly sharp bends. Moreover, recently, large efforts have been made to develop so called hybrid RANS-LES methods, new promising approaches whereby the computationally heavy eddy resolving approach can be switched on or off depending on local flow conditions (Keylock *et al.*, 2012). Unfortunately, these models are still too difficult and computationally time consuming to be implemented in the context of morphodynamic applications of relevance to engineering and geomorphological practice,

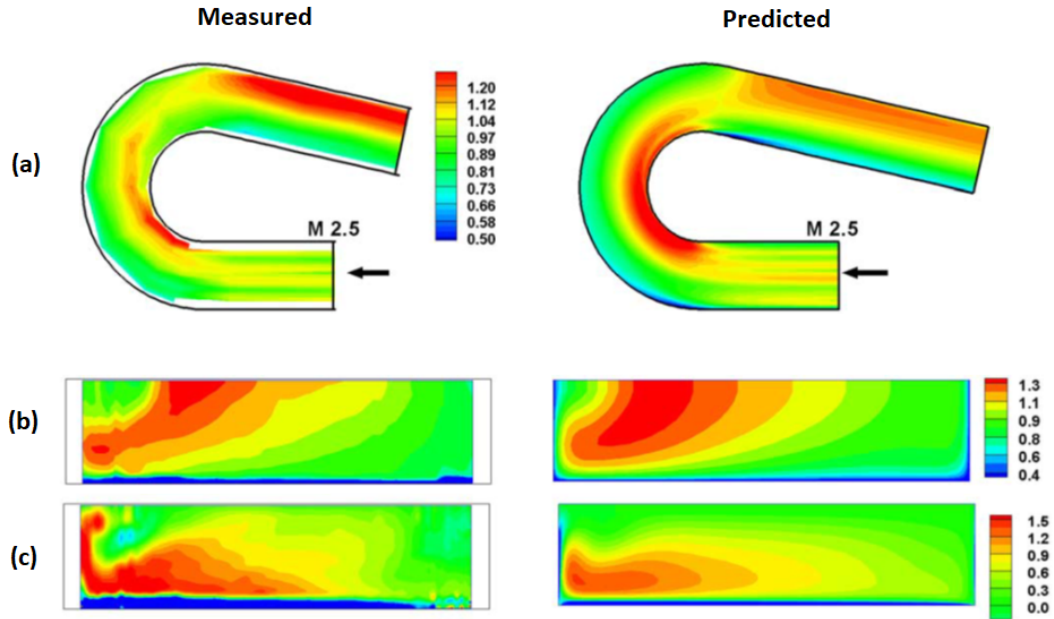


Figure 48. Summary of simulation results of Zeng *et al.* (2008b) (right) compared with observations of Blanckaert (2002). (a) Spatial development of the depth averaged longitudinal velocity U , scaled by the cross-sectionally averaged speed U . Cross sectional distributions of (b) normalized streamwise velocity u_s/U , (c) normalized streamwise vorticity $\omega_s/(U/D_u)$. Plots (b,c) refer to the cross-section at 90° (reproduced from Zeng *et al.*, 2008b, under the permission of WRR, license number 5704690904617).

a state of affairs that will likely last for many years to go. This has motivated efforts to formulate simpler models able to incorporate in some approximate way the knowledge made available by the scientific investigations.

The main physical effects, ignored or under-represented in models for weakly meandering channels, that were found to play a significant role in sharp bends are the lateral redistribution of longitudinal flow momentum by the secondary flow and turbulence anisotropy which controls the formation of the outer bank secondary cell and flow separation. However, outer bank secondary cells affect morphological calculations indirectly through their possible effect on the mechanism of bank erosion, which still awaits to be fully understood. Flow separation is a characteristic of very sharp bends with fixed beds, but is a fairly minor feature of natural bends. Indeed, even in sharp bends the formation of a separation bubble drives sediment settling which weakens the strength of the recirculating bubble.

The only remaining factor that needs to be properly addressed is the lateral momentum redistribution. In this respect one should note that, unlike stated sometimes in the literature, this effect is not ignored in perturbation approaches, that are too often and inappropriately described as *linear*. Let us clarify this point referring to our analysis of flow in constant curvature channels discussed in Section 2.4. The effect of lateral momentum redistribution is associated with the term $\mathfrak{b} u_n \partial u_s / \partial n$ in the right hand side of equation (57b). This term is significant provided the lateral velocity component is large and the longitudinal velocity component experiences non negligible variations in the transverse direction. In weakly curved bends, we have seen that $u_n \sim \mathcal{O}(\delta)$. In wide bends with flat horizontal beds (see Section 2.4.2) transverse variations of u_s are also $\mathcal{O}(\delta)$. Hence, in weakly curved bends with flat horizontal bed, the lateral momentum redistribution is a very weak ($\mathcal{O}(\delta^2)$) process, a finding in qualitative agreement with Rozovskij (1957) observations. On the other hand, in the presence of topographic steering (see Section 2.4.3) transverse variations of u_s are $\mathcal{O}(1)$ quantities, hence the lateral redistribution is a less weak ($\mathcal{O}(\delta)$) process. One would then like to know up to what values of (δ) the perturbation approach may be taken as a reasonable

approximation of the full solution. In other words, to what extent can we push the validity of the weakly nonlinear approach in the field of moderately sharp bends?

An attempt to answer this question has been carried out by Blanckaert and de Vriend (2003). In order to account for nonlinear effects on the vertical flow structure, they developed a semi-empirical model based on the flow equations for curved flow, evaluated at the bend centerline and reduced to their simplest form.

We do not discuss this model, which relies on a number of empirical approximations. It suffices to point out that the Authors identify a parameter which would allow to distinguish bends for which a linear approach is appropriate from those for which it is moderately acceptable or fails. Unfortunately this parameter is not readily estimated in terms of external dimensionless parameters like those introduced in this chapter. Indeed, it also depends on the lateral derivative of the longitudinal depth averaged velocity evaluated at the channel centerline, a quantity which is not known a priori.

3. Forced bars in sinuous channels

In this Chapter we focus on the morphodynamics of a curved channel with the characteristics described in Section 2.1.1 except for the additional feature of the channel bed being now cohesionless.

3.1. Formulation of the problem of morphodynamics of sinuous channels

The problem is readily formulated adding to the hydrodynamic framework discussed in the previous Chapter (Section 2.1) the governing equations, closures and boundary conditions for the motion of the solid phase introduced in Chapter 4I. They will be rewritten employing the curvilinear coordinate system appropriate to sinuous channels introduced in Section 2.1.1.

3.1.1 The motion of the solid phase in sinuous channels: dimensional formulation

Governing equations

Referring the motion to the orthogonal curvilinear coordinates (s, n, z) and adopting the notations introduced in Chapter 4(I), the evolution equation of the bed interface (equation 245(I)) takes the form:

$$\frac{\partial(DC)}{\partial t} + c_M \frac{\partial \eta}{\partial t} + \frac{1}{h_s} \frac{\partial Q_{ss}}{\partial s} + \frac{1}{h_s} \frac{\partial (h_s Q_{sn})}{\partial n} = 0. \quad (174)$$

with C *depth averaged concentration* of the sediment contained in the water column and Q_s *depth integrated total sediment flux per unit width*. These quantities are defined in the form:

$$DC = \int_{\eta}^h \langle c \rangle dz, \quad Q_{sj} = \int_{\eta}^h \langle q_{sj} \rangle dz \quad (j = s, n). \quad (175)$$

Here, $\langle c \rangle$ is the Reynolds (macroscopically) averaged local sediment concentration and $\langle q_{ss} \rangle$, $\langle q_{sn} \rangle$ are the longitudinal and lateral components of the local Reynolds averaged total sediment flux, respectively. Moreover, we recall that:

$$Q_{sj} = Q_{sj}^b + Q_{sj}^s \quad (j = s, n), \quad (176)$$

where Q_{sj}^b and Q_{sj}^s are the bedload and suspended load components of the depth integrated sediment flux Q_{sj} , respectively. The evolution equation of the bed interface must then be associated with appropriate mathematical tools to evaluate C , Q_{sj}^b and Q_{sj}^s .

Evaluating the suspended load

The *macroscopically averaged* form of the equation of continuity of the solid phase (equation 221(I)), in curvilinear coordinates, reads:

$$\begin{aligned} \frac{\partial \langle c \rangle}{\partial t} + \frac{1}{h_s} \frac{\partial (\langle c \rangle u_s)}{\partial s} + \frac{1}{h_s} \frac{\partial (h_s \langle c \rangle u_n)}{\partial n} + \frac{\partial (\langle c \rangle u_z)}{\partial z} \\ + \frac{1}{h_s} \frac{\partial \langle c' u'_s \rangle}{\partial s} + \frac{1}{h_s} \frac{\partial (h_s \langle c' u'_n \rangle)}{\partial n} + \frac{\partial \langle c' u'_z \rangle}{\partial z} - w_s \frac{\partial \langle c \rangle}{\partial z} = 0. \end{aligned} \quad (177)$$

This conservation equation must be solved with the boundary conditions listed in Chapter 4(I), i.e. the impermeability condition for the free surface (eq. 255(I)) and the constraint (eq. 257(I)) at the bed interface. In curvilinear coordinates and with the help of (16) they read:

$$\left[-\frac{\langle c' u'_s \rangle}{h_s} \frac{\partial H}{\partial s} - \langle c' u'_n \rangle \frac{\partial H}{\partial n} + \langle c' u'_z \rangle - w_s \langle c \rangle \right]_H = 0 \quad (178a)$$

$$\left[\frac{\langle c' u'_s \rangle}{h_s} \frac{\partial \eta}{\partial s} + \langle c' u'_n \rangle \frac{\partial \eta}{\partial n} - \langle c' u'_z \rangle + w_s \langle c_a \rangle \right]_{\eta+a} = 0, \quad (178b)$$

where appropriate conditions at the open boundary will have to be included.

Finally, the differential system (177), (178a), (178b) will require a *closure* for the turbulent diffusive flux $\langle \mathbf{u}'c' \rangle$. Following the classical approach introduced in Section 3.5.4(I), we employ a gradient-diffusion assumption, that in curvilinear coordinates takes the form:

$$\langle u'_s c' \rangle = -\frac{\mathfrak{D}_s}{h_s} \frac{\partial \langle c \rangle}{\partial s}, \quad \langle u'_n c' \rangle = -\mathfrak{D}_n \frac{\partial \langle c \rangle}{\partial n}, \quad \langle u'_z c' \rangle = -\mathfrak{D}_z \frac{\partial \langle c \rangle}{\partial z}, \quad (179)$$

where \mathfrak{D}_j ($j = s, n, z$) is the j -th component of the *turbulent diffusivity* vector, usually estimated using the Reynolds analogy (i.e., $\mathfrak{D}_j = \nu_T$). We recall that the rational framework underlying the above formulation holds for suspensions sufficiently *dilute* to allow neglecting the effect of fluid-solid particles and particle-particle interactions. Moreover, the associated hydrodynamic equations do not feel the presence of solid particles, that must then be *small enough* to induce negligible disturbances of the turbulence field down to its smallest scales (*one way coupling*). Once the solutions for $\langle c \rangle$, $\langle u_s \rangle$ and $\langle u_n \rangle$ have been obtained, the depth integrated components of the suspended sediment flux are immediately calculated from the following relationships:

$$Q_{ss}^s = \int_{\eta}^H \langle c \rangle \langle u_s \rangle dz - \frac{1}{h_s} \int_{\eta}^H \mathfrak{D}_s \frac{\partial \langle c \rangle}{\partial s} dz, \quad (180a)$$

$$Q_{sn}^s = \int_{\eta}^H \langle c \rangle \langle u_n \rangle dz - \int_{\eta}^H \mathfrak{D}_n \frac{\partial \langle c \rangle}{\partial n} dz \quad (180b)$$

Evaluating the bed load

In Chapter 4(I) we have presented a generalized bedload transport relationship and examined the particular case of weakly sloping beds ($|\nabla_h \eta| \rightarrow 0$), which is of special interest to morphodynamics. The outcome of the analysis was the set of relationships (equations 334a(I), 334b(I), 350(I) and 351(I)). However, as already pointed out in the treatment of fluvial bars in straight channels (Chapter 6(I)), those relationships refer to a cartesian coordinate system with x aligned with the tangential stress $\boldsymbol{\tau}$ at the bottom. As illustrated in Figure 49, in the present context, the longitudinal coordinate s lies on a horizontal plane and is aligned with the longitudinal component of flow velocity. Hence, the above relationships must be adapted to include the effect of rotation of the (x, y) coordinate axes by an angle equal to the angle χ that the bottom stress forms with

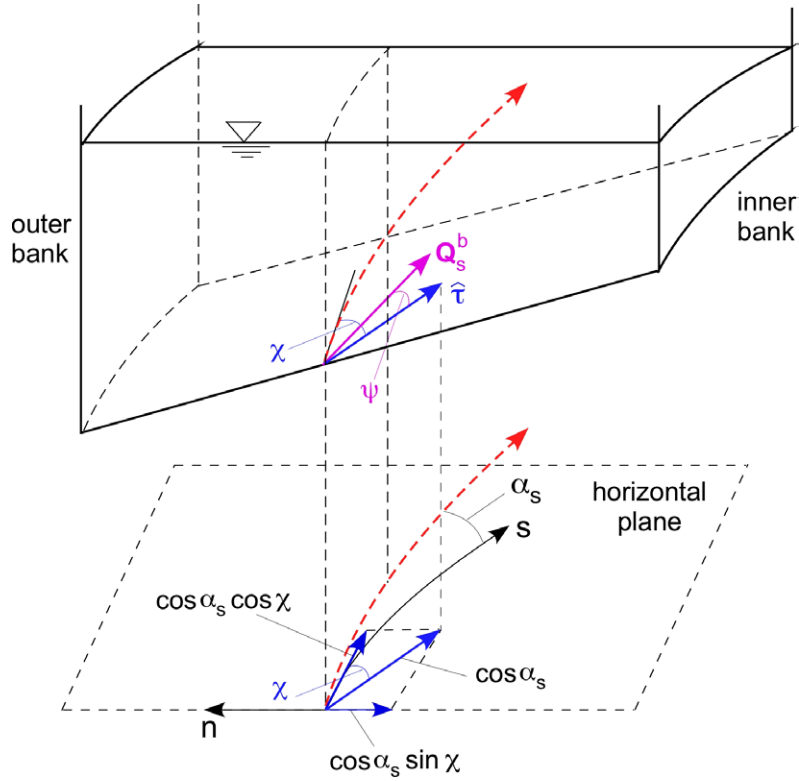


Figura 49. Sketch illustrating the deviation (measured by the angle χ) of the bed shear stress vector τ from the longitudinal direction induced by the secondary flow. Also shown is the deviation of the bedload flux vector Q_s^b from the bed shear stress vector. Deviation is measured by the angle ψ and is associated with the action of gravity on sediment particles in motion on the lateral sloping bed.

the longitudinal axis. In the context of the weakly sloping approximation adopted herein, the following closures for Q_{ss}^b and Q_{sn}^b , written in curvilinear coordinates, are found:

$$Q_{ss}^b = Q_{s0}^b \left[\cos \alpha_s \cos \chi - \frac{1}{h_s} \left(-\frac{1}{\Phi_{s0}^b} \frac{d\Phi_{s0}^b}{d\tau_{*c}} \right)_{\tau_{*c0}} \frac{\tau_{*c0}}{\mu_s} \frac{\partial \eta}{\partial s} \right] \quad (181a)$$

$$\simeq Q_{s0}^b \left[1 - \frac{1}{h_s} \left(-\frac{1}{\Phi_{s0}^b} \frac{d\Phi_{s0}^b}{d\tau_{*c}} \right)_{\tau_{*c0}} \frac{\tau_{*c0}}{\mu_s} \frac{\partial \eta}{\partial s} \right],$$

$$Q_{sn}^b = Q_{s0}^b \left[\cos \alpha_s \sin \chi - \frac{r}{\sqrt{\tau_*}} \frac{\partial \eta}{\partial n} \right] \simeq Q_{s0}^b \left[\sin \chi - \frac{r}{\sqrt{\tau_*}} \frac{\partial \eta}{\partial n} \right], \quad (181b)$$

where we have set $\cos \chi \simeq \cos \alpha_s \simeq 1$. Moreover, the angle χ will be evaluated through the following relationship:

$$\sin \chi = \left[\frac{T_{zn}}{|\tau|} \right]_{z_0} = \left[\frac{T_{zn}}{\sqrt{T_{zs}^2 + T_{zn}^2}} \right]_{z_0} \simeq \left[\frac{\partial u_n / \partial z}{\partial u_s / \partial z} \right]_{z_0}. \quad (182)$$

Note that we have taken advantage of the weak longitudinal channel slope to assume that the components of the shear stress vector τ acting on the bottom can be approximated by $T_{zs}|_{z_0}$ and $T_{zn}|_{z_0}$: this approximation is a direct consequence of the assumption $\cos \chi \simeq \cos \alpha_s \simeq 1$. Furthermore, notations are again those employed in Chapter 4(I). In particular, Q_{s0}^b is the

equilibrium dimensional bedload flux per unit width evaluated for the local and instantaneous hydrodynamic conditions, namely the local value of the Shields stress

$$\tau_* = \frac{|\boldsymbol{\tau}|}{(\rho_s - \rho) g d_s}. \quad (183)$$

3.1.2 The motion of the solid phase in sinuous channels: dimensionless formulation

Let us make the mathematical formulation for the motion of the solid phase dimensionless adopting the following scaling:

$$(\tilde{s}, \tilde{n}, \tilde{z}) = \left(\frac{s}{L}, \frac{n}{B}, \frac{z}{D_u} \right), \quad \tilde{t} = \frac{t}{D_u/U_u}, \quad (184a)$$

$$(\tilde{D}, \tilde{H}, \tilde{\eta}) = \left(\frac{D}{D_u}, \frac{H}{F_{ru}^2 D_u}, \frac{\eta}{D_u} \right), \quad (\tilde{u}_s, \tilde{u}_n, \tilde{u}_z) = \frac{(u_s, u_n, u_z \beta_u)}{U_u}, \quad (184b)$$

$$(\tilde{\nu}_T, \tilde{\mathfrak{D}}_j) = \left(\frac{\nu_T, \mathfrak{D}_j}{u_{\tau u} D_u} \right), \quad ((\tilde{c}), \tilde{C}) = \left(\frac{(c), C}{C_u} \right), \quad (184c)$$

$$(\tilde{Q}_{ss}^s, \tilde{Q}_{sn}^s) = \left(\frac{Q_{ss}^s, Q_{sn}^s}{C_u U_u D_u} \right), \quad (\tilde{Q}_{ss}^b, \tilde{Q}_{sn}^b) = \frac{(Q_{ss}^b, Q_{sn}^b)}{\sqrt{(s-1) g d^3}}, \quad (184d)$$

Note that the lateral coordinate has been scaled by the channel half width B , the longitudinal coordinate by some reference length L (e.g. meander wavelength), the vertical coordinate by some reference flow depth D_u , time by a hydrodynamic temporal scale associated with flow depth D_u/U_u , namely the time required by the reference uniform flow to travel a distance equal to the vertical scale D_u with the reference speed U_u . Moreover, the eddy diffusivity \mathfrak{D}_j has been scaled by $u_{\tau u} D_u$, with $u_{\tau u}$ friction velocity. Finally, the Reynolds averaged concentration and its depth averaged value have been scaled by some reference value C_u (e.g., the equilibrium concentration at the bed), the Einstein scale has been adopted for the components of the bedload flux and the components of the depth integrated suspended sediment flux have been scaled by the reference flux $C_u U_u D_u$. Note that the suffix u suggests that, just like in the previous Chapter, the reference state is a uniform flow in equilibrium with its cohesionless bed, to be precisely defined in each case.

With the help of the above scalings, the complete dimensionless form of the evolution equation of the bed interface in curvilinear coordinates reads:

$$\frac{C_u}{c_M} \frac{\partial(\tilde{D}\tilde{C})}{\partial\tilde{t}_m} + \frac{\partial\tilde{\eta}}{\partial\tilde{t}_m} + \frac{\mathfrak{L}}{\mathfrak{b}} \frac{1}{h_s} \left[\frac{\partial\tilde{Q}_{ss}^b}{\partial\tilde{s}} + r_{sb} \frac{\partial\tilde{Q}_{ss}^s}{\partial\tilde{s}} \right] + \frac{1}{h_s} \left[\frac{\partial(h_s \tilde{Q}_{sn}^b)}{\partial\tilde{n}} + r_{sb} \frac{\partial(h_s \tilde{Q}_{sn}^s)}{\partial\tilde{n}} \right] = 0. \quad (185)$$

Here, $\tilde{t}_m = \epsilon_m \tilde{t}$ with $\epsilon_m \left(\equiv \sqrt{(s-1) g d^3} / (c_M B U_u) \right)$ a small parameter that represents the ratio between the chosen hydrodynamic and morphological time scales. Moreover, $r_{sb} \left(\equiv C_u D_u U_u / \sqrt{(s-1) g d^3} \right)$ is the dimensionless parameter measuring the ratio between the scales of suspended load and bed load. Hence, the role of suspended load is negligible compared with that of bed load if $r_{sb} \ll 1$ and viceversa. Finally, \mathfrak{L} and \mathfrak{b} are the dimensionless parameters defined in the previous Chapter (equations 54) and their ratio is also the ratio B/L between the lateral and longitudinal spatial scales.

Note that, just like in the straight case discussed in Section 6.2(I), the first (*storage*) term present in (185) is often negligible because C_u/c_M is typically $\mathcal{O}(10^{-4})$ or smaller. However, this estimate is based on the choice we made for the hydrodynamic time scale (D_u/U_u), that is typically much smaller than the morphodynamic time scale. In general, other hydrodynamic time scales may play an important role. In particular, a *flood time scale* may be externally imposed if the flow discharge supplied to the channel reach varies in time. Flood and morphological time scales are often comparable with each other. Under these circumstances the flow field may no longer be

assumed to adapt instantaneously to temporal variations of supply and morphological changes and the first (storage) term in (185) is no longer negligible.

The evolution equation (185) requires closures in dimensionless forms.

The dimensionless forms of the relationships (181a) and (181b) for the components of the bedload flux read:

$$\tilde{Q}_{ss}^b = \Phi_{s0}^b \left[1 - \frac{\mathfrak{L}R_x}{\mathfrak{b}h_s} \frac{\partial \tilde{\eta}}{\partial \tilde{s}} \right], \quad (186a)$$

$$\tilde{Q}_{sn}^b = \Phi_{s0}^b \left[\sin \chi - R_y \frac{\partial \tilde{\eta}}{\partial \tilde{n}} \right]. \quad (186b)$$

Here Φ_{s0}^b is the equilibrium dimensionless bedload flux per unit width evaluated for the local and instantaneous hydrodynamic conditions, namely the local value of the Shields stress

$$\tau_* = \frac{\tau_{*u}}{\sqrt{C_{fu}}} \sqrt{\left(\tilde{\nu}_T \frac{\partial \tilde{u}_s}{\partial \tilde{z}} \right)_{\tilde{z}_0}^2 + \left(\tilde{\nu}_T \frac{\partial \tilde{u}_n}{\partial \tilde{z}} \right)_{\tilde{z}_0}^2}, \quad (187)$$

with

$$\tau_{*u} = \frac{u_{\tau u}^2}{(s-1)gd} \quad (188)$$

the Shields stress under uniform flow conditions. Moreover, R_x and R_y are the parameters defined by equations (484a,b)(I).

It is convenient at this stage to neglect the diffusive contributions of suspended load in the longitudinal and lateral directions, as they are found to be proportional to the friction coefficient C_{fu} , a typically small quantity. The dimensionless versions of (180) for the components of the depth integrated suspended flux then read:

$$\tilde{Q}_{ss}^s = \int_{\tilde{\eta}}^{F_{ru}^2 \tilde{H}} \langle \tilde{c} \rangle \langle \tilde{u}_s \rangle d\tilde{z}, \quad (189a)$$

$$\tilde{Q}_{sn}^s = \int_{\tilde{\eta}}^{F_{ru}^2 \tilde{H}} \langle \tilde{c} \rangle \langle \tilde{u}_n \rangle d\tilde{z}. \quad (189b)$$

Finally, the dimensionless form of the *macroscopically averaged* equation of continuity of the solid phase (177), written in curvilinear coordinates, takes the form:

$$\begin{aligned} \frac{1}{\sqrt{C_{fu}}} \frac{\partial \langle \tilde{c} \rangle}{\partial \tilde{t}} + \frac{\mathfrak{L}}{h_s} \frac{\partial (\langle \tilde{c} \rangle \tilde{u}_s)}{\partial \tilde{s}} + \frac{\mathfrak{b}}{h_s} \frac{\partial (h_s \langle \tilde{c} \rangle \tilde{u}_n)}{\partial \tilde{n}} + \mathfrak{b} \frac{\partial (\langle \tilde{c} \rangle \tilde{u}_z)}{\partial \tilde{z}} \\ - \frac{\partial}{\partial \tilde{z}} \left(\tilde{\mathfrak{D}}_z \frac{\partial \langle \tilde{c} \rangle}{\partial \tilde{z}} \right) - \frac{w_s}{u_{\tau u}} \frac{\partial \langle \tilde{c} \rangle}{\partial \tilde{z}} = 0. \end{aligned} \quad (190)$$

The boundary conditions associated with (190) are:

$$\left[-\tilde{\mathfrak{D}}_z \frac{\partial \langle \tilde{c} \rangle}{\partial \tilde{z}} - \frac{w_s}{u_{\tau u}} \langle \tilde{c} \rangle \right]_{F_{ru}^2 \tilde{H}} = 0, \quad (191a)$$

$$\left[\tilde{\mathfrak{D}}_z \frac{\partial \langle \tilde{c} \rangle}{\partial \tilde{z}} + \frac{w_s}{u_{\tau u}} \langle \tilde{c}_a \rangle \right]_{\tilde{\eta} + \tilde{a}} = 0. \quad (191b)$$

The above formulation must be completed imposing appropriate boundary conditions at the open boundaries that will be made explicit in each of the cases examined in the next sections.

Below, we will replace \tilde{z} by the transformed coordinate $\zeta = (\tilde{z} - \tilde{\eta})/\tilde{D}$.

3.2. Forced (point) bars in single bends of cohesionless channels with constant curvature

The case of a single bend can be treated extending the approach adopted in the previous Chapter to include the effects associated with the mobile nature of the bed. Essentially, the bed elevation η will no longer be assigned and the flow depth D will no longer vary only as a result of variations of the free surface elevation, but will feel the much stronger effect of variations of bed elevation. The physical mechanism that we wish to describe in the following is the formation of a point bar at the inner bend and of a pool at the outer bend. The driving effect is the occurrence of secondary flow at the bend entrance. This generates an inward directed lateral component of the bottom stress that drives an inward lateral component of sediment transport, whereby sediment particles are displaced from the outer region of the bend towards the inner region where they progressively build up the point bar. The process develops downstream until a new fully developed state is reached. As pointed out by Engelund (1974), equilibrium in this state is ensured by a balance between the inward directed tangential force acting on sediment particles as a result of the secondary flow and the outward directed tangential force resulting from the projection of gravity onto the tangent plane (Figure 50). Thus, in the fully developed state, the lateral component of the bedload flux vanishes, i.e. the bedload flux is a vector aligned with the longitudinal direction. Note that the distance required for the bed to achieve its fully developed equilibrium state will exceed, in general, the distance required for the hydrodynamics to fully develop.

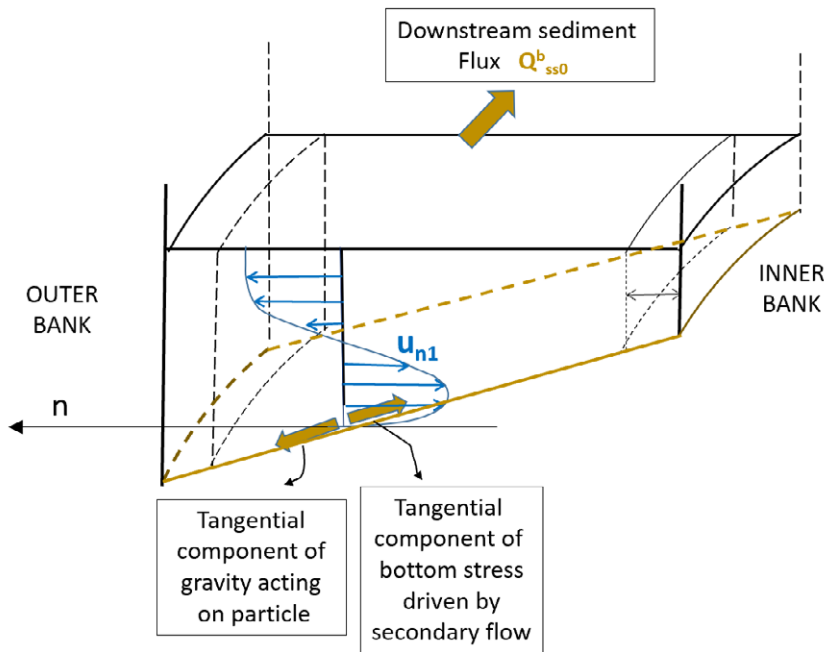


Figure 50. Sketch illustrating the physical mechanism that controls the establishment of a lateral slope of the channel under fully developed conditions and dominant bedload.

The dimensionless formulation of the problem follows the lines presented in the previous Section. However, note that, in the constant curvature case, there is no external longitudinal scale, hence we set $L = B$ and replace the dimensionless parameter \mathcal{L} with \mathfrak{b} throughout.

3.2.1 Fully developed point bar in mildly curved bends: linear theory

Let us start examining the case of *mildly curved* bends, assuming:

$$\delta \ll 1. \quad (192)$$

This assumption allows us to employ the perturbation approach presented in the previous Chapter. We will examine the fully developed state and leave to the reader the investigation of the spatial transition from the straight configuration to the fully developed state asymptotically reached as $s \rightarrow \infty$. Below, for the sake of simplicity, we will remove the tilde from notations for dimensionless quantities.

The hydrodynamics of the steady state (in particular in the fully developed case) is governed by the equations and boundary conditions introduced in Section 2.4.1 and will not be repeated here. The only novel feature to be introduced in that formulation concerns the flow depth that will have to be considered as an unknown variable rather than a given quantity. In order to set up the appropriate perturbation expansion, let us consider the bedload dominated case and note that, under equilibrium conditions ($Q_{sn}^b = 0$), the order of magnitude of the lateral bed slope established in the cross section is controlled by a *balance between the lateral stress contribution* ($\propto \sin \chi$) and *the gravitational term in the closure relationship* (186b). The former is proportional to the lateral component of the secondary flow u_n which is $\mathcal{O}(\delta)$ for weakly curved bends. The size of the latter is $\mathcal{O}(R_{yu} \partial \eta / \partial n)$. Hence, the magnitude of the lateral slope depends on the parameter R_{yu} . If the latter is $\mathcal{O}(1)$, then the above balance implies that the lateral slope $\partial \eta / \partial n$ is $\mathcal{O}(\delta)$, i.e. perturbations of bottom elevation are small and a linear theory is appropriate. This is the case most commonly examined in the literature and will be discussed in this Section. We will see in Section 3.2.2 that a rational approach can be set up also for mildly curved bends characterized by small values of the parameter R_{yu} (as typically found in nature), in which case the perturbations of bed elevation are finite ($\mathcal{O}(1)$) although the secondary flow keeps small.

In the linear case, the perturbation expansion reads:

$$\begin{aligned} [u_s, u_n, u_z, H, D, \nu_T, Q_{ss}, Q_{sn}] = & \\ \delta^0 [u_{s0}(\zeta), 0, u_{z0}(\zeta), H_u(s) + h_0, 1 + F_{ru}^2 h_0, \nu_{T0}(\zeta), Q_{ss0}, 0] + & \\ \delta [u_{s1}(n, \zeta), u_{n1}(\zeta), u_{z1}(n, \zeta), h_1(n), D_1(n), \nu_{T1}(n, \zeta), Q_{ss1}(n), Q_{sn1}(n)] + & \\ \mathcal{O}(\delta^2), & \end{aligned} \quad (193)$$

Here, as usual, H_u is the dimensionless free surface elevation of the unperturbed uniform flow in a straight channel with constant slope S of the channel axis. Moreover, in a linear context the flow depth at the leading order is the unperturbed uniform flow depth, but we allow for a dimensionless perturbation $F_{ru}^2 h_0$, i.e. a correction of the free surface elevation and, possibly, of the free surface slope. This correction is required to satisfy the two integral constraints to be imposed at the open boundaries, entailing a constant water flux (equation (60)) and a constant sediment flux, namely

$$\int_{-1}^1 Q_{ss} dn = 2 Q_{ssu}, \quad (194)$$

with Q_{ssu} depth integrated sediment flux per unit width in the straight channel upstream of the bend.

Substituting from (193) into the differential problem governing the flow hydrodynamics (Section 2.4.1), one again finds a sequence of differential problems at the various orders of approximation which are nearly identical with their fixed bed counterparts. The reader will readily verify that the solution up to $\mathcal{O}(\delta)$ reads:

$$u_{s0} = \mathcal{F}_0(\zeta), \quad u_{z0} = F_{ru}^2 \frac{dH_u}{ds} u_{s0}, \quad h_0 = 0, \quad U_0 = 1, \quad D_0 = 1, \quad (195a)$$

$$u_{n1} = \mathcal{F}_0(\zeta) I_{\mathcal{G}_{11}} - \mathcal{G}_{11}(\zeta), \quad h_1 = -\frac{\sqrt{C_{fu}}}{\mathfrak{b}} I_{\mathcal{G}_{11}} n, \quad (195b)$$

$$u_{s1} = \frac{1}{2} \left(\frac{7}{6} D_1 - \frac{n}{\mathfrak{b}} \right) \mathcal{F}_0(\zeta), \quad u_{z1} = F_{ru}^2 \frac{dH_u}{ds} \mathcal{F}_0(\zeta) \left(\frac{7}{12} D_1 - \frac{3}{2} \frac{n}{\mathfrak{b}} \right), \quad (195c)$$

where notations are those employed in the fixed bed case. In particular, we recall that $I_{G_{11}} = \int_{\zeta_0}^1 G_{11} d\zeta$. Note that the procedure to prove that h_0 vanishes is identical to that used in the fixed bed case. A similar procedure allows one to show that h_{10} must also vanish in order to satisfy the integral constraint (60). Finally, D_1 must satisfy the integral constraint (60). With the help of (195), one finds that the latter becomes:

$$\int_{-1}^1 D_1 dn = 0. \quad (196)$$

In order to proceed with the evaluation of the flow depth perturbation D_1 (and of the associated bottom pattern) we need to examine the consequences of the mobile character of the bed. In the fully developed region of the bend, the steady Exner equation (185) reduces to the simple statement:

$$\frac{\partial(h_s Q_{sn})}{\partial n} = 0. \quad (197)$$

Imposing the boundary condition that constrains the lateral component of the sediment flux to vanish at the channel banks, the latter relationship leads to the following solution:

$$Q_{sn} = 0. \quad (198)$$

It is instructive, at this stage, to distinguish between the case when sediment transport is dominated by bedload and the general case where suspended load is also significant.

The bedload dominated case

In the bedload dominated case, with the help of (186b) and (182) the equation (198) at $\mathcal{O}(\delta)$ becomes:

$$Q_{sn1}^b = \Phi_{s0}^b \left[\left(\frac{du_{n1}}{d\zeta} / \frac{du_{s0}}{d\zeta} \right)_{\zeta_0} - R_{yu} \frac{d\eta_1}{dn} \right] = 0, \quad (199)$$

and, consequently, the solution for the bottom elevation is:

$$\eta_1 = \frac{1}{R_{yu}} \left[\frac{du_{n1}}{d\zeta} / \frac{du_{s0}}{d\zeta} \right]_{\zeta_0} n. \quad (200)$$

Observing that $\eta_1 = F_{ru}^2 h_1 - D_1$, and using (195b) for h_1 , one finds:

$$D_1 = - \left(F_{ru}^2 \frac{\sqrt{C_{fu}}}{b} I_{G_{11}} + \frac{1}{R_{yu}} \left[\frac{du_{n1}}{d\zeta} / \frac{du_{s0}}{d\zeta} \right]_{\zeta_0} \right) n. \quad (201)$$

This result is quite instructive. Noting that $[du_{n1}/d\zeta]_{\zeta_0}$ is a negative quantity, (200) predicts the formation of a point bar at the inner bend, where η_1 is maximum, and a pool at the outer bend, where η_1 is minimum. Moreover, it suggests that the amplitude of the perturbation of bed elevation scales with the parameter γ defined as follows:

$$\gamma = \frac{\delta}{R_{yu}} = \frac{\nu_0 \sqrt{\tau_{*u}}}{r \sqrt{C_{fu}}}. \quad (202)$$

Hence, as pointed out by Seminara and Solari (1998), scour increases linearly with the curvature ratio ν_0 and with the square root of the average Shields stress τ_{*u} . Notice that the parameter γ controls the intensity of bottom scour and attains typically $\mathcal{O}(1)$ values. In other words, the maximum scour may be a finite quantity in spite of the fact that curvature (and the associated secondary flow) is small, an observation that restricts the formal validity of the linear approach proposed above to bends characterized by small values of the γ parameter. In the next Section, we show that a rational approach may be readily formulated for mildly curved bends with finite perturbations of the bottom topography, where the latter restriction is removed.

The additional effect of suspended load

If suspended load is also significant, then the average concentration field as well as the suspended flux must also be expanded in powers of the small parameter δ in the form

$$[\langle c \rangle, Q_{ss}^s, Q_{sn}^s] = [\langle c \rangle_0(\zeta), Q_{ss0}^s, 0] + \delta [\langle c \rangle_1(n, \zeta), Q_{ss1}^s(n), Q_{sn1}^s] + O(\delta^2), \quad (203)$$

where $\langle c \rangle_0(\zeta)$ and Q_{ss0}^s are the vertical distribution of the average concentration and the suspended sediment flux per unit width in the straight basic configuration, respectively. However, a glance at the advection diffusion equation (190) for $\langle c \rangle$ immediately suggests that, in the present linear fully developed case, no forcing is induced on $\langle c \rangle$ by the secondary flow, at least up to $\mathcal{O}(\delta)$. Hence $\langle c \rangle_1 = 0$. Indeed, neither $\langle c \rangle_0$ nor u_{n1} depend on n and the term describing the transverse diffusion can be neglected being proportional to $b^2 C_{fu}$. Moreover, in the fully developed case, one readily appreciates that the longitudinal component of the suspended sediment flux does not affect the solution of the Exner equation (198) that, at $\mathcal{O}(\delta)$, becomes:

$$Q_{sn1}^b + r_{sb} Q_{sn1}^s = \Phi_{s0}^b \left[\left(\frac{du_{n1}}{d\zeta} / \frac{du_{s0}}{d\zeta} \right)_{\zeta_0} - R_{yu} \frac{d\eta_1}{dn} \right] + r_{sb} \int_{\zeta_0}^1 \langle c \rangle_0 u_{n1} d\zeta = 0. \quad (204)$$

Here, the lateral component of the suspended sediment flux Q_{sn1}^s has been obtained from the definition (189b) and consists of the advective contribution only. Indeed, the diffusive contribution vanishes, as the leading order average concentration $\langle c \rangle_0$ is independent of the lateral coordinate and $\langle c \rangle_1$ vanishes. One ends up with the following solution for the perturbation of bed elevation:

$$\eta_1 = \frac{1}{R_{yu}} \left\{ \left[\frac{du_{n1}}{d\zeta} / \frac{du_{s0}}{d\zeta} \right]_{\zeta_0} + \frac{r_{sb}}{\Phi_{s0}^b} \int_{\zeta_0}^1 \langle c \rangle_0(\zeta) u_{n1}(\zeta) d\zeta \right\} n. \quad (205)$$

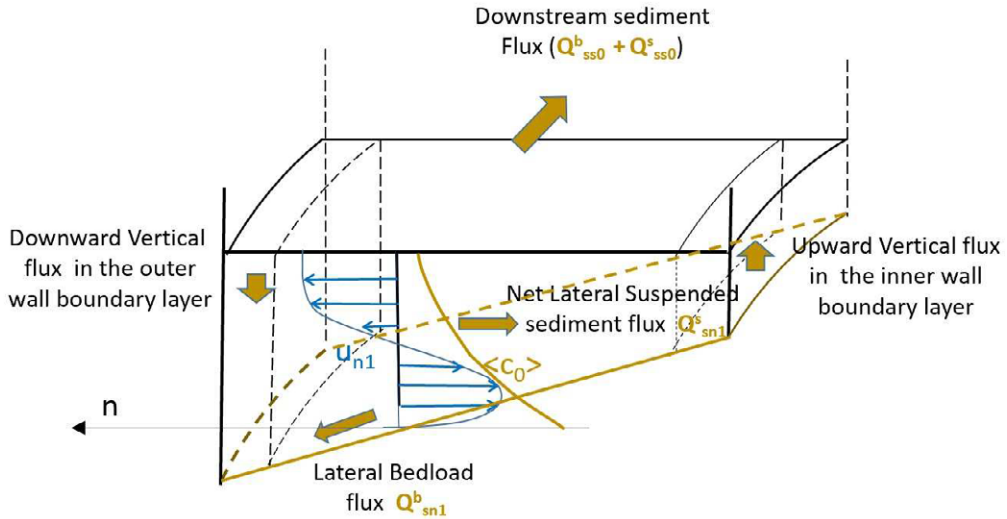


Figure 51. Sketch illustrating the physical mechanism that determines the negative sign of the net lateral component of the suspended sediment flux.

Note that the lateral component of the suspended flux (i.e. the integral in the right hand side of equation 205) is a negative quantity as the sediment concentration is higher close to the bed, where the secondary flow is directed inward and lower close to the free surface, where the secondary

flow is directed outward (Figure 51). As a result, *at equilibrium the lateral slope of the bed must increase relative to the bedload dominated case*, such to generate a positive contribution of the lateral component of the bedload flux able to balance the negative contribution of the suspended sediment flux.

The output of the analysis can be summarized by the following relationship for the magnitude of the maximum scour at the outer bank. Recalling that η is the bed elevation relative to the undisturbed horizontal bed, the magnitude of the maximum scour coincides with the magnitude of the minimum bed elevation of the cross section η_{min} :

$$|\eta_{min}| = \gamma \left(s_1 + \frac{r_{sb}}{\Phi_{s0}^b} s_2 \right), \quad (206)$$

where the coefficients s_1 and s_2 are plotted in Figure 52 (a),(b).

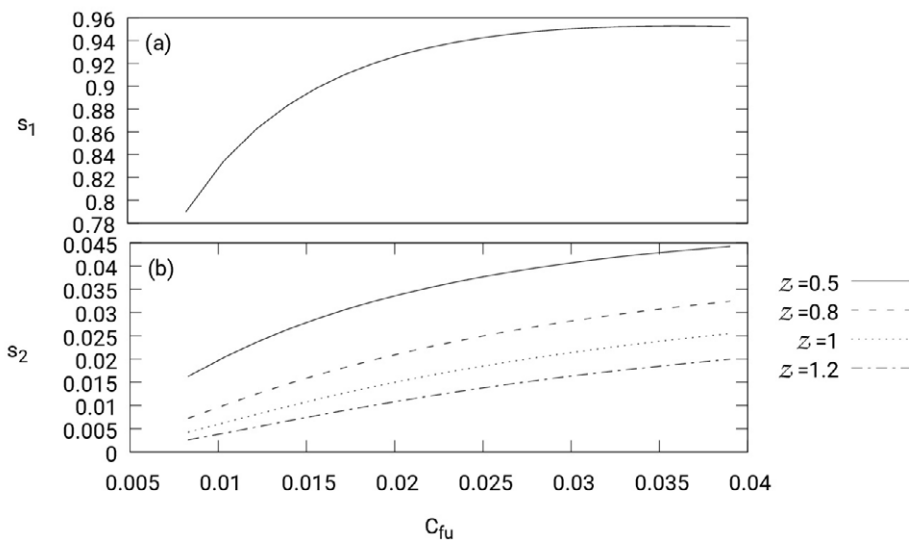


Figure 52. (a),(b) The coefficients s_1 and s_2 of the relationship (206) yielding the magnitude of maximum scour at the outer bank, $|\eta_{min}|$, are plotted as functions of the friction coefficient C_{fu} for uniform flow conditions. Different values of the Rouse number \mathcal{Z} have been considered to account for the intensity of suspended load.

For pure bedload conditions, the maximum scour at the outer bank increases as the friction coefficient of the undisturbed uniform flow increases (Figure 52a). The contribution of suspended load to the maximum scour increases with C_{fu} and with the Rouse number \mathcal{Z} (Figure 52b). Application of the above theory is reported in Figure 53 for the Po and Magdalena Rivers, note that results agree satisfactorily in the case of Magdalena River (Figures 53(c) and 54).

3.2.2 Finite amplitude fully developed point bars in mildly constant curvature bends

We have seen in Section 3.2.1 that perturbations of bed elevation driven by curvature in weakly curved channels may be finite quantities although the secondary flow is small. We now illustrate a rational theory originally proposed by Seminara and Solari (1998), that is able to account for finite amplitude perturbations of bed topography (and flow depth) within the context of a perturbation approach still valid in the limit of *small* δ .

Two basic novel ideas underlie this theory:

- we treat the flow field at the leading order of approximation as a slowly varying sequence of locally uniform flows characterized by the local values of flow depth;

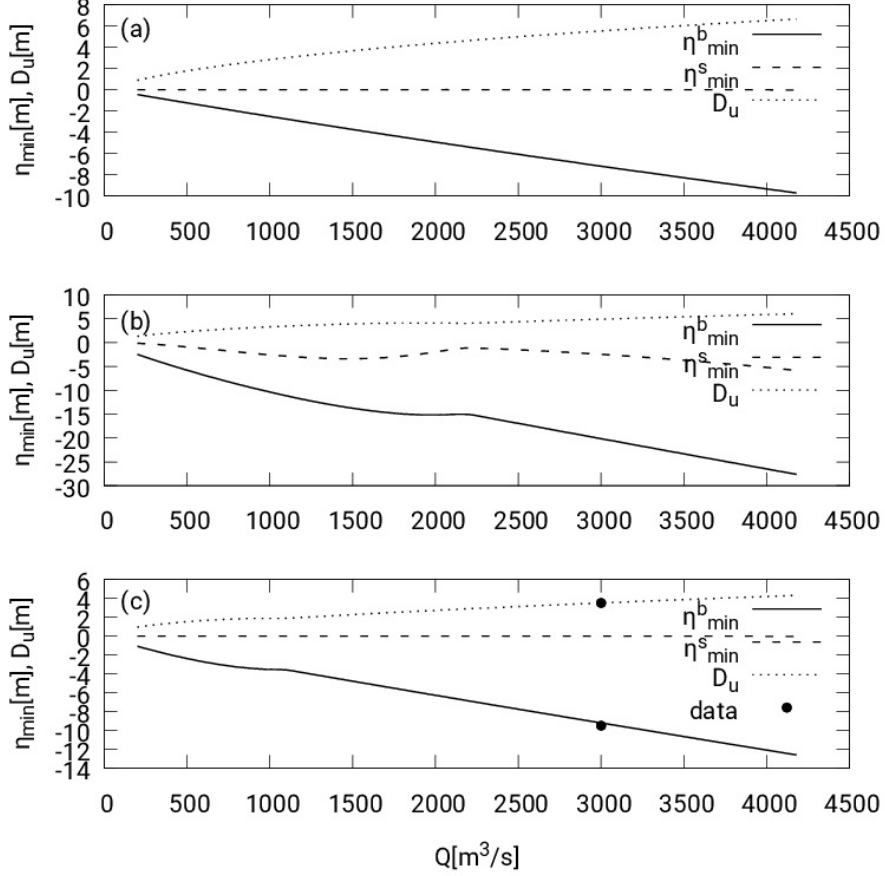


Figure 53. Uniform flow depth (black line); minimum bed elevation at the outer bank for pure bedload conditions, η_{min}^b (magenta line) and suspended sediment contribution to the minimum bed elevation at the outer bank, η_{min}^s (green line) as functions of the flow discharge, for (a) an upstream reach of the Po River ($S=0.001$, $d=5$ mm, $B=100$ m, $R_0=1$ km), (b) a downstream reach of the Po River ($S=0.0001$, $d=0.15$ mm, $B=150$ m, $R_0=1$ km) and (c) the Magdalena River ($S=0.00038$, $d=0.55$ mm, $B=150$ m, $R_0=1.3$ km). Dots refer to field data (see Figure 54).

- we take advantage of the fact that the coefficient of the lateral slope term in the closure relationship for the lateral bedload flux (186b) is typically small, and set:

$$R_{yu} = c_{ls} \delta, \quad (207)$$

with c_{ls} an $\mathcal{O}(1)$ quantity.

The former assumption is formally justified for weakly curved sufficiently wide bends and has an important physical consequence. The solutions for both the flow depth and the longitudinal flow velocity are allowed to vary in the lateral direction at the leading order of approximation, hence the important mechanism of lateral redistribution of flow momentum that leads to distortion of the longitudinal flow operates at first order (rather than at second order as in the linear theory of Section 3.2.1).

The latter assumption applies commonly in the field where the product $\beta_u \sqrt{\tau_{*u}}$ is sufficiently large.

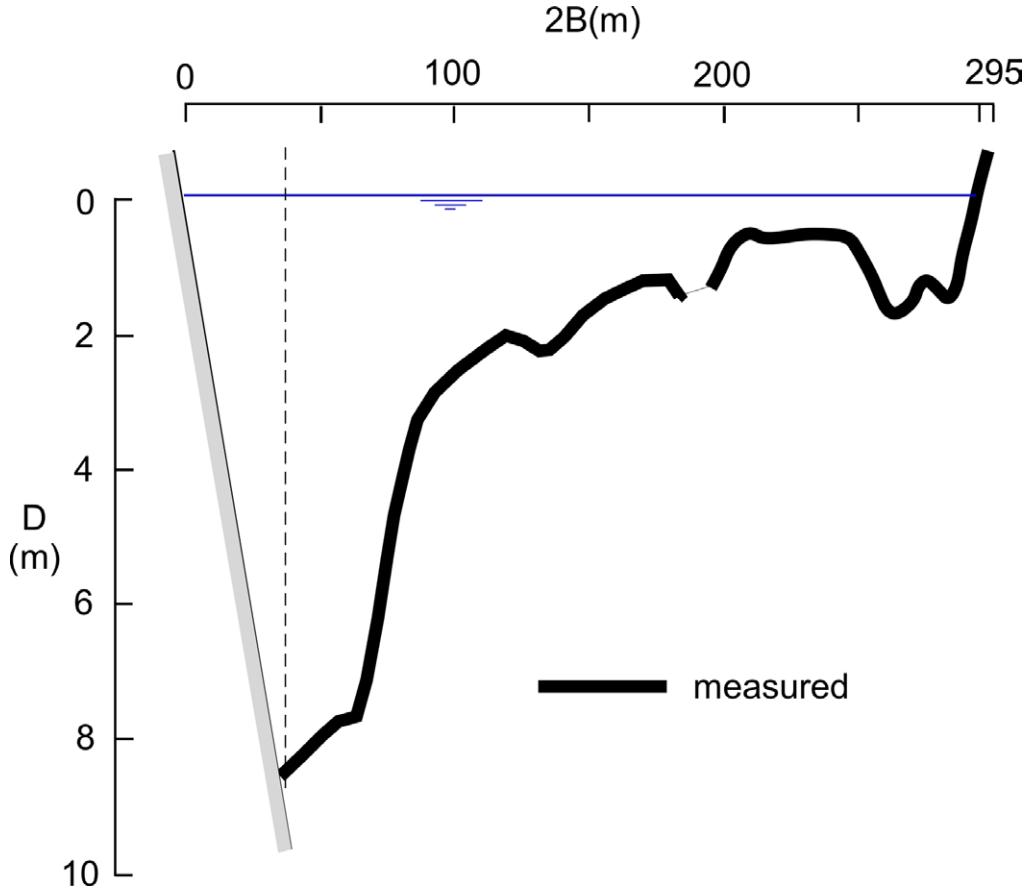


Figura 54. Cross section of Magdalena River downstream of Pto. Triunfo (data from Jansen et al., 1979).

Under the above assumptions, we may set up a perturbation expansion similar to that employed in the fixed bed case discussed in Section 2.4.3:

$$\begin{aligned}
 [u_s, u_n, u_z, H, D, \nu_T, Q_{ss}^b, Q_{sn}^b] &= \\
 &= \delta^0 [u_{s0}(n, \zeta), 0, u_{z0}(n, \zeta), H_u(s) + h_0(s), D_0(s, n), \nu_{T0}(n, \zeta), Q_{ss0}^b(n), Q_{sn0}^b(n)] \\
 &+ \delta [u_{s1}(n, \zeta), u_{n1}(n, \zeta), u_{z1}(n, \zeta), h_1(s, n), D_1(s, n), \nu_{T1}(n, \zeta), Q_{ss1}^b(n), Q_{sn1}^b(n)] \\
 &+ \delta^2 [u_{n2}(n, \zeta), h_2(s, n)] + \mathcal{O}(\delta^2).
 \end{aligned} \tag{208}$$

The main novel feature with respect to that formulation concerns the flow depth components, D_0 and D_1 , which are unknown variables rather than given quantities. A second feature that needs to be accounted for is the correction of the longitudinal slope (S) of the unperturbed free surface, due to the perturbation of the free surface elevation $h(s, n)$ relative to its unperturbed uniform configuration $H_u(s)$. As a result, the forcing term in the dimensionless form of the longitudinal momentum equation ($-\sqrt{C_{fu}}$) must be replaced by ($-\sqrt{C_{fu}}\mathfrak{R}$) where:

$$\mathfrak{R} = \frac{\partial H}{\frac{dH_u}{ds}} = -\frac{\mathfrak{b}}{\sqrt{C_{fu}}} \frac{\partial H}{\partial s}. \tag{209}$$

The quantity \mathfrak{R} represents the ratio between the free surface slope in the curved bend and its unperturbed value in the straight reach. \mathfrak{R} may also be expanded in powers of δ as follows:

$$\mathfrak{R} = \mathfrak{R}_0(s) + \delta \mathfrak{R}_1(s, n) + \mathcal{O}(\delta^2). \quad (210)$$

Substituting from (208) and (210) into the governing differential problem for the flow hydrodynamics, one finds a sequence of differential problems at the various orders of approximation quite similar to their fixed bed counterparts.

The only difference is related to the term dH_u/ds that is now replaced by

$$\frac{\partial H}{\partial s} = -\frac{\mathfrak{R}_0 \sqrt{C_{fu}}}{\mathfrak{b}} \left[1 + \delta \frac{\mathfrak{R}_1}{\mathfrak{R}_0} + \delta^2 \frac{\mathfrak{R}_2}{\mathfrak{R}_0} + \mathcal{O}(\delta^3) \right]. \quad (211)$$

where

$$\mathfrak{R}_0 = 1 - \frac{\mathfrak{b}}{\sqrt{C_{fu}}} \frac{dh_0}{ds}, \quad \mathfrak{R}_1 = -\frac{\mathfrak{b}}{\sqrt{C_{fu}}} \frac{\partial h_1}{\partial s}, \quad \mathfrak{R}_2 = -\frac{\mathfrak{b}}{\sqrt{C_{fu}}} \frac{\partial h_2}{\partial s} \quad (212)$$

Bottom pattern at the leading order

In order to determine the lowest order approximation for the bed profile, it is sufficient to determine the solution for u_{s0} , u_{n1} and h_1 . The reader will readily find that:

$$u_{s0} = \mathfrak{R}_0^{1/2} D_0^{7/12} \mathcal{F}_0(\zeta), \quad u_{z0} = u_{s0} F_{ru}^2 \mathfrak{R}_0 \frac{dH_u}{ds}, \quad (213a)$$

$$u_{n1} = \mathfrak{R}_0^{1/2} D_0^{7/4} \mathcal{G}_1(\zeta), \quad \mathcal{G}_1(\zeta) = I_{\mathcal{G}_{11}} \mathcal{F}_0(\zeta) - \mathcal{G}_{11}(\zeta), \quad (213b)$$

$$h_1 = h_{10}(s) - \frac{\sqrt{C_{fu}}}{\mathfrak{b}} I_{\mathcal{G}_{11}} \mathfrak{R}_0 \int_{-1}^n D_0^{7/6} dn', \quad (213c)$$

where notations are those employed in the fixed bed case.

A major difference between the present nonlinear slowly varying solution (213) and the linear solution (195) is the dependence of the former on the as yet unknown distribution of flow depth D_0 that displays $\mathcal{O}(1)$ lateral variations. Also, note that $I_{\mathcal{G}_1}$ vanishes like in the fixed bed case, a constraint arising again from flow continuity. Indeed, integrating the continuity equation and imposing the kinematic boundary condition at the free surface, one ends up with the following relationship:

$$\frac{d}{dn} (D_0 I_{u_{n1}}) = 0. \quad (214)$$

Hence, recalling that the lateral flux must vanish at the walls, it follows that the lateral water flux must vanish identically.

In order to complete the analysis to determine the function $D_0(n)$ we must solve the Exner equation. We limit ourselves to the case of dominant bedload, leaving to the reader the task to evaluate the additional effect of suspended load. In the bedload dominated case, with the help of (182), (186b) and (207), the equation (198) at $\mathcal{O}(\delta)$ becomes:

$$Q_{sn1}^b = \Phi_{s0}^b \left[\left(\frac{\partial u_{n1} / \partial \zeta}{\partial u_{s0} / \partial \zeta} \right)_{\zeta_0} + \sqrt{\frac{\tau_{*u}}{\tau_{*0}}} c_{ts} \frac{dD_0}{dn} \right] = 0. \quad (215)$$

From the definition of Shields stress (187), one readily finds that

$$\tau_{*0} = \frac{\tau_{*u}}{\sqrt{C_{fu}}} \frac{1}{D_0} \left(\nu_{T0} \frac{\partial u_{s0}}{\partial \zeta} \right)_{\zeta_0}, \quad (216)$$

or, recalling the differential problem for u_{s0} , integrating over the depth and assuming that $(1 - \zeta_0) \simeq 1$:

$$\tau_{*0} = \frac{\tau_{*u}}{\sqrt{C_{fu}}} (D_0 \mathfrak{R}_0 \sqrt{C_{fu}}) = \tau_{*u} D_0 \mathfrak{R}_0. \quad (217)$$

Hence:

$$\sqrt{\frac{\tau_{*u}}{\tau_{*0}}} = D_0^{-1/2} \mathfrak{R}_0^{-1/2}. \quad (218)$$

Substituting from (213) and (218) into (215) the following nonlinear ordinary differential equation for D_0 is found;

$$\frac{dD_0}{dn} = \left(\left[\frac{d\mathcal{G}_{11}/d\zeta}{d\mathcal{F}_0/d\zeta} \right]_{\zeta_0} - I_{\mathcal{G}_{11}} \right) \frac{\mathfrak{R}_0^{1/2}}{c_{ls}} D_0^{5/3}. \quad (219)$$

This is immediately solved to give:

$$D_0 = \left(d_{01} \mathfrak{R}_0^{1/2} n + D_{00} \right)^{-3/2}, \quad d_{01} = \frac{2}{3 c_{ls}} \left(I_{\mathcal{G}_{11}} - \left[\frac{d\mathcal{G}_{11}/d\zeta}{d\mathcal{F}_0/d\zeta} \right]_{\zeta_0} \right). \quad (220)$$

with D_{00} constant to be determined. Thus, we are left with a solution that depends on two constants, namely \mathfrak{R}_0 and D_{00} . They are determined imposing two integral conditions that constrain the water and sediment longitudinal fluxes to keep constant and equal to the values experienced in the straight reach upstream. The former condition is the integral constraint (60) that, with the help of (213a), takes the form:

$$\mathfrak{R}_0^{1/2} \int_{-1}^1 D_0^{19/12} dn = 2. \quad (221)$$

Using the solution (220) and some algebra, one finds:

$$\left(-d_{01} \mathfrak{R}_0^{1/2} + D_{00} \right)^{-11/8} - \left(d_{01} \mathfrak{R}_0^{1/2} + D_{00} \right)^{-11/8} = \frac{11}{4} d_{01}, \quad (222)$$

The second condition may be written in the form:

$$\int_{-1}^1 Q_{ss0}^b dn = \int_{-1}^1 \Phi_{s0}^b(\tau_{*0}) dn = 2 \Phi_u, \quad (223)$$

Adopting Meyer-Peter and Müller (1948) formula for Φ_{s0}^b and recalling the relationships (217) and (220), some algebra finally leads to the following form of the latter constraint:

$$\int_{-1}^1 \left[\mathfrak{R}_0 \tau_{*u} \left(d_{01} \mathfrak{R}_0^{1/2} n + D_{00} \right)^{-3/2} - \tau_{*c} \right]^{3/2} dn = 2(\tau_{*u} - \tau_{*c})^{3/2}. \quad (224)$$

The two relationships (222) and (224) can be solved by a trial and error procedure for the two unknown constants \mathfrak{R}_0 and D_{00} .

Bottom pattern at first order

A supplement of analysis is needed if one wishes to determine the distortion of the longitudinal velocity profile driven by the lateral redistribution of flow momentum. We then need to determine the solutions for u_{z1} and u_{s1} , that depend on the first order correction for the flow depth (D_1). To determine the latter quantity one needs to find the solution of Exner equation at $\mathcal{O}(\delta^2)$, which requires the availability of the solutions for u_{n2} and h_2 . The algebraic work needed to determine u_{z1} and u_{s1} is similar to that pursued in the fixed bed case and is left to the reader, who will show that these quantities read:

$$u_{s1} = \frac{1}{2} u_{s0} \left[\frac{7}{6} \frac{D_1}{D_0} - \frac{n}{\mathfrak{b}} + \frac{\mathfrak{R}_1}{\mathfrak{R}_0} \right] + \mathfrak{b} \mathfrak{R}_0^{1/2} D_0^{23/12} \frac{dD_0}{dn} \left(\mathcal{F}_{11} - \frac{1}{2} I_{\mathcal{F}_{11}} \mathcal{F}_0 \right). \quad (225a)$$

$$u_{z1} = \mathfrak{R}_0^{1/2} D_0^{7/4} \frac{dD_0}{dn} \left[-\frac{11}{4} \mathcal{I}_{\mathcal{G}_1} + (\zeta - 1) \mathcal{G}_1 \right] - \mathfrak{R}_0 \frac{\sqrt{C_{fu}}}{\mathfrak{b}} F_{ru}^2 \left[u_{s1} - \frac{n}{\mathfrak{b}} u_{s0} + \frac{\mathfrak{R}_1}{\mathfrak{R}_0} u_{s0} \right], \quad (225b)$$

Here, the second major difference with respect to the linear solution (195c) emerges. The $\mathcal{O}(\delta)$ correction of the longitudinal velocity is now affected by the momentum redistribution driven by the secondary flow, that in the present context occurs at $\mathcal{O}(\delta)$ (see the second term in the right hand side of equation (225a)). Note that a similar effect of momentum redistribution was obtained in the fixed bed case (Section 2.4.3). The only difference between the *fixed bed solution* (equation (127)) and the present one is the fact that the flow depth was assigned in Section 2.4.3, while it is an unknown in the mobile bed case. The solution for u_{s1} depends on the unknown quantities D_1 and \mathfrak{R}_1 that are related to each other through the integral constraint (60) that, at $\mathcal{O}(\delta)$ reads:

$$\int_{\zeta_0}^1 d\zeta \int_{-1}^1 (u_{s0} D_1 + u_{s1} D_0) dn = 0, \quad (226)$$

or, recalling the solutions for u_{s0} and u_{s1} :

$$\frac{\mathfrak{R}_1}{\mathfrak{R}_0} = \frac{\frac{1}{\mathfrak{b}} \int_{-1}^1 n D_0^{19/12} dn - \frac{19}{6} \int_{-1}^1 D_0^{7/12} D_1 dn - \frac{12}{47} \mathfrak{b} I_{\mathcal{F}_{11}} \left[D_0 \Big|_1^{47/12} - D_0 \Big|_{-1}^{47/12} \right]}{N_{19/12}}, \quad (227)$$

In order to evaluate D_1 we must solve the Exner equation at $\mathcal{O}(\delta^2)$, which, in turn, involves the second order component of the lateral velocity u_{n2} . Let us then substitute from (208) and (105) into the governing differential problem for u_n , and equate terms of $\mathcal{O}(\delta^2)$ to find:

$$\begin{aligned} \frac{1}{D_0^2} \frac{\partial}{\partial \zeta} \left(\nu_{T0} \frac{\partial u_{n2}}{\partial \zeta} \right) &= -\frac{1}{D_0^2} \left(\frac{U_1}{U_0} - \frac{7}{6} \frac{D_1}{D_0} \right) \frac{\partial}{\partial \zeta} \left(\nu_{T0} \frac{\partial u_{n1}}{\partial \zeta} \right) + \frac{\mathfrak{b}}{D_0} u_{z1} \frac{\partial u_{n1}}{\partial \zeta} \\ &+ \mathfrak{b} \frac{\partial h_2}{\partial n} + \frac{n}{\mathfrak{b}} u_{s0}^2 - 2 u_{s0} u_{s1} - \frac{\mathfrak{b}}{D_0} \frac{\partial u_{n1}}{\partial \zeta} F_{ru}^2 \frac{dh_0}{ds} \left(u_{s1} - \frac{n}{\mathfrak{b}} u_{s0} \right) \\ &- \frac{\mathfrak{b}}{D_0} u_{s0} \frac{\partial u_{n1}}{\partial \zeta} F_{ru}^2 \frac{dh_1}{ds} + \mathfrak{b} \left[u_{n1} \frac{\partial u_{n1}}{\partial n} - \frac{u_{n1}}{D_0} (\zeta - 1) \frac{dD_0}{dn} \frac{\partial u_{n1}}{\partial \zeta} \right] \\ &+ \frac{\mathfrak{b}}{D_0} \left[\frac{\partial u_{n2}}{\partial \zeta} - \frac{D_1}{D_0} \frac{\partial u_{n1}}{\partial \zeta} \right] \left[u_{z0} - u_{s0} F_{ru}^2 \frac{dh_0}{ds} \right], \end{aligned} \quad (228a)$$

$$u_{n2} \Big|_{\zeta_0} = 0, \quad \frac{\partial u_{n2}}{\partial \zeta} \Big|_1 = 0, \quad (228b)$$

or, using the solutions for u_{z0} and u_{z1} :

$$\begin{aligned} \frac{1}{D_0^2} \frac{\partial}{\partial \zeta} \left(\nu_{T0} \frac{\partial u_{n2}}{\partial \zeta} \right) &= \left(-\frac{U_1}{U_0} + \frac{7}{6} \frac{D_1}{D_0} \right) \left(\mathfrak{b} \frac{\partial h_1}{\partial n} - u_{s0}^2 \right) + \mathfrak{b} \frac{\partial h_2}{\partial n} + \frac{n}{\mathfrak{b}} u_{s0}^2 \\ &- 2 u_{s0} u_{s1} - \frac{\mathfrak{b}}{D_0} \frac{\partial u_{n1}}{\partial \zeta} \frac{\partial (D_0 \mathcal{I} u_{n1})}{\partial n} + \mathfrak{b} u_{n1} \frac{\partial u_{n1}}{\partial n} \end{aligned} \quad (229a)$$

$$u_{n2}|_{\zeta_0} = 0, \quad \frac{\partial u_{n2}}{\partial \zeta} \Big|_1 = 0, \quad (229b)$$

Let us next define:

$$u_{n2} = \mathfrak{R}_0^{1/2} \left\{ \left[U_{20} + U_{21} \frac{D_1}{D_0} + a_2(n) U_{22} \right] \mathcal{F}_0(\zeta) + \left[U_{23} \frac{D_1}{D_0} + U_{24} \right] \mathcal{G}_{11}(\zeta) + U_{25} \mathcal{G}_{21}(\zeta) \right\}, \quad (230a)$$

$$\frac{\partial h_2}{\partial n} = \mathfrak{R}_0 a_2(n). \quad (230b)$$

With the help of the latter definitions and of the solutions for u_{s0} , u_{n1} and u_{s1} , the system (229) can be solved to find:

$$U_{20} = -I_{G_{11}} D_0^{7/4} \left[-\frac{n}{2\mathfrak{b}} + \frac{\mathfrak{R}_1}{2\mathfrak{R}_0} + \mathfrak{b} D_0^{4/3} \frac{dD_0}{dn} \frac{I_{\mathcal{F}_{11}}}{2} \right], \quad U_{21} = \frac{7}{12} I_{G_{11}} D_0^{7/4} \quad (231a)$$

$$U_{22} = -\frac{\mathfrak{b}}{\sqrt{C_{fu}}} D_0^{7/2}, \quad U_{23} = -\frac{7}{4} D_0^{7/4}, \quad (231b)$$

$$U_{24} = D_0^{7/4} \left[\frac{3n}{2\mathfrak{b}} - \frac{\mathfrak{R}_1}{2\mathfrak{R}_0} \right] + \frac{3}{2} \mathfrak{b} D_0^{37/12} \frac{dD_0}{dn} I_{\mathcal{F}_{11}} \quad U_{25} = \mathfrak{b} D_0^{37/12} \frac{dD_0}{dn}, \quad (231c)$$

and the function \mathcal{G}_{21} is the solution of the following differential system:

$$\frac{d}{d\zeta} \left[\mathcal{N}(\zeta) \frac{d\mathcal{G}_{21}}{d\zeta} \right] = -2 \mathcal{F}_0 \mathcal{F}_{11} + \frac{7}{4} \mathcal{G}_1^2 - \frac{11}{4} \frac{d\mathcal{G}_1}{d\zeta} \int_{\zeta_0}^{\zeta} \mathcal{G}_1 d\zeta, \quad (232a)$$

$$\mathcal{G}_{21}|_{\zeta_0} = 0, \quad \frac{d\mathcal{G}_{21}}{d\zeta} \Big|_1 = 0. \quad (232b)$$

Moreover, $a_2(n)$ is obtained imposing the constraint of vanishing depth integrated lateral flux at second order, to find:

$$a_2 = -\frac{\sqrt{C_{fu}}}{\mathfrak{b}} \left(a_{20} + a_{21} \frac{D_1}{D_0} \right), \quad (233a)$$

$$a_{20} = I_{G_{11}} D_0^{7/6} \left(-\frac{2n}{\mathfrak{b}} + \frac{\mathfrak{R}_1}{\mathfrak{R}_0} \right) - \mathfrak{b} D_0^{5/2} \frac{dD_0}{dn} \left(I_{\mathcal{F}_{11}} I_{G_{11}} + I_{G_{21}} \right), \quad (233b)$$

$$a_{21} = \frac{7}{6} I_{G_{11}} D_0^{7/6}. \quad (233c)$$

We can now determine the $\mathcal{O}(\delta)$ correction for the flow depth D_1 solving at $\mathcal{O}(\delta)^2$ the Exner equation that reads:

$$Q_{sn2}^b = 0, \quad (234)$$

hence:

$$\left[\frac{\partial u_{n2}/\partial \zeta}{\partial u_{s0}/\partial \zeta} \right]_{\zeta_0} - \left[\frac{\partial u_{s1}/\partial \zeta}{\partial u_{s0}/\partial \zeta} \frac{\partial u_{n1}/\partial \zeta}{\partial u_{s0}/\partial \zeta} \right]_{\zeta_0} - c_{ls} \sqrt{\frac{\tau_{*u}}{\tau_{*0}}} \left[-\frac{dD_1}{dn} + F_{ru}^2 \frac{\partial h_1}{\partial n} + \frac{1}{2} \frac{\tau_{*1}}{\tau_{*0}} \frac{dD_0}{dn} \right] = 0. \quad (235)$$

Recalling the relationship (187) that expresses τ_* in terms of the velocity field, and using the available solutions for u_{s0} and u_{s1} , with the help of some algebra one eventually finds:

$$\tau_{*1} = \tau_{*0} \left[\frac{D_1}{D_0} + t_{10} \right], \quad (236)$$

where τ_{*0} is given by (217) and t_{10} reads:

$$t_{10} = -\frac{n}{\mathfrak{b}} + \frac{\mathfrak{R}_1}{\mathfrak{R}_0} + \frac{\mathfrak{b}}{\sqrt{C_{fu}}} D_0^{4/3} \frac{dD_0}{dn} \left[\mathcal{N} \frac{d\mathcal{F}_{11}}{d\zeta} \right]_{\zeta_0} \quad (237)$$

We can finally employ (237) and (236) and the solutions for u_{s1} , u_{n1} and u_{n2} to reduce the Exner equation at $\mathcal{O}(\delta^2)$ (235) to the following form:

$$\frac{dD_1}{dn} + d_{11}(n) D_1 = d_{10}(n), \quad (238)$$

where

$$d_{10}(n) = \frac{1}{2} \frac{dD_0}{dn} t_{10} + F_{ru}^2 \frac{\partial h_1}{\partial n} - \frac{\mathfrak{R}_0^{1/2}}{c_{ls}} \left\{ D_0^{5/3} \frac{n}{\mathfrak{b}} \left(\frac{d\mathcal{G}_{11}}{d\zeta} \Big|_{\zeta_0} - I_{\mathcal{G}_{11}} \right) + \mathfrak{b} \frac{dD_0}{dn} D_0^3 \left[\left(\frac{d\mathcal{G}_{21}}{d\zeta} \Big|_{\zeta_0} - I_{\mathcal{G}_{21}} \right) + \left(\frac{d\mathcal{G}_{11}}{d\zeta} \Big|_{\zeta_0} - I_{\mathcal{G}_{11}} \right) \left(\frac{d\mathcal{F}_{11}}{d\zeta} \Big|_{\zeta_0} + I_{\mathcal{F}_{11}} \right) \right] \right\}, \quad (239a)$$

$$d_{11}(n) = -\frac{1}{2} \frac{1}{D_0} \frac{dD_0}{dn} + \frac{7}{6} \frac{\mathfrak{R}_0^{1/2}}{c_{ls}} D_0^{2/3} \left(I_{\mathcal{G}_{11}} - \frac{d\mathcal{G}_{11}}{d\zeta} \Big|_{\zeta_0} \right). \quad (239b)$$

The numerical solution of the ordinary differential equation (238) for D_1 is obtained numerically, but depends on two unknowns: the value of D_1 at a side wall and the unknown slope correction \mathfrak{R}_1 . They can be determined with the help of two integral constraints arising from the conditions of constant water and sediment fluxes.

The former constraint, at $\mathcal{O}(\delta)$ was derived before and has the form of equation (227). The constraint on sediment flux, at $\mathcal{O}(\delta)$, reads:

$$\int_{-1}^1 Q_{ss1}^b dn = 0. \quad (240)$$

Expanding the formula for the bed load flux in powers of δ , we find:

$$Q_{ss1}^b = \frac{\partial \Phi_{s0}^b}{\partial \tau_*} \Big|_{\tau_{*0}} \tau_{*1}, \quad (241)$$

where τ_{*0} and τ_{*1} have the forms (217) and (236), respectively.

We can finally substitute from (241), (217) and (236) into (240) to find:

$$\int_{-1}^1 (D_1 + D_0 t_{10}) \frac{\partial \Phi_{s0}^b}{\partial \tau_*} \Big|_{\tau_{*0}} dn = 0. \quad (242)$$

In particular, using the Meyer-Peter and Müller (1948) formula, the above integral becomes:

$$\int_{-1}^1 (\tau_{*u} \mathfrak{R}_0 D_0 - \tau_{*c})^{1/2} (D_1 + D_0 t_{10}) dn = 0. \quad (243)$$

The dependence of the quantities $D_0(n = \pm 1)$ and $D_1(n = \pm 1)$ on the parameter γ is plotted in Figure 55. Figure 55a) also shows the same dependence as predicted by the linear theory. Note that the curve obtained by the nonlinear theory tends to the linear curve as the parameter γ tends to zero. Furthermore nonlinear predictions for the maximum depth significantly exceed the linear values for large values of γ .

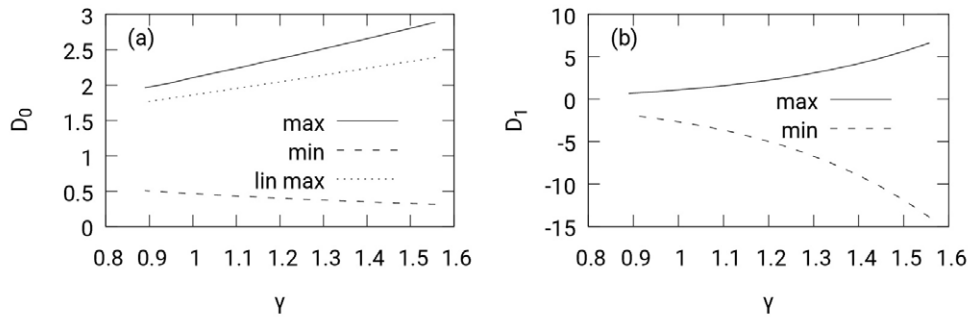


Figure 55. Maximum scour and deposit predicted by the present theory at (a) the leading and (b) the first order. Values of dimensionless parameters: $C_{fu} = 0.004$, $\nu_0 = 0.1$ and $\beta_u = 20$.

3.3. Finite amplitude morphodynamics in meandering channels

3.3.1 Finite amplitude bars in slowly varying meandering channels with constant width

We now extend to the mobile bed case the analysis of the hydrodynamics of meandering channels with fixed bed performed in Section 2.5. We consider a rectangular channel with constant width $2B$ and axis consisting of a curved 3D line $\eta = \eta_a(s)$, lying on the vertical ($z-s$) coordinate surface and characterized by constant slope $S = -d\eta_a/ds$ (recall the sketch in Figure 33). Moreover, $\mathcal{C}(s)$ will denote the dimensionless curvature of the longitudinal coordinate line s , with s dimensionless and scaled by the meander wavelength L . Again, we assume that the channel is *weakly meandering* such that $\delta \ll 1$. Also, the rate of longitudinal variations of channel curvature is *slow*, such that $\Lambda = R_0/L \sim O(1)$ and, consequently, $\mathfrak{L} = \Lambda \delta \ll 1$ (recall equation (140)).

Formulation

We employ the same notations as in the fixed bed case and simply update the dimensionless formulation to include the only novel feature of the mobile bed case. The bed elevation $\eta(s, n)$, rather than a given fixed quantity, is an unknown function that must be determined solving the Exner equation coupled with the governing equations. As a consequence, the flow depth $D(s, n)$ does no longer satisfy the equation (138).

The hydrodynamic problem in dimensionless form, with the steady (139a) and wide channel (139b) assumptions, is formulated in terms of the (s, n, ζ) coordinates by the governing equations (51a), (51b), (51c), with the closure relationships and boundary conditions presented in Section 2.2.

The hydrodynamic equations need be complemented by the steady form of the Exner equation. Recalling that, $h_s = 1 + \nu_0 \mathcal{C}(s) n = 1 + \delta \mathcal{C}(s) n/b$, in the case of dominant bed load, with the

present notations and in dimensionless form, from equation (185) we obtain:

$$\frac{\delta \Lambda}{\mathfrak{b} + \delta \mathcal{C}(s)n} \frac{\partial Q_{ss}^b}{\partial s} + \frac{\partial Q_{sn}^b}{\partial n} = - \frac{\delta \mathcal{C}(s)}{\mathfrak{b} + \delta \mathcal{C}(s)n} Q_{sn}^b. \quad (244)$$

The closure relationships associated with (244) are obtained from (186a) and (186b). Just like in the constant curvature case, we take advantage of the smallness of the coefficient of the lateral slope term in the closure relationship for the lateral bedload flux and employ the assumption (207). Moreover, we neglect the $\mathcal{O}(\delta)$ sloping effect on the longitudinal component of sediment transport. With these assumptions, (186a) and (186b) become:

$$Q_{ss}^b = \Phi_{s0}^b(\tau_*), \quad Q_{sn}^b = \Phi_{s0}^b(\tau_*) \left[\frac{\frac{\partial u_n}{\partial \zeta} \Big|_{\zeta_0}}{\frac{\partial u_s}{\partial \zeta} \Big|_{\zeta_0}} + \delta \sqrt{\frac{\tau_{*u}}{\tau_*}} c_{ls} \frac{\partial (F_{ru}^2 H - D)}{\partial n} \right], \quad (245)$$

where the tilde has again been removed. The above formulation is completed enforcing the usual constraints whereby the flow discharge and the total sediment flux must keep constant at any cross section through the meandering channel.

Derivation

We seek a fully analytical approach following essentially the framework of Seminara and Solari (1998), extended to meandering channels by Bolla et al. (2009), with some formal modifications already introduced in the fixed bed case, mainly related to a different closure relationship for the friction coefficient C_f .

The solution for the flow field is expanded in powers of the small parameter δ according to (142), with the only exceptions of the free surface elevation $H(s, n)$ and the flow depth D that are now expanded in the form:

$$\begin{aligned} [H(s, n), D(s, n)] &= [H_{-1}(s), 0] \delta^{-1} + [H_0(s), D_0(s, n)] \\ &\quad + \delta [H_1(s, n), D_1(s, n)] + \mathcal{O}(\delta^2) \end{aligned} \quad (246)$$

Note that, an $\mathcal{O}(\delta^{-1})$ contribution to the free surface elevation, $H_{-1}(s)$, is now present in the expansion. However, unlike in the fixed bed case treated in Section 2.5, this contribution is not only associated with the basic uniform solution, hence it does not have the form (143). As shown below, a correction is required in the mobile case in order to satisfy the constraint of constant total sediment flux in the cross section. Also, the closure for ν_T is again obtained from (105) with D and U functions of both s and n .

The usual perturbation machinery allows to determine the solution at the various orders of approximation.

$\mathcal{O}(\delta^0)$

The continuity equation, at the leading order has a form identical to the fixed case (equation 145). However, unlike $H_u(s)$, the quantity $H_{-1}(s)$ is now unknown, and the solution for u_{z0} becomes:

$$u_{z0} = \frac{\Lambda}{\mathfrak{b}} F_{ru}^2 \frac{dH_{-1}}{ds} u_{s0}. \quad (247)$$

At the same order, the longitudinal momentum equation leads to a differential problem that differs from the fixed bed case and reads:

$$\begin{aligned} \frac{1}{D_0^2} \frac{\partial}{\partial \zeta} \left(\nu_{T0} \frac{\partial u_{s0}}{\partial \zeta} \right) &= \Lambda \frac{dH_{-1}}{ds} + \frac{1}{D_0} \frac{\partial u_{s0}}{\partial \zeta} \left(-\Lambda F_{ru}^2 \frac{dH_{-1}}{ds} u_{s0} + \mathfrak{b} u_{z0} \right) \\ &= \Lambda \frac{dH_{-1}}{ds} = -\mathfrak{R}_0(s) \sqrt{C_{fu}}, \end{aligned} \quad (248a)$$

$$u_{s0} \Big|_{\zeta_0} = 0, \quad \frac{du_{s0}}{d\zeta} \Big|_1 = 0, \quad (248b)$$

where use has been made of (247) and we have introduced the following definition:

$$\mathfrak{R}_0(s) = -\frac{\Lambda}{\sqrt{C_{fu}}} \frac{dH_{-1}}{ds}. \quad (249)$$

The function $\mathfrak{R}_0(s)$ is clearly related to the ratio between the local slope of the free surface at each cross section and its average uniform value. Recalling (105a), the governing equation (248) is readily solved in the form

$$u_{s0} = \mathfrak{R}_0^{1/2}(s) D_0^{7/12}(s, n) \mathcal{F}_0(\zeta). \quad (250)$$

This solution again displays $\mathcal{O}(1)$ lateral and longitudinal variations of the flow speed. A difference with the respect to the fixed bed case is the form taken by the integral constraint (60), that now involves the quantity dH_{-1}/ds , through the function \mathfrak{R}_0 (see equation (249)), rather than the correction $H_0(s)$ of the uniform flow depth required to ensure the flow discharge keeps constant along the channel. The constraint (60) now reads:

$$\int_{-1}^1 U_0 D_0 dn = \mathfrak{R}_0^{1/2}(s) \int_{-1}^1 D_0^{19/12} dn = 2. \quad (251)$$

The leading order component of the flow depth $D_0(s, n)$ remains unknown at this order. Indeed, at the leading order, the Exner equation does not involve $D_0(s, n)$ and is automatically satisfied as H_{-1} is independent of the lateral coordinate.

$\mathcal{O}(\delta)$

Let us move to the lateral component of the momentum equation which, at $\mathcal{O}(\delta)$, reads:

$$\mathfrak{R}_0^{1/2} D_0^{-7/12} \frac{\partial}{\partial \zeta} \left[\mathcal{N}(\zeta) \frac{\partial u_{n1}}{\partial \zeta} \right] = \mathfrak{b} \frac{\partial H_1}{\partial n} - \mathfrak{R}_0 \mathcal{C}(s) D_0^{7/6} \mathcal{F}_0^2(\zeta), \quad (252a)$$

$$u_{n1}|_{\zeta=\zeta_0} = 0, \quad \frac{\partial u_{n1}}{\partial \zeta} \Big|_{\zeta=1} = 0. \quad (252b)$$

The solution for u_{n1} is readily obtained in the form:

$$u_{n1} = \mathfrak{R}_0^{1/2} \left[-D_0^{7/12} \mathcal{F}_0(\zeta) a_1(s, n) - \mathcal{C}(s) D_0^{7/4} \mathcal{G}_{11}(\zeta) \right], \quad (254)$$

where the function $\mathcal{G}_{11}(\zeta)$ is given by a relationship identical to (87) and we have set:

$$\frac{\partial H_1}{\partial n} = \frac{\sqrt{C_{fu}}}{\mathfrak{b}} \mathfrak{R}_0 a_1(s, n), \quad (255)$$

with $a_1(s, n)$ a function to be determined through the continuity equation.

At $\mathcal{O}(\delta)$, the latter may be written in a form identical to that obtained for the fixed bed case (see equation 152). Imposing the no slip condition at the bed, with the help of (250) and (254), the equation is again solved for u_{z1} . Expanding the kinematic boundary condition at the free surface at $\mathcal{O}(\delta)$ one finds a relationship for $u_{z1}|_{\zeta=1}$. Imposing consistency with the solution for u_{z1} , one ends up with an equation for a_1 similar to (156) except for the presence of the unknown function $\mathfrak{R}_0(s)$. It reads:

$$\mathfrak{R}_0^{1/2} \frac{\partial(D_0^{19/12} a_1)}{\partial n} = -I_{\mathcal{G}_{11}} \frac{\partial(D_0^{11/4})}{\partial n} \mathcal{C}(s) \mathfrak{R}_0^{1/2} + \frac{\Lambda}{\mathfrak{b}} \frac{\partial(\mathfrak{R}_0^{1/2}(s) D_0^{19/12})}{\partial s} \quad (256)$$

With the help of some algebra (256) can again be solved for a_1 to give:

$$a_1 = -I_{G_{11}} D_0^{7/6} \mathcal{C}(s) + \frac{\Lambda}{\mathfrak{b}} \mathfrak{R}_0^{-1/2} D_0^{-19/12} \int_{-1}^n \frac{\partial(\mathfrak{R}_0^{1/2}(s) D_0^{19/12})}{\partial s} dn' + c_1(s) D_0^{-19/12} \quad (257)$$

with $c_1(s)$ function determined imposing the no lateral flux condition at the walls. Indeed, recalling (254) we find:

$$\left[\int_{\zeta_0}^1 u_{n1} d\zeta \right]_{n=-1} = 0 \quad \Rightarrow \quad a_1|_{n=-1} = -I_{G_{11}} D_0^{7/6}|_{n=-1} \mathcal{C}(s) \quad (258)$$

Using this condition, one also finds that the function $c_1(s)$ must vanish and the solution for a_1 becomes:

$$a_1 = -I_{G_{11}} D_0^{7/6} \mathcal{C}(s) + \frac{\Lambda}{\mathfrak{b}} \mathfrak{R}_0^{-1/2} D_0^{-19/12} \int_{-1}^n \frac{\partial(\mathfrak{R}_0^{1/2}(s) D_0^{19/12})}{\partial s} dn'. \quad (259)$$

The last step required to complete the derivation of the leading order solution is the analysis of the Exner equation at $\mathcal{O}(\delta)$ that reads:

$$\frac{\Lambda}{\mathfrak{b}} \frac{\partial Q_{ss0}^b}{\partial s} + \frac{\partial Q_{sn1}^b}{\partial n} = 0, \quad (260)$$

where:

$$Q_{ss0}^b = \Phi_{s0}^b(\tau_{*0}), \quad (261a)$$

$$Q_{sn1}^b = \Phi_{s0}^b(\tau_{*0}) \left(\frac{\partial u_{n1}}{\partial \zeta} \Big|_{\zeta_0} + D_0^{-1/2} \mathfrak{R}_0^{-1/2} c_{ls} \frac{\partial D_0}{\partial n} \right). \quad (261b)$$

Substituting from (261) into (260), one ends up with the following nonlinear partial differential equation for the unknown function $D_0(s, n)$:

$$n_1 \frac{\partial^2 D_0}{\partial n^2} + n_2 \left(\frac{\partial D_0}{\partial n} \right)^2 + n_3 \frac{\partial D_0}{\partial n} + n_4 + n_5 \frac{\partial D_0}{\partial s} + n_6 = 0, \quad (262)$$

where

$$n_1 = c_{ls} \frac{R_0^{1/2} D_0^{1/2}}{\tau_{*0}} \frac{\Phi_{s0}^b}{\partial \Phi_{s0}^b / \partial \tau_*} \Big|_{\tau_{*0}}, \quad (263a)$$

$$n_2 = \mathfrak{R}_0^{1/2} c_{ls} D_0^{-1/2} \left(1 - \frac{1}{2 \tau_{*0}} \frac{\Phi_{s0}^b}{\partial \Phi_{s0}^b / \partial \tau_*} \Big|_{\tau_{*0}} \right), \quad (263b)$$

$$n_3 = -\mathfrak{R}_0 a_1 - \left(1 + \frac{7}{6 \tau_{*0}} \frac{\Phi_{s0}^b}{\partial \Phi_{s0}^b / \partial \tau_*} \Big|_{\tau_{*0}} \right) \mathfrak{R}_0 D_0^{7/6} \mathcal{C}(s) \frac{dG_{11}}{d\zeta} \Big|_{\zeta_0}, \quad (263c)$$

$$n_4 = -\frac{\Phi_{s0}^b}{\partial \Phi_{s0}^b / \partial \tau_*} \Big|_{\tau_{*0}} \frac{1}{\tau_{*u}} \frac{\partial a_1}{\partial n}, \quad n_5 = \frac{\Lambda}{\mathfrak{b}} \mathfrak{R}_0, \quad n_6 = \frac{\Lambda}{\mathfrak{b}} \frac{d\mathfrak{R}_0}{ds} D_0 \quad (263d)$$

The solution of (262) is coupled with the solution for $a_1(s, n)$ (equation (259)) and must satisfy the hydrodynamic constraint (251) and the morphodynamic constraint. The latter imposes that the

total sediment flux in the cross section must keep constant and equal to the given sediment supply associated with the average reach slope. Recalling equation (261a), at leading order one finds:

$$\int_{-1}^1 Q_{s0}^b dn = \int_{-1}^1 \Phi_{s0}^b(\tau_{*0}) dn = 2 \Phi_u \quad (264)$$

The procedure followed by Bolla et al. (2009) to calculate the solution was as follows. They employed the Meyer-Peter and Müller (1948) formula for the sediment flux and solved the differential problem formulated above numerically, marching in n for every single cross section. In particular, at each cross section j , trial values of the flow depth at the inner bank $D_{0j}|_{n=-1}$ and of the free surface slope correction \mathfrak{R}_{0j} were chosen. With the latter choices, the quantity $\frac{\partial D_{0j}}{\partial n}|_{n=-1}$ was evaluated from (261b) imposing the condition of vanishing lateral sediment flux at the inner wall. The Exner equation, coupled with (259), could then be solved numerically in the whole domain. The differences between the values of the liquid and solid discharges associated with the computed solution and the assigned values were then computed and the trial initial values of $D_{0j}|_{n=-1}$ and \mathfrak{R}_{0j} were modified correspondingly. Iterations were then pursued until residual errors reduced below some chosen value. The implementation of this trial and error procedure allowed Bolla et al. (2009) to determine the sought functions $D_0(s, n)$ and $\mathfrak{R}_0(s)$. The Authors also checked whether non unique solutions of the problems might exist. The numerical tests performed by the Authors suggested that this is not the case, at least provided sediment transport occurs in the entire cross section.

Bolla et al. (2009) pursued the perturbation approach further and evaluated the $\mathcal{O}(\delta)$ component of the longitudinal velocity and flow depth, as well as the $\mathcal{O}(\delta^2)$ component of the lateral velocity and lateral slope. The analysis is conceptually straightforward. The interested reader may usefully refer to the above paper for details. Below, we provide an overview of some of the main results.

The test case investigated in depth concerned the so called sine generated meanders (Langbein and Leopold, 1966) already discussed in the fixed bed case. The dimensionless curvature of the channel axis \mathcal{C} was then assumed to read $\cos(2\pi s)$ (recall equation 280). Two periodic sequences of sine generated meanders characterized by different *dimensionless wave numbers* were analyzed. The dimensionless wavenumber, λ_{BS} in Bolla et al. (2009) notations, was equal to $2\pi BL$ in the present notations. The first wavenumber considered was fairly small ($\lambda_{BS} = 0.07$), the latter was fairly large ($\lambda_{BS} = 0.185$). As we know, the degree of smallness of this parameter measures the degree to which the longitudinal variations of the flow field may be considered as slowly varying. For very long meanders the spatial scale over which variations occur, namely the meander wavelength, are much larger than the adaptation length required for the flow to adjust to the varying curvature. The consequences emerge clearly from Figure (56). Indeed, the phase lag of bed topography relative to channel curvature is fairly small when convective effects play a negligible role, i.e., for small wave numbers (Figure (56a)). As the wavenumber increases, the maximum scour moves from downstream to upstream of the bend apex and the pattern of scour and deposits displays oscillations larger than those found for smaller wave numbers (Figure (56b)). The high-velocity core of the vertically averaged longitudinal velocity (Figures 56c and 56d) shifts from one side to the other side of the channel through the meander length and peaks just downstream to the bend apex.

Figure 57 shows the complete flow field at four cross sections along the shorter meander ($\lambda_{BS} = 0.185$). The contour lines represent the values of the dimensionless longitudinal velocity. The vectors visualize the secondary flow, whilst the arrowed lines are the projection of a few streamlines on the cross section. The first important observation is that the values of the secondary flow velocity are typically one order of magnitude smaller than those of the longitudinal motion, in spite of the fact that the perturbation of the bottom elevation are not small. At the inflection point (Figure 57a) the secondary flow is nearly uniform in the cross section and is directed from the left to the right bank except close to the banks. There, the curvature driven component gives rise to secondary cells such to satisfy the boundary conditions of vanishing transverse component of the flow rate at the side walls. Moving downstream, the secondary flow driven by both streamline curvature and topography is initially enhanced near the bottom and close to the outer bank (Figure

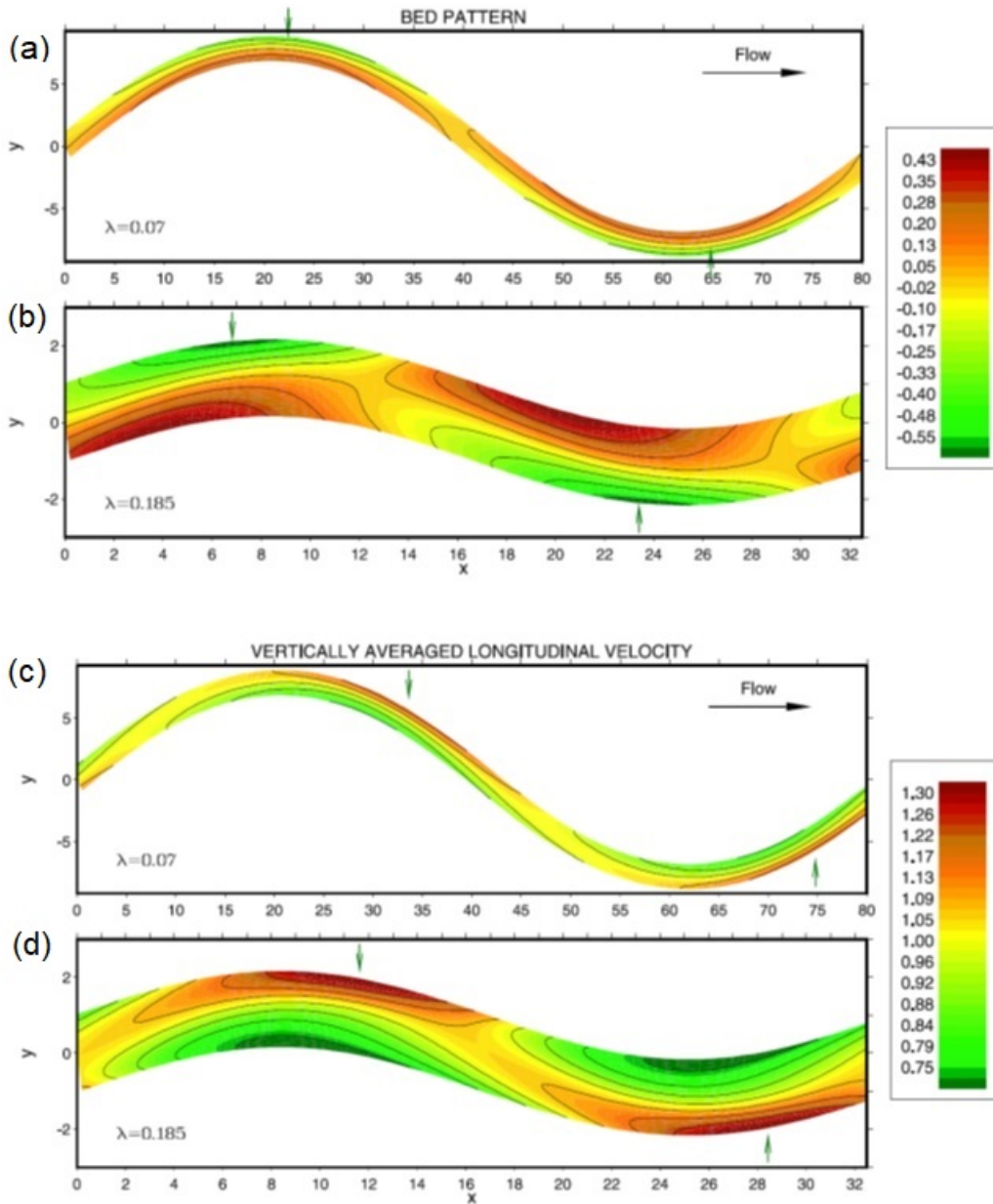


Figure 56. Patterns of bed topography and vertically averaged longitudinal velocity in two periodic sequences of sine generated meanders, characterized by different dimensionless wave numbers. (a,b) Dimensionless bed elevation relative to the undisturbed bed; (c,d) dimensionless value of the vertically averaged longitudinal velocity. Values of dimensionless parameters: $d_{su} = 5 \cdot 10^{-3}$ (hence $\sqrt{C_{fu}} = 0.059$), $\nu_0 = 0.04$ and $\beta_u = 7$ (hence $\delta = 0.097$ and $b = 2.42$), $\lambda_{BS} = 0.07$ (corresponding to $\mathcal{L} = 0.027$) and $\lambda_{BS} = 0.185$ (corresponding to $\mathcal{L} = 0.071$), $\tau_{*u} = 0.1$. Green arrows show the locations of maximum scour and maximum velocity (modified from Bolla et al., 2009).

57b). Further downstream it spreads towards the outer deeper region of the cross section (Figure 57c); in the shallower inner region it is directed inwards except close to the inner bank where the secondary flow with vanishing depth average again prevails. Downstream of the bend apex (Figure 57d) the bed elevation is nearly constant in the lateral direction and the secondary flow is driven

by convective effects.

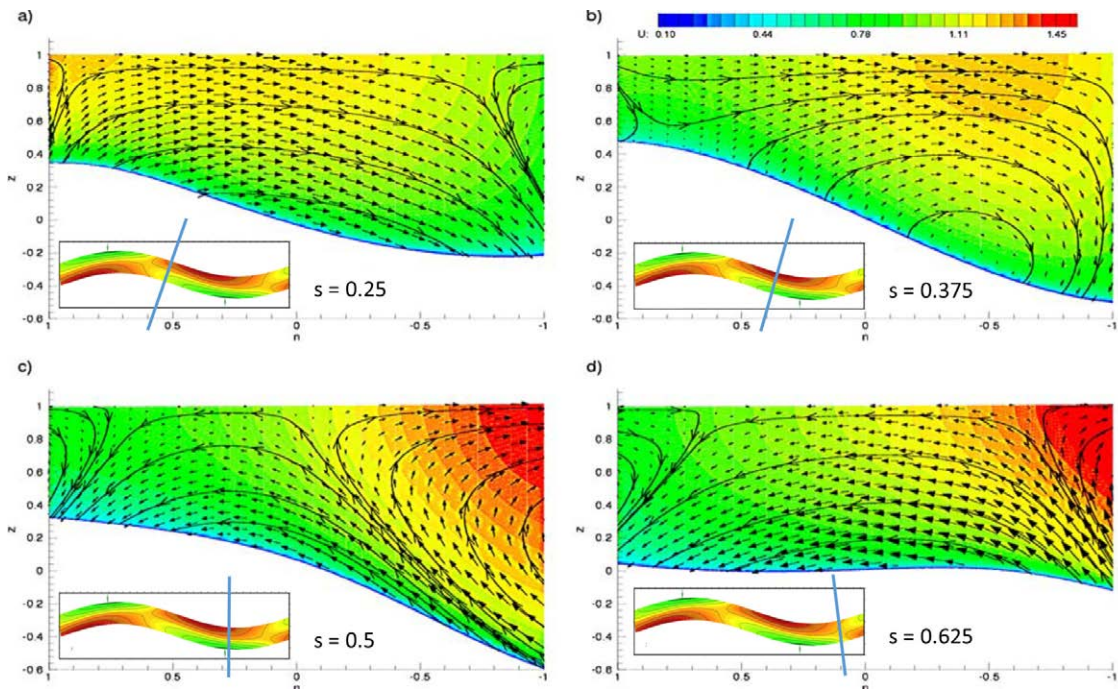


Figure 57. Isocontours of dimensionless downstream velocity at different cross sections of the sine generated meander of Figure (56) for $\lambda_{BS} = 0.185$. (a), $s = 0.25$; (b), $s = 0.375$; (c), $s = 0.5$; (d), $s = 0.625$. Vectors visualize the secondary flow velocity; arrowed lines represent the projection of some streamlines on the cross section. Values of the relevant dimensionless parameters are the same as in the Figure 56 (modified from Bolla *et al.*, 2009).

Note that the secondary cells present close to the banks in these computations have nothing to do with the turbulence-driven secondary flows discussed in the previous Chapter. The present model ignores the side wall boundary layers and our simple turbulence closures would be unable to predict their formation. However, the wide character of our channels make their role negligible anyway.

3.3.2 Extension to the case of meandering channels undergoing spatial variations of channel width

Luchi *et al.* (2012) extended the nonlinear analysis of flow and bed topography in meandering channels with constant width discussed in the previous section to allow for spatial variations of the channel width. The analysis of Luchi *et al.* (2012) was aimed at explaining the field observations that suggest that spatially periodic variations of channel width are indeed a common characteristics of fluvial channels (see Section 5.6.1). It is of interest to note that the constant width model of Bolla *et al.* (2009) showed that an equilibrium configuration of flow and bed topography does exist for given flow discharge and associated sediment flux. However, in order to achieve equilibrium, spatial variations of the longitudinal free surface slope must be allowed. In the development of Luchi *et al.* (2012) the channel width undergoes spatial oscillations. Under these conditions, the meandering channel is able to accommodate prescribed values of flow and sediment discharges with the longitudinal free-surface slope kept constant.

The latter paper was also able to show that, in a meandering channel, the equilibrium width oscillates with a frequency twice the frequency of channel curvature and experiences the maximum width close to inflection points. This pattern is typically observed in so called canaliform rivers. Luchi *et al.* (2012) also point out that a similar behavior is readily understood to be characteristic of so called sinuous point bar rivers, provided one recognizes that, in this case, the hydrodynamic

width (width of the free surface) must be replaced by the active width, namely the width of the portion of the cross section where sediment transport occurs at formative conditions.

3.4. Further approaches to the morphodynamics of sinuous channels

The theoretical framework set in the previous sections provides a description of the physical processes which govern the bed topography in sinuous channels and the key controlling factors. The solutions for the flow field and the bed topography obtained at the various degrees of approximation have also a practical relevance, inasmuch as the assumptions entailed in their derivation are satisfied in many real cases. Moreover, rational perturbation approaches allow one to restrict the analysis to the essential physical processes, leading to a reduction of the large computational effort required by detailed numerical simulations. They also ensure a simpler analysis of sensitivity to parameter uncertainties, changes in geometry and boundary conditions of the computational domain (Lanzoni, 2022).

Needless to say, perturbation approaches have their own limits, in particular:

- perturbation parameters in the real world are not always as 'small' as theory would require;
- complex river geometries are not readily accommodated.

In order to overcome these limitations one may resort to one of the following tools: laboratory measurements, field observations, numerical simulations. However, the reader should immediately appreciate the major difference between analytical models and laboratory-field-numerical approaches: the former ones apply to a wide class of fluvial configurations, the latter concern a single specific configuration. Moreover, the effort required in the former case is much smaller than in the latter case.

This notwithstanding, in the last few decades, we have witnessed a considerable, technologically driven progress in research based on each of the three mentioned approaches.

Additional tools, besides those presented in this Monograph, are needed to implement them. In particular, Computational Morphodynamics may well be taken as a fairly mature branch of Morphodynamics, that will deserve a specific attention. It falls outside our scopes to cover these aspects in the present Monograph. Below, we then limit ourselves to briefly present few examples of how particular features of sinuous channels can be investigated complementing theoretical analysis with experimental observations and numerical simulations.

3.4.1 Laboratory observations: bed topography in movable bed meandering channels with a Kinoshita planform

The first example concerns the experimental investigation carried out by Abad (2008) in a laboratory flume, which was integrated with three-dimensional numerical simulations (but see also Abad and García, 2009; Abad et al., 2013). The experiments were carried out in a movable bed meandering flume reproducing a sequence of three upstream skewed bends shaped according to the classical configuration suggested by Kinoshita (1961). The bed topography that developed in the presence of bed load was characterized by the formation of progressive dune-type bedforms superimposed on point bars.

The bed elevation was measured by sonar transducers while the velocity measurements were carried out by means of Acoustic Doppler Velocimeters (ADV). Because of the intrinsic difficulties encountered in the measurements (migration of bed forms and ADVs limitations) only the structure of the mean flow field was quantified. Numerical simulations, carried out solving the incompressible RANS equations with the help of a $k-\epsilon$ closure model, were employed to obtain a detailed characterization of flow velocities and shear stresses after a calibration based on measured values of water surface elevations and mean velocities.

Results reported in Figure 58 show that, not surprisingly, the erosion peak in the upstream-skewed case is located upstream of the bend apex, while in the downstream-skewed case it is located downstream of the bend apex. Moreover, numerical simulations of the flow field associated with the measured topographies show that the presence and location of bedforms on a bend may strongly affect secondary circulations. The highest modification of the flow field is observed when a dune crest crosses a given cross section. This modification creates the highest near-bed and

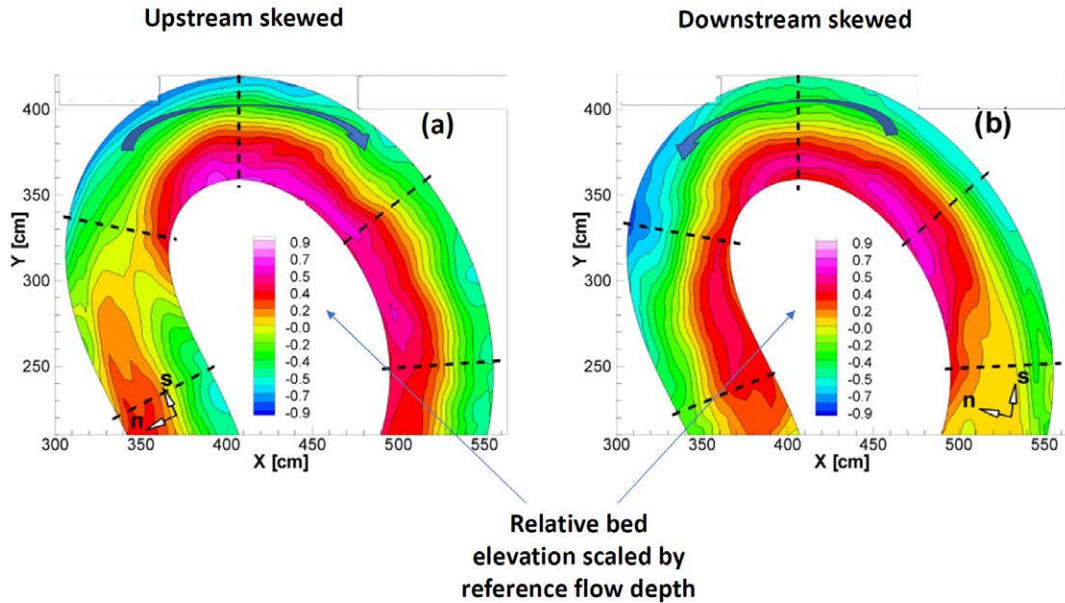


Figure 58. Average bed elevation relative to the unperturbed topography and scaled by the unperturbed flow depth in a Kinoshita channel: (a) upstream-skewed. (b) downstream-skewed. Positive values denote deposition while negative values imply erosion (modified from Abad, 2008).

near-bank shear velocities, thus enhancing (as much as 50%) fluvial erosion and possibly stream bank scour.

3.4.2 Field observations: three-dimensional flow structure and bed morphology in large elongated meander loops

Theoretical models do not readily accommodate the effects of heterogeneities, notably those associated with a non uniform roughness distribution. Under these circumstances, field observations may shed some light. In particular, we know (Section 4.5.6(I)) that the presence of macroscopic roughness (e.g. topographic undulations) on the banks leads to a form drag which can strongly affect the flow field and the boundary shear stresses close to the banks. This was indeed confirmed by the field observations collected by Konsoer (2014) (but see also Konsoer et al., 2016) within two elongated meander loops of the Wabash River (Figure 59).

Detailed channel bathymetry was surveyed in the two meander loops using a multibeam echo sounder (MBES), while the three-dimensional velocity field was measured in various cross sections using a boat-mounted Acoustic Doppler Current Profiler (ADCP). An interesting observation was that the depth-averaged near-bank velocities observed for a near-bankfull discharge were, in general, greater than those measured for overbank flow.

The Authors suggest that observations confirm that the point bars forced by the curvature of the channel axis induce a strong topographic steering which adds to the curvature-driven secondary motion. A glance at Figures 59b and 59c shows that the flow velocity peaks well downstream of the bend apex, unlike scour, which displays a maximum ahead of the apex. This effect is driven by flow acceleration in a reach where bedrock is exposed along the outer bank (area delimited by the white-dashed line in Figure 59b). Furthermore, the presence of abundant large woody debris along the outer bank of the Horseshoe bend increases the flow resistance, leading to the development of a zone of low velocities adjacent to the bank and inhibiting there the effects of secondary flow circulations.

3.4.3 Coupled hydro-morphodynamic simulations at the meander reach scale

As mentioned above, the recent advances in numerical techniques coupled with a continuous growth of computing power are nowadays leading to an increasing number of high-resolution morphodynamic simulations for complex river bathymetry (Sotiropoulos, 2015). The detailed information provided by these simulations can then be used in conjunction with comprehensive experimental observations to further unravel specific details of sinuous channel morphodynamics not covered or only approximately envisaged by theoretical analyses.

While an assessment of the state of the art in Computational Morphodynamics will have to await a forthcoming Monograph, here we limit ourselves to provide an interesting example of such efforts, namely the numerical hydro-morphodynamic simulation of large dune dynamics in meandering streams carried out by Khosronejad *et al.* (2015). In the simulation the unsteady RANS equations (URANS) with a $k-\epsilon$ turbulence closure were solved. The free water surface was treated using the rigid-lid approximation (Struiksma *et al.*, 1985). A Curvilinear Immersed Boundary (CURVIB) method (Ge and Sotiropoulos, 2007) was used to deal with the geometric complexity of the channel banks and the channel bed. The temporal variation of the bed elevation was computed by solving the Exner equation. The bedload flux was related to the sediment concentration in the bedload layer following the method of van Rijn (1984a). The contribution of suspended load to the bed variation rate was accounted for in terms of the difference between the rates of net sediment deposition on the bed and net sediment entrainment from the bed. This difference was taken to be proportional to the difference between the concentration immediately above the bedload layer and the equilibrium (Rouse) concentration. Periodic boundary conditions were used, i.e. the sediment flux was numerically recirculated through the simulated meandering reach. A dual time stepping approach was used to account for the different time scales controlling bedform dynamics and turbulent eddies, i.e. adopting a morphodynamic time step significantly greater than the time step used to advance the hydrodynamic equations.

Khosronejad *et al.* (2015) applied their model to a small meandering gravel-bed river ($d_{50} = 32$ mm, width = 27 m and depth = 1 m).

While it appears that URANS simulations are reasonably successful in predicting the quasi-equilibrium bed topography at the meander scale, it is hard to evaluate their ability to reproduce the onset and development of dunes. No comparison with experimental observations is reported in the paper of Khosronejad *et al.* (2015), which contains also a discussion of the intrinsic difficulties encountered in this type of simulations.

Finally, it is worthwhile to mention that numerical results correspond to a physical time of nearly two months and have been carried out on 160 CPUs for about 15 days of CPU clock-time (Sotiropoulos, 2015). This computational cost is likely to increase significantly when simulating a river with size similar to those typical of the Wabash River (average bankfull depth in the range 4-8 m and a bankfull width between 200 and 350 m).

3.4.4 Field observations through remote sensing

The use of remotely sensed imagery for high spatio-temporal resolution of river morphodynamics has lately enjoyed an increasing popularity. Indeed, the massive availability of satellite imagery (e.g. Landsat, <http://landsat.usgs.gov/>) and processing tools has greatly expanded the spatial and temporal scales on which river morphology and dynamics can be investigated. A growing number of studies (Gautier *et al.*, 2007; Rowland *et al.*, 2016; Schwenk, 2016; Schwenk *et al.*, 2017; Monegaglia, 2017; Monegaglia *et al.*, 2018) have thus leveraged Landsat imagery in order to estimate planform changes, bank migration and sediment bar dynamics of large meandering rivers (much wider than the typical resolution (30 m) of actual satellite images). A much finer spatial resolution (up to 2 m) can be achieved using aerial photographs.

Satellite images can be easily extracted using the Google Earth Engine or the USGS's Earth Explorer website. Images first need to be classified using suitable algorithms for identifying the pixels corresponding to sediment, water, land, or cloud cover. Images are then combined into annual composites and bankfull-resolving channel masks are eventually obtained.

User friendly toolboxes (e.g SCREAM (Rowland et al., 2016), RivMAP (Schwenk et al., 2017), PyRIS (Monegaglia et al., 2018)) have been developed taking advantage of the image-processing functions available in languages as IDL (SCREAM), MATLAB (RivMAP) and Python (PyRIS). These toolboxes allow one to extract centerline and bankline, widths, lengths, and properties of the channel axis (e.g. curvatures) from channel masks. Changes in channel widths, rates of bank migration, accretion and erosion areas, as well as spatio-temporal characteristics of cutoff dynamics can then be retrieved by comparison of multitemporal images. The information provided by these outputs can then be exploited to compute morphodynamic metrics needed for the application of theoretical and numerical models, as well as for comparing observed and predicted river planforms.

Figure 60 provides an example which shows the annually resolved centerline for a reach of the Ucayali River (1500 *km*) in the period 1985-2015, created using RivMAP. As pointed out by Schwenk et al. (2017), the observed patterns reveal a variety of features of channel migration. Quantitative analysis of such features may provide a useful benchmark for theoretical investigations like those presented in the next Chapters.

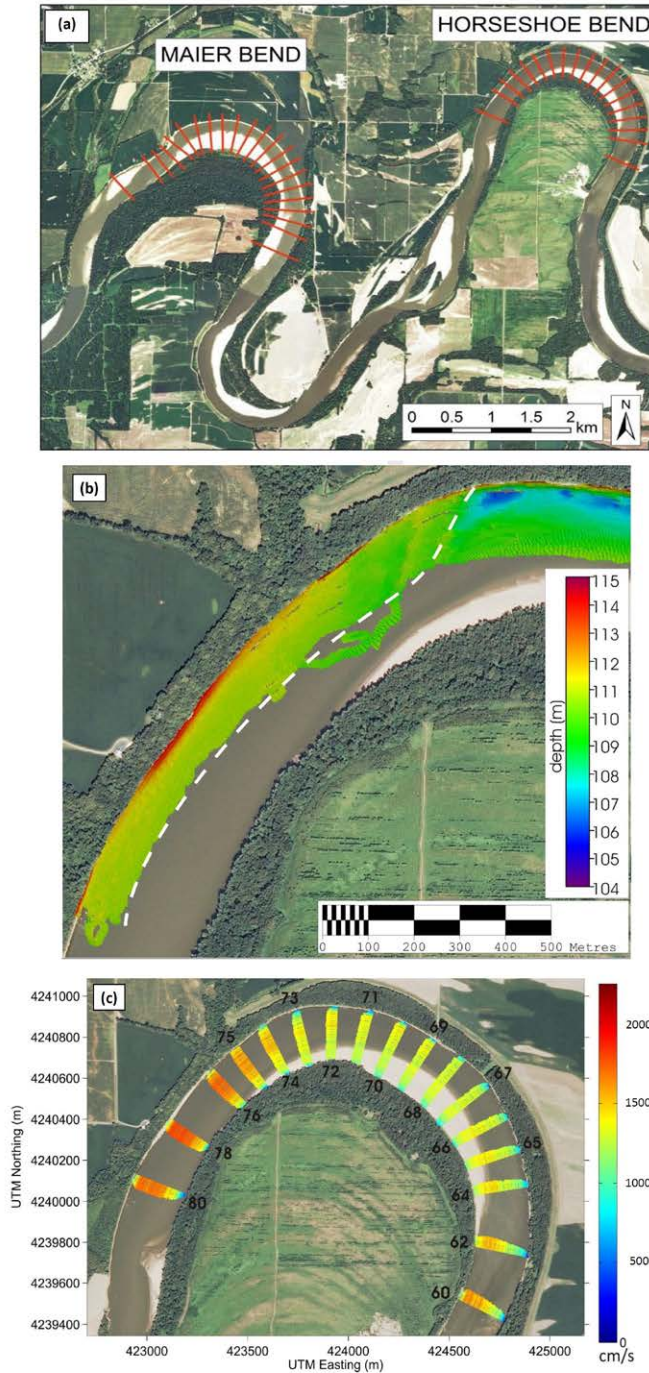


Figure 59. (a) Location of the two meander bends (Horseshoe and Maier) of the Wabash River surveyed by Konsoer (2014), with indication of the locations of the ADCP cross sections. (b) Bathymetric map derived from 2008 and 2013 multibeam surveys for Horseshoe bend. The white-dashed line marks the boundary of the region of bedrock outcrop within the channel. (c) Depth-averaged velocity vectors at Horseshoe Bend for campaign 1. Black arrows denote the direction of the flow (reproduced from Figures 3.1, 3.5 and 5.5 of Konsoer, 2014).

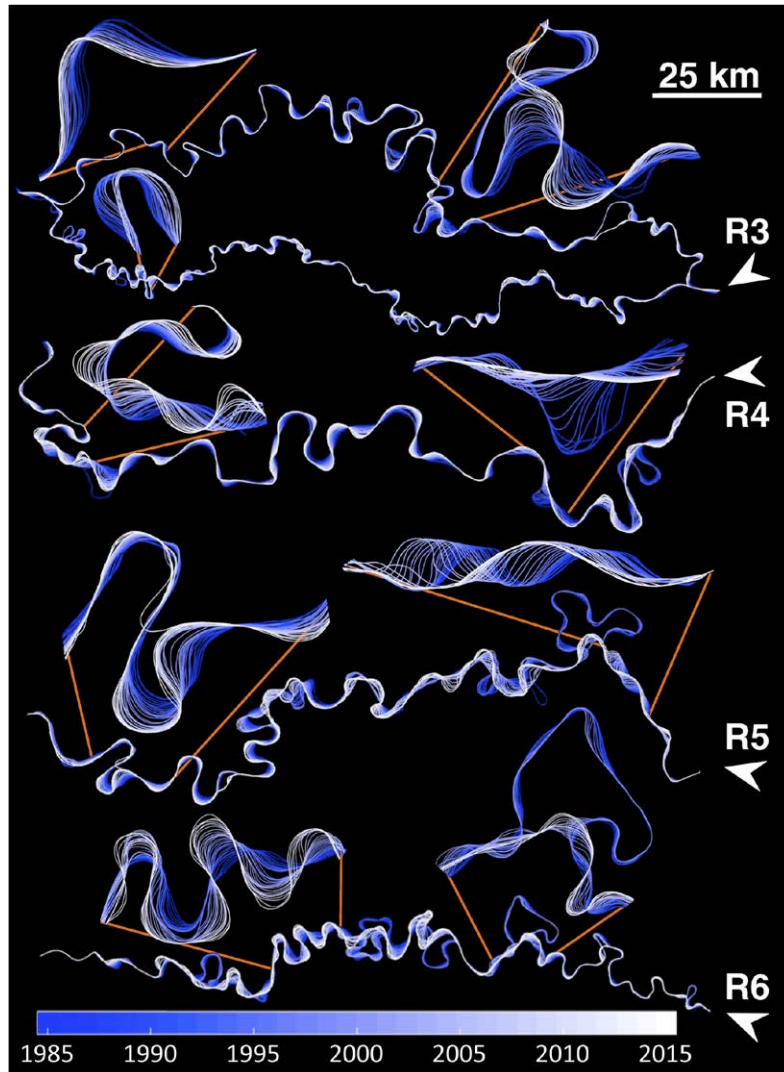


Figura 60. Centerlines of meandering patterns along the Ucayali River (Peru) obtained from the analysis of Landsat images using the RivMAP toolbox by Schwenk (2016). North arrows indicate the flow direction which travels from R6 to R3. Zoom views highlight some of the complex migration patterns and cutoffs (reproduced from Figure 4.13 of Schwenk, 2016).

4. The theory of river meanders

4.1. Introduction

The analysis developed in the previous two Chapters have hopefully clarified how curvature driven forcing mechanisms contribute to determining the flow field and the bed topography pattern in meandering channels. However, forcing effects do not tell the whole story.

Indeed, so far we have ignored the possible role that the free morphodynamic response of the channel may play in the process. Mathematically, we have not accounted for the fact that the homogeneous component of the governing differential problem admits of *free* solutions. They are the free bars that we have investigated in Chapter 6I for straight channels. Removing the straight channel assumption turns out to be quite instructive as it allows to tackle and clarify a number of important issues.

A first major issue arises from the fact that the spatial periodicity of forcing associated with channel curvature may *resonate* with the *natural* free response of the channel. To grasp this concept, one must recall that the spectrum of free bars allowed by a straight channel comprises also a class of non migrating and non amplifying bars characterized by wavenumber λ_R and aspect ratio of the channel β_R . As already pointed out in Section 6.3I, they do not form spontaneously as their growth rate vanishes, but they may be forced by external effects. In essence, a meandering channel with aspect ratio β_R and wavenumber λ_R would *resonate* with the natural non migrating and non amplifying free bar. This was first discovered by Blondeaux and Seminara (1985). Of course, such ideal coincidence never occurs in practice, but the flow field and bed topography of meandering channels is strongly influenced by resonance within a wide neighborhood of the exact resonance conditions. This will be discussed in Section 4.3.

A second related issue concerns another fundamental aspect of the problem that may be understood if one considers a curved channel connected to straight reaches both upstream and downstream. Curvature gives rise to a deformation of the bed in the bend. One may then reasonably wonder whether the effects of this deformation are felt in the downstream and/or upstream straight reaches. This is a general problem that was posed by Zolezzi and Seminara (2001), who described it as the *problem of morphodynamic influence*. The reader should not be surprised that morphodynamic influence may be felt not only downstream but also upstream. Indeed, influence is essentially the propagation of morphodynamic information which occurs through bottom waves consisting of migrating bars. We know from Section 6.3I that a class of bars able to migrate upstream exists for values of the aspect ratio of the channel exceeding the *resonant* value β_R . Again, they do not form spontaneously as they are not the fastest growing perturbations, but may be excited by some forcing mechanism, like e.g. bed deformation in curved bends. The problem of morphodynamic influence will be discussed in Section 4.4.

A third major issue can be intuitively grasped noting that the periodic sequence of point bars and pools that form in a meandering channel have characteristics that resemble quite closely those of free bars in straight channels. However, a major difference between point bars and free bars is that the former are steady (except for possible oscillations driven by temporal variations of the flow and sediment supply) whilst the latter are usually migrating features even under steady

supply conditions. Moreover, free migrating bars are typically shorter than meanders. One may then wonder whether free bars may coexist with point bars. And, indeed, the early fundamental observations of Kinoshita (1961) and Kinoshita and Miwa (1974) clarified that coexistence is possible as long as meander sinuosity is sufficiently small. In other words, alternate bars can migrate through mildly meandering channels. We will discuss these observations and provide their theoretical explanation in Section 4.5.

It turns out that all the above issues can be investigated adopting a depth averaged model. In Tubino and Seminara (1990) and Zolezzi and Seminara (2001) a version of the depth averaged model including the memory of the secondary flow with zero depth average was employed. Indeed, nonlinearity of convective acceleration implies that the zero depth average contribution to secondary flow does induce a non vanishing (*dispersive*) contribution to the lateral transport of longitudinal momentum, as first pointed out by Kalkwijk and De Vriend (1980). In Chapters 2 and 3 we have clarified the effects of this contribution on the hydrodynamics and morphodynamics of river bends, respectively. However, in the present Chapter, where our goal is to illustrate a number of fundamental mechanisms controlling the morphodynamics of meandering rivers, we ignore dispersive effects as they complicate the analysis considerably without modifying the main features of the relevant processes.

4.2. Depth averaged model of meander morphodynamics

Below, for the sake of generality, we derive a depth averaged model of meander hydrodynamics including the role of dispersive contributions.

Let us represent the flow field in the following form:

$$u_s = U(s, n) + \mathbf{u}(s, n, \zeta), \quad u_n = V(s, n) + \mathbf{v}(s, n, \zeta) \quad (265)$$

where U and V are the longitudinal and lateral depth averaged components of the flow velocity whilst \mathbf{u} and \mathbf{v} are the corresponding components of the secondary flow with zero depth average, i.e. such that $I_{\mathbf{u}} = I_{\mathbf{v}} \equiv 0$ (recall that $I_f = \int_{\zeta_0}^1 f d\zeta$). In principle, one could obtain a formally justified form of the fluctuations \mathbf{u} and \mathbf{v} using the general solution obtained in Section 2.5. This approach would retain the memory of the zero average component of the secondary flow through velocity fluctuations with the same structure they exhibit in the case of slowly meandering channels.

The differential problem for the *steady* flow in *wide* sinuous channels with dimensionless curvature distribution $\mathcal{C}(s)$ is obtained from (51a, 51b, 51c), setting $\partial/\partial t \equiv 0$. Moreover, in order to allow for a simple comparison with the free bar treatment presented in Chapter 6I, we will not distinguish between the lateral spatial scale B and the longitudinal spatial scale L . We thus set $L = B$ or, in dimensionless terms, $\mathfrak{L} = \mathfrak{b}$. Finally, we neglect the effect of normal stresses and note

that $\nu_0 = \delta/\mathbf{b}$, to find:

$$\begin{aligned} & \frac{1}{1 + \nu_0 \mathcal{C}(s) n} \left[\frac{\partial u_s}{\partial s} - \left(\frac{F_{ru}^2}{D} \frac{\partial H}{\partial s} + \frac{\zeta - 1}{D} \frac{\partial D}{\partial s} \right) \frac{\partial u_s}{\partial \zeta} \right] + \frac{\partial u_n}{\partial n} \\ & - \left(\frac{F_{ru}^2}{D} \frac{\partial H}{\partial n} + \frac{\zeta - 1}{D} \frac{\partial D}{\partial n} \right) \frac{\partial u_n}{\partial \zeta} + \frac{1}{D} \frac{\partial u_z}{\partial \zeta} + \frac{\nu_0 \mathcal{C}(s)}{1 + \nu_0 \mathcal{C}(s) n} u_n = 0, \end{aligned} \quad (266a)$$

$$\begin{aligned} & \frac{1}{1 + \nu_0 \mathcal{C}(s) n} \left[\frac{\partial u_s^2}{\partial s} - \left(\frac{F_{ru}^2}{D} \frac{\partial H}{\partial s} + \frac{\zeta - 1}{D} \frac{\partial D}{\partial s} \right) \frac{\partial u_s^2}{\partial \zeta} \right] + \frac{1}{D} \frac{\partial (u_s u_z)}{\partial \zeta} + \frac{\partial (u_s u_n)}{\partial n} \\ & - \left(\frac{F_{ru}^2}{D} \frac{\partial H}{\partial n} + \frac{\zeta - 1}{D} \frac{\partial D}{\partial n} \right) \frac{\partial (u_s u_n)}{\partial \zeta} + \frac{2 \nu_0 \mathcal{C}(s)}{1 + \nu_0 \mathcal{C}(s) n} u_s u_n \\ & = - \frac{1}{1 + \nu_0 \mathcal{C}(s) n} \frac{\partial H}{\partial s} + \frac{\sqrt{\mathcal{C}_{fu}}}{\mathbf{b} D} \frac{\partial T_{zs}}{\partial \zeta}, \end{aligned} \quad (266b)$$

$$\begin{aligned} & \frac{1}{1 + \nu_0 \mathcal{C}(s) n} \left[\frac{\partial (u_s u_n)}{\partial s} - \left(\frac{F_{ru}^2}{D} \frac{\partial H}{\partial s} + \frac{\zeta - 1}{D} \frac{\partial D}{\partial s} \right) \frac{\partial (u_s u_n)}{\partial \zeta} \right] + \frac{1}{D} \frac{\partial (u_n u_z)}{\partial \zeta} + \frac{\partial u_n^2}{\partial n} \\ & - \left(\frac{F_{ru}^2}{D} \frac{\partial H}{\partial n} + \frac{\zeta - 1}{D} \frac{\partial D}{\partial n} \right) \frac{\partial u_n^2}{\partial \zeta} + \frac{\nu_0 \mathcal{C}(s)}{1 + \nu_0 \mathcal{C}(s) n} (u_n^2 - u_s^2) \\ & = - \frac{\partial H}{\partial n} + \frac{\sqrt{\mathcal{C}_{fu}}}{\mathbf{b} D} \frac{\partial T_{zn}}{\partial \zeta}, \end{aligned} \quad (266c)$$

where the tilde (denoting dimensionless quantities) has been dropped for the sake of simplicity. Next, we substitute from the decomposition (265) into (266a,266b,266c) and perform a depth integration. This operation generates five types of contributions:

- i) terms that depend on depth averaged quantities: they give rise to corresponding terms in the classical shallow water equations;
- ii) terms which involve the 3-D solution evaluated at the bed: those containing the flow velocity vanish in order to satisfy the no slip condition at the bed; those involving the stress at the bed do not vanish and give rise to the frictional terms of the shallow water equations;
- iii) terms which involve the 3-D solution evaluated at the free surface: their sum vanishes in order to satisfy the kinematic and dynamic conditions at the free surface;
- iv) terms which involve linearly fluctuations with respect to the depth-average: they vanish by definition of zero average fluctuations;
- v) terms which involve fluctuations nonlinearly: they do not vanish in general and represent the memory of the effect of zero average secondary flow in the context of a depth averaged formulation (dispersive terms).

We now illustrate the procedure in detail for the continuity equation (266a) whilst analogous derivations for the momentum equation are left to the reader.

The depth integration of (266a) gives:

$$\begin{aligned} & \frac{1}{D} u_z \Big|_{\zeta_0}^1 + \frac{1}{1 + \nu_0 \mathcal{C}(s) n} \left[\frac{\partial}{\partial s} (U + I_u) - \frac{F_{ru}^2}{D} \frac{\partial H}{\partial s} u_s \Big|_{\zeta_0}^1 + \frac{1}{D} \frac{\partial D}{\partial s} (\zeta - 1) u_s \Big|_{\zeta_0}^1 \right. \\ & \left. + \frac{1}{D} \frac{\partial D}{\partial s} (U + I_u) \right] + \frac{\partial}{\partial n} (V + I_v) - \frac{F_{ru}^2}{D} \frac{\partial H}{\partial n} u_n \Big|_{\zeta_0}^1 + \frac{1}{D} \frac{\partial D}{\partial n} (\zeta - 1) u_n \Big|_{\zeta_0}^1 \\ & + \frac{1}{D} \frac{\partial D}{\partial n} (V + I_v) + \frac{\nu_0 \mathcal{C}(s)}{1 + \nu_0 \mathcal{C}(s) n} (V + I_v) = 0. \end{aligned} \quad (267)$$

Terms of the second type are proportional to $u_s|_{\zeta_0}$, $u_n|_{\zeta_0}$ or $u_z|_{\zeta_0}$, hence they vanish. No stress contribution arises in the continuity equation. Terms of the third type give rise to the following contribution:

$$\frac{1}{D} \left[-\frac{1}{1 + \nu_0 \mathcal{C}(s) n} F_{ru}^2 \frac{\partial H}{\partial s} u_s|_1 - F_{ru}^2 \frac{\partial H}{\partial n} u_n|_1 + u_z|_1 \right], \quad (268)$$

which vanishes identically due to the constraint imposed by the steady dimensionless form of the kinematic boundary condition (53c) with $\mathfrak{L} = \mathfrak{b}$.

Terms of the fourth type are those proportional to I_u or I_b (or their derivatives) and vanish. Finally, no term of the fifth type arises as the continuity equation is linear. Under the assumption that ζ_0 does not depend on s and n , the continuity equation then reads:

$$\frac{1}{1 + \nu_0 \mathcal{C}(s) n} \frac{\partial(DU)}{\partial s} + \frac{\partial(DV)}{\partial n} + \frac{\nu_0 \mathcal{C}(s)}{1 + \nu_0 \mathcal{C}(s) n} (DV) = 0, \quad (269)$$

Performing a similar analysis for the momentum equation, with the help of some algebra, one ends up with the following form of the sought depth averaged governing equations:

$$\begin{aligned} & \frac{1}{1 + \nu_0 \mathcal{C}(s) n} \frac{\partial(DU^2)}{\partial s} + \frac{\partial(DVU)}{\partial n} + \frac{D}{1 + \nu_0 \mathcal{C}(s) n} \frac{\partial H}{\partial s} + \beta_u C_{fu} \tau_s + \frac{2\nu_0 \mathcal{C}(s)}{1 + \nu_0 \mathcal{C}(s) n} (DUV) \\ & = -\frac{1}{1 + \nu_0 \mathcal{C}(s) n} \frac{\partial(DI_u^2)}{\partial s} - \frac{\partial(DI_{uv})}{\partial n} - \frac{2\nu_0 \mathcal{C}(s)}{1 + \nu_0 \mathcal{C}(s) n} (DI_{uv}) \end{aligned} \quad (270)$$

$$\begin{aligned} & \frac{1}{1 + \nu_0 \mathcal{C}(s) n} \frac{\partial(DUV)}{\partial s} + \frac{\partial(DV^2)}{\partial n} + D \frac{\partial H}{\partial n} + \beta_u C_{fu} \tau_n + \frac{\nu_0 \mathcal{C}(s)}{1 + \nu_0 \mathcal{C}(s) n} D(V^2 - U^2) = \\ & -\frac{\partial(DI_v^2)}{\partial n} - \frac{1}{1 + \nu_0 \mathcal{C}(s) n} \frac{\partial(DI_{uv})}{\partial s} - \frac{\nu_0 \mathcal{C}(s)}{1 + \nu_0 \mathcal{C}(s) n} (I_{v^2} - I_{u^2}), \end{aligned} \quad (271)$$

where τ_s and τ_n are the dimensionless longitudinal and lateral components of the bottom stress, respectively. They may be expressed through the following classical closure relationships:

$$\tau_s = \frac{C_f}{C_{fu}} U \sqrt{U^2 + V^2}, \quad \tau_n = \frac{C_f}{C_{fu}} V \sqrt{U^2 + V^2}. \quad (272)$$

The reader should note that the right hand sides of (270) and (271) contain terms of the fifth type (I_{u^2} , I_{v^2} , I_{uv}) which provide the depth averaged effect of the zero average secondary flow on momentum transfer. Note that such dispersive terms are in principle always present in depth averaged models of shallow flows. In practice, they are usually neglected, but they may play some role in curvilinear flows. This notwithstanding, as pointed out above, as a first approximation, in what follows we will neglect their contributions.

With the help of the continuity equation (269) the depth averaged momentum equations can then be simplified and read:

$$\frac{\partial(DU)}{\partial s} + [1 + \nu_0 \mathcal{C}(s) n] \frac{\partial(DV)}{\partial n} + \nu_0 \mathcal{C}(s) DV = 0, \quad (273a)$$

$$\begin{aligned} & U \frac{\partial U}{\partial s} + [1 + \nu_0 \mathcal{C}(s) n] V \frac{\partial U}{\partial n} + \frac{\partial H}{\partial s} \\ & + \beta_u C_f [1 + \nu_0 \mathcal{C}(s) n] \frac{U \sqrt{U^2 + V^2}}{D} = -\nu_0 \mathcal{C}(s) UV, \end{aligned} \quad (273b)$$

$$\begin{aligned} & U \frac{\partial V}{\partial s} + [1 + \nu_0 \mathcal{C}(s) n] V \frac{\partial V}{\partial n} + [1 + \nu_0 \mathcal{C}(s) n] \frac{\partial H}{\partial n} \\ & + \beta_u C_f [1 + \nu_0 \mathcal{C}(s) n] \frac{V \sqrt{U^2 + V^2}}{D} = \nu_0 \mathcal{C}(s) U^2. \end{aligned} \quad (273c)$$

The reader should note that, setting $\mathcal{C}(s) = 0$, the above equations reduce to the classical steady shallow water equations valid for straight channels (see equations 470(I), 471(I) and 472(I)).

To complete the hydrodynamic formulation, appropriate boundary conditions must be specified. The no flux condition at the side walls reads:

$$V = 0, \quad (n = \pm 1) \quad (274)$$

The conditions appropriate to the upstream and downstream open boundaries will be formulated in Section 4.4.

The hydrodynamic equations are coupled to the Exner equation and related closures presented in Section 3.1.2. Below, for the sake of simplicity, we restrict ourselves to the bedload dominated case. Removing the tilde as usual, setting $\mathfrak{L} = \mathfrak{b}$ and recalling that $\beta_u \sqrt{C_{fu}} = 1/\mathfrak{b}$, the governing equation (185) then becomes:

$$\frac{\partial \eta}{\partial t_m} + \frac{1}{h_s} \frac{\partial Q_{ss}^b}{\partial s} + \frac{1}{h_s} \frac{\partial (h_s Q_{sn}^b)}{\partial n} = 0, \quad (275)$$

where:

$$Q_{ss}^b = Q_{s0}^b(\tau_*; \tau_{*c}, R_p), \quad Q_{sn}^b = Q_{s0}^b(\tau_*; \tau_{*c}, R_p) \left[\sin \chi - \frac{r}{\beta_u \sqrt{\tau_*}} \frac{\partial \eta}{\partial n} \right]. \quad (276)$$

Here we have neglected the weak effect of perturbations of the longitudinal slope on sediment transport and closure is needed for the angle χ according to the definition (182). In this respect, although we have neglected the dispersive effects of secondary flows with zero depth average in the governing momentum equations, following the lead of Blondeaux and Seminara (1985), we wish to preserve the memory of the latter in the closure adopted for χ . This is not essential for the development of the theory of river meandering presented in this Chapter, but it has some quantitative effect on the prediction of the lateral bed slope and can be accounted for at very low computational cost.

We then assume the following closure for $\sin(\chi)$:

$$\sin \chi = \frac{V}{\sqrt{U^2 + V^2}} + \nu_0 \mathcal{C}(s) D^{7/4} c_\chi, \quad c_\chi = \frac{1}{\beta_u \sqrt{C_{fu}}} \left(I_{\mathcal{G}_{11}} - \frac{d\mathcal{G}_{11}}{d\zeta} \Big|_{\zeta_0} \right) \quad (277)$$

where the first contribution in the right hand side of the expression for $\sin \chi$ is associated with the depth averaged component and the second contribution is an estimate of the effect of the zero average component of secondary flow.

Let us clarify the latter result. The estimate of the second contribution to $\sin \chi$ is based on the expression valid, at the linear level, for fully developed flow in constant curvature channels with topography (Section 2.4.3), assumed to hold locally in channels with arbitrary distribution of curvature. We recall that, in the context of weakly sloping beds, the angle χ that the bottom stress forms with the longitudinal axis can be expressed as in Section 3.1.1, equation (182). On the other hand, in the case of steady flow in weakly meandering channels with non-flat topography (Section 2.5), the longitudinal and lateral velocity components (equations 147, 151) take the form

$$u_s(s, n, \zeta) = U_0(s, n) \mathcal{F}_0(\zeta) + \mathcal{O}(\delta), \quad (278a)$$

$$u_n(s, n, \zeta) = \delta \left\{ V_1(s, n) \mathcal{F}_0(\zeta) + U_0(s, n) \mathcal{C}(s) \left[I_{\mathcal{G}_{11}} \mathcal{F}_0(\zeta) - \mathcal{G}_{11}(\zeta) \right] \right\}. \quad (278b)$$

As a consequence, recalling equation (182) and assuming for the calculation of $\sin \chi$ $U \simeq U_0$ and $V \simeq \delta V_1$, the closure for $\sin \chi$ takes the form (277).

Note that the latter appears to be the simplest approximation one may envisage. Although it is not fully justified in the context of rational perturbation schemes, it is sufficient for the present purposes.

Finally, under steady conditions, the usual integral constraints impose that the water flux and the sediment discharge must keep constant in the longitudinal direction, hence:

$$\int_{-1}^1 U D \, dn = 2, \quad \int_{-1}^1 Q_{ss}^b \, dn = 2 Q_{s0}^b \Big|_{\tau_u = \tau_{*u}} = 2 Q_{su}. \quad (279)$$

4.3. Resonance in meandering channels

We can now investigate the morphodynamics of meandering channels based on the above depth averaged formulation, that will allow us to disclose its subtle relationship to the morphodynamics of free bars in straight channels. We will start with the simplest approach where we assume that meanders are in their infancy, hence characterized by small amplitudes and small curvatures (Section 4.3.1). Resonance will then emerge naturally as a process occurring under fairly special conditions, but such to influence the response of the channel also when these conditions are not exactly met. We will next investigate how nonlinearities damp the resonance mechanism under weakly nonlinear conditions (i.e., not too far from resonance) (Section 4.3.2) and complete our analysis discussing how the effects of resonance are felt under fully nonlinear conditions (Section 4.3.3).

4.3.1 Linear theory and the resonance mechanism

Following the usual notations and recalling that in this Chapter we will employ the half-width of the channel (B) as scale for both the longitudinal and lateral coordinates, we consider a channel characterized by longitudinal axis such that its projection onto the horizontal plane (s, n) is a sine generated curve characterized by dimensionless channel curvature $\mathcal{C}(s)$ (Figure 61):

$$\mathcal{C}(s) = \exp(i \lambda_m s) + c.c., \quad (280)$$

where $\lambda_m = 2 \pi B / L_m$ is the intrinsic meander wavenumber, with L_m intrinsic meander wavelength. The word intrinsic implies that lengths are measured along the s axis.

Let us assume that ν_0 is a small parameter, hence:

$$\nu_0 \ll 1, \quad (281)$$

and use this assumption to linearize the governing equations and the related boundary and integral conditions around the uniform straight channel solution.

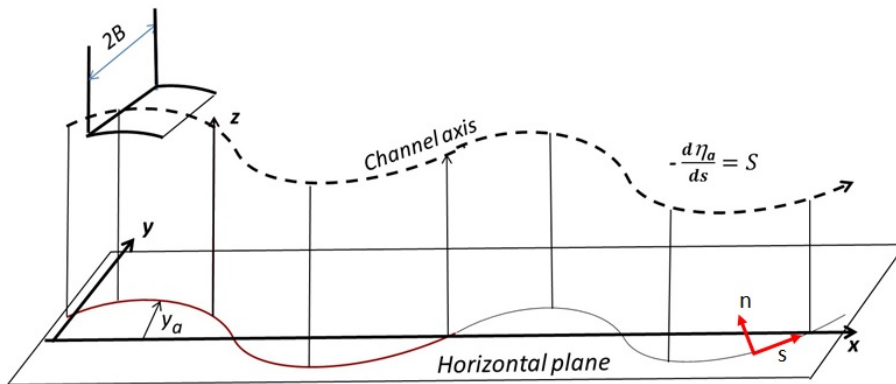


Figure 61. Cartesian reference frame for a sinuous channel and notations

We then look for *linear periodic solutions* of the depth averaged equations and set:

$$(U, V, H, D) = (1, 0, H_0, 1) + \nu_0 (U_1, V_1, H_1, D_1) e_1 + c.c. + \mathcal{O}(\nu_0^2) \quad (282)$$

where we have employed the following notation:

$$e_1 = \exp(i \lambda_m s) \quad (283)$$

Note that the quantities U_1, V_1, H_1, D_1 are in general complex quantities such that we could also write

$$U_1 e_1 + c.c. = 2 \operatorname{Re}(U_1) \cos(\lambda_m s) - 2 \operatorname{Im}(U_1) \sin(\lambda_m s) = 2 |U_1| \cos(\lambda_m s + \varphi), \quad (284)$$

where φ is the phase lag of the longitudinal velocity relative to curvature, and reads:

$$\varphi = \arctan \frac{\operatorname{Im}(U_1)}{\operatorname{Re}(U_1)}. \quad (285)$$

The latter expansion is closely related to, but differs slightly from the one originally employed by Blondeaux and Seminara (1985). The small parameter employed by Blondeaux and Seminara (1985) was the meander amplitude ϵ which appears in the cartesian equivalent of (280) that reads:

$$y_a = \epsilon \exp(i k_m x) + c.c.. \quad (286)$$

Here, y_a is the lateral cartesian coordinate of the channel axis, x is a cartesian longitudinal coordinate aligned with the valley, $k_m = 2\pi B/L_x$ is a cartesian meander wavenumber (with L_x the cartesian meander wavelength) and ϵ is a small meander amplitude (Figure 61).

The cartesian scheme is appropriate when the analysis is adopted to investigate the process of incipient meander formation (see Chapter 5). As pointed out by Blondeaux and Seminara (1985), the cartesian and intrinsic approaches are related to each other as channel curvature in cartesian coordinates reads:

$$\nu_0 \mathcal{C} = \frac{d^2 y_a / dx^2}{\left[1 + (dy_a / dx)^2\right]^{3/2}} = -\epsilon k_m^2 \exp(i k_m x) + c.c. + \mathcal{O}(\epsilon^2 k_m^2). \quad (287)$$

Moreover, as the element of the s -coordinate line ds is related to the corresponding cartesian element dx through the relationship $ds = \sqrt{1 + (dy_a / dx)^2} dx$, it follows that ds coincides with dx (and correspondingly λ_m with κ_m) except for higher order contributions of $\mathcal{O}(\epsilon^2 k_m^2)$. Hence, it follows that:

$$\nu_0 = \epsilon k_m^2 \simeq \epsilon \lambda_m^2. \quad (288)$$

This relationship implies that the forcing terms associated with curvature in Blondeaux and Seminara (1985) analysis include a factor λ_m^2 that is absent in the present approach.

Let us then return to our perturbation analysis, which follows closely the lines of the linear stability analysis for free bars (Section 6.3I), except for the steady character of the present perturbations and for the presence of forcing (non homogeneous) terms driven by curvature. Using the same notations as in the free bar case, the reader will readily show that the perturbation amplitudes U_1, V_1, H_1 and D_1 satisfy the following linear ordinary differential system:

$$a_{1j} U_1 + a_{2j} V_1 + a_{3j} H_1 + a_{4j} D_1 = a_{5j} \quad (j = 1, 4), \quad (289)$$

Moreover, the coefficients of the above linear system of differential equations read:

$$a_{11} = i \lambda_m, \quad a_{21} = \frac{d}{dn}, \quad a_{31} = 0, \quad a_{41} = i \lambda_m, \quad (290a)$$

$$a_{12} = i \lambda_m + 2 \beta_u C_{fu}, \quad a_{22} = 0, \quad a_{32} = i \lambda_m, \quad a_{42} = \beta_u C_{fu} (c_{fD} - 1), \quad (290b)$$

$$a_{13} = 0, \quad a_{23} = i \lambda_m + \beta_u C_{fu}, \quad a_{33} = \frac{d}{dn}, \quad a_{43} = 0, \quad (290c)$$

$$a_{14} = 2 i \lambda_m \Phi_T^b, \quad a_{24} = \frac{d}{dn}, \quad a_{34} = -F_{ru}^2 R_{nu} \frac{d^2}{dn^2}, \quad a_{44} = -\frac{a_{34}}{F_{ru}^2} + a'_{44}, \quad (290d)$$

$$a_{51} = 0, \quad a_{52} = -n a'_{52} = -n \beta_u C_{fu}, \quad a_{53} = 1, \quad a_{54} = 0. \quad (290e)$$

and

$$a'_{44} = \Phi_T^b i \lambda_m c_{fD}, \quad a'_{52} = \beta_u C_{fu}, \quad (291)$$

Note that the homogeneous part of the above differential system reduces exactly to the algebraic system (equations 505(I) and 506(I)) with vanishing growth rate ($\omega = 0$) if the lateral dependence of the perturbations (U_1 , V_1 , H_1 and D_1) is given the normal form of free bar perturbations adopted in the linear stability analysis of Section 6.3.1I, and longitudinal slope effect on bedload is neglected.

The differential system (289) is solved with the following boundary conditions:

$$V_1|_{n=\pm 1} = 0, \quad Q_{sn1}^b|_{n=\pm 1} = 0 \rightarrow \left[F_{ru}^2 \frac{dH_1}{dn} - \frac{dD_1}{dn} \right]_{n=\pm 1} = \frac{c_\chi}{R_{nu}}. \quad (292)$$

Some algebraic manipulations are needed to reduce the system of four first order differential equations (289) to a single non-homogeneous fourth order ordinary differential equation with constant coefficients¹. The outcome of this procedure is as follows:

$$\frac{d^4 V_1}{dn^4} + \Gamma_1 \frac{d^2 V_1}{dn^2} + \Gamma_2 V_1 = \Gamma_0, \quad (293a)$$

$$V_1|_{n=\pm 1} = 0, \quad \frac{d^2 V_1}{dn^2} \Big|_{n=\pm 1} = \Gamma_3, \quad (293b)$$

where:

$$\Gamma_1 = \frac{a'_{44} - a_{14}}{R_{nu}} + \frac{a_{32} a_{23} a_{11}}{a_{12}} - \frac{1 + F_{ru}^2 R_{nu} a_{23}}{a_{12} R_{nu}} (a_{41} a_{12} - a_{42} a_{11}) + a_{14} \frac{a_{12} - a_{42}}{a_{12} R_{nu}}, \quad (294a)$$

$$\Gamma_2 = \frac{a_{32} a_{23}}{a_{12} R_{nu}} (a'_{44} a_{11} - a_{14} a_{41}), \quad \Gamma_0 = \frac{a'_{44} a_{11} - a_{14} a_{41}}{a_{12} R_{nu}} (a'_{52} + a_{32} a_{53}), \quad (294b)$$

$$\Gamma_3 = \frac{a_{41} a_{12} - a_{11} a_{42}}{a_{12}} \left(-\frac{c_\chi}{R_{nu}} + F_{ru}^2 a_{53} \right) + \frac{a_{11}}{a_{12}} (a'_{52} + a_{32} a_{53}). \quad (294c)$$

The equation (293) is readily solved in closed form to find:

$$V_1 = \frac{\Gamma_0}{\Gamma_2} + \gamma_1 \cosh(\mu_1 n) + \gamma_2 \cosh(\mu_2 n). \quad (295)$$

where

$$\mu_1 = \sqrt{\frac{1}{2} \left(-\Gamma_1 + \sqrt{\Gamma_1^2 - 4\Gamma_2} \right)}, \quad \mu_2 = \sqrt{\frac{1}{2} \left(-\Gamma_1 - \sqrt{\Gamma_1^2 - 4\Gamma_2} \right)}, \quad (296a)$$

$$\gamma_1 = \frac{\mu_2^2 \Gamma_0 / \Gamma_2 + \Gamma_3}{(\mu_1^2 - \mu_2^2) \cosh \mu_1}, \quad \gamma_2 = \frac{\mu_1^2 \Gamma_0 / \Gamma_2 + \Gamma_3}{(\mu_2^2 - \mu_1^2) \cosh \mu_2}. \quad (296b)$$

Similar solutions can be obtained for the remaining unknowns U_1 , H_1 and D_1 (see Blondeaux and Seminara, 1985). This exercise is left to the reader.

In Figure 62 we plot the real part of U_1 , i.e. the amplitude of the component of the longitudinal perturbation velocity in phase with curvature, as a function of the meander wavenumber λ_m for $n = 1$ and given values of the unperturbed Shields stress τ_{*u} , the friction coefficient C_{fu} and the unperturbed aspect ratio β_u . The plot suggests that, for some values of λ_m and β_u with given τ_{*u} and C_{fu} , the morphodynamic response displays a very high peak. A glance at the solution (295),

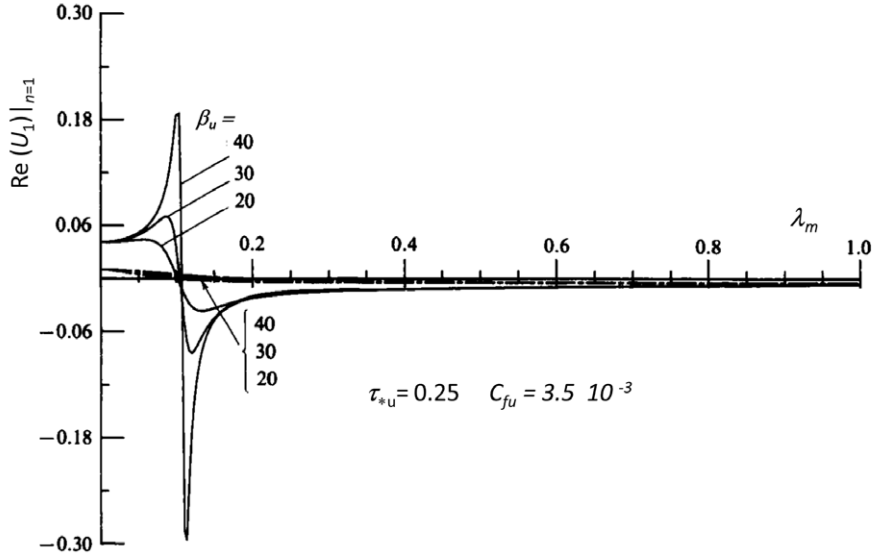


Figure 62. The amplitude of the longitudinal component of the perturbation velocity in phase with curvature $Re(U_1)$, evaluated at the outer bank, is plotted versus the meander wavenumber λ_m . Calculations were performed according to the theory of Blondeaux and Seminara (1985), modified as discussed in the text, and assuming the absence of small scale bedforms (i.e. plane bed conditions).

296b) clarifies that, indeed, it becomes unbounded for values of the dimensionless parameters such that

$$\mu_1^2 = \mu_2^2. \quad (297)$$

Under these conditions curvature forces a natural solution of the system and resonance occurs.

To understand the origin of resonance the reader should appreciate that the forcing terms associated with curvature in the system (289) can be thought of as the sum of lateral Fourier modes identical with those characterizing free bars. This is immediately understood noting that the coefficient a_{52} can be expanded in Fourier series (Churchill and Brown, 1987), observing that, in the interval $-1 \leq n \leq 1$,

$$n = \sum_{m=0}^{\infty} A_m \sin(Mn), \quad A_m = \int_{-1}^1 n \sin(Mn) dn = (-1)^m \frac{2}{M^2}, \quad M = \frac{(2m+1)\pi}{2}. \quad (298)$$

This expansion thus generate terms proportional to $\mathcal{S}^m(n)$ or $\mathcal{C}^m(n)$ with m odd or even (recall the definitions (6.34I)). And we know that, for given τ_{*u} and C_{fu} the first lateral mode associated with the homogeneous part of the system (289) is characterized by vanishing growth rate ($\omega = 0$) if the aspect ratio β_u and the wavenumber λ take the values β_R and λ_R , respectively (see Section 6.3I). It is then clear that a sine generated meander with $\lambda_m = \lambda_R$ and $\beta_u = \beta_R$ would force a natural steady and non-amplifying free bar solution.

It is a well-known feature of linear resonators (Kevorkian and Cole, 1981, p. 141) that the phase of the response of the system to the oscillatory forcing changes quadrant on crossing the resonance conditions. In order to fully understand this concept, the interested reader may find

¹ Use eq. (289) ($j = 3$) to express dH_1/dn in terms of V_1 . Substitute this expression into eq. (289) ($j = 2$) differentiated with respect to n to express dU_1/dn in terms of dD_1/dn . Substitute this expression into eq. (289) ($j = 1$) differentiated with respect to n , to express dD_1/dn (and consequently dU_1/dn) in terms of V_1 and its second derivative. Finally, differentiate with respect to n the eq. (289) ($j = 4$) and use the previously derived relationships to express dU_1/dn , d^3H_1/dn^3 , d^3D_1/dn^3 and dD_1/dn in terms of V_1 and its second and fourth derivative.

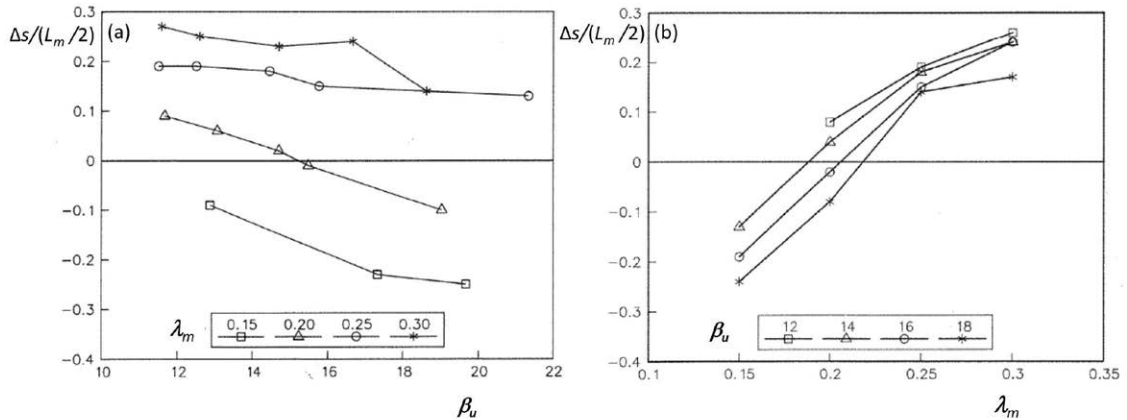


Figure 63. The dimensionless quantity $\Delta s/(L_m/2)$, is plotted versus (a) the aspect ratio of the channel β_u for different values of the meander wavenumber λ_m and versus (b) the meander wavenumber λ_m for given values of the aspect ratio of the channel β_u . Here, Δs is the longitudinal distance of the peak scour from the bend apex in the experiments of Colombini *et al.* (1991) (modified from Colombini *et al.*, 1991).

it useful to read Section 8.1 of the Mathematical Appendix, where we outline the behavior of forced oscillatory systems in a neighborhood of resonant conditions for a simple toy model. For the present meandering problem it is sufficient to point out a major implication of the above feature. On crossing resonance (i.e. as the meander wavenumber λ_m increases for given aspect ratio β_u or, viceversa, as the aspect ratio increases for given meander wavenumber), the location where the peak flow occurs crosses the bend apex. This theoretical prediction has been experimentally confirmed (see Figure 6 of Colombini *et al.* (1991) and Garcia and Niño (1993)). In particular, the former Authors have located the position of the peak scour in a sequence of experimental tests carried out for trains of sine generated meanders characterized by different values of meander wavenumber and aspect ratio. Results are plotted in Figure 63 in terms of the dimensionless quantity $\Delta s/(L_m/2)$, where Δs is the longitudinal distance of the peak scour from the bend apex. The latter ratio may range from -0.5 (peak scour located $L_m/4$ upstream of the bend apex) to 0.5 (peak scour located $L_m/4$ downstream of the bend apex). Figure 63 shows a fairly regular behavior for $\Delta s/(L_m/2)$ which decreases with β_u (the peak scour moves upstream as discharge decreases) and increases with λ_m (the peak scour moves downstream as the meander wavelength decreases).

The importance of the above results is related to the problem of planform evolution of meandering rivers, that is extensively discussed in the next Chapter. We will see that theoretical predictions (Seminara *et al.*, 2001a) and numerical simulations (Lanzoni and Seminara, 2006) suggest that sub-resonant trains of periodic meanders migrate downstream while super-resonant trains migrate upstream. This feature is precisely related to the observation that the location of the peak scour crosses the meander apex as the resonant conditions are crossed.

Before we proceed, it is worth mentioning that the reason why the existence of the resonance phenomenon disclosed by Blondeaux and Seminara (1985) had been overlooked in the previous important contribution of Ikeda *et al.* (1981) was the fact that, in that paper, bed topography was not determined through the solution of Exner equation coupled with the hydrodynamic equations. It was related to the flow field only empirically thus preventing the effects of the free bar response of the system to emerge. This shortcoming was later recognized and corrected by Johannesson and Parker (1989) in a paper that has enjoyed a great popularity and confirmed all the findings of Blondeaux and Seminara (1985).

4.3.2 Weakly nonlinear theory of near resonant meanders

Results discussed in the previous Section call for the need of a number of important develop-

ments.

Linear theory predicts an infinite response of flow and bed topography at resonant conditions. This is obviously an un-physical behavior that can be removed accounting for nonlinear effects. Such a development will also allow us to answer a related question: how wide is the range of meander wave-numbers and aspect ratios of the channel cross section where the effects of resonance are significantly felt?

These issues are discussed in detail in the Mathematical Appendix, Section 8.1 for a toy model of nonlinear resonator. The reader not familiar with the subject is advised to read that Section before proceeding. There, it is shown that nonlinearity turns out to widen the resonant range and leads to further interesting features like non-uniqueness of the nonlinear response.

Below, we simply discuss the main outcomes of the weakly nonlinear analysis of Seminara and Tubino (1992), which is based on a perturbation expansion valid in a neighborhood of resonance following the lines of the approach discussed in the Mathematical Appendix. Results suggest that nonlinear nearly resonant meanders do behave like other classical nonlinear resonators. Their response differs significantly from the linear response within a fairly wide range of meander wave-numbers of practical significance and may be non-unique.

The approach followed by Seminara and Tubino (1992) is based on the recognition that, at lowest order in the sought expansion in powers of the small parameter ν_0 , the leading order contribution must have the structure of the *natural* solution of the homogeneous linear problem describing marginally stable non-migrating and non-amplifying free bars, with an amplitude A to be determined at higher order. In other words, at lowest order, the near resonant solution for any relevant variable, say the longitudinal component of the velocity U , reads:

$$U = [A u_{11} e_1^R \mathcal{S}_1(n)] \nu_0^\xi + c.c., \quad (299)$$

where ξ is an exponent to be determined and e_1^R denotes the function e_1 evaluated for $\lambda_m = \lambda_R$. The classical argument employed in the analysis of weakly nonlinear resonant oscillations (see Section 8.1.5) shows that the singular resonant behavior occurring at the linear level is suppressed by nonlinear effects provided $\xi = 1/3$. This suggests to set up the following expansion:

$$\begin{aligned} U = & [A u_{11} e_1^R \mathcal{S}_1(n) + c.c.] \nu_0^{1/3} + \\ & + [A^2 e_2^R (u_{22} \mathcal{C}_2(n) + u_{20}) + A \bar{A} (u_{02} \mathcal{C}_2(n) + u_{00}) + c.c.] \nu_0^{2/3} \\ & + (u_{31} e_1^R \mathcal{S}_1(n) + c.c.) \nu_0 + \mathcal{O}(e_3^R \nu_0, \nu_0^{4/3}), \end{aligned} \quad (300)$$

with similar expansions envisaged for V , H and D .

Moreover, we expand the width to depth ratio β_u and the meander wavenumber λ_m in neighborhoods of their resonant values β_R and λ_R , respectively, such that we may explore the width of the *resonant range* where the effects of resonance are felt. The usual argument suggests the following expansion:

$$\beta_u = \beta_R (1 + b \nu_0^{2/3}), \quad \lambda_m = \lambda_R + \lambda_1 \nu_0^{2/3}. \quad (301)$$

Finally, the time variable appropriate to describe the transient evolution of the amplitude function A is the *slow* variable T defined as:

$$T = \nu_0^{2/3} t. \quad (302)$$

On substituting from the above expansions into the governing equations and equating terms of order $\mathcal{O}(\nu_0^{1/3})$ one recovers the unforced linear algebraic problem governing spatial free modes presented in Section 6.3I. Similarly, equating terms of order $\mathcal{O}(\nu_0^{2/3})$ we recover problems for the harmonics 22, 20, 02 and 00 of weakly nonlinear spatial modes which are still unaffected by curvature (see Section 6.5.2I). At order $\mathcal{O}(\nu_0)$ the differential problem governing the fundamental reproduced by nonlinear interactions includes non-homogeneous terms associated with curvature. Since the homogeneous part of this differential problem admits of a non-trivial solution, one must

impose a solvability condition. We omit details of the analysis and refer the reader to the original paper of Seminara and Tubino (1992). The fundamental result of this theory is the following amplitude equation:

$$\frac{dA}{dT} = [i \lambda_1 \alpha^R + b \beta_R (\mu_\beta^R + i \nu_\beta^R)] A + a^R A |A|^2 + \alpha_3^R, \quad (303)$$

where α^R , μ_β^R , ν_β^R and a^R are identical to the corresponding complex coefficients of the amplitude equation (548(I)), describing the finite-amplitude development of spatially growing bars. Moreover, α_3^R is the non-homogeneous term associated with the forcing effect of curvature. The solution of (303) gives the dependence of the complex amplitude A on time for given values of the dimensionless parameters of the problem. Through the expansions (300) and (301), it then completely determines the solution for the flow and bottom topography in weakly meandering channels up to third order.

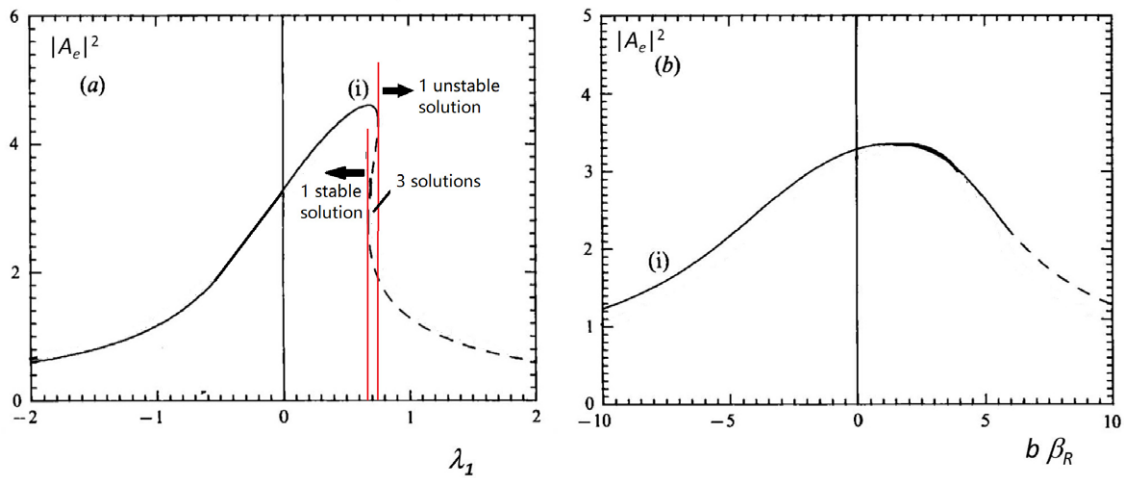


Figure 64. The weakly nonlinear steady-state solution for the amplitude function of near-resonant meanders is plotted versus the perturbations of the meander wavenumber λ_m (λ_1) and of the width ratio β_u ($b \beta_R$) with respect to their resonant values, for Shield stress $\tau_{*u} = 0.1$, and grain roughness $d_s = 0.01$. Solid and dashed lines denote stable and unstable solutions, respectively (modified from Seminara and Tubino, 1992).

Under steady state conditions ($dA/dT = 0$) equation (303) admits of equilibrium solutions A_e that are discussed in some detail in Seminara and Tubino (1992). A simpler treatment for a model problem is given in Section 8.1. The steady state equation exhibits in general one real and two complex-conjugate solutions. Hence, under these conditions, the complex solutions being meaningless, the steady response of the channel is unique. This is shown in Figure 64. However, the same figure shows that, for given τ_{*u} and d_s , ranges of A_e exist in which the three solutions of (303) are all real. Hence, the response of the channel may not be unique, a feature typical of nonlinear oscillators close to resonance. One is then led to investigate which of the three real solutions is appropriate for a given set of initial conditions. The issue is resolved investigating the stability of the three solutions. Numerical solutions of the full amplitude equation, performed following the approach outlined in Section 8.1, reveal that the upper branch of the solution (solid line in Figure 64) is invariably stable. Conversely, the lower branch and the loop joining the upper branch to the lower branch (dashed line in Figure 64) are invariably unstable. Moreover, further analysis allows one to show that the unstable steady solution corresponding to the lower branch bifurcates into a time-periodic solution, while the unstable solution corresponding to the loop bifurcates into the steady upper-branch solution. Hence, theory predicts that, as the wavenumber increases, the solution abruptly shifts from the steady upper-branch behavior to a time-periodic behavior. In other words, two different types of behavior arise for sub- or super-resonant meanders.

This can be physically understood noting that, close to resonance, two distinct responses of free migrating bars exist. Below resonance they do not amplify (hence no homogeneous solution of the linear unsteady problem exists); above resonance they do amplify. Hence, under super-resonant conditions, the linearly unstable homogeneous part of the solution interacts nonlinearly with the steady forced part giving rise to the time-periodic pattern detected in the numerical solution of (303).

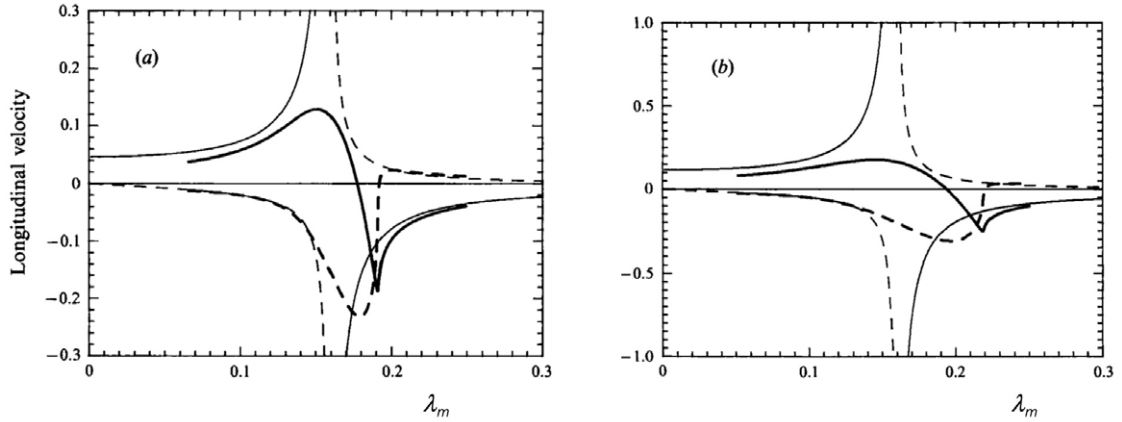


Figure 65. The linear solution and the fundamental component of the weakly nonlinear solution for the perturbation of the longitudinal velocity at the outer wall ($U|_{n=1}$) are plotted versus meander wavenumber λ_m for different values of the curvature ratio ν_0 ($\tau_{*u} = 0.08$, $d_s = 0.05$, $\beta_u = 12$). Thin curves: linear theory $[\nu_0 U_1]_{n=1}$, thick curves: nonlinear theory $[\nu_0^{1/3} A u_{11}]_{n=1}$. Solid and dashed curves denote real and imaginary parts respectively. (a) $\nu_0 = 0.01$; (b) $\nu_0 = 0.025$ (modified from Seminara and Tubino, 1992).

It is also instructive to compare the weakly nonlinear resonant solution developed here with the linear forced solution. This is shown in Figure 65. Notice that in the plots only the contribution associated with the fundamental harmonic in the longitudinal direction e_1^R , i.e. the $\mathcal{O}(\nu_0^{1/3})$ component of the weakly nonlinear expansion (300), has been kept. The figure shows that, the sharp linear peak at resonance is smoothed out and the system response follows a fairly smooth trend with a relatively weak maximum for values of meander wavenumber larger than the resonant value. In other words, not only do nonlinear effects suppress the singularity exhibited by the linear solutions at (λ^R, β^R) , but they also control the bed response within a fairly wide range of values of meander wavenumber whose amplitude depends on the curvature ratio ν_0 through (301).

Experimental verification of the resonant response of meandering channels

Systematic laboratory experiments aimed at providing some substantiation to the picture emerging from theoretical efforts were performed by Colombini *et al.* (1991) and, few years later, by Garcia and Niño (1993). Detailed descriptions and discussions of the experimental procedure can be found in those papers. Let us summarize their main results.

The sinuous channel in each of the experiments of Colombini *et al.* (1991) consisted of at least 3.5 meanders, and was characterized by a channel axis following a sine curve. The values of the curvature ratio ν_0 , the average slope S and the grain size were kept constant through all the experiments, whilst the channel wavenumber and the width ratio were varied in a range as broad as possible close to their resonant values. The value chosen for ν_0 was 0.05, large enough to expect that free migrating bars would be suppressed (see Section 4.5), but small enough for the perturbation approach to be expected to be sufficiently valid. This value of ν_0 corresponds typically to natural meanders in the initial-intermediate stage of development. The Cartesian wavenumber k_m , fell in the range 0.15 – 0.30, and the width ratio in the range 11 – 20. Sediment consisted of coarse sand ($d_{50} = 0.76$ mm) and small-scale bedforms (ripples, dunes) did not form. In each experiment forced bars reached an equilibrium configuration, sometimes disturbed by small

propagating sand waves born within the pool at the concave bank and disappearing downstream. For the smallest wavenumber ($k_m = 0.15$), migrating alternate bars with amplitude smaller than that of the forced bars did also form.

The typical spectrum of the amplitudes of bottom harmonics found by Colombini *et al.* (1991) clearly supported the weakly nonlinear nature of the response of bed topography, as the fundamental 11 harmonic was dominant and higher harmonics decayed. Moreover, a nonlinear resonance effect was indeed operating in the experimental process. In the absence of resonance, a straightforward perturbation scheme in integer powers of ν_0 would be appropriate. As extensively discussed for the model problem in Section 8.1.5, such an expansion predicts a decay of the intensity of higher harmonics produced by nonlinear interactions much faster than the one observed. In particular, second-order harmonics should have an intensity of the order of 5% of the intensity of the fundamental, very far from observed values of roughly 30%.

Figure 66 shows a comparison between the amplitude of the first harmonic of the solution for the bottom elevation as predicted by linear and weakly nonlinear theories and the values observed for the two set of experiments with $k_m = 0.2$ and $k_m = 0.15$, respectively. The comparison seems to be fairly satisfactory if account is taken of the fact that the weakly nonlinear solution strictly applies only within a neighborhood $\mathcal{O}(\nu_0^{2/3})$ of the resonant values λ_R and β_R (the resonant range roughly sketched in the figures). Note that β_R in the experiments was close to 13 and λ_R fell in the range 0.165 – 0.175 for the values of Shields and roughness parameters typical of these experiments.

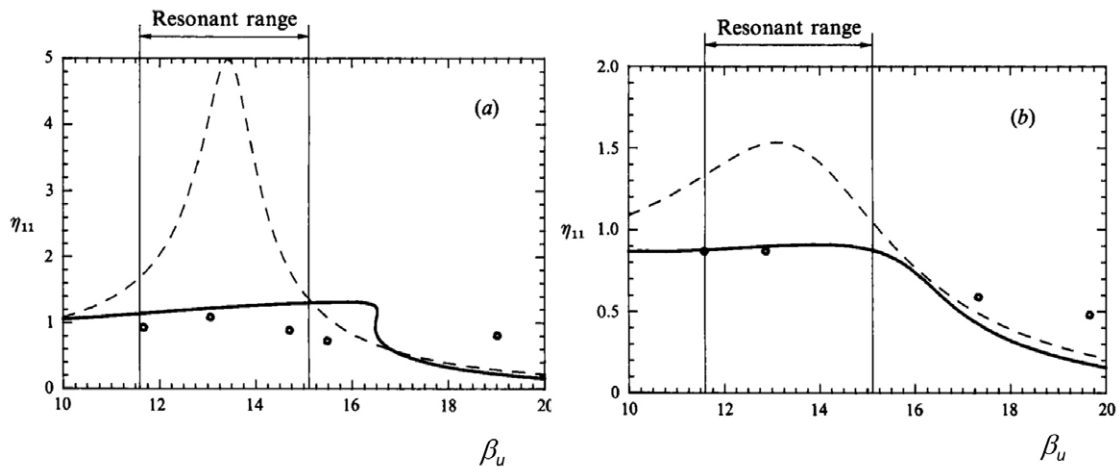


Figure 66. The dimensionless amplitude of the first harmonic of bottom elevation η_{11} predicted by the weakly nonlinear theory of Seminara and Tubino (1992) (solid curve) and by the linear theory (dashed curve) is plotted versus the width ratio of the channel β_u and compared with the experimental findings of Colombini *et al.* (1991) for two values of the meander wavenumber. The resonant range is defined by (301) with $b\beta_R = \pm 1$. (a) $k_m = 0.2$; (b) $k_m = 0.15$ (modified from Seminara and Tubino, 1992).

4.3.3 The nonlinear response far from resonance

Let us finally analyze how the effects of resonance decay as we move farther from the resonant conditions. To fulfill this aim, we employ the model developed by Bolla *et al.* (2009) and discussed in Section 3.3.1, which applies to meandering channels with constant widths and slowly varying weak curvature, but is not restricted to small amplitude perturbations of the bottom topography.

The Figure 67 reports the peak value (Figure 67a) and relative phase lag (Figure 67b) of the vertically averaged dimensionless longitudinal velocity in a sine generated meander characterized by different values of β_u and given values of the relevant dimensionless parameters (d_s , ν_0 and τ_{*u}). It is noticeable that, for each value of β_u , the curves representing the intensity of the maximum

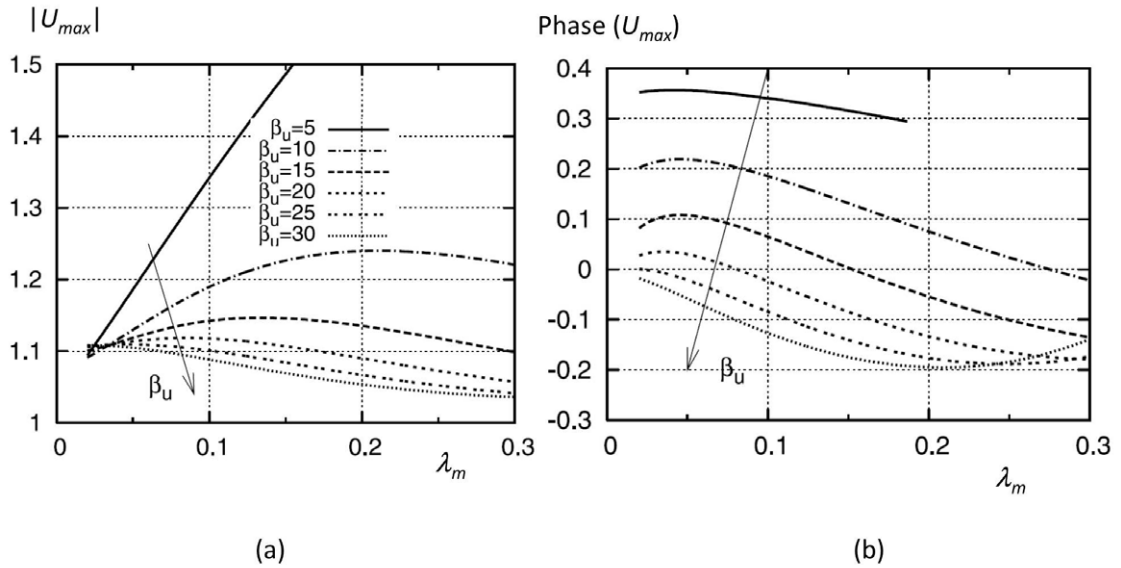


Figura 67. Maximum value (a) and relative phase lag (b) of the vertically averaged dimensionless longitudinal velocity computed in sine generated meanders for different values of β_u far from resonance ($d_s = 5 \cdot 10^{-3}$, $\nu_0 = 0.04$, and $\tau_{*u} = 0.1$) (modified from Bolla et al., 2009).

velocity exhibit a peak except for $\beta_u = 5$. In this case, the curve is interrupted because the value of the Shields stress falls below the threshold of motion somewhere along the meander. Also, note that, for increasing values of β_u and keeping ν_0 constant, the perturbation parameter δ in the expansion of Bolla et al. (2009) decreases, hence smaller values of the maximum speed are experienced. Moreover, Figure 67 indicates that, for small values of β_u , as the wave number increases the cross section where the maximum velocity is located moves from downstream (positive phase lag) to upstream (negative phase lag) relative to the bend apex. For larger values of β_u the trend is similar but the maximum speed is located upstream of the bend apex even for small wave numbers.

In conclusion, similarly to the weakly nonlinear case, the channel response exhibits a peak of the longitudinal velocity even for values of the aspect ratios far from its resonant value, but the intensity of the peak decays. This concludes our overview of the linear and nonlinear aspects of the resonance mechanism discovered by Blondeaux and Seminara (1985).

4.4. Morphodynamic influence

Let us now investigate the fundamental issue of *morphodynamic influence*, i.e. the question of whether the perturbation of bottom topography driven by channel curvature is able to affect the river morphodynamics downstream and/or upstream of the curved reach.

4.4.1 What influence?

Let us first clarify that the type of influence we will discuss here does not concern one-dimensional perturbations of bottom topography. Indeed, it has been known since the work of de Vries (1969) that an upstream 1-D influence may indeed occur in supercritical streams (where hydrodynamic influence is prevented) through the slow upstream propagation of 1-D bottom waves.

We are concerned here with two-dimensional, bar-type, perturbations of bottom topography. This problem can be illustrated at best considering the experimental configuration examined by Struiksma et al. (1985): a curved reach with constant curvature of the channel axis connected to two straight reaches located upstream and downstream of the curved reach, respectively (Figure 68).

Under such conditions, Struiksmas *et al.* (1985) showed that, at the entrance region of the curved reach, bottom topography adjusts to the new equilibrium through a sequence of damped steady oscillations of transverse bed slope occurring downstream of the abrupt change of channel curvature. The development of such non-migrating spatially decaying bars at the bend entrance represents the clearest example of *downstream influence* in river morphodynamics as the morphodynamic effects of the discontinuity in channel curvature is felt downstream. This phenomenon was called *overdeepening*, it was numerically reproduced by Struiksmas *et al.* (1985) and later confirmed by Johannesson and Parker (1989).

The reader should note that the non-migrating spatially decaying bars associated with overdeepening represent the *free* contribution to the entrance flow and bed topography.

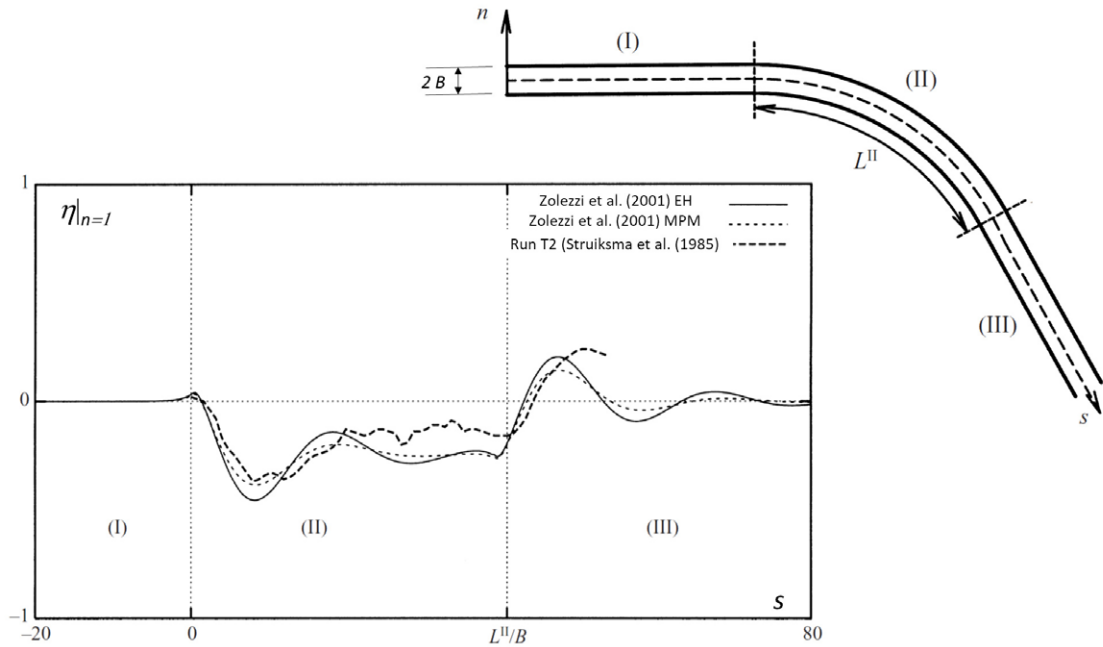


Figura 68. The dimensionless bed elevation at the outer bank in the experiment T2 of Struiksmas *et al.* (1985) shows the phenomenon of over-deepening. At the entrance region of a curved channel issuing from a straight reach, bottom topography adapts through a sequence of damped steady oscillations of transverse bed slope that represent an example of morphodynamic influence. Also shown are the predictions of Zolezzi and Seminara (2001) using two different closures for sediment transport, namely Meyer-Peter & Müller (MPM) and Engelund & Hansen (EH) (modified from Zolezzi and Seminara, 2001).

Yet, a natural question arises: are there any conditions such that the morphodynamics of meandering rivers is characterized by upstream influence? This is a reasonable question. Indeed we recall that in Section 6.4I we pointed out that spatially oscillatory free perturbations which decay fairly slowly are possible solutions of the homogeneous problem. Their influence is felt over a considerable channel length and grow exponentially in the linear regime downstream or upstream under sub- or super-resonant conditions, respectively. In other words, it is reasonable to expect that super-resonant channels may exhibit upstream influence. In the experimental configuration considered by Struiksmas *et al.* (1985), upstream influence would manifest itself through the formation of a periodic sequence of bars in the upstream straight reach.

The occurrence of upstream influence has an obvious implication. In order for the upstream reach to receive the *morphodynamic information* required to give rise to the bottom modifications, sufficiently long two-dimensional bed perturbations of the alternate bar type must be able to migrate upstream. And we know that this is an established property of super-resonant free bars (see Section 6.3.1I).

4.4.2 The exact solution of the linear problem of meander morphodynamics

The concepts outlined above can be mathematically framed seeking the exact solution of the linear problem of meander morphodynamics, i.e. the solution for flow and bed topography in a meandering channel with arbitrary, albeit mildly, curvature distribution. We then look for solutions of the depth averaged equations of the form:

$$(U, V, H, D) = (1, 0, H_0, 1) + \nu_0 (U_1, V_1, H_1, D_1) + \mathcal{O}(\nu_0^2) \quad (304)$$

Substituting from (304) into (273a, 273b, 273c, 275, 276, 277) and equating terms of order $\mathcal{O}(\nu_0)$, we obtain the following non-homogeneous, linear differential problem, describing the linear response of the flow field and of the bed configuration to the forcing induced by an arbitrary distribution of channel curvature:

$$\frac{\partial U_1}{\partial s} + \frac{\partial V_1}{\partial n} + \frac{\partial D_1}{\partial s} = 0, \quad (305a)$$

$$\left(\frac{\partial}{\partial s} + a_1\right)U_1 + \frac{\partial H_1}{\partial s} + a_2 D_1 = b_1 n \mathcal{C}(s), \quad (305b)$$

$$\left(\frac{\partial}{\partial s} + a_3\right)V_1 + \frac{\partial H_1}{\partial n} = b_2 \mathcal{C}(s), \quad (305c)$$

$$a_4 \frac{\partial U_1}{\partial s} + a_5 \frac{\partial D_1}{\partial s} + \frac{\partial V_1}{\partial n} - a_6 \frac{\partial^2 H_1}{\partial n^2} + a_6 \frac{\partial^2 D_1}{\partial n^2} = 0, \quad (305d)$$

satisfying the non-homogeneous boundary conditions

$$V_1 = 0 \quad (n = \pm 1), \quad (306a)$$

$$\frac{d(F_{ru}^2 H_1 - D_1)}{dn} = b_3 \mathcal{C}(s) \quad (n = \pm 1), \quad (306b)$$

where:

$$a_1 = 2\beta_u C_{fu}, \quad a_2 = (c_{fD} - 1)\beta_u C_{fu}, \quad a_3 = \beta_u C_{fu}, \quad (307a)$$

$$a_4 = 2Q_{sT}, \quad a_5 = Q_{sT} c_{fD}, \quad a_6 = R_{nu} \quad (307b)$$

$$b_1 = -\beta_u C_{fu}, \quad b_2 = 1, \quad b_3 = \frac{c_\chi}{R_{nu}}. \quad (307c)$$

The linear partial differential problem (305, 306, 307), governs the morphodynamics of weakly meandering wide rivers with constant width and arbitrary distribution of curvature of the channel axis. It was derived in a quite similar, but not identical form by Zolezzi and Seminara (2001). More precisely, for the sake of simplicity, in the present case we have assumed plane bed conditions, such that the friction coefficient depends only on the relative roughness, and the sediment flux on the Shields stress.

Moreover, we have ignored all the effects related to dispersive terms. As a result, forcing, i.e. non-homogeneous, terms in (305b) and (305c) arise from purely metric effects. The forcing term in (306b) drives a non-vanishing local lateral bed slope at the walls, required for gravity to balance the lateral bottom stress associated with secondary flow with zero depth average.

In order to allow for the role of the free component of the solution to emerge clearly, it is convenient to expand (U_1, V_1, H_1, D_1) in Fourier series in the lateral direction and remove the

effect of the non homogeneous terms of the boundary conditions by setting:

$$\begin{aligned}
 U_1(s, n) &= \sum_{m=0}^{\infty} u_m(s) \sin(M n) \\
 V_1(s, n) &= \sum_{m=0}^{\infty} v_m(s) \cos(M n) \\
 D_1(s, n) &= \bar{d}_1 \mathcal{C} n + \sum_{m=0}^{\infty} d_m(s) \sin(M n) \\
 H_1(s, n) &= \bar{h}_1 \mathcal{C} n + \sum_{m=0}^{\infty} h_m(s) \sin(M n)
 \end{aligned} \tag{308}$$

where $M = (2m + 1)\pi/2$ ($m = 0, 1, 2, \dots$). Note that the expansion (308) respects the symmetric character of V_1 and the antisymmetric character of U_1 , H_1 and D_1 . Moreover, we choose the quantities \bar{d}_1 and \bar{h}_1 such that the lateral momentum equation (305c) and the boundary conditions for (u_m, v_m, d_m, h_m) become homogeneous. We thus set:

$$\bar{h}_1 = b_2, \quad \bar{d}_1 = F_{ru}^2 b_2 - b_3. \tag{309}$$

Substituting from (308) and (309) into (305a), (305b), (305c) and (305d), and expanding n in Fourier series (see equation 298), one ends up with the following linear system of four first order ordinary differential equations:

$$\frac{du_m}{ds} - M v_m + \frac{dd_m}{ds} = -A_m \bar{d}_1 \frac{d\mathcal{C}}{ds}, \tag{310a}$$

$$\left(\frac{d}{ds} + a_1 \right) u_m + \frac{dh_m}{ds} + a_2 d_m = A_m \left[(b_1 - a_2 \bar{d}_1) \mathcal{C}(s) - \bar{h}_1 \frac{d\mathcal{C}}{ds} \right], \tag{310b}$$

$$\left(\frac{d}{ds} + a_3 \right) v_m + M h_m = 0, \tag{310c}$$

$$a_4 \frac{du_m}{ds} + a_5 \frac{dd_m}{ds} - M v_m + a_6 M^2 (F_{ru}^2 h_m - d_m) = -a_5 \bar{d}_1 A_m \frac{d\mathcal{C}}{ds}. \tag{310d}$$

A large amount of algebra allows one to reduce the above system to a single fourth order ordinary differential equation with constant coefficients for u_m , that may be expressed in the following form:

$$\left(\sigma_4 \frac{d^4}{ds^4} + \sigma_3 \frac{d^3}{ds^3} + \sigma_2 \frac{d^2}{ds^2} + \sigma_1 \frac{d}{ds} + \sigma_0 \right) u_m = -A_m \sum_{j=0}^6 \rho_{j+1} \frac{d^j \mathcal{C}}{ds^j} \tag{311}$$

where the m -th Fourier terms A_m are given by (298) while the coefficients σ_j ($j = 0 - 4$) and ρ_j ($j = 0 - 6$) are expressions involving the coefficients of the differential system.

Once u_m is known, the remaining unknowns v_m , h_m and d_m are obtained from the following relationships:

$$(v_m, d_m, h_m) = \sum_{j=0}^4 (v_{mj}, d_{mj}, h_{mj}) \frac{d^{j-1} u_m}{ds^{j-1}} + A_m \sum_{j=5}^9 (v_{mj}, d_{mj}, h_{mj}) \frac{d^{j-1} \mathcal{C}}{ds^{j-1}} \tag{312}$$

Note that the presence of the coefficient A_m ensures that the role of higher harmonics decays fairly rapidly, whilst the coefficients v_{mj} , d_{mj} , h_{mj} are again given by expressions in terms of the coefficients of the differential system and depend on the relevant dimensionless parameters

$(\beta_u, d_s, \tau_{*u})$. The above coefficients, as well as the coefficients σ_j and ρ_j , will be provided to the interested reader on request to the Authors.

In the case of a periodic sequence of sine generated meanders, equation (311) reduces to the periodic forced equation (293a) which admits of the solution (295).

For channels with arbitrary curvature distributions, the general solution is obtained as the sum of the homogeneous solution and of a particular solution of the full non homogeneous ordinary differential equation (311). Hence, the general solution for $u_m(s)$ may be written in the form:

$$u_m(s) = u_m^h(s) + u_m^p(s). \quad (313)$$

The homogeneous solution has the usual form

$$u_m^h(s) = \sum_{j=1}^4 c_{mj} e^{\lambda_{mj} s} \quad (314)$$

where λ_{mj} ($j = 1, 4$) are the characteristic exponents of the homogeneous differential equation and c_{mj} are integration constants to be determined imposing the boundary conditions at the channel ends. It is of great relevance to note that the characteristic exponents λ_{mj} ($j = 1, 4$) coincide with the complex wavenumbers that define the spatial bar modes discussed in Section 6.4.1I. This implies that a suitable mix of spatial bars is needed in order for the river morphodynamics forced by channel curvature to adapt to the conditions assigned at the end sections of the river reach under investigation.

Let us recall the main properties of the above characteristic exponents which emerge from Figure 96(I):

- one of the exponents is invariably real and positive, one is real and negative, the last two are complex conjugates;
- the real part of the complex exponents is negative, provided the dimensionless parameter β_u does not exceed a threshold value that, for the first mode ($m = 1$) coincides with the resonant value β_R ;
- for higher order modes ($m > 1$), the following relationships hold:

$$\beta_R^m = m \beta_R, \quad \lambda_{mj}(\beta_u; \tau_{*u}, d_s) = m \lambda_{1j}\left(\frac{\beta_u}{m}; \tau_{*u}, d_s\right). \quad (315)$$

Hence, for sub resonant modes ($\beta_u < \beta_R^m$) the complex exponents describe spatial bars whose amplitudes decay exponentially downstream; viceversa, for super-resonant modes ($\beta_u > \beta_R^m$) the bar amplitudes decay exponentially upstream.

To clarify the effect of the above findings, we first consider the case of a meandering reach connected both upstream and downstream to infinitely long straight reaches (Figure 69). Under these conditions, the perturbations driven by channel curvature progressively vanish in both the upstream and downstream straight reaches such that the homogeneous solution is not needed to adapt to the end conditions, i.e. the integration constants c_{mj} vanish identically. For this configuration, the solution for the amplitude $u_m(s)$ of the m -th mode reduces to the particular solution $u_m^p(s)$, which accounts for the forcing effect associated with channel curvature. A classical approach to derive $u_m^p(s)$ is the so called *method of variation of parameters* (see e.g. Coddington and Levinson, 1955, p. 75). Here, we only report the structure of $u_m^p(s)$ and its physical interpretation, referring to Zolezzi and Seminara (2001) for details.

For all sub-resonant modes, i.e. for values of m such that $\beta_u < \beta_R^m$ the solution for $u_m^p(s)$ has the

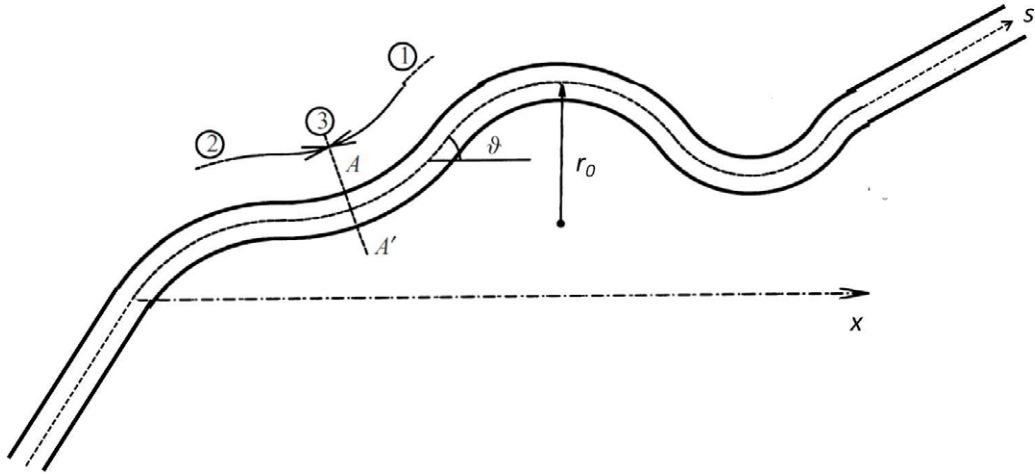


Figura 69. Sketch of a meandering reach, connected both upstream and downstream to infinitely long straight reaches, with indication of the regions of morphodynamic influence.

following structure:

$$\begin{aligned}
 u_m^p = & \underbrace{A_m u_{m1} \int_s^\infty \exp[-\lambda_{m1}(t-s)] \mathcal{C}(t) dt}_{\text{upstream influence}} \\
 & + \underbrace{A_m \sum_{j=2}^4 u_{mj} \int_{-\infty}^s \exp[\lambda_{mj}(s-t)] \mathcal{C}(t) dt}_{\text{downstream influence}} \\
 & + \underbrace{A_m \sum_{j=5}^8 u_{mj} \frac{d^{(j-5)} \mathcal{C}}{ds^{(j-5)}}}_{\text{local effect of curvature}} \quad (316)
 \end{aligned}$$

where the coefficients u_{mj} ($j = 1, 8$) are functions of the relevant dimensionless parameters. The upstream distribution of channel curvature is felt downstream through the three convolution integrals corresponding to $j = 2, 3, 4$. As λ_{m2} is a real order-one number, its influence decays along a distance of the order of few channel widths. On the contrary, λ_{m3} and λ_{m4} are complex conjugate and their influence decays over a much greater distance as their damping rates ($Re(\lambda_{m3})$ and $Re(\lambda_{m4})$, respectively) are an order of magnitude smaller than λ_{m2} (at least for the lower modes). Moreover, they display spatial (*bar-type*) oscillations with frequencies $Im(\lambda_{m3})$ and $Im(\lambda_{m4})$, respectively. The downstream distribution of channel curvature is only weakly felt upstream through the first convolution integral ($j = 1$), which decays fast upstream (as λ_{m1} is an order-one real number). Finally, the local value of curvature and its local derivatives have a direct effect on the particular solution through the last term of (316).

For any super-resonant mode, i.e. provided that the aspect ratio β_u exceeds the resonant value

β_R^m associated with some mode m , the particular solution takes the form:

$$\begin{aligned}
 u_m^p = & \underbrace{A_m \sum_{j=1,3,4} u_{mj} \int_s^\infty \exp[-\lambda_{mj}(t-s)] \mathcal{C}(t) dt}_{\text{upstream influence}} \\
 & + \underbrace{A_m u_{m2} \int_{-\infty}^s \exp[\lambda_{m2}(s-t)] \mathcal{C}(t) dt}_{\text{downstream influence}} \\
 & + \underbrace{A_m \sum_{j=5}^8 u_{mj} \frac{d^{(j-5)} \mathcal{C}}{ds^{(j-5)}}}_{\text{local effect of curvature}}. \tag{317}
 \end{aligned}$$

Here, the upstream distribution of channel curvature is felt downstream only through the second convolution integral (corresponding to $j = 2$). This downstream influence is restricted to a short reach upstream of the examined cross section, as λ_{m2} is an $\mathcal{O}(1)$ real number. The downstream distribution of channel curvature is now felt upstream through the three convolution integrals corresponding to $j = 1, 3, 4$. The first ($j = 1$) decays fast downstream ($\lambda_{m1} = \mathcal{O}(1)$ real number), hence its effect is felt within a short reach. The other two ($j = 3, 4$) decay slowly and display spatial oscillations (as $\lambda_{m3}, \lambda_{m4}$ are complex conjugate with fairly small real parts). Finally, the local value of curvature and its local derivatives have again a direct effect on the particular solution through the last term of (317). Of course, once the solution for u_m is known, the remaining dependent variables are readily obtained from (312).

The above solution has been derived including only contributions that keep bounded within the flow domain. In other words, exponentially growing contributions have been discarded as, in the present linear context, they would be unbounded at infinity. This is an obvious limitation of the linear approach as it does not account for the possibility that exponentially growing perturbations may evolve in the nonlinear regime such to reach a finite equilibrium amplitude. The issue of whether, in a nonlinear context, growing and decaying perturbations may coexist can ultimately be resolved by means of a fully nonlinear analysis. We leave this problem aside for the time being as the linear theory is sufficient to disclose the existence of the phenomenon of upstream influence which is our present concern.

The picture arising from the above solution may be simply summarized by stating that the morphodynamic influence concerning sub-resonant modes is dominantly felt downstream. In other words, the channel curvature at a given cross section affects the amplitude and phase of sub-resonant modes in the river reach located downstream of that cross section. On the contrary, the channel curvature at a given cross section affects the amplitude and phase of super-resonant modes in the river reach located upstream of that cross section.

In the case of a meandering reach of finite length L (Figure 70), the above solution must be completed by adding homogeneous terms. These terms allow to fit the conditions imposed at the initial cross section ($s = s_0$) and the final cross section ($s = s_0 + L$), respectively (Figure 70). They read:

$$u_m^h = \underbrace{c_{m1} \exp[-\lambda_{m1}(s_0 + L - s)]}_{\text{upstr. effect of downstr. BC}} + \underbrace{\sum_{j=2}^4 c_{mj} \exp[\lambda_{mj}(s - s_0)]}_{\text{downstr. effect of upstr. BC}}, \tag{318}$$

for sub-resonant modes and

$$u_m^h = \underbrace{\sum_{j=1,3,4} c_{mj} \exp[-\lambda_{mj}(s_0 + L - s)]}_{\text{upstr. effect of downstr. BC}} + \underbrace{c_{m2} \exp[\lambda_{m2}(s - s_0)]}_{\text{downstr. effect of upstr. BC}}, \tag{319}$$

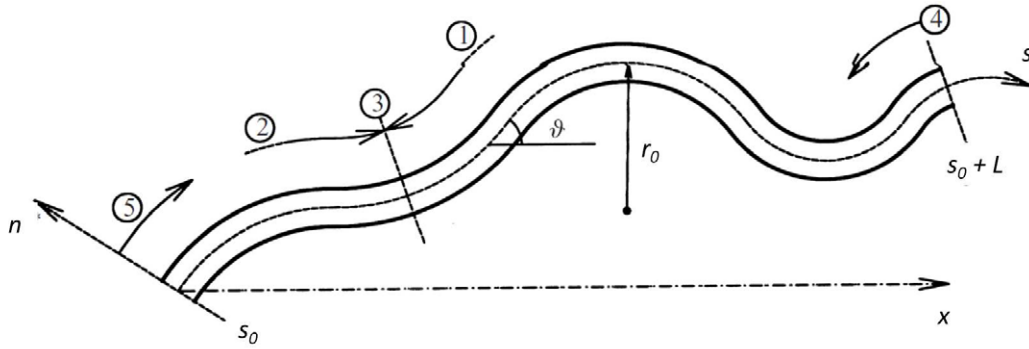


Figura 70. Sketch of a meandering reach of finite length L with indication of the regions of morphodynamic influence.

for super-resonant modes.

4.4.3 Testing linear predictions in the sub-resonant case: downstream influence

Zolezzi and Seminara (2001) employed the exact solution derived in the previous Section to ascertain its ability to predict the over-deepening phenomenon outlined in Section 4.4.1. They examined the configuration depicted in Figure 68, namely a constant curvature channel reach (II) connected to indefinitely long straight reaches located upstream (I) and downstream (III).

As the curvature of channel axis exhibits discontinuities in the two cross sections located at $s = 0$ and $s = s_L$, the solution must be obtained for the three reaches separately imposing matching at the latter cross sections. We also note that the experiments of Struiksmas *et al.* (1985) considered only sub-resonant configurations for any mode. Hence, imposing that perturbations of the flow and bottom topography keep finite as $s \rightarrow \pm\infty$, the solution for u_m in the three regions takes the form:

Region I

$$u_m = c_{m1}^I \exp(\lambda_{m1} s), \quad (320)$$

Region II

$$u_m = c_{m1}^{II} \exp \left[\lambda_{m1} \left(s - \frac{L_{II}}{B} \right) \right] + \sum_{j=2}^4 c_{mj}^{II} \exp(\lambda_{mj} s) + A_m u_{m5} C \quad (321)$$

Region III

$$u_m = \sum_{j=2}^4 c_{mj}^{III} \exp \left[\lambda_{mj} \left(s - \frac{L_{II}}{B} \right) \right], \quad (322)$$

where, for each free mode m , in the infinitely long straight reaches located upstream and downstream of the constant curvature bend we have included only the contributions that decay exponentially at infinity. Of course, once the solution for u_m is known, the remaining dependent variables are readily obtained from (312). Note that eight unknown constants arise, namely c_{m1}^I , c_{mj}^{II} ($j = 1, 4$) and c_{mj}^{III} ($j = 2, 3, 4$). They are readily determined imposing matching of the solutions for u_m , v_m , h_m and d_m in regions I and II at $s = 0$, and in regions II and III at $s = s_L$.

Comparison with the experimental observations of Struiksmas *et al.* (1985) was pursued by Zolezzi and Seminara (2001) by retaining the first five modes in the expansion and good agreement

was found as demonstrated by Figure 68. Comparison is fairly satisfactory both for the wavelength and the amplitude of bed deformations. Downstream overdeepening does indeed occur at the entrance of both the curved reach (II) and of the straight reach (III), induced by the discontinuities in channel curvature. It is also fair to note that the linear model appears to work sufficiently well. This is due to the fact that the dimensionless parameter controlling the amplitude of bed deformations, discussed in Section 3.2.1, keeps sufficiently small in all experiments of Struiksmā *et al.* (1985).

4.4.4 Testing linear predictions in the super-resonant case: upstream influence

Zolezzi and Seminara (2001) examined theoretically the occurrence of upstream over-deepening applying the super-resonant solution to a very simple channel configuration. Again with reference to Figure 68, they considered a straight reach (I) and a curved reach (II) long enough for the effect of the upstream and downstream ends not to be felt in the region of interest. This allowed to isolate the upstream influence effect due to a discontinuity in channel curvature. The aspect ratio of the channel exceeded its resonant value for the first mode only. Under these conditions, in reach (I), the response of the system is characterized by three oscillating and exponentially growing free modes, whereas the solution in reach (II) was obtained by adding the solution forced by curvature to the free response consisting of an exponentially damped free mode only. Hence, the solution for the first mode ($m = 1$) reads:

Region I

$$u_1 = \sum_{j=1,3,4} c_{1j}^I \exp \lambda_{1j} s, \quad (323)$$

Region II

$$u_1 = c_{12}^{II} \exp \lambda_{12} s + A_1 u_{15} \mathcal{C}, \quad (324)$$

whilst solutions for higher modes ($m > 1$) are of the form:

Region I

$$u_m = c_{m1}^I \exp \lambda_{m1} s, \quad (325)$$

Region II

$$u_m = \sum_{j=2}^4 c_{mj}^{II} \exp \lambda_{mj} s + A_m u_{m5} \mathcal{C}, \quad (326)$$

Figure 71 shows the bed profile predicted by the linear solution close to the left bank of the channel, i.e., at the outer bank of the bend. Notice that finite bed deformations reach a distance of various tens channel widths in the upstream straight reach, whilst no overdeepening is experienced in the curved reach.

In order to substantiate the above findings Zolezzi *et al.* (2005) performed a detailed experimental work on a 180° constant curvature bend, connected upstream and downstream with straight channel reaches. As discussed below, the main conclusion of linear theory, namely the occurrence of downstream and upstream over-deepening under sub- and super-resonant conditions was confirmed by these experiments. However, the picture arising from experimental observations was somewhat more complicated than linear theory suggests. This was due to two main reasons.

Firstly, in each run free migrating alternate bars were observed to coexist with the steady point bars forced by curvature, as well as with the steady spatially oscillating bars associated

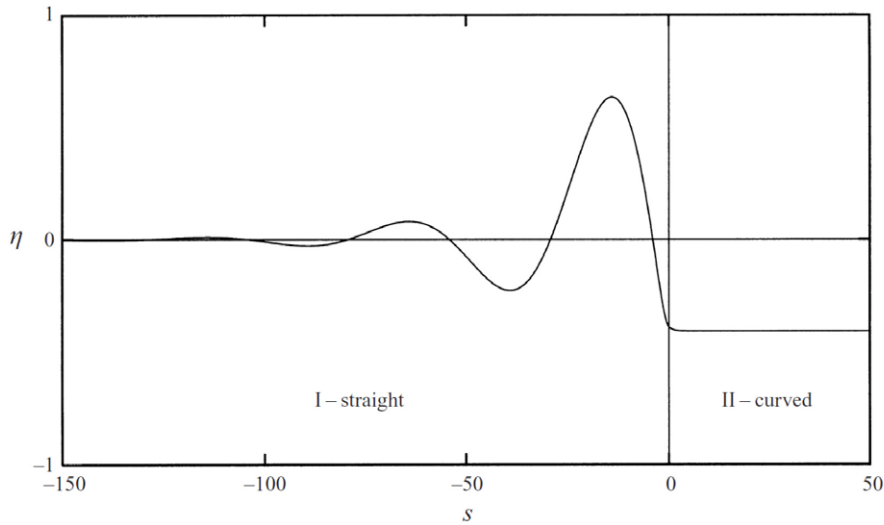


Figure 71. The over-deepening phenomenon occurring upstream of a 180° constant curvature reach under super-resonant conditions according to linear predictions are obtained for $\tau_{*u} = 0.1$, $d_s = 0.01$, $\beta_R = 16.5$, $\beta = 30$. Flow direction is left to right. The bed elevation η is computed at the left bank of the channel ($n = 1$).

with downstream or upstream overdeepening. This was not surprising as we have known since the early work of Kinoshita (1961) and Kinoshita and Miwa (1974) that free migrating bars may coexist with forced (stationary) bars driven by curvature in river meanders. In particular, it was conclusively shown by Kinoshita and Miwa (1974) that a single bend is unable to suppress the migration of free bars. The mechanism underlying free bar suppression was investigated by Tubino and Seminara (1990) and will be discussed in the next Section.

The second reason is a consequence of an intrinsic limit of the linear theory. Indeed, within a linear context, exponentially growing modes must be discarded as they become unbounded at infinity, whereas in a nonlinear context perturbations may evolve from a linear exponential growth into a finite amplitude regime reaching asymptotically an equilibrium amplitude, as clarified by Seminara and Tubino (1992).

For both the above reasons, the pattern observed by Zolezzi *et al.* (2005) was much richer than linear predictions suggest. In order to analyze the structure of the bottom perturbation, Zolezzi *et al.* (2005) extracted the steady component of the signal using a filtering procedure whereby the contribution of migrating bars to bed elevation was removed. In other words, the steady bed topography was obtained along the whole flume by time averaging the bed elevation at any location. As the time data set included more than one period of migrating bars, the averaging procedure was performed either over single or multiple periods, leading to almost identical results. This was taken as a proof that the experiments had reached an average equilibrium configuration. Figure 72 shows the outcome of the filtering procedure for run U2, one of the three super-resonant configurations tested in the experiment.

The theory of Zolezzi and Seminara (2001) predicts that upstream influence takes place only under super-resonant conditions. This has invariably been confirmed by the observations of Zolezzi *et al.* (2005). Indeed, steady bed deformations were detected in the upstream straight reach only in the three super-resonant runs (U1, U2 and U3). On the contrary, in both the sub-resonant runs (D1 and D2) no significant steady bed deformation was detected in the same reach. An example of the above findings is reported in Figure 73.

Moreover, direct inspection of Figures 72 and 73 suggests that over-deepening was associated with an alternate bar configuration. This is consistent with the theory of Zolezzi and Seminara (2001), which states that upstream over-deepening is associated with super-resonant modes. And, indeed, the experimental conditions of runs U1, U2 and U3, were such that only the first (alternate

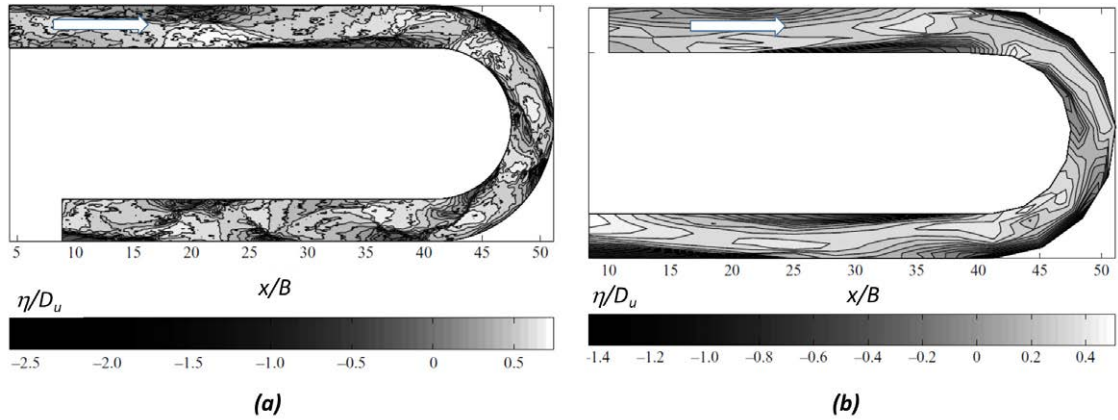


Figure 72. (a) Instantaneous bed topography measured at the end of run U2 ($\tau_{*u} = 0.1$, $d_s = 0.067$, $\beta_R = 11.7$, $\beta = 20$) by Zolezzi *et al.* (2005); (b) steady component of bed topography obtained filtering the instantaneous signal. Run U2 was super-resonant and indeed upstream overdeepening was observed (modified from Zolezzi *et al.*, 2005).

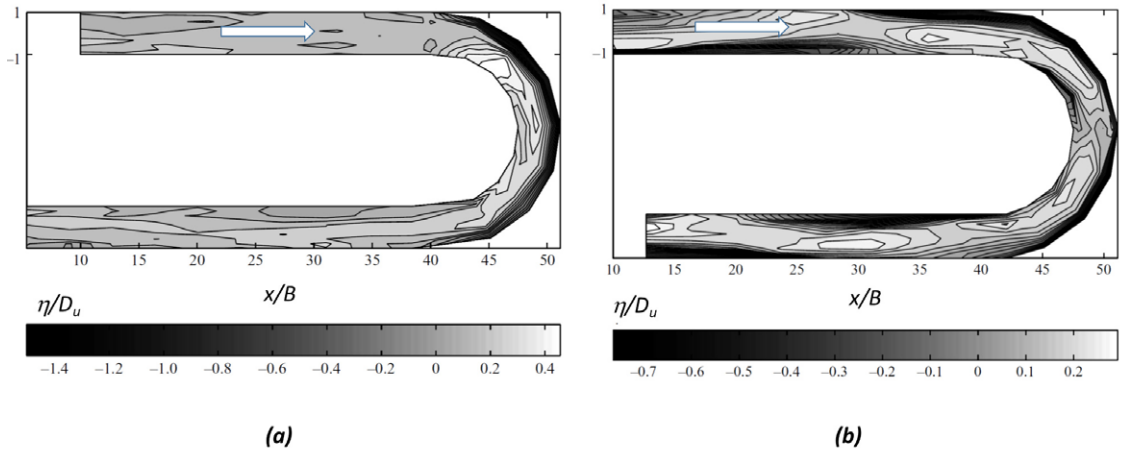


Figure 73. Experimental observations of over-deepening carried out by Zolezzi *et al.* (2005). (a) Sub-resonant run D2 ($\tau_{*u} = 0.133$, $d_s = 0.05$, $\beta_R = 22.1$, $\beta = 8.6$): over-deepening occurs only downstream; (b) super-resonant run U3 ($\tau_{*u} = 0.1$, $d_s = 0.01$, $\beta_R = 14.6$, $\beta = 15$): over-deepening occurs both upstream and downstream (modified from Zolezzi *et al.*, 2005).

bar) mode ($m = 1$) was super-resonant.

These observations are confirmed by the two-dimensional Fourier analysis of the steady bed deformation. Figure 74 refers to the steady bottom pattern occurred in the upstream reach in run U2 and D2. For super-resonant conditions (Figure 74a) the bed shape arises essentially from the contribution of two largely dominant harmonics, the 11 and the 02, where the ij Fourier component corresponds to the i -th longitudinal mode and the j -th transverse mode. Thus harmonic 11 represents an alternate sequence of riffles and pools, while the 02 pattern is a longitudinally uniform central deposit (or scour). The latter is triggered by migrating alternate bars through nonlinear effects, as shown in Colombini *et al.* (1987). On the other hand, the same Fourier analysis carried out in the same reach for the sub-resonant runs confirms the absence of significant steady bed deformation under sub-resonant conditions in accordance with equation (316).

Although the results obtained by Zolezzi *et al.* (2005) do confirm the general picture of morphodynamic influence suggested by Zolezzi and Seminara (2001), however differences arise in the way over-deepening occurs in the curved and downstream straight reaches. As shown in

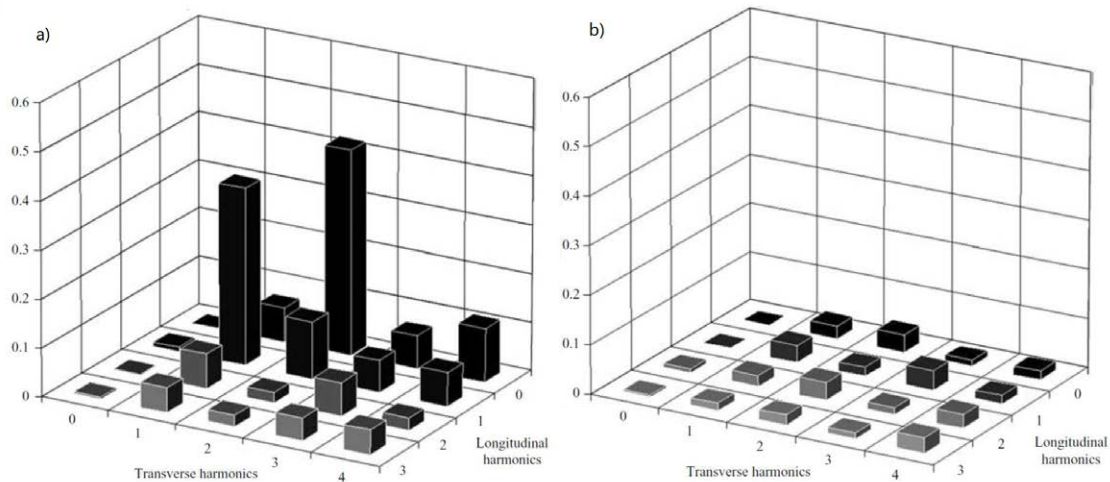


Figure 74. Two-dimensional Fourier analysis of the steady bed deformation observed in the upstream straight reach of flume experiments (a) U2 and (b) D2 carried out by Zolezzi *et al.* (2005). Under super-resonant conditions of run U2 bed deformation originated from the contribution of two largely dominant harmonics, the 11 and the 02. On the contrary, in the sub-resonant run D2 no significant steady bed deformation was observed in the upstream straight reach (modified from Zolezzi *et al.*, 2005).

Figure 73, under sub-resonant conditions over-deepening occurs only in the curved and downstream straight reaches, in agreement with linear theory and experimental observations of Struiksma *et al.* (1985). Similarly, a significant steady bottom deformation is detected in the straight downstream reach, under super-resonant conditions (for the first mode). This is also in general agreement with the theory of Zolezzi and Seminara (2001) but with a major difference. The linear theory predicts that in the downstream straight reach only sub-resonant transverse modes, i.e. modes higher than the first for the conditions of runs U1, U2 and U3, should be present. On the contrary, a spectral analysis similar to that shown in Figure 74 showed the presence of a contribution of the first mode 11 with amplitude comparable to those associated with higher transverse modes. As already pointed out, this feature cannot be predicted in a linear context, where the exponentially growing first mode in the downstream reach would not keep bounded at infinity. Similar arguments explain also the presence of the first mode in the bottom pattern of the curved reach under sub-resonant conditions. A fully nonlinear numerical solution is then called for in order to provide a complete reproduction of the experimentally observed patterns.

4.4.5 Morphodynamic regime in the field

The obvious question that one would like to answer at this stage is: to what extent does the theoretical framework built in this Chapter apply to field conditions? A significant contribution to the analysis of this important problem was made by Luchi (2009) (but see also Zolezzi *et al.*, 2009).

These Authors analyzed the morphodynamic regime of a set of 134 alluvial gravel bed rivers belonging to the relatively wide and tested data set from different geographical locations employed by Parker *et al.* (2007). Field data were used as input conditions to be fed into the morphodynamic model of Zolezzi and Seminara (2001) that assumes *dominant bed load* and requires the knowledge of reach-averaged representative values of flow discharge, channel width, water depth, down-channel slope and mean sediment size. Bankfull conditions were assumed to be appropriate to characterize the medium-long term morphodynamics. Two main subsets were employed; the North American (NA) subset and the United Kingdom (UK) subset. The complete solution for the flow and bed topography was then used to predict the resonant conditions for each of the 134 gravel bed river reaches. The outcome of the analysis is reported in Figure 75, which shows that, in most cases (96

reaches, i.e. 71% of the total), super-resonant conditions were found, while only 25 reaches (19%) turned out to be sub-resonant and 13 reaches (10%) could be defined as near resonant (Figure 75a). The plot of Figure 75b shows a comparison between the resonant value of $\beta_R(\tau_*)$ and the value

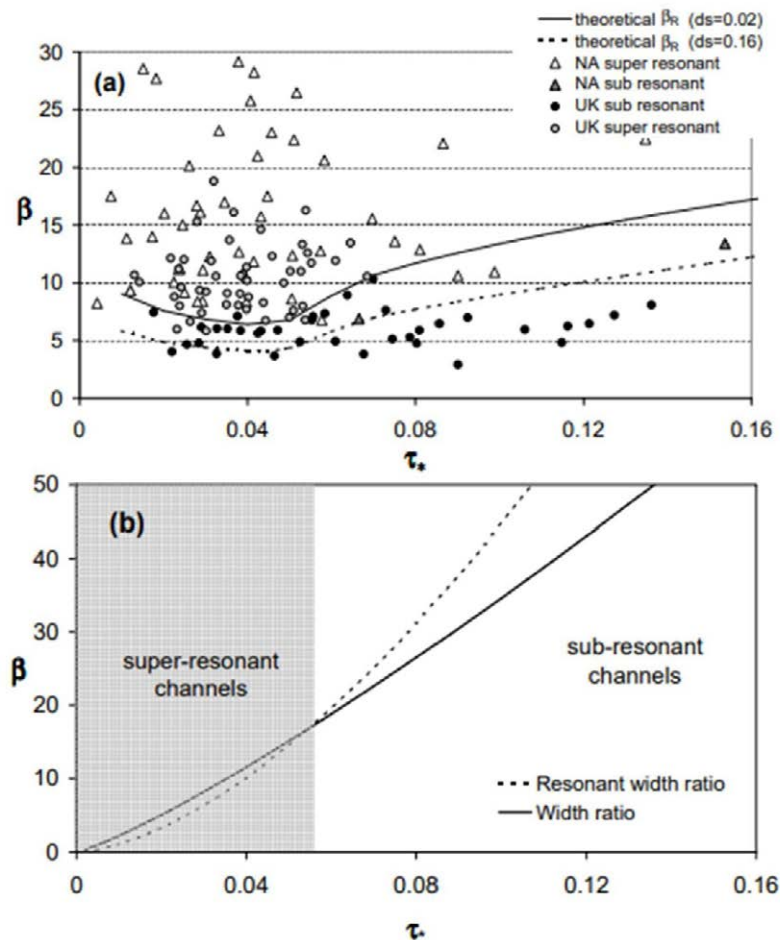


Figure 75. (a) Morphodynamic regime of the gravel bed river reaches belonging to the set analyzed by Luchi (2009). The sub- super-resonant regime is defined in the $\beta - \tau_*$ plane. Triangles correspond to North American (NA) rivers, circles to United Kingdom (UK) streams. (b) Comparison between the resonant value of $\beta_R(\tau_*)$ and the value of the aspect ratio $\beta(\tau_*)$ predicted by the quasi-universal bankfull geometry regime relationship proposed by Parker *et al.* (2007) (reproduced from Figure 4.2 of Luchi, 2009).

of the aspect ratio $\beta(\tau_*)$ predicted by the quasi-universal bankfull geometry regime relationship proposed by Parker *et al.* (2007). This comparison is quite instructive. Gravel bed rivers are quasi-universally super-resonant at low Shields stresses, and sub-resonant in the higher τ_* range (with dominant bed load). A rule of thumb was then proposed by Luchi (2009) to estimate the threshold value of β for which the transition sub-super resonant is expected to occur. Reaches with $\beta < 7.5$ are likely to be sub-resonant, wider and shallower gravel bed streams are likely super-resonant.

The latter work has filled a gap in our attempt to construct a rational framework to the morphodynamics of meandering rivers. An extension of this contribution to the case of sand bed rivers would be extremely useful to complete the picture.

4.5. Free bar suppression in meandering channels

4.5.1 Experimental and field observations

In the late 1950s, a systematic investigation on the morphodynamics of the Ishikari River was commissioned to a Japanese geomorphologist, R. Kinoshita, by the Natural Resources Division of the Ministry of Science and Technology of Japan. This investigation exploited aerial surveys as well as earlier photos taken by reconnaissance flights performed during the second world war. The output was a monumental report (Kinoshita, 1961), rich of interesting observations and seminal ideas parallel to the innovative ideas that were emerging from the independent work of the great American geomorphologist Luna Leopold and his coworkers. Among the cute observations contained in that report, was the recognition of the distinction between free migrating bars and forced stationary bars associated with curvature in meandering rivers and the identification of some measure of channel sinuosity as the appropriate parameter to define the threshold between two distinct regimes. For sufficiently small sinuosities free bars coexisted with forced bars and were able to migrate through meandering channels. Exceeding some threshold value of sinuosity, free bars were suppressed and only forced bars were observed. In Figure 76 we report the original plot of Kinoshita (1961). The measure of channel sinuosity adopted by Kinoshita (1961) was the angle θ between straight segments tangent to the channel axis at two consecutive inflection points. This figure suggests that the threshold value of θ marking the transition between the two regimes is about 25° for weak river slopes, and decreases as the slope increases.

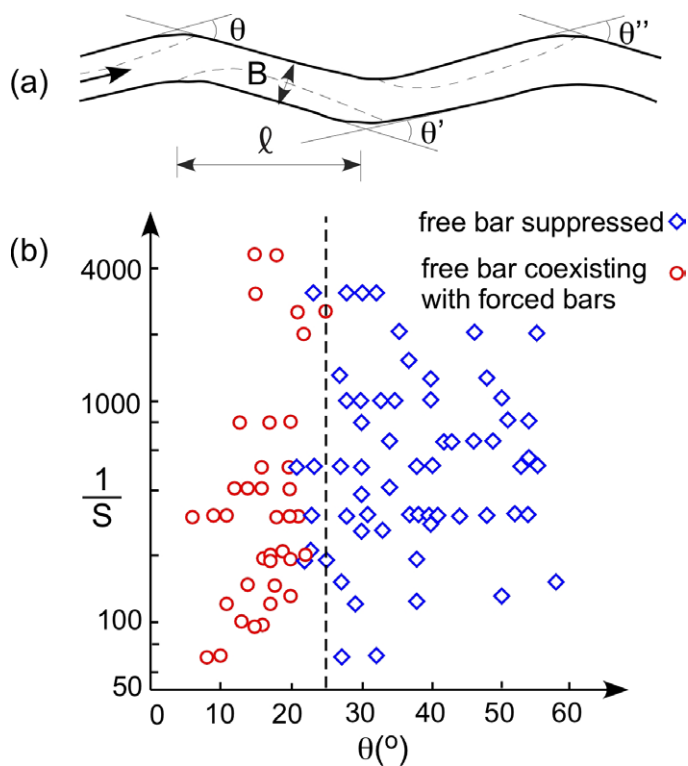


Figura 76. The plots of Kinoshita (1961), showing results of field observations in the Ishikari River. The vertical coordinate is the inverse of the river slope. The abscissa is the angle θ formed by the straight segments tangent to the channel axis at two consecutive inflection points, as shown in the upper sketch. Circles denote meandering reaches where free bars coexisted with forced bars. Diamonds denote meandering reaches where free bars were suppressed (redrawn from Kinoshita, 1961).

The above field observations were experimentally tested in the later work of Kinoshita and Miwa

(1974), hereinafter referred to as KM, who wrote an interesting paper published in Japanese, which remained unknown to the western scientific community until Professor Parker kindly provided a copy of his English translation of it. The paper described the experiments carried out in an apparatus consisting of a meandering channel formed “*from straight segments at an angle α to each other*”. Preliminary runs on a straight channel with identical flow and sediment characteristics provided the length of free bars forming in the absence of channel curvature. The wavelength of the meandering channel (2ℓ in figure 77a reproduced from Kinoshita and Miwa, 1974) was chosen to be either equal to, or a fraction of, the wavelength of free bars.

Results of the meander runs (Figure 77b) confirmed the existence of two distinct morphodynamic regimes:

- for $\theta < \theta_c$, a train of free bars formed and migrated even after reaching an apparently *naturally stable* state where they were perfectly in phase with steady forced bars;
- for $\theta > \theta_c$ free bars ceased migration, i.e. temporal bed oscillations disappeared at any given cross section.

Moreover, the threshold value θ_c was found to vary in the range $20^\circ - 40^\circ$, depending on the wavelength of the meandering channel. KM's results suggest that it is the interaction between

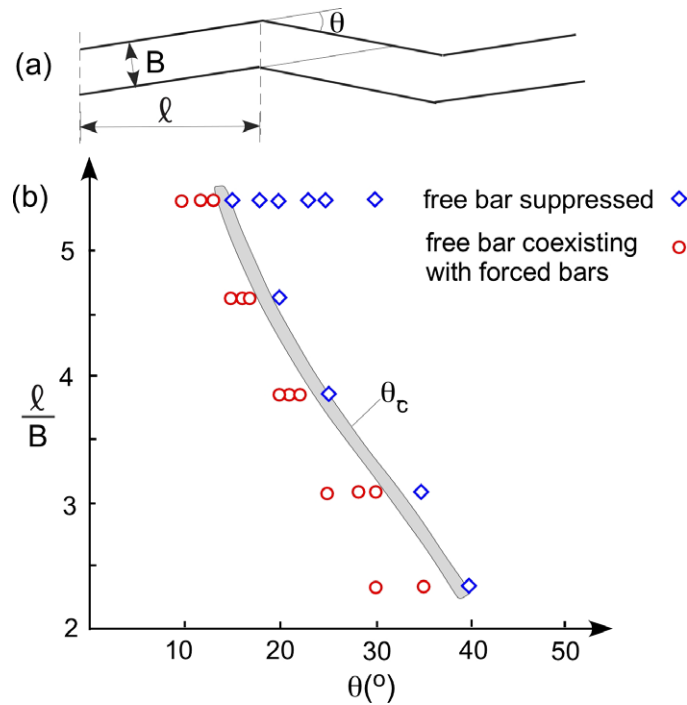


Figure 77. The plot of Kinoshita and Miwa (1974), showing results of laboratory observations on a schematic meandering channel formed by straight segments at an angle θ to each other. The meandering wavelength 2ℓ was chosen to be either equal to, or a fraction of, the wavelength of free bars formed in preliminary runs on straight channels under similar conditions. Circles denote runs where free bars coexisted with forced bars. Diamonds denote runs where free bars were suppressed (redrawn from Kinoshita and Miwa, 1974).

migrating free and steady forced bars which is likely responsible for the suppression of the former perturbations. It is reasonable to infer that, for suppression to occur, the amplitude of forced bars, which increases with channel curvature, i.e. with θ , must exceed a threshold value dependent on meander wavelength.

4.5.2 Theoretical interpretation of the suppression mechanism

A successful attempt to provide a theoretical interpretation of the above observations was made by Tubino and Seminara (1990) (but see also Seminara and Tubino (1989)). The analysis, based on a perturbation approach, is conceptually straightforward but formally complicated. In order to help mathematically inclined readers to fully appreciate this analysis, we have provided in Section 8.2 of the Mathematical Appendix an application of the same ideas to a simplified model as a preliminary step to the full treatment contained in Tubino and Seminara (1990). Here, we limit ourselves to outlining the main ideas of the mathematical approach and its physical meaning.

Let us consider a meandering channel characterized by the usual sine-generated curvature distribution. Let λ_m and β_u denote the meander wavenumber and the aspect ratio under uniform conditions, respectively. Moreover, let us set ourselves within a neighborhood of the critical conditions for the onset of free migrating bars by assuming that:

$$\beta_u = \beta_c + \epsilon^2 b, \quad \lambda = \lambda_c, \quad \omega = \omega_c \quad (327)$$

Here, ϵ denotes a small parameter, and b is the dummy parameter introduced in Chapter 6I (see equation 528(I)) that allows to consider either supercritical ($b = 1$) or sub-critical ($b = -1$) conditions; λ_c is the wavenumber of free bars at critical conditions and ω_c the corresponding angular frequency.

Under supercritical conditions and *in the absence of curvature*, we expect to observe the development of free migrating perturbations, say of bed elevation η^f , of the form:

$$\eta^f = \epsilon A(\tau) \sin(M n) E_1 + c.c. \quad (328)$$

where, using notations as in Chapter 6I,

$$E_1 = \exp[i(\lambda_c s - \omega_c t)]. \quad (329)$$

The above perturbations consist of harmonic waves with longitudinal wavenumber λ_c and lateral mode m such that $M = \pi/2 m$. They propagate in the s -direction with migration speed ω_c/λ_c and amplitude proportional to the square root of the distance ($\beta_u - \beta_c$) of the control parameter β_u from its critical value. These waves grow *slowly* in time, i.e. they amplify on the slow time scale ($\tau = \epsilon^2 t$). Linearly, the growth is exponential, whilst, reaching the finite amplitude regime, growth is progressively damped until the free bar reaches an equilibrium amplitude satisfying the solution of a Landau-Stuart amplitude equation (eq. 534(I)).

On the other hand, in the presence of curvature and *in the absence of free bars*, we expect to observe the development of forced stationary perturbations of bed elevation η^m , of the form:

$$\eta^m = \nu_0 \eta_1(n) e_1 + c.c. \quad (330)$$

where

$$e_1 = \exp(i \lambda_m s), \quad (331)$$

as in Section 4.3.1. These perturbations then consist of stationary waves with longitudinal wavenumber λ_m and complex amplitude proportional to the curvature ratio ν_0 , assumed to be sufficiently small.

The problem we wish to solve is: does the presence of spatially forced modes prevent the development of free temporal modes? Are there any threshold conditions in the space of the relevant physical parameters separating regions where coexistence is possible from regions where free modes are suppressed?

In order to answer these subtle questions, one needs to follow the cascade of interactions arising when the $\mathcal{O}(\epsilon)$ free temporal mode coexists with the $\mathcal{O}(\nu_0)$ forced spatial mode. The word interaction, in a weakly nonlinear context, is simply equivalent to seeking the consequences of taking products of free modes with themselves, forced modes with themselves and free modes with forced modes. Then, one immediately recognizes that, at second order one finds:

- the $\mathcal{O}(\epsilon^2)$ free-free interactions already analyzed in Chapter 6I when dealing with the weakly nonlinear stability theory (Section 6.5.1I);

- the $\mathcal{O}(\nu_0^2)$ forced-forced interactions already analyzed in the present Chapter when dealing with the weakly nonlinear forced response (Section 4.3.2).
- additional second order $\mathcal{O}(\nu_0 \epsilon)$ mixed terms which account for the interactions between free and forced modes, proportional to $E_1 e_1 = \exp[i(\lambda_c + \lambda_m)s - \omega t]$, $E_1 \bar{e}_1$ and their complex conjugates.

At third order, we are interested only in interactions that reproduce the fundamental free mode, as those interactions determine the fate of the temporal evolution of free bars. It is readily seen that the free mode is reproduced by three types of interactions: free $\mathcal{O}(\epsilon)$ -free $\mathcal{O}(\epsilon^2)$, free $\mathcal{O}(\epsilon)$ -forced $\mathcal{O}(\nu_0^2)$ and mixed $\mathcal{O}(\nu_0 \epsilon)$ -forced $\mathcal{O}(\nu_0)$. These three contributions occur at the same order of approximation provided one sets:

$$\nu_0 = k_r \epsilon, \quad (332)$$

with k_r a real $\mathcal{O}(1)$ quantity.

Hence, we may expect that, provided the forcing parameter ν_0 is of the order of ϵ , i.e. the amplitudes of the fundamental free and forced modes are of the same order of magnitude, then the free-forced interaction is significant and may alter the usual picture of weakly nonlinear free modes amplifying and reaching an equilibrium amplitude asymptotically in time.

The above intuitive arguments can be formalized seeking a solution of the governing equations in the form of a composite expansion in terms of the two parameters ν_0 and ϵ subject to the condition (332), including free, forced and mixed interactions. The approach is described in detail by Tubino and Seminara (1990). The outcome of the analysis is a modified amplitude equation obtained, as usual, imposing that secular terms generated at third order must vanish. One finds:

$$\frac{dA}{d\tau} = [b\beta_c(\mu_\beta + i\nu_\beta) + k_r^2\alpha_{11}]A + [a_r + ia_i]A^2\bar{A}. \quad (333)$$

where coefficients μ_β , ν_β , a_r and a_i are identical with those found for free bars (recall equation 534(I)) and α_{11} is a new complex coefficient. Each of the above coefficients is a function of the unperturbed Shields stress τ_{*u} and of the dimensionless grain size d_s . The coefficient α_{11} is also a function of the meander wavenumber λ_m .

Equation (333) is of Landau-Stuart type and reduces to the amplitude equation for free bars in straight channels derived by Colombini *et al.* (1987) as $k_r \rightarrow 0$. For finite k_r , equation (333) admits of supercritical equilibrium solutions as $T \rightarrow \infty$ provided the ratio $[b\beta_c\mu_\beta + k_r^2\text{Re}(\alpha_{11})]/a_r$ is negative. Thus curvature does affect the presence of free bars in meandering channels. We know from Colombini *et al.* (1987) that $b\beta_c\mu_\beta/a_r$ is always negative. Hence, curvature can suppress free alternate bars provided $\text{sgn}[\text{Re}(\alpha_{11})] \neq \text{sgn}[\mu_\beta]$. Under the latter conditions $[b\beta_c\mu_\beta + k_r^2\text{Re}(\alpha_{11})]$ changes sign when the following condition is satisfied

$$k_r = k_{rc1} = \sqrt{-\frac{b\beta_c\mu_\beta}{\text{Re}(\alpha_{11})}}. \quad (334)$$

Here, the threshold value k_{rc1} depends on the unperturbed Shields parameter τ_{*u} , the dimensionless grain size d_s and the meander wavenumber λ_m .

For values of λ_m/λ_c such that the critical value k_{rc1} defined by (334) exists, the critical value ν_{0c1} of the curvature ratio able to suppress free bars is given by the following relationship

$$\nu_{0c1} = k_{rc1} \sqrt{\frac{\beta_u - \beta_c}{b}}. \quad (335)$$

Physically, equation (335) is equivalent to simply stating that, the larger the amplitude of free bars the more sinuous the channel should be in order to suppress them. Although the dependence

of ν_{0c1} on β_u predicted by (335) is fairly strong, it could not be detected in the experiments of Kinoshita and Miwa (1974) where β_u was held constant.

A second important outcome of the modified amplitude equation (333) is the prediction of the effect of curvature on the speed of free bars. At equilibrium, we can write

$$A = |A_e| \exp(i \hat{\omega} \tau), \quad (336)$$

with $\hat{\omega}$ real. Substituting from (336) into (333) one finds:

$$\hat{\omega} = b \beta_c \nu_\beta + k_r^2 \text{Im}(\alpha_{11}) + |A_e|^2 a_i \quad (337)$$

The dimensionless wavespeed of free bars in a meandering channel, c_m , is affected by curvature according to the following relationship :

$$c_m = (\omega_c - \epsilon^2 \hat{\omega}) / \lambda_c = (\omega_1 + \nu_0^2 \omega_2) / \lambda_c \quad (338)$$

where ω_1 is the angular frequency of weakly nonlinear bars in a straight channel ($\omega_1 = \omega_c - \epsilon^2 (b \beta_c \nu_\beta + |A_e|^2 a_i)$) and $\nu_0^2 \omega_2$ is the correction of the angular frequency of weakly nonlinear bars in a meandering channel ($\omega_2 = -\text{Im}(\alpha_{11})$). Thus curvature will slow down or speed up the propagation of free bars depending on ω_2 being negative or positive.

If the former condition is satisfied, then (338) allows one to define a second critical value of the curvature ratio ν_{0c2} as the minimum value of ν_0 such that c_m vanishes. One finds:

$$\nu_{0c2} = \sqrt{-\frac{\omega_1}{\omega_2}} \quad (339)$$

where ν_{0c2} will depend on the values of the relevant parameters τ_{*u} , d_s , λ_m and β_u .

Summarizing the above findings, we suggest the existence of the following regimes:

- i) $\nu_{0c1} < \nu_{0c2}$: free bars are damped by curvature and slow down for $\nu_0 < \nu_{0c1}$, whereas they are suppressed for $\nu_0 > \nu_{0c1}$;
- ii) $\nu_{0c1} > \nu_{0c2}$:
 - free bars are damped, slow down and migrate downstream for $\nu_0 < \nu_{0c2}$;
 - free bars are damped and migrate upstream (possibly at a very low rate) for $\nu_{0c2} < \nu_0 < \nu_{0c1}$;
 - free bars are suppressed for $\nu_0 > \nu_{0c1}$.

A quantitative comparison between the above theoretical predictions of the critical values of $k_{rc1} = \nu_{0c1}/\epsilon$ and $k_{rc2} = \nu_{0c2}/\epsilon$ and the experimental results of Kinoshita and Miwa (1974) was pursued by Tubino and Seminara (1990) and is reported in the figures 78a,b. The procedure followed to perform such comparison was to evaluate ν_{0c1} and ν_{0c2} , from (335) and (339), respectively, using the experimental values of the relevant parameters. The corresponding critical values θ_{c1} and θ_{c2} of the angle between straight segments of the experimental channel were then estimated using relationships obtained by modeling the channel as a sequence of meanders. The centreline of the latter is given in Cartesian coordinates by a sinusoid with maximum curvature and intrinsic wavenumber respectively equal to those characteristic of the equivalent *sine generated curve* adopted in the theoretical model. Various observations arise from Figure 78.

The signs of $\text{Re}(\alpha_{11})$ and $\text{Im}(\alpha_{11})$ are found to be such that critical values ν_{0c1} and ν_{0c2} exist in a wide range of values of λ_m/λ_c including those corresponding to the experiments of Kinoshita and Miwa (1974). The distributions of ν_{0c1} and ν_{0c2} are very close to each other and both appear to be in fairly good agreement with experimental observations. Note that the criterion employed by Kinoshita and Miwa (1974) to define θ_c , was to ascertain “*whether an initially formed bar train*

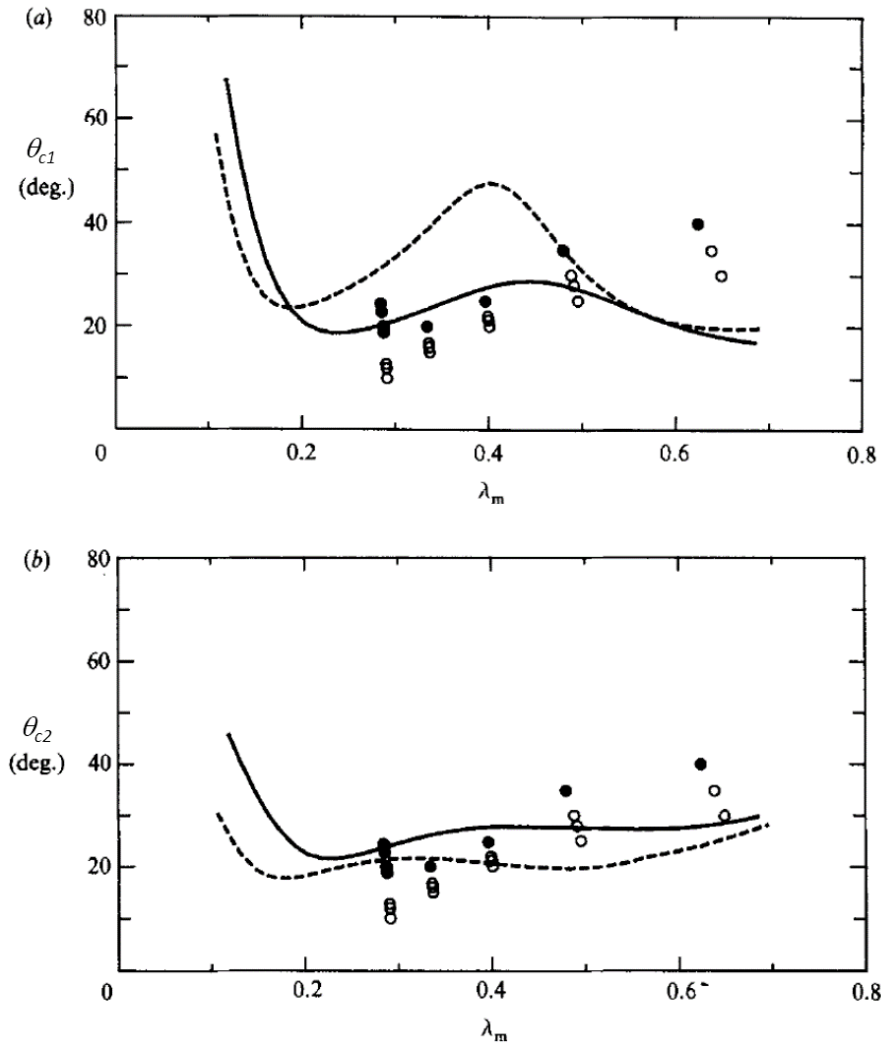


Figure 78. The critical values θ_{c1} and θ_{c2} predicted by the theory of Tubino and Seminara (1990) are compared with the experimental observations of Kinoshita and Miwa (1974) for two different values of the slope parameter r in the closure equation for sediment transport (276). Solid lines $r = 0.5$, dashed lines $r = 0.3$ • non migrating bars; ○ migrating bars (modified from Tubino and Seminara, 1990).

could migrate more than one wavelength downstream" but the boundary between the *migrating* and *non-migrating* regimes was not completely clear. Let us quote Kinoshita and Miwa (1974): "It was sometimes observed that clearly visible bar fronts would be unable to migrate more than one wavelength downstream and would tend to vanish . . . , but that nevertheless the point of deepest scour along the bank would subsequently be subject to oscillations in elevation that would not fade in time . . . ". This notwithstanding, the agreement exhibited by figures 78a and 78b appears to be strongly supportive of the present theoretical interpretation.

A second notable feature emerging from Figure 78 is the observation that in some ranges of values of λ_m it appears that $\nu_{0c1} > \nu_{0c2}$. Tubino and Seminara (1990) pointed out that it should then be possible to perform an experiment in these ranges where bars migrating upstream should be observed, suggesting that experiments or strongly nonlinear computations might be able to prove the actual existence of this regime.

A third feature is the existence of a minimum in the curves $\nu_{0c1}(\lambda_m)$ and $\nu_{0c2}(\lambda_m)$. This

property is further displayed in Figure 79b showing that the dependence of k_{rc1} on the ratio λ_m/λ_c exhibits two minima. In addition, Figure 79a shows that the fundamental forced component of bottom elevation has a near resonant elevation peak for a meander wavenumber corresponding to maximum free bar suppression. Such a result clearly supports the interpretation that the minimum values of ν_{0c1} and ν_{0c2} , are attained within the resonant wavenumber range of Blondeaux and Seminara (1985). This is not surprising as, close to resonance, the forced bar exhibits a peak, hence lower sinuosities are sufficient to damp free bars.

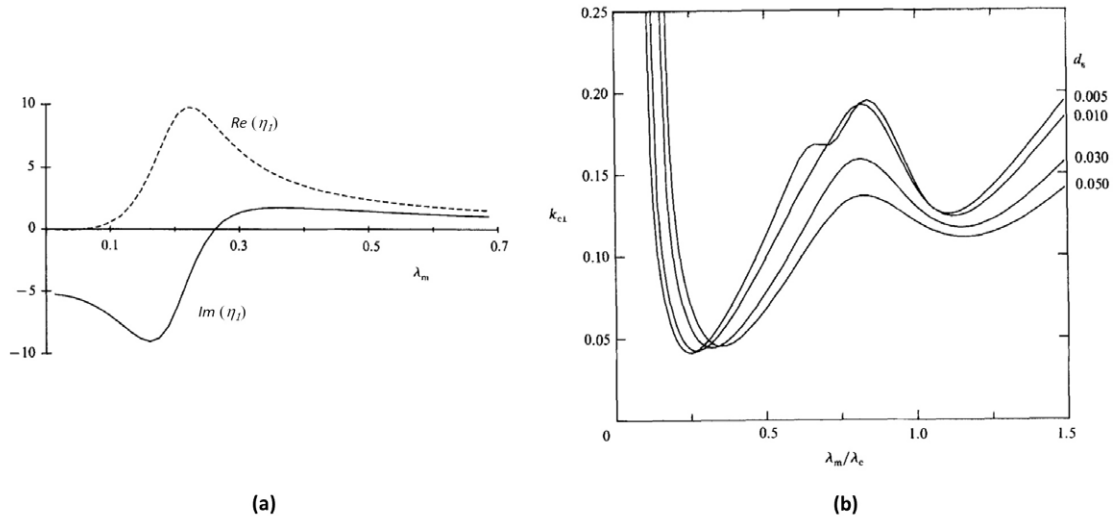


Figura 79. (a) The fundamental forced component of bed elevation, η_1 , is plotted versus meander wavenumber, λ_m , showing that the near resonant elevation peak is associated with a meander wavenumber corresponding to maximum free bar suppression. Data as in Kinoshita and Miwa (1974). (b) The critical value of k_{rc1} is plotted versus the ratio λ_m/λ_c for $\tau_{*u} = 0.1$ and various values of d_s (modified from Tubino and Seminara, 1990).

The last noticeable feature of Figure 78 is the behavior of θ_{c1} and θ_{c2} as $\lambda_m \rightarrow 0$ that clearly suggests that free bars are no longer suppressed by curvature if meanders are long enough. This result conforms to the field observations of Kinoshita (1961) and Whiting and Dietrich (1993) who noticed that in tortuous bends several alternate bars may be superimposed over a primary point bar.

An additional attempt to test the theory of Tubino and Seminara (1990) by laboratory experiments was performed by Niño (1992), but see also Garcia and Niño (1993). Comparison was less satisfactory than the one based on experimental observations of Kinoshita and Miwa (1974). The Figure 80 shows that agreement required some empirical adjustment of the value of k_{rc1} predicted by the theory, suggesting that in Niño (1992) free bars required less sinuosity to be suppressed.

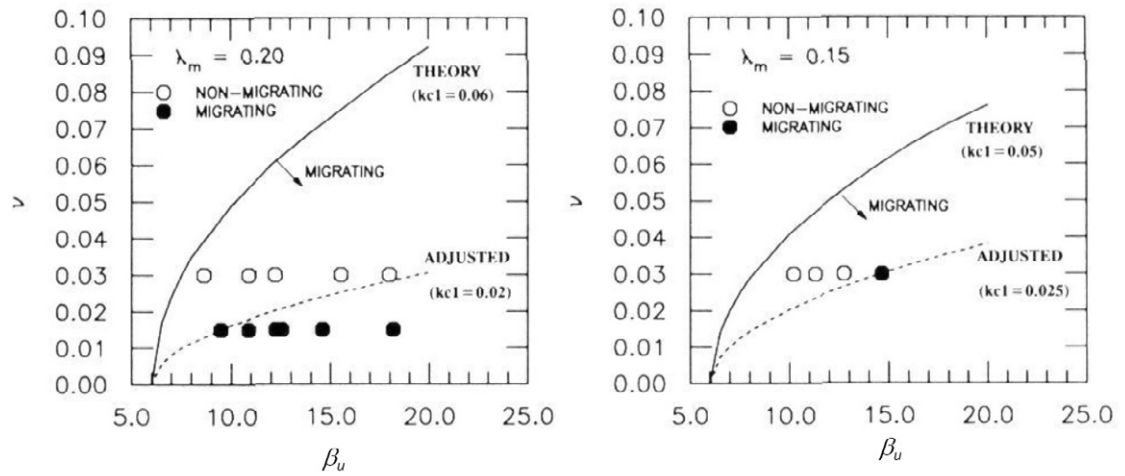


Figure 80. Comparison between theoretical predictions and experimental results of Niño (1992) for the suppression of migrating bars in meandering channels (reproduced from Figures 6.23 and 6.24 of Niño, 1992).

5. Planform evolution of meandering rivers

As discussed in Chapter 1, the picture of meander evolution emerging from field observations shows that meanders undergo a life cycle whereby they are generated, often following the *death* of a previous meander. They grow and migrate developing mature shapes displaying several characteristic features, including skewing and fattening of single loops, as well as the formation of multiple loops. They eventually *die* through the process of *cutoff*. The formation of an *oxbow lake* buried into the flood plain is the heritage left by the abandoned meander loop. Each of these stages has distinct characteristics and poses challenging problems of physical and mathematical interpretation that are the subject of the present Chapter. In order to tackle these problems, we must preliminarily model the driving mechanism of meander evolution, i.e. the process whereby *outer* banks of the meandering channel are progressively eroded, whilst sediment deposition is experienced by *inner* banks.

5.1. Bank erosion and migration rules

Understanding the mechanism of bank retreat has long attracted the attention of the scientific community. The goal of most investigations focused on the detailed processes occurring when a bank is subjected to weak or intense flow events. Such detailed processes are not directly relevant to our major present undertaking, namely the mechanics of long-term planform evolution of meandering river. It is sufficient for our purposes, to formulate a *migration rule* able to interpret in an averaged sense the outcome of the sequence of erosion events determined by the actual series of flow hydrographs. The migration rule must be simple enough to be suitable to the long-term planform evolution models required to understand the gross features of how meanders evolve from incipient formation to cutoff and beyond.

Let us recall that banks are usually classified on the basis of their composition and their stratigraphy, as *non-cohesive*, *cohesive* or *composite*. Thorne (1991) notes that strictly non-cohesive banks are fairly rare, i.e. most alluvial bank materials exhibit cohesion either real (due to the presence of silt and clay fractions), or apparent (due to capillary suction in unsaturated layers or to the binding effect of vegetation). Composite banks (Figure 81) have typically a stratified structure, with non-cohesive sandy-gravel deposits typically originating from relic channel bars interspersed with cohesive sandy silt and clay deposited by overbank flow on emergent bars (Thorne and Tovey, 1981).

Bank retreat is a complex process which occurs in a variety of forms that can ultimately be attributed to two main mechanisms.

- The first is *fluvial erosion*, consisting of a continuous process of removal of bank material, occurring when gravitational and hydrodynamic forces acting on bank particles exceed the resistive forces associated with friction (in non cohesive banks) and interparticle bonds (in cohesive banks).
- The second mechanism is that of *mass failure*. *Bank collapse* consists of sudden events (micro-landslides) whereby a portion of the bank fails. Destabilizing effects are the action of gravity, the effect of pore pressure of the interstitial fluid, flow erosion of the bank toe which



Figura 81. A composite bank in the Cecina river (Tuscany, Italy) (courtesy of L. Solari).

increases the bank height (Thorne, 1991) and undercutting, which increases the bank angle. Bank failure is opposed by friction and soil cohesion that resist movement.

However, the ultimate control on the rate of bank retreat must arise from the ability of the stream to actually remove the material stored at the bank toe. Indeed, bank-toe erosion occurs if the rate of removal of sediment by the flow in the basal area exceeds the rate of sediment supplied from the bank erosion process. In this case, called *excess basal capacity*, scour of the basal area causes both the bank height and the bank slope to increase thus decreasing bank stability to mass failure. On the contrary, bank-toe aggradation and berm formation (*impeded removal*) occurs when the rate of sediment supply to this zone exceeds the rate of sediment removal by the flow. Under these conditions, bank erosion leads to enhancing riverbank stability.

This is essentially the concept of *basal endpoint control* of bank erosion introduced by Thorne (1991). It links the sedimentary processes occurring at the bank and channel scales. It also suggests that the long-term rate of bank retreat at a cross-section is ultimately dominated by fluvial erosion independently of the nature of the bank and of the detailed sequence of bank erosion events that determine the bank retreat.

Indeed, recent numerical simulations of bank collapse, carried out using a detailed finite element model (Zhao *et al.*, 2021), have shown that as a river bend evolves from a small amplitude sinusoidal configuration, the initially scattered bank collapse events progressively concentrate at the outer bank and converge toward the section where the bed shear stress attains a maximum, implying a transition from a bank-stability-dominated state (controlled by the ratio between near-bank water depth and bank height) to a hydraulically-dominated state (dictated by the near-bank distribution of bed shear stress). Moreover, the intermittent outer bank collapse and the continuous inner bank accretion lead to a catch-up behavior, whereby the channel maintains a nearly constant channel width.

Bank migration rule

Outer bend erosion and inner bend deposition determine the progressive planform migration of the river. We recall that, as discussed in Chapter 2, the channel axis of a meandering river is a curved line in the 3-D space. Nevertheless, it is convenient to refer the flow to an orthogonal system of coordinates (s , n and z , respectively, in Figure 82) such that the longitudinal s axis

is the projection of the channel axis onto a horizontal plane, the transverse rectilinear axis n is horizontal and orthogonal to the s axis, while z is the vertical axis pointing upward.

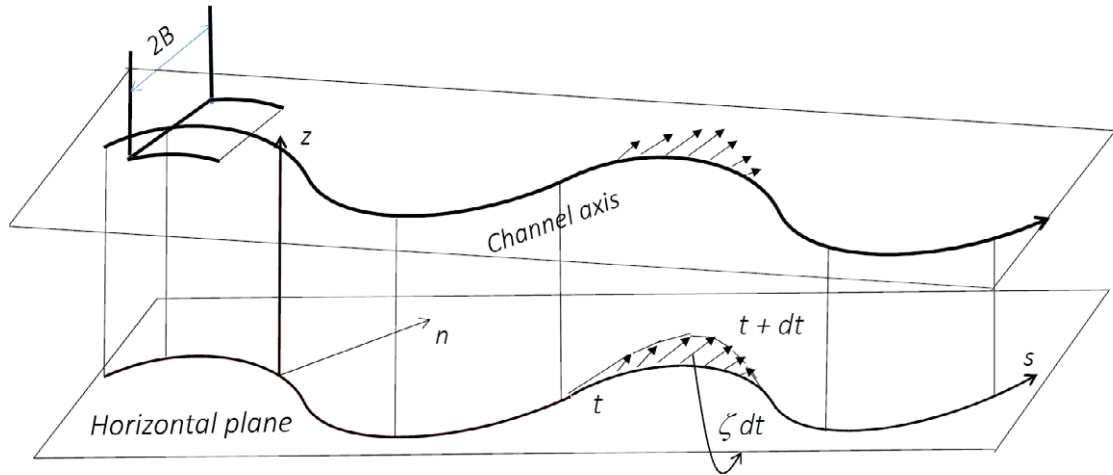


Figura 82. Sketch of a sinuous channel showing the lateral migration of the channel axis.

The planform evolution of the river channel can be conveniently described in terms of the continuous deformation of the coordinate line s driven by the lateral migration of the river. Let us denote by $\zeta(s, t)$ the *average bank erosion rate*, i.e. the rate of displacement of the coordinate line s in the direction normal to the line. In general, ζ will depend on the characteristics of the flow field, of bed topography and of the geological texture of the banks.

In the early kinematical models proposed by geomorphologists (e.g. Howard and Knutson, 1984; Howard, 1996), the lateral migration speed was empirically assigned. A major development of the subject was achieved when bank erosion was coupled to some measure of the deviations of the flow field from some equilibrium state of the meandering reach. Essentially, this approach assumes that any perturbation of the flow field at equilibrium drives bank erosion, which in turn leads to planform evolution and consequently to further modification of the flow field.

This novel idea was first introduced in the cornerstone paper of Ikeda *et al.* (1981) (which built upon the previous Japanese contribution of Ikeda *et al.*, 1976) where a dynamic approach was proposed. Bank erosion was assumed to be driven by an excess flow speed at the outer bank while bank deposition was conversely associated with a defect of flow speed at the inner bank, excess or defect being referred to the reach-averaged flow velocity. Hence, the erosion law reads:

$$\zeta = E (U|_{out} - U|_{inn}). \quad (340)$$

Here, U is the depth-averaged longitudinal velocity, the subscript *out* (*inn*) indicates that the velocity is evaluated at the outer (inner) bank and E is a dimensionless long-term erosion coefficient. The above linear rule has received some substantiation from field observations on rivers with fairly uniform cohesive banks (Pizzuto and Meckelnburg, 1989). The erosion law (340) has an important feature: it preserves channel width throughout the process of meander development. Indeed, pure width variations would lead to identical values of the perturbations of flow velocities at the inner and outer banks (i.e. $U|_{out} - U|_{inn} = 0$) such that (340) predicts vanishing value of the displacement of the channel centreline.

A number of alternative erosion laws have been proposed in the literature. In particular, proportionality between bank erosion rate and excess shear stress has been suggested by Blondeaux and Seminara (1985). These Authors implicitly assumed that the unperturbed straight channel configuration is in equilibrium, i.e. erosion is only caused by secondary flow associated with curvature. The rate of bank retreat can also be expected to be correlated with bank height.

However, note that an increase of water depth is associated with an increase of longitudinal velocity, which leads to increasing longitudinal bed shear stress. Hence, as pointed out by Blondeaux and Seminara (1985), the former assumption does implicitly account for the expected deepening of the cross-section close to the outer bank. Models in which the bank erosion rate is assumed to be explicitly proportional to the excess near-bank water depth have also been proposed (see Mosselman (1998) and references therein).

It is worth pointing out at this stage that, in the context of a linear theory of meander hydrodynamics, perturbations of the flow velocity, flow depth and bottom shear stress are simply proportional to each other. Hence, in planform evolution models adopting a linear hydrodynamics, the above erosion laws are essentially equivalent and different choices simply correspond to a change of the erosion coefficient. This conclusion does not hold if one adopts a nonlinear model of meander hydrodynamics. However, the computational effort associated with the latter choice is still prohibitive if long-term simulations are pursued. Hence, as we will see in the next Sections, these type of simulations have mostly been based on hydrodynamic linear models. Anyhow, as discussed in the next section, *the kinematics of planform evolution of meandering rivers is intrinsically geometrically nonlinear, independently of the linear or nonlinear character of the hydrodynamic model*. As a result, the shape of river meanders will be shown to exhibit a number of features typical of nonlinear systems even using a linear hydrodynamic model.

Below, we start adopting the erosion law (340) and show that a lot can be learned on the fundamental mechanisms of meander evolution with the help of this simple assumption. More recent developments on bank erosion rules allowing to decouple the dynamics of the outer bank from that of the inner bank will be discussed in the Section 5.6.2.

5.2. The integro-differential equation of planform evolution

On the fairly large timescale characterizing the planform evolution of meandering rivers, the equation governing the process of continuous deformation of meander shape can be derived by purely kinematic arguments applied to the migration of the longitudinal coordinate line, along with some erosion law coupling the lateral rate of migration ζ to the flow hydrodynamics. The first attempt in this direction was pursued by Ikeda *et al.* (1981) who referred the channel centreline to a cartesian reference frame. Moreover, the meander model employed by these Authors was based on a major approximation whereby the bed topography was assigned rather than derived with the help of a morphodynamic model. This was pointed out by Blondeaux and Seminara (1985) who showed that the missing coupling between hydrodynamics and morphodynamics rules out a number of important features of the process (resonance, upstream influence), that have been extensively discussed in Chapter 4.

Later, Seminara *et al.* (1994) and Seminara *et al.* (2001b) derived a form of the planform evolution equation in intrinsic coordinates which displays a nonlinear and integro-differential character and is coupled through the erosion rate ζ to the governing equations of meander morphodynamics. This form of the evolution equation proves quite instructive. In particular, it is amenable to analytical solutions in the geometrically nonlinear regime, i.e. when meanders have developed large amplitudes.

Before we proceed with the derivation of this important equation, it is appropriate to quote a recent contribution of Camporeale *et al.* (2007). These Authors, revisiting the models of river meandering proposed in the literature, quoted an important paper of Brower *et al.* (1984) where the kinematics of moving interfaces in two or more dimensions was investigated in terms of their intrinsic geometric properties. The interest of Brower *et al.* (1984) focused on the "motion of a boundary between time-dependent phase domains in which the interface itself satisfies an equation of motion". Moreover, "competing stabilizing and destabilizing forces act on the phase boundary to produce irregular or patterned structures, such as those which occur in solidification". The planform evolution of river meanders turns out to be a particular case of the class of processes analyzed there. This paper was not known to Seminara *et al.* (1994) and Seminara *et al.* (2001b). The Authors adopted an independent physical approach which led to an identical form of the evolution equation. Below, we will then follow the latter approach.

As mentioned above, the river planform (Figure 83) is represented through the coordinate line s , which lies on a horizontal plane. At a given time t , this line can be described by the distribution $\theta(s, t)$ of the angle that the local tangent to the line forms with the direction of a Cartesian axis x . This angle is related to the radius of curvature $r_0(s, t)$ of the line through the geometrical relationship:

$$r_0(s, t) d\theta = -ds, \quad (341)$$

where the sign of $r_0(s, t)$ is negative or positive depending on whether the line is locally convex or concave. In dimensionless form and recalling the definition of dimensionless curvature \mathcal{C} introduced in Section 2.2 (see equations (22) and (23)) the latter relationship becomes:

$$\nu_0 \mathcal{C}(\tilde{s}, \tilde{t}) = -\frac{d\theta}{d\tilde{s}}. \quad (342)$$

Here, ν_0 is the curvature ratio, defined as the ratio of half channel width B to some characteristic value of the radius of curvature R_0 , say its minimum value in the meandering reach, whilst \tilde{s} and \tilde{t} are dimensionless longitudinal coordinate and time scaled by B and B/U_0 , respectively, with U_0 some reference velocity scale.

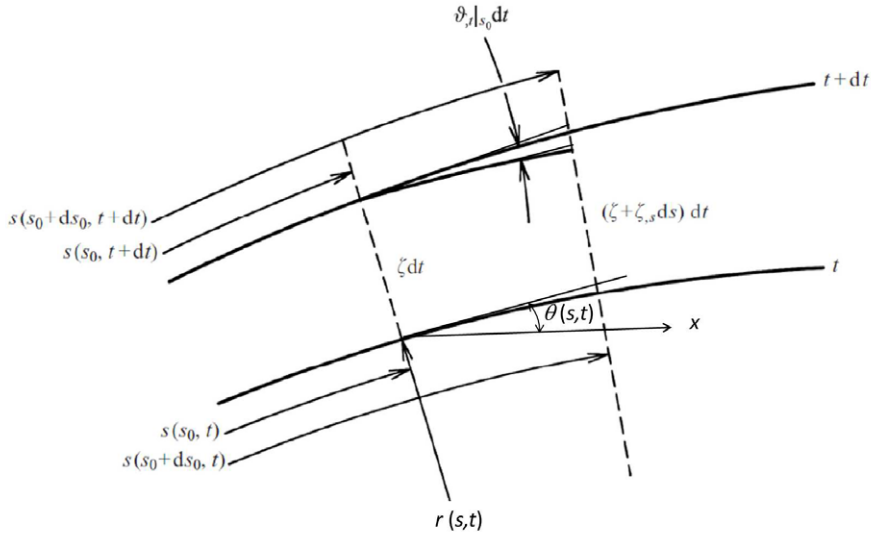


Figure 83. Sketch of the planform evolution of the coordinate line s defined as the projection of the axis of a meandering channel onto a horizontal plane.

We then stipulate that each point of this coordinate line moves in the normal direction n with a lateral migration speed ζ driven by bank erosion. Let us express this simple statement in mathematical terms.

Firstly, we introduce the function $s = s(s_0, t)$ which maps the longitudinal coordinate s of the channel cross section at time t onto its location s_0 at the initial time t_0 . Hence, we can write $\theta = \theta[s(s_0, t), t]$, i.e. the angle θ is a function of time both explicitly and implicitly, through the map $s(s_0, t)$. We can now calculate the material derivative $d\theta/dt$, which reads

$$\frac{d\theta}{dt} = \frac{\partial\theta}{\partial t} + \frac{\partial\theta}{\partial s} \frac{ds}{dt} \quad (343)$$

and is seen to involve the material derivative of the arc length ds/dt .

The next step is to evaluate the latter quantity. This is obtained observing that, in the time interval dt , simple geometrical reasoning shows that each infinitesimal portion of the channel axis varies its initial length ds by an amount

$$d(ds) = \frac{\zeta dt}{r} ds. \quad (344)$$

Recalling that the local radius of curvature is defined in the form $1/r = -\partial\theta/ds$, integration in s gives

$$\frac{ds}{dt} = - \int_0^s \zeta \frac{\partial\theta}{\partial s'} ds', \quad (345)$$

where s' is a dummy variable and the integral accounts for the spatial distribution of the channel deformation process.

Finally, kinematical arguments illustrated in Figure 83 imply that the relative displacement of two adjacent points of the coordinate line s in a time interval dt drives a temporal variation of the angle θ associated with the material element ds , such that

$$\frac{\partial\zeta}{\partial s} ds dt = \frac{d\theta}{dt} dt ds. \quad (346)$$

Substituting from (345) and (346) into (343) we end up with the following planform evolution equation of river meanders (Seminara *et al.*, 1994; Seminara *et al.*, 2001b):

$$\frac{\partial\zeta}{\partial s} = \frac{\partial\theta}{\partial t} - \frac{\partial\theta}{\partial s} \int_0^s \zeta \frac{\partial\theta}{\partial s'} ds' \quad (347)$$

or, in dimensionless form:

$$\frac{\partial\tilde{\zeta}}{\partial\tilde{s}} = \frac{\partial\theta}{\partial\tilde{t}} - \frac{\partial\theta}{\partial\tilde{s}} \int_0^{\tilde{s}} \tilde{\zeta} \frac{\partial\theta}{\partial\tilde{s}'} d\tilde{s}'. \quad (348)$$

Here, the dimensionless lateral migration rate $\tilde{\zeta}$ is scaled by U_0 . Three major observations on the form of (347) are in order.

- The evolution equation is nonlinear. A first source of nonlinearity is present in the integral term and arises from purely geometrical constraints.
- The evolution equation is integro-differential and, as such, it accounts for the spatial history of the deformation process, including upstream and downstream influence.
- Finally, the evolution equation is coupled to the morphodynamics of the channel through the erosion law (340) (or alternative forms). Hence, besides geometric nonlinearities, also flow nonlinearity may affect the planform evolution of the river channel through the dependence of the lateral migration rate ζ on the flow field.

5.3. Meander formation: an instability process

The question of why and when meanders form has long puzzled the scientific community. However, in spite of the ubiquitousness of river meandering, few field observations of meandering initiation have been reported and they have not supported any conclusive interpretation of the initiation mechanism. On the other hand, as discussed in the next section, laboratory observations have also proven rather elusive until recently.

5.3.1 Modern field and laboratory observations

The starting point of the modern understanding of river channel patterns may possibly be associated with the seminal work of Leopold and Wolman (1957). Various major observations are reported in that paper. They can be summarized as follows:

- Channel patterns were defined as belonging to three main categories, straight, sinuous-meandering, or braided, with gradual merging of one pattern into another.
- Reaches that keep straight for distances exceeding ten times the channel width are rare. Moreover, “*although the channel itself is straight, the thalweg wanders back and forth from positions near one bank and then the other*”. The Authors note explicitly that: “*In an idealized sense, this plan view of straight channels appears to bear a remarkable resemblance to a meander*”.
- Another characteristic of natural streams even in straight reaches is the occurrence of pools and riffles, but the Authors do not mention the possible migrating character of this pattern.

More recently, the data collected from aerial photos and topographic maps allowed the analysis of a large number of meandering bends (Lagasse *et al.*, 2004) and led to the mechanistically based classification reported in Section 2.3. Here, as an additional information, we recall that the sinuosity of observed meandering bends, defined as the ratio of the intrinsic to the cartesian meander wavelengths can reach values up to about 3 before neck cutoff (Figure 84). Moreover, according to the database collected by Lagasse *et al.* (2004), the median sinuosity takes the value 1.69, with a standard deviation of 0.399.

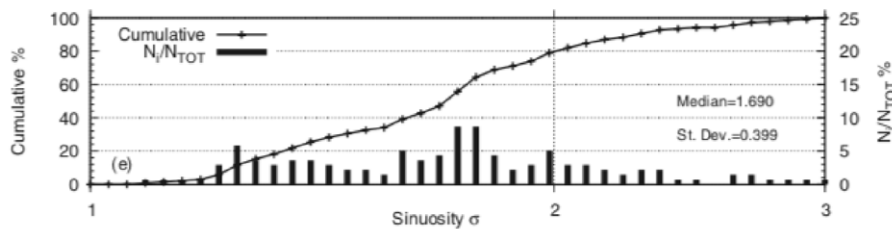


Figura 84. Typical frequency distribution and cumulative frequency curve of the mean meander bend sinuosity σ , computed for the alluvial river reaches contained in the database of Lagasse *et al.* (2004) (reproduced from Bolla Pittaluga and Seminara, 2011).

As discussed in Chapter 6(I), Leopold and Wolman (1957) identify the characteristics of bars in nature but do not detect the difference between free and forced bars. On the contrary, they tend to consider the bar pattern as a unique feature, emphasizing that the observed wavelengths in both straight and meandering channels correlate clearly with channel width. Note that meander wavelength was defined as twice the distance between successive points of inflection, hence a sort of cartesian (rather than intrinsic) wavelength. Figure 3(I) shows a celebrated plot, that has had significant influence on the development of the subject. Based on flume and field data of various Authors, it shows a clear correlation between channel width and wavelengths of either meanders or pool-riffle sequences in straight channels. Wavelength turns out to be proportional to the 1.1-power of channel width, with coefficient equal to 6.5.

The above observations have led geomorphologists to speculate on alternate bars being precursors of river meandering. However, this suggestion has various major shortcomings. Before we clarify this important point, let us first give an overview of the outcome of laboratory observations and clarify why, rather surprisingly, laboratory observations have for long been unable to provide crucial insight on the mechanism of meander formation. The main reason for this failure is now clear: cohesionless sediments were most often employed in these experiments. Typically, an initially straight channel was incised through a flat layer of cohesionless material. When flow was allowed into the channel, a sequence of processes were then observed. They were reported by Friedkin (1945) and Wolman and Brush (1961) among others, but a clearest illustration was made in the more recent contribution of Federici (1999) (but see also Federici and Paola, 2003; Eaton and Church, 2004). Briefly

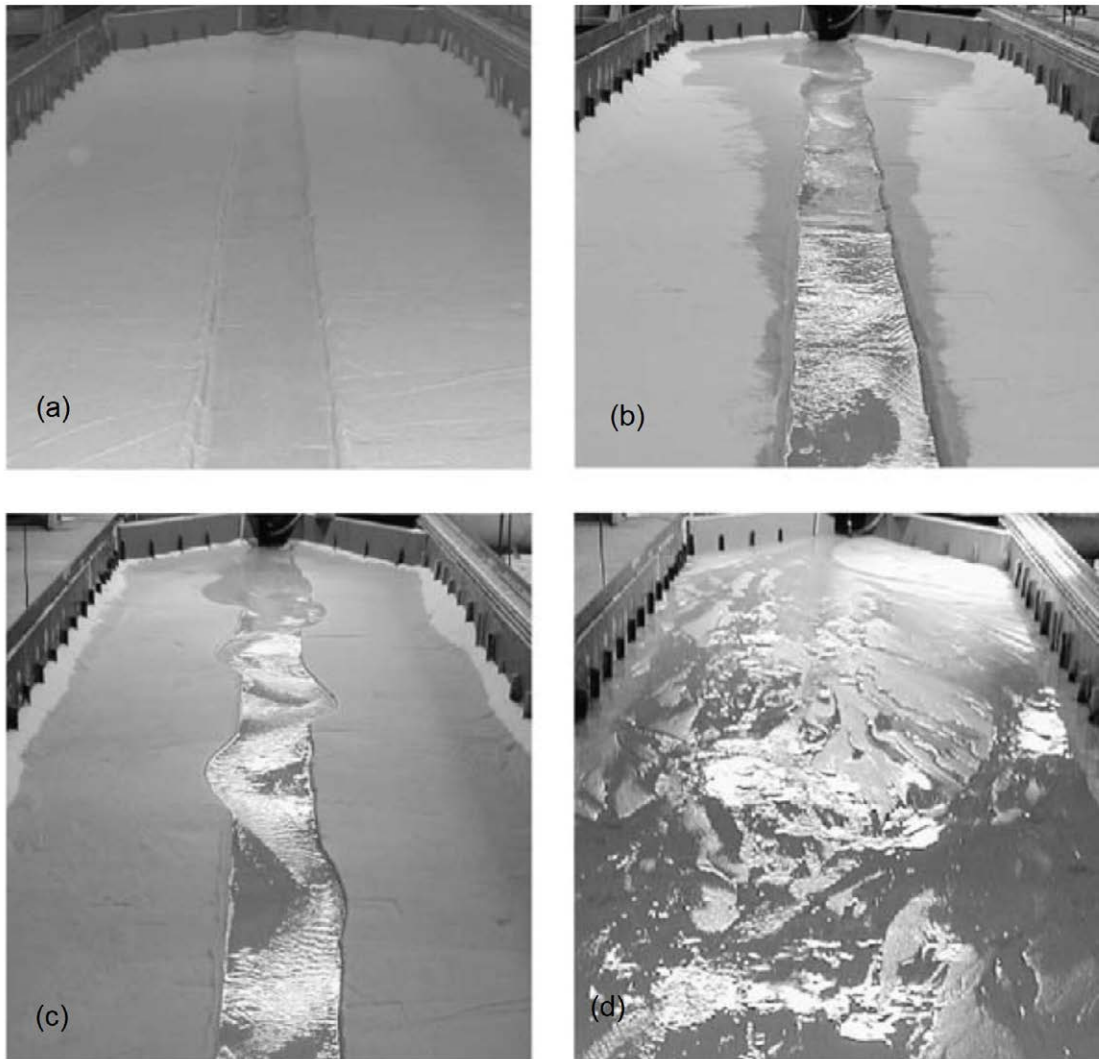


Figura 85. The sequence of processes observed in the experiments of Federici (1999) (reproduced from Federici and Seminara, 2003).

- The width of the initial channel is not in equilibrium, hence the channel banks are progressively eroded, the flow depth decreases and the aspect ratio of the cross section increases.
- Channel widening leads to the formation and downstream migration of alternate bars (Figure 85b).
- However, widening of the channel does not stop. Rather, after a while, preferential widening occurs at bar pools leading to the formation of a "*rhythmic sequence of indentations... on both banks, while the stream displays a tendency to meander*" (Figure 85c). Note that, at this stage, the cohesionless character of the floodplain plays a crucial role. Pools may represent preferential sites for bank erosion in spite of the migrating character of alternate bars because in the laboratory experiments the time scale of bank erosion is not larger than that associated with bottom erosion.

- The consequence of the onset of a periodic variation of channel width and channel curvature is the suppression of alternate bar migration. This mechanism is similar to that discussed in Section 4.5 and was given a theoretical interpretation by Repetto and Tubino (1999), who showed that bar migration may indeed be suppressed in channels with periodic variations of channel width of sufficiently large amplitude.
- The fixed character of the pools and the development of curvature of the stream do enhance bank erosion leading the bank indentations to grow and migrate downstream. As the stream undergoes further widening, chute cutoffs form and they drive the development of central bars.
- As the channel continues to widen, irregular smaller scale bars form in the central part of the channel (Figure 85d), showing the tendency of the stream to develop a multibar pattern that, eventually, transforms into a multichannel pattern induced by the emergence of bars.

In conclusion, the formation of a braided channel is the fate of any such experiment if the floodplain is modeled as cohesionless.

The idea that the persistence of a coherent meandering pattern requires a cohesive floodplain was investigated by Schumm and Khan (1972). In the latter experiments, after an initial phase when sand was supplied to the stream and submerged bars formed, the addition of a 3 % concentration of kaolinite, along with a decrease in sand supply led to enhanced bank stability, channel deepening and bar emergence until erosion ceased. The resulting channel pattern kept straight, though with a sinuous thalweg. Later, Jin and Schumm (1987) employed a two layer setting, with a lower sand layer and a thicker upper layer consisting of over 50 % kaolinite. The resulting pattern was sinuous with active point bars, but, as pointed out by Paola (2001), its inability to reform the ad hoc substrata suggests that the single thread meandering pattern was a transient feature. In other words, if these experiments had lasted long enough, the upper clay layer would have been removed by lateral migration and the stream would have eventually produced a braided pattern.

A similar attempt was more recently made by Smith (1998) using a variety of granular materials mixed with kaolinite. The effort was successful in that high sinuosity channels were actually produced with active point bars and chute channels. However, migration ceased once sinuosity developed such that the final equilibrium state of the channel was static.

A significant step forward was made by Gran (2000) (but see also Gran and Paola, 2001) and Tal and Paola (2007). They performed a series of ingenious experiments where the goal to give strength to the banks of the laboratory channel was achieved seeding the flume with *alfalfa* (*Medicago sativa*) and allowing the seeds to grow. It turned out that, starting from an initial braided network formed in the absence of vegetation, the growth of vegetation led to drastic modification of the channel pattern. In particular, the Authors note: "*In the run with the highest vegetation density, width-to-depth ratios approached those of natural single-thread channels and in plan view the model resembled a wandering river, with one to two main channels flowing around larger vegetated islands . . . vegetation plays an important role in stabilizing the banks, constraining channel migration, and allowing deeper and narrower channels to develop. These are all effects that move the channel pattern in the direction of meandering*" (Figure 86).

As pointed out by Braudrick *et al.* (2009), the alfalfa experiments reproduced many features of natural meanders, including avulsions and cutoffs, but the meandering character of the channel pattern was not stable and it was only present in part of the flume.

Two further laboratory experiments (Peakall *et al.* (2007), Braudrick *et al.* (2009)) tried to overcome the apparent inability of previous attempts to generate self-maintaining laterally migrating channels with cutoffs. In particular, Braudrick *et al.* (2009) point out that the key challenge is to allow both outer bank erosion and inner bank deposition at the same rate, discouraging the flow from occupying and enlarging chute channels which would typically lead to flow diversion down the chute and the development of multiple channels. More precisely, they suggested that laboratory experiments need the following ingredients:

- "*bank strength greater than that due to deposited bedload (to slow outer bank erosion rate)*", a goal they achieved using alfalfa sprouts in analogy with the approach of Tal and Paola (2007);



Figura 86. Image of the channel pattern observed in run 5 of Gran (2000). The run was characterized by the highest spatial vegetation density. A wandering stream developed, consisting of one to two main channels separated by large, vegetated islands (reproduced from Gran, 2000, courtesy of Karen Gran).

- “the addition of suspended load (to both settle out in the chutes, reducing the tendency for a low sinuosity cutoff, and to become deposited on the bar top, raising the surface to floodplain level)”. Hence, both a coarse (sand) and fine (lightweight plastic) sediment were fed separately at the upstream end of the flume.

A third ingredient, namely the occurrence of “periodic overbank flow (to raise the depositional surface of the point bar and to disperse suspended sediment into nearby low areas)” turned out not to be actually necessary. The main results of the experiments may be summarized as follows (Figure 87).

- The experiment, lasting 136 h, led to the formation of a meandering channel composed of five bends that experienced both lateral and longitudinal migration, as well as five distinct cutoff events. Fine sediment was crucial for connecting bars to the floodplain.
- No migrating alternate bars were observed in spite of the fact that morphodynamic conditions would have been favorable for alternate bar development.
- Migration rates were fastest in the initial stage of bend growth, as well as immediately after cutoffs.
- The channel width increased during the experiment, reaching asymptotically a fairly stable value.
- The channel sinuosity increased throughout the experiment to a maximum value of 1.19.

In conclusion, “increasing the bank strength relative to noncohesive sediment and promoting deposition of fine sediment in troughs between point bars and the floodplain”, turned out to be

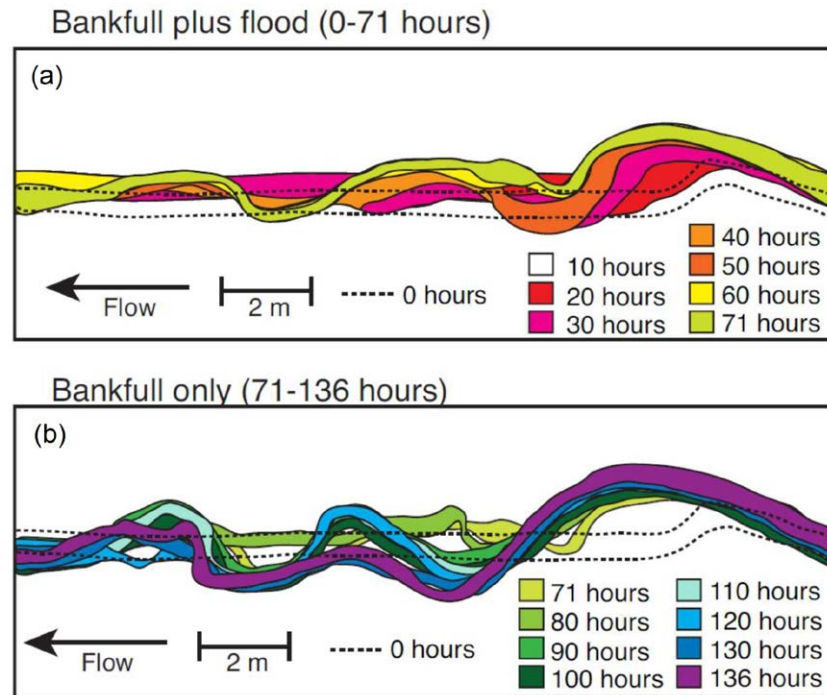


Figure 87. Planform evolution of the meandering channel formed in the experiments of Braudrick *et al.* (2009). (a) The first 71 *h* of the experiment: discharge included both a bankfull and flood flow; (b) planform evolution from 71 – 136 *h* under steady bankfull flow (reproduced from Braudrick *et al.*, 2009, under the CC BY-NC-ND license).

necessary and sufficient conditions for the generation of a self-sustaining meandering channel in a laboratory flume. In order to achieve meander sinuosities closer to natural values (hence larger than 1.19, see Figure 84), Braudrick *et al.* (2009) note that it would be necessary to reduce the migration rates of laboratory channels to field values. This would likely allow for an increase of the amount of fine sediment deposited in the chutes and a decrease of the frequency of chute cutoff. However, the time required for the experiments would significantly increase, which leaves this as the next challenge for experimentalists.

One further laboratory investigation (Schuurman *et al.*, 2016) deserves to be mentioned. The viewpoint adopted by these Authors is different from the previous ones and originates from the consideration that meander instability has been shown (Lanzoni and Seminara, 2006) to have convective nature (Section 9.3.5(I)). This issue and its experimental substantiation will be discussed in the next Section.

In summary, the picture emerging from the laboratory observations suggests that the driving mechanism of meandering initiation is bank erosion, which occurs whenever an initial perturbation of channel alignment is present. In most experiments an initial bend was carved at the inlet to hasten the onset of meandering. Hence, the original speculation of geomorphologists on alternate bars being precursors of river meandering is not confirmed. This is not surprising as alternate bars are migrating feature, hence they can hardly be responsible for the localized erosion of cohesive banks driving meander formation, unless the time scales of bottom erosion and bank erosion are comparable, a condition satisfied only in laboratory experiments where cohesionless sediments are employed. And, indeed, alternate bars did not form in many of the laboratory experiments discussed above (Smith, 1998; Peakall *et al.*, 2007; Braudrick *et al.*, 2009).

Moreover, as discussed in Section 4.5, alternate bars are observed to coexist with and migrate through weakly meandering channels, an observation which contradicts the idea that they would evolve into the fixed-point bars of river meanders.

In conclusion, the *bend* mechanism, that we analyze in the next Section, appears to be the only rational scheme able to explain various features of the meandering initiation process.

5.3.2 Bend instability: linear theory

The concept of bend instability was first introduced by Ikeda *et al.* (1981). Essentially, it is the process whereby a sinuous perturbation of channel alignment relative to an initially straight configuration, generates an alternate sequence of pools and point bars, which lead to outer bank erosion, that in turn amplifies the perturbation. This process leads eventually to the development of a meandering pattern. The linear theory of Ikeda *et al.* (1981) was based on a flow model that neglected the coupling between hydrodynamics and bed deformation. As a result, various aspects of the phenomenon were unavoidably overlooked. The later contribution of Blondeaux and Seminara (1985) did account for coupling and, as a result, the mechanisms of resonance and morphodynamic influence discussed in Section 4.4, emerged from the analysis.

Here, we follow the lead of Seminara (2006) who employs an instructive classical normal mode approach. We then consider a perturbed state consisting of a sinuous channel formed by a sequence of so called sine-generated bends (Langbein and Leopold, 1966). Let us use dimensionless variables (dropping the tilde for the sake of simplicity) and express the inclination angle θ as follows:

$$\theta = \theta_1 \exp i(\lambda s - \omega t) + c.c., \quad (349)$$

with θ_1 small initial amplitude of the perturbation, λ the intrinsic meander wavenumber, scaled by half the channel width B , and ω the complex angular frequency, scaled by U_0/B . The temporal growth rate of perturbations is the imaginary part $Im(\omega)$ of the complex angular frequency, the dimensionless wavespeed is given by $c = Re(\omega)/\lambda$ while the complex group velocity reads $\partial\omega/\partial\lambda$.

Let us illustrate the mechanism of bend instability analyzing two cases.

Bank erosion in phase with curvature

Let us arbitrarily assume that the dimensionless lateral migration speed ζ is *proportional to and in phase with local curvature*, i.e.

$$\zeta = -\zeta_1 \frac{\partial\theta}{\partial s}, \quad (350)$$

with ζ_1 real constant, taken to be sufficiently small to justify linearizing the planform evolution equation (348). Substituting from (350) and (349) into the linearized form of (348), one finds

$$-i\omega\theta = -\zeta_1 (i\lambda)^2 \theta, \quad (351)$$

hence

$$\omega = i\zeta_1 \lambda^2. \quad (352)$$

This leaves us with an unsatisfactory picture of the process, as:

- $Im(\omega)$ would be equal to $\zeta_1 \lambda^2$, i.e. meanders would amplify with a rate increasing indefinitely as the wavenumber increases;
- moreover, $Re(\omega)$ would vanish, i.e. meanders would not migrate ($c = 0$).

Bank erosion out of phase relative to curvature

Let us next add an important ingredient, namely a phase lag of the lateral migration speed ζ relative to the local curvature ($-\partial\theta/\partial s$). Let the dimensional spatial lag be δB , and write

$$\zeta = -\zeta_1 \frac{\partial\theta}{\partial s} \exp(-i\lambda\delta). \quad (353)$$

Substituting from (349) and (353) into the linearized form of (348), one finds

$$Im(\omega) = \zeta_1 \lambda^2 \cos(\lambda\delta), \quad c = \zeta_1 \lambda \sin(\lambda\delta). \quad (354)$$

This is quite a satisfactory picture of the process. Indeed (Figure 88):

- meanders grow for values of meander wavenumbers falling in the range $-\pi/2 < \lambda \delta < \pi/2$, with the growth rate peaking at some preferred wavenumber;
- moreover, unstable meanders migrate downstream if the erosion peak is located downstream of the bend apex (positive c , Figure 88a) and conversely they migrate upstream (negative c , Figure 88b) if the erosion peak is located upstream of the bend apex.

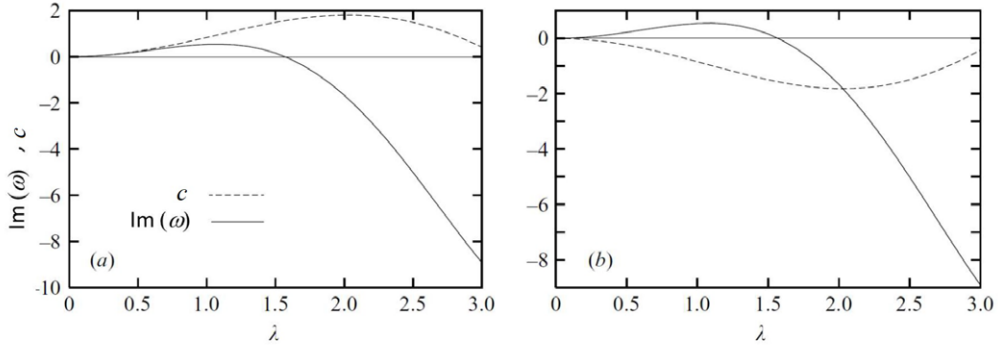


Figure 88. Dependence of growth rate ($\text{Im}(\omega)$, continuous lines) and migration speed (c , dashed lines) of meanders obeying the erosion law (353) on meander wavenumber for (a) positive or (b) negative value of the phase lag δ between bank erosion and curvature. Both ζ_1 and $|\delta|$ have been conventionally set equal to one (modified from Seminara, 2006).

As discussed below, in nature, the phase lag δ is not a constant but rather a function of the flow hydrodynamics and the erosion rule. This notwithstanding, the above picture is quite close to the real one and provides the simplest mathematical illustration of the basic mechanism of bend instability. The occurrence of a phase lag between flow perturbations (hence bank erosion) and curvature is the crucial ingredient to allow meander growth.

In order to refine the picture we must now replace the arbitrary assumption on the lateral migration speed with an appropriate erosion rule mimicking the coupling between bank erosion and flow field.

Hydrodynamic control on the phase lag δ

Let us employ the erosion rule (340), which couples lateral migration to meander hydrodynamics. We may then make use of the exact solution of the linear problem of meander morphodynamics discussed in Section 4.4.2, with $\mathcal{C}(s)$ replaced by the following relationship, immediately derived from (349),

$$\nu_0 \mathcal{C}(s, t) = -\frac{\partial \theta}{\partial s} = -i \lambda \theta_1 \exp i(\lambda s - \omega t) + c.c. \quad (355)$$

Note that we can still treat the flow as steady (albeit parametrically dependent on time) as the time scale associated with planform evolution is much larger than the hydrodynamic time scale.

As usual, we take advantage of the typically weak curvature of many river bends and assume that the curvature ratio ν_0 is a small quantity. The equations governing the flow field can then be linearized and their solution obtained through the expansions (304, 308) presented in Section 4.4.2. With the help of those expansions and the migration rule (340), one readily finds

$$\zeta = 2 \nu_0 E \sum_{m=0}^{\infty} (-1)^m u_m. \quad (356)$$

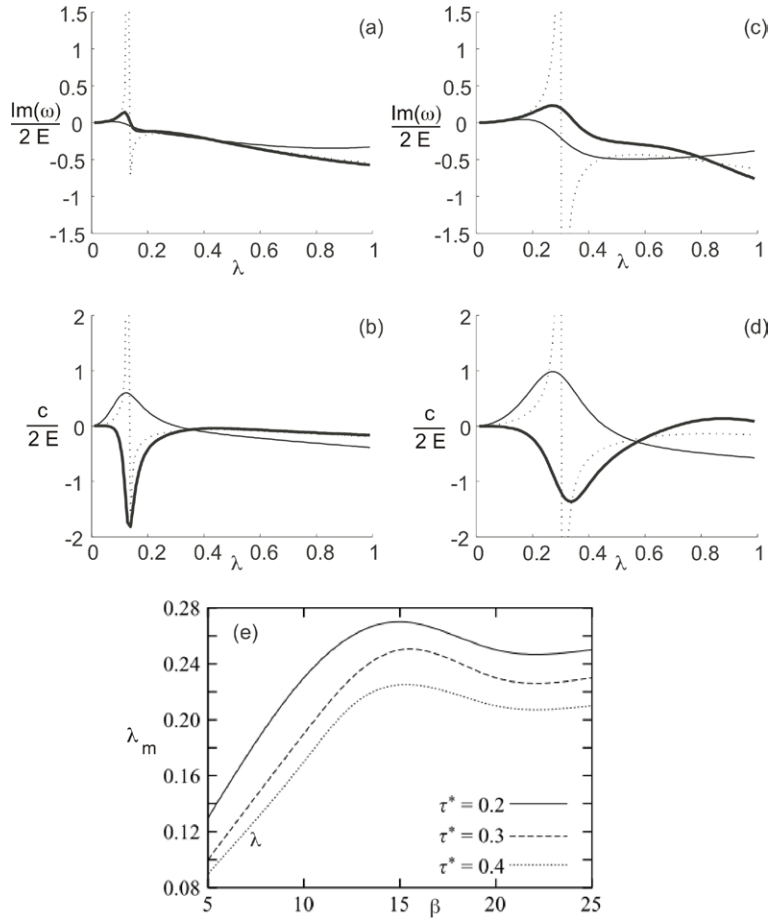


Figura 89. Dependence of the temporal growth rate $Im(\omega)$ and migration speed $c (= Re(\omega)/\lambda)$ on the (real) meander wave number λ . Three lateral Fourier modes have been used to describe the flow field as the effect of further modes proves quantitatively negligible. (a) and (b) refer to plane bed conditions ($\tau_{*0} = 0.1$, $d_s = 0.01$) while (c) and (d) were obtained assuming a dune-covered bed ($\tau_{*0} = 0.3$, $d_s = 0.005$). Thin lines denote sub-resonant conditions (plots a and b, $\beta = 10$; plots c and d, $\beta = 5$); thick lines denote super-resonant conditions (plots a and b, $\beta = 25$; Plots (c) and (d), $\beta = 15$); dotted lines denote resonant conditions (plots (a) and (b), $\beta_R = 20$; plots (c) and (d), $\beta_R = 10$). (e) Dependence of the dimensionless wavenumber λ selected by bend instability on the aspect ratio β for a few values of the Shields stress τ_{*0} , $d_s = 0.001$, and a dune-covered bed.

Substituting this expression and (349) into the linearized form of the bend evolution equation (348) leads to

$$-i\omega\theta = 2\nu_0 E \sum_{m=0}^{\infty} (-1)^m \frac{du_m}{ds}. \quad (357)$$

The dispersion relationship for bend instability is thus readily obtained using the solution of the linear problem of meander morphodynamics developed in Section 4.4.2. Multiplying equation (311) by $(-1)^m$, differentiating it, summing over m and making use of (355) eventually yields the

following relation (Seminara *et al.*, 2001b; Seminara, 2006)

$$\omega = 2E \sum_{m=0}^{\infty} (-1)^{m+1} A_m \lambda \frac{\sum_{j=1}^7 \rho_j (i\lambda)^j}{4 \sum_{j=0}^7 \sigma_j (i\lambda)^j}, \quad (358)$$

where A_m is the coefficient of the m -th term of the Fourier expansion of the function n in the lateral direction, given by the relation (298), while ρ_j and σ_j (see Section 4.4.2) are functions of the aspect ratio β , the Shields parameter τ_{*0} and the average friction coefficient C_{f0} of the basic uniform flow in the initially straight channel.

Figure 89 shows the dispersion relationship (358) for realistic values of the relevant parameters. Various features arise:

- A peak in the growth rate is observed at a value of the dimensionless wavenumber ranging about 0.1 – 0.3 (corresponding to wavelengths of about 30 – 10 channel widths, respectively) (Figure 89a,c);
- The meandering pattern migrates while amplifying and, indeed, the migration speed may change sign (Figure 89b,d).

According to our previous discussion, this implies that the erosion peak may shift from downstream to upstream of the bend apex. One would then like to know what mechanism controls the occurrence of a clear peak in meander growth as well as the predicted shift of the location of the erosion peak.

Resonance, selection of meander wavelength and migration speed

The answer to the first of the above questions is straightforward if one recalls the theory of linear meanders discussed in Section 4.3.1. There, we have shown that linear meanders behave as linear oscillators which resonate at specific values λ_R and β_R of the meander wavenumber and of the aspect ratio of the channel, respectively. Moreover, we know that λ_R and β_R depend on the intensity of sediment transport (through τ_{*0}) and friction (through the relative roughness d_s). The plots of the functions $\lambda_R(\tau_{*0})$ and $\beta_R(\tau_{*0})$ for given values of d_s , reported in Seminara and Tubino (1992), are reproduced in the Figure 90 and Figure 91, respectively. Of course, in nature, the aspect ratio of the channel is determined by the equilibrium arguments discussed in Chapter 5(I) and will differ in general from the exact resonant values. However, we know from Section 4.3.3 that the effects of resonance are felt within a fairly wide range of values in a neighborhood of β_R . In other words, a peak in the bend growth rate (albeit a finite rather than an infinite peak) occurs for any value of β not too far from β_R and selects a meander wavenumber λ_m not too far from λ_R . This is clearly demonstrated in Figure 89.

The answer to the second question, concerning the change in sign of meander migration speed is also related to the resonance phenomenon. Indeed, the migration speed changes sign as the resonance conditions are crossed. This feature is related to the property of linear resonators already discussed in Section 4.3.1, whereby the phase of the response changes quadrant (i.e. the location of peak flow crosses the bend apex) as the resonance conditions are crossed. As a result, sub-resonant (super-resonant) trains of periodic meanders migrate downstream (upstream).

The convective nature of bend instability

Let us complete our analysis of bend instability with some discussion of its fundamental nature: are we dealing with a convective or absolute type of instability? We have already clarified the physical aspects of this distinction when we discussed free bar instability (Section 6.3.3(I)).

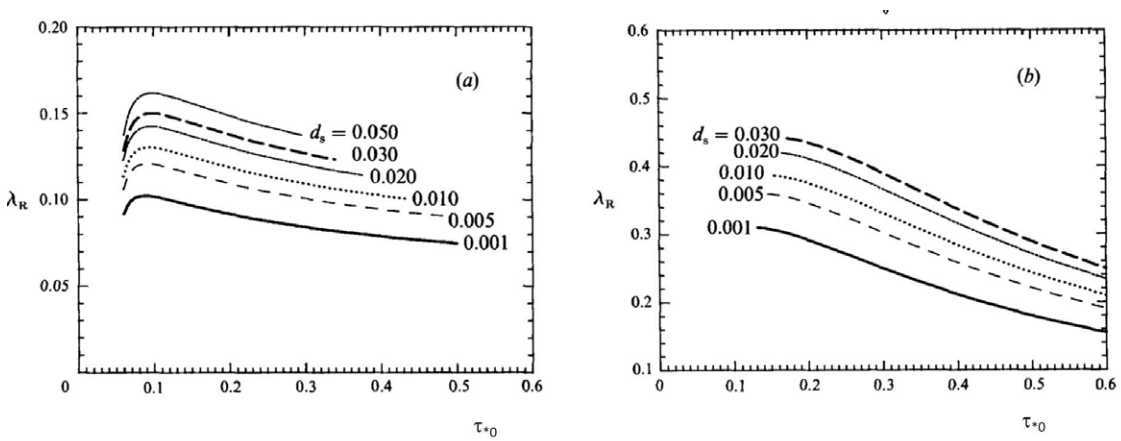


Figure 90. The resonant values of the meander wavenumber λ_R are plotted versus the Shields stress τ_{*0} for given values of the dimensionless grain roughness d_s . (a) plane bed; (b) dune-covered bed (modified from Seminara and Tubino, 1992).

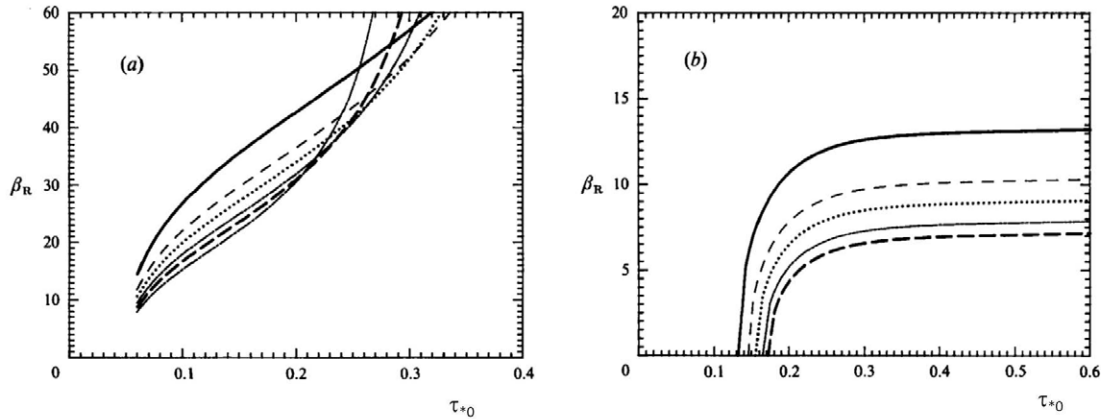


Figure 91. The resonant values of the aspect ratio of the channel β_R , are plotted versus the Shields stress τ_{*0} for given values of the dimensionless grain roughness (d_s values are those of figure 90). (a) plane bed; (b) dune-covered bed (modified from Seminara and Tubino, 1992).

Here, it suffices to recall that the convective/absolute nature of bend instability can be assessed by investigating the response of the channel planform in response to a spatially localized perturbation of the initially straight configuration, imposed at some cross section at the initial time. Such a response has typically the form of a wave packet in the (s, t) plane and, in order to distinguish between convective and absolute instability, one must examine its long-term behavior along the ray $s/t = 0$ at a fixed spatial location (Figure 93(I)). The theory explained in Section 9.3.5(I) shows that such a behavior is imprinted in the structure of the dispersion relationship. An application of the theory to bend instability was pursued by Camporeale and Ridolfi (2006) and Lanzoni and Seminara (2006). Results suggest the existence of two typical scenarios. The first scenario arises for low values of β : under such conditions, at a linear level, bend instability turns out to be invariably convective. The second scenario is associated with higher Fourier modes and suggests a transition to absolute instability for large values of β , dune covered bed and large values of τ_{*0} . In the absence of dunes this behavior is found for unrealistically high values of β . A further interesting feature emerging from the analysis concerns the group velocity $[\partial Re(\omega)/\partial \lambda]_{\lambda_{max}}$, with λ_{max} the wavenumber characterized by the maximum growth rate. It is found that the group

velocity changes sign as resonance is crossed. In other words, under super-resonant conditions the meander pattern propagates upstream. These results will be more clearly illustrated in Section 5.4.5 where we will report results of numerical simulations performed by Lanzoni and Seminara (2006).

It is appropriate at this stage to mention the laboratory investigations of van Dijk *et al.* (2012) and Schuurman *et al.* (2016) which were designed to experimentally test the importance of a persisting upstream perturbation in the process of meander formation and development. In the experiment, the initially straight channel had a transversely moving upstream inlet and silt-sized silica flour was added to the sediment feed to allow for floodplain formation. A dynamic meandering river with scroll bars, chute cutoffs and floodplain building was reproduced and the Authors concluded that “*the necessary and sufficient conditions for dynamic meandering gravel bed river are a sustained dynamic upstream perturbation and floodplain formation*”. The latter conclusion lends experimental support to the theoretical predictions of the convective nature of meander instability discussed above.

5.4. Nonlinear evolution from incipient meandering to neck cutoff: the origin of fattening and skewing of meander bends

5.4.1 Formulation

Let us next investigate the nonlinear planform evolution of river meanders. Our major goal is to provide a theoretical explanation of a number of field observations described in Chapter 1. In particular, we wish to answer the following questions.

- Can we clarify why single meanders develop typically the regular forms described by the fattened and skewed Kinoshita shape (Kinoshita, 1961)?
- Can we actually infer from an aerial photo what is the flow direction of a meandering river, on the ground that meanders would be invariably *upstream skewed*?
- Can we predict the observations according to which the amplitude of single bends increases up to a peak and then decreases while their migration speeds decrease monotonically (Nanson and Hickin, 1983)?
- Is the model formulated in the previous Section able to reproduce the fact that the continuous evolution of river meanders leads to neck cutoff, at least in the absence of geological constraints (like the confining valley walls of the Beaver river (Figure 11)?

To answer these questions, let us investigate the spatial-temporal evolution of a periodic sequence of fluvial meanders with the help of the theoretical model formulated above. The flow field evolves on a time scale much smaller than that characterizing the planform evolution of the channel, which is driven by the average bank erosion. In other words, the flow field is assumed to adapt instantaneously to planform changes and, hence, at any time t of the evolutionary process we can assume steady flow conditions within the channel.

Substituting from (356) into the dimensionless form of the evolution equation of the channel axis (348) yields:

$$2\nu_0 E \sum_{m=0}^{\infty} (-1)^m \frac{\partial u_m}{\partial s} = \frac{\partial \theta}{\partial t} - 2\nu_0 E \frac{\partial \theta}{\partial s} \sum_{m=0}^{\infty} \int_0^s (-1)^m u_m \frac{\partial \theta}{\partial s'} ds'. \quad (359)$$

In Section 5.3.2 we have analyzed the linear approximation of the latter equation and shown that it admits of a simplest solution consisting of a periodic sequence of sine generated meanders (equation (355)). The amplitude of these meanders grows exponentially in time within specific wavenumber ranges depending on the parameters of the problem (equation (358)). Moreover, these planform shapes migrate either downstream or upstream depending on the sub- super-resonant character of the channel. Clearly, this linear solution is no more valid as the meander amplitude

increases too much and, in particular, it fails under near resonant conditions. In the latter case, a nonlinear solution for the flow field of the type discussed in Section 4.3.2 must replace the linear solution.

Below, we restrict our attention to non-resonant conditions and consider the geometric nonlinearity embodied by the integral term appearing in the planform evolution equation (359). To account for this spatial memory effect we introduce a modified Fourier expansion of the form:

$$\theta(s, t) = \sum_{k=1}^{\infty} \theta_k(t) e^{i \lambda_k(t) s} + c.c. \quad (360)$$

The peculiar character of this expansion consists of the fact that both the coefficients θ_k and the wavenumbers $\lambda_k = (2k - 1) \lambda(t)$ depend on time. Also, note that, the expansion of equation (359) involves only odd harmonics. This is due to the fact that the unknown function θ occurs in cubic form in the planform evolution equation (359) (recall that $u_m \propto \tau \propto d\theta/ds$). Similarly, we account for the dependence of the coefficients u_m on s by similar Fourier series expansions of the form:

$$u_m = \frac{1}{\nu_0} \sum_{k=1}^{\infty} u_{mk} \theta_k(t) e^{i \lambda_k(t) s} + c.c. \quad (361)$$

Recalling that u_m satisfy the equation (311), it is easily demonstrated that

$$u_{mk} = A_m \frac{\sum_{j=1}^7 \rho_j (i \lambda_k)^j}{\sum_{j=0}^4 \sigma_j (i \lambda_k)^j}. \quad (362)$$

We can then rewrite the channel lateral migration rate (356) as

$$\zeta = \sum_{k=1}^{\infty} \zeta_k e^{i \lambda_k(t) s} + c.c., \quad (363)$$

with

$$\zeta_k = 2 E \sum_{m=0}^{\infty} (-1)^m u_{mk} \quad (364)$$

Substituting from (360) and (363) into the integro-differential equation (359), and equating terms proportional to $\exp(i \lambda_k s)$ ($k = 0, 1, 2, \dots, N$), we obtain a coupled system of N nonlinear ordinary differential equations for the amplitudes $\theta_k(t)$ ($k = 1, 3, 5, \dots, N$) and an equation for the meander wavenumber $\lambda(t)$ of the form:

$$\begin{aligned} \frac{d\theta_1}{dt} &= i \lambda \mathcal{F}_1(\theta_1, \theta_3, \theta_5, \dots) \\ \frac{d\theta_3}{dt} &= i \lambda \mathcal{F}_3(\theta_1, \theta_3, \theta_5, \dots) \\ \frac{d\theta_5}{dt} &= i \lambda \mathcal{F}_5(\theta_1, \theta_3, \theta_5, \dots) \\ &\dots \\ \frac{d\lambda}{dt} &= \lambda^2 [i (\bar{\zeta}_1 \theta_1 \bar{\theta}_1 + 3 \bar{\zeta}_3 \theta_3 \bar{\theta}_3 + 5 \bar{\zeta}_5 \theta_5 \bar{\theta}_5 + \dots) + c.c.], \end{aligned} \quad (365)$$

where \mathcal{F}_k ($k = 1, 3, 5, \dots$) are nonlinear functions of the amplitudes θ_k (Seminar *et al.*, 2001b) and, as usual, an overbar denotes the complex conjugate of a complex number. This set of equations describes the nonlinear planform development of periodic trains of river meanders starting from an initial sine-generated shape with wavenumber $\lambda(t)|_{t=0}$.

It is appropriate to note that the above formulation was first presented in a national meeting (Seminar *et al.*, 1994) and in a paper invited at an international conference (Seminar, 1995). An expansion identical to that formulated above (albeit relying on the model of Ikeda *et al.*, 1981), was employed by Edwards and Smith (2002) in a paper published one year after Seminar *et al.* (2001b) and seventeen years after Blondeaux and Seminar (1985). We will come back to the latter paper below.

5.4.2 A Landau-Stuart amplitude equation for the fundamental harmonic

Let us now consider a particular case of the system (365). Assume that all the harmonics higher than the first can be neglected. This approximation is not extreme as it may appear. Indeed, the numerical solution of the planform evolution equation that will be discussed below shows that, under sub-resonant conditions, even at the late stage of meander development, third harmonics remain usually much smaller than the fundamental. Under these conditions, the full system (365) reduces to the following form:

$$\frac{d\theta_1}{dt} = i\lambda \left[\zeta_1 \theta_1 - \frac{1}{2} \zeta_1 \theta_1^3 - \frac{1}{2} (\zeta_1 \theta_1^2 \bar{\theta}_1 + c.c.) \right], \quad (366)$$

$$\frac{d\lambda}{dt} = \lambda^2 [i \bar{\zeta}_1 \theta_1 \bar{\theta}_1 + c.c.]. \quad (367)$$

The reader will note that (366) bears a superficial similarity with the classical Landau-Stuart (LS) equation governing the weakly nonlinear evolution of a linear Fourier mode excited by the instability of steady basic states in a neighborhood of the critical conditions (see equation 534(I)) in Section 6.5.1(I)). However, (366) has a few distinct features:

- the second and fourth terms in the right-hand side of (366) are not present in Landau-Stuart equation;
- furthermore, the coefficients of the linear and cubic terms of (366) depend on time through their dependence on the fundamental wavenumber λ and on the coefficient $\zeta_1(\lambda)$. This feature arises from the integrodifferential nature of the original planform evolution equation. Indeed, the history of channel deformation is accounted for through the progressive channel elongation associated with the temporal development of the fundamental wavenumber λ .

5.4.3 Can meanders of permanent form exist?

Equation (366) can be used to investigate whether meanders of permanent form exist. Such meanders, migrating in the longitudinal direction with no growth or decay in the absence of geological constraints have never emerged from the available field observations. We now show that equation (367) strongly tends to exclude this possibility.

Note that the above issue was first raised by Parker *et al.* (1983), who found a nonlinear solution of permanent form in a neighborhood of the wavenumber characterized by vanishing growth rate. However, such a solution was later shown to be unstable by Parker and Andrews (1986). The theoretical model described in Section 5.4.1 allows us to revisit this problem fairly easily using the LS-type amplitude equation. In fact, subtracting the complex conjugate of (366) multiplied by θ_1 from (366) multiplied by $\bar{\theta}_1$, we find:

$$2 \frac{d}{dt} |\theta_1|^2 = i\lambda (\zeta_1 - \bar{\zeta}_1) |\theta_1|^2 (2 - |\theta_1|^2), \quad (368)$$

where $|\theta_1|$ denotes the modulus of the complex number θ_1 . This equation clarifies that, in order to achieve equilibrium, the meander amplitude, expressed in terms of the real quantity $|\theta_1|$, should

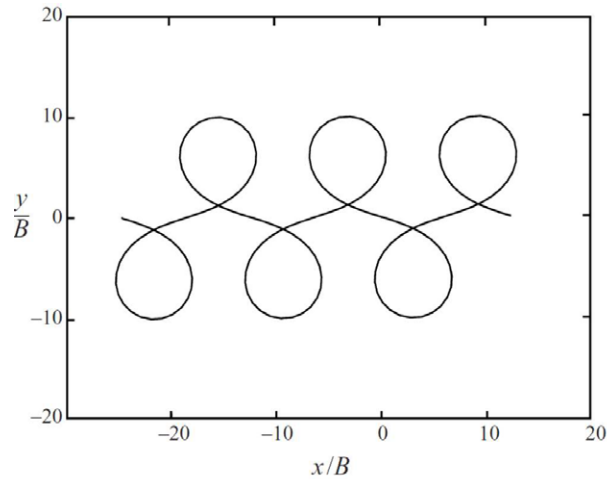


Figure 92. Theoretical shape predicted by equation (366) for the finite amplitude equilibrium of single harmonic meanders, such that $|\theta_1| = \sqrt{2}$ (reproduced from Seminara *et al.*, 2001b).

reach the value $\sqrt{2}$. Figure 92 shows the shape that such a *meander in equilibrium* would attain. Such a shape is obviously non-realistic as a train of sine-generated meander bends would undergo cutoff before reaching this stage. Moreover, equilibrium is incompatible with the lengthening process predicted by equation (367), that would continue even if $|\theta_1|$ had reached a constant value.

This result relies on the assumption that the dominant contribution to meander shape arises from the fundamental in our expansion (360) and is strongly suggestive of the absence of any equilibrium configuration of meander evolution in the absence of geological constraints. However, as pointed out by Seminara *et al.* (2001b), “*it does not conclusively rule out the possibility that equilibrium might be achieved through the development of more complex shapes with higher harmonics playing a non-negligible role*”. The numerical experiments discussed below have not shown any such tendency.

5.4.4 General features of the planform development of river meanders in the sub-resonant and super-resonant cases

Seminara *et al.* (2001b) investigated the short-term planform evolution of meandering rivers solving numerically the differential system (365), neglecting the contribution of harmonics higher than the fifth. Note, that by *short term* we mean that simulations have been stopped at incipient cutoff conditions.

First the sub-resonant case was investigated starting from the initial condition $Re(\theta_1) = 0.001$, $Re(\theta_3) = Re(\theta_5) = Im(\theta_1) = Im(\theta_3) = Im(\theta_5) = 0$. Results are described in Figure 93, which clearly shows that the sub-resonant evolution is characterized by two distinct phases. A linear growth of the fundamental harmonic, θ_1 , followed by a slower nonlinear growth in which the third harmonic reaches values of the order of 20 % of the fundamental, while the fifth harmonic remains always negligible (Figure 93a). As a consequence, the meander length, that increases quite slowly during the initial linear phase, grows quite rapidly in the nonlinear stage (Figure 93b). In particular, the growth of the third harmonic induces a progressive fattening and upstream skewing of the meander shape (Figure 94a). Predicted meander shapes thus develop the classical regular forms suggested by Kinoshita (1961). This is not surprising as the expansion (360), truncated at second order, coincides with Kinoshita shape. The fact that spatial harmonics higher than the third do not play a significant role as suggested by Kinoshita (1961), is simply due to the fact that neck cutoff typically occurs before higher harmonics have had a chance to amplify. Under sub-resonant conditions meanders are skewed upstream and migrate downstream. The migration speed decreases monotonically throughout meander development and tends to vanish prior to

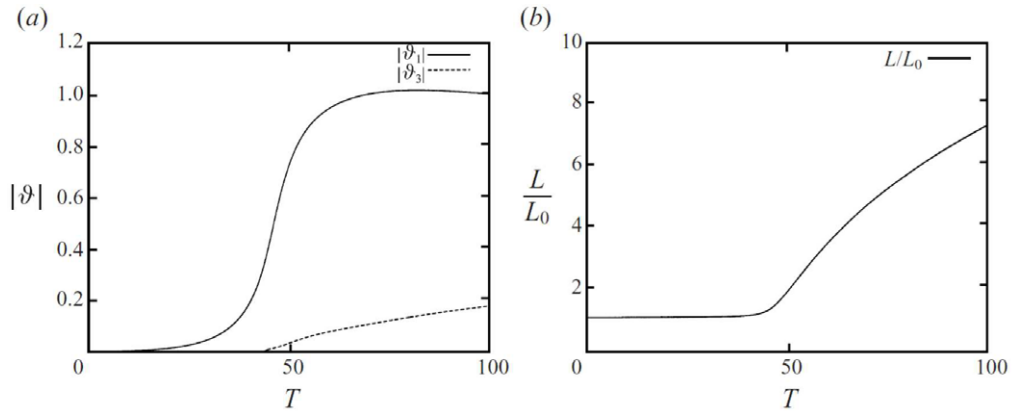


Figure 93. Time evolution of (a) the amplitude of the first and third harmonics, and (b) of the normalized intrinsic wavelength under sub-resonant conditions ($\beta = 10 < \beta_R$, $\tau_* = 0.2$, $d_s = 0.01$, plane bed conditions). The T time variable is defined as $T = 2Et/\nu_0$ (reproduced from Seminara *et al.*, 2001b).

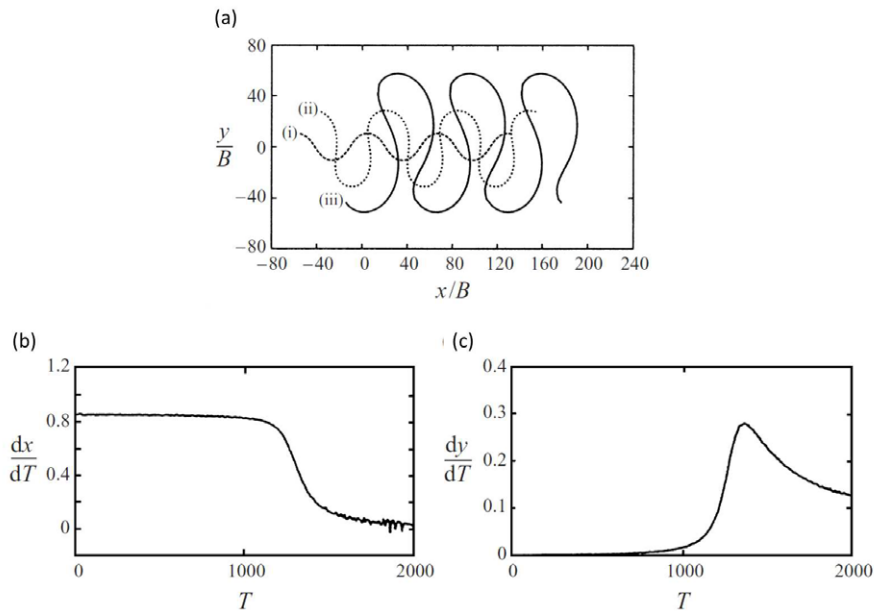


Figure 94. (a) Sub-resonant evolution of periodic meanders; (b) downstream migration rate; (c) bend amplification as functions of dimensionless time T of meander evolution ($\beta = 10 < \beta_R$, $\tau_* = 0.2$, $d_s = 0.01$, plane bed conditions) (reproduced from Seminara *et al.*, 2001b).

cutoff (Figure 94b). On the contrary, the rate of bend amplification does not show a monotonic behavior, it grows to a peak and then slowly decays (Figure 94c). Both these results agree with field observations (e.g. Nanson and Hickin, 1983).

A different scenario has been found in the super-resonant case. Figure 95a shows the planimetric development of meander shape for the same set of parameters employed for the sub-resonant case, except for the width ratio which now exceeds β_R . In this case meanders are skewed downstream and migrate upstream. This result differs drastically from that emerging from the model of Ikeda *et al.* (1981), which is shown in Figure 95b.

This feature is associated with a variation of the phase of the third harmonics relative to the fundamental as explained in Seminara *et al.* (2001b). More precisely, classical upstream skewing

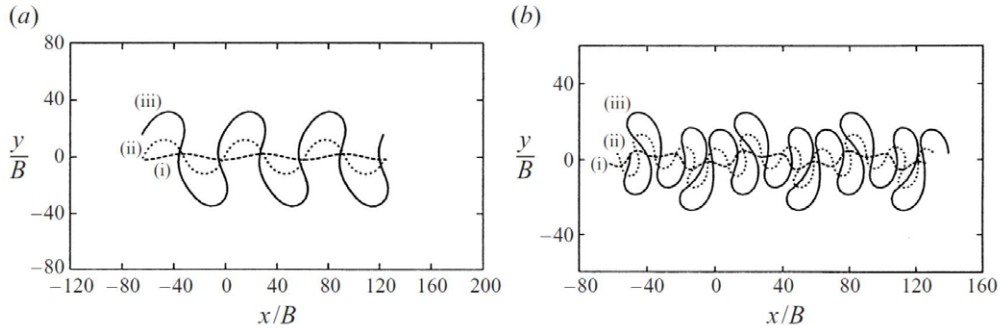


Figure 95. (a) Super-resonant evolution of periodic meanders. (b) Ikeda *et al.* (1981) model ($\tau_{*0} = 0.2$, $\beta = 30$, $d_s = 0.01$, plane bed conditions, reproduced from Seminara *et al.*, 2001b).

occurs when the phase lag lies in the range $(0, \pi)$ whereas values in the range $(\pi, 2\pi)$ determine downstream skewing. Downstream skewing is often observed in nature, as shown in the examples reported by Lanzoni and Seminara (2006) and reproduced in Figure 96.

Can the morphodynamic regime change during the planform evolution process?

Luchi (2009) investigated if the channel lengthening associated with the planform evolution of meandering rivers prior to neck cutoff may drive a transition of the morphodynamic regime of alluvial single-thread channels. Indeed, channel lengthening implies a progressive increase of channel sinuosity, hence a continuous variation of the down-channel slope at the timescale of planform evolution. As a consequence, the reach-averaged characteristics, that affect both β and β_R , vary and may induce a variation of the regime of morphodynamic influence. Channel width also adjusts to gradual variations of channel slope. This effect has so far been neglected (but see the recent developments discussed in Section 5.6).

In order to ascertain whether the above mechanism do lead to variations of the morphodynamic regime, Luchi (2009) performed a series of simulations of planform evolution from incipient meander formation to cutoff. Input data were the reference dimensionless parameters of the data set already considered in Section 4.4.5, concerning gravel bed rivers. Results of the simulations are plotted in Figure 97. Essentially, almost half (49%) of the examined river reaches kept within the initial morphodynamic regime (either sub-resonant or super-resonant), the remaining transitional streams almost invariably moved from the super-resonant to the sub-resonant regime due to the progressive decrease of β and increase of β_R as channel elongates and its slope decreases.

Compound and multiple loops

Another peculiar feature of the super-resonant case is the formation of compound meander shapes *prior to neck cutoff*. This is a consequence of the faster amplification of higher harmonics, a mechanism that was pointed out by Seminara *et al.* (2001b) and clarified by Luchi (2009) (but see also Zolezzi *et al.*, 2009). The role of the fifth harmonic θ_5 usually remains negligible before cutoff. However, relatively rapid growth of θ_5 is observed to occur when β approaches β_R . The mechanism responsible for this growth can be explained analyzing the effects of channel elongation. Indeed, at the beginning of each simulation, the fundamental meander wavelength coincides with the linearly most unstable meander wavelength for the initial values of the relevant parameters, whilst the third and fifth harmonic fall within the linearly stable range, i.e. they are associated with shorter and non-amplifying meander modes. As the meander elongates, the wavelengths associated with the third and fifth harmonics progressively increase and move toward the linearly unstable range. The relatively fast growth of θ_5 starts around $T/T_{cutoff} \simeq 0.8$, when β approaches β_R . This is illustrated in Figure 98

We may conclude this section noting that the theoretical framework built up above, which accounts for the geometric nonlinearities intrinsic in the meander deformation process, appears

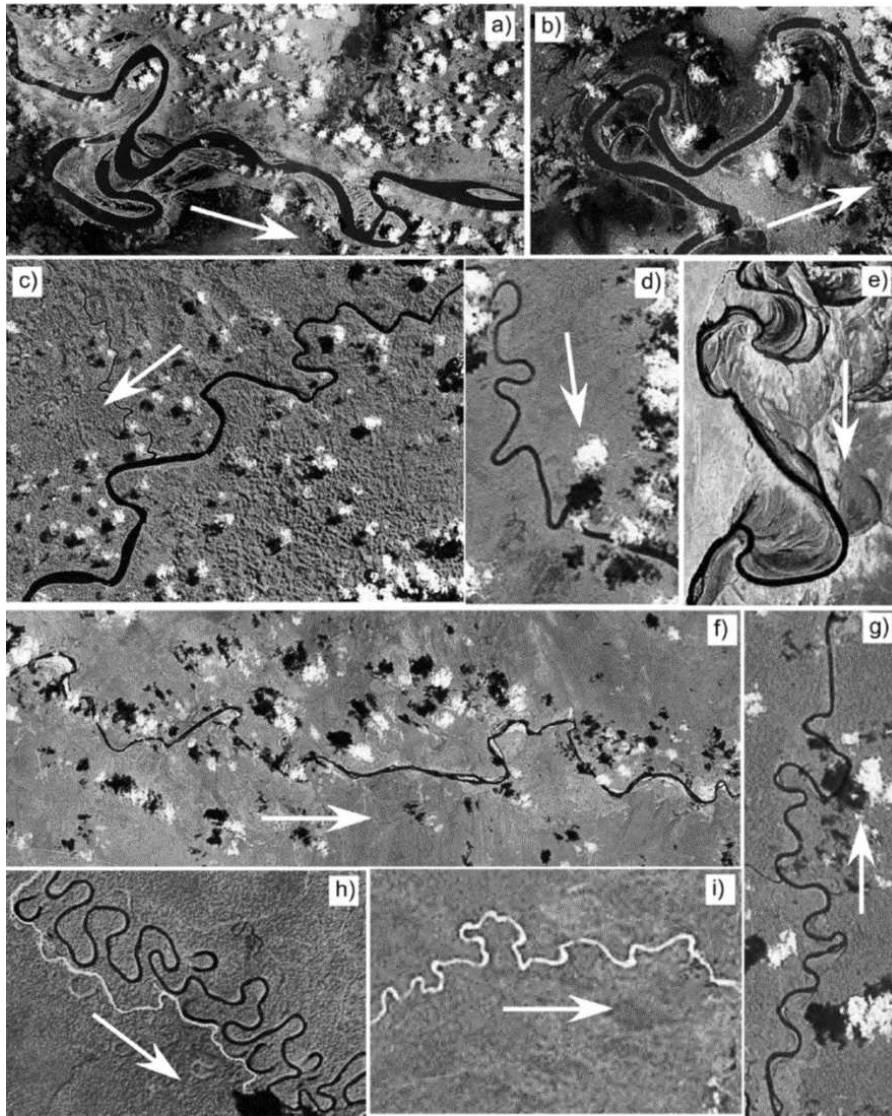


Figure 96. A few examples of planform patterns of meandering rivers exhibiting downstream skewed meandering loops. The rivers are located in (a, b, c) the southern part of Papua New Guinea (in particular, (a) and (b) refer to some reaches of lower and middle Fly River), (d, h, g) the northeastern coast of Papua New Guinea, (e) Namibia, (f) Kenya, and (i) Tanzania. Landsat mosaic images (<https://zulu.ssc.nasa.gov/mrsid/mrsid.pl>). The arrows indicate flow direction (reproduced from Lanzoni and Seminara, 2006).

to give a qualitatively satisfactory insight into the mechanics of planform evolution, reproducing most of the features of the process emerging from field observations.

5.4.5 The nature of bend instability in the nonlinear regime

In Section 5.3.2 we have noted that linear bend instability is convective except, possibly, in the highly super-resonant regime.

Lanzoni and Seminara (2006) have ascertained that this property persists in the (geometrically) nonlinear regime. They solved the planform evolution equation numerically, starting from a configuration obtained by adding small random perturbations to the straight initial state. The

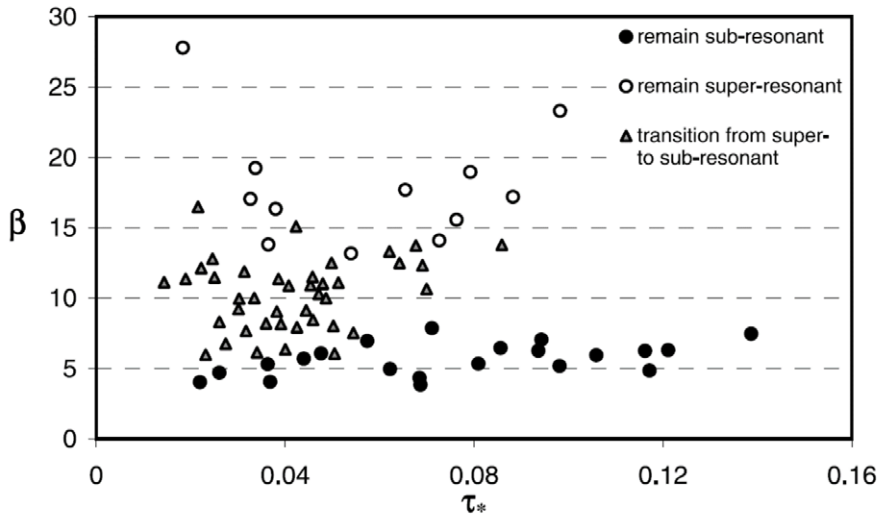


Figure 97. Transitions between sub- and super-resonant regimes, as predicted by Luchi (2009) for a wide range of conditions associated with the set of gravel bed rivers examined therein (reproduced from Figure 4.2 of Luchi, 2009).

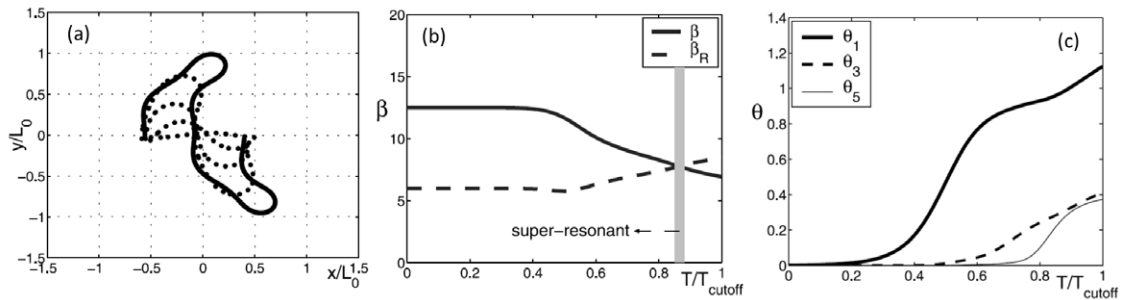


Figure 98. Meander evolution leading to (a) the formation of compound meander planforms. As the meander amplitude grows starting from super-resonant conditions, the progressive changes in the relevant parameters produce (b) the transition to the sub-resonant regime. The tendency to multilobing is due to the role of the fifth harmonic (c) which, under these conditions, attains values comparable with θ_3 before the occurrence of cutoff (reproduced from Figures 4.6 and 4.7 of Luchi, 2009).

planform was allowed to evolve freely, no constraint was imposed at the end cross-sections. The channel morphodynamics was modeled using the complete solution for flow and bed topography of Zolezzi and Seminara (2001) (Section 4.4) and both the sub-resonant and the super-resonant scenarios were examined.

Results are reported in Figure 99. They confirm the picture emerged from linear theory, including two scenarios. Convective instability leads to the development of meander groups migrating downstream for sub-resonant values of β (Figure 99a). Under super-resonant conditions, but not too large values of τ_{*0} , instability is still convective, but meander groups migrate upstream (Figure 99b). For large values of both β and τ_{*0} , and dune covered beds a transition to absolute instability is observed (Figure 99c). The physical implication of the above findings is noteworthy. In super-resonant meanders morphodynamic information propagates upstream, a result that would not emerge in the context of the uncoupled model of Ikeda *et al.* (1981), where bend instability is also convective but wave groups can only migrate downstream.

5.5. Beyond neck cutoff: Long-term evolution

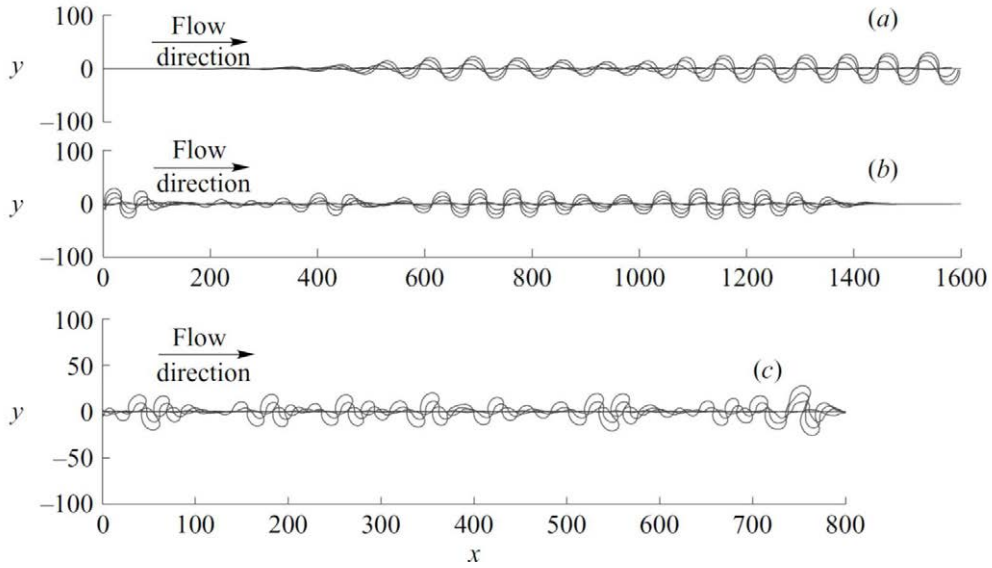


Figure 99. Numerical simulations of the nonlinear response of a river to bend instability: wave groups develop and migrate downstream (upstream) under sub-resonant (super-resonant) conditions. (a) Sub-resonant conditions ($\tau_{*0} = 0.2$, $\beta = 22$, $d_s = 0.004$, flat bed, $E = 2 \cdot 10^{-8}$): instability is convective; (b) Super-resonant conditions ($\tau_{*0} = 0.1$, $\beta = 30$, $d_s = 0.01$, flat bed, $E = 2 \cdot 10^{-8}$): instability is convective; (c) Super-resonant conditions ($\tau_{*0} = 0.7$, $\beta = 25$, $d_s = 0.005$, dune covered bed, $E = 1.85 \cdot 10^{-8}$): instability is absolute (reproduced from Seminara (2006).)

5.5.1 Further effects generating the complexity of meander patterns

On the long time scales (of the order of decades or centuries) typical of river meander evolution the geometry of planform patterns is further complicated by the strongly nonlinear effects arising from abrupt channel shortening via cutoff processes. These processes provide local mechanisms to straighten the channel axis, thus limiting the growth of the channel sinuosity σ . Two different types of cutoff are usually recognized in natural channels, chute and neck cutoffs. *Chute cutoffs* are relatively long flow diversions which occur when a meander loop is bypassed through a new channel which forms across the bar enclosed by the loop. This process occurs most frequently in wide channels with large curvature bends, high discharges, poorly cohesive, weakly vegetated banks, and high gradients (Howard and Knutson, 1984). *Neck cutoffs* occur when the local sinuosity becomes so large that adjacent loops approach each other sufficiently for the stream to abruptly choose the much shorter path which connects the upstream branch to the downstream branch directly, thus excluding the meander loop. The latter progressively transforms into a so called *oxbow lake* when sedimentation closes the ends of the abandoned loop (see Figure 100).

On the one hand, cutoff events limit the spatial evolution of meander loops, on the other hand they generate an intermittent short noise that disturbs (in space and time) the deterministic dynamics (Camporeale *et al.*, 2007). Additional nonlinear effects, that sum to those associated with the planform evolution equation (348) discussed in the previous section, are associated with spatio-temporal heterogeneities of the floodplain, resulting in a variable bank erodibility. All these nonlinearities concur to determine the wide range of bend shapes usually observed in nature. They are summarized in Figure 6 and, as already pointed out, encompass downstream and upstream skewed bends, compound bends and multiple loops.

In order to ascertain which novel features are associated with the intermittent occurrence of cutoffs a full numerical approach is required.

5.5.2 Numerical simulations

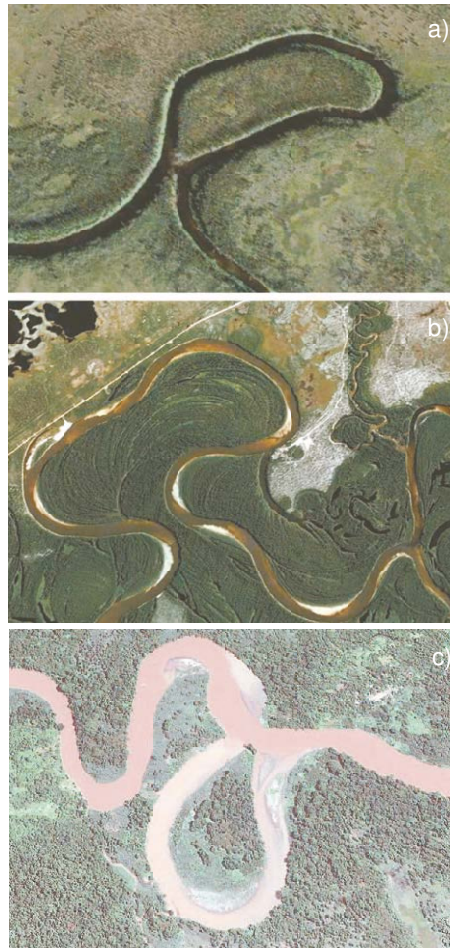


Figura 100. (a) and (b) Examples of incipient neck cutoffs. (c) Formation of an oxbow lake after a neck cutoff event.

Development of the subject

The semi-empirical model of Howard and Knutson (1984) was possibly the first attempt to performing long-term numerical simulations of meander evolution, although a previous application of Ikeda *et al.* (1981) model was performed by Parker (1982). The approach employed by Howard and Knutson (1984) was purely kinematic as the lateral migration rate was assumed to be proportional to local channel curvature. However, the Authors recognized the role played by the spatial memory of the deformation process by introducing an adjusted migration rate obtained by weighting the nominal migration rate calculated in the upstream reach. This assumption turns out to be equivalent to Ikeda *et al.* (1981) model, i.e. it accounts for downstream influence. It thus enabled Howard and Knutson (1984) to predict meandering patterns typical of the sub-resonant regime (super-resonant features emerge only if upstream influence is also accounted for).

Few years later, Howard (1992) performed long-term numerical simulations of meander evolution using the coupled version of Ikeda *et al.* (1981) model developed by Johannesson and Parker (1989). The paper of Howard (1992), along with the previous pioneering contribution of Parker (1982), represent milestones as they mark the starting point of various generations of numerical models. Note, that this model was more advanced than many of the models that will be proposed in the following years. Indeed, unlike the later contributions of Sun *et al.* (1996), Stolum (1996) and Edwards and Smith (2002), which relied on the uncoupled Ikeda *et al.* (1981) approach, it

employs a coupled morphodynamic model, hence it would have been potentially equipped to disclose the difference between sub- and super-resonant patterns. Moreover, it accounts for the interaction between the channel and the floodplain not only through the mechanism of bank erosion but also allowing for overbank sediment deposition, a feature ignored in most of the later works. This process was modeled semiempirically as a combination of settling and diffusion with rate decreasing with the distance from the channel. It is fair to say that most (though not all) observed features of the long-term planform evolution of meandering rivers *in the sub-resonant regime* were satisfactorily predicted in this paper. In particular: fattening, upstream skewing and downstream migration of meander bends in the initial phase of the process, neck-cutoffs, formation of complex loops (attributed to the role of cutoffs), oxbow lakes, overbank deposits with increasing elevation away from the channel, gradual infilling of the oxbow lakes, strongly asymmetric shape of confined meanders. Howard (1992) also noted a sensitivity to initial conditions of the meandering pattern generated by the simulations, an observation suggestive of the possible chaotic character of meander morphodynamics. We will come back to this point in Section 5.5.5.

Many of the latter results will be totally or partially replicated by simulations of other members of what may be called *the first generation of numerical modelers*, namely those who employed the morphodynamic approach of Ikeda *et al.* (1981). In particular, Sun *et al.* (1996) explored further the importance of the reduced erodibility of oxbow lake deposits in controlling confinement as well as river diversions within the *meander belt*, namely the strip of the valley within which meander activity keeps confined. Stolum (1996) also explored whether river meandering could be interpreted in the light of the new fashionable paradigm of self organization, an issue that we will analyze in Section 5.5.5.

A second generation of numerical models was based on the coupled theory of Blondeaux and Seminara (1985) and Zolezzi and Seminara (2001) (or the similar theory of Johannesson and Parker, 1989). They include the contributions of Seminara *et al.* (2001b), Lanzoni and Seminara (2006), Frascati and Lanzoni (2009) and Zolezzi *et al.* (2009). The main novel ingredient of these contributions was their ability to explore fully the implications of the morphodynamic regime of the channel on the characteristics of planform evolution, relying on the theoretical framework discussed in the last Section. Two further works (Sun *et al.*, 2001a,b) have attempted to extend the model of Johannesson and Parker (1989) such to allow for the sorting of sediments with different grain sizes. They also claim to have included the effect of migrating alternate bars on the planform evolution process. We will refer to these works in the next Chapter, where we outline the role of sorting on meander morphodynamics. Finally, let us mention the coupled model of Crosato (1990), based on the theory of Struiksma *et al.* (1985), and the later contribution (Crosato, 2007) which devoted considerable attention to computational issues.

A different viewpoint was taken by Camporeale *et al.* (2005) and Camporeale *et al.* (2007). Their goal was to ascertain whether one could envisage a universal character in the statistical long-term behavior of meandering rivers. To pursue this goal they assessed the outcomes of coupled versus uncoupled approaches in the context of long-term simulations of planform evolution. Their conclusion was that an equilibrium state does exist and is “*largely unaffected by the details of the fluid dynamic processes that govern the short-term river behavior*”. The latter statement was later challenged by Frascati and Lanzoni (2009) who showed that distinct equilibria characterize the long-term evolution of meandering rivers under sub- or super-resonant conditions.

Below, we analyze most of the above issues referring to the analysis of Frascati and Lanzoni (2009) which appears to us the most comprehensive contribution covering all the aspects emerged in the above works. Of course, we will refer to other results wherever appropriate.

The numerical approach

The channel axis is discretized through a sequence of equally spaced nodes $P_i = (x_i, y_i)$. At every time step Δt , the planform evolution of the channel axis is obtained by displacing each node in the direction orthogonal to the channel axis by an amount $\zeta_i \Delta t$. On the slow time scale associated with the planform development of the channel, bank erosion is modeled as a continuous process and described in terms of the slow temporal variable $T = Et$. Although the long-term evolution of meandering rivers produces a rearrangement of the floodplain, as a first approximation we

assume a constant value of the erodibility coefficient (say $E = 10^{-8}$, e.g. Johannesson and Parker, 1989). In other words, for the moment we neglect the heterogeneity in the spatial distribution of the erodibility of the undisturbed floodplain that would be associated, e.g. with point bar deposits or oxbow lake deposits (see Figure 100). In addition, differential changes in base level, as well as possible geological constraints are neglected. Hence, the valley gradient is assumed to be constant and no constraints at either channel end are imposed. We will discuss in Section 5.5.4 the possible role of the features neglected here. Finally, we are only able to model the formation of neck cutoffs since the mechanics of chute cutoffs are as yet poorly understood. A brief account of recent progress in modeling of the latter process is given in Section 5.7.

The flow field is evaluated using the linearized solution presented in Section 4.4.2. In particular, the longitudinal velocity is obtained from the expansions (304), (308) and the solutions (316) or (317) under sub- or super-resonant conditions, respectively. With the help of these relationships, at each time step, we are able to evaluate the local value of the lateral migration rate ζ_i of the channel axis. The local value of the dimensionless channel curvature \mathcal{C}_i is also needed to calculate the local velocity. This value is determined approximating the geometrical relationship (342) through a centered finite difference scheme, with the spatial distribution of the angle θ determined by averaging back and forth, hence:

$$\theta_i = \frac{1}{2} \left(\arctan \frac{y_{i+1} - y_i}{x_{i+1} - x_i} + \arctan \frac{y_i - y_{i-1}}{x_i - x_{i-1}} \right). \quad (369)$$

In order to reduce the computational effort required to evaluate the four convolution integrals appearing in the solution (316) or (317) for the Fourier coefficients u_m^p , a semi-analytical integration is carried out, assuming that the curvature varies linearly between two consecutive nodes. Moreover, taking advantage of the exponential decay of the function to be integrated, the integration is truncated when the function is smaller than a given tolerance (say 0.0001), with a further significant reduction of the computational time. A predictor-corrector method (Crosato, 1990) is used to improve the accuracy and effectiveness of the time marching procedure. The forward time step is performed using for each node the normalized migration rate obtained as the average of its values at the previous and present time steps. The step size ΔT is controlled by requiring that

$$\Delta T \leq \epsilon_{step} \frac{\Delta s}{\Delta U_{max}}, \quad (370)$$

where Δs is the distance between two consecutive nodes, and ϵ_{step} is an empirical parameter defining the threshold between stable and unstable computations. The choice of this parameter (= 0.005), is made through preliminary simulation tests. As the channel migrates, the distance Δs between individual nodes may increase or decrease. A standard cubic spline interpolation is used to re-mesh the points uniformly after each time step. Moreover, new nodes are periodically added to maintain the size of the spatial step in the range 0.8 – 0.9. A discussion about the effects of interpolation and node remesh, as well as the effects of the algorithm employed to compute the curvature is reported in Schwenk *et al.* (2015).

At each time step, the presence of potential neck cutoffs is detected by controlling whether the dimensional distance between the i -th node P_i and the $(i+k)$ -th nodes P_{i+k} (with $1 < i + k < N$) approaches some critical value (say $2.2B_0$). When such a distance is reached, all the points P_{i+j} , $j = 1, k$, representing the abandoned channel loop, are removed. To recognize the nodes (say P_i and P_{i+k}) at distance smaller than the selected critical value, Frascati and Lanzoni (2009) used a matrix algorithm proposed by Camporeale *et al.* (2005) that allows a significant reduction of the computational effort. Furthermore, in order to avoid the presence of physically nonrealistic cusp-like regions with very high curvature at a reconnection, they chose to remove also three nodes upstream of P_i and three nodes downstream of P_{i+k} . Such somehow artificial procedure is justified by the fact that the rapid smoothing of sharp bends is a well-known phenomenon observed in meandering rivers at cutoff (see, e.g. Figure 100).

5.5.3 Results of numerical simulations: sub- versus super-resonant

The Figure 101 shows two typical examples of the simulated planform configurations obtained by Frascati and Lanzoni (2009) under initially sub-resonant (Figure 101a) or super-resonant (Figure 101b) conditions, starting from a configuration obtained adding a small random perturbation to the initial straight state.

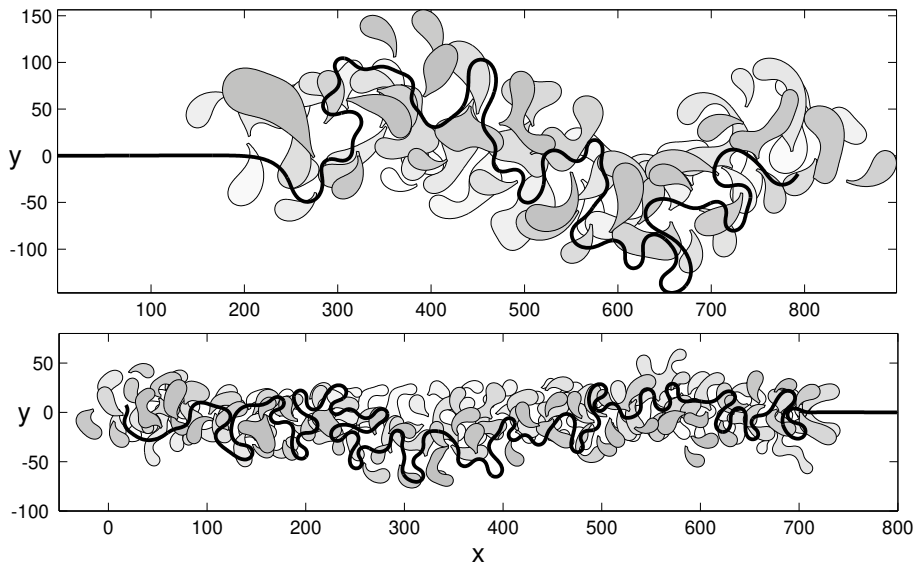


Figure 101. Examples of the long-term ($2 \cdot 10^6$ time steps) planform evolution of a meandering river, computed starting from a straight channel subject to random perturbations. (a) Sub-resonant conditions: $\beta = 8.5$; $\tau_{*0} = 0.35$; $d_s = 0.0007$. (b) Super-resonant conditions: $\beta = 22.0$; $\tau_{*0} = 0.6$; $d_s = 0.0025$. Both simulations have been carried out setting $E = 1.5 \cdot 10^{-8}$ and assuming a dune-covered bed. The age of oxbow lakes is measured by a grey-scale. Darker oxbows are the most recent ones, whiter oxbows are the oldest ones.

The numerical results confirm the picture that emerged from the theoretical analysis described in the previous section. Bend instability turns out to be generally convective and the group velocity of bend perturbations changes sign as the resonant conditions are crossed. This implies that, under sub-resonant conditions, non-persistent initial perturbations develop into wave groups which amplify and migrate downstream, leaving the upstream reach unperturbed, i.e. recovering the initial straight configuration (Figure 101a). Conversely, under super-resonant conditions wave groups migrate upstream and the initially straight planform is recovered downstream (Figure 101b). As demonstrated by Lanzoni and Seminara (2006), absolute instability whereby wave groups migrate upstream, but spread over the entire domain, can occur under super-resonant conditions, for dune-covered beds and fairly high values of the Shields stress (see Figure 99c).

It is also important to observe that the mathematical model employed by Frascati and Lanzoni (2009) is able to reproduce most of the bend shapes observed in nature (Figure 6) without invoking changes in external controls such as formative discharge, heterogeneities in the erodibility of the flood plain, nonlinearities of the flow field and bed topography. The Figure 102 summarizes the typical patterns emerged from numerical computations. The similarity with natural forms is remarkable. Simple bends (upstream or downstream skewed), compound bends, and multiple loops (the cumuliform shapes observed by Howard, 1992) are correctly generated by the model. Particularly remarkable is the ability of the model to reproduce the formation, often observed in nature (Brice, 1974; Hooke and Harvey, 1983), of a compound bend evolving from a simple bend which develops a curvature reversal along the bend itself (Figure 102c-f). This ability is strictly related to the transition from super-resonant to sub-resonant conditions, as discussed in Section 5.4.4 (recall Figure 98). In other words, *the formation of compound bends does not need the locking of the system around a resonant state triggered by a neck cutoff event*, as suggested by the numerical simulations of Howard (1992) and Sun *et al.* (2001b). Similarly, heterogeneity of

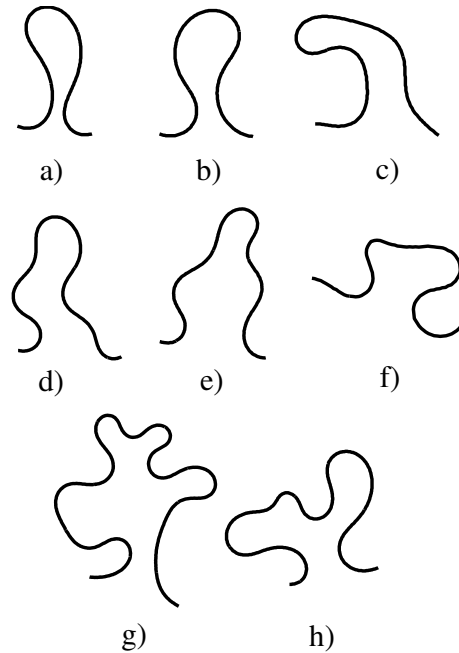


Figure 102. Examples of the shapes of meandering bends generated synthetically using the ZS linearized flow field model. (a) Upstream-skewed bend, (b) downstream-skewed bend, (c)-(f) compound bends, and (g,h) multiple loops. Flow is from left to right, (reproduced from Frascati and Lanzoni, 2009).

bank erodibility, invoked by Sun *et al.* (1996) to explain multiple loops (see Section 5.5.4), is not actually needed to reproduce these bend shapes, although it may surely contribute to causing the process.

5.5.4 Effects of floodplain heterogeneity

Various aspects of floodplain heterogeneity can be identified. The first consists of mechanisms that make the erodibility of the floodplain much smaller than the erodibility of the point bar deposits. Vegetated floodplains, as well as meandering rivers confined by valley walls consisting of rocky hillslopes or earlier terraces, provide common examples. A most striking one is shown in Figure 103 (but recall also Figure 11) and refers to the Beaver River (Saskatchewan province, Canada). The clear effect of confinement is to give rise to a peculiar meander shape, sometimes called *rectangular meander* (Sun *et al.*, 1996).

This feature was described as a characteristic of constrained meandering rivers as early as Allen (1985) and was first predicted in the simulations of the planform evolution of confined meandering rivers by Howard and Knutson (1984) and Howard (1992). Similar simulations were performed by Sun *et al.* (1996). These works were able to reproduce the shape of confined meanders (Figure 103) assuming a value of floodplain erodibility much smaller than the erodibility of point bar deposits. Simulations showed that a pattern consisting of a train of regular sine generated bends developed in the initial stage and evolved into a sequence of *Beaver-type* meanders when the lateral migration led the channel to impact on the highly more resistant floodplain sediments. It is precisely the laterally impeded development of the channel that causes the appearance of the *rectangular* meander shape. Note that predicted meander loops were upstream skewed and concave upstream.

A second aspect that has received considerable attention (Howard, 1992; Sun *et al.*, 1996; Frascati and Lanzoni, 2009) is the heterogeneity driven by the formation and filling of oxbow lakes. In particular, Sun *et al.* (1996) were interested in ascertaining whether their model would support the concept of *meander belt*, namely the existence of a strip of the valley within which meander

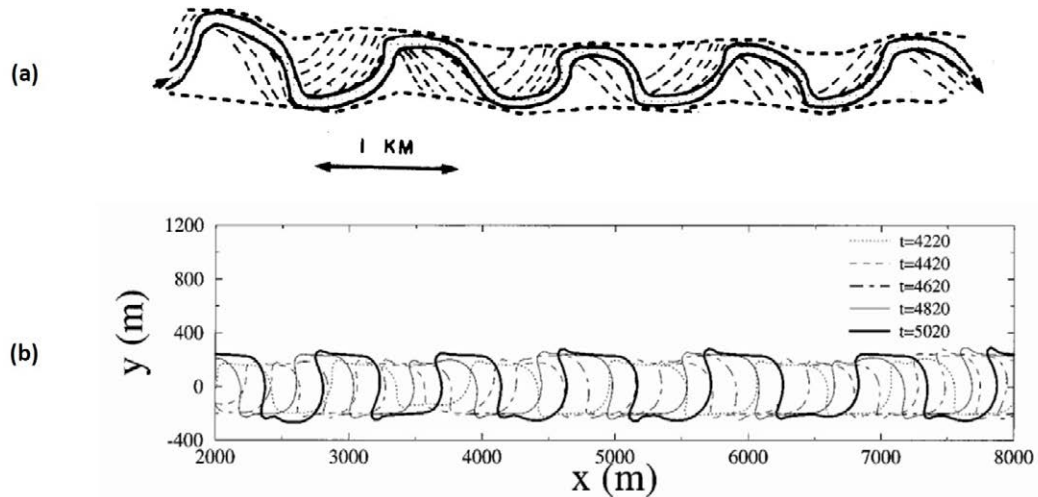


Figure 103. Results of numerical simulations of planform evolution of meandering rivers under conditions of erodibility of the floodplain much smaller than the erodibility of the point bar deposits (modified from Howard and Knutson (1984)(a) and Sun *et al.* (1996)(b), respectively).

activity would keep confined. This idea was introduced by Jefferson (1902), who suggested that the width of the meander belt would be about 18 times the width of the river. Later, Fisk (1952), based on his field observations of the Mississippi River, emphasized the importance of the reduced erodibility of oxbow lake deposits in controlling confinement as well as river diversions within the belt. The assumption that oxbow lake deposits are actually responsible for the formation of meander belts was first explicitly formulated by Allen (1965), but the issue has continued to be investigated for decades for its obvious stratigraphic relevance and its implications for the development of oil reservoir models.

Sun *et al.* (1996) examined the problem adopting two different deposition scenarios. In the former case, they modeled the formation of oxbow lakes, their filling and consolidation as instantaneous. Simulations showed that the continuously generated oxbow lakes merge into resistant barriers distributed along the river. However, no stable, well-defined meander belt was identified. The latter deposition scenario allowed for a significant delay between the formation of an oxbow lake, its filling and consolidation into a resistant material. Indeed, as pointed out by Gagliano and Howard (1983), filling an oxbow lake can take as long as centuries to thousands of years. Sun *et al.* (1996) claim that allowing for such a delay bears an important consequence for meander belts. Indeed according to their simulations it turns out that recently formed oxbows are easily eroded when neighboring bends migrate into them, whereas abandoned loops located at great distance from the river have more time to consolidate. This mechanism opposes the attempts of the river to migrate far from its present course and leads to the development of a fairly stable meander belt.

The role of floodplain heterogeneity was also investigated by Bogoni *et al.* (2017) with the help of the model of planform evolution developed by Frascati and Lanzoni (2009). Figure 104 summarizes the migration history of the river planforms based on six scenarios obtained with different choices for the erodibility of the pristine floodplain, of scroll bar units and infilled oxbow lakes. The first scenario concerns a floodplain with an erodibility that is not modified by the river evolution, i.e. the river has no memory of its own past configurations. The second scenario assumes the formation of oxbow lakes that, after their disconnection and infilling, develop a resistance to erosion larger than that of the pristine floodplain, while scroll bars are assumed not to modify floodplain erodibility. The third and the fourth scenarios concern the formation of scroll bars

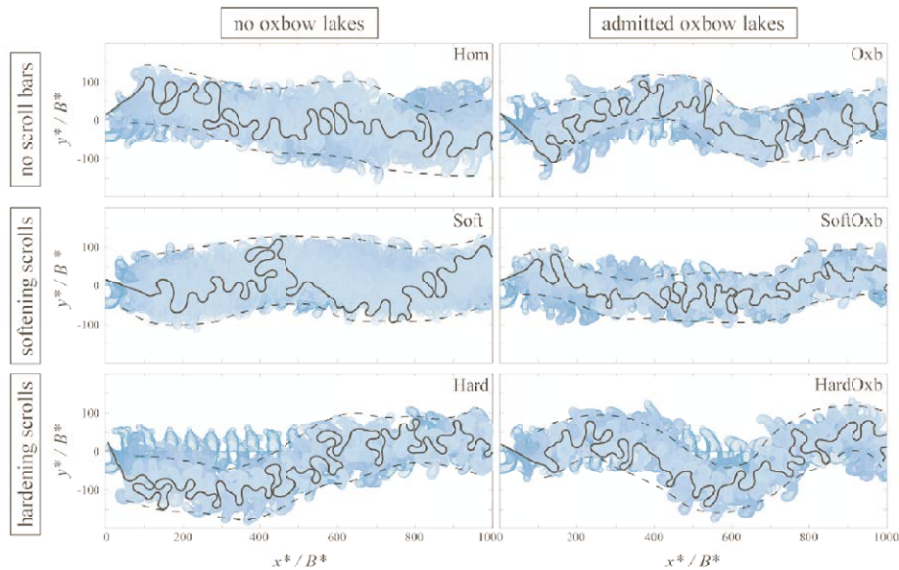


Figure 104. Examples of migration history of river planforms, simulated for six erodibility scenarios by Bogoni et al. (2017). The dimensionless parameters used for the initial straight configuration are $\beta = 20$, $\tau_{*0} = 0.7$; $d_s = 0.0005$. Darker regions are older, lighter are younger. Dashed lines provide a qualitative view of the active meander belt width (reproduced from Bogoni et al., 2017).

which are more erodible than the surrounding floodplain (softening scroll bars). Oxbow lake effects are either excluded or included. The latter two scenarios might roughly correspond to rivers which flow over fine sediment deposits which, during the falling stage of floods, allow coarser sediment to settle on the point bars at inner bends. These coarse sediment deposits (arranged in layers) increase scroll bar erodibility and this effect is assumed to dominate over that given by fine layers deposited during the falling flood stage. Alternatively, one may attempt to mimic the dynamics of rivers where bank erosion develops on a time scale smaller than that required by the strengthening actions of soil compaction and vegetation encroachment at point bars. The fifth and the sixth scenarios assume that scroll bars are less erodible than the surrounding floodplain. The river then migrates more slowly when it flows across them. Also in this case, oxbow lake effects are either excluded or accounted for. These two scenarios might roughly correspond to a river which flows through floodplain deposits formed by relatively coarse material and deposits mainly fine sediment on the point bars. The effect of the finer layers of the scroll bar on bed erodibility is assumed to be stronger than that due to the coarser layers. Alternatively, the scenarios may mimic the rapid formation of a vegetation cover that stabilizes the point bar, leading to a bank strengthening as the river impinges again on that area.

To summarize, numerical simulations (Sun *et al.*, 1996; Bogoni et al., 2017) confirm that variability in erosional resistance affects the generation of irregular planform patterns of meandering rivers. The final channel planform, as well as the structure of the meander belt turn out to be highly sensitive to floodplain variations in the erosional resistance. The hardening scenarios whereby oxbow lakes and/or scroll bars are less erodible than the pristine floodplain generate a wavy meander belt of about 50–60 river widths. The remaining two scenarios (the homogeneous case and the softening scenario without oxbow lakes) exhibit a meander belt that is nearly straight and has a width of about 90–100 channel widths.

The introduction of heterogeneities in the modelling framework also improves the overall similarity between simulated and observed planforms. This is discussed in detail in Bogoni et al. (2017), where a statistical comparison is performed among natural river shapes and simulated planforms.

5.5.5 Long-term meander evolution in the light of the modern paradigms of complexity

Parallel to the physically based literature discussed above, since the early 1990s, various contributions have attempted to ascertain whether the dynamics of river meandering can be interpreted in the light of modern paradigms of the theory of dynamical systems. The questions they wished to answer can be summarized as follows: Are meanders fractal forms? Is meandering a chaotic process? Can one detect the signs of self-organized criticality (SOC) in meandering dynamics? Answering these questions requires some technicalities that cannot be discussed in detail here. The reader with no previous knowledge of the notions of fractals, chaos and SOC are referred to the wide literature on the subject. Just few suggestions: at undergraduate level, an entertaining introduction can be found in Strogatz (1994), at higher level Bar-Yam (1997) and Kantz and Schreiber (1997). A fractal theory of river networks is the subject of the treatise by Rodriguez-Iturbe and Rinaldo (2010).

Below, after a brief introduction to the notions of fractals, chaos and SOC we will limit ourselves to provide overview of results of applications of the above notions to answer the questions listed above. The reader is also referred to the paper of Seminara and Bolla Pittaluga (2012), where the same issues are discussed in the hopefully entertaining form of a Socratic dialogue between supporters of opposite views, namely a reductionist versus a holistic view of meandering processes.

Are meanders fractal forms?

Fractals are geometrical objects investigated by the branch of Mathematics called *Topology*. Let us focus on *fractal curves*: they are topologically one-dimensional objects. However, in simplest terms, their *fractal* nature implies that they are too detailed to be one-dimensional, but too simple to be two-dimensional (Harte, 2001). They are strange objects, which are characterized by a so called *fractal dimension*, that is larger than one but smaller than two. The fractal dimension provides a measure of the space-filling capacity of the fractal pattern. These concepts can be generalized to higher dimensions, so that one may define a fractal surface, characterized by a fractal dimension larger than two but smaller than three, and so on.

To clarify the above statements, let us consider a classical example of fractal curve, the *Koch snowflake* (Figure 105). This object can be constructed by the following iterative procedure. Consider an equilateral triangle, with side length equal to one (iteration 1). Then subdivide each side into three segments of equal length ($1/3$) and replace the middle segments by two further oblique segments with the same length, chosen such that, along with the middle segment, they would form an equilateral triangle with side length $1/3$ (iteration 2). The procedure can be repeated ad libitum and, as the number of iterations tends to infinity, the geometric object emerging from the above construction is a Koch fractal. This example exhibits some of the characteristics of fractals. In particular: fractals are self-similar objects, which display similar patterns as one looks at the object in increasing detail; moreover, they are usually nowhere differentiable.

A Koch fractal is still a line of the Euclidean space, i.e. a geometrical object with a topological dimension of 1, but the length of the fractal line between any two points is infinite. Measuring this length with the help of a *finite stick* then leads to a result depending on the length of the stick. This is clarified in Figure 105 where the length L of the fractal line is clearly dependent on the order n of the iteration, i.e. on the length of the unit segment $\ell(n)$, which may be interpreted as the length of the measuring stick. This apparent paradox was resolved by Benoit Mandelbrot, in a paper (Mandelbrot, 1967) with a suggestive title: *How Long Is the Coast of Britain?*. The idea of a *fractal dimension* emerged there is rooted in the earlier works of great mathematicians of the past, including Weierstrass, Cantor, Poincare, Koch, Sierpinski. It was formally introduced in the early 1900s by Hausdorff (Hausdorff, 1919) and Besicovitch (Besicovitch, 1929; Besicovitch and Ursell, 1937).

In very simple terms, the fractal dimension D of a line can be defined as follows:

$$L = a \ell^{1-D}, \quad (371)$$

where L is the length of the line obtained by approximating the actual line by a sequence of segments of length ℓ and a is a constant. Fractality is suggested by the existence of a sufficiently

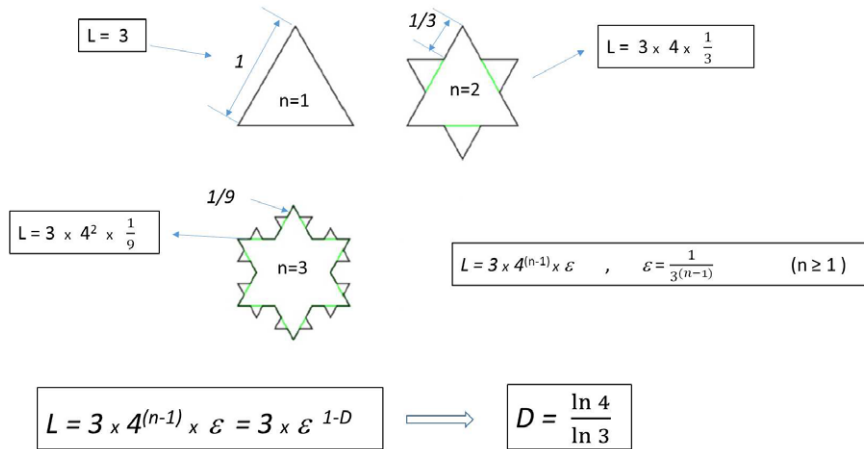


Figure 105. The sketch shows the first three steps of the iterative procedure leading to the construction of the Koch snowflake fractal curve. The length of the curve L increases as the number of iterations n increases. The dependence of L on the length $\ell(n)$ of each segment at the n -th iteration, allows one to introduce the notion of fractal (or Hausdorff-Besicovitch) dimension D

wide range of values of ℓ where a straight line with nonzero, non-integer slope fits closely the pattern of data obtained by plotting $\log L$ against $\log \ell$. Figure 105 shows that the Koch snowflake is indeed a fractal curve with fractal dimension $D = \ln 4 / \ln 3 = 1.2619$.

The irregularity of channel planforms has motivated the longstanding interest of geomorphologists to identify some objective measure of this property. In particular, self-similarity of meander planforms was recognized since the early work of Leopold and Wolman (1960). Fractality of meander centerlines was first suggested by Mandelbrot (1982). Various attempts to substantiate this suggestion on the basis of field observations have then appeared, starting from Snow (1989) with the following contributions of Nikora (1991), Montgomery (1996) and Stolum (1996). In particular, Nikora (1991) analyzed the topographic maps of 41 single thread river reaches in Moldavia and concluded that six reaches were non-fractal, whilst the remaining 35 reaches could be interpreted as fractals over less than an order of magnitude, with fractal dimension ranging between 1.04 and 1.33. Moreover, fractal dimension and channel sinuosity turned out to be highly correlated. Montgomery (1996) examined 46 reaches from 42 alluvial and non-alluvial perennial rivers of North America, characterized by average sinuosities in the range 1.2 – 2.7, various climates and degrees of channel confinement. His main results can be summarized as follows: (i) the average fractal dimension of alluvial rivers was 1.28; (ii) the eight incised meanders were non fractal; (iii) the high correlation between fractal dimension and channel sinuosity was confirmed; (iv) fractal dimension was uncorrelated to channel width. Finally, Stolum (1996) found fractal dimensions in the range of 1.18 – 1.47 over 1.2 – 2.3 orders of magnitude for five reaches of the Central Amazon river, long enough to justify fractal analysis with minimum external constraints ¹.

Stolum (1996) also attempted to ascertain the fractal behavior of meander planforms on the basis of numerical simulations performed with the help of the model of Howard (1992). The fractal dimension of the numerical output was 1.28 over two orders of magnitudes. However, Montgomery (1996) noted that, in his sinuosity versus fractal dimension plot, the point corresponding to the simulation of Stolum (1996) result was a clear outlier, due to the excessive sinuosity and *insufficient intricacy* of the numerical outputs.

From the above picture, one might be tempted to conclude that meandering patterns are *likely* to be fractal over fairly short scales (say of the order of 100 channel widths, see Seminara and

¹ The scaling found by Stolum (1996) was actually anisotropic. This suggests that meander planforms are self-affine forms (see Rodriguez-Iturbe and Rinaldo, 2010).

Bolla Pittaluga, 2012). However, the reader must be warned on the limits of the latter conclusion. They depend on an intrinsic conflict arising when attempting to apply fractal analysis to river patterns. On one hand, the length of the analyzed river reach should be short enough to minimize the impact of non-homogeneities (due, e.g. to variations of flow discharge, sediment size, sediment supply, presence of tributaries), on the other hand it should be long enough to make a fractal analysis significant. It is uncertain whether the short length over which fractality seems to emerge is sufficient to justify the above conclusion. These problems, in particular the issue of whether one may actually identify morphologically homogeneous river reaches were discussed by Nikora (1991).

Is meandering a chaotic process?

Chaos is one of the great discoveries of the last century and its main feature has become popular through the so called *butterfly effect*. In 1972 Edward Lorenz, a meteorologist of M.I.T., presented to the American Association for the Advancement of Science in Washington, D.C., the paper: *Predictability: Does the flap of a butterfly's wings in Brazil set off a tornado in Texas?* The major concept implied by this apparently paradoxical question is the main characteristic of chaotic processes, namely their *sensitivity to initial conditions*. A small change in the initial conditions of a chaotic dynamical system (the flapping wing) moves the system dynamics into a significantly different trajectory. As a consequence, since initial conditions are most commonly known with some uncertainty, the exponential divergence of the trajectories issuing from slightly different initial conditions, implies that, in spite of the deterministic character of the dynamical system, one is unable to predict its state for sufficiently large times. This is not the only characteristic of chaotic dynamical systems (Devaney, 1989), but it is the feature which bears the most important practical consequences.

Ascertaining the possibly chaotic behavior of the planform evolution of meandering channels on the basis of field data would require sufficiently long records of planform changes over historical timescales, for sufficiently long, yet homogeneous, river reaches. Although some good historical data are now available for some highly mobile channels (Hooke, 2004; Gautier *et al.*, 2007; Schwenk *et al.*, 2015), they do not encompass a sufficiently long observation period for chaotic analysis to be feasible. For these reasons a different approach, relying on the use of time series obtained from physics-based mathematical models, was employed by Frascati and Lanzoni (2010). Note that a *necessary (but by no means sufficient) condition for a dynamical system to be chaotic is its nonlinearity*. This condition is satisfied by meander evolution which is known to be affected by the, albeit fairly weak, geometric nonlinearities associated with the deformation process, as well as by the strong nonlinearity arising from the abrupt channel shortening events due to cutoff processes and in the case of sharp bends, by hydrodynamic nonlinearities.

Figure 106a shows the long-term synthetic planform evolution generated by Frascati and Lanzoni (2010) for subsequent chaotic analysis. Oxbow lakes generated during the entire simulation are highlighted. Moreover, Figure 106b plots the intrinsic length of oxbow lakes versus the time of cutoff occurrence. Results of the simulations, that provide a continuous description of the dynamics of the system, can be transformed into discrete maps of the forms (Frascati and Lanzoni, 2010)

$$\mathbf{x}_{i,n+1} = \mathbf{F}(\mathbf{x}_{i,n}) \quad (i = 1, 2, 3, \dots N). \quad (372)$$

Here, $\mathbf{x}_{i,n}$ is a 2D vector describing the position of the projection of the i -th point of the channel axis onto a horizontal plane at the n -th time step ($T = n \Delta T$). The spatio-temporal patterns given by the sequences of points $\mathbf{x}_{i,n}$ identify a set of trajectories of the dynamical system: they are uniquely determined once the initial conditions $\mathbf{x}_{i,0}$ are specified. However, the nonlinear analysis of spatio-temporal maps of the type (372) is a yet unsettled subject and no general method to ascertain the chaotic nature of the process is available. Hence, the various Authors who confronted themselves with this problem were forced to simplify the problem, replacing the spatio-temporal map (372) either by a spatial map (Perucca *et al.*, 2005; Schwenk and Foufoula-Georgiou, 2017) of the channel curvature at a given time or by a temporal map (Stolum, 1996; Frascati and Lanzoni, 2010) of the type

$$x_{n+1} = F(x_n), \quad (373)$$

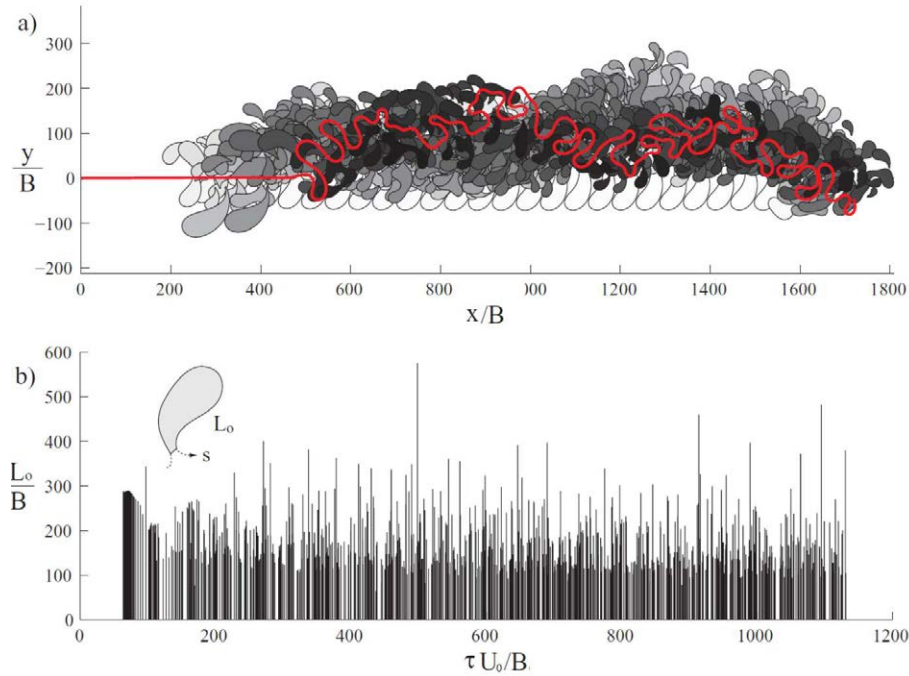


Figure 106. (a) Results of a long-term simulation of the planform evolution of a meandering river evolving from an initially straight, randomly perturbed, configuration. The initial values of the parameters used in the simulation are $\beta = 11$, $d_s = 0.001$, $\tau_* = 1.3$ (dune covered bed, sub-resonant conditions). Here, T is the dimensionless slow time variable Et appropriate to describe the planform evolution. The oxbow lakes generated during the entire simulation are highlighted using grey-scale tones, with dark indicating recent and white old. (b) The intrinsic length of the oxbow lakes L_0 is plotted versus time of cutoff occurrence (modified from Frascati and Lanzoni, 2010).

where x_n is some average measure of the intricacy of the spatial pattern of the channel axis in the reach considered at the n -th time step. A convenient choice made in the above papers was to set $x = \sigma$, with σ the average reach sinuosity.

Figure 107a shows the temporal sequence of σ for the simulation of Figure 106. Three stages of the evolution process emerge: an initial monotonic growth lasting until cutoff occurs (region I); a decay stage with fluctuations (region II); an asymptotic statistically stationary state characterized by fluctuations around a constant value (region III). Note that some cutoff clustering is observed only at the initial stage of the simulation and is clearly an artificial consequence of the ideal configuration adopted for the initial state (a straight channel axis with small perturbations). The meander train developing from such ideal configuration exhibits a high degree of regularity, such that that adjacent meanders approach neck cutoff nearly simultaneously. However, the latter artificial regularity is destroyed by cutoffs. Clustering then becomes much less likely and sinuosity fluctuations are driven by single cutoff events. In addition, Figures 107a,b clarify that the introduction of a small disturbance in the river planform at a certain instant ($T = \tau_3 U_0/B = 760$) of its evolution modifies the temporal series of sinuosity to some extent, a possible sign of the chaotic nature of the long-term behavior of the planform pattern.

In order to ascertain whether this suggestion is real, one should resort to the various techniques of nonlinear series analysis specifically developed for this purpose. Indeed, chaos looks like noise if one analyzes it adopting conventional linear tools, such as Fourier transforms. On the contrary, it turns out to exhibit well-defined structural features when analyzed in an appropriate phase space with the help of nonlinear time series analysis (Schwenk and Foufoula-Georgiou, 2017). These techniques were indeed employed by Frascati and Lanzoni (2010). However, as warned by the Authors themselves, nonlinear analysis is far less established than its linear counterpart

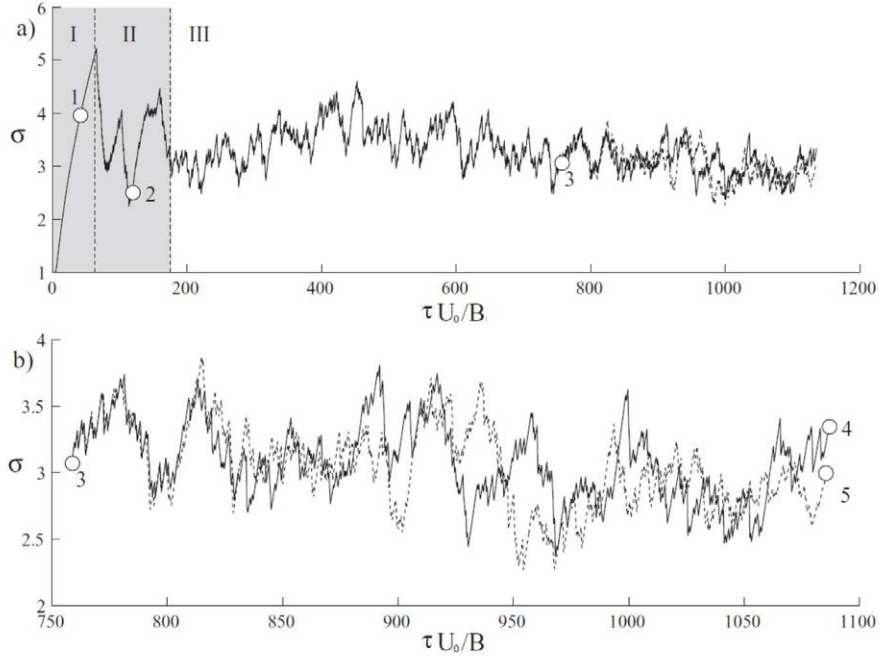


Figura 107. (a) Time series of the reach sinuosity σ . In the initial phase (Region I) the average reach sinuosity progressively grows monotonically, reaching very high and unrealistic values (up to five). As cutoff conditions are reached (Region II) sinuosity starts decreasing with oscillations and, after a sequence of cutoff events, it reaches a stationary state (Region III) characterized by sinuosity fluctuations around a constant value. Point 3 denotes the instant at which a small perturbation is introduced in the planform configuration after a given cutoff event. (b) Expansion of the steady region for $\tau > \tau_3$. The continuous and dashed lines denote the unperturbed and the perturbed sinuosity time series, respectively (modified from Frascati and Lanzoni (2010))

such that the application of the various techniques may in some cases yield results that cannot be unambiguously interpreted (Kantz and Schreiber, 1997; Sprott, 2003).

The first step in the nonlinear time series analysis is the so called *phase-space reconstruction*, i.e the conversion of observed data into an appropriate state vector. The most important phase space reconstruction technique is the so called *method of delays*. Starting from the scalar series x_n ($n = 1, 2, \dots, N_T$), one may construct m -dimensional vectors \mathbf{x}_n ($n = 1, 2, \dots, N_T$) in a new space, called the *embedding space*, assembling time-delayed values of the scalar data as follows (Kantz and Schreiber, 1997):

$$\mathbf{x}_n = \{x_{n-(m-1)d}, x_{n-(m-2)d}, \dots, x_{n-d}, x_n\} \quad (n = 1, 2, 3, \dots, N_T). \quad (374)$$

Here, the number m of elements of each vector is called the *embedding dimension*, while the time $T_d = d \Delta T$ is known as the *time delay* (or *lag*). Different quantitative tools are available to guide the choice of the optimal values of m (Frascati and Lanzoni, 2010).

The second step of the analysis is to evaluate a few parameters which provide information on the chaotic nature of the system. The so called *correlation dimension of the attractor* reflects the mean probability that the states at two different times are closer than a given distance ϵ . The *Lyapunov exponents* tell us whether nearby points in the phase space do diverge exponentially, as typical of chaotic phenomena.

The correlation dimension D_C may be calculated starting from the correlation sum (Grassberger and Procaccia, 1983a,b)

$$C(m, \epsilon) = \frac{2}{N_T(N_T - 1)} \sum_{i=1}^{N_T} \sum_{j=1+1}^{N_T} \mathcal{H}(\epsilon - \|\mathbf{x}_i - \mathbf{x}_j\|). \quad (375)$$

Here, \mathcal{H} is the Heaviside step function and $\|\mathbf{x}_i - \mathbf{x}_j\|$ is the spatial separation between two points \mathbf{x}_i and \mathbf{x}_j of the m -dimensional embedding space. The correlation dimension D_C is then obtained from the relation

$$D_C = \lim_{\epsilon \rightarrow 0} \lim_{N_T \rightarrow \infty} \frac{\partial \log C(m, \epsilon)}{\partial \log \epsilon}, \quad (376)$$

and can be determined by plotting $\log C(m, \epsilon)$ versus $\log \epsilon$. Provided saturation of the curve occurs, the slope of the straight line fitted through the plateau is precisely the sought value of the correlation dimension. If the latter is non-integer then the attractor of the system is chaotic (also called *strange attractor*).

The exponential divergence of the trajectories of a dynamical system is characterized by the spectrum of so called Lyapunov exponents (Eckmann and Ruelle, 1985). However, it is common to just refer to the maximum Lyapunov exponent (λ_M) which is a simple measure of the overall predictability of the system. A positive λ_M indicates that the system is chaotic. Its value allows one to estimate the time scale over which predictability is ensured (e.g. a few days for weather systems). A consistent and unbiased estimate of the maximum Lyapunov exponent can be obtained from the following relationship (Kantz and Schreiber, 1997):

$$S(m, \epsilon, T) = \left\langle \ln \frac{1}{|\mathcal{I}(\mathbf{x}_0)|} \sum_{\mathbf{x}_i \in \mathcal{I}(\mathbf{x}_0)} \left(\|\mathbf{x}_0(T) - \mathbf{x}_i(T)\| \right) \right\rangle, \quad (377)$$

where \mathbf{x}_0 is the reference point in the embedding space, and $\mathcal{I}(\mathbf{x}_0)$ is a neighborhood of \mathbf{x}_0 with diameter ϵ . The latter formula is implemented using the algorithm of Rosenstein *et al.* (1993). If $S(m, \epsilon, t)$ exhibits a linear trend with identical slope for all m larger than some m_0 and for a reasonably wide range of values of ϵ , then this slope can be taken as an estimate of the maximum exponent λ_M .

The correlation dimension calculated by Frascati and Lanzoni (2010) for the sinuosity time series is shown in Figure 108. No saturation of the curves (plateau) is obtained varying the embedding dimension and the delay. Hence, no scaling range exists and no unique value of the correlation dimension can be identified. Similar results were found for the spatial series of channel curvature.

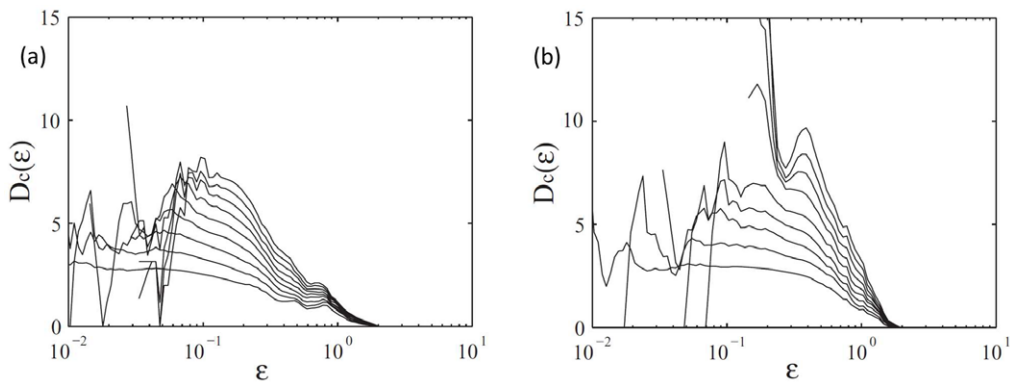


Figure 108. Local slope estimation of the correlation dimension D_C for various embedding dimensions ($m = 2, 3, \dots, 12$). (a) and (b) show estimates based on sinuosity time series for time delays $d = 5$ and $d = 60$, respectively. Similar results have been found using time delays $d = 30$ and $d = 150$. No clear saturation is detected (modified from Frascati and Lanzoni, 2010).

Finally, the estimate of the maximum Lyapunov exponent λ_M for the sinuosity time series is reported in Figure 109. A wide range of values of m and d has been examined. This notwithstanding, no linear increase of the plotted curves can be clearly detected. Similar results were found for the spatial series of channel curvature at a given time.

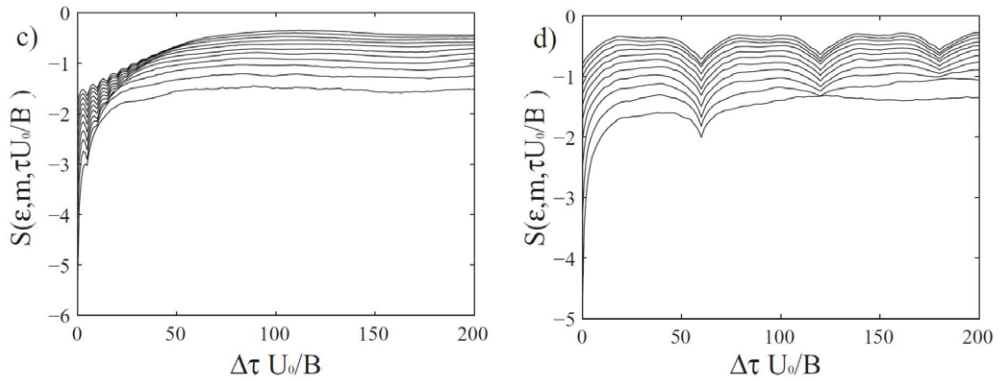


Figure 109. Estimates of the maximum Lyapunov exponent for the sinuosity time series using a time delay (a) $d = 5$ and (b) $d = 60$. Embedding dimension varies over the range $m = 2, \dots, 12$. No linear increase is clearly detectable, reflecting the lack of exponential divergence of nearby trajectories. Similar results have been found using time delays $d = 30$ and $d = 150$ (modified from Frascati and Lanzoni, 2010).

We may conclude from the latter findings that *meander planform patterns at a given time, as well as the overall process of river meandering are not chaotic.*

Does meandering show signs of self-organization?

The notion of self-organized criticality (SOC) stems from the original work of Bak *et al.* (1987) who showed that “*certain extended dissipative dynamical systems naturally evolve into a critical state, with no characteristic time or length scales. The temporal fingerprint of the self-organized critical state is the presence of flicker noise or $1/f$ noise; its spatial signature is the emergence of scale invariant (fractal) structure*”. The prototype of large, highly nonlinear dissipative systems with many degrees of freedom considered by Bak *et al.* (1987) was a cellular automaton called *sandpile* due to its superficial similarity with an actual sandpile. Indeed, this schematic system consists of a square grid of boxes, each of which may receive or loose particles according to the following rules:

- at each time step a particle is dropped into a randomly selected box;
- as soon as a box contains four particles, all of them are redistributed to the four adjacent boxes leaving the original box empty;
- in the case of edge boxes, particles crossing the grid boundary are lost by the system.

The reader may readily check that the redistribution mechanism, starting when the *least stable* part of the system reaches the four-particle threshold, triggers a burst of activity that propagates through the entire system. Each sequence of redistributions, leads to a number of particles lost by the grid and is defined as a *model avalanche*. Avalanches generate chain reactions of global size. For *sandpiles* the state of the system may be defined by the average number of particles present in the boxes. *This state is found to fluctuate about a quasi-equilibrium value.* Bak *et al.* (1987) showed that the sandpile algorithm naturally evolves towards a SOC state characterized by spatial and temporal power-law scaling behavior, i.e. the distinct feature of a SOC state is the absence of characteristic spatial or temporal scales. Indeed, if one plots the number of avalanches n_{av} versus the area A_{av} involved (defined by the number of boxes that participate in the avalanches) one finds a power law distribution. For a 50×50 grid, the distribution is shown in Figure 110. Thus the *spatial behavior* of the system is scale invariant. Similarly, defining the time T as the number of particle redistributions during an avalanche and denoting by n_T the number of events with T redistributions, then one finds that $n_T \sim T^{-1}$.

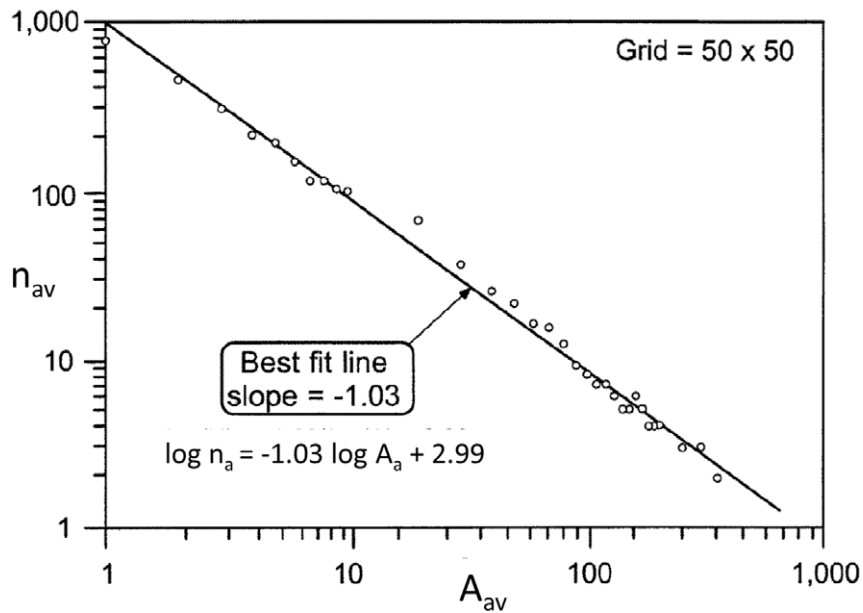


Figura 110. Avalanche–frequency versus avalanche area distribution for a sandpile model on a 50×50 grid (modified from Turcotte, 1999).

As soon as the SOC paradigm was put forward, a number of contributions attempting to interpret geophysical processes as examples of SOC were published (see the review of Turcotte, 1999). In particular, an application to river meandering was attempted by Stolum (1996), who proposed an analogy between clusterings of neck cutoffs and avalanches. This Author analyzed the cumulative area frequency distribution of the oxbow lakes synthetically generated through numerical simulations based on the model of Ikeda *et al.* (1981) and found that it follows a power-law over nearly two orders of magnitude. However, Frascati and Lanzoni (2010) noted that “*if meandering systems really tend to SOC then not only spatial but also temporal power-law scaling should be expected. On the contrary, the analysis of the temporal distribution of neck cutoff occurrences, . . . reveals that the time inter-arrivals of cutoff events x_T are exponentially distributed*”. Exponential distributions are an example of probability distributions describing processes characterized by events occurring independently of each other, as typically occurs for Poisson processes. These processes are devoid of memory effects and do not exhibit any evidence of temporal clustering. All these features argue against the idea that meandering patterns would tend to a dynamical SOC state. This is not surprising if one recognizes that the consequences of a cutoff event affect a fairly short river reach. This observation, which is contrary to the chain reaction paradigm embodied by SOC, is suggested by both the solution of the morphodynamic problem (see Section 4.4), where upstream and downstream influence are felt through convolution integrals decaying fairly rapidly, and by the field observations carried out by Brice (1973) on the White River.

Seeking universality

The excursus reported above suggests that, in spite of major efforts of the scientific community to seek universal properties in the long-term evolution of meandering rivers with the help of the modern paradigms of complex systems, we are left with a fairly meager outcome.

Let us conclude our discussion returning to the interesting result concerning the asymptotic behavior of the temporal evolution of the averaged sinuosity emerged from numerical simulations. It was pointed out before that this evolution tends to a dynamical stationary state characterized by

fluctuations around a constant value of the averaged sinuosity (Figure 107). This finding was first reported by Howard and Knutson (1984) and Stolum (1996). Later Camporeale *et al.* (2005) have revisited this issue comparing the response of various models and reached the following conclusions:

- *the statistical long-term behavior of meandering rivers proves to be universal and largely unaffected by the details of the fluid dynamic processes that govern the short-term river behavior;*
- *the long-term equilibrium conditions are essentially governed by only one spatial scale, proportional to the ratio of the river depth and the friction coefficient and one temporal scale, proportional to the square of the spatial scale divided by the river width, the mean longitudinal velocity, and the erodibility coefficient.*

The first conclusion, if totally correct, would be a bit disappointing. What the Authors call *details of the fluid dynamic processes* is the morphodynamic model employed. One would then be surprised to learn that correct (albeit linear) models (BS, Blondeaux and Seminara (1985); JP, Johannesson and Parker (1989); ZS, Zolezzi and Seminara (2001)) and models that miss a significant part of the solution of the problem (IPS, Ikeda *et al.*, 1981), lead to identical results. Camporeale *et al.* (2005) argue that cutoffs select the morphodynamic processes that are really important in the long-term dynamics, thus implying that for the occurrence of cutoffs *details* of the morphodynamic model would be irrelevant, in spite of the facts that planform patterns obtained with the help of different models are substantially different (Figure 111).

However, at a more careful examination, one finds that the first conclusion depends strictly on the choice made by Camporeale *et al.* (2005) to consider only rivers falling in the sub-resonant regime. This was conclusively demonstrated by Frascati and Lanzoni (2009).

In order to clarify this point, it is convenient to examine the second conclusion, which concerns the spatial scale of fluvial meanders. According to the celebrated diagram proposed by Leopold and Wolman (1957), the Cartesian length of meanders observed in vastly different environments is correlated with channel width (Figure 3(I)). Assuming that the preferred wavelength L_m is selected by the bend instability mechanism, theoretical results show that the dimensionless meander wavenumber ($\lambda_m = 2\pi B/L_m$) should fall in the range 0.1 – 0.3, depending on the values attained by the relevant physical parameters. Figure 3(I) shows that most experimental points do indeed fall within the predicted range.

More recently, Edwards and Smith (2002) have repeated some of the linear and nonlinear analyses previously developed by other Authors, employing the IPS model. One of the statements of Edwards and Smith (2002) concerns the length scale of river meanders which they suggest, on dimensional grounds, would coincide with the ratio between a typical flow depth and a typical friction coefficient of the flow. But the above suggestion was not new. A decade earlier Parker and Johannesson (1989) (p. 384) had already proposed a similar scaling for the dimensionless meander wavenumber. However, the rescaled wavenumber varied over more than two orders of magnitude in the 75 field cases they examined, a correlation worse than that obtained through the classical Leopold scaling. The length suggested by Edwards and Smith (2002) is purely hydrodynamic, owing to the decoupled character of the IPS model. It represents the unique length over which the morphodynamic influence is felt in the context of IPS model (Sun *et al.*, 1996). One may then wonder how an hydrodynamic based scale can account for meandering occurring in vastly different sedimentary environments. The exact solution of the linear problem of meander morphodynamics presented in Section 4.4.2 shows that the morphodynamic influence displays a more complex behavior involving four spatial scales depending on the aspect ratio of the channel, as well as on the intensity of sediment transport (τ_{*0}) and friction (C_{f0}). This response arises from the contributions of four convolution integrals (equation 316). Each of them involves distinct spatial scales associated with the inverse of the exponents $\lambda_{m,j}$ appearing in the integrals. Two of these exponents are complex conjugates and determine the upstream and downstream morphodynamic influence felt through spatial bars, i.e. spatially oscillating perturbations that decay either upstream or downstream. They allow one to define a morphodynamic length scale \mathcal{L}^m equal to the inverse of the imaginary parts of the two dominant complex conjugate exponents.

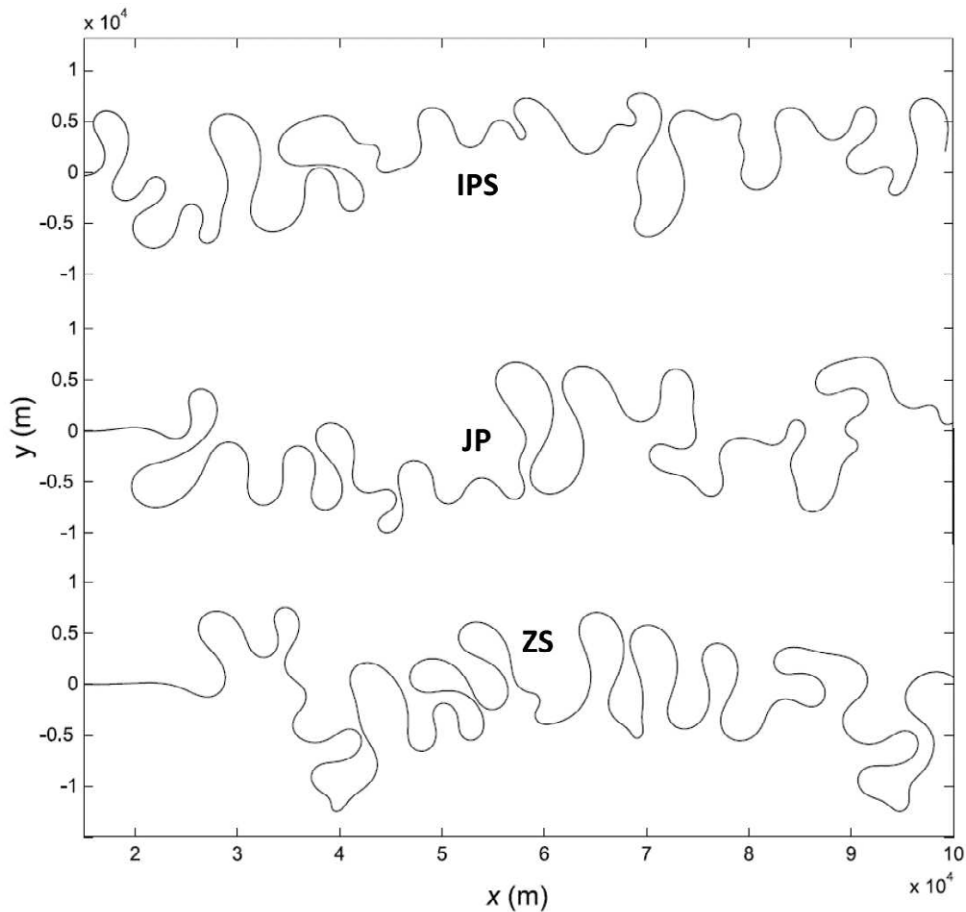


Figure 111. Comparison performed by Camporeale *et al.* (2005) between the outcomes of long-term planform simulations obtained with the help of different morphodynamic models: IP = Ikeda *et al.* (1981), JP = Johannesson and Parker (1989), ZS = Zolezzi and Seminara (2001): $d_s = 0.004$, $\tau_{*0} = 0.4$, $\beta = 7.4$, $C_{f0} = 0.0032$ (modified from Camporeale *et al.*, 2005).

The *hydrodynamic* and *morphodynamic* spatial scales \mathcal{L}^h and \mathcal{L}^m attain similar values only in the sub-resonant regime and for a limited range of the relevant parameters. Conversely, these two scales differ significantly (by a factor larger than 2) in the super-resonant regime.

Camporeale *et al.* (2005) and Frascati and Lanzoni (2009) have calculated the probability density functions (PDF) of channel curvature based on results of simulations obtained using the IPS and ZS models. If data are restricted to sub-resonant simulations (Camporeale *et al.*, 2005), the PDFs, scaled by \mathcal{L}^h , tend to collapse into a common trend (Figure 112a). However, if data referring to both the morphodynamic regimes are included (Frascati and Lanzoni, 2009), then the scatter exhibited by ZS curves is significantly higher (Figure 112b). This result is not surprising as the hydrodynamic scale \mathcal{L}^h is a good approximation of the actual length scale only in the sub-resonant regime. Conversely, a remarkable collapse on two distinct common trends is obtained if \mathcal{L}^m is adopted to scale the PDFs of curvature associated with the ZS planforms (Figure 112c).

This is reassuring. The signature of the morphodynamic regime (sub- or super-resonant), hence the physics of the process, is not lost in the long-term behavior of planform evolution. While the occurrence of repeated cutoffs plays an important role, however it is not sufficient to filter out the physical complexity associated with the major process of morphodynamic influence.

An additional contribution on this issue has been recently proposed by Schwenk and Foufoula-

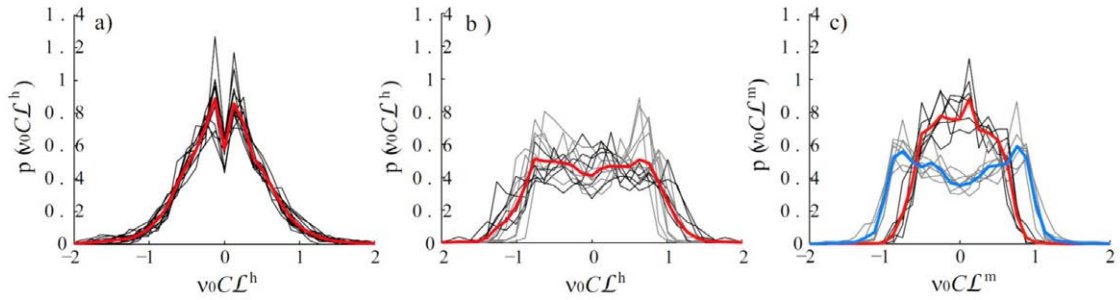


Figure 112. Probability density function (PDF) of the channel axis curvature \mathcal{C} resulting from simulations of planform evolution performed using different models. (a) IPS model, sub-resonant simulations, PDFs scaled by \mathcal{L}^h ; (b) ZS model, both sub- and super-resonant simulations, PDFs scaled by \mathcal{L}^h ; (c) ZS model, both sub- and super-resonant simulations, PDFs scaled by \mathcal{L}^m . Black lines denote sub-resonant patterns; grey lines denote super-resonant patterns; red and blue lines denote mean PDF distributions (modified from Frascati and Lanzoni (2009)).

Georgiou (2017) who, introducing an appropriate metric, analysed the strength of planform nonlinearities. They concluded that a nonlinear structure could be detected from trajectory densities in phase space. This finding confirms that the nonlinearity in the underlying deterministic dynamics of meandering river evolution indeed leaves its signature on the resulting planform.

5.6. Planform evolution and meander width

One of the main assumptions of the models of planform evolution of meandering rivers discussed in this Chapter is the spatially and temporally constant value of channel width. This is partly justified by field observations (Lagasse *et al.*, 2004). Indeed, while many rivers keep a fairly constant mean channel width as they evolve, systematic width variations have also been reported (see Brice, 1982).

Note that the relationship between variations of channel width and channel curvature is by no means obvious. At a first glance, in some cases (Figure 99(I)a) channel width appears to be maximum at, or close to bend apexes and minimum at, or close to bend crossings. Conversely, in other cases (Figure 99(I)b) channel width appears to peak at inflection points.

The presence of distinct width patterns was used by Brice (1984) to classify meandering rivers into two main classes. *Sinuuous point bar rivers* are fluvial patterns that display larger widths at bend apexes and prominent point bars, typically scrolled and visible at normal stage. On the contrary, *sinuuous canaliform rivers* are rivers with fairly constant width, no clear width-curvature correlation and narrow, crescent-shaped, point bars. Moreover, sinuuous canaliform rivers exhibit typically a bank resistance higher than that experienced by sinuuous point bar rivers, and, as a result, have lower rates of lateral bend migration (Brice, 1982; Lagasse *et al.*, 2004).

In order to ascertain what mechanisms determine the establishment of the above patterns, one may pursue two different lines of investigation, an *equilibrium approach* or a *dynamic analysis*. The rationale behind the equilibrium approach is to try and answer the following question: what is the spatial distribution of channel width in a meandering channel with constant longitudinal slope of the free surface in order to satisfy the constraints of morphodynamic equilibrium (constant flow discharge and sediment flux)? The dynamic approach pursues a more ambitious goal: decoupling outer bank erosion from inner bank deposition in planform evolution models, thus removing the constant width constraint and allowing the coevolution of channel width and channel sinuosity to emerge. Below, we briefly outline recent contributions based on each of these approaches.

5.6.1 The equilibrium approach: Spatial variations of channel width in meandering channels at equilibrium

The equilibrium approach was pursued by Luchi *et al.* (2012) following a previous contribution of Solari and Seminara (2005). The first observation of Luchi *et al.* (2012) concerns a fundamental aspect of the problem, namely the very definition of channel width. Luchi *et al.* (2012) noted that,

if the channel width is taken to coincide with the width of the free surface, then Brice classification (Brice, 1984) becomes stage-dependent in sinuous point bar rivers. Indeed, the lateral bed profile at point bars is quite gentle, so that small changes in water level cause relatively large changes in channel width. On the contrary, channel width is fairly objectively identified and weakly stage dependent for canaliform rivers.

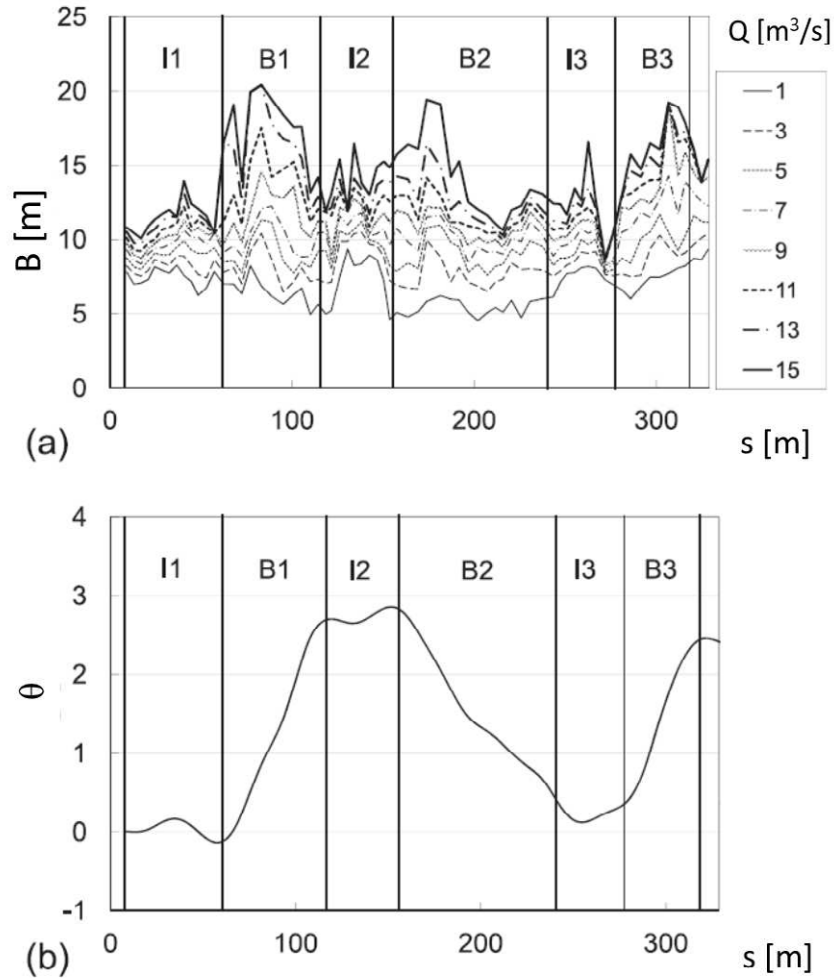


Figura 113. (a) Channel width variation along a reach of the Bollin River at different flow stages and (b) spatial variation of the inclination angle of the channel centerline θ in the same reach. I and B denote crossings and bends, respectively (modified from Luchi *et al.*, 2012).

Figure 113, which refers to the active meandering gravel river Bollin in NW England surveyed by Luchi *et al.* (2010a), clarifies this concept. The 330 m river reach is composed of three bends freely evolving in a highly erodible floodplain, with fairly uniform grain size distribution (d_{50} falling in the range 26 – 35 mm) and uniform riparian areas covered by grassland. These uniformities ensure that the observed variations of channel width are independent of variations of bank resistance. Luchi *et al.* (2012) substantiated the notion of the stage dependence of channel width throughout the reach, using a 1D hydraulic numerical model to calculate the width of the free surface using the surveyed cross sections for a set of flow discharges ranging from $1 m^3 s^{-1}$ (mean annual flow), to $15 m^3 s^{-1}$ (bankfull discharge). Results of these calculations are reported in Figure 113a, which shows that, at low flow, the free surface width at crossings is larger than at bends. On the contrary, at

high flow, the maximum widths occur within the regions B1, B2, and B3 whilst minimum widths are experienced at crossings. The above observations call for a reconsideration of the mechanistic basis of the distinction between sinuous point bar and canaliform meandering rivers proposed by Brice (1984).

In order to clarify the latter issue, Luchi *et al.* (2012) extended the nonlinear analysis of flow and bed topography in meandering channels proposed by Bolla *et al.* (2009) (recall Section 3.3.1) to allow for spatial variations of channel width. It is of interest to note that the constant width model of Bolla *et al.* (2009) showed that an equilibrium configuration of flow and bed topography does exist for given flow discharge and associated sediment flux. However, in order to achieve equilibrium, spatial variations of the longitudinal free-surface slope must be allowed. In the development of Luchi *et al.* (2012), the channel width undergoes spatial oscillations. Under these conditions, the meandering channel is able to accommodate prescribed values of flow and sediment discharges with the longitudinal free-surface slope kept constant. In general, Luchi *et al.* (2012) find that, at equilibrium, *channel width attains its maximum close to the inflection points and its minimum close to the bend apex* (Figure 114). The main assumption required for this model to be rational is that flow and bottom topography must be *slowly varying* in both longitudinal and lateral directions, i.e. the channel must be *wide* enough and its width and channel alignment must vary on a longitudinal scale much larger than channel width.

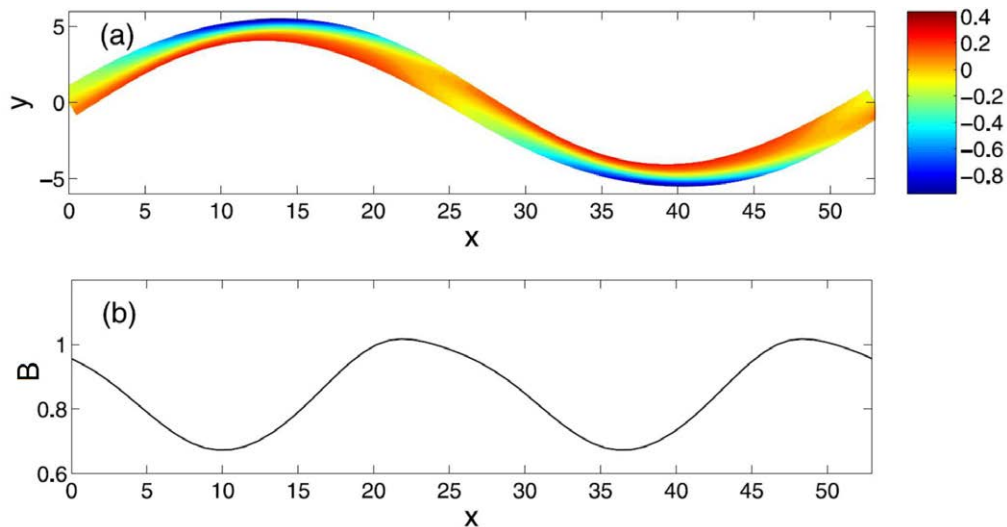


Figure 114. (a) Dimensionless bed elevation in a periodic sequence of sine generated meanders; (b) spatial oscillations of the dimensionless channel width B in equilibrium with the prescribed flow rate and sediment flux. Bed elevation and channel width are scaled by the uniform flow depth and the channel width of the equivalent unperturbed straight channel. In both plots the longitudinal coordinate x is scaled by half channel width. The values of the parameters adopted in the computations are: $d_s = 0.005$, $\tau_{*u} = 0.09$, $\beta = 7$, $\lambda_m = 0.11$, $\nu_0 = 0.06$. Flow is from left to right (reproduced from Luchi *et al.*, 2012).

Results of Luchi *et al.* (2012) fit clearly the canaliform pattern. In order to substantiate this finding, Luchi *et al.* (2012) applied their model to a 1225 km long meandering reach of the Lower Mississippi River. The morphology of this reach was investigated by Hudson (2002) who, with the help of surveys from the late 1800s and early 1900s, showed that the bankfull channel width at riffles was unambiguously greater than at pools. This observation was confirmed by the calculations of Luchi *et al.* (2012), who obtained the following results:

- the minimum width is invariably experienced just downstream from the bend apex and the maximum width downstream from the inflection point;
- the relative variation of the channel width increases as the curvature parameter ν_0 increases;

- for typical values of ν_0 in the range 0.125 – 0.14, appropriate to various subsets of meanders in the Lower Mississippi River (Harmar and Clifford, 2006), the maximum width is roughly from 12% to 14.5% larger than the minimum width, with a slight overestimation with respect to the field observation (8.5%).

The above picture suggests that width variations driven by the constraint of morphodynamic equilibrium do not support the distinction between canaliform and sinuous point bar meandering rivers. The resolution of this apparent contradiction between theory and observations is immediately understood if one notes that the equilibrium constraint does not involve the entire cross section, but rather the active portion of it, namely the portion where transport occurs at formative conditions. Assuming that these conditions correspond to bankfull discharge and seeking the portion of the cross section where the Shields stress is lower than critical, Luchi *et al.* (2012) have obtained the spatial distribution of the active width at bankfull conditions for the reach of the Bollin River discussed above. Figure 115 shows the comparison between the spatial distributions of active width and width of the free surface. It clarifies that the distinction canaliform-sinuous point bar depends on the definition of *river width* adopted in the classification. The reach of the Bollin River should be classified of *sinuous point bar* type if the free surface width is adopted; the same reach has canaliform features if the active width is employed instead. In other words: the equilibrium constraint has similar consequences for canaliform and sinuous point bar rivers if the active portion of the cross section is taken to define the river width considered (Figure 115b).

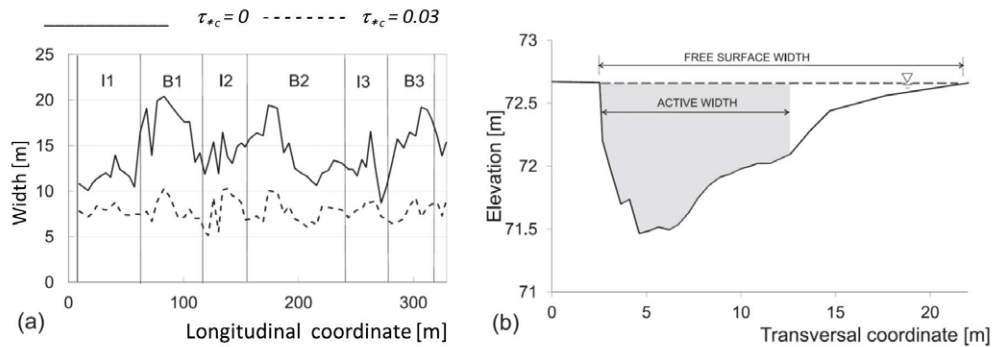


Figure 115. (a) Spatial distributions of free-surface width (solid line) and active width (dashed line) for a meandering reach of the River Bollin according to calculations of Luchi *et al.* (2012); (b) sketch of a cross section at a point bar (reproduced from Luchi *et al.*, 2012).

The conclusion of Luchi *et al.* (2012) is then that “*The difference between canaliform and sinuous point bar rivers may be simply stated noting that, in the former case, the active width roughly coincides with the width of the free surface, while in the latter case a nonactive portion of the point bar exists. . . the confining role of a high bank resistance (due to dense vegetation or clay content) in canaliform rivers prevents the formation at high stage of the ‘inactive’ part of the point bar.*”

A complementary viewpoint to explain the occurrence of systematic variations of channel width in meandering channels was taken by Luchi (2009) (but see also Zolezzi *et al.*, 2012). Essentially, these Authors investigated whether spatial oscillations in width may be due to in-stream (or *autogenic*) morphodynamic processes, i.e. processes that do not arise from the effect of external factors, like spatial variations in bank material composition. The autogenic process investigated by Luchi (2009) is the growth of mid-channel bars diverting the flow towards the banks. This mechanism was studied employing a perturbation approach that relies on the observations that the 2D dimensionless equations governing the morphodynamics of meandering channels with width variations is forced by terms involving two main dimensionless parameters, the curvature ratio ν_0 and a parameter δ measuring the dimensionless amplitude of width oscillations. One may then distinguish three contributions:

- the *forcing of curvature* due to both first order terms $\mathcal{O}(\nu_0)$ and second order terms $\mathcal{O}(\nu_0^2)$ typical of meandering channels with constant width;
- the *forcing of channel width variations*, leading to an $\mathcal{O}(\delta)$ contribution as in straight channels with variable width (recall Section 6.4.2(I));
- the *mixed forcing* arising from $\mathcal{O}(\nu_0 \delta)$ interactions between the effects of width and curvature variations.

The model equations were then solved expanding the solution in powers of the two perturbation parameters ν_0 and δ . Details of the analysis are left to the mathematically inclined reader who is referred to the original paper. The basic ideas are summarized below.

At $\mathcal{O}(\nu_0)$ one recovers the classical linear solution forced by curvature, which describes the occurrence of an excess longitudinal velocity at one bank with respect to the reference uniform flow, and a symmetrical defect at the opposite bank, i.e. the classical point bar morphology.

At $\mathcal{O}(\delta)$ the spatial variations of channel width force a laterally symmetrical flow-bed topography pattern of the central bar type. This is known to promote the growth of width oscillations in straight channels through a planform instability mechanism analogous to that of bend instability, as shown by Repetto *et al.* (2002). Luchi *et al.* (2010b) argue that the latter mechanism can cause the growth of mid-channel bars also in meandering rivers when the advance rate of one bank cannot keep pace with the rate of retreat of the opposite bank. This was documented by Hooke (1986) and Hooke and Yorke (2011), who observed that widening preceded central bed deposition in most of the field sites they analyzed.



Figura 116. (a) Aerial view of a meandering reach of the River Bollin. Flow is from right to left. (b,c) Pictures showing downstream views of a region adjacent to an inflection point of the channel axis. Pictures were taken before (April 2008) and after (July 2009) several channel-forming events (courtesy of Rossella Luchi).

The novel features of this analysis arise at a nonlinear level:

- The $\mathcal{O}(\nu_0^2)$ component of the solution describes a mid-channel bar component of the bed topography, that is known may have amplitudes up to half that of the point bar (Colombini

et al., 1991). Hence, mid-channel bars are not exclusively associated with preexisting spatial width variations, but can arise from nonlinear effects in equi-width meandering channels. Luchi (2009) substantiates this theoretical finding referring again to the field observations on the River Bollin, whose “*high lateral mobility makes it particularly suitable to study meander processes*” (Hooke, 2004). Figure 116 shows the development of a mid-channel bar in a reach adjacent to an inflection point, monitored in the period 2008-2009. The bar growth is readily appreciated comparing the Figures 116b and 116c, showing pictures taken before and after several channel-forming events.

- The $\mathcal{O}(\nu_0^2)$ contribution suggests that curvature variations can drive a laterally symmetrical mechanism able to promote the development of width variations. The reciprocal effect, i.e. the effect of width variations on the evolution of channel curvature, and hence on meander growth, is governed by the mixed $\mathcal{O}(\nu_0 \delta)$ component of the solution. It turns out that, for typical aspect ratios of meandering rivers, width variations do affect bend instability shifting the instability region in the $\lambda - \beta$ plane toward wavenumber values higher ($\lambda \sim 0.2 - 0.3$) than those found in classical linear bend theories for equi-width channels (Figure 117a). This is good news as it is known that the latter theories lead to a systematic wavelength overestimation. This emerges from the comparison between predicted and measured intrinsic wave numbers of some low sinuous rivers extracted from the data set of Hey and Thorne (1986) performed by Zolezzi *et al.* (2012). They suggest that this discrepancy may be corrected if one accounts for the presence of width variations.

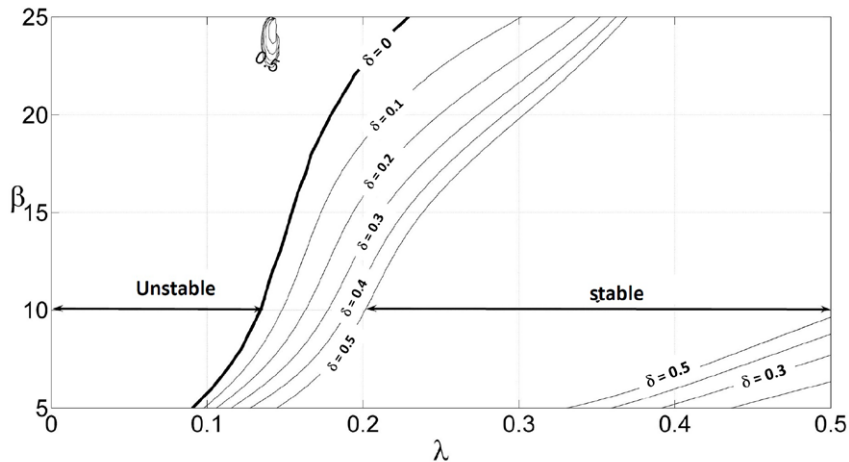


Figura 117. Marginal bend stability curves in the $\lambda - \beta$ plane for different amplitudes δ of relative spatial width variations ($d_s = 0.08$, $\tau_{*u} = 0.1$). Courtesy of Rossella Luchi.

5.6.2 The dynamic approach: Coevolution of meander width and sinuosity

The dynamic approach ultimately aims at ascertaining the mechanism whereby meandering rivers determine their own widths through a coevolution of sinuosity and width. This is the goal pursued by Eke (2013) (but see also Eke *et al.*, 2014b,a), following a previous contribution of Parker *et al.* (2011). More recently an alternative approach has been proposed by Lopez Dubon and Lanzoni (2019).

The starting point of the analysis of Eke (2013) was the recognition that, if bankfull fluid discharge Q , bedload discharge at bankfull flow Q_s , grain size d_s and channel-forming Shields number τ_{*f} are specified in a straight channel, then the uniform flow momentum balance and a

bedload transport relation impose three constraints of the general form:

$$S = S(Q, Q_s, d_s, \tau_{*f}), \quad (378a)$$

$$2B = 2B(Q, Q_s, d_s, \tau_{*f}), \quad (378b)$$

$$\mathcal{D} = \mathcal{D}(Q, Q_s, d_s, \tau_{*f}). \quad (378c)$$

where S is the bed slope, \mathcal{D} is the bankfull average flow depth and $2B$ is the channel width at bankfull stage. In other words, slope, flow depth and channel width are uniquely determined. Eke (2013) notes that, if one applies the above relationships to a sinuous channel at a given time, with S now interpreted as reach-averaged bed slope and τ_{*f} assigned a constant value, then an unrealistic consequence arises. Consider a river reach that is initially nearly straight with bed slope S_i and subsequently evolves towards a meandering pattern. Simple estimates reported by Eke (2013) suggest that, as S drops from the straight-channel value S_i to one corresponding to a sinuosity of 2.5, the width should correspondingly drop to 40% of its initial value at the nearly straight state. No such sharp drop in width as sinuosity increases is observed in reality.

This notwithstanding, Eke (2013) wishes to employ the relationships (378) in the context of their planform evolution model. To avoid the above contradiction, they resort to a trick. With the help of empirical observations of Li *et al.* (2014), they relax the assumption of constant value of τ_{*f} and replace it by the following empirical relation for channel-forming (bankfull) Shields number, valid across the range from silt-bed to cobble-bed rivers:

$$\tau_{*f} = 1220 R_p^{2/3} S^{0.53}. \quad (379)$$

Here, R_p denotes the particle Reynolds number. According to (379), as the sinuosity of a reach increases and the reach slope decreases, τ_{*f} drops and the uniform flow relationships (378) now predict a rather modest channel narrowing. It is appropriate to point out that the latter approach assumes that sinuosity increases in inverse proportion to channel lengthening, thus ignoring the possible role of aggradation and degradation processes undergone by the river reach as a consequence of planform evolution. This assumption has been recently challenged by Monegaglia (2017) and Monegaglia and Tubino (2019), as discussed below.

The analysis of Eke (2013) proceeds as follows. With the help of (378, 379), the Authors are able to associate a value for the channel-forming Shields number τ_{*f} to any sinuous configuration. However, unlike in straight channels, in meandering rivers the bed shear stress varies both longitudinally and laterally. As a result, adjacent to a bank, the streamwise bed shear stress may exceed or be smaller than the channel-forming bottom stress. In the former case, the bank is eroded, in the latter case the bank accretes. Erosion is modeled by an approach able to capture sediment removal mitigated by armoring due to slump blocks. Accretion is treated by a submodel capturing vegetal encroachment damped by the effect of near-bank flow. Both migration rules are expressed in the following form:

$$\frac{dn_b}{dt} = \zeta + \frac{1}{S_b} \frac{\partial \eta_b}{\partial t}. \quad (380)$$

Here:

- dn_b/dt denotes the rate of migration of the left ($n_b(t) = B$) or right ($n_b(t) = -B$) bank;
- ζ denotes the lateral erosion (accretion) rate due to sediment removal from (supply to) the bank. This process is triggered as the local Shields stress at the bank deviates from its formative value associated with the reach averaged slope. ζ is given an empirical form in terms of parameters measuring the effects of slump blocks, flood intermittency and vegetation.
- S_b is the bank slope, taken to be constant. Of course, the Authors are implicitly assuming that the banks are *gently* sloping as the second term in (380) would be unbounded for a vertical bank.

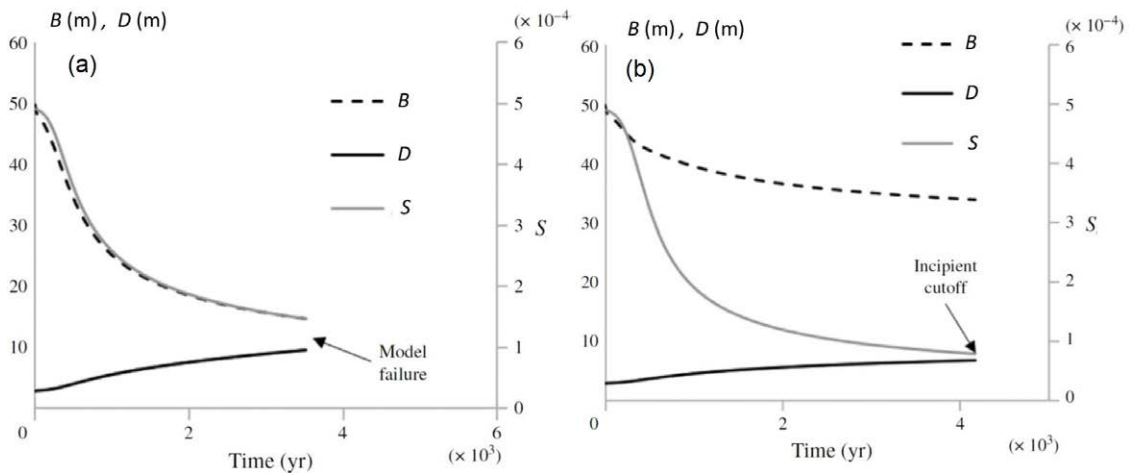


Figure 118. Adjustment of reach-averaged/reference channel characteristics over time in response to increasing channel sinuosity. As slope S decreases, the channel half-width B decreases and the flow depth D increases. (a) Analysis based on a constant channel-forming Shields number. (b) Analysis based on a slope-dependent channel-forming Shields number (modified from Figures 3.11 and 3.13 of Eke, 2013).

A nonlinear depth-averaged submodel for river morphodynamics is then employed to evaluate the spatial distribution of the bed shear stress in a meandering channel with variable width. Moreover, a standard numerical scheme is adopted to simulate the kinematics of channel shift. The above approach was applied to a test case. Starting from a constant width, low-amplitude meander with an initial sine-generated waveform, the planform evolution was followed up to incipient cut-off conditions. Data were chosen such to mimic an actively meandering sand bed stream, namely the reach of the Pembina River investigated by Beck *et al.* (1983). Various results have emerged from this application.

Firstly, assuming that the channel-forming Shields number keeps constant at its initial value leads to a channel that becomes unacceptably narrow as sinuosity increases (Figure 118a). This problem is fully resolved adopting the empirical relation (379) for channel-forming (bankfull) Shields number (Figure 118b).

Secondly, simulations show that the curvature at the apex, the relative amplitude of width variations and the maximum migration rate rapidly increase, reach a peak value and then decline slowly. Values for the peak migration rates and width variations are within the range of values observed for the investigated reach of the Pembina River.

Thirdly, the predicted location of the maximum width is just upstream of the bend apex and the minimum width is found to occur around the crossings, a trend similar to that observed in the Pembina River.

Recently, Monegaglia (2017) (but see also Monegaglia and Tubino, 2019) has taken a different approach to simulate the co-evolution of sinuosity and channel width in meandering channels. These Authors make use of recent progress in remote sensing analysis. Fairly detailed data on the evolution of channel width at the bend scale for four meandering rivers of the Amazon Basin are used to test model predictions. Figure 119a provides a detailed documentation of the planform development of an individual meander bend of the Rio Ucayali (Perù) in the time period 1988-2009. Also shown (Figure 119b) is the coevolution of channel width and meander sinuosity in the same period.

The starting point of the analysis of Monegaglia (2017) is the recognition that changes of channel geometry at bankfull conditions during the planform evolution of a meandering river are not driven only by the reduction of channel slope due to the elongation of a channel connecting two floodplain points (Eke *et al.*, 2014b). Indeed, a reduction of slope implies a reduction of the sediment transport capacity. Monegaglia (2017) then argues that the models for meander

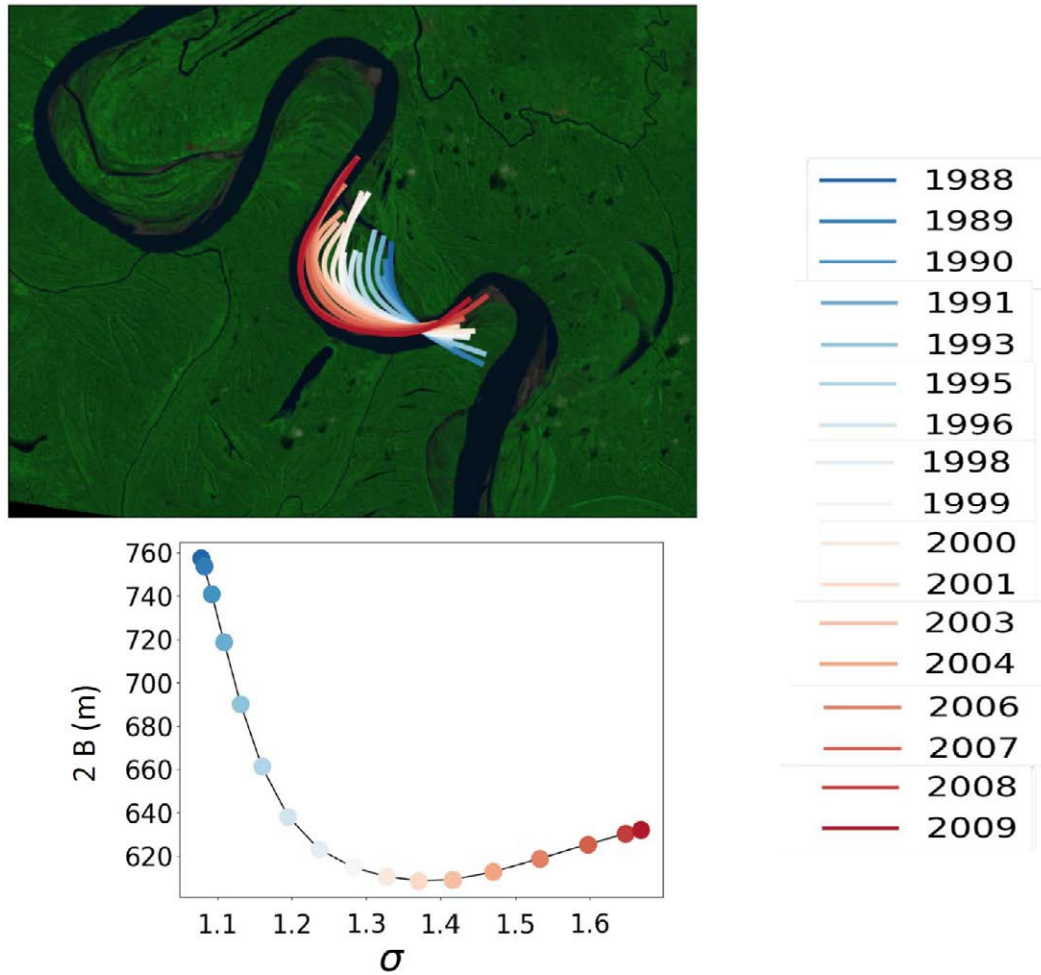


Figura 119. (a) Planform development of an individual meander bend of the Rio Ucayali (Perù) in the time period 1988-2009. Coevolution of channel width $2B$ and meander sinuosity σ in the same period (modified from Figure 6.8 of Monegaglia, 2017).

morphodynamics developed so far overlook the capability of evolving meander bends to rework the river bed through aggradation/degradation processes such to counteract the variations of channel slope associated with planform development. They then propose a new, physically based model for the bankfull hydraulic geometry of a periodic train of evolving meanders based on the *assumption that the rate of sediment supply to the meandering reach keeps constant*.

Briefly, the analysis proceeds as follows. Sinuosity-width coevolution is described by the following two rules:

$$\zeta = \frac{1}{2} E (U_{bl} - U_{br}), \quad (381a)$$

$$\frac{dB}{dt} = E (U_{bl} + U_{br} - 2\mathcal{U}_R) \quad (381b)$$

with ζ lateral migration rate, E bank erosion rate, U_{bl} (U_{br}) depth averaged longitudinal velocity at the left (right) bank and \mathcal{U}_R some cross sectionally averaged velocity threshold, above (below) which bank erosion (accretion) occurs. Moreover, unlike Eke et al. (2014b), Monegaglia (2017) assumes that the threshold value \mathcal{U}_R is univocally determined once the hydrology and the grain

size are given. The reader will note that, according to the above rules, laterally symmetrical components of the perturbations of the depth averaged longitudinal velocity (such that $U_{bl} = U_{br}$) do not affect the lateral channel migration but do drive width variations.

To close the problem, an evolution equation for the reach averaged channel slope is needed to replace the common assumption whereby slope reduction would be inversely proportional to channel lengthening. Indeed, consider the mathematical definition of reach slope $S = \Delta\eta/L$, with L reach length and $\Delta\eta$ drop in cross sectionally averaged bed elevation. Differentiation of this definition immediately clarifies that, besides channel lengthening, bed aggradation-degradation may also play a role. Temporal differentiation of the definition of reach averaged slope allows one to express the rate of slope reduction dS/dt in terms of the rates of reach lengthening dL/dt and bed aggradation-degradation $d\Delta\eta/dt$. The latter three quantities must satisfy a relationship imposing sediment continuity at the reach scale. Essentially, this condition requires that the disequilibrium between the rate of sediment supply, assumed to be constant, and the rate of sediment transport, which varies as meander evolves, must be balanced by the rate at which sediment is stored in (or subtracted from) the meander reach due to bed aggradation (degradation), lateral migration and average width change.

Making also use of the evolution equations for channel curvature and meander length derived by Seminara *et al.* (2001b), the analysis leads to a system of coupled ordinary differential equations, for channel curvature, average meander width, meander length and drop of bed elevation. It turns out that the response of the system depends crucially on a dimensionless parameter that measures the ratio between the timescale of planform evolution T_e and that associated with bed aggradation-degradation T_B . It reads:

$$\mathcal{R}_T = \frac{T_e}{T_B}. \quad (383)$$

Here:

$$T_e = \frac{B_0}{E U_0}, \quad T_B = \frac{B_0 (1-p) S_0 L_0^2}{Q_{s0}} \quad (384)$$

with the subscript 0 denoting an equilibrium value in the quasi-straight initial configuration and p sediment porosity. If the value of \mathcal{R}_T is small, planform evolution is too fast for the river bed to adapt to the evolving planform configuration. As a result, the bed slope tends to the classical inverse dependence on meander length. On the contrary, if \mathcal{R}_T is large, then settling compensates the slope change due to meander elongation. As a result, the sediment transport capacity balances the sediment supply and the bankfull hydraulic geometry converges to the equilibrium conditions.

Results of the numerical simulations display a general tendency of channel slope and average width to decrease uniformly as the sinuosity of river planform increases. On the contrary, the average reach depth increases.

As for the role played by the parameter \mathcal{R}_T , it turns out that the larger is the value of \mathcal{R}_T , the smaller is the departure of the bankfull hydraulic geometry from the initial equilibrium configuration. For values of \mathcal{R}_T as large as 10, the bankfull hydraulic geometry keeps almost constant as meander develops. In this case, the river bed maintains its slope in equilibrium with the sediment supply. Conversely, at low values of \mathcal{R}_T , the river bed is unable to keep up with channel elongation, hence the bankfull width and slope must decrease accordingly. Comparison with remote sensing data (Figure 120) for the trajectory of the correlation $B - \sigma$ between half-channel width and sinuosity appears to be fairly encouraging. Monegaglia (2017) notes that the observed values of \mathcal{R}_T are typically correlated with the average sediment concentration and their values span the range 0.1 – 10, with few values in the low range. The Authors then conclude that the general tendency of the bankfull geometry should be to keep nearly constant or change slightly as meanders develop.

An alternative approach to deal with the coupled evolution of river planform and channel width has been developed by Lopez Dubon and Lanzoni (2019), who simulate the river bank evolution through a statistically constrained physical model. The analysis of a wide sample of river planforms extracted from Landsat images shows that the median of the half-channel width, normalized by its mean varies within a relatively limited range (0.904 to 1.013). On the contrary the interquartile range can differ significantly from river to river (Figure 121). For a given river, the reach averaged

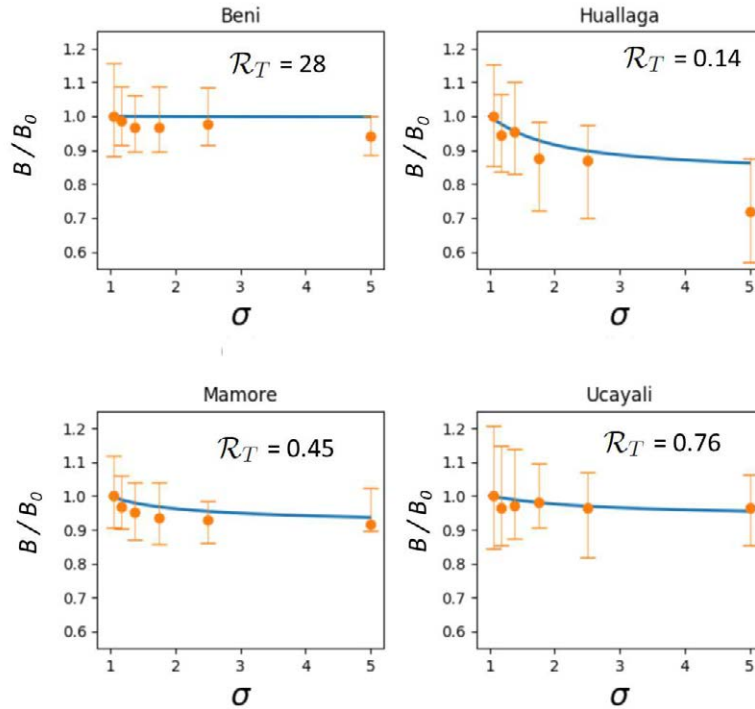


Figure 120. Comparison of the predicted trajectory of the correlation width-sinuosity for four large rivers of the Amazon basin and remote sensing data. The important role played by the \mathcal{R}_T parameter appears to be reasonably confirmed. Courtesy of Federico Monegaglia.

mean width B_{avg} can change in time as the river migrates across the floodplain. In particular, significant variations are observed when the river undergoes important morphological changes, such as those due to the occurrence of cutoffs. Nevertheless, these fluctuations are usually centered around a statistically steady value. This value can be taken as a signature of the hydrological and sedimentological regimes characterizing the river, of the overall strength of the banks, and of the sedimentary structure of the surrounding floodplain.

A generalized extreme value (GEV) probability distribution is usually found to provide the best fit of along-channel distribution of channel width. Even though the three parameters controlling the GEV shape can change from year to year, the differences of the statistical distances between each distribution keep relatively limited, thus implying an almost complete similarity of the distributions. Meaningful variations in the GEV parameters occur when the river planform experiences important shortening due to cutoffs. However, a few years after these changes, the GEV parameters tend to recover the preexisting values that can thus be taken as river specific (Figure 122).

The above findings led Lopez Dubon and Lanzoni (2019) to develop the following statistically constrained physical model. The outer bank erosion and the inner bank accretion are treated separately, thus allowing for spatial width fluctuations with respect to the mean when the river migrates. However, these fluctuations are constrained within a meaningful range of values using the GEV distribution that better fits the spatio-temporal sequences of widths observed for the investigated river. The accretion of the inner bend is computed through the deposition relation of Mehta and Partheniades (1975), whilst the erosion rate at the outer bank is estimated through an excess threshold linear formula of Darby *et al.* (2002). Note that the above approach allows to account not only for the water and sediment inputs that, on average, control the river morphology, but also for heterogeneities in the bank composition and in the floodplain structure that concur to

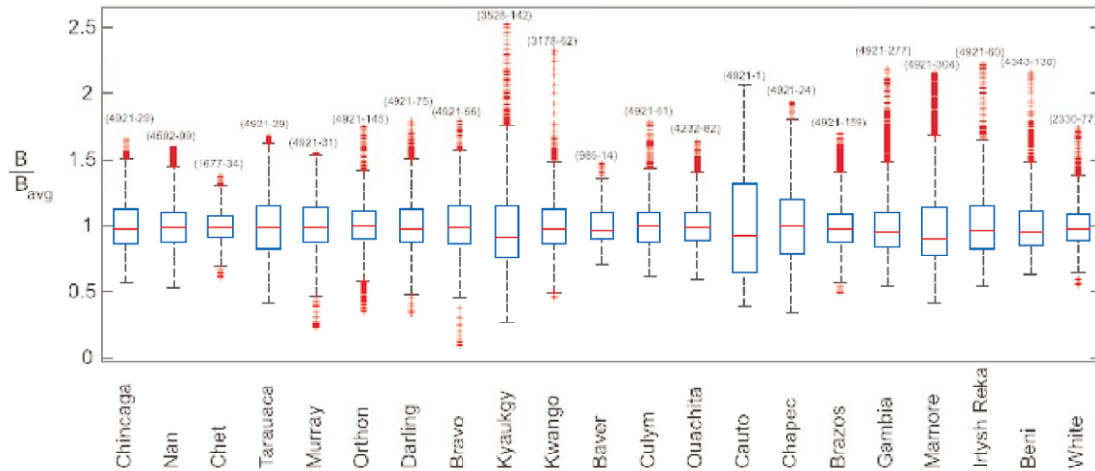


Figure 121. Box and whisker plots computed for the along-channel distributions of the dimensionless half-width $B(s)/B_{avg}$, observed in various rivers across the world. The boxes represent the interquartile ranges corresponding to 50% of the data; the horizontal line within each box denotes the median; the whiskers extend up to 1.5 times the interquartile range. All the values outside the whiskers are considered as outliers. The numbers in the upper part of the plot, delimited by round brackets, denote the size of the sample and the number of outliers (modified from Lopez Dubon and Lanzoni, 2019).

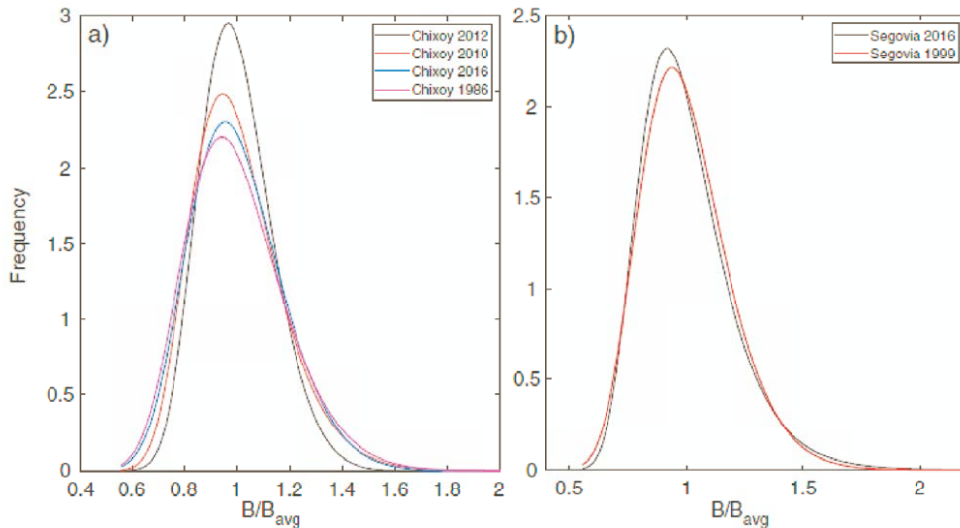


Figure 122. Examples of the temporal variations experienced by the generalized extreme value (GEV) PDF (probability density distribution) fitted to dimensionless $B(s)/B_{avg}$ distribution observed in (a) the Chixoy River and (b) the Segovia River in different years (modified from Lopez Dubon and Lanzoni, 2019).

determine the river shape.

The value of the bank shear stress used to drive the bank evolution can be obtained using any flow model. Figure 123 shows an example of application to the Ucayali River (Peru), carried out by using the linearized morphodynamic model of Frascati and Lanzoni (2013), which computes the in-channel bed topography and the corresponding flow field in meandering rivers with weakly, but arbitrarily varying spatial distributions of channel curvature and channel width.

5.7. Mechanics of chute-cutoffs

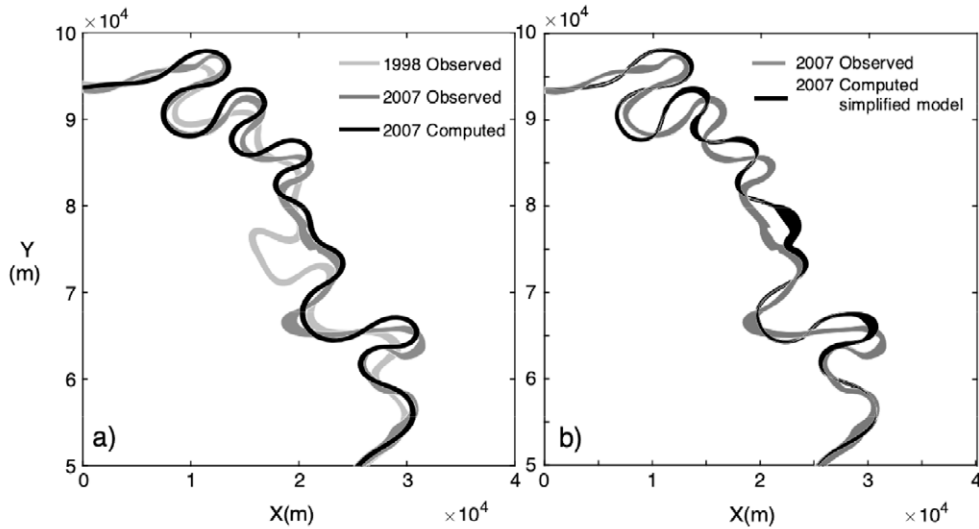


Figure 123. Short-term (10 years) simulations of planform evolution experienced by a reach of the Ucayali River (Peru). Panel (a) shows a comparison between the planform observed in 2007 and that predicted starting from the observed 1998 configuration using the statistically constrained model of Lopez Dubon and Lanzoni (2019). Panel (b) shows a similar comparison where predictions have been obtained also without including the statistical constraint on the temporal width evolution (modified from Lopez Dubon and Lanzoni, 2019).

Chute cutoffs are autogenic features observed in many meandering rivers (Figure 124). They consist of relatively long flow diversions that occur when a meander loop is bypassed by a new channel that cuts through the floodplain enclosed by the loop (Constantine et al., 2010). They usually form in rivers with wide cross sections, large curvature bends, high discharges and high overbank flow gradients (Howard and Knutson, 1984). Indeed, unlike neck cutoffs, chutes may be incised only when the floodplain adjacent to the channel is inundated, thus requiring high water levels and high rates of bed load transport. The chute incision and the consequent channel shortening enhance the downstream sediment delivery, giving rise to sediment pulses that promote the downstream formation of bars and an overall rearrangement of meandering bends adjacent to that bypassed by the chute. The incision process may be very fast (Iwasaki et al., 2016) or may last for a long period (Gay *et al.*, 1998). The original meander loop may either be filled with sediments or, less frequently, remain active together with the chute channel (Grenfell *et al.*, 2012).

Even though a number of different processes concur to the formation of chute cutoffs, three main mechanisms have been identified (Constantine et al., 2010). The first is related to the presence of sequences of ridges and swales within the meander loop. The swales may act as preferential paths for the flow and, consequently, they are subject to a gradual erosion due to the stronger water surface gradient. Eventually, one of these paths becomes large enough to convey most of the discharge, leading to the formation of a chute cutoff (Figure 125).

A second mechanism is related to the progressive incision of small embayments formed along the channel banks by localized erosion events. These embayments can be found either upstream or downstream of the meander loop that undergoes the chute cutoff (Figure 125). In the first case, when the water inundates the floodplain, the embayment is subject to a progressive extension, controlled by the inertia and the direction of the in-channel incoming flow. Conversely, in the second case, the embayment undergoes a progressive elongation by headward incision, controlled by surface gradient of the overbank flow and floodplain topography.

Chute extension by upstream incision can also form as a result of a natural obstruction of the river (e.g. due to the encroachment of woody debris) that forces overbank flow. The stage difference across the floodplain that forms upstream and downstream of this dam drives a flow that returns into the channel and, hence, impinges on the riverbank. The bank can thus be carved,

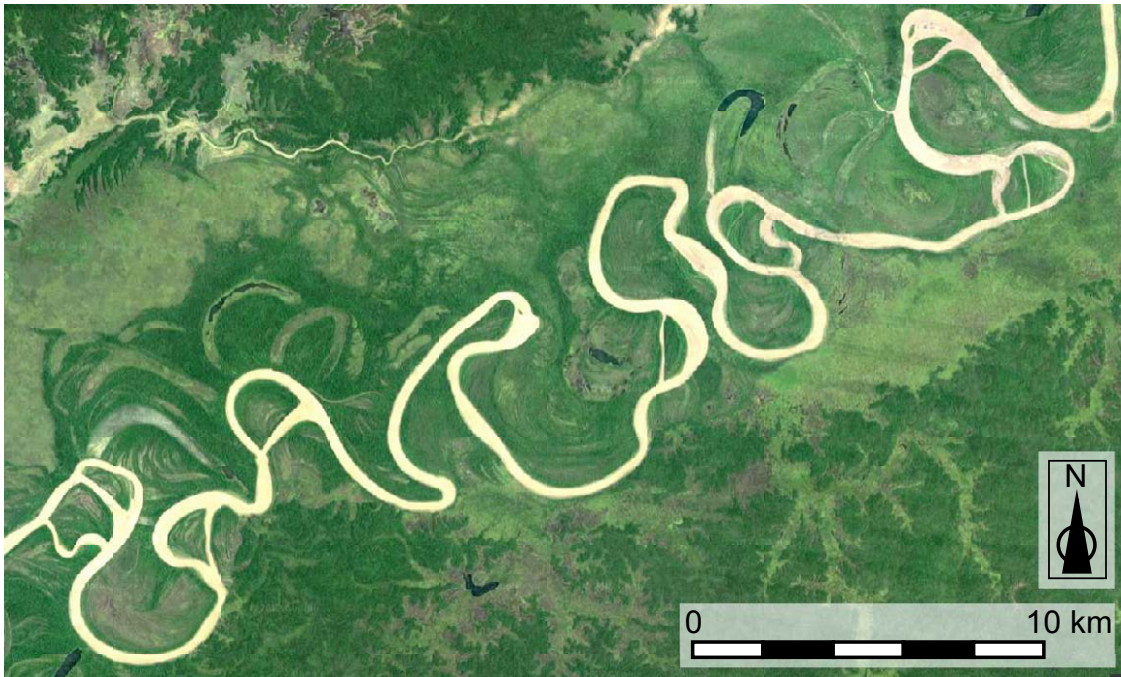


Figura 124. Examples of chute cutoffs in the Strickland River (Papua New Guinea) about 50 km north-east of the confluence with the Fly River (aerial photo from Google Earth, 2017, lat. 7° 13' 21" S; lon., 141° 46' 02" E).

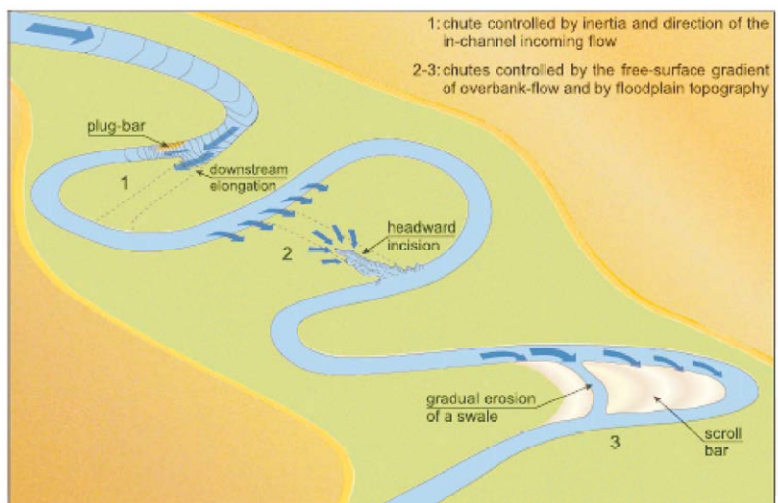


Figura 125. Possible mechanisms driving chute cutoff formation in meandering rivers. 1) Downstream elongation of a chute, controlled by inertia and direction of the in-channel incoming flow; 2) headward incision; and 3) swale enlargement aligned to main scroll bar direction (modified from Viero *et al.*, 2018).

creating an embayment that propagates upstream by headcut incision until it forms a chute.

Figure 126 shows an example of chute cutoff likely produced by the downstream extension of a small embayment. These data refer to two consecutive meandering bends of the Sacramento River (California, USA) surveyed in 1976 (continuous lines) and 1981 (dashed lines). An embayment (delimited by a magenta line) is present in the 1976 configuration downstream of the apex of

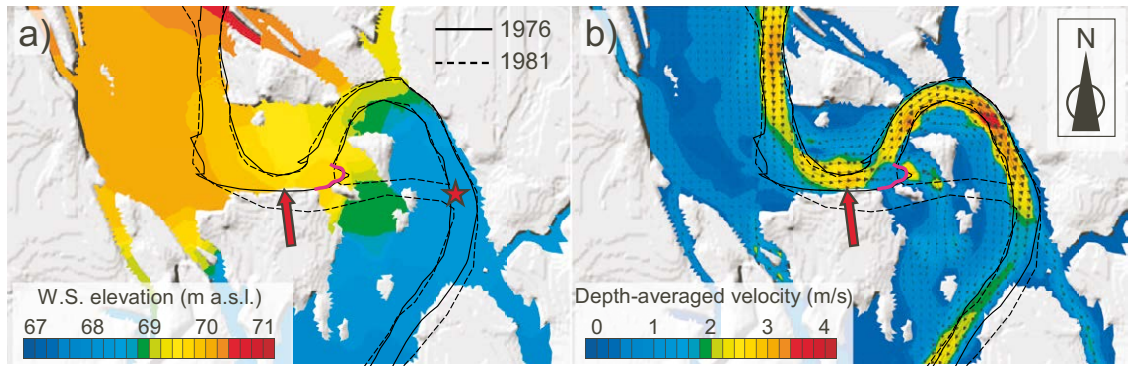


Figure 126. (a) Water surface elevation and (b) depth-averaged flow velocity in a bend of the Sacramento River (California, USA) near Bend Bridge gauge station, upstream of Red Bluff. The flow has been computed with the help of a two-dimensional finite element model considering a total discharge of $3000 \text{ m}^3 \text{ s}^{-1}$. Continuous and dotted lines denote the 1976 and 1981 river configurations, respectively. Red arrows denote the cross-section narrowing at the apex of the first bend; the magenta lines locate the embayment likely originating the chute cutoff; the red star in panel a) denotes the end cross-section of the chute that will be formed across the floodplain (modified from Viero *et al.*, 2018).

the first bend, at the outer bank. It was possibly originated by the presence of a more erodible portion of soil associated with the presence of a palaeo-meander, and precluded to the formation of the chute cutoff (dashed lines) characterizing the 1981 configuration. Numerical simulations, carried out with the help of a finite element model solving the two-dimensional shallow water equations, suggest that the narrowing of the main channel nearby the bend apex (red arrows) tends to concentrate the water flux and to increase the in-channel velocity. As a consequence, a high momentum current is directed against the outer bank and impinges on the embayment. This favours a progressive erosion of the bank material and hence meander migration, as well as the progressive downstream extension of a chute by the overbank flow ($340 \text{ m}^3 \text{ s}^{-1}$). Note that, in this example, the directions of the initial embayment and of the final chute tend to be aligned with that of the in-channel flow at the bend apex. This behaviour is promoted by the sharpness of the bend and the inertia of the incoming channelized flow, which is predominant with respect to the effects exerted by the floodplain characteristics (topography, vegetation, etc.). The palaeo-meander present in the floodplain, rather than driving the overbank flow, provides a more erodible portion of soil close to the outer channel bank, where shear stresses concentrate. Also, note that the cross-section enlargement caused by the embayment tends to reduce the flow velocity at the centre of the main channel. This reduction enhances sediment deposition, favouring the formation of a central-bar (Seminara, 2006) or a plug-bar (Eekhout and Hoitink, 2015) and, hence, the discharge diversion through the forming chute.

A second type of chute cutoff is depicted in Figure 127, referring to a meander of the Cecina River (Tuscany, Italy). In this case, the free-surface gradient, the topographic irregularities and the sedimentological composition of the floodplain area within the meander loop play a major role in triggering a chute cutoff. When a sufficiently large discharge is conveyed by the river (Figure 127b), the presence of poorly developed point bar deposits generates a gradient advantage and, hence, a preferential flow path (dashed lines) promoting the chute cutoff incision.

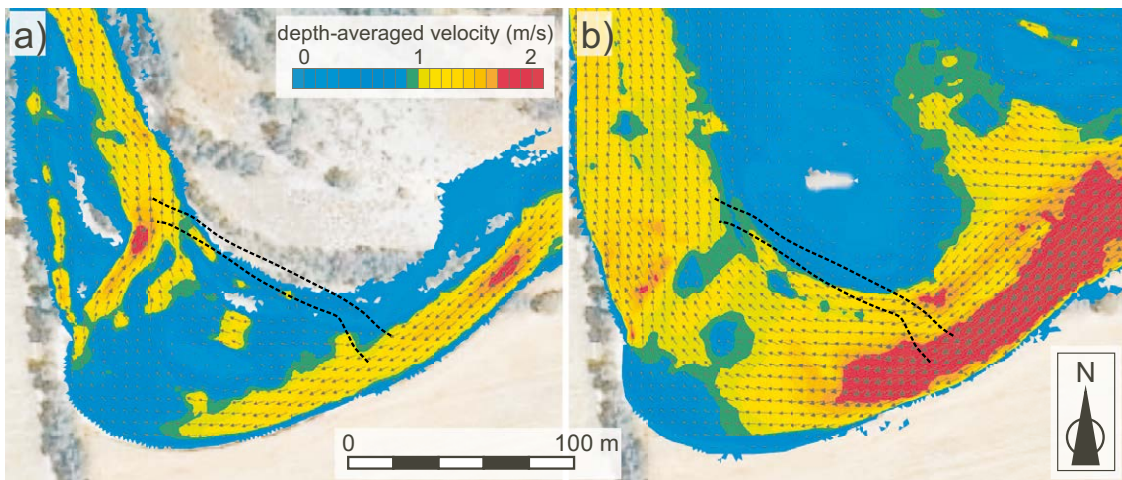


Figure 127. Spatial distribution of the depth-averaged flow velocity in a bend of the Cecina River (Tuscany, Italy). The flow has been computed with the help of a two-dimensional finite element model for values of river discharge equal to (a) $40 \text{ m}^3/\text{s}$ and (b) $200 \text{ m}^3/\text{s}$. Dashed lines denote the location of the chute occurred between 2010 and 2013. Elevations of the nodes of the numerical grid were reconstructed from a LiDAR survey carried out in 2008 and an aerial image (shaded in background) taken in 2010. Flow is from right to left (modified from Viero *et al.*, 2018).

6. Additional features of fluvial meandering

Two further important features of fluvial meandering, that we have ignored so far, deserve some attention. The first concerns the nature of natural sediments, that are known to be heterogeneous, so the issue arises of what sorting pattern develops on the sloping beds of meander bends; conversely, one may reasonably wonder whether sorting has any appreciable effect on bed topography. A second aspect regards the sediment supply: throughout all the previous chapters, we have invariably tacitly assumed that enough sediment was supplied to the channel, such to meet the transport capacity of the stream everywhere. This assumption is typically not satisfied in the upper portions of the watershed, where mixed alluvial-bedrock channels are often encountered.

Below, we address both issues reviewing the yet limited available knowledge on these subjects.

6.1. Sorting effects on fluvial meanders

Field observations on river meanders suggest that the heterogeneous character of sediments results in a fairly consistent sorting pattern: point bars on the inside of bends tend to be finer than the pools at the outer bends. Moreover, the upper parts of point bars display a tendency to be coarser upstream and finer downstream. This is illustrated in Figure 128, reporting field observations for a stream with a mixture of sand and gravel collected by Bridge and reproduced in Parker and Andrews (1985).

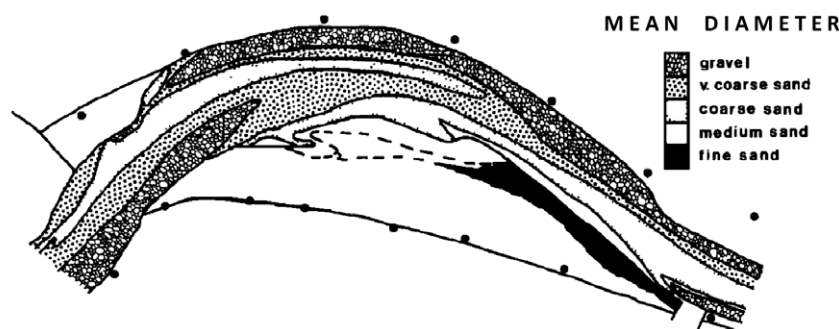


Figura 128. Pattern of sediment sorting in a bend of the South Esk River. Flow is from left to right. Field observations of Bridge as reproduced in Parker and Andrews (1985).

More recently, detailed observations of surface sorting were performed by Clayton (2010) in various reaches of two gravel bed rivers, namely the Colorado River at Rocky Mountain National Park (USA) and the Fall River (USA). The main result of this investigation was to show that increasing channel curvature enhances the degree of sorting (Figure 129a). Moreover, the standard deviation of surface grain sizes was found to decrease with distance downstream (Figure 129c), an effect increasing slightly with channel curvature.

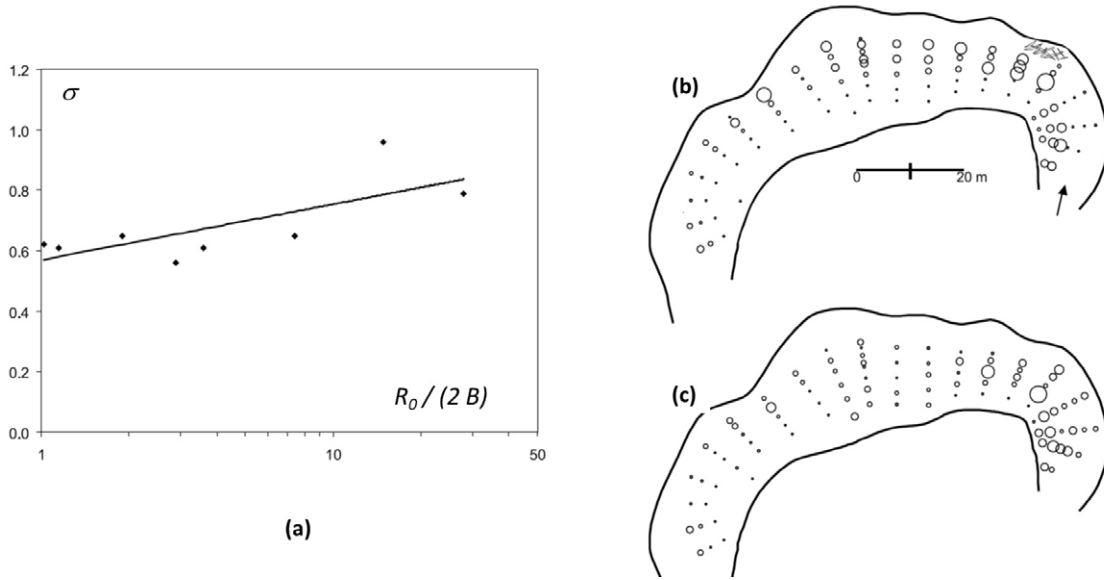


Figure 129. (a) Relationship between reach averaged standard deviation of the grain size distribution of surface sediments and radius of curvature scaled by channel width for all Colorado River and Fall River sites analyzed by Clayton (2010). The radius of curvature R_0 of the bend was obtained approximating the channel centerline with a fraction of a circle. Note that sorting is enhanced with increasing bend sharpness. The maps on the right show the distribution of (b) the average grain size d_{50} and (c) the standard deviation σ of the grain size distribution, measured at a number of locations in bend CR2. The size of symbols is proportional to the magnitude of the corresponding quantity. Values for d_{50} ranged from 7.5 to 56.9 mm. Values for σ ranged from 0.42 to 1.14. Flow is from right to left (modified from Clayton, 2010).

A number of early attempts to obtain a mechanistic interpretation of sediment sorting in bends appeared in the '70s. They are reviewed by Parker and Andrews (1985). The latter paper can be considered the first modern contribution attempting at finding a mechanistic solution of the bend sorting problem. Let us then outline the basic physics of the sorting process in the bedload dominated case emerging from the latter work. Recall the expression (390b(I)) for the lateral component of the dimensional bedload flux per unit width Q_{yd}^b in cartesian coordinates. In the (s, n) curvilinear coordinates employed in the previous Chapters and according to the linear approximation appropriate to weakly sloping beds, Q_{nd}^b reads:

$$Q_{nd}^b = Q_{0d}^b \left[\sin \chi - \frac{r}{\sqrt{\tau_{*g}}} \sqrt{\frac{d}{d_g} \mathcal{H}(d/d_g) \frac{\partial \eta}{\partial n}} \right]. \quad (385)$$

The coefficient of the lateral slope in (385) is seen to be proportional to $[(d/d_g) \mathcal{H}]^{1/2}$ hence, recalling (377(I)), it is a (weakly) increasing function of the ratio d/d_g . It then follows that coarser grains feel the down-slope pull of gravity more intensely than finer grains. In other words, *sorting is accomplished as coarser grains move preferentially toward the base of transverse slopes*, a mechanism which is supported by the observations that we have just outlined. As this mechanism was pointed out in the 1980's, it is somewhat surprising that the above ideas have not been fully implemented in a sound model of sorting in meandering rivers yet. Indeed, to our knowledge, the only fairly conclusive contribution available so far concerns the case of constant curvature bends that was analyzed by Seminara *et al.* (1997) modifying a previous contribution of Ikeda *et al.* (1987). The analysis considers a wide rectangular bend with constant width and constant curvature issuing from a straight channel subject to a uniform flow carrying a constant discharge of heterogeneous sediments with a given grain size distribution. The basic idea of the analysis

of Seminara *et al.* (1997) is to assume *complete sorting*. This means that the differential lateral mobility of grains of different sizes has led to a lateral redistribution of sediment sizes such that, at each lateral coordinate, sediments are characterized by only one size in equilibrium with the local lateral slope (Figure 130). This is obviously a simplifying assumption, but it is qualitatively supported by the field observations quoted above (Figure 128).

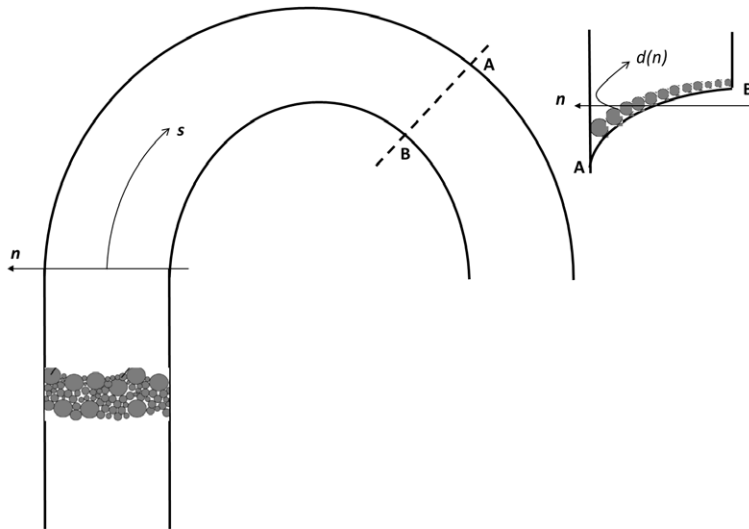


Figura 130. Sketch illustrating the assumption of *complete sorting* adopted by Seminara *et al.* (1997) to investigate the process of sorting in constant curvature bends.

The second ingredient needed by Seminara *et al.* (1997) was the availability of a morphodynamic model for flow and bed topography in constant curvature channels. This goal was fulfilled using a modified version of the nonlinear model of Seminara and Solari (1998) that we have extensively discussed in Section 3.2.2. The only modification required concerns the implementation of the constraint of vanishing lateral component of bedload transport, expressed through equation (385). Here, the grain diameter d appearing in the definition of the Shields stress is now an unknown function of the lateral coordinate n . Moreover, the hiding function in the complete sorting assumption is equal to one (sediment is effectively uniform at each lateral coordinate). The constraint to be satisfied in order to determine the function $d(n)$ is sediment continuity. It requires that the sediment supply associated with any given grain size (that is transported everywhere in the straight reach) must be equal to the flux of sediments transported through the longitudinal strip corresponding to the lateral coordinate where that grain size concentrates as a result of sediment sorting. Mathematically this constraint reads:

$$2 B Q_d^b \Delta d = Q_0^b |_{\tau_{*d}} \Delta n, \quad (386)$$

where $Q_d^b \Delta d$ is the flux per unit width transported by a sediment mixture as bed load in the size range $(d, d + \Delta d)$ (recall equation 381(I)).

Note that, in the limit of infinitesimal increments, (386) becomes an ordinary differential equation that can be solved provided the lateral distribution of the Shields stress in the cross section is known from the hydrodynamic model, for given distribution of grain size in the lateral direction. The problem is then solved using a trial and error approach. One starts from an initial tentative distribution of grain size (say uniform). This allows to determine the flow and bed topography with the help of the model of Seminara and Solari (1998). One can then solve (386) for the distribution $d(n)$ imposing that the finest size is located at the inner bend ($d|_{n=-1} = d_{min}$). Of course, the first trial will not allow one to satisfy the further condition ($d|_{n=+1} = d_{max}$) at the outer bend. One then iterates on the parameter \mathcal{R} (recall equation 209), which represents the

ratio between the free surface slope in the curved bend and its unperturbed value in the straight reach. Iterations then proceed until the boundary condition on the grain size at the outer bend is also satisfied.

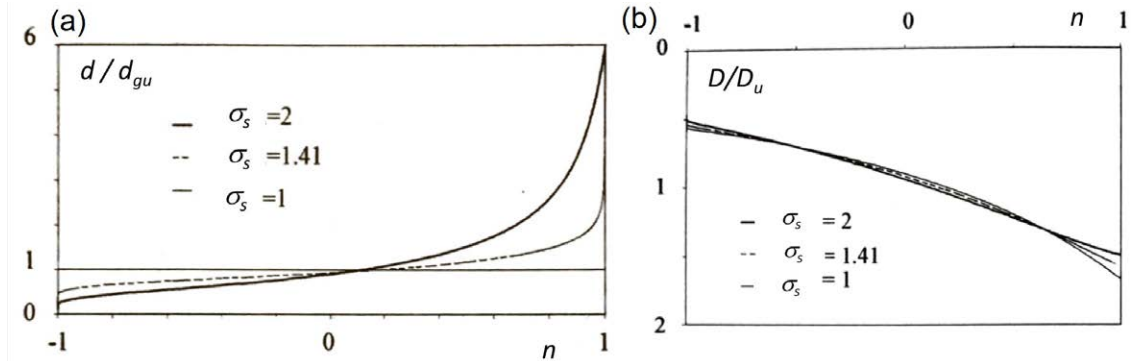


Figure 131. Grain size distribution (a) and bed topography (b) in a constant curvature wide rectangular bend issuing from a straight channel subject to a uniform flow carrying a constant discharge of heterogeneous sediments according to results of Seminara and Solari (1998). The size distribution is log-normal with diameters in the range $(0.1 - 6) d_{gu}$, with d_{gu} geometric average size and σ_s geometric standard deviation of the surface layer. D_u denotes the average flow depth in the upstream straight channel. Values of parameters are: $d_{gu} = 16 \text{ mm}$; free surface slope of the fully developed stream in the curved reach $= 5 \cdot 10^{-4}$; parameter controlling the amplitude of bed perturbations $\nu_0 (\sqrt{\tau_{*g}}/r) C_f = 10$; average friction coefficient in the bend $C_f = 0.0004$.

Figure 131 shows results obtained by Seminara *et al.* (1997). Not surprisingly, it turns out that sorting becomes more pronounced as the standard deviation of the sediment mixture increases. Moreover, the geometric average grain size is found to be located close to the channel centerline. The effect of sorting on bed topography appears to be quite weak. It remains to be ascertained how promptly sorting at the entrance of the bend develops into its fully developed (complete) state. To our knowledge, this problem has not been tackled yet.

The above model takes advantage of the fact that, under ideal fully developed conditions in constant curvature channels, no lateral bedload transport occurs. This is not the case in meandering channels where sediment continuity requires that longitudinal variations of the longitudinal component of bedload (driven by longitudinal variations of channel curvature) must be balanced by lateral variations of the lateral component of bedload. The only theoretical attempt known to us to tackle the meandering case is the early attempt of Parker and Andrews (1985). Although that work bears a major historical importance as it was the first to clarify the physics of the sorting process, however the way those ideas were implemented (assumption of weak sorting and lowest order treatment of the hydrodynamics) severely limits the significance of the actual results. In particular, the Authors were forced to include in their model some effect of the side wall boundary layers, the only regions where the longitudinal flow at lowest order exhibits lateral variations. If the Authors had restricted their attention to the central region, their theory would have predicted the absence of sorting.

A similar approach was later employed by Sun *et al.* (2001a,b), who developed a computer model based on the hydrodynamic approach of Johannesson and Parker (1989) and the sorting model of Parker and Andrews (1985). Sorting results again from the artificial inclusion of side wall effects. Also, the model adopts the assumption of small amplitude of the perturbations of the grain size distribution, which is again hardly justified.

In conclusion, mathematical modeling of sorting in meandering rivers is a still open issue even if one restricts oneself to the case of dominant bedload. The role of suspension further complicates the problem and is left as one of the future challenges for research.

6.2. Meanders in mixed bedrock-alluvial channels

Let us finally investigate how the available knowledge on alluvial meandering can be extended to the mixed bedrock-alluvial case. The very existence of meandering rivers in bedrock environments poses a number of questions, most notably the problem of how they originated. We outline the available knowledge on this problem in Section 6.2.2. However, preliminarily, it is appropriate to analyze how the morphodynamics of meandering alluvial channels is modified when the sediment supply rate is lower than the transport capacity and the thickness of the alluvial cover is finite. We provide an overview of the latter issue in the next section.

6.2.1 Morphodynamics of mixed bedrock-alluvial meandering channels

Some progress on this subject has been made with the help of laboratory observations, as well as theoretical modeling.

Laboratory observations

The development of point bars on the inside of bends whose outside is bare rock was reproduced in various laboratory experiments. Some of them (Shepherd and Schumm, 1974; Mishra *et al.*, 2018; Fernández *et al.*, 2019) were ultimately interested in understanding the mechanics of vertical and lateral incision in bedrock-alluvial meanders, hence they will be discussed in the next subsection.

Experiments in a laboratory meandering flume aimed at addressing the development of morphology in mixed bedrock-alluvial meanders were performed by Papangelakis *et al.* (2020). These Authors analyzed the effects of sediment supply and channel curvature on the spatial distribution and extent of the alluvial cover in a fixed-bed sinuous channel under conditions of *insufficient* sediment supply (ranging between 0.3 and 1.2 times the estimated channel capacity under constant discharge). A poorly sorted sand mixture ($d_{10} = 0.39 \text{ mm}$, $d_{50} = 1.2 \text{ mm}$, $d_{90} = 3.5 \text{ mm}$) was employed to construct the fixed bed and feed the channel.

Experiments started from a condition of bare bed. Feeding sediments at a constant rate, the cover fraction increased from zero to an equilibrium value, invariably lower than one, that was found to increase with the sediment supply rate. Similar trend was displayed by the volume of the alluvial cover stored in the channel. The Authors state explicitly that “*even as the cover fraction reached a limit with increasing sediment supply, additional increases in supply continued to be stored as increasing cover thickness but not areal extent*”. To what extent the latter statement can be extended to higher sediment supplies is a yet unanswered question.

The development of alluvial cover led to the formation of a periodic sequence of *steady forced bars* located at channel bends. The outside of bends between apexes remained bare in all experiments. More precisely, 20% of the bed area remained bare even in the run characterized by supply rate slightly larger than the estimated channel capacity (Figure 132). Bars developed simultaneously in all channel bends but at different rates, the upstream bends responding faster than downstream ones.

The heterogeneous character of the sediment led to the development of sorting patterns associated with the morphologic features of the alluvial cover. The sorting pattern changed depending on the feed rate. Essentially, bar deposits were fine at the top of the bars, whilst coarse sediment deposited along the outlines of the bars and the crossover features were coarser than the bars.

Modeling

While considerable progress has been made in understanding flow and bed topography in curved alluvial channels (see Chapters 2 and 4, the analogous problem for mixed bedrock-alluvial meandering channels is still largely unexplored.

Some preliminary insight was gained in the recent contribution of Nelson *et al.* (2014) who investigated how channel curvature affects sediment deposition and bedrock exposure in mixed bedrock-alluvial rivers. To achieve this goal Nelson *et al.* (2014) extended the analytical approach of Seminara and Solari (1998) and Bolla *et al.* (2009) such to account for three novel features:

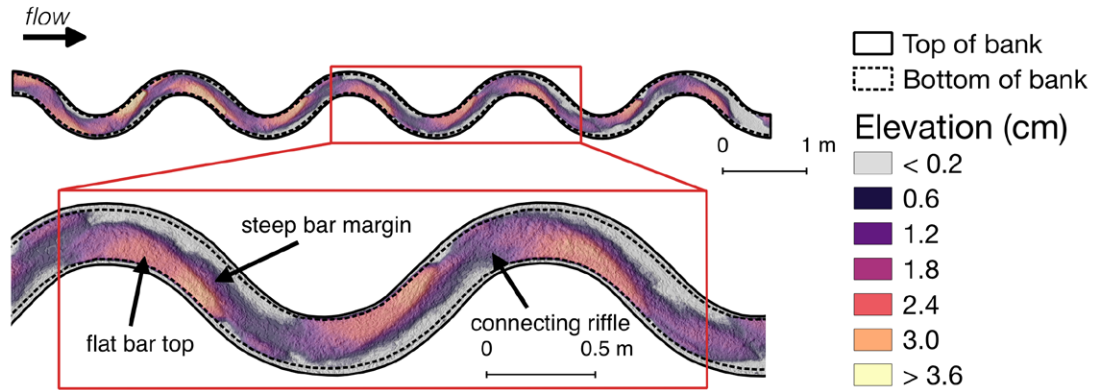


Figura 132. Spatial distribution of the elevation (z) of the alluvial cover above the channel bed surveyed at the end of the experiment of Papangelakis *et al.* (2020) characterized by the highest supply rate. The latter was slightly larger than the estimated channel capacity. Inset shows details for one meander wavelength (courtesy of Elli Papangelakis).

the alluvial layer has finite thickness, bedrock and alluvial portions of the bed have different roughnesses, and the sediment supply is less than the local sediment transport capacity. This new model allowed for the investigation of the mechanisms that control the bed topography as well as the distribution of sediment and bedrock cover through the cross section.

Following Seminara and Solari (1998), Nelson *et al.* (2014) consider a *wide* channel bend with channel centerline consisting of a circular helix with constant radius of curvature r_0 *large* relative to the constant channel width $2B$ (Figure 133). The curvature driven secondary flow generates perturbations of the sediment transport field which ultimately lead to the development of a point bar at the inner bank. However, in the mixed alluvial-bedrock case, the bar forms at the top of a bedrock layer (the flat interface in Figure 133). It is thus the goal of the model to determine whether and how much of the bedrock is exposed, as well as the shape of the bar.

We adopt the notations of Figure 133 and consider the steady flow of a constant fluid discharge Q under *fully developed* conditions, i.e. such that the properties of the flow field, sediment transport field, and bed topography do not vary in the downstream direction ($\partial/\partial s = 0$). Let us denote by U_u , D_u and C_{fu} the average speed, flow depth, and friction coefficient of the uniform flow field in the upstream straight reach with constant slope S_u . Let S_b denote the constant slope of the bottom centerline in the fully developed portion of the bend. It is then convenient to model the flow field in the bend as a perturbation of a uniform flow with average speed, flow depth, and friction coefficient U_b , D_b and C_{fb} , modified from the straight values by the effects of curvature, bed topography, and roughness. We recall that from the appropriate scaling of the governing equations for flow and bed topography, the following dimensionless parameters emerge:

$$\nu = \frac{B}{r_0}, \quad \beta_b = \frac{B}{D_b}, \quad \delta = \frac{\nu}{\beta_b \sqrt{C_{fb}}} \quad (387)$$

The assumptions of wide and weakly curved channel, with typical values of the friction coefficient, imply that

$$\nu \ll 1, \quad \beta_b \gg 1, \quad \delta \ll 1 \quad (388)$$

Following Seminara and Solari (1998), Nelson *et al.* (2014) set up a perturbation expansion of the solution for flow and bed topography in powers of the small parameter δ , i.e. in a neighborhood of the straight solution, assuming that the cross-sectional shape of the bend is described by some unknown function $D(n)$ to be determined. The analysis follows the lines of Seminara and Solari (1998) with some modifications. Essentially, one derives a nonlinear ordinary differential

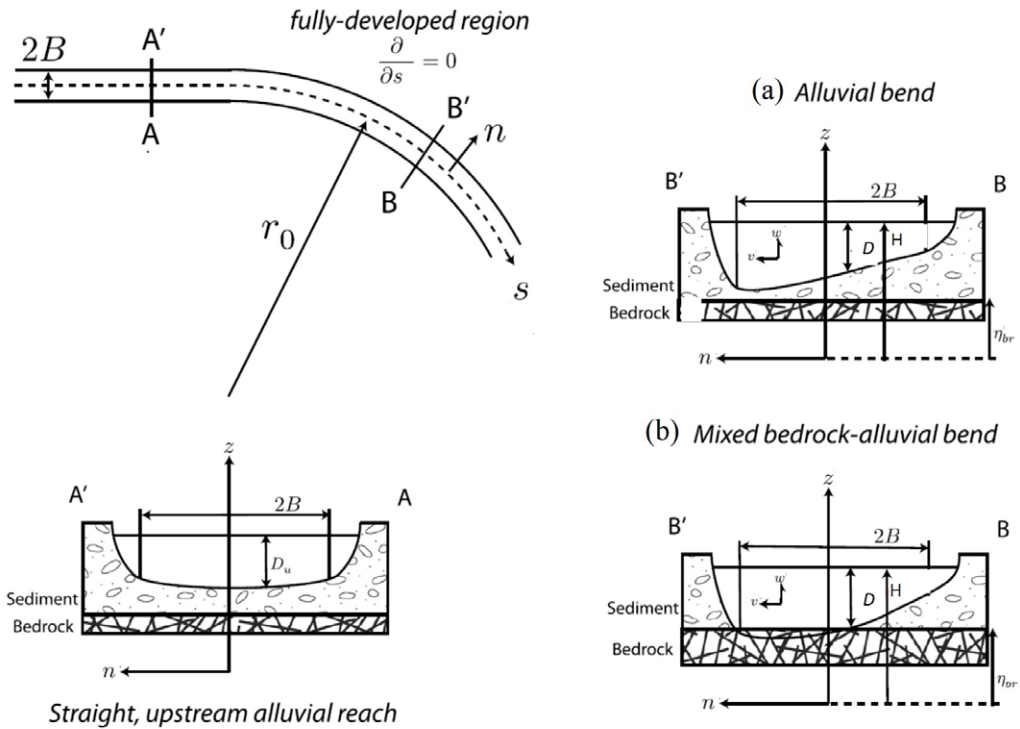


Figure 133. Sketch and notations for a mixed alluvial-bedrock channel bend. (a) Fully alluvial case: the maximum bedrock elevation is lower than the deepest point of scour. (b) Mixed bedrock-alluvial case: part of the bed surface is exposed bedrock. The channel is *wide*, the curvature parameter ν being approximately 0.05. The analysis is restricted to the central flow region spanning $2B$ and ignores the boundary layers at the side walls (modified from Nelson *et al.*, 2014).

equation for the local flow depth D as a function of the lateral coordinate at the various order of approximations. This is solved by a trial and error procedure starting from some initial guess for the value of D at the inner bank and iterating until the flow discharge in the whole cross section meets the assigned value. At some stage, the computed bed elevation may locally reach values lower than the local bedrock elevation η_{br} , indicating a transition from alluvial bed conditions to exposed bedrock. The computational approach must then recognize that the bed elevation in the exposed bedrock region is no longer unknown. At each iteration, the bed slope in the bend necessary to satisfy the sediment integral constraint must also be evaluated at each order of approximation, assuming that no sediment flux occurs in the exposed area. The updated value of the bed slope is then used to update the solution for $D(n)$ and the procedure iterates until the changes from one iteration to the next become negligible.

Results of Nelson *et al.* (2014) show that, in mixed bedrock-alluvial bends, there is a characteristic relationship between the various parameters controlling the bend morphology: dimensionless curvature, rate of sediment supply, morphology of the point bar, and amount of bedrock exposure. The points in Figure 134a show the predicted fraction of bedrock exposed in the bend as a function of the ratio Q_{sup}/Q_b of the rate of sediment supply to the total sediment transport capacity in the bend, for values of dimensionless curvature in the range 0.02 – 0.08. A clear, nearly linear relationship between Q_{sup}/Q_b and the fraction of bedrock exposed emerges (point cloud as compared to the dashed line in Figure 134a), a finding in close agreement with the exposure term proposed by Sklar and Dietrich (2004).

In Figure 134b the dimensionless bar height (difference in elevation between the bar top and the pool or bedrock surface, scaled by D_b) is plotted as a function of the ratio Q_{sup}/Q_b and for

different values of the curvature ratio. Note that, increasing either the bend curvature or the rate of sediment supply, the point bar height increases.

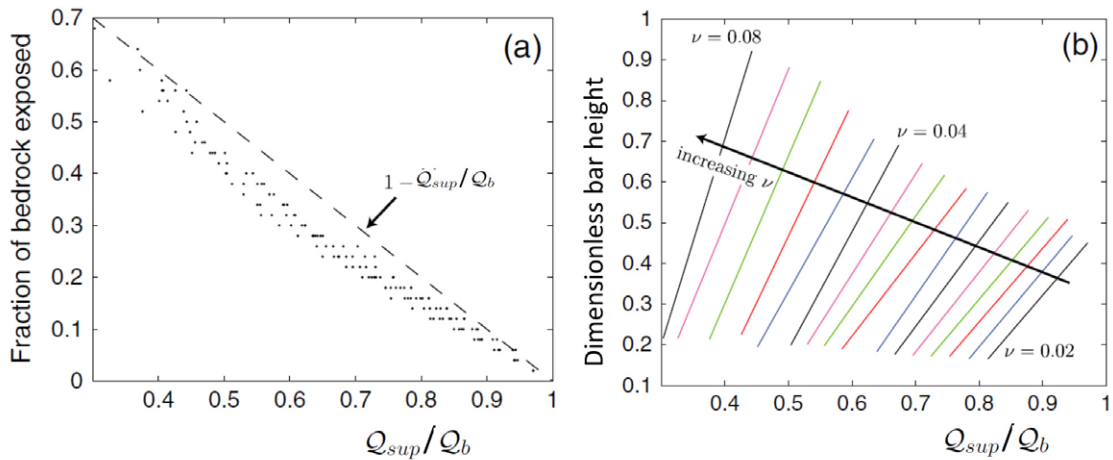


Figure 134. (a) Fraction of bedrock exposed as a function of the ratio Q_{sup}/Q_b of upstream rate of sediment supply to total sediment transport capacity in the bend. The points correspond to the results of Nelson *et al.* (2014) while the dashed line shows the linear cover relationship of Sklar and Dietrich (2004). (b) Dimensionless bar height (scaled by D_b) as a function of the ratio Q_{sup}/Q_b , for different values of the dimensionless channel curvature ν . In the computations, the bedrock elevation was assigned and the areal concentration of bed sediment in the straight upstream channel was set equal to one (fully alluviated). Moreover, the bedrock roughness was assumed to be equal to the roughness of the alluvial bed (modified from Nelson *et al.*, 2014).

Nelson *et al.* (2014) have tested the model using data provided by Nittrouer *et al.* (2011) for the lower Mississippi River, which has characteristics of a mixed bedrock-alluvial river as sand is transported over a consolidated bedrock-like substratum, which becomes exposed at some locations along the river (recall Figure 143(I)). Using those data, Nelson *et al.* (2014) varied the curvature parameter ν from 0 to 0.08. In Figure 135 the fraction of the bedrock exposed is plotted as a function of dimensionless curvature. The model predicts a threshold value of ν equal to 0.029 below which the bed is fully alluviated (i.e. no bedrock is exposed). This threshold nicely agrees with the observations of Nittrouer *et al.* (2011). Furthermore, adopting parameters characteristic of bends in the lower Mississippi, the model predicts the formation of point bars with a finite amplitude height of about 25 m and sediment coverage spanning about 60% of the channel, values falling within the range of observations reported by Nittrouer *et al.* (2011).

Various developments of the above model await to be pursued. In particular, its extension to the case of arbitrary curvature is the next obvious step (see, the slowly varying model of Bolla *et al.* (2009) for the alluvial case). The assumption of uniform sediment also needs to be relaxed in order to explore the effects of sorting on finite amplitude morphology.

6.2.2 How do meanders incise bedrock?

An ambitious goal of investigations concerning incised meandering rivers is settling a long-standing issue (Leopold *et al.*, 1964, p. 313), namely that of ascertaining which fundamental mechanism underlies their formation.

Entrenched vs incised meanders

Due to its complexity, the state of the art on this problem does not seem to have progressed much from the picture outlined in Shepherd and Schumm (1974). The ongoing debate at that time, based on early contributions by Davis (1893a,b) and Winslow (1893), identified two distinct types of bedrock meanders, sometimes referred to as *entrenched* and *incised*, respectively.

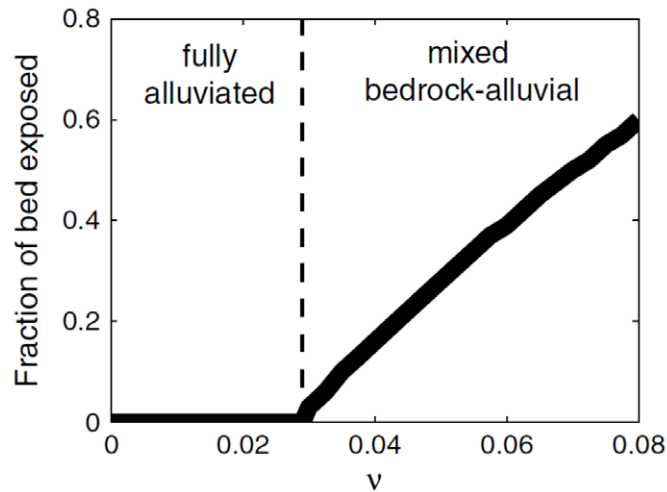


Figure 135. Fraction of bedrock exposed in a constant curvature bend of a mixed bedrock-alluvial channel as a function of dimensionless curvature for values of the dimensionless parameters characteristic of the lower Mississippi River (Nitttrouer *et al.*, 2011): $S_u = 10^{-5}$, $d = 1 \text{ mm}$, $B = 430 \text{ m}$, and $D_u = 35 \text{ m}$. The value $\nu = 0.029$ turns out to be the threshold between full alluvial coverage and partial bedrock exposure (reproduced from Nelson *et al.*, 2014).

Winslow (1893) suggested that *incised* meanders originate from streams with minor sinuosities which would then increase through a combined process of both downward and lateral cutting, possibly favored by the essentially horizontal character of the rock formations, as in the Ozark plateau cut by the Osage River. A major expression of this process would be the existence of *slip-off slopes at the convex banks* of meander spurs and *undercutting at the concave banks* of the same meanders (Figure 136).



Figure 136. Sketch of the mechanism of meander incision suggested by Winslow (1893) (modified from Tarr, 1924).

Davis (1893a) proposed a different mechanism for the origin of the so called *entrenched meanders*: they would originate from an initial pattern formed when the river flowed through a low-gradient alluvial plain. Later, uplifting of the alluvial plain would lead to entrenching of the meandering stream through a process of *vertical cutting* into the rising rock mass.

Tarr (1924) and Moore (1926a,b) argued that both types of meandering are present in nature. In particular, Moore (1926a), analyzing the San Juan River and other incised rivers in the Colorado Plateau, suggested that it is the effective resistance of the various strata through which the stream incises that controls the relative amount of vertical versus lateral incision. In resistant rocks, the erosive load is low and the stream becomes under-loaded, which favors vertical cutting. This is the case of the San Juan River in southeast Utah, which incised straight down for several hundred meters in bedrock while maintaining a highly sinuous and regular pattern (Figure 12). On the

contrary, in less resistant rocks, streams are overloaded, which would cause lateral cutting as illustrated in Figure 136.

In order to make any progress with the latter interpretations, one should investigate how the morphodynamics of mixed bedrock-alluvial meandering channels determines their vertical and lateral incisions. Some progress in this direction has been made with the help of laboratory investigations as well as theoretical contributions.

Insight from laboratory observations

A pioneering laboratory investigation was performed by Shepherd and Schumm (1974) in a laboratory channel realized using a mixture of water and well-mixed fine sand with 19% silt-clay and kaolinite, added to provide additional cohesion. After drying, this procedure provided a uniform, cohesive and isotropic material that had the desired characteristics, allowing to simulate bedrock, including its erosive response to hydraulic stresses and sediment transport, within an experimentally feasible time period. In one of the four experiments performed in this work, a channel was excavated in the simulated bedrock with a curved cross-sectional shape and a sinuous pattern (Figure 137a).

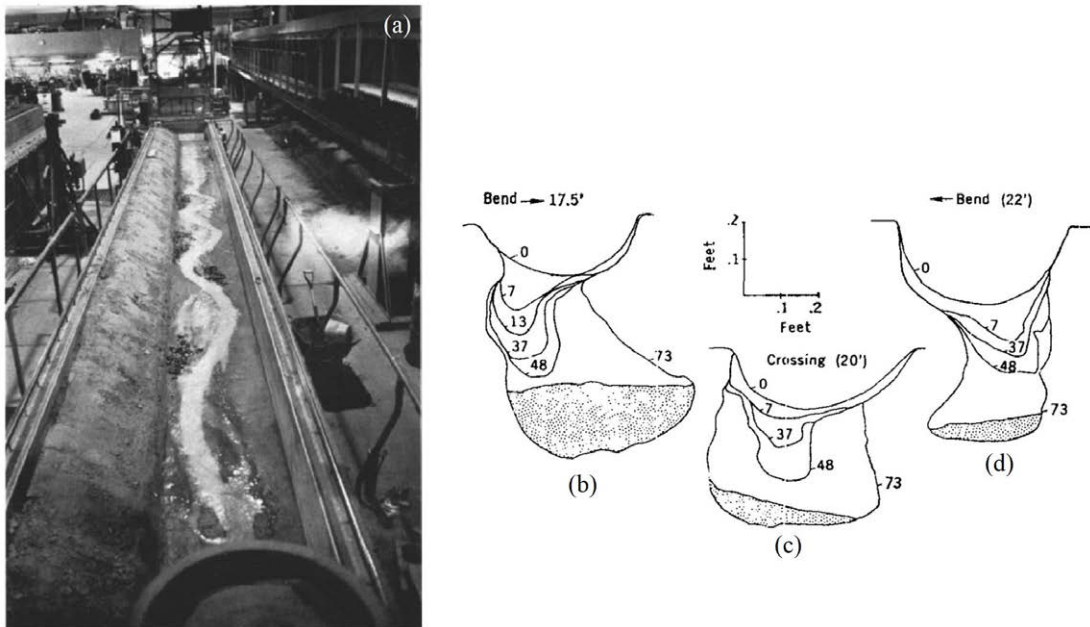


Figure 137. (a) Initial channel precut with a sinuous course in the fourth experiment of Shepherd and Schumm (1974). Note that gravel was used to prevent overflow at initial bankfull stage. Initial sinuosity was 1.05. (b-d) Lateral profiles of cross sections monitored at two bends (b,d) and at the crossing inbetween (c). Arrows point to concave banks. Stippled areas represent sand deposition; elapsed time is shown for each profile (modified from Shepherd and Schumm, 1974).

Fine sand was then fed upstream and various hydraulic and morphological properties (transverse and longitudinal water-surface profiles, channel cross sectional profile) were monitored at given time intervals. Figure 137b,c,d shows the lateral profiles of the experimental channel at two successive bends and at a crossing, representative of the trend observed at all bends and crossings. At each bend, erosion initially occurred at the inside bank. This is not surprising recalling that, at the entrance of bends with fixed bottoms, the longitudinal velocity (and the bottom stress) is known to peak at the inner bank. After 73 *h*, as gradient had decreased leading to sediment deposition, the maximum erosion had moved to the outer bank which was undercut. After 107 *h*, erosion had exposed the flume wall at the 17.5 *ft* bend. At the crossing between the two bends the

channel incised almost vertically into the bedrock (Figure 137c). Shepherd and Schumm (1974) also note that the relative intensity of lateral versus vertical incision was controlled by the amount of load entrained by the flow.

More recently, Fuller (2014) (but see also Fuller *et al.*, 2016) performed systematic laboratory experiments to investigate how bedload particle impacts may provide an efficient mechanism of lateral bedrock erosion and how the latter mechanism may be influenced by changes in channel bed roughness and bedload supply rate.

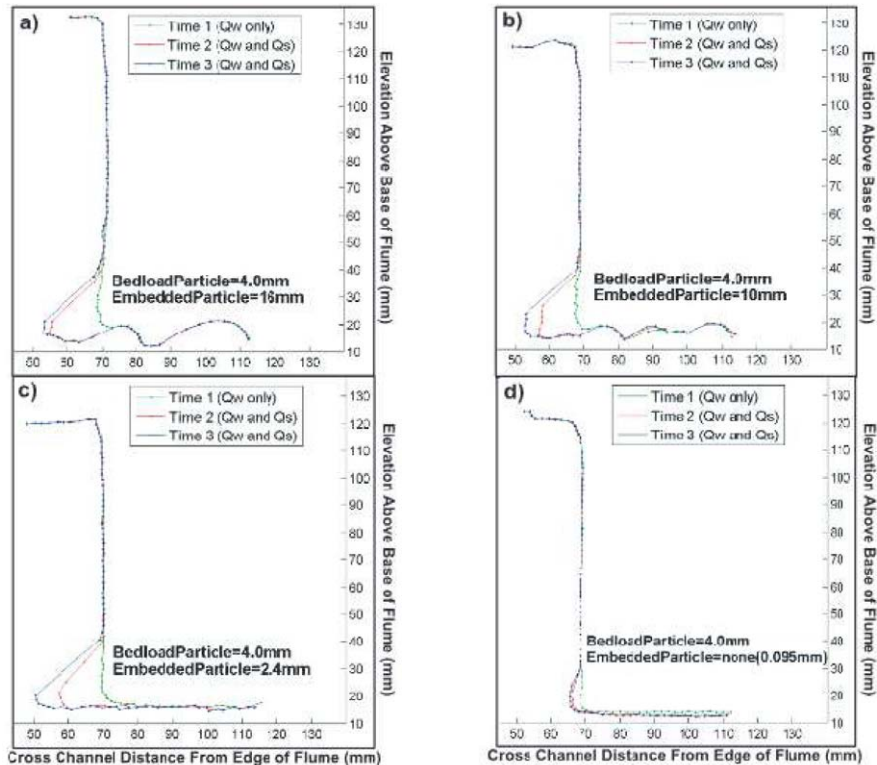


Figure 138. Profiles of the undercut portion of the channel wall in cross sections characterized by different roughnesses, observed in the flume experiment of Fuller (2014) at the end of the following periods: clear-water flow (Time 1, green dot); initial bed load supply (Time 2, red circle); and second bed load supply (Time 3, blue triangle). Legend time refers to the total time (in hours and minutes) elapsed since beginning of experiment (reproduced from Figure 2.9 of Fuller, 2014).

Using different amounts of sand and cement, the experimental channel was constructed such that the bed was non-erodible whilst channel walls were erodible. The bottom roughness was determined by the size of larger particles embedded in the sand-cement mixture. Results of the experiments can be summarized as follows:

- clear water did not produce significant lateral erosion (green lines in Figure 138);
- bank undercut was driven by bedload, which eroded preferentially the base of the channel walls, leading to the removal of up to 3% of the initial wetted cross-sectional area;
- adding bottom roughness of size exceeding a threshold (roughly equal to half the median bedload particle diameter) led to a large increase of lateral erosion, up to a factor of 7 (compare Figure 138d with Figure 138c);

- further increase of bottom roughness did not lead to significant variation of lateral erosion (compare Figure 138c with Figure 138a).

Fuller (2014) interpreted the above findings suggesting that saltating bed load particles were deflected into the channel wall by the fixed roughness elements and this mechanism drove the observed increase in lateral erosion rates. This interpretation was supported by the following arguments. Firstly, the rates of lateral erosion in the smooth channel sections did not increase significantly over clear flow values, suggesting that the downstream transport of saltating bed load particles cannot be major drivers of lateral erosion. Secondly, maximum erosion heights were found to be 3 times larger than the hop height predicted using a saltation model, suggesting that bed load particles are deflected by the tops of the protruding roughness elements, and thus reach higher elevations. Thirdly, a distinct correlation was observed between the degree of longitudinal variability in lateral erosion rates and the size of roughness elements. The lateral erosion rate was quasi-continuous when the size of roughness elements was comparable with the size of bedload particles and became increasingly discontinuous as the roughness size increased.

Fuller (2014) concludes that “*Given the ability of most bedrock rivers to transport sediment and the relatively wide distribution of grain sizes present in bedrock channels, lateral erosion by deflected particle impact is likely an active mechanism in most bedrock channels*”. They also note that particle deflection may also be driven by strong secondary flows like those observed at the entrance of canyons (Venditti *et al.*, 2014) or those driven by bar development, which could increase lateral fluid accelerations and enhance the lateral momentum of saltating bed load particles.

Most effective source of secondary flows, as we know, is channel curvature. The distinct features of lateral erosion in curved meandering channels have thus attracted the attention of Mishra (2017), but see also Mishra *et al.* (2018). The starting point of this work was the recognition that three distinct patterns are typically observed in bedrock meandering rivers: bedrock benches (namely exposed strips of bedrock with little sediment cover) at the outer banks, alluvial point bars and strath terraces at the inner banks (Figure 139). The Authors tried to interpret these observations performing experiments on a U-shaped channel with soft mortar bed and banks. Results displayed some interesting features. The thickness of the sediment layer as well as the sediment supply rates adopted in the experiments ensured that the bed in the straight, upstream and downstream, parts of the channel was fully covered. In the curved part, both regions of exposed bedrock and point bar developed, moreover vertical and lateral erosions were observed. These features are summarized in Figure 140, where red and green represent exposed bedrock and sediment covering, respectively.

As the sediment supply rate was increased, the height or width of the point bar increased and the exposed area decreased. Note that a part of the bed area in the bend was exposed even when the sediment supply rate was twice the initial transport capacity, although it is reasonable to predict that for sufficiently high values of the sediment supply rate or of the initial alluvial thickness, the channel bed would become fully covered, i.e. the alluvial limit would eventually be attained.

Vertical and lateral erosion were experienced in different portions of the bend, whilst no erosion occurred in the straight parts (Figure 140). The Author argues that: “*the vector direction of bedload near the outer bank is critical for eroding the walls of channel*” and “*with increased sediment input, the height of point bar increases . . . the effect of lateral bed slope dominates over effect of secondary flow making more and more sediment collide with the walls of the bank . . . , causing more and more erosion to the banks*”. Lateral abrasion was located in the region adjacent to the cross section at 135° and its amplitude increased linearly with the sediment supply rate. However, erosion was only experienced by the lowermost part of the bank. Vertical erosion peaked in the region adjacent to the cross section at 157° , although some weak erosion occurred also in the region adjacent to the cross section at 45° , where it concentrated in the central part of the cross section. In this region, bedrock near the outer bank was fully exposed and experienced less sediment transport over it, i.e. a bedrock bench developed. On the contrary, the bedrock near the inner bank was fully covered by sediment, hence the central part of the cross section was the only portion amenable to erosion.

The above observations will have to be extended and interpreted with the help of theoretical modeling that represents a major challenge for future research.



Figura 139. Image of a bend of the Shimanto River (Japan) showing various morphological units: bedrock bench at the outer bank, alluvial point bar and strath terrace at the inner bank (modified from Figure 2.1 of Mishra, 2017).

Let us conclude this section noting that one further mechanism that may play a role in lateral erosion is physical weathering of rock via wetting and drying cycles, as shown by Montgomery (2004) and Stock *et al.* (2005) for channels that cut through clay-rich lithologies. While weathering weakens the wall rock, it is the hydrodynamics, hence the wall shear stress, which is ultimately responsible for bedrock removal in this case.

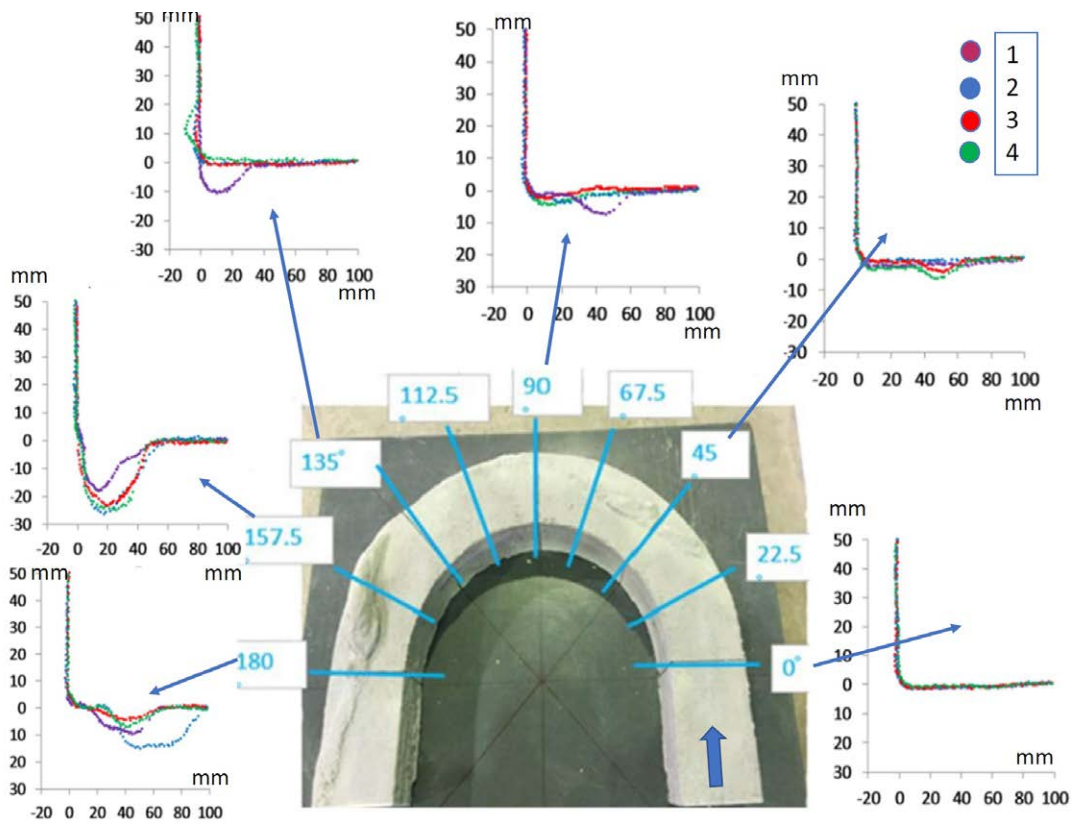


Figure 140. Mixed bedrock-alluvial bed observed at the end of the flume experiments of Mishra (2017). The lateral plots show cross-sectional profiles of bedrock surface measured from 3D scan of the mold at 4 locations in the channel. The zero reference elevation corresponds to the initial bed elevation at each section; values of the abscissa measure distances from the outer bank. Coloured dots are the experimental data: the four runs were characterized by different values of the sediment supply rate, increasing from $35 \text{ cm}^3/\text{min}$ in case 1 to 70, 100, $140 \text{ cm}^3/\text{min}$ in cases 2, 3, 4 respectively (modified from Figure 2.10 of Mishra, 2017).

7. Concluding remarks

In this Monograph, we have learnt that there is wide consensus on the nature of the physical process which determines the spatial-temporal development of meanders once they have formed. We have seen that research has conclusively ascertained that it is the combined outcome of outer bank erosion and inner bend accretion that controls meander development. Indeed, models based on the adoption of simple semiempirical 'long term' erosion rules have been able to reproduce most of the major features observed in nature: most notably meander growth, meander migration, skewing and fattening, shapes of meander loops and neck cutoff.

Consensus has also been reached on when and why free bars may migrate through low amplitude meanders. The ability of alternate bars to coexist with point bars without triggering bank erosion does not seem to point at the former features as the actual cause of incipient meander formation. And, indeed, as discussed in Section 5.3, in many modern experiments where meandering (rather than braiding) was reproduced in the laboratory, alternate bars did not form.

A further feature of the meandering process that may be considered as definitively ascertained is the role of bank cohesion, which turns out to be crucial to prevent the tendency of channels to evolve into braiding patterns.

Needless to say, there is room to improve our understanding of the meandering evolution process. In particular, decoupling outer bank erosion from inner bank deposition is still an open subject of research that calls for improved, physically based, modeling of both bank erosion and inner bend accretion, possibly accounting for the active role of vegetation and the distinct effects of bedload and suspended load. Indeed, planform evolution in alluvial valleys is affected by long term exchanges of water and sediments between the river and the flood plain, a process mediated by the vegetation dynamics, a feature which suggests that ecology will soon intrude in meandering research.

Also, available evolution models assume that planform changes are free to occur, independently of end effects that may constrain the channel to follow given paths. The role of upstream and downstream boundary conditions in meandering models remains an unexplored subject.

A few, non-irrelevant, unsolved modeling problems also remain.

One such problem concerns the modeling of the sorting patterns observed in meandering rivers. As discussed in Section 6.1, field observations are clear: point bars on the inside of bends tend to be finer than the pools at the outer bends, moreover, the upper parts of point bars display a tendency to be coarser upstream and finer downstream. The physical mechanism of sorting has been clarified in the early work of Parker and Andrews (1985) as driven by the size-dependent component of gravity in the direction tangent to the lateral bed profile. It is then somewhat surprising that a phenomenon whose characteristics are clear from field observations and theoretical arguments, has so far defeated attempts to formulate sound theoretical models. As pointed out in Section 6.1 the available models of sorting in meandering rivers are based on two weak assumptions: sorting requires the artificial inclusion of side wall effects and the perturbation of the grain size distribution driven by channel curvature is assumed to have small amplitude. The topic is open to improvements.

Progress in the available knowledge on meandering initiation and meander development in mixed bedrock-alluvial channels is also needed. Indeed, as discussed in Section 6.2, no conclusive answer is

yet available to the issue of which of the two proposed mechanisms (entrenched vs. incised) prevails depending on the type of rock formation and the history of uplifting of the valley plain. This is an active area of research that calls for a close collaboration between geomorphologists and hydraulic engineers and will strongly benefit from further laboratory observations and theoretical modeling to support interpretations of combined vertical and lateral incisions of mixed bedrock-alluvial meandering channels.

Finally, a fundamental question that one may ask is: *Can meanders form in the absence of point bars?*

We have shown in Chapter 4 that a straight fluvial pattern is not stable in general, in that a planform instability is triggered by bank erosion-deposition processes in cohesionless channels, and all the mechanisms of meander formation reviewed in this book (except, possibly, the insufficiently explored process of meandering in bedrock channels) rely on the existence of point bars.

However, a well known early explanation of river meandering, proposed by Albert Einstein (Einstein, 1926), did not rely on point bars. It was based on a tea cup analogy and captured the role of centrifugally driven secondary flow in a curved bend. *“At every cross-section of its course, where it is bent, a centrifugal force operates in the direction of the outside of the curve (from A to B). This force is less near the bottom, where the speed of the current is reduced by friction, than higher above the bottom. This causes a circular movement of the kind illustrated in the diagram”* (Figure 141b). It also captured the mechanism of lateral redistribution of momentum associated with the secondary flow: *“The particles of liquid in most rapid motion will be farthest away from the walls, that is to say, in the upper part above the center of the bottom. These most rapid parts of the water will be driven by the circulation toward the right-hand wall, while the left-hand wall gets the water which comes from the region near the bottom and has a specially low velocity”*. And concluded: *“Hence in the case depicted in Figure 141a the erosion is necessarily stronger on the right side than on the left”*. The reader should note that Einstein’s picture ignores the metric effect that drives flow acceleration at the inner bend and delays the weak effect of the lateral redistribution of longitudinal momentum, but it does contain the essential idea that meander formation is caused by bank erosion at the ‘outer banks’. However, it is noticeable that, in this picture, the flow concentration towards the outer bank responsible for bank erosion is exclusively attributed to the centrifugally driven component of the secondary flow. In other words, although

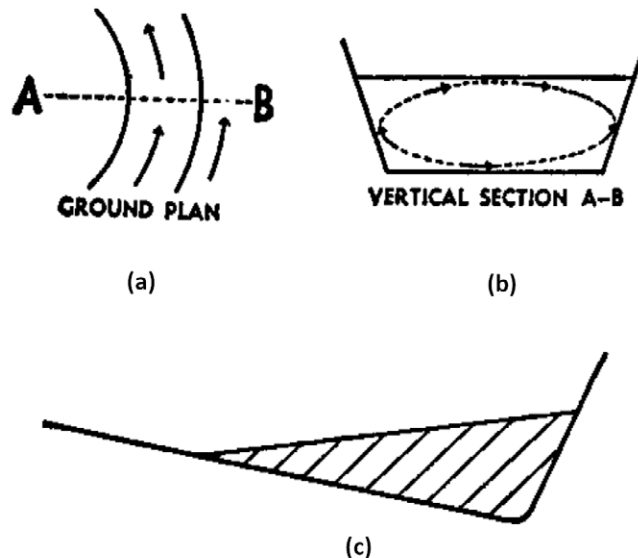


Figure 141. Einstein’s sketch illustrating the formation of centrifugally driven secondary flows in curved bends.

Einstein (1926) was fully aware of channel deepening at the outer bank, he ignored the role of the topographically driven component of secondary flow, which is now known to dominate over the

centrifugal component as soon as the bottom deforms. Indeed, he writes: “*We have now revealed the causes of the formation of meanders. Certain details can, however, also be deduced without difficulty from these facts. Erosion will be comparatively extensive not merely on the right-hand wall but also on the right half of the bottom, so that there will be a tendency to assume a profile as illustrated in Figure 141c*”. Hence, in the latter picture, outer channel deepening would be the mere consequence of the redistribution of longitudinal momentum driven by the centrifugal secondary flow.

One is then led to formulating the fundamental question raised above, that none seems to have conclusively tackled yet. Proving that a channel with no point bar could meander would fit Einstein’s picture; proving the opposite would show that the part of the real process captured by Einstein’s intuition was insufficient to explain meander initiation! Such an investigation would also help clarifying recent experimental observations suggesting that irregular bends in peat bogs are strongly controlled by vegetation, migrate only sporadically and have rather unfrequent scroll bars (G. Parker, Personal communication).

Note that the answer to the latter question is by no means obvious. Indeed, the absence of point bars is equivalent to assuming a fixed horizontal bed. Employing the model discussed in Section 2.5 and forcing the bed to be horizontal ($S_n = 0$), one ends up with a picture of the flow field (see Figure 37, uppermost panel) suggesting that the thread of high velocity is located at the inner bend and is in phase with curvature: a pattern that definitely leads to bend stability. However, the model presented in Section 2.5, in the case of horizontal bed, accounts for the free vortex effect but does not include the very weak effect of lateral redistribution of longitudinal momentum associated with the centrifugal secondary flow. The fact that this effect is very weak emerges clearly for the experiments of Rozovskij (1957): indeed, a glance at Figure 26 shows that the free vortex effect prevails through the whole bend and the thread of high velocity is displaced towards the outer bend only around the bend exit. Momentum redistribution requires lateral variations of the basic longitudinal flow, a feature that is enhanced in narrow channels. Hence, one may not rule out the possibility that in narrow, sufficiently long meandering channels with fixed horizontal bed, the thread of high velocity may be displaced to the outer bank, possibly leading to bend instability.

Finally, engineering calls for the need of models of reduced complexity. Indeed, the most recent research developments in the field of hydrodynamics and morphodynamics of meandering channels focus on the refinement of fully 3D numerical models of flow and bed topography, with the aim to extend applications to the complex configurations relevant for practical purposes (e.g. Nabi *et al.*, 2012, 2013a,b; Sotiropoulos, 2019). However, investigations of the long term morphodynamic evolution of large scale fluvial reaches, an important issue in the century of global warming, can hardly be tackled with the help of 3D numerical models. Future progress may perhaps be sought in the opposite direction, namely that of deriving from the general formulation simpler, but physically and theoretically sound, models of reduced complexity that may be more suitable to long term simulations. Some attempts in this direction have been performed by Blanckaert and de Vriend (2003) and Ottevanger *et al.* (2013). Although such attempts should be welcomed, however achieving reduced complexity is much harder (though possibly more enjoyable) than running a computer model including all the necessary (and possibly unnecessary) ingredients. The hard job is to adopt approximations that can be rationally justified. In this respect, we feel that the problem is still open to future contributions.

8. Mathematical Appendix

The aim of this Chapter is to provide the reader with some basic knowledge on linear and nonlinear forced oscillators, as well as on the mathematics of the interaction between free and forced responses of oscillatory systems.

8.1. Forced oscillations and resonance

8.1.1 Toy model

Let us consider a new toy model consisting of the following nonlinear partial differential equation

$$\frac{du}{dt} + Lu + Nu = \nu \exp i\lambda_m x + c.c.. \quad (389)$$

The reader should note that, unlike in the toy-model (665, 666)(I) discussed in Chapter 9(I), a non-homogeneous forcing term is present in the right-hand side of equation (389).

Here, ν is a small parameter. Moreover, $L(\cdot)$ and $N(\cdot)$ are linear and nonlinear differential operators, respectively, defined in the form:

$$L \equiv \frac{\partial^4}{\partial x^4} + \frac{\partial^3}{\partial x^3} + 2R \frac{\partial^2}{\partial x^2} + 2\frac{\partial}{\partial x} + 1, \quad (390a)$$

$$N \equiv \left(\frac{\partial}{\partial x} \right)^2. \quad (390b)$$

8.1.2 Free oscillations: Temporal normal modes

In order to provide a complete picture of the behavior of the solutions of our toy model, it is convenient to start with a linear stability analysis, whereby we seek the response of the non-forced system ($\nu = 0$) to *infinitesimal perturbations* of the steady basic solution $u = 0$. To pursue this goal we write:

$$u(x, t) = \epsilon u_1(x, t) + \mathcal{O}(\epsilon^2), \quad (391)$$

with ϵ an infinitesimal parameter.

The assumption of infinitesimal perturbations allows us to *linearize* the differential problem. Substituting from (391) into (389) after setting $\nu = 0$ and neglecting terms of order ϵ^2 or higher we obtain:

$$\left(\frac{d}{dt} + L \right) u_1 = \left[\frac{d}{dt} + \frac{\partial^4}{\partial x^4} + \frac{\partial^3}{\partial x^3} + 2R \frac{\partial^2}{\partial x^2} + 2\frac{\partial}{\partial x} + 1 \right] u_1 = 0. \quad (392)$$

At this stage, it is convenient to restrict the class of perturbations considered, performing a *normal mode analysis* similar to that presented in Section 9.3.4(I). The *eigen-relationship* in the present case is found to read:

$$-i\omega + L_1(\lambda, R) = -i\omega + \lambda^4 - i\lambda^3 - 2R\lambda^2 + 2i\lambda + 1 = 0, \quad (393)$$

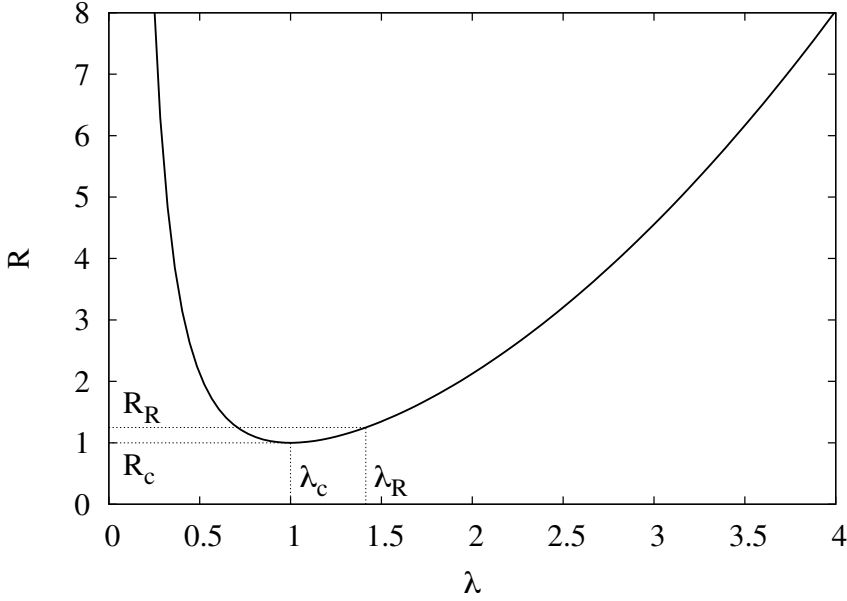


Figura 142. The marginal stability curve of the toy model (389) is plotted in the plane (λ, R) . The absolute minimum of the curve defines the critical values (λ_c and R_c) of the wavenumber and of the control parameter, respectively. The values λ_R and R_R denote marginal perturbations with vanishing wavespeed.

where λ is a real number, ω is complex (in general) and L_p ($p = 0, 1, 2, \dots$) denotes the algebraic operator:

$$L_p(\lambda, R; p) = p^4 \lambda^4 - i p^3 \lambda^3 - 2 R p^2 \lambda^2 + 2 i p \lambda + 1. \quad (394)$$

The eigenrelationship (393) shows that, for our toy model, ω is indeed a complex number. If we set $\omega_i = 0$, then the real part of (393) gives:

$$R = \frac{\lambda^4 + 1}{2\lambda^2}. \quad (395)$$

The relationship (395) determines the *marginal (or neutral) stability curve* in the plane (λ, R) plotted in Figure 142. It exhibits an absolute minimum for the following *critical values* of the control parameter R and wavenumber λ :

$$R_c = 1, \quad \lambda_c = 1. \quad (396)$$

The wavespeed c of marginal perturbations reads:

$$c = \frac{\omega_r}{\lambda} \Big|_{\text{marginal}} = \frac{2\lambda - \lambda^3}{\lambda} = 2 - \lambda^2. \quad (397)$$

In particular, at criticality, one finds $c_c = 1$. Moreover, we denote by $\lambda_R = \sqrt{2}$ the wavenumber of the marginal perturbations characterized by vanishing wavespeed which occur for $R_R = 5/4$.

8.1.3 Free oscillations: spatial modes

A second class of free oscillations allowed by the system is the spectrum of *spatial modes*, namely the set of normal modes characterized by vanishing values of ω and complex values of λ .

Needless to say these are non-migrating modes. The associated eigen-relationship is obtained from (393) with λ complex simply setting $\omega = 0$, to find:

$$L_1(\lambda, R) = 0. \quad (398)$$

A special role is played by spatial modes with vanishing *spatial growth rate* λ_i . The corresponding wavenumber is λ_R . The real and imaginary parts of (398) under these conditions read:

$$\lambda_R^4 - 2R_R\lambda_R^2 + 1 = 0, \quad (399a)$$

$$2\lambda_R - \lambda_R^3 = 0. \quad (399b)$$

These equations are readily solved to give:

$$\lambda_R = \sqrt{2}, \quad R_R = \frac{5}{4}. \quad (400)$$

Hence, a harmonic spatial oscillation with wavenumber λ_R is a free solution of the system provided the control parameter takes the value R_R .

8.1.4 Forced oscillations: linear solution at the steady state and resonance

Let us next move to analyze the forced response of the system ($\nu \neq 0$) at the steady state ($\frac{\partial}{\partial t} \equiv 0$). The obvious approach is to take advantage of the assumption that $\nu \ll 1$ and assume a regular straightforward expansion of the solution in powers of the small parameter. Truncating the expansion at the linear level, one finds:

$$u(x) = \nu U_1(x) + \mathcal{O}(\nu^2), \quad (401)$$

Substituting from (401) into (389) at $\mathcal{O}(\nu)$ we find:

$$L_1^m U_1(x) = e_1 + \bar{e}_1 = e^{i\lambda_m x} + c.c., \quad (402)$$

where L_1^m is the algebraic operator L_1 evaluated for $\lambda = \lambda_m$ and we have used the following notation:

$$e_p = e^{p i \lambda_m x}, \quad (p = 0, 1, 2, \dots). \quad (403)$$

The equation (402) is readily solved assuming the following structure of the solution:

$$U_1(x) = U_{11} e_1 + c.c.. \quad (404)$$

Hence:

$$U_{11} = \frac{1}{L_1^m}. \quad (405)$$

The modulus $|U_{11}|$ and the phase ϕ of the complex amplitude U_{11} are plotted versus λ_m for different values of R in Figure 143.

Two important features of the solution deserve to be noted. The first is that the amplitude of the response exhibits an infinite peak if λ_m and R take the values λ_R and R_R , respectively. This condition is called *resonance*: the forcing oscillation excites a natural (free) oscillation allowed by the system.

The second observation concerns the phase ϕ which changes sign as the resonant conditions are crossed: this is a typical feature of linear resonators that has important physical implications for meander evolution, as discussed in Chapter 4 and Chapter 5..

8.1.5 Forced oscillations: weakly nonlinear solution

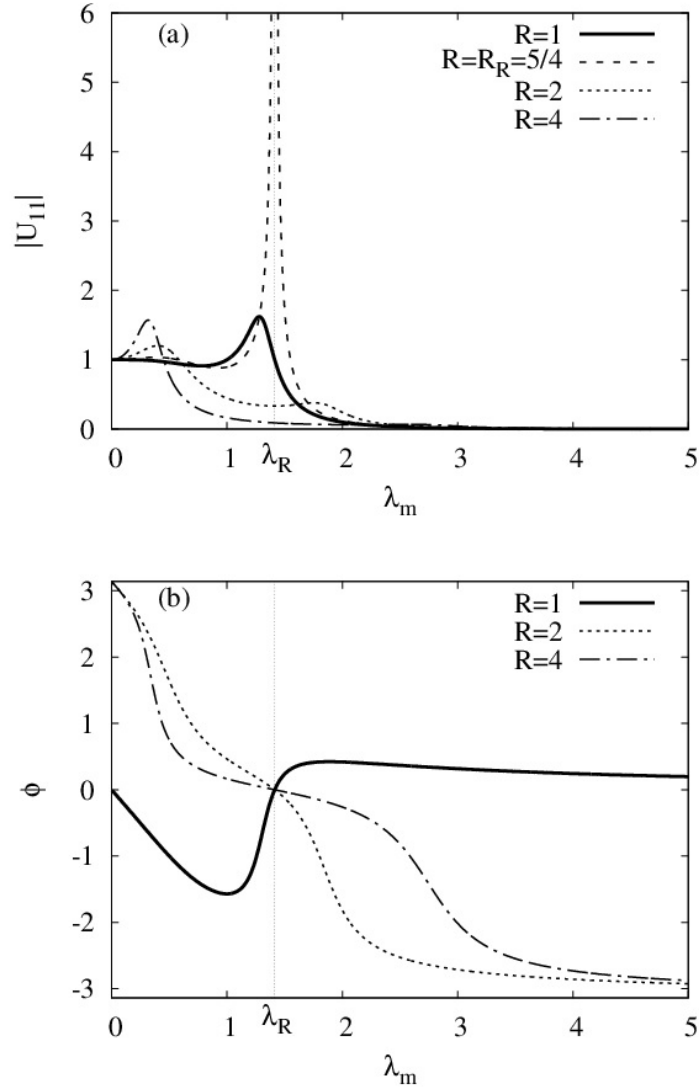


Figure 143. The modulus $|U_{11}|$ and the phase ϕ of the complex amplitude U_{11} of the linear forced response of the toy model (389) are plotted versus λ_m for different values of R . Note that an infinite resonant peak of the modulus of the response is experienced as λ_m and R take the values λ_R and R_R , respectively. Also, note that the phase of the response changes sign as the resonant conditions are crossed.

To complete the analysis of the solutions of our toy model, we now examine the role played by nonlinearity. It is convenient, in this respect to distinguish between non-resonant and near-resonant conditions.

Solution far from resonance.

Under non-resonant conditions, a weakly nonlinear solution is obtained proceeding with the expansion (401) up to the required order of approximation. This is an exercise which is left to the reader. Here, we simply report the $\mathcal{O}(\nu^2)$ term of the solution, which reads:

$$U_2(x) = U_{22} e_2 + 2U_{20} e_0 + \bar{U}_{22} \bar{e}_2 = U_{22} e_2 + U_{20} e_0 + c.c., \quad (406)$$

with

$$U_{22} = \frac{\lambda_m^2}{L_2^m} U_{11}^2, \quad U_{20} = -\lambda_m^2 U_{11} \bar{U}_{11}. \quad (407)$$

This solution fails at resonance ($\lambda_m = \lambda_R$), where $L_1^R = 0$ and, hence, U_{11} becomes unbounded. Close to resonance (407) must be replaced by the solution derived below.

Solution near resonance.

Let us now investigate the forced solution assuming that the wavenumber of the forcing spatial oscillation λ_m and the control parameter R fall within a neighborhood of the resonant values, λ_R and R_R . We look for a solution of our nonlinear toy model such that the singular resonant behaviour occurring at the linear level be suppressed. This is another example of non-uniformity of the straightforward expansion. In the present case non-uniformity does not occur for large values of the independent variable x as in the weakly damped oscillator discussed in Section 9.2.1(I). Rather, non-uniformity is driven by a singularity occurring in a neighborhood of some specific region of the parameter space.

The main questions to which we need preliminary answers are:

(i) what is the order of magnitude of the amplitude of the solution in terms of the small parameter ν such that suppression of the singularity may be achieved?

(ii) how wide is the range of values of λ_m and R within which nonlinear effects are felt and needed to suppress the singularity?

The classical argument employed to answer the above questions goes as follows. Let us assume that the fundamental component of the perturbation is of order $\mathcal{O}(\nu^y)$ with y a real exponent to be determined. At the lowest order and exactly at resonance, the oscillatory solution must coincide with the *natural* solution of the homogeneous linear problem describing marginally stable (i.e., non-amplifying) and non-migrating free oscillations. Hence, at the lowest order of approximation we may assume the following form of the solution

$$u_1(x) = \nu^y (A e_1^R + \bar{A} \bar{e}_1^R), \quad (408)$$

with A a complex amplitude to be determined. Let us analyze how secular terms are generated in the present case. Substituting from the lowest order of approximation into the nonlinear term $N(u)$, one finds:

$$N[u_1(x)] = -\nu^{2y} \lambda_R^2 (A^2 e_2^R + \bar{A}^2 \bar{e}_2^R - 2A\bar{A} e_0^R) = -\nu^{2y} \lambda_R^2 (A^2 e_2^R - A\bar{A} e_0^R + c.c.). \quad (409)$$

Hence it is clear that the nonlinear term $N(u)$ involving the fundamental (408), produces at second order, $\mathcal{O}(\nu^{2y})$, second harmonics proportional to e_2^R or e_0^R and at third order, $\mathcal{O}(\nu^{3y})$, the fundamental through interactions of second and first harmonics (Figure 144). The reader will check that $\bar{e}_1^R e_2^R = e_1^R$ and $e_1^R e_0^R = e_1^R$. Terms reproducing the fundamental are secular and must be suppressed. The only condition that can ensure that suppression does not lead to the trivial

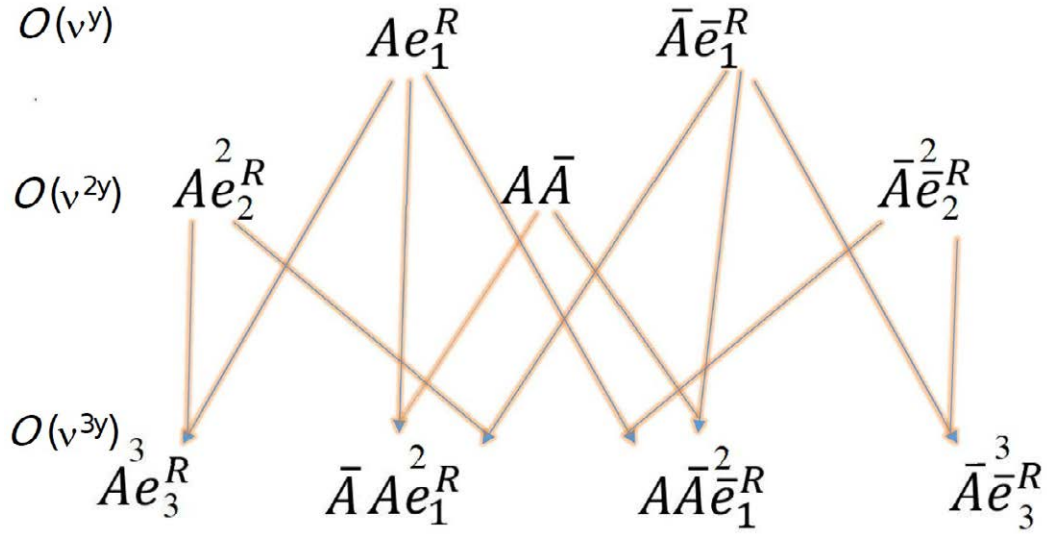


Figura 144. The sketch depicts the nonlinear interactions of the second and first harmonics associated with the nonlinear term $N(u)$ (equation (390b)) that lead to reproducing the fundamental mode at third order.

solution $A = 0$, is that the reproduction of the fundamental occurs at the same order, $\mathcal{O}(\nu)$, as that of the forcing oscillation. Below we will show that the above condition implies:

$$3y = 1. \quad (410)$$

Similarly, for variations of λ_m and R in a neighborhood of λ_R and R_R respectively, to be felt at order $\mathcal{O}(\nu)$, their order must be $\mathcal{O}(\nu^{\frac{2}{3}})$.

Let us then set the following expansions:

$$u(x) = A e_1 \nu^{\frac{1}{3}} + [U_{20} e_0 + U_{22} e_2] \nu^{\frac{2}{3}} + [U_{31} e_1 + U_{33} e_3] \nu + c.c. + \mathcal{O}(\nu^{\frac{4}{3}}), \quad (411a)$$

$$\lambda_m = \lambda_R + \lambda_1 \nu^{\frac{2}{3}}, \quad (411b)$$

$$R = R_R + R_1 \nu^{\frac{2}{3}}. \quad (411c)$$

On substituting from the expansion (411) into our toy differential equation, the linear terms give:

$$\begin{aligned} Lu = & L_1^R A e_1^R \nu^{\frac{1}{3}} + [L_2^R U_{22} e_2^R + L_0^R U_{20} e_0^R] \nu^{\frac{2}{3}} + \\ & + [L_1^R U_{31} e_1^R + L_3^R U_{33} e_3^R] \nu \\ & + \left[i\lambda_1 x L_1^R + \frac{\partial L_1}{\partial R} \Big|_{\lambda_R, R_R} R_1 + \frac{\partial L_1}{\partial \lambda} \Big|_{\lambda_R, R_R} \lambda_1 \right] A e_1^R \nu, \end{aligned} \quad (412)$$

having employed the following notation:

$$L_p^R = L_p(\lambda_R, R_R). \quad (413)$$

Recalling the definition (398) one finds:

$$L_0^R = 1, \quad (414a)$$

$$L_1^R = \lambda_R^4 - i\lambda_R^3 - 2R_R \lambda_R^2 + 2i\lambda_R + 1 = 0, \quad (414b)$$

$$L_2^R = 16\lambda_R^4 - 8i\lambda_R^3 - 8R_R \lambda_R^2 + 4i\lambda_R + 1 = 45 - 12\sqrt{2}i, \quad (414c)$$

$$\begin{aligned} \frac{\partial L_1}{\partial R} \Big|_{\lambda_R, R_R} R_1 + \frac{dL_1^R}{d\lambda} \Big|_{\lambda_R, R_R} \lambda_1 &= (-2\lambda_R^2) R_1 + (4\lambda_R^3 - 3i\lambda_R^2 - 4R_R\lambda_R + 2i)\lambda_1 \quad (414d) \\ &= (3\sqrt{2} - 4i)\lambda_1 - 4R_1. \end{aligned}$$

On substituting from the expansion (411) into the nonlinear term of our toy differential equation, we find

$$\begin{aligned} Nu &= \left[(i\lambda_R A e_1^R) \nu^{\frac{1}{3}} + (2i\lambda_R U_{22} e_2^R) \nu^{\frac{2}{3}} + c.c. + \mathcal{O}(\nu) \right]^2 = \\ &= -\lambda_R^2 (A^2 e_2^R - A \bar{A}) \nu^{\frac{2}{3}} + [4\lambda_R^2 (e_1^R U_{22} \bar{A} - A U_{22} e_3^R)] \nu + c.c. + \mathcal{O}(\nu^{\frac{4}{3}}). \quad (415) \end{aligned}$$

Substituting from (412) and (415) into the governing equation (389) and equating terms of different orders of magnitude we find the following sequence of algebraic equations.

$$\mathcal{O}(\nu^{\frac{1}{3}})$$

$$L_1^R A = 0. \quad (416)$$

This equation is identically satisfied for any amplitude A , which is left undetermined at this order.

$$\mathcal{O}(\nu^{\frac{2}{3}})$$

The amplitude U_{22} of the second harmonics satisfies the following algebraic equation:

$$L_2^R U_{22} - \lambda_R^2 A^2 = 0, \quad (417)$$

hence:

$$U_{22} = \frac{2}{45 - 12\sqrt{2}i} A^2. \quad (418)$$

Moreover, the amplitude U_{20} of the x -independent component reads:

$$U_{20} = -\lambda_R^2 A \bar{A} = -2A \bar{A}. \quad (419)$$

$$\mathcal{O}(\nu)$$

Finally, let us consider the equation that governs the amplitude U_{31} of the fundamental component of the solution reproduced at third order $\mathcal{O}(\nu)$. It reads:

$$L_1^R (U_{31} + i\lambda_1 A x) + [(3\sqrt{2} - 4i)\lambda_1 - 4R_1] A + \frac{16}{45 - 12\sqrt{2}i} A^2 \bar{A} = 1. \quad (420)$$

Recalling (413a), it follows that suppression of secular terms implies that the amplitude A must satisfy the following complex algebraic equation:

$$\alpha_1 A + \alpha_2 A^2 \bar{A} = 1, \quad (421)$$

where

$$\alpha_1 = (3\sqrt{2} - 4i)\lambda_1 - 4R_1, \quad \alpha_2 = \frac{16}{45 - 12\sqrt{2}i}. \quad (422)$$

The complex amplitude equation (421) is readily reduced to a cubic algebraic equation for $|A|^2$ multiplying the product of (421) and \bar{A} by its complex conjugate:

$$\alpha_2 \bar{\alpha}_2 |A|^6 + (\alpha_1 \bar{\alpha}_2 + \bar{\alpha}_1 \alpha_2) |A|^4 + \alpha_1 \bar{\alpha}_1 |A|^2 - 1 = 0. \quad (423)$$

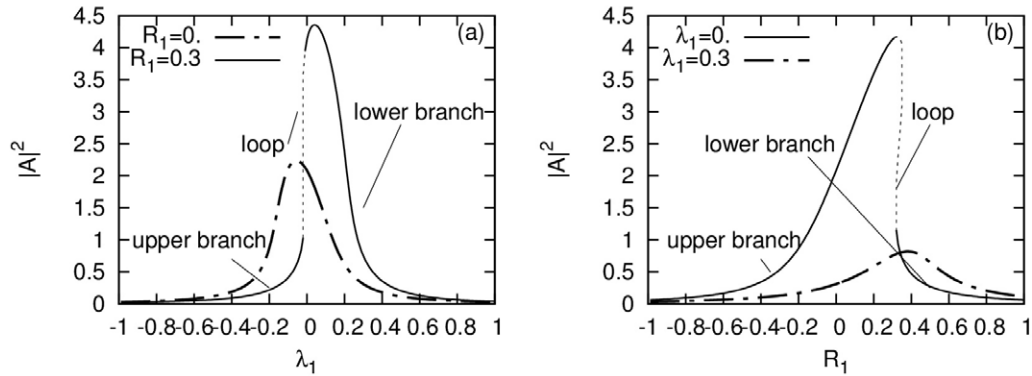


Figura 145. The square of the modulus of the solution of the amplitude equation (421) $|A|^2$ is plotted versus the parameters (a) λ_1 and (b) R_1 which measure the distance of λ_m and R from their resonant values λ_R and R_R . Solid and dashed lines denote stable and unstable solutions, respectively.

Once the latter equation is solved, one may derive A (hence its phase) from (421).

In general (423) exhibits one real and two complex-conjugate solutions. Under these conditions, the complex solutions being meaningless, the response of the system is unique. This is shown in the figures 145a and 145b, where $|A|^2$ is plotted as a function of λ_1 and R_1 , respectively.

However, this figure shows that ranges of λ_1 and R_1 exist, in which the three solutions of (423) are all real. In other words, the response of the system may not be unique, a feature characteristic of the nonlinear behavior of resonant oscillators (see, for instance, Thompson and Stewart, 1986, p. 72). In order to ascertain which of the three real solutions is appropriate for a given set of initial conditions, we investigate the linear stability of the above three solutions. Let us then set:

$$A = A_e + a(T), \quad (424)$$

where A_e is the equilibrium solution obtained above and a is an infinitesimally small perturbation. Moreover, we have introduced an appropriate time variable, describing the rate at which the system responds to perturbations in the near resonant region, namely

$$T = \nu^{\frac{2}{3}} t. \quad (425)$$

Note that T has been chosen such to affect the solution at order $\mathcal{O}(\nu)$, i.e. such to affect the amplitude equation for A . Indeed, including the temporal derivative in our toy model, the amplitude equation takes the form appropriate to investigate transient processes, that is readily seen to be:

$$\frac{dA}{dT} + \alpha_1 A + \alpha_2 A^2 \bar{A} = 1. \quad (426)$$

On substituting from (424) into (426) and linearizing we find the following linear ordinary differential equation for $a(T)$:

$$\frac{da}{dT} = \gamma_1 a + \gamma_2 \bar{a}, \quad (427)$$

where

$$\gamma_1 = -(\alpha_1 + 2|A_e|^2 \alpha_2), \quad \gamma_2 = -\alpha_2 A_e^2, \quad (428)$$

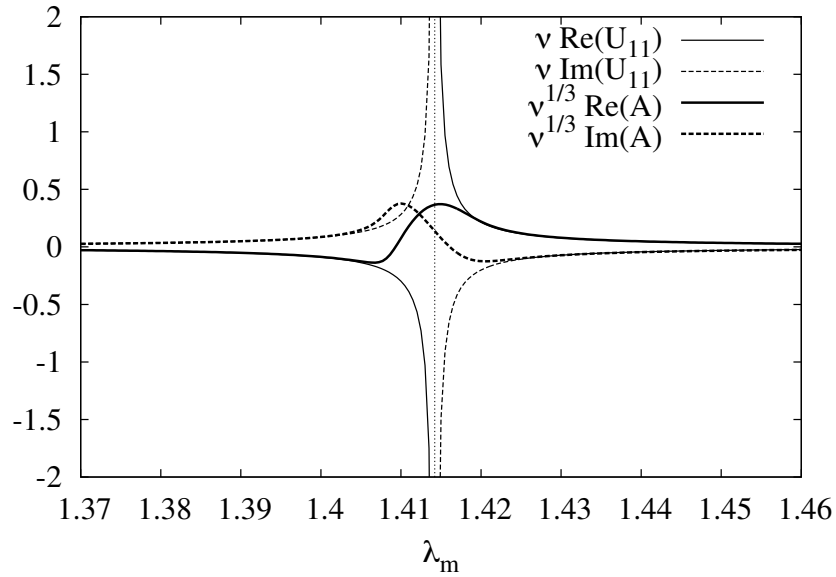


Figure 146. The amplitude of the linear solution, νU_{11} (equation (405), thin lines), and the amplitude of the fundamental component of the weakly nonlinear solution, $\nu^{1/3} A$ (equation (421), thick lines), are plotted as functions of the wavenumber λ_m of the forcing oscillation for $\nu = 0.01$. Solid and dashed curves denote real and imaginary parts, respectively.

Differentiating (427) once and using (427) to express $\frac{d\bar{a}}{dT}$ and \bar{a} in terms of $\frac{da}{dT}$ and a , one ends up with the following second order ordinary differential equation with constant coefficients for the sought function $a(T)$.

$$\frac{d^2 a}{dT^2} = (\gamma_1 + \bar{\gamma}_1) \frac{da}{dT} + (\gamma_2 \bar{\gamma}_2 - \gamma_1 \bar{\gamma}_1) a. \quad (429)$$

This equation admits of exponentially growing solutions provided the quantity $(\gamma_2 \bar{\gamma}_2 - \gamma_1 \bar{\gamma}_1)$ is positive. Alternatively, if the latter quantity is negative, $(\gamma_1 + \bar{\gamma}_1)$ must also be positive. Otherwise the equilibrium solution A_e is stable. Calculations show that the upper branch of the solution for $|A|^2$ depicted in Figures 145 is invariably stable with the lower branch and the loop joining the upper branch to the lower branch invariably unstable. In order to ascertain the nature of the possibly unsteady solutions bifurcating from the unstable steady solutions, one has to solve numerically the fully nonlinear equation (426). This exercise is left to the reader (but see also Seminara and Tubino (1992), sect. 6 for a specific example of relevance to morphodynamics).

Finally, in Figure 146 we compare the amplitude of the linear solution, νU_{11} (equation (405)), with the amplitude of the fundamental component of the weakly nonlinear solution, $\nu^{1/3} A$ (equation (421)), for a given value of the small parameter $\nu = 0.01$. Rather than exhibiting a sharp peak within the resonant range, the nonlinear response follows a fairly smooth trend with a relatively weak maximum for values of the forcing wavenumber larger than the resonant value. In other words, not only do nonlinear effects suppress the singularity exhibited by the linear solutions at $\lambda_m = \lambda_R$, but they also control the response of the system within a fairly wide range of values of the wavenumber of the forcing oscillation.

8.2. Interaction between temporal free modes and forced modes

In the previous Section we have analyzed a toy model which allows for the development of free temporal modes as well as forced modes associated with an oscillatory spatial forcing. In fluvial morphodynamics they correspond to free migrating bars and forced (point) bars, respectively.

The next problem we wish to analyze is that of ascertaining whether free and forced modes may coexist. More precisely: does the presence of spatially forced modes prevent the development of free temporal modes? Are there any threshold conditions separating regions where coexistence is possible from those where free modes are suppressed?

In order to answer this subtle question, we consider again the toy model (389) and employ the notations of the previous Section. Let us set ourselves within a neighborhood of the critical conditions for the onset of free temporal modes by assuming that:

$$R = R_c + \epsilon^2 R_1, \quad \lambda = \lambda_c, \quad \omega = \omega_c. \quad (430)$$

It is instructive to follow the flow of interactions arising when an $\mathcal{O}(\epsilon)$ free temporal mode, say

BASIC STATE

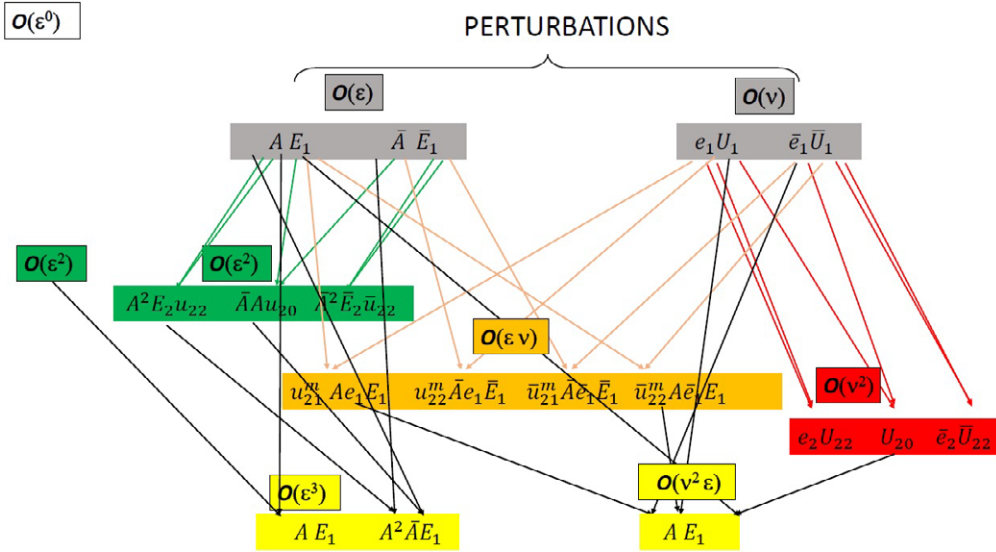


Figure 147. The sketch depicts the weakly nonlinear interactions between temporal free modes and forced modes for the toy model (389) which lead to reproducing the fundamental free temporal mode at third order.

$\epsilon(AE_1 + c.c.)$ coexists with an $\mathcal{O}(\nu)$ forced spatial mode, say $\nu(U_{11}e_1 + c.c.)$. Below, we will implicitly assume that $E_1 = E_1|_{\lambda=\lambda_c, \omega=\omega_c}$. As depicted in the sketch of Figure 147, at second order we find the $\mathcal{O}(\epsilon^2)$ free-free interactions and the $\mathcal{O}(\nu^2)$ forced-forced interactions already analyzed in the previous sections when dealing with the weakly nonlinear stability theory and the weakly nonlinear forced response. Here, we find additional second order $\mathcal{O}(\nu\epsilon)$ mixed terms which account for the interactions between free and forced modes. At third order, the fundamental free mode is readily seen to be reproduced by three types of interactions: free $\mathcal{O}(\epsilon)$ - free $\mathcal{O}(\epsilon^2)$, free $\mathcal{O}(\epsilon)$ -forced $\mathcal{O}(\nu^2)$ and mixed $\mathcal{O}(\nu\epsilon)$ - forced $\mathcal{O}(\nu)$.

The three contributions occur at the same order of approximation provided one sets:

$$\nu = k\epsilon, \quad (431)$$

with k an $\mathcal{O}(1)$ quantity. Hence, we may expect that, provided the forcing parameter ν is of the order of ϵ , i.e. the amplitudes of the fundamental free and forced modes, are of the same order of magnitude, the free-forced interaction is significant and may alter the usual picture of weakly nonlinear free modes amplifying and reaching an equilibrium amplitude asymptotically in time.

These intuitive arguments suggest the opportunity to seek a solution in the form of the following expansion:

$$\begin{aligned}
 u(x, t; T) = & \epsilon[A E_1 + c.c.] + \nu[U_{11} e_1 + c.c.] \\
 & + \nu^2[U_{20} e_0 + U_{22} e_2 + c.c.] \\
 & + \epsilon^2[A\bar{A} u_{20} E_0 + A^2 E_2 u_{22} + c.c.] \\
 & + \epsilon\nu[u_{21}^m A e_1 E_1 + u_{22}^m \bar{A} e_1 \bar{E}_1 + c.c.] \\
 & + \epsilon^3[u_{31} A^2 \bar{A} E_1 + u_{33} A^3 E_3 + c.c.] \\
 & + \nu^2\epsilon[Au_{31}^m E_1 + Au_{32}^m \bar{e}_2 E_1 + Au_{33}^m e_2 E_1 + c.c.] \\
 & + \mathcal{O}(\epsilon^2\nu, \nu^3),
 \end{aligned} \tag{432}$$

where $A(T)$ is an amplitude function of the slow temporal variable T defined as in the classical weakly nonlinear analysis:

$$T = \epsilon^2 t. \tag{433}$$

Substituting from (432) into the governing differential equation (389) and equating terms of the same order of magnitude, one finds a sequence of algebraic equations for the coefficients of the expansion. At $\mathcal{O}(\epsilon)$ and $\mathcal{O}(\nu)$ the linear free and forced problems are recovered, respectively.

At higher order the contribution of the nonlinear operator Nu must be accounted for. One readily finds that:

$$\begin{aligned}
 Nu = & + \nu^2[-(i\lambda_m)^2 U_{11} \bar{U}_{11} e_0 + (i\lambda_m)^2 U_{11}^2 e_2 + c.c.] \\
 & + \epsilon^2[-(i\lambda_c)^2 A\bar{A} E_0 + (i\lambda_c)^2 A^2 E_2 + c.c.] \\
 & + \epsilon\nu[-2\lambda_c\lambda_m A U_{11} e_1 E_1 + 2\lambda_c\lambda_m \bar{A} U_{11} e_1 \bar{E}_1 + c.c.] \\
 & + \epsilon^3[2(2i\lambda_c)(-i\lambda_c) A\bar{A} u_{22} E_1 + c.c. + \dots] \\
 & + \nu^2\epsilon \{ A E_1 [2i(\lambda_c + \lambda_m)(-i\lambda_m) \bar{U}_{11} u_{21}^m + \\
 & \qquad \qquad \qquad 2i(\lambda_c - \lambda_m)(i\lambda_m) U_{11} \bar{u}_{22}^m] + c.c. + \dots \} \\
 & + \mathcal{O}(\epsilon^2\nu, \nu^3).
 \end{aligned} \tag{434}$$

The reader should note that at $\mathcal{O}(\epsilon^3)$ and $\mathcal{O}(\epsilon\nu^2)$ other harmonics are also reproduced, but they are not included as they do not play any role in the derivation of the amplitude equation that is the main scope of our analysis. With the help of the latter relationship, the solution at higher order is found as follows.

$\mathcal{O}(\epsilon^2)$

The solutions for u_{20} and u_{22} satisfy the following relationships:

$$\begin{aligned}
 [L_2^c - 2i\omega_c]u_{22} & = \lambda_c^2, \\
 L_0^c u_{20} & = -\lambda_c^2,
 \end{aligned} \tag{435}$$

hence:

$$u_{20} = -\lambda_c^2 = -1 \quad , \quad u_{22} = \frac{\lambda_c^2}{(16\lambda_c^4 - 8R_c\lambda_c^2 + 1) + i(-8\lambda_c^3 + 4\lambda_c - 2\omega_c)} = \frac{1}{9 - 6i}. \tag{436}$$

$\mathcal{O}(\nu^2)$

The solutions for U_{20} and U_{22} are identical to (407) with L_p^m calculated for $R = R_c$.

$\mathcal{O}(\nu\epsilon)$

The solutions for u_{21}^m and u_{22}^m satisfy the following relationships:

$$\begin{aligned} [L_1^{c+m} - i\omega_c]u_{21}^m &= 2\lambda_c\lambda_m U_{11}, \\ [L_1^{-c+m} + i\omega_c]u_{22}^m &= -2\lambda_c\lambda_m U_{11}, \end{aligned} \quad (437)$$

where the following notations have been used:

$$L_1^{c+m} = L_1|_{\lambda=\lambda_c+\lambda_m, R=R_c} \quad , \quad L_1^{-c+m} = L_1|_{\lambda=-\lambda_c+\lambda_m, R=R_c}. \quad (438)$$

Hence:

$$u_{21}^m = \frac{2\lambda_c\lambda_m U_{11}}{L_1^{c+m} - i\omega_c} \quad , \quad u_{22}^m = -\frac{2\lambda_c\lambda_m U_{11}}{L_1^{-c+m} + i\omega_c}. \quad (439)$$

$\mathcal{O}(\epsilon^3, \nu^2\epsilon)$

At third order we are interested in suppressing the secular terms generated only by the reproduction of the fundamental free mode E_1 . Using the assumption (431), the $\mathcal{O}(\epsilon^3)$ and $\mathcal{O}(\nu^2\epsilon)$ nonlinear interactions occur at the same order, hence, taking into account also the effects of the slow temporal dependence of the amplitude function A and of the perturbation ($\epsilon^2 R_1$) of the control parameter R , one readily finds:

$$[L_1^c - i\omega_c](A^2 \bar{A} u_{31} + A k^2 u_{31}^m) = -\frac{dA}{dT} + \alpha_1 A + \alpha_2 A^2 \bar{A}, \quad (440)$$

where

$$\alpha_1 = k^2 [-2\lambda_m(\lambda_c + \lambda_m) \bar{U}_{11} u_{21}^m + 2\lambda_m(\lambda_c - \lambda_m) U_{11} \bar{u}_{22}^m] + 2R_1 \lambda_c^2, \quad (441)$$

$$\alpha_2 = -4\lambda_c^2 u_{22}. \quad (442)$$

As the left hand side of (440) vanishes, a similar condition must hold for the right hand side. This leads to the following amplitude equation of Landau-Stuart type:

$$\frac{dA}{dT} = \alpha_1 A + \alpha_2 A^2 \bar{A}. \quad (443)$$

The discussion of the solutions of this amplitude equation has been given in Section 9.3.6(I). We know that (443) admits of supercritical equilibrium solutions provided $Re(\alpha_2)$ is negative. The reader will readily show that, in the absence of forcing ($\nu = 0$, $k = 0$), the bifurcation is indeed supercritical and the equilibrium amplitude reads:

$$|A_e| = \sqrt{-\frac{Re(\alpha_1)}{Re(\alpha_2)}} = \sqrt{-\frac{2R_1 \lambda_c^2}{Re(\alpha_2)}} = \sqrt{\frac{13}{2}} R_1. \quad (444)$$

Finally, in the presence of forcing ($k \neq 0$), we can answer the original question that motivated the present analysis: is there any threshold condition separating the region where coexistence of temporal free modes with spatially forced modes is possible from that where free modes are suppressed? In the present context suppression implies the inability of the perturbation to grow. We recall that the growth rate of the perturbations is the real part of the linear coefficient α_1 in the amplitude equation (443) (see Section 9.3.6(I)). The threshold condition is thus seen to be the condition such that $Re(\alpha_1)=0$. This occurs at a threshold value (k_t) of the parameter (k), i.e. when the amplitude of the forcing ν exceeds a critical value depending on the wavenumber of the forcing oscillation λ_m and the control parameter R . The reader will readily find that:

$$k_t^2 = -\frac{2R_1 \lambda_c^2}{Re[-\lambda_m(\lambda_c + \lambda_m) \bar{U}_{11} u_{21}^m + \lambda_m(\lambda_c - \lambda_m) U_{11} \bar{u}_{22}^m]}. \quad (445)$$

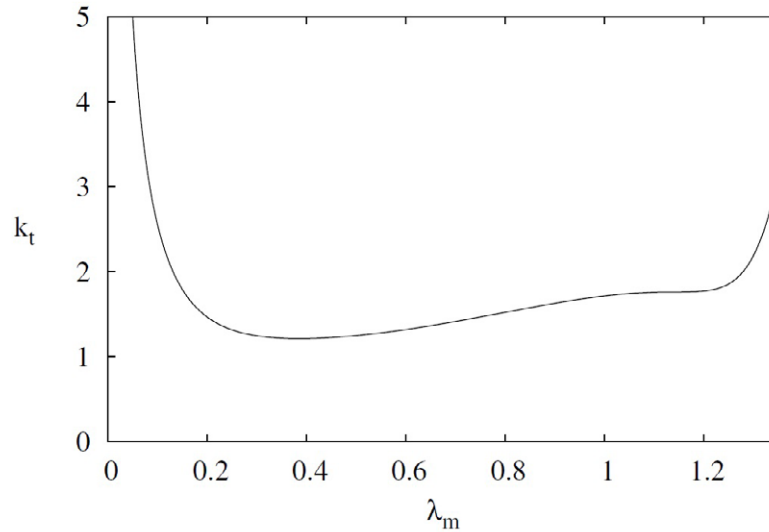


Figure 148. The threshold k_t for suppression of the modes is plotted as a function of λ_m for $R_1 = 1$

The plot of $k_t(\lambda_m)$ reported in Figure 148 suggests that suppression is inhibited when the wavenumber of the spatial forcing tends to vanish ($\lambda_m \rightarrow 0$).

Differently from the problem of the free bar suppression in meandering channels (Figure 79), Figure 148 does not show any local minimum for λ_m equal to λ_R . It occurs because in our toy problem, $R_R (= 1.25)$ is significantly higher than $R_c (= 1)$. Indeed, by slightly modifying the linear operator of the model problem (389) with the introduction of a constant larger than 1 and lower than 2 (e.g. equal to 1.2) before the third derivative in (390a), the resonant value of R becomes closer to R_c (e.g. equal to 1.134). In this case, as shown in Figure 149, the value of k_t has a local minimum close to resonance, hence lower intensities of the forcings are sufficient to damp the growth of instabilities.

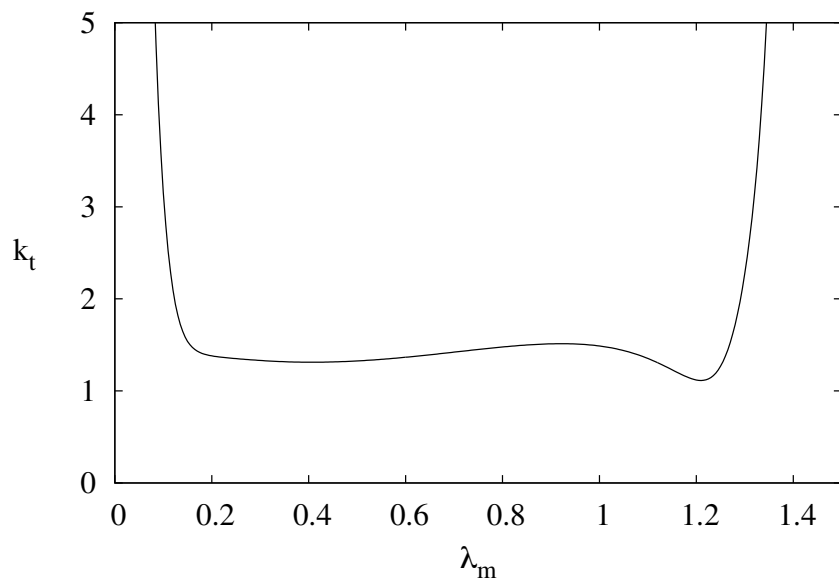


Figura 149. The threshold k_t for suppression of the modes is plotted as a function of λ_m for the modified model problem with $R_c = 1$, $R_R = 1.134$ and $R_1 = 1$.

9. Bibliography

- Abad, J. D. (2008) Hydrodynamics and morphodynamics in Kinoshita meandering channels, Dissertation submitted in partial fulfillment of the requirements for the degree of Doctor of Philosophy in Civil Engineering in the Graduate College of the University of Illinois at Urbana-Champaign.
- Abad, J. D., and M. H. García (2009), Experiments in a high-amplitude Kinoshita meandering channel: 2. Implications of bend orientation on bed morphodynamics, *Water Resour. Res.*, 45, W02402, doi:10.1029/2008WR007017.
- Abad, J. D., Frias, C. E., Buscaglia, G. C., and García, M. H. (2013). Modulation of the flow structure by progressive bedforms in the Kinoshita meandering channel, *Earth Surface Processes and Landforms*, 38(13), 1612-1622. <https://doi.org/10.1002/esp.3460>.
- Allen, J. R. L. (1965) A review of the origin and characteristics of recent alluvial sediments, *Sedimentology*, 5, 89-191.
- Allen, J. R. L. (1985). *Principles of Physical Sedimentology*, Chapman and Hall, New York.
- Azpiroz-Zabala, M., Cartigny, M. J. B., Sumner, E. J., Clare, M. A., Talling, P. J., Parsons, D. R., and Cooper, C. (2017). A general model for the helical structure of geophysical flows in channel bends. *Geophysical Research Letters*, 44, 11,932-11,941. <https://doi.org/10.1002/2017GL075721>
- Bagnold, R. A. (1960), Some aspects of the shape of river meanders, U.S. Geol. Surv. Prof. Pap. 282-E, U.S. Geol. Surv., Washington, D.C.
- Bak, P., Tang, C. and Wiesenfeld, K. (1987) Self-organized criticality, *Phys. Rev. Lett.*, 59, 381-4.
- Bar-Yam, Y. (1997) Dynamics of Complex Systems, (Addison-Wesley, Reading, 1997).
- Bathurst, J. C., C. R. Thorne, and R. D. Hey (1977), Direct measurements of secondary currents in river bends, *Nature*, 269, 504-506, doi:10.1038/269504a0.
- Bathurst, J. C., C. R. Thorne, and R. D. Hey (1979), Secondary flow and shear stress at river bends, *J. Hydraul. Div. Am. Soc. Civ. Eng.*, 105(10),1277-1295.
- Beck, S., Harrington, R. A. and Andres, D. D. (1983). Lateral channel stability of the Pembina River near Rossington, Alberta. *Alberta Research Council Report No. SWE 83-2*.
- Besicovitch, A. S. (1929). On Linear Sets of Points of Fractional Dimensions. *Mathematische Annalen*. 101 (1): 161-193. doi:10.1007/BF01454831.
- Besicovitch, A. S. and H. D. Ursell (1937). Sets of Fractional Dimensions. *Journal of the London Mathematical Society*. 12 (1): 18-25. doi:10.1112/jlms/s1-12.45.18.
- Blanckaert, K. (2002), Flow and turbulence in sharp open-channel bends, *Ph.D. thesis n. 2545, Ecole Polytechnique Fédérale Lausanne, Switzerland*.
- Blanckaert, K. (2009), Saturation of curvature induced secondary flow, energy losses, and turbulence in sharp open channel bends: Laboratory experiments, analysis, and modeling, *J. Geophys. Res.*, 114, F03015, doi:10.1029/2008JF001137.

- Blanckaert, K. (2010), Topographic steering, flow recirculation, velocity redistribution and bed topography in sharp meander bends, *Water Resour. Res.*, 46, W09506, doi:10.1029/2009WR008303.
- Blanckaert, K. (2011), Hydrodynamic processes in sharp meander bends and their morphological implications, *J. Geophys. Res.*, 116, F01003, doi:10.1029/2010JF001806.
- Blanckaert, K., and H. J. de Vriend, (2003) Nonlinear modeling of mean flow redistribution in curved open channels, *Water Resour. Res.*, 39(12), 1375, doi:10.1029/2003WR002068.
- Blanckaert, K., and H. J. de Vriend (2004), Secondary flow in sharp open-channel bends, *J. Fluid Mech.*, 498, 353-380, doi:10.1017/S0022112003006979.
- Blanckaert, K., and W. H. Graf (2004), Momentum transport in sharp open channel bends, *J. Hydraul. Eng.*, 130(3), 186-198, doi:10.1061/(ASCE)0733-9429(2004)130:3(186).
- Blanckaert, K., F. Buschman, R. Schielen, and J. H. A. Wijnbenga (2008), Redistribution of velocity and bed shear stress in straight and curved open channels by means of a bubble screen. Laboratory experiments, *J. Hydraul. Eng., Am. Soc. Civ. Eng.*, 134(2), 184-195, doi:10.1061/(ASCE)0733-9429(2008)134:2(184).
- Blanckaert, K., A. Duarte, Q. Chen, and A. J. Schleiss (2012), Flow processes near smooth and rough (concave) outer banks in curved open channels, *J. Geophys. Res.*, 117, F04020, doi:10.1029/2012JF002414.
- Blondeaux, P., and G. Seminara (1985), A unified bar-bend theory of river meanders, *J. Fluid Mech.*, 157:449-479.
- Blondeaux, P., Colombini, M., Seminara, G. and G. Vittori, (2018), Introduction to Morphodynamics of Sedimentary Patterns, *Monograph Series on Morphodynamics of Sedimentary Patterns*, Ed. Genova University Press.
- Bogoni, M., Putti, M., and Lanzoni, S. (2017). Modeling meander morphodynamics over self-formed heterogeneous floodplains. *Water Resources Research*, 53, 5137-5157. <https://doi.org/10.1002/2017WR020726>.
- Bolla Pittaluga, M., G. Nobile, and G. Seminara (2009), A nonlinear model for river meandering, *Water Resour. Res.*, 45, W04432, doi:10.1029/2008WR007298.
- Bolla Pittaluga, M. and G. Seminara (2011) Nonlinearity and unsteadiness in river meandering: a review of progress in theory and modelling *Earth Surf. Process. Landforms* 36, 20-38, doi:10.1002/esp.2089
- Booij, R. 2003 Measurements and large-eddy simulations of the flows in some curved flumes. *J. Turbulence* 4, 1-17.
- Braudrick, C. A., W. E. Dietrich, G. T. Leverich, and L. S. Sklar (2009), Experimental evidence for the conditions necessary to sustain meandering in coarse bedded rivers, *Proc. Natl. Acad. Sci. U. S. A.*, 106, 16,936-16,941, doi:10.1073/pnas.0909417106.
- Brice, J. C. (1973). Meandering pattern of the White River in Indiana: An analysis. In *Fluvial Geomorphology. Morisawa M. (ed.) University of New York: Binghamton*.
- Brice, J. (1974), Evolution of meander loops, *Geol. Soc. Am. Bull.*, 85, 215-235.
- Brice, J. (1982). Stream channel stability assessment. *Report no. FHWA/RD, Federal Highway Administration, Offices of Research and Development*.
- Brice, J. C. (1984), Planform properties of meandering rivers, Keynote paper, in *River Meandering, Proceedings of the Conference Rivers, '83 New Orleans, LA, 24-26 October 1983, edited by C. M. Elliott, pp. 1-15, American Society of Civil Engineers, N. Y.*
- Bridge, J. S., and J. Jarvis (1977), Velocity profiles and bed shear stress over various bed configurations in a river bend, *Earth Surf. Processes Landforms*, 2, 281-294, doi:10.1002/esp.3290020402.
- Brower, R. C., D. A. Kessler, J. Koplik, and H. Levine (1984), Geometrical models of interface evolution, *Phys. Rev. A*, 29, 1335-1342.
- Camporeale, C., and Ridolfi, L. (2006). Convective nature of the planimetric instability in meandering river dynamics. *Physical Review E - Statistical, Nonlinear, and Soft Matter Physics* 73(2).

- Camporeale, C., P. Perona, A. Porporato and L. Ridolfi (2005), On the long-term behavior of meandering rivers, *Water Resour. Res.*, 41, W12403, doi:10.1029/2005WR004109
- Camporeale, C., P. Perona, A. Porporato, and L. Ridolfi (2007), Hierarchy of models for meandering rivers and related morphodynamic processes, *Rev. Geophys.*, 45, RG1001, doi:10.1029/2005RG000185.
- Chang, Y. C. (1971) Lateral mixing in meandering channels, *Ph.D. thesis, University of Iowa, USA*.
- Cheng, K. C., Lin, R.C. and Ou, J. W. 1976 Fully developed laminar flow in curved rectangular channels. *Trans. ASME: J. Fluids Engng* 98, 41-48.
- Christensen, B., Gislason, K. and J. Fredsoe, (1999) Secondary turbulent flow in an infinite bend. *1st RCEM Symp., Genova, Italy, vol. 1, pp. 543-553*.
- Churchill, R. V., Brown, J. W., 1987. Fourier Series and Boundary value problems, McGraw-Hill, New York.
- Clayton, J. A. (2010), Local sorting, bend curvature, and particle mobility in meandering gravel bed rivers, *Water Resour. Res.*, 46, W02601, doi:10.1029/2008WR007669.
- Coddington, E. A. and Levinson, N. (1955) *Theory of Ordinary Differential Equations*. McGraw-Hill.
- Colombini, M., G. Seminara, and M. Tubino (1987), Finite-amplitude alternate bars, *J. Fluid Mech.*, 181:213-232.
- Colombini, M., Tubino, M. and Whiting, P. (1991) Topographic expression of bars in meandering channels. In *Dynamics of Gravel-bed Rivers* (ed. P. Billi, R. D. Hey, C. R. Thorne and P. Tacconi). John Wiley and Sons.
- Constantinescu, G., Koken, M., Zeng, J., (2011), The structure of turbulent flow in an open channel bend of strong curvature with deformed bed: Insight provided by detached eddy simulation. *Water Resour. Res.* 47, W05515.
- Constantine, J.A., McLean, S.R. and Dunne, T. (2010). A mechanism of chute cutoff along large meandering rivers with uniform floodplain topography, *Geol. Soc. Am. Bull.*, 122, 855–869, doi:10.1130/B26560.1
- Crosato, A. (1990), Simulation of meandering river processes, in Communication on Hydraulic and Geotechnical Engineering, Rep. 903, Delft Univ. of Technol., Delft, Netherlands.
- Crosato, A. (2007), Effects of smoothing and regridding in numerical meander migration models, *Water Resour. Res.*, 43, W01401, doi:10.1029/2006WR005087.
- Darby, S. E., Alabyan, A. M., and Van de Wiel, M. J. (2002). Numerical simulation of bank erosion and channel migration in meandering rivers. *Water Resources Research*, 38(9), 2–21.
- Davila, J. and J. C. R. Hunt, 2001. Settling of small particles near vortices and in turbulence. *J. Fluid. Mech.* 440:117-145.
- Davis, W. M. (1893a) The Topographic Maps of the United States Geological Survey *Science*, 21 (534), 225-227.
- Davis, W. M. (1893b) The Osage River and the Ozark uplift *Science*, 22, 276-279.
- de Vriend, H. J. 1981 Velocity redistribution in curved rectangular channels. *J. Fluid Mech.* 107, 423-439.
- Vries, M. de (1969) Riverbed variations. Aggradation and degradation. *IAHR Seminar, New Delhi*.
- Dean, W. R. (1927). Note on the motion of fluid in a curved pipe. *Phil. Mag.* 20 (20): 208-223. doi:10.1080/14786440708564324.
- Demuren, A. O., and Rodi, W. (1986). Calculation of flow and pollutant dispersion in meandering channels. *J. Fluid Mech., Cambridge, U.K.*, 172, 63-92.
- Devaney, R. L. (1989) An Introduction to Chaotic Dynamical Systems, 2nd edn. Addison-Wesley.
- Dietrich WE, Smith JD. 1983. Influence of the point bar on flow through curved channels. *Water Resour. Res.* 19:1173-92

- Duarte, A. (2008), An experimental study on main flow, secondary flow and turbulence in open channel bends with emphasis on their interaction with the outer bank geometry, *Ph.D. thesis 4227, Ecole Polytech. Fed. Lausanne, Lausanne, Switzerland*
- Eaton B. C. and Church M. (2004) A graded stream response relation for bed load-dominated streams. *J Geophys Res* 109:F03011 doi:10.1029/2003JF000062.
- Eckmann, J. P. and Ruelle, D. (1985). Ergodic theory of chaos and strange attractors. *Reviews of Modern Physics* 57: 617.
- Edwards, B. and Smith, D. (2002) River meandering dynamics. *Phys. Rev. E* 65, 046303.
- Eekhout, J.P.C. and Hoitink, A.J.F. (2015). Chute cutoff as a morphological response to stream reconstruction: The possible role of backwater, *Water Resour. Res.*, 51, 3339-3352, doi:10.1002/2014WR016539.
- Einstein, A. (1926). Die Ursache der Mäanderbildung der Flussläufe und des sogenannten Baerschen Gesetzes Die Naturwissenschaften, 14 (11), 223-224 doi:10.1007/BF01510300.
- Eke, E. C. (2013) Numerical Modeling of river migration incorporating erosional and depositional bank processes. Dissertation submitted in partial fulfillment of the requirements for the degree of Doctor of Philosophy in Civil Engineering in the Graduate College of the University of Illinois at Urbana-Champaign.
- Eke, E., Parker, G. and Shimizu, Y. (2014a). Numerical modeling of erosional and depositional bank processes in migrating river bends with self-formed width: morphodynamics of bar push and bank pull. *J. Geophys. Res.* 119 (7), 1455-1483.
- Eke, E. C., Czapiga, M. J., Viparelli, E., Shimizu, Y., Imran, J., Sun, T and G. Parker (2014b). Coevolution of width and sinuosity in meandering rivers, *J. Fluid Mech.* 760, 127-174, doi:10.1017/jfm.2014.556
- Engelund, F. (1974), Flow and bed topography in channel bends, *J. Hydraul. Div.*, 574 100 (11), 1631-1648.
- Federici, B. (1999) Experimental observations on bifurcations in braided rivers. Thesis, University of Genova. (In Italian.)
- Federici, B., and C. Paola (2003) Dynamics of channel bifurcations in noncohesive sediments, *Water Resour. Res.*, 39(6), 1162, doi:10.1029/2002WR001434.
- Federici, B., and G. Seminara (2003), On the convective nature of bar instability, *J. Fluid Mech.*, 487, 125-145.
- Ferguson, R. I., D. R. Parsons, S. N. Lane, and R. J. Hardy (2003), Flow in meander bends with recirculation at the inner bank, *Water Resour. Res.*, 39(11), 1322, doi:10.1029/2003WR001965
- Fernández, R., Parker, G. and Stark C. P. (2019) Experiments on patterns of alluvial cover and bedrock erosion in a meandering channel, *Earth Surf. Dynam.*, 7, 949-968.
- Finotello, A., Lanzoni, S., Ghinassi, M., Marani, M., Rinaldo, A., and D'Alpaos, A. (2018). Field migration rates of tidal meanders recapitulate fluvial morphodynamics. *Proceedings of the National Academy of Sciences*, 115(7), 1463-1468. <https://doi.org/10.1073/pnas.1711330115>
- Finotello, A., D'Alpaos, A., Bogoni, M., Ghinassi, M., and Lanzoni, S. (2020). Remotely-sensed planform morphologies reveal fluvial and tidal nature of meandering channels. *Scientific Reports*, 1-13. <https://doi.org/10.1038/s41598-019-56992-w>
- Fisk, H. N. (1952) Mississippi river valley geology relation to river regime, *Trans. Am. Soc. Civ. Eng.*, 117, 667-689.
- Frascati, A. and Lanzoni, S. (2009) Morphodynamic regime and long-term evolution of meandering rivers. *Journal of Geophysical Research* 114: F02002, doi:10.1029/2008JF001101
- Frascati, A. and Lanzoni, S. (2010) Long-term river meandering as a part of chaotic dynamics? A contribution from mathematical modelling, *Earth Surface Process. and Landforms* 35, 791-802 doi:10.1002/esp.1974

- Frascati, A., and Lanzoni, S. (2013). A mathematical model for meandering rivers with varying width. *Journal of Geophysical Research: Earth Surface*, 118, 1–17. <https://doi.org/10.1002/jgrf.20084>
- Friedkin, J. F., (1945) A laboratory study of the meandering of alluvial rivers: U. S. Waterways Expt. Sta., Vicksburg, Miss., 40 p.
- Fukuoka, S. (1971) Longitudinal dispersion in sinuous channels. *Ph.D. thesis, University of Iowa, USA*.
- Fuller, T. K. (2014) Field, Experimental and Numerical Investigations into the Mechanisms and Drivers of Lateral Erosion in Bedrock Channels A Dissertation submitted to the faculty of the University of Minnesota in partial fulfillment of the requirements for the degree of Doctor of Philosophy
- Fuller, T. K., Gran, K. B., Sklar, L. S., and Paola, C. (2016). Lateral erosion in an experimental bedrock channel: The influence of bed roughness on erosion by bed load impacts: Lateral Bedrock Erosion by Impact Wear. *Journal of Geophysical Research: Earth Surface*, 121(5), 1084-1105. <https://doi.org/10.1002/2015JF003728>.
- Gagliano, S. M., and P. C. Howard (1983) The neck cutoff oxbow lake cycle along the lower Mississippi river, in *River Meandering, Proceedings of the Conference Rivers '83*, edited by Charles M. Elliott, pp. 147-158, Am. Soc. of Civ. Eng., New York.
- Garcia, M. and Niño, Y. (1993) Dynamics of sediment bars in straight and meandering channels: experiments on the resonance phenomenon. *J. Hydr. Res.* 31, 739-761.
- Gautier, E., Brunstein, D., Vauchel, P., Roulet, M., Fuertes. O., Guyot, J. L., Darozzes, J. and Bourrel, L. (2007). Temporal relations between meander deformation, water discharge and sediment fluxes in the floodplain of the Rio Beni (Bolivian Amazonia). *Earth Surface Processes and Landforms* 32: 230-248.
- Gay, G.R., Gay, H.H., Gay, W.H., Martinson, H.A., Meade, R.H. and Moody, J.A. (1998). Evolution of cutoffs across meander neck in Powder River, Montana, USA, *Earth Surf. Proc. Land.*, 23, 651–662.
- Ge L, Sotiropoulos F. (2007). A numerical method for solving the 3D unsteady incompressible Navier Stokes equations in curvilinear domains with complex immersed boundaries, *J Comput Phys*, 225, 1782-809. <http://dx.doi.org/10.1016/j.jcp.2007.02.017>.
- Ghanmi, A. (1999). Modeling of flows between two consecutive reverse curves. *J. Hydraul. Res.*, 37:1, 121-135.
- Görtler, H. (1955). Dreidimensionales zur Stabilitätstheorie laminarer Grenzschichten. *Journal of Applied Mathematics and Mechanics*. 35 (9-10): 362-363. [doi:10.1002/zamm.19550350906](https://doi.org/10.1002/zamm.19550350906)
- Gran, K. B. (2000) Effects of riparian vegetation on braided stream dynamics: Experimental results, M.S. thesis, 138 pp., Univ. of Minnesota, Minneapolis.
- Gran K. and Paola C. (2001) Riparian vegetation controls on braided stream dynamics. *Water Resour Res* 37:3275-3283.
- Grassberger, P. and Procaccia, I. (1983a). Characterization of strange attractors. *Physics Review Letters* 50: 346-349.
- Grassberger, P. and Procaccia, I. (1983b). Measuring the strangeness of strange attractors. *Physica D* 9: 189-208.
- Grenfell, M., Aalto, R. and Nicholas, A. (2012). Chute channel dynamics in large, sand-bed meandering rivers, *Earth Surf. Proc. Land.*, 37, 315–331, [doi:10.1002/esp.2257](https://doi.org/10.1002/esp.2257).
- Harmar, O. P., and N. J. Clifford (2006). Planform dynamics of the Lower Mississippi River, *Earth Surf. Processes Landforms*, 31(7), 825-843, [doi:10.1002/esp.1294](https://doi.org/10.1002/esp.1294).
- Harte, D. (2001). Multifractals. *Chapman & Hall*. pp. 3-4.
- Hausdorff, F. (1919). Dimension und äußeres Maß. *Mathematische Annalen*. 79 (1-2): 157-179. [doi:10.1007/BF01457179](https://doi.org/10.1007/BF01457179).
- Hey, R. and Thorne, C. (1986) Stable Channels with Mobile Gravel Beds, *Journal of Hydraulic Engineering*, 112(8), 671-689.

- Hille, P., Vehrenkamp, R. and Schulz-Dubois, E. O. 1985 The development and structure of primary and secondary flow in a curved square duct. *J. Fluid Mech.* 151, 219-241.
- Hooke, R. LeB., (1974). Distribution of sediment and shear stress in a meander bend, *Jour. Geol.*, v. 83, p. 543-565.
- Hooke, J. M. (1986). The significance of mid-channel bars in an active meandering river, *Sedimentology*, 33, 839-850.
- Hooke, J. M. (2004) Cutoffs galore! Occurrence and causes of multiple cutoffs on a meandering river. *Geomorphology* 61: 225-238.
- Hooke, J.M., and Harvey, A.M. (1983), Meander changes in relation to bend morphology and secondary flows. In: *Collinson, J., Lewin, J. (Eds.), Modern and Ancient Fluvial Systems Int. Assoc. Sediment Sp. Publs., vol. 6. Blackwells, Oxford, pp. 121-132.*
- Hooke, J. M., and L. Yorke (2011). Channel bar dynamics on multi-decadal timescales in an active meandering river, *Earth Surf. Processes Landforms*, 36, 1910-1928, doi:10.1002/esp.2214.
- Howard, A. D. (1992) Modeling channel migration and floodplain sedimentation in meandering streams. In *Lowland floodplain rivers: Geomorphological Perspectives (ed. Carling, P. A. and Petts, G. E.)*, pp. 1-41. John Wiley and Sons.
- Howard, A. D. (1996) Modelling channel evolution and floodplain morphology. In *Floodplain Processes (ed. M. G. Anderson, D. E. Walling and P. D. Bates)*, pp. 15-62. John Wiley and Sons.
- Howard, A. D. (2009) How to make a meandering river, PNAS, vol. 106n. 4117245-17246
- Howard, A. D. and Knutson, T. R. (1984) Sufficient conditions for river meandering: a simulation approach. *Water Resour. Res.* 20, 1659-1667.
- Hudson, P. F. (2002). Pool-riffle morphology in an actively migrating alluvial channel: The Lower Mississippi River, *Phys. Geogr.*, 23(2), 154-169.
- Ikeda, S., Hino, M. and Kihhawa, H., (1976) Theoretical study on the free meandering of rivers. *Proc. Japan Soc. Civ. Engrs*, 255, 63-73 (in Japanese).
- Ikeda S, Parker G, Sawai K. 1981. Bend theory of river meanders. Part 1. Linear development. *J. Fluid Mech.*, 112:363-77
- Ikeda, S., M. Yamasaka and M. Chiyoda (1987). Bed topography and sorting in bends, *J. Hydraul. Eng.*, 113(2), 190-206.
- Inoue, T., G. Parker, and C. P. Stark (2017), Morphodynamics of a bedrock-alluvial meander bend that incises as it migrates outward: approximate solution of permanent form. *Earth Surf. Process. Landforms*, 42, 1342-1354, doi:10.1002/esp.4094.
- Iwasaki, T., Shimizu, Y. and Kimura, I. (2016). Numerical simulation of bar and bank erosion in a vegetated floodplain: A case study in the Otofuke River. *Adv. Water Resour.*, 93, 118-134, doi:10.1016/j.advwatres.2015.02.001.
- Jansen, P. Ph, van Bendegom, L., van den Berg, J., de Vries, M, and Zanen, A (Editors), 1979. Principles of River Engineering: The Non-tidal Alluvial River. *Pitman Publishing Ltd.*, London, Great Britain, ISBN 90-6562-146-6.
- Jefferson, W. S. (1902) Limiting width of meander belts, *Natl. Geogr. Mag.*, 13, 373-383.
- Jin, D., and Schumm, S. A., (1987) A new technique for modeling river morphology, in *Gardiner, V., ed., International Geomorphology, Part I: Chichester, U.K., John Wiley & Sons, p. 681-690.*
- Johannesson, H. and Parker, G. 1989 Linear theory of river meanders. In *River Meandering (ed. S. Ikeda & G. Parker)*. *Water Res. Monograph 12*, pp. 181-214. AGU.
- Kalkwijk, J. P. Th. and De Vriend, H. J. (1980) Computation of the flow in shallow river bends. *J. Hydraul. Res.* 18, 327-342.
- Kantz, H. and Schreiber, T. (1997). Nonlinear Time Series Analysis. *Cambridge University Press: Cambridge, UK.*
- Karlstrom, L., P. Gajjar, and M. Manga (2013), Meander formation in supraglacial streams, *J. Geophys. Res. Earth Surf.*, 118, doi:10.1002/jgrf.20135.

- Kevorkian, J. and Cole, J. D. (1981) *Perturbation Methods in Applied Mathematics*. Springer.
- Keylock, C.J., Constantinescu, G. and Hardy, R.J. (2012) The application of computational fluid dynamics to natural river channels: Eddy resolving versus mean flow approaches. *Geomorphology*, 179, 1-20. ISSN 0169-555X
- Khosronejad, A., C. Rennie, S. Neyshabouri, and R. D. Townsend (2007), 3D numerical modeling of flow and sediment transport in laboratory channel bends, *J. Hydraul. Eng.*, 133(10), 1123-1134.
- Khosronejad, A., Kozarek, J. L., Palmsten, M. L., and Sotiropoulos, F. (2015). Numerical simulation of large dunes in meandering streams and rivers with in-stream rock structures. *Advances in Water Resources*, 81, 45-61. <https://doi.org/10.1016/j.advwatres.2014.09.007>.
- Kinoshita, R. (1961) An investigation of channel deformation of the Ishikari River. *Tech. Rep., Natural Resources Division, Ministry of Science and Technology of Japan*, Tokio, 36 , pp. 1-174
- Kinoshita, R. and Miwa, H. 1974 River channel formation which prevents downstream translation of transverse bars. *Shinsabo* 94, 12-17 (in Japanese).
- Knighton, A. D. (1981). Channel Form and Flow Characteristics of Supraglacial Streams, Austre Okstindbreen, Norway, *Arctic and Alpine Research*, 13(3), 295-306.
- Konsoer, K. M. (2014) Influence of riparian vegetation on near bank flow structure and rates of erosion on a large meandering river. Dissertation submitted in partial fulfillment of the requirements for the degree of Doctor of Philosophy in Geography in the Graduate College of the University of Illinois at Urbana-Champaign.
- Konsoer, K. M., Rhoads, B. L., Best, J. L., Langendoen, E. J., Abad, J. D., Parsons, D., and García, M. H. (2016). Three-dimensional flow structure and bed morphology in large elongate meander loops with different outer bank roughness characteristics. *Water Resources Research*, 52, 9621-9641. <https://doi.org/10.1111/j.1752-1688.1969.tb04897.x>
- Lagasse, P.F., Spitz, W.J., Zevenbergen, L.W., and Zachmann, D.W. (2004) Handbook for Predicting Stream Meander Migration. NCHRP Report 533, TRB, National Research Council: Washington, DC.
- Langbein, W. B. and L. B. Leopold (1966), River Meanders: Theory of Minimum Variance, *Physiographic and Hydraulic Studies of Rivers. Geological Survey Professional Paper 422-H*
- Lanzoni, S. (2022). Morphodynamic Modeling of Alluvial Rivers and Floodplains. In *Treatise on Geomorphology* (2nd ed., pp. 83-104). Elsevier Inc. <https://doi.org/10.1016/B978-0-12-818234-5.00154-1>
- Lanzoni, S. and Seminara, G., (2006). On the nature of meander instability. *J. Geophys. Res.* 111, F04006. <http://dx.doi.org/10.1029/2005JF000416>.
- Lauder, E. and Spalding, B. (1974) The numerical computation of turbulent flow. *Comp. Meth. Appl. Mech. & Engng* 3, 269-289.
- Leeder, M. R., and P. H. Bridges (1975), Flow separation in meander bends, *Nature*, 253(5490), 338-339, doi:10.1038/253338a0.
- Leopold, L. B. and Wolman, M. G. (1957) River channel patterns, braided, meandering and straight. *US Geol. Survey, Profes. Paper 282-B*, pp. 45-62. Reproduced in *Rivers Morphology* (ed. S. A. Schumm), *Benchmark papers in Geology*, pp. 283-300, Hutchinson, Ross and Dowden 1972.
- Leopold, L. B., and M. G. Wolman (1960), River Meanders, *Geol. Soc. Am. Bull.*, 71(6), 769-793.
- Leopold, L. B., R. A. Bagnold, M. G. Wolman, and L. M. Brush, (1960) Flow resistance in sinuous and irregular channels, *U.S. Geol. Surv. Prof. Pap.*, 282D, 111-134.
- Leopold, L. B., J. P. Miller, and G. M. Wolman (1964), *Fluvial processes in geomorphology*, Freeman, San Francisco, p. 522.
- Leschziner, A. and Rodi, W. (1979) Calculation of strongly curved open channel flow. *J. Hydraul.Div. ASCE 105 (HY10)*, 1297-1314.

- Li, C., Czapiga, M. J., Eke, E. C., Viparelli, E. and Parker, G. (2014). River bankfull geometry: shear velocity is viscosity-dependent but grain size-independent. *J. Hydraul Res.*, doi: 10.1080/00221686.2014.939113.
- Lopez Dubon, S., and Lanzoni, S. (2019). Meandering Evolution and Width Variations : A Physics-Statistics-Based Modeling Approach. *Water Resources Research*, 55, 1–19. <https://doi.org/10.1029/2018WR023639>.
- Lorenz, E.N. (1972). Predictability: does the flap of a butterfly's wings in Brazil set off a tornado in Texas? *139th Annual Meeting of the American Association for the Advancement of Science (29 Dec 1972)*, in *Essence of Chaos (1995), Appendix 1, 181*
- Luchi, R. (2009) Effect of curvature and width variations on the morphodynamics of meandering rivers. PhD thesis submitted in partial fulfillment of the requirements for the degree of Doctor of Philosophy in Environmental Engineering, University of Trento (Italy)
- Luchi, R., J. M. Hooke, G. Zolezzi, and W. Bertoldi (2010a), Width variations and mid-channel bar inception in meanders: River Bollin (UK), *Geomorphology*, 119(1-2), 1-8, doi:10.1016/j.geomorph.2010.01.010.
- Luchi, R., G. Zolezzi, and M. Tubino (2010b). Modelling midchannel bars in meandering channels, *Earth Surf. Processes Landforms*, 35(8), 902-917, doi:10.1002/esp.1947.
- Luchi, R., M. Bolla Pittaluga, and G. Seminara (2012), Spatial width oscillations in meandering rivers at equilibrium, *Water Resour. Res.*, 48, W05551, doi:10.1029/2011WR011117.
- Mandelbrot, B. (1967). How Long Is the Coast of Britain? *Science*. 156 (3775): 636-638
- Mandelbrot, B. B. (1982) *The Fractal Geometry of Nature*. W. H. Freeman and Company, New York
- Marani, M., S. Lanzoni, D. Zandolin, G. Seminara, and A. Rinaldo, (2002). Tidal meanders, *Water Resour. Res.*, 38(11), 1225, doi:10.1029/2001WR000404.
- Markham, A. J., and C. R. Thorne (1992), Geomorphology of gravel bed river bends, in *Dynamics of Gravel Bed Rivers*, edited by P. Billi et al., pp. 433-456, Wiley, Chichester, U. K.
- Matsubara, Y., A.D. Howard, D.M. Burr, R.M.E. Williams, W.E. Dietrich, J.M. Moore (2014). River meandering on Earth and Mars: A comparative study of Aeolis Dorsa meanders, Mars and possible terrestrial analogs of the Usuktuk River, AK, and the Quinn River, NV., *Geomorphology*, <http://dx.doi.org/10.1016/j.geomorph.2014.08.031>
- Mehta, A. J. and Partheniades, E. (1975). An investigation of the depositional properties of flocculated fine sediments, *Journal of Hydraulic Research*, 134, 22–1686.
- Menter, F. R. (1994), Two-equation eddy-viscosity turbulence models for engineering applications, *AIAA J.*, 32(8), 1598-1605.
- Meyer-Peter, E. and Müller, R. (1948) Formulas for bedload transport, *2nd IAHR Congress, Int Assoc. for Hydraul. Res., Stockholm*.
- Mishra J. (2017) Erosion in Bedrock and Alluvial Meanders through 2 D Numerical Models, Laboratory Experiments and Field Observations. Thesis submitted in partial fulfillment of the requirements for the degree of Doctor of Philosophy in Engineering, Hokkaido University
- Mishra, J., T. Inoue, Y. Shimizu, T. Sumner and J. M. Nelson (2018) Consequences of Abrading Bed Load on Vertical and Lateral Bedrock Erosion in a Curved Experimental Channel, *Journal of Geophysical Research: Earth Surface*, 123, 3147-3161, doi:10.1029/2017JF004387
- Mockmore, C. A. (1943), Flow around bends in stable channels, *Trans. Am. Soc. Civ. Eng.*, 109, 593-628.
- Monegaglia, F. (2017). Meandering rivers morphodynamics - integrating nonlinear modeling and remote sensing, PhD Dissertation in fulfillment of the Erasmus Mundus Joint Doctorate School in Science for Management of Rivers and their Tidal System.
- Monegaglia, F. and Tubino, M. (2019). The hydraulic geometry of evolving meandering rivers. *Journal of Geophysical Research: Earth Surface*, 124, 2723-2748. <https://doi.org/10.1029/2019JF005309>

- Monegaglia, F., Zolezzi, G., Güneralp, I., Henshaw, A. J., and Tubino, M. (2018). Automated extraction of meandering river morphodynamics from multitemporal remotely sensed data. *Environmental Modelling and Software*, 105, 171-186. <https://doi.org/10.1016/j.envsoft.2018.03.028>
- Montgomery, K. (1996). Sinuosity and fractal dimension of meandering rivers. *Area* 28, 491-500.
- Montgomery, D. R. (2004). Observations on the role of lithology in strath terrace formation and bedrock channel width, *Am. J. Sci.*, 304(5), 454-476.
- Moore, R. C. (1926a) Origin of inclosed meanders on streams of the Colorado Plateau *Jour. Geology*, 34, 29-57.
- Moore, R. C. (1926b) Significance of inclosed meanders in the physiographic history of the Colorado Plateau country *Jour. Geology*, 34, 97-130.
- Mosselman, E. (1998) Morphological modelling of rivers with erodible banks, *Hydrol. Process.* 12, 1357-1370
- Nabi, M., H. J. de Vriend, E. Mosselman, C. J. Sloff, and Y. Shimizu (2012), Detailed simulation of morphodynamics: 1. Hydrodynamic model, *Water Resour. Res.*, 48, W12523, doi: 10.1029/2012WR011911.
- Nabi, M., H. J. de Vriend, E. Mosselman, C. J. Sloff, and Y. Shimizu (2013a), Detailed simulation of morphodynamics: 2. Sediment pick-up, transport and deposition, *Water Resour. Res.*, doi:10.1002/wrcr.20303.
- Nabi, M., H. J. de Vriend, E. Mosselman, C. J. Sloff, and Y. Shimizu (2013b) Detailed simulation of morphodynamics: 3. Ripples and dunes *Water Resour. Res.*, 49, 5930-5943, doi: 10.1002/wrcr.20457.
- Nanson, G. C. and Hickin, E. J. (1983). Channel migration and incision on the Beatton River, *J. Hydraul. Div. ASCE* 109(3), 327-337.
- Nelson, P. A., M. Bolla Pittaluga, and G. Seminara (2014), Finite amplitude bars in mixed bedrock-alluvial channels, *J. Geophys. Res. Earth Surface*, 119, 566-587, doi:10.1002/2013JF002957.
- Niño, Y. (1992) Sediment bars in straight and meandering channels: experiments on the resonance phenomenon. Thesis submitted in partial fulfillment of the requirements of the degree of Master of Science. Graduate School of Civil Engineering. University of Illinois at Urbana-Champaign.
- Nikora, V. (1991). Fractal structures of river planforms. *Water Resources Research* 6, 1327-1333.
- Nittrouer, J. A., D. Mohrig, M. A. Allison and A-P. B. Peyret (2011) *Sedimentology* 58, 1914-1934, doi:10.1111/j.1365-3091.2011.01245.x
- Ottevanger, W., Blanckaert, K., J. Uijttewaal, W. S., and De Vriend, H. J. (2013). Meander dynamics: A reduced-order nonlinear model without curvature restrictions for flow and bed morphology. *Journal of Geophysical Research: Earth Surface*, 118(2), 1118–1131. <https://doi.org/10.1002/jgrf.20080>
- Ovidio, *Metamorphoses*, Vol. 8, line 162.
- Paola, C., (2001) Modelling stream braiding over a range of scales, in *Mosley, M.P., ed., Gravel-bed Rivers V: Christchurch, New Zealand, Caxton Press, p. 11-46.*
- Papangelakis, E., M. Welber, P. Ashmore and B. MacVicar (2020) Controls of alluvial cover formation, morphology and bedload transport in a sinuous channel with a non-alluvial boundary, *Earth Surf. Process. Landforms*, doi:10.1002/esp.5032.
- Parker, G. (1975) Meandering of supraglacial melt streams *Water Resour. Res.*, 11(4), 551– 552.
- Parker, G. (1982) Stability of the channel of the Minnesota River Near State Bridge n. 93, Minnesota. *Project Report n. 205, St. Anthony Falls Hydraulic Laboratory n. 33*
- Parker, G., and E. D. Andrews, (1985) Sorting of bed load sediment by flow in meander bends, *Water Resources Reserach*, 21(9), 1361-1373.
- Parker, G. and Andrews, E. D. (1986) On time development of meander bends. *J. Fluid Mech.* 162, 139-156.

- Parker, G. and Johannesson, H. (1989) Observations on several recent theories of resonance and overdeepening in meandering channels. In *River Meandering* (ed. S. Ikeda and G. Parker) *Water Res. Monograph 12*, pp. 379-415. AGU.
- Parker, G., Diplas, P. and Akiyama, J. (1983) Meander bends of high amplitude. *J. Hydraul. Engng. ASCE 109*, 1323-1337.
- Parker, G., P. R. Wilcock, C. Paola, W. E. Dietrich, and J. Pitlick (2007), Physical basis for quasi-universal relations describing bankfull hydraulic geometry of single-thread gravel bed rivers, *J. Geophys. Res.*, 112, F04005, doi:10.1029/2006JF000549.
- Parker, G., Shimizu, Y., Wilkerson, G. V., Eke, E. C., Abad, J. D., Lauer, J. W., Paola, C., Dietrich, W. E. and Voller, V. R. (2011). A new framework for modeling the migration of meandering rivers. *Earth Surf. Process. Landf.* 36, 70-86.
- Peakall J., Ashworth P. J., Best J. L. (2007) Meander-bend evolution, alluvial architecture, and the role of cohesion in sinuous river channels: A flume study. *J. Sed. Res.* 77:197-212.
- Perucca, E., Camporeale, C. and Ridolfi, L. (2005) Nonlinear analysis of the geometry of meandering rivers. *Geophysical Research Letters* 32:L03402, doi:10.1029/2004GL021966.
- Pizzuto, J. E., and T. S. Meckelnburg (1989), Evaluation of a Linear Bank Erosion Equation, *Water Resources Research*, 25(5), 1005-1013.
- Prandtl, L. 1942 *Führer durch die Strömungslehre*. Vieweg, Braunschweig.
- Rattray, M. and Mitsuda, E. (1974) Theoretical Analysis of Conditions in a Salt Wedge, *Estuarine and Coastal Marine Science* 2, 375-394
- Repetto, R., and M. Tubino, (1999) Transition from migrating alternate bars to steady central bars in channels with variable width, *Proc. of first IAHR-RCEM Symposium, Int. Assoc. for Hydraul. Res., Genoa, Italy, 6-10 Sept.*
- Repetto, R., M. Tubino, and C. Paola (2002), Planimetric instability of channels with variable width, *J. Fluid Mech.*, 457, 79-109.
- Rodriguez-Iturbe, I. and Rinaldo, A., (2010). *Fractal River Basins. Chance and Selforganization*, Cambridge University Press, 564 pp.
- Rosenstein, M. T., Collins, J. J. and De Luca, C. J. (1993). A practical method for calculating largest Lyapunov exponents from small data sets. *Physica D* 65: 117-134.
- Rowland, J. C., Shelef, E., Pope, P. A., Muss, J., Gangodagamage, C., Brumby, S. P., and Wilson, C. J. (2016). A morphology independent methodology for quantifying planview river change and characteristics from remotely sensed imagery. *Remote Sensing of Environment*, 184, 212-228. <https://doi.org/10.1016/j.rse.2016.07.005>
- Rozovskij, I. L., (1957) Flow of water in bends of open channels, *Acad. Sci. Ukrainian USSR*.
- Schumm S. A. and Khan H. R. (1972) Experimental study of channel patterns. *Geol. Soc. Amer. Bull.* 83:1755-1770.
- Schuurman F. (2015). Bar and channel evolution in meandering and braiding rivers using physics-based modeling, *Utrecht Studies in Earth Sciences* 079.
- Schuurman F., Shimizu Y., Iwasaki T., Kleinhans M. G., (2016) Dynamic meandering in response to upstream perturbations and floodplain formation, *Geomorphology*, 253, 94-109
- Schwenk J. (2016) Meandering rivers: interpreting dynamics from planform geometry and the secret lives of migrating meanders A dissertation submitted to the faculty of the graduate school of the University of Minnesota in partial fulfillment of the requirements for the degree of Doctor of Philosophy
- Schwenk, J., and Foufoula-Georgiou, E. (2017). Are process nonlinearities encoded in meandering river planform morphology? *Journal of Geophysical Research*, (1), 1534-1552 <https://doi.org/10.1002/2016JF003929>.
- Schwenk, J., Lanzoni, S., and Foufoula-Georgiou, E. (2015). The life of a meander bend: Connecting shape and dynamics via analysis of a numerical model. *Journal of Geophysical Research F: Earth Surface*, 120(4), 690-710 <https://doi.org/10.1002/2014JF003252>.

- Schwenk, J., Khandelwal, A., Fratkin, M., Kumar, V., and Foufoula-Georgiou, E. (2017). High spatiotemporal resolution of river planform dynamics from landsat: The rivMAP toolbox and results from the Ucayali river. *Earth and Space Science*, 4(2), 46-75. <https://doi.org/10.1002/2016EA000196>
- Seminara, G. (1995) in *Nonlinear Dynamics and Pattern Formation in the Natural Environment*, edited by A. Doelman and A. van Harten, Pitman Research Notes in Mathematics Series Vol. 335 Longman, New York, pp. 269-294.
- Seminara G. 2006. Meanders. *J. Fluid Mech.* 554, 271-97
- Seminara G. and M. Bolla Pittaluga (2012) Reductionist versus holistic approaches to the study of river meandering: An ideal dialogue, *Geomorphology (163-164)* 110-117
- Seminara, G. and Solari, L. (1998). Finite amplitude bed deformations in totally and partially transporting wide channel bends. *Water Resour. Res.*, 34 (6), 1585-1598.
- Seminara G. and Tubino M. (1989). Alternate bars and meandering: free, forced and mixed interactions. In *River Meandering (ed. S. Ikeda & G. Parker)*. AGU Water Resour. Monograph, 12, pp. 267–320.
- Seminara G. and Tubino M. (1992) Weakly nonlinear theory of regular meanders. *J. Fluid Mech.* 244:257-88
- Seminara, G., Tubino, M. and Zardi, D. 1994 Evoluzione planimetrica dei corsi d'acqua meandri-formi dall'incipiente formazione al cut-off. *XXIV Convegno di Idraulica e Costr. Idrauliche, Napoli, 20-22 settembre, T4-207* (In Italian).
- Seminara, G., L. Solari and M. Tubino (1997). Finite amplitude scour and grain sorting in wide channel bends, *Proceedings of Theme B, 27th IAHR Congress, S. Francisco*.
- Seminara, G., Zolezzi, G., Tubino, M. and Zardi, D. (2001a) Downstream and upstream influence in river meandering. Part 2. Planimetric development. *J. Fluid Mech.*, 438, 213-230.
- Seminara, G., L. Solari, and G. Parker, (2001b) Bed-load transport on arbitrarily sloping beds at low Shields stress and validity of Bagnold's hypothesis. *2nd IAHR Symposium on River, Coastal and Estuarine Morphodynamics, RCEM 2001*, 10-14 September 2001, Obihiro Japan.
- Seminara G. and S. Lanzoni and N. Tambroni (2023) Theoretical Morphodynamics: Straight Channels, *Firenze University Press*.
- Shepherd, R.G. and S.A. Schumm (1974), Experimental study of river incision, *Geological Society of America Bulletin*, 85, 257-268.
- Shimizu, Y., H. Yamaguchi, and T. Itakura (1990), Three-dimensional computation of flow and bed deformation, *J. Hydraul. Eng., Am. Soc. Civ. Eng.*, 116(9), 1090-1108.
- Siebert W. (1982), Stroemungscharakteristiken in einem Kanal mit 180-Kruemmungen, Mitteilungen 168. Theodor-Rehbock Flussbaulaboratorium, Karlsruhe.
- Sklar, L. S., and W. E. Dietrich (2004), A mechanistic model for river incision into bedrock by saltating bed load, *Water Resour. Res.*, 40, W06301, doi:10.1029/2003WR002496.
- Smith C. (1998) Modeling high sinuosity meanders in a small flume. *Geomorphology* 25:19-30.
- Smith, J. D., and McLean S. R. (1984). A Model for Flow in Meandering Streams, *Water Resour. Res.*, 20(9), 1301– 1315, doi:10.1029/WR020i009p01301.
- Snow, R.S. (1989). Fractal sinuosity of stream channels. *Pure Appl. Geophys.* 131, 99-109.
- Solari, L., Seminara, G. (2006). On width variations in meandering rivers, In: *River, Coastal and Estuarine Morphodynamics: RCEM 2005 - Proceedings of the 4th IAHR Symposium on River, Coastal and Estuarine Morphodynamics*, Urbana, IL, 4-7 October, 2, pp. 745-751.
- Sotiropoulos, F. (2015). Hydraulics in the era of exponentially growing computing power. *Journal of Hydraulic Research*, 53(5), 547-560. <https://doi.org/10.1080/00221686.2015.1119210>
- Sotiropoulos, F. (2019) Hydraulic Engineering in the Era of Big Data and Extreme Computing: Can Computers Simulate River Turbulence?, *J. Hydraul. Eng.*, 145(6): 02519002 [https://doi.org/10.1061/\(ASCE\)HY.1943-7900.0001594](https://doi.org/10.1061/(ASCE)HY.1943-7900.0001594)

- Spalart, P. R. (2000), Trends in turbulence treatments, *AIAA Paper 2000-2306, Fluids 2000, Denver*.
- Sprott, J. C. (2003). *Chaos and Time Series Analysis*. Oxford University Press: New York.
- Stock, J. D., D. R. Montgomery, B. D. Collins, W. E. Dietrich, and L. S. Sklar (2005), Field measurements of incision rates following bedrock exposure: Implications for process controls on the long profiles of valleys cut by rivers and debris flows, *Geol. Soc. Am. Bull.*, 117(1-2), 174-194, doi:10.1130/B25560.1.
- Stoesser, T., Ruether, N. and Olsen, N. R. B. (2010) Calculation of primary and secondary flow and boundary shear stresses in a meandering channel. *Advances in Water Resources* 33, 158-170.
- Stolum, H. H. (1996), River meandering as a self-organized process, *Science*, 271, 1710-1713.
- Strabo, (around 10), *The geography of Strabo. Literally translated, with notes, Book 12, Ch. 8, Sect. 15, H.G. Bohn Ltd., London, 1854-1857*, downloadable at: <https://archive.org/details/geograofstrablit02strauoft>.
- Strogatz, S. H. (1994) *Nonlinear Dynamics and Chaos. Addison-Wesley, Reading*.
- Struiksma, N., K. W. Olesen, C. Flokstra, and H. J. de Vriend, Bed deformation in a curved alluvial channel, *J. Hydraul. Res.*, 23(1), 57- 79.
- Sun, T., P. Meaking, T. Jossang, and K. Schwarz (1996), A simulation model for meandering rivers, *Water Resour. Res.*, 32(9), 2937-2954
- Sun, T., P. Meakin, and T. Jossang (2001a) A computer model for meandering rivers with multiple bed load sediment sizes: 1. Theory, *Water Resour. Res.*, 37(8), 2227-2241
- Sun, T., P. Meakin, and T. Jossang (2001b), A computer model for meandering rivers with multiple bed load sediment size: 2. Computer simulations, *Water Resour. Res.*, 37, 2243-2258.
- Tal M. and Paola C. (2007) Dynamic single-thread channels maintained by the interaction of flow and vegetation. *Geology* 35:347-350.
- Tarr W. A. (1924) Intrenched and Incised Meanders of Some Streams on the Northern Slope of the Ozark Plateau in Missouri, *The Journal of Geology*, 32 (7), 583-600 <https://doi.org/10.1086/623142>
- Thompson, J. M. T. and Stewart, H. B. (1986) *Nonlinear Dynamics and Chaos. Wiley & Sons*.
- Thorne, C. R. (1991). Bank erosion and meander migration of the Red and Mississippi Rivers, USA. In: *Hydrology for the water management of large river basins, Proceedings of IAHS Symposium Publ. 201, pages 301-313, Vienna, Austria*.
- Thorne, C. R., and R. D. Hey (1979), Direct measurements of secondary currents at a river inflexion point, *Nature*, 280, 226-228, doi:10.1038/280226a0.
- Thorne, C. R. and Tovey, K. (1981). Stability of composite river banks. *Earth Surface Processes and Landforms*, 6:469-484.
- Thorne, C. R., S. R. Abt, and S. T. Maynard (1995), Prediction of nearbank velocity and scour depth in meander bends for design of riprap revetments, in *River, Coastal and Shoreline Protection: Erosion Control Using Riprap and Armourstone*, edited by C. R. Thorne et al., pp. 115-133, John Wiley, Chichester, U. K.
- Titus Livius, *The History of Rome*, Book 38, Chapter 13 Evan T. Sage, Ph.D., Ed.
- Tubino, M. and Seminara, G. (1990) Free-forced interactions in developing meanders and suppression of free bars. *J. Fluid Mech.* 214, 131-159
- Turcotte, D. L. (1999) Self-organized criticality, *Rep. Prog. Phys.* 62 1377-1429.
- van Balen, W., W. S. J. Uijttewaal, and K. Blanckaert (2009), Large-eddy simulation of a mildly curved open-channel flow, *J. Fluid Mech.*, 630, 413-442, doi:10.1017/S0022112009007277.
- van Dijk, W. M., W. I. van de Lageweg, and M. G. Kleinans (2012), Experimental meandering river with chute cutoffs, *J. Geophys. Res.*, 117, F03023, doi:10.1029/2011JF002314.
- van Rijn, L.C. (1984a) Sediment transport, I, Bed load transport, *J. Hydraul. Eng. Am. Soc. Civ. Eng.*, 110(10): 1431-1456.

- Venditti, J. G., and M. Church (2014), Morphology and controls on the position of a gravel-sand transition: Fraser River, British Columbia, *J. Geophys. Res. Earth Surf.*, 119, 1959-1976, doi:10.1002/2014JF003147.
- Venditti, J. G., C. D. Rennie, J. Bomhof, R. W. Bradley, M. Little, and M. Church (2014), Flow in bedrock canyons, *Nature*, 513(7519), 534-537.
- Viero, D. P., Dubon, S. L., and Lanzoni, S. (2018). Chute cutoffs in meandering rivers: formative mechanisms and hydrodynamic forcing. *International Association of Sedimentologists*, 47(11), 201-229.
- Whiting, P. J. and W. E. Dietrich (1993) Experimental studies of bed topography and flow patterns in large-amplitude meanders: 1. Observations *Water Resources Research*, 29(11), 3605-3614
- Wilcox, D. C. (1994). Simulation of transition with a two-equation turbulence model. *AIAA J.*, 42(2), 247-255.
- Winslow, A. (1893). The Osage River and its meanders, *Science*, 22, 31-3.2.
- Winters, K. H. 1987 A bifurcation study of laminar flow in a curved tube of rectangular cross section. *J. Fluid Mech.* 180, 343-369.
- Wolman M. G. and Brush L. M. (1961) Factors controlling the size and shape of stream channels in coarse, noncohesive sands. *U. S. Geol. Surv. Prof. Paper 282-G:183-210.*
- Xenophon, Anabasis, Book 1, Ch. 2, Sect. 8, Harvard University Press, Cambridge, Massachusetts; William Heinemann, Ltd., London. 1980. OCLC 10290977. ISBN 0-674-99100-1.
- Yen, C. L., (1970) Bed topography effect on flow in a meander. *J. Hydr. Div., Amer. Soc. Civ. Eng.*, 96(HY1), 57-74.
- Zeng L., Balachandar S., Fischer P. and F. M. Najjar 2008. Interactions of a stationary finite-sized particle with wall turbulence. *J. Fluid Mech.* 594:271-305
- Zeng, J., S. G. Constantinescu, and L. Weber (2008a), A 3D non-hydrostatic model to predict flow and sediment transport in loose bed channel bends, *J. Hydraul. Res.*, 46(3), 356-372, doi:10.3826/jhr.2008.3328.
- Zeng, J., G. Constantinescu, K. Blanckaert, and L. Weber (2008b), Flow and bathymetry in sharp open-channel bends: Experiments and predictions, *Water Resour. Res.*, 44, W09401, doi:10.1029/2007WR006303.
- Zhao, K., Lanzoni, S., Gong, Z., and Coco, G. (2021). A numerical model of bank collapse and river meandering, *Geophysical Research Letters*, 48, e2021GL093516. <https://doi.org/10.1029/2021GL093516>.
- Zolezzi, G., and G. Seminara (2001), Downstream and upstream influence in river meandering. Part 1. General theory and application to overdeepening, *J. Fluid Mech.*, 438, 183-211.
- Zolezzi G, Guala M, Seminara G, Termini D. 2005. Experimental observations of upstream overdeepening. *J. Fluid Mech.* 531:191-219
- Zolezzi, G., R. Luchi, and M. Tubino (2009), Morphodynamic regime of gravel bed, single-thread meandering rivers, *J. Geophys. Res.*, 114, F01005, doi:10.1029/2007JF000968.
- Zolezzi, G., Luchi, R. and Tubino, M. (2012). Modeling morphodynamic processes in meandering rivers with spatial width variations. *Rev. Geophys.* 50, RG4005, doi:10.1029/2012RG000392.

10. Notations

- f

f any scalar, vectorial or tensorial quantity

\bar{f} dimensionless form of f

$\langle f \rangle$ large scale turbulent flow (macroscopic) average of f

f' fluctuations of f

f^+

\bar{f} overbar is used for the instantaneous and local value of the volume (spatial) average of f (microscopic average) and to denote the conjugate of a complex number

∇_h two dimensional gradient operator ($\partial/\partial x, \partial/\partial y$)

$|\mathbf{f}|$ modulus of the vector \mathbf{f}

- a A bar or, in general, perturbation amplitude

- b

B half width of the free surface

- c

c wavespeed of the perturbations

C depth averaged value of the Reynolds averaged local sediment concentration

C_f friction coefficient

C_{fu} friction coefficient associated with the uniform flow

\bar{C}_f cross sectionally averaged friction coefficient

\bar{C}_{fw} free surface averaged wind friction coefficient

C dimensionless curvature

- d

d sediment particle diameter

d_g geometric mean grain size of a sediment mixture

d_s relative roughness d/D_u

d_{50} average grain size

d_{90} sediment size such that 90% percent of the sample is finer

$D(x, y, t)$ local instantaneous flow depth

D_u uniform flow depth

D_b average flow depth in the bend

\mathfrak{D}_j j -th-component of the *turbulent diffusivity* vector

- e

E erosion coefficient

- f

\mathcal{F}_0 shape function for the logarithmic vertical velocity profile

F_r Froude number

F_{ru} uniform flow Froude number

- g

\mathbf{g} gravity vector

- h

h_s, h_n, h_z metric coefficients

$H(x, y, t)$ local, instantaneous free surface elevation

- k

k von Karman constant

k_m cartesian meander wavenumber

- l

L scale of spatial variations of the flow field in the longitudinal direction

L wavelegth in Chapter I.1.

L_m and L_s ntrinsic meander wavelength

L_x the cartesian meander wavelength

L_0 intrinsic length of the oxbow lakes

L_r the intrinsic length of the curved channel reach

- n

\mathcal{N} shape function for eddy viscosity

$\hat{\mathbf{n}}$ unit vector normal to the element, oriented in the outward direction

- p

$p(\mathbf{x}, t)$ pressure

P average pressure

- q

q_s local total sediment flux per unit width

$q_s^{b,s}$ local (b bedload; s suspended) sediment flux per unit width

Q local fluid discharge per unit width

Q (modulus of the) local fluid discharge per unit width

\mathcal{Q} flow discharge

Q_s local depth integrated total sediment flux per unit width

$Q_s^{b,s}$ local depth integrated (b bedload; s suspended) sediment flux per unit width

Q_s modulus of the depth integrated total sediment flux per unit width

$Q_s^{b,s}$ modulus of the depth integrated (b bedload; s suspended) sediment flux per unit width

\tilde{Q}_s^b dimensionless modulus of the depth integrated bedload sediment flux per unit width (it

coincides with Φ^b under plane bed conditions)

$Q_s[L^3T^{-1}]$ total longitudinal sediment flux transported in the cross section $Q_s^i[L^3T^{-1}]$ ($i=b$ bedload; $i=s$ suspended) sediment flux transported in the cross section

- r

R_p particle Reynolds number

R_u hydraulic radius of the reference flow

R_0 radius of curvature of the channel axis

- s

s relative particle density

s also longitudinal curvilinear coordinate

S channel slope

- t

t time

T dimensionless slow time variable

$\mathbf{T}(\mathbf{x}, t)$ fluid stress tensor

\mathbf{T}^t Reynolds stress tensor

- u

u_τ friction velocity

$u_{\tau u}$ friction velocity of the uniform flow

$\mathbf{u} = (u, v, w)$ Reynolds averaged fluid velocity

U_u depth averaged uniform flow velocity

U depth averaged longitudinal velocity

U_0 scale of fluid velocity

\mathcal{U} cross sectionally averaged flow speed

- v

V lateral component of the depth averaged velocity

V_0 scale of the lateral component of velocity

- w

w_s asymptotic steady value of the sediment settling speed

W_0 scale of the vertical velocity component

W_f wake function

- x

\mathbf{x} position

$x_j, j = 1, 2, 3$ Cartesian coordinate system

- z

z axis orthogonal to the channel axis

$\hat{\mathbf{z}}$ unit vector

ζ normalized vertical coordinate

Z Rouse parameter

z_0 elevation where no-slip is imposed at the wall

- α

α_s stream-wise inclination angle of the bottom

α_n transverse inclination angle of the bottom

- β

β aspect ratio of the channel cross-section defined as half width over depth

- δ

δ phase lag between bank erosion and curvature

- ζ

ζ dimensionless form of the z coordinate

ζ also average bank erosion rate in Section 1

- η

η elevation of the bed interface

η_a elevation of the channel axis

$\bar{\eta}$ cross sectionally averaged bottom elevation

- θ

θ angle between straight segments tangent to the channel axis at two consecutive inflection points

$\theta(s, t)$ angle that the local tangent to the channel center line forms with the direction of a Cartesian axis x

- λ

λ_m intrinsic meander wavenumber

- ν

ν viscosity

ν_T eddy viscosity

- ϕ

ϕ phase lag

Φ^b dimensionless depth integrated bedload sediment flux per unit width under plane bed conditions

Φ^s dimensionless depth integrated suspended sediment flux per unit width

- χ

χ flow conductance

χ also angle that the bottom stress forms with the longitudinal axis

χ_u *flow conductance* of uniform flows

- ψ
 ψ angle that the velocity of the bedload particles forms with the bottom shear stress vector $\boldsymbol{\tau}$

- ϱ
 ϱ water density
 ϱ_s density of sediment particles

- σ
 σ standard deviation of the grain size distribution
 σ_s standard deviation of the grain size distribution of the surface layer

- τ
 τ flow shear stress
 τ_u bottom value of the uniform shear stress
 τ_c threshold shear stress for incipient sediment motion
 τ_s, τ_n dimensionless longitudinal and lateral components of the bottom stress
 $\bar{\tau}_u$ uniform shear stress averaged over the wet boundary

 τ_* local value of the dimensionless Shields stress
 $\bar{\tau}_*$ laterally averaged value of the dimensionless Shields stress
 τ_{*c} critical value of the Shields stress for incipient motion
 τ_{*c0} critical value of the Shields stress for incipient motion under conditions of nearly vanishing bed slope
 τ_{*g} Shields stress associated with the geometric mean size of the sediments in the surface layer
 τ_{*u} dimensionless Shields stress of the uniform flow

- ω
 ω vorticity
 ω complex perturbations growth rate
 Ω mean vorticity, averaged over turbulence

STUDIES IN SCIENCES AND TECHNOLOGY

TITOLI PUBBLICATI

1. Giovanni Seminara, Stefano Lanzoni, Nicoletta Tambroni, *Theoretical Morphodynamics: Straight Channels*, 2023
2. Giovanni Seminara, Stefano Lanzoni, Nicoletta Tambroni, *Theoretical Morphodynamics: River Meandering*, 2023

Studies in Sciences and Technology

2

This monograph discusses the mechanics of Meandering Rivers with the help of the mathematical and modeling tools built up in the previous monograph of the same Authors (monograph 1 of the present series). After introducing the reader to the ubiquitous character of meandering streams, we discuss the hydrodynamics of curved channels with fixed beds and banks. Next, we extend the analysis to account for the mobile character of the bed and show that it gives rise to the alternate sequence of riffles and pools that characterize river meanders. Allowing for the erodible character of the river banks then allows to build up a rational theory of meander formation able to explain most of the features observed in nature: meander growth, migration, skewing, multiple loops, cutoffs and meander belts.

GIOVANNI SEMINARA, Master in Civil Engineering (University of Genoa), PhD in Applied Math (Imperial College, London), Professor Emeritus at the University of Genoa and Socio Nazionale of Accademia Nazionale dei Lincei.

STEFANO LANZONI, Master in Hydraulic Engineering (University of Padua), PhD in Hydrodynamics (joint program, Universities of Genoa, Florence, Padua and Trent), Professor of Fluid Mechanics at the University of Padua.

NICOLETTA TAMBRONI, Master in Civil Engineering (University of Genoa), PhD in Fluid dynamics and Environmental Processes in Engineering (University of Genoa), Associate Professor of Fluid Mechanics at the University of Genoa.

ISBN 979-12-215-0302-9 (Print)
ISBN 979-12-215-0303-6 (PDF)
ISBN 979-12-215-0304-3 (XML)
DOI 10.36253/979-12-215-0303-6

www.fupress.com